

University of Southampton Research Repository ePrints Soton

Copyright © and Moral Rights for this thesis are retained by the author and/or other copyright owners. A copy can be downloaded for personal non-commercial research or study, without prior permission or charge. This thesis cannot be reproduced or quoted extensively from without first obtaining permission in writing from the copyright holder/s. The content must not be changed in any way or sold commercially in any format or medium without the formal permission of the copyright holders.

When referring to this work, full bibliographic details including the author, title, awarding institution and date of the thesis must be given e.g.

AUTHOR (year of submission) "Full thesis title", University of Southampton, name of the University School or Department, PhD Thesis, pagination

UNIVERSITY OF SOUTHAMPTON

FACULTY OF NATURAL AND ENVIRONMENTAL SCIENCES

School of Ocean and Earth Science

National Oceanography Centre, Southampton

**LARGE SUBMARINE LANDSLIDE AND TURBIDITY CURRENT FREQUENCY:
IMPLICATIONS FOR HAZARDS AND CLIMATE CHANGE**

by

Michael Andrew Clare

MGeol CGeol EurGeol FGS

Thesis for the degree of Doctor of Philosophy in Ocean and Earth Science

September 2015

ABSTRACT

UNIVERSITY OF SOUTHAMPTON
FACULTY OF NATURAL AND ENVIRONMENTAL SCIENCES
SCHOOL OF OCEAN AND EARTH SCIENCE

Doctor of Philosophy

LARGE SUBMARINE LANDSLIDE AND TURBIDITY CURRENT FREQUENCY: IMPLICATIONS FOR HAZARDS AND CLIMATE CHANGE

By **Michael Andrew Clare**

Submarine landslides are one of the most important processes for moving sediment across our planet. Landslides that are fast enough to disintegrate can generate potentially hazardous tsunamis, and produce long run-out turbidity currents that break strategically important cable networks. It is therefore important to understand their frequency and triggers. This thesis aims to do so using extensive datasets ($N > 100$) suitable for statistical analysis. The influence of temporally non-random variables on landslide and turbidity current frequency is assessed statistically. In light of predicted future global and sea level rises this is a timely study.

Analysis of large volume turbidites ($> 0.1 \text{ km}^3$) reveals two distinct frequency distribution forms for submarine landslide recurrence. A Poisson (time-independent) form is observed in three basins which may indicate similar controls on landslide frequency and triggers occur in disparate areas. A log-normal (time-dependent) distribution is seen in the Iberia Abyssal Plain over much longer timescales (20 Myr). Physiographic and palaeoclimatic effects are thought to explain the two different distribution forms.

The influence of sea level is either shown to be statistically insignificant (Poisson form) or has a significantly delayed ($\sim 1.2 \text{ Myr}$) influence (log-normal form) on landslide and turbidite recurrence. Two sequences that cross the Initial Eocene Thermal Maximum (IETM) hyperthermal, show a reduction in turbidity current and landslide activity, rather than the increase hypothesised by many studies. Therefore, predicted future sea level rise and global warming may not necessarily result in significantly increased submarine landslide or turbidity current frequency on human timescales.

Finally, a unique direct monitoring dataset from the Squamish Prodelta, British Columbia provides new insights into the links between rivers and offshore deltas on very short ($< \text{months}$) timescales. It is shown that elevated river discharge is the primary control for the ‘switch on’ of turbidity current activity, but the trigger for flows is related to a combination of tide and river-controlled elevated shear stresses on the submarine delta top. Extreme flood peaks do not correspond to hyperpycnal flows, but instead cause rapid accumulation of sediment leading to delta lip failures.

Contents

| | |
|---|------------|
| ABSTRACT | iii |
| Contents | v |
| List of tables | xi |
| List of figures | xiii |
| List of accompanying materials | xviii |
| DECLARATION OF AUTHORSHIP | xix |
| Acknowledgements | xxv |
| Definitions and Abbreviations | xxvii |
| Chapter 1: Thesis introduction | 1-1 |
| 1.1 The largest mass flows on earth..... | 1-2 |
| 1.2 Why landslide and turbidity current frequency is important..... | 1-3 |
| 1.2.1 Overarching thesis aim | 1-4 |
| 1.3 Thesis outline and key science questions posed | 1-5 |
| 1.4 Research drivers: Understanding seafloor hazards and sediment transport | 1-7 |
| 1.4.1 Triggering of large submarine landslides | 1-7 |
| Why focus on sea level as a possible control on landslide frequency? | 1-8 |
| 1.4.2 Potentially fatal landslide-triggered tsunamis | 1-9 |
| 1.4.3 Hazards for strategically important subsea cable networks..... | 1-10 |
| 1.4.4 Implications for expensive oil and gas infrastructure..... | 1-13 |
| 1.4.5 Connecting the two major processes for sediment transport on earth - river systems and turbidity currents | 1-16 |
| 1.5 How can we acquire records of landslide-turbidity current recurrence?..... | 1-19 |
| 1.5.1 Depositional records of submarine landslides and turbidity currents..... | 1-20 |
| 1.5.1.1 <i>Limitation 1: Incomplete sedimentary records</i> | 1-25 |
| 1.5.1.2 <i>Limitation 2: Limited number of events for analysis</i> | 1-26 |
| 1.5.1.3 <i>Limitation 3: Issues with dating individual events</i> | 1-29 |
| 1.5.2 Indirect observations | 1-30 |
| 1.5.3 Direct Observations | 1-33 |
| 1.6 Key questions addressed by this thesis | 1-37 |
| <u>Question 1:</u> How can we measure the recurrence of potentially damaging landslides and turbidity currents? | 1-37 |
| <u>Question 2:</u> How can we quantitatively analyse recurrence of potentially damaging landslides and turbidity currents? | 1-37 |
| <u>Question 3:</u> Do large submarine landslides show time-dependent behaviour? | 1-38 |
| <u>Question 4:</u> Is sea level a dominant control on large submarine landslide recurrence? | 1-39 |
| <u>Question 5:</u> Does millennial-scale dramatic global warming result in an increased frequency of submarine landslides and turbidity currents? | 1-39 |

| | |
|---|------|
| <u>Question 6:</u> Can large submarine landslides catalyse global warming? Did large submarine landslides trigger global warming at the Initial Eocene Thermal Maximum? | 1-40 |
| <u>Question 7:</u> How does long term (>10 Myr) global warming affect turbidity current frequency? . | 1-40 |
| <u>Question 8:</u> How are mass failures and flows triggered at offshore bedload-dominated river deltas? ... | 1-41 |

Chapter 2: Geological setting of study areas 2-1

| | |
|---|------|
| 2.1. Introduction | 2-2 |
| 2.2. Marnoso-arenacea Formation, Italian Apennines..... | 2-4 |
| 2.1.1 Tectonic setting..... | 2-4 |
| 2.1.2 Physiography and sediment input sources | 2-5 |
| 2.1.3 Interval analysed in this study..... | 2-6 |
| 2.3. Zumaia Series, North-East Spain | 2-7 |
| 2.1.4 Tectonic setting..... | 2-7 |
| 2.1.5 Physiography and sediment input sources | 2-8 |
| 2.1.6 Interval analysed in this study..... | 2-8 |
| 2.4. Iberia Abyssal Plain | 2-9 |
| 2.1.7 Tectonic setting..... | 2-9 |
| 2.1.8 Physiography and sediment input sources | 2-10 |
| 2.1.9 Interval analysed in this study..... | 2-11 |
| 2.5. Madeira Abyssal Plain | 2-11 |
| 2.1.10 Tectonic setting | 2-12 |
| 2.1.11 Physiography and sediment input sources..... | 2-12 |
| 2.1.12 Interval analysed in this study | 2-13 |
| 2.6. Balearic Abyssal Plain | 2-16 |
| 2.1.13 Tectonic setting | 2-16 |
| 2.1.14 Physiography and sediment input sources..... | 2-16 |
| 2.1.15 Interval analysed in this study | 2-18 |
| 2.7. Squamish Prodelta..... | 2-18 |
| 2.1.16 Tectonic setting | 2-19 |
| 2.1.17 Physiography and sediment input sources..... | 2-19 |
| 2.1.18 Interval analysed in this study | 2-19 |

Chapter 3: Methods for calculating landslide and turbidite recurrence intervals..... 3-1

| | |
|--|------|
| 3.1 Introduction | 3-2 |
| 3.1.1 Identifying long-term records of large landslides and flows from distal basin plains | 3-2 |
| 3.1.2 Rationale for selection of distal basin plain sites | 3-3 |
| 3.1.3 Visual sedimentary logging | 3-6 |
| 3.1.4 Geochemical logging | 3-10 |
| 3.1.5 Identification of hemipelagic deposits | 3-11 |
| 3.1.6 Erosion by turbidity currents | 3-13 |
| 3.1.7 Age control | 3-15 |
| 3.1.8 Short term fluctuations in hemipelagic mud accumulation rates | 3-22 |
| 3.1.9 Minimum resolvable time intervals for study areas | 3-22 |

| | | |
|-------------------|--|------------|
| 3.1.10 | Reconstructed sea level curves..... | 3-22 |
| 3.2 | Direct monitoring of flows at Squamish..... | 3-23 |
| 3.2.1 | Repeat Seafloor Surveys | 3-24 |
| 3.2.2 | ADCP monitoring | 3-26 |
| Chapter 4: | Methodologies for statistical analysis of landslide and turbidite recurrence intervals | |
| | | 4-1 |
| 4.1 | Introduction | 4-2 |
| 4.2 | Data..... | 4-3 |
| 4.2.1 | Data censoring..... | 4-4 |
| 4.3 | Statistical analysis of landslide recurrence | 4-4 |
| 4.3.1 | What is the characteristic frequency of landslide recurrence?..... | 4-5 |
| 4.3.2 | Are landslides clustered in time?..... | 4-8 |
| 4.3.3 | Do different time periods feature different characteristic recurrence? | 4-12 |
| 4.3.4 | Is sea level a dominant control on landslide recurrence? | 4-12 |
| 4.4 | Valid sample size determination..... | 4-17 |
| 4.5 | Conclusions | 4-18 |
| Chapter 5: | Frequency distribution of large submarine landslides and implications for sea level control | |
| | | 5-1 |
| 5.1 | Introduction | 5-2 |
| 5.2 | Aims | 5-4 |
| 5.3 | Methods | 5-4 |
| 5.3.1 | Erosion by turbidity currents..... | 5-4 |
| 5.3.2 | Short-term fluctuations in hemipelagic mud accumulation rates | 5-5 |
| 5.3.3 | Were these extensive basin plain turbidity currents triggered by large landslides? | 5-5 |
| 5.4 | Results | 5-6 |
| 5.4.1 | Common frequency distribution form of landslide recurrence intervals..... | 5-6 |
| 5.4.2 | Is this distribution time-independent (Poissonian)? | 5-6 |
| 5.4.3 | Effects of variable erosion beneath beds | 5-9 |
| 5.4.4 | Effects of short-term changes in hemipelagic accumulation rates..... | 5-9 |
| 5.4.5 | Results of tests that are independent of frequency distribution | 5-10 |
| 5.5 | Discussion..... | 5-11 |
| 5.5.1 | Geological significance of Poisson distribution | 5-11 |
| 5.5.2 | Landslide frequency and sea-level | 5-11 |
| 5.5.3 | Comparison to the frequency distribution of large magnitude earthquakes | 5-12 |
| 5.5.4 | Multiple local or sequential controls along a basin margin | 5-13 |
| 5.6 | Conclusions | 5-18 |
| Chapter 6. | Implications of millennial-scale dramatic climate change for landslide and turbidite recurrence | |
| | | 6-1 |
| 6.1 | Introduction | 6-2 |
| 6.1.1 | Landslide and turbidity current recurrence frequency and climate change | 6-3 |

| | | |
|-------------------|---|------------|
| 6.1.2 | Turbidites as a record of disintegrative landslides | 6-3 |
| 6.1.3 | Geohazards and global sediment flux | 6-4 |
| 6.1.4 | Previous work | 6-5 |
| 6.2 | Aims | 6-5 |
| 6.3 | Study areas | 6-6 |
| 6.3.1 | Regional tectonic setting..... | 6-7 |
| 6.3.2 | Palaeoceanographic setting..... | 6-8 |
| 6.4 | Methods..... | 6-11 |
| 6.4.1 | Calculating recurrence intervals..... | 6-11 |
| 6.4.2 | Identification of hemipelagic mud | 6-11 |
| 6.4.3 | Age framework | 6-14 |
| 6.4.4 | Carbon isotopic records | 6-16 |
| 6.4.5 | Comparison with sea level curve | 6-16 |
| 6.5 | Results | 6-16 |
| 6.5.1 | Turbidite switch off during IETM | 6-16 |
| 6.5.2 | Modelling of uncertainty in recurrence intervals | 6-17 |
| 6.5.3 | Is the switch off genuine? | 6-18 |
| 6.5.4 | Post-IETM reduction in turbidite frequency | 6-20 |
| 6.6 | Discussion | 6-23 |
| 6.6.1 | Long term controls on turbidite recurrence..... | 6-23 |
| 6.6.2 | IETM-related control on turbidity current recurrence intervals..... | 6-26 |
| | <i>Reduced landslide frequency during the IETM.....</i> | 6-26 |
| | <i>Did flows route elsewhere during IETM?</i> | 6-26 |
| | <i>Was there a tectonic influence?</i> | 6-27 |
| | <i>Did ocean circulation control turbidite frequency?</i> | 6-29 |
| 6.6.3 | Why did turbidity current activity reduce post-IETM?..... | 6-29 |
| 6.6.4 | IETM turbidite frequency – global review..... | 6-30 |
| 6.6.5 | Implications for geohazards..... | 6-31 |
| 6.6.6 | Implications for future short-term climate change..... | 6-34 |
| 6.7 | Conclusions..... | 6-34 |
| Chapter 7. | Implications of long-term climate change for turbidite recurrence..... | 7-1 |
| 7.1 | Introduction | 7-2 |
| 7.1.1 | Climatic implications and geohazards | 7-3 |
| 7.1.2 | Turbidity currents as geohazards | 7-4 |
| 7.1.3 | Long-term records of sediment transport..... | 7-5 |
| 7.1.4 | Limitations of existing studies | 7-5 |
| 7.2 | Aims..... | 7-6 |
| 7.3 | Methods..... | 7-7 |
| 7.3.1 | Rationale for selection of study site..... | 7-7 |
| 7.3.2 | Determination of recurrence intervals..... | 7-8 |
| 7.4 | Statistical analysis | 7-9 |
| 7.4.1 | Testing for temporal clustering | 7-10 |

| | | |
|---|--|------------|
| 7.4.2 | Testing for significance of sea level..... | 7-10 |
| 7.5 | Results | 7-11 |
| 7.5.1 | Log-normal distribution of long-term (20 Myr) turbidite frequency..... | 7-11 |
| 7.5.2 | Common log-normal distribution of shorter-term turbidite frequency..... | 7-16 |
| 7.5.3 | Does sea level change influence turbidite recurrence? | 7-18 |
| 7.6 | Discussion..... | 7-21 |
| 7.6.1 | Implications of a log-normal distribution of turbidite recurrence for long (>10 Myr) timescales..... | 7-21 |
| 7.6.2 | Differences in distribution form from other deep-sea basins | 7-22 |
| 7.6.3 | What does a common distribution reveal about controls on shorter-term (<1 Myr) turbidite recurrence..... | 7-22 |
| 7.6.4 | Long term intensification of turbidity current activity – Tectonic or climate control? | 7-24 |
| 7.6.5 | Is sea level a dominant control on short-term turbidite recurrence?..... | 7-25 |
| 7.6.6 | Implications for short-term global warming..... | 7-30 |
| 7.6.7 | Implications for future geohazards..... | 7-30 |
| 7.7 | Conclusions | 7-31 |
| Chapter 8. Mass failure and turbidity current frequency at a modern bedload-dominated submarine river delta..... | | 8-1 |
| 8.1 | Introduction | 8-3 |
| 8.2 | Aims | 8-6 |
| 8.3 | Methods | 8-9 |
| 8.3.1 | Squamish delta: An outstanding natural laboratory..... | 8-9 |
| 8.3.2 | Repeat multibeam echo-sounder (MBES) surveys..... | 8-9 |
| 8.3.3 | Acoustic Doppler current profiler (ADCP) monitoring..... | 8-10 |
| 8.3.4 | Tidal, river discharge and earthquake data..... | 8-11 |
| 8.3.5 | Calculation of channel bed shear stress..... | 8-12 |
| 8.3.6 | Calculation of residual pore pressures due to tidal elevation change | 8-13 |
| 8.3.7 | Statistical analysis | 8-15 |
| 8.3.8 | Recurrence intervals and frequency distribution form | 8-16 |
| 8.3.9 | Optimal sample sizes..... | 8-16 |
| 8.4 | Results | 8-17 |
| 8.4.1 | Recurrence distribution | 8-17 |
| 8.4.2 | Delta lip collapses | 8-19 |
| 8.4.3 | Triggering of events during river floods – is it by hyperpycnal flow or slope failure? | 8-20 |
| 8.4.4 | Did earthquakes trigger slides or flows? | 8-21 |
| 8.4.5 | Does river discharge control the ‘switch on’ and frequency of flows? | 8-21 |
| 8.4.6 | Do slope failures and flows coincide with low tides? | 8-24 |
| 8.4.7 | Does flow timing relate to a combination of tide and river discharge effects? | 8-26 |
| 8.5 | Discussion..... | 8-29 |
| 8.5.1 | Extreme river flood discharge leads to delta lip failures not hyperpycnal flows..... | 8-29 |
| 8.5.2 | Conditioning and triggering of delta lip failures | 8-30 |
| 8.5.3 | River discharge is the primary conditioner for flow activity..... | 8-33 |

| | | |
|------------------------|---|------------|
| 8.5.4 | Tidal effects amplify the effects of river discharge to trigger flows | 8-34 |
| 8.6 | Conclusions | 8-34 |
| Chapter 9. | Summary and future work | 9-1 |
| 9.1 | Overview | 9-1 |
| 9.2 | Responses to initial questions posed in this thesis | 9-1 |
| | <u>Question 1:</u> How can we measure the recurrence of potentially damaging landslides and turbidity currents? | 9-2 |
| | <u>Question 2:</u> How can we quantitatively analyse recurrence of potentially damaging landslides and turbidity currents? | 9-4 |
| | <u>Question 3:</u> Do large submarine landslides show time-dependent behaviour? | 9-5 |
| | <u>Question 4:</u> Is sea level a dominant control on large submarine landslide recurrence? | 9-6 |
| | <u>Question 5:</u> Does millennial-scale dramatic global warming result in an increased frequency of submarine landslides and turbidity currents? | 9-7 |
| | <u>Question 6:</u> Can large submarine landslides catalyse global warming? Did large submarine landslides trigger global warming at the Initial Eocene Thermal Maximum? | 9-8 |
| | <u>Question 7:</u> How does long term (>10 Myr) global warming affect turbidity current frequency? ... | 9-8 |
| | <u>Question 8:</u> How are mass failures and sediment flows triggered at offshore bedload-dominated river deltas? | 9-9 |
| 9.3 | Future research | 9-10 |
| 9.3.1 | Are geohazards time-independent and can they be predicted? | 9-10 |
| 9.3.2 | How will future climate change affect geohazards (and will geohazards affect climate change)? | 9-17 |
| 9.3.3 | Is there a gradual continuum of geohazard frequency and magnitude? If not, what are the threshold-limits for extreme events? | 9-18 |
| 9.4 | Concluding remarks | 9-23 |
| References..... | Following thesis chapters | |

List of tables

| | |
|--|------|
| Table 1.1: Factors that may contribute to the initiation of submarine landslides | 1-8 |
| Table 1.2: Possible mitigation measures for landslide-turbidity current hazard posed to seafloor structures (from Clare et al., 2015) | 1-14 |
| Table 1.3: Summary of global submarine landslide recurrence studies | 1-20 |
| Table 1.4: Summary of regional and local landslide and turbidity current recurrence studies..... | 1-22 |
| Table 1.5: Summary of published monitoring data for submarine sediment density flows | 1-31 |
| Table 2.1: Summary of sites considered in this study | 2-3 |
| Table 3.1: Summary of datasets analysed in this study | 3-8 |
| Table 3.2: Examples of facies identified from cores in the Balearic Abyssal Plain..... | 3-9 |
| Table 3.3: Minimum resolvable time intervals for study areas | 3-22 |
| Table 4.1: Examples of Power Law, log-normal and exponential distributions in the natural world | 4-7 |
| Table 5.1: Summary of statistical results for Generalised Linear Model and Proportional Hazards Model for the Balearic and Madeira Abyssal Plain datasets testing for significance of sea level and its first derivative | 5-8 |
| Table 5.2: Results of rescaled range analysis for Madeira Abyssal Plain. | 5-16 |
| Table 5.3: Summary of statistical results for Generalised Linear Model and Proportional Hazards Model for subsets of the Madeira Abyssal Plain turbidite record. Bold italicised values are significant results ($p < 0.05$). | 5-17 |
| Table 6.1: Summary of study area locations, turbidite records | 6-14 |
| Table 6.2: Results of non-parametric unpaired Mann-Whitney and Kolmogorov-Smirnov tests | 6-21 |
| Table 6.3: Results of non-parametric unpaired Mann-Whitney and Kolmogorov-Smirnov tests | 6-22 |
| Table 6.4: Summary of other deep-water IETM sites with reference to turbidite recurrence. | 6-33 |
| Table 7.1: Results of Cox Proportional Hazards Modelling | 7-19 |
| Table 7.2: Results of non-parametric unpaired Mann-Whitney tests | 7-33 |
| Table 7.3: Results of non-parametric unpaired Kolmogorov-Smirnov tests | 7-36 |
| Table 8.1: Natural triggering mechanisms hypothesised for slope failures and flows at offshore river deltas..... | 8-8 |
| Table 8.2: Results of Chi Squared statistic testing for conformance of event recurrence data to different distributions | 8-17 |
| Table 8.3: Results of non-parametric statistical tests to determine significance of difference between annual range in variables against the range coincident with events detected by the ADCP..... | 8-24 |
| Table 8.4: Time required for 90% dissipation of excess pore pressures following sediment loading. The time to dissipate pore pressures is highly dependent on the consolidation (or hydraulic diffusivity) | |

coefficient (c_v ; based on values from Fraser River in Chillarige et al., 1997) as well as the rate and amount of sediment loading. Results based on methods in Terzaghi (1943) and Iverson (2005)8-30

| | |
|--|------|
| Table 8.5: Review of triggering mechanisms for failures and flows during surveyed interval at Squamish. | 8-34 |
| Table 8.6: Results of GLM and PHM analysis for ADCP events. | 8-35 |
| Table 8.7: Results of GLM and PHM analysis for MBES events. | 8-38 |
| Table 8.8: Results of GLM and PHM analysis for Central Channel MBES events. | 8-39 |
| Table 8.9: Results of GLM and PHM analysis for North Channel MBES events. | 8-40 |
| Table 8.10: Results of GLM and PHM analysis for South Channel MBES events. | 8-41 |
| Table 9.1: Preliminary results of Generalised Linear Model and Proportional Hazards Model for Balearic Abyssal Plain | 9-16 |

List of figures

| | |
|--|------|
| Figure 1.1: Demonstration of the potentially large volumes transported by landslide-triggered turbidity currents. This is just one example of many such deposits identified worldwide (see Figure 1.12 for more examples). Individual landslide-triggered flow volumes of >100 km ³ have been correlated in the Moroccan Turbidite System, offshore NW Africa | 1-3 |
| Figure 1.2: Idealised schematic showing evolution from submarine landslide (left) to turbidity current (right) | 1-5 |
| Figure 1.3: Sources of historical tsunamis in South and South-east Asia | 1-9 |
| Figure 1.4: Global network of submarine fibre-optic telecommunication cables | 1-10 |
| Figure 1.5: Seafloor rendering of the giant Storegga Slide (above) that occurred 8,200 years ago | 1-11 |
| Figure 1.6: Evidence of cable breaks that demonstrate the fast speeds and long travel distance of turbidity currents | 1-12 |
| Figure 1.7: Example seafloor images from active and proposed oil and gas development areas..... | 1-13 |
| Figure 1.8: Some potential implications for pipelines, cables and umbilicals in relation to impact by a turbidity current..... | 1-15 |
| Figure 1.9: Two of the world's largest sediment accumulations, the Indus and Bengal submarine fan.. | 1-16 |
| Figure 1.10: Water discharge profile for the Gaoping River during Typhoon Morakot in 2009 | 1-17 |
| Figure 1.11: Record of Homathko River discharge at Bute Inlet, British Columbia during monitoring period | 1-18 |
| Figure 1.12: Global database of large (>>1 km ³) submarine landslides..... | 1-20 |
| Figure 1.13: Examples of large submarine landslide deposits from core and outcrop. | 1-21 |
| Figure 1.14: Examples of large volume distal basin plain turbidite-hemipelagite sequences from which turbidite recurrence intervals can be derived..... | 1-24 |
| Figure 1.15: Photos of submarine outcrop of turbidites acquired using a remotely operated submarine from the Eel Canyon, offshore California | 1-26 |
| Figure 1.16: Outcrop photographs from the Miocene Marnoso-arenacea Formation, Italian Apennines where hemipelagic mud can be clearly discerned from turbidite mud | 1-27 |
| Figure 1.17: Bathymetric profile along Gaoping Canyon and into Manilla Trench showing cable breaks in 2009. 1-28 | |
| Figure 1.18: Example of waveforms (seismometer vertical component) of the three different types of signal observed in the western Ionian Sea..... | 1-29 |
| Figure 1.19: Spectrograms of four hydrophones from West Mata volcano, Lau Basin | 1-29 |
| Figure 1.20: Seafloor imagery showing morphological similarities between shallow and deep water sites | 1-32 |
| Figure 1.21: Example techniques for flow monitoring..... | 1-33 |
| Figure 2.1: Location of the study areas analysed in this thesis. | 2-2 |
| Figure 2.2: Outcrop photograph illustrating the tabular nature of beds of the Marnoso-arenacea and the basal sandstone of the Contessa and Fiumicello megaturbidites | 2-4 |

| | |
|--|------|
| Figure 2.3: Schematic palaeogeographic reconstruction of the Marnoso-arenacea foredeep basin during the mid-Miocene | 2-5 |
| Figure 2.4: Palaeogeographic reconstruction of the Marnoso-arenacea foreland basin during the Miocene. | 2-6 |
| Figure 2.5: Panoramic view of the Zumaia series, north-east Spain..... | 2-7 |
| Figure 2.6: Palaeogeographic reconstruction for the Bay of Biscay during the late Palaeocene | 2-8 |
| Figure 2.7: Outcrop photograph illustrating section analysed in this study from Itzurun Beach, Zumaia | 2-9 |
| Figure 2.8: Location map (A) showing ODP Site 1068 and reference to Zumaia site in NE Spain; Palaeogeographic reconstruction (B) for Iberian Margin and ODP Site 1068 during late Palaeocene/Early Eocene (modified from Whitmarsh et al., 1995); (C) Regional palaeogeography during late Palaeocene (modified from Kaminski et al., 1998)..... | 2-10 |
| Figure 2.9: Map of the Moroccan Turbidite System, offshore Northwest Africa..... | 2-11 |
| Figure 2.10: Location of the Madeira Abyssal Plain (grey) and sources of turbidites since 7 Ma. | 2-13 |
| Figure 2.11: Bulk geochemical cross-plots of mudcap compositions in the Madeira Abyssal Plain that are used to infer different sources. | 2-14 |
| Figure 2.12: Summary of literature concerning the many potential sediment input sources to the Balearic Abyssal Plain. Core LC05 (used in this study) is annotated. | 2-16 |
| Figure 2.13: Photograph of the Howe Sound, British Columbia with the Squamish River delta lip annotated..... | 2-17 |
| Figure 2.14: Location of the Howe Sound, with reference to the Squamish delta and other minor input sources | 2-19 |
| Figure 3.1: (A) Example landslide frequency study (Geist and Parsons, 2010) from the Santa Barbera Channel (N=7); Summary sedimentary log (B) from the Balearic Abyssal Plain (N=151; this study); Schematic (C) showing comparison between typical frequency of deposits in proximal and distal settings | 3-3 |
| Figure 3.2: Requirements for the selection of sites..... | 3-5 |
| Figure 3.3: Field photographs of the Marnoso-arenacea Formation..... | 3-7 |
| Figure 3.4: Field photographs from Zumaia, NE Spain..... | 3-10 |
| Figure 3.5: Identification of hemipelagic mud from core studies | 3-11 |
| Figure 3.6: Identification of hemipelagic mud from outcrop studies..... | 3-12 |
| Figure 3.7: Example bed correlation in Marnoso-arenacea | 3-13 |
| Figure 3.8: Variation in hemipelagic bed thickness determined from scanlines at Zumaia..... | 3-14 |
| Figure 3.9: Photo of Cabelli section at the Marnoso-arenacea annotated with biostratigraphic control points (from Clare et al., 2014) | 3-15 |
| Figure 3.10: Age plot for hemipelagic sedimentation at the Iberia Abyssal Plain..... | 3-16 |
| Figure 3.11: Available age control for the studied interval at Zumaia | 3-17 |
| Figure 3.12: Age plot for hemipelagic sedimentation at the Madeira Abyssal Plain..... | 3-18 |
| Figure 3.13: Comparison of Sr and Ca records from hemipelagic deposits in core LC05 from the Balearic Abyssal Plain | 3-19 |

| | |
|---|------|
| Figure 3.14: Correlation of ITRAX elemental data (Ca:Si ratio) acquired as part of this study | 3-20 |
| Figure 3.15: Correction for core stretching for LC06 | 3-21 |
| Figure 3.16: Correction for core stretching at LC05 | 3-21 |
| Figure 3.17: (A) Seafloor bathymetry as surveyed by multibeam echosounder at the Squamish site..... | 3-24 |
| Figure 3.18: Illustrations of ADCP deployment..... | 3-25 |
| Figure 3.19: Two examples of the ADCP data from Squamish in 2011. The arrival of each turbidity current is annotated as $t=0$ and can be seen from both the measurements of velocity (lower panel) and backscatter intensity (upper panel). Modified from Hughes Clarke et al. (2012)..... | 3-26 |
| Figure 3.1. Location of sites and time windows referenced in this paper. | 4-4 |
| Figure 3.2: Plots showing cumulative distributions (left) and probability density (right) functions of four ideal distributions. | 4-5 |
| Figure 3.3: Example exceedence plots | 4-6 |
| Figure 3.4: Parameters required for the rescaled range analysis from Chen and Hiscott (1999) | 4-9 |
| Figure 3.5: Example time series plot of the Iberian Abyssal Plain | 4-10 |
| Figure 3.6: Example hazard function, $h(x)$, plot illustrating different values of α for Gamma curves.... | 4-12 |
| Figure 3.7: Results of a simulation study for Cox PHM from Vittinghoff and McCulloch (2006)..... | 4-14 |
| Figure 5.1: Location map (A). Frequency histograms of hemipelagic mud thickness (B to D). Recurrence intervals plotted on (E) log-linear axes, (F) log-log axes and (G) with recurrence intervals normalized by rate parameter (λ). | 5-7 |
| Figure 5.2: Dispersion parameters plotted for GLM results on exceedance plot (left) and cumulative hazard function plot (right)..... | 5-8 |
| Figure 5.3: Comparison of 100 sequences of randomly generated synthetic data (black) with actual data (green) normalized to λ | 5-9 |
| Figure 5.4: (A) Influence of erosion on hemipelagic thickness. Ten modified datasets (grey) account for random amounts of erosion (between 0.0 m and 0.1 m) below turbidites thicker than the mean bed thickness from the Balearic Abyssal Plain. (B) Influence of short term variations in hemipelagic accumulation rates | 5-10 |
| Figure 5.5: Results of rescaled range analysis..... | 5-10 |
| Figure 5.6: Probability density function plot shows datasets (solid lines) superimposed on global earthquake data (points and dashed line)..... | 5-12 |
| Figure 5.7: Times series plot of turbidites from the Madeira Abyssal Plain differentiated by distinct geochemical signatures..... | 5-14 |
| Figure 5.8: (A) Exceedence plot on log-linear scale for subsets of Madeira abyssal plain turbidites differentiated by geochemical signature, | 5-15 |
| Figure 6.1: Palaeogeographic reconstructions at the end-Palaeocene | 6-7 |
| Figure 6.2: Summary of tectonic and palaeoceanographic variations | 6-10 |
| Figure 6.3: Identification of hemipelagic mud from turbidite mudcap from ODP 1068 borehole samples. HP refers to hemipelagic mud, TBT is turbidite..... | 6-12 |

| | |
|---|------|
| Figure 6.4: Identification of hemipelagic (HP) mud from turbidite (TBT) mudcap deposits | 6-13 |
| Figure 6.5: Available age control for the studied interval at Zumaia | 6-15 |
| Figure 6.6: A) Location of study areas annotated with mean turbidite recurrence interval, λ | 6-17 |
| Figure 6.7: Modelling of random variations (grey) in sediment accumulation rate between +/-30% for Zumaia (A) and ODP site 1068 (B) compared with measured data (black) analysed in this study ... | 6-18 |
| Figure 6.8: Turbidite recurrence time series for Zumaia and ODP 1068 sites..... | 6-19 |
| Figure 6.9: Box and whisker plots of turbidite recurrence expressed for different time windows relative to the IETM..... | 6-23 |
| Figure 6.10: Scenarios that generate different frequency distributions | 6-25 |
| Figure 6.11: Turbidite recurrence intervals for Ermua, NE Spain based on detailed lithostratigraphic logs | 6-27 |
| Figure 6.12: Conceptual model explaining effects of climate change on deep-water turbidity current activity at Zumaia (distal basin plain) | 6-29 |
| Figure 6.13: Summary of other deep-water IETM sites | 6-32 |
| Figure 7.1: Location map..... | 7-9 |
| Figure 7.2: Log-probability exceedence plot for full (N=1571) turbidite recurrence record..... | 7-12 |
| Figure 7.3: Turbidite recurrence (circles) and thickness (grey bars) time series for ODP Site 1068..... | 7-14 |
| Figure 7.4: Time series including turbidite recurrence for unfiltered record..... | 7-15 |
| Figure 7.5: Cumulative turbidite recurrence | 7-16 |
| Figure 7.6: (A) Time series plot of the Iberian Abyssal Plain record | 7-17 |
| Figure 7.7: Frequency histograms of sea level (A) and rate of change (B) based on analysis of global sea level from Miller et al. (2005) during the studied interval..... | 7-20 |
| Figure 7.8: Consideration of variables that may affect the frequency distribution of turbidites in deep-sea basin plains..... | 7-23 |
| Figure 7.9: Comparison of global carbon and oxygen isotope records (from Zachos et al., 2001) with global temperature (Zachos et al., 2001)..... | 7-25 |
| Figure 7.10: Cartoon schematics to illustrate the Iberian margin at different sea level states | 7-28 |
| Figure 8.1: Illustration of various hypotheses for the triggering of slides and flows at offshore bedload-dominated river deltas. Slope angles based on Squamish Prodelta example. | 8-5 |
| Figure 8.2: Location of northern, central and southern channels..... | 8-6 |
| Figure 8.3: Time series of event occurrence, river discharge (annotated with earthquakes and all monitored flow events), tidal elevation (with ADCP flow events), recurrence of flows at ADCP location (green), and flow frequency per 10 day bins based on MBES data (grey)..... | 8-11 |
| Figure 8.4: Schematic channel cross section showing how parameters H (height) and B (width of base) vary during different tidal elevations. | 8-12 |
| Figure 8.5: Variation in consolidation coefficient and pore fluid compressibility for different degrees of pore fluid saturation. | 8-14 |
| Figure 8.6: Plots of binned flow recurrence determined from the ADCP monitoring..... | 8-18 |

| | |
|--|------|
| Figure 8.7: Plots of binned flow recurrence determined by MBES surveys to visually assess the goodness of fit for different frequency distributions. | 8-18 |
| Figure 8.8: Location of headwalls of large delta lip failures seen on MBES data. | 8-21 |
| Figure 8.9: Detailed view on river discharge and tidal elevation during delta lip failure events A to E. | 8-22 |
| Figure 8.10: River discharge (left) and tidal elevation (right) plotted against flow recurrence as measured from the ADCP. | 8-25 |
| Figure 8.11: Results of Generalised Linear Model and Proportional Hazards Model analysis for events timing from ADCP (left) and MBES (right) monitoring. | 8-26 |
| Figure 8.12: Time series of river discharge (top), residual pore pressure (middle), and bed shear stress variable as determined by Q/BH^2 (lower). | 8-27 |
| Figure 8.13: Comparison of background annual variations in variables analysed in this chapter with those at the time of observed ADCP events. | 8-28 |
| Figure 8.14: Time series variation. | 8-31 |
| Figure 9.1: Summary of data sets used for determining landslide and turbidity current frequency. Methods used in this thesis outlined in orange. More detail on the methods is outlined in Chapter 1. | 9-3 |
| Figure 9.2: Initial compilation of mudcap geochemistry for individual turbidites in core LC05 (Balearic Abyssal Plain). Subtle changes in geochemistry may indicate shifts in the point or nature of sediment input | 9-12 |
| Figure 9.3: Comparison of periods defined by ITRAX analysis from Figure 9.2 with published variations in sediment input from published studies | 9-13 |
| Figure 9.4: AMS radiocarbon data and their calibrated (and corrected) ages for Lake Ríñihue turbidite record 9-14 | |
| Figure 9.5: Exceedence plots of turbidite recurrence both showing close to a straight-line fit on log-probability axes which is indicative of a log-normal distribution | 9-15 |
| Figure 9.6: Summary of other deep-water IETM sites that could form the initial basis of a global inventory. | 9-17 |
| Figure 9.7: Schematic illustrating the hypothesized step-change between normal and extreme events, comparing different scales of magnitude and time | 9-19 |
| Figure 9.8: Exceedence plot comparing modern Iberia Abyssal Plain record with data sets from Chapters 5 and 6 (from Allin, Clare et al., In Prep.) | 9-20 |
| Figure 9.9: Proposed deployment of monitoring instruments for proposed 2015-2018 Monterey Canyon experiment | 9-22 |

List of accompanying materials

| | |
|------------|---|
| Appendix 1 | Publications arising from this thesis |
| Appendix 2 | Summary sedimentary core logs |
| Appendix 3 | Data tables |
| Appendix 4 | Code for statistical analysis using <i>R</i> |
| Appendix 5 | ITRAX geochemical data for core LC05 (Balearic Abyssal Plain) |

DECLARATION OF AUTHORSHIP

I, Michael Andrew Clare, declare that the thesis entitled

“Large landslide and turbidity current frequency: Implications for hazards and climate change”

and the work presented in the thesis are both my own, and have been generated by me as the result of my own original research. I confirm that:

- this work was done wholly or mainly while in candidature for a research degree at this University;
- where any part of this thesis has previously been submitted for a degree or any other qualification at this University or any other institution, this has been clearly stated;
- where I have consulted the published work of others, this is always clearly attributed;
- where I have quoted from the work of others, the source is always given. With the exception of such quotations, this thesis is entirely my own work;
- I have acknowledged all main sources of help;
- where the thesis is based on work done by myself jointly with others, I have made clear exactly what was done by others and what I have contributed myself;
- Parts of this work have been published as:

Clare, M.A., Talling, P.J., Challenor, P., Hunt, J.E. and Malgesini, G. (2014) Distal turbidites reveal a common distribution for large ($>0.1 \text{ km}^3$) submarine landslide recurrence intervals, *Geology*, 43, 263-266.

Clare, M.A., Talling, P.J., and Hunt, J. (2015) Implications of reduced turbidity current and landslide activity for the Initial Eocene Thermal Maximum – evidence from two deep-water sites *Earth and Planetary Science Letters*, 420, 102-115.

Clare, M.A., Talling, P.J., Challenor, P.G. and Hunt, J.E. (In Press) Tempo and triggering of large submarine landslides - Statistical analysis for hazard assessment, Submarine mass movements and their consequences: 7th International Symposium, Wellington, New Zealand. (Advances in Natural and Technological Hazards Research).

Hunt, J., Talling, P.J., **Clare, M.A.**, Jarvis, I. and Wynn, R.B. (2014), Long term (17Ma) turbidite record of the timing and frequency of large flank collapses of the Canary Islands:

insight for landslide and tsunami hazards, *Geochemistry, Geophysics, Geosystems*. 15, 3322-3345.

Clare, M.A., Thomas, S., Mansour, M. and Cartigny, M. (2015) Turbidity current hazard assessment for field layout planning, *Proceedings of the 3rd International Symposium on Frontiers in Offshore Geotechnics*.

Clare, M.A., Thomas, S. and Spinewine, B. (2013) Sediment Density Flow Impact Assessment and Mitigation Studies for Deepwater Developments: A Challenge on Multiple Scales, *Proceedings of the Offshore Technology Conference*, 6 - 9 May 2013, Houston, TX, USA, <http://dx.doi.org/10.4043/23993-MS>, ISBN 978-62748-339-1.

Clare, M.A., Cartigny, M.J., North, L.J., Talling, P.J., Vardy, M.E., Hizzett, J.L., Sumner, E.J., Hughes Clarke, J.E., Spinewine, B. and Cooper, C. (2015) Quantification of Near-bed Dense Layers and Implications for Seafloor Structures: New Insights into the Most Hazardous Aspects of Turbidity Currents, *Proceedings of the Offshore Technology Conference*, May 2015, Houston, TX, USA.

- Parts of this work have been submitted as:

Clare, M.A., Talling, P.J and Hunt, J.E., (Submitted) Long term (20 Myr) tempo of long run-out turbidity currents in the Iberian Abyssal Plain: Persistent log-normal distribution and relationship to major climatic events. *Marine Geology*.

- Work during preparation of this thesis has also contributed to:

Clare, M.A., Talling, P.J., Hughes-Clarke, J. (In Prep.) How are mass failures and flows triggered at offshore bedload-dominated river deltas? *Geology*.

Talling, P.J., **Clare, M.A.**, Urlaub, M., Hunt, J.E., and Pope, E. (2014) “Large submarine landslides on continental slopes: Geohazards and role in methane release and climate change”, *Oceanography*, 27, 32-45.

Urlaub, M., Talling, P.J. and **Clare, M.A.** (2014) “Sea level-induced seismicity and submarine landslide occurrence: Comment”, *Geology*, 42, 337.

Talling, P.J., **Clare, M.A.** et al. (2015) “Key future directions for research on turbidity currents and their deposits”, *Journal of Sedimentary Research*, 85, 153-169.

- Other papers that I have contributed to during my doctoral studies, but are not detailed within this thesis, include:

Azpiroz, M., Cartigny, M., Talling, P.J., **Clare, M.A.**, Cooper, C., Parsons, D., Sumner, E.J., Simmons, S. and Pope, E. (In Prep.). The structure and dynamics of run-away turbidity currents in the deep ocean, *Nature*.

Clare, M.A., Smith, C.A., Unterseh-Dan, G. and Spinewine, B. (2014) Early stage geohazard assessments in tectonically active areas – application to potential developments in South-East Asia, *Proceedings of 2014 Offshore Technology Conference Asia*, <http://dx.doi.org/10.2118/24922-MS>, ISBN 978-1-61399-312-5.

Spinewine, B., **Clare, M.A.** and Unterseh, G. (2013) Numerical Modelling of Runout and Velocity for Slide-Induced Submarine Density Flows: A Building Block of an Integrated Geohazards Assessment for Deepwater Developments, *Proceedings of the Offshore Technology Conference*, 6 - 9 May 2013, Houston, TX, USA, <http://dx.doi.org/10.4043/24180-MS>, ISBN 978-62748-339-1

Pope, E., Talling, P.J., Urlaub, M., Hunt, J.E., **Clare, M.A.** and Challenor, P. (2015) Are large submarine landslides temporally random or do uncertainties in available age constraints make it impossible to tell?, *Marine Geology*.

Moernaut, J., Van Daele, M., Strasser, M., **Clare, M.A.**, Heirman, K., Viel, M., Cardenas, J., Kilian, R., Ladrón de Guevara, B., Pino, M., Urrutia, R., De Batist, M. (In Review) Lacustrine turbidites produced by surficial slope failure: a mechanism for continuous and consistent turbidite paleoseismic records, *Marine Geology*.

Symons, W.O., Sumner, E.J., Cartigny, M.J., Talling, P.J. and **Clare, M.A.** (Submitted) Large-scale sediment waves and scours on the modern seafloor and their implications for the prevalence of supercritical flows, *Marine Geology*.

Allin, J., Hunt, J.E., Talling, P.J., **Clare, M.A.**, Pope, E., Masson, D.G. (Submitted) Different controls on canyon filling and flushing events in Central Portuguese Margin canyons, *Marine Geology*.

- Work related to this thesis has been presented at the following conferences:

Clare, M.A., Talling, P.J., Hunt, J.E. (2014) Long term (20 Myr) tempo of long run-out turbidity currents in the Iberia Abyssal Plain: Persistent log-normal distribution and relationship to major climatic events, *British Sedimentological Research Group Annual Meeting*, Nottingham, December 2014.

Clare, M.A., Talling, P.J., and Cartigny, M.J. (2014) Can biogenic modification trigger landslides and inhibit erosion from turbidity currents? British Sedimentological Research Group Annual Meeting, Nottingham, December 2014.

Clare, M.A., Mason, A., Mason, C. and Nicholls, J. (2014) Determination of slope failure mechanics from an integration of high resolution seismic and sedimentological core data, Proceedings of the First Applied Shallow Marine Geophysics Conference (Extended Abstract).

Clare, M.A., Talling, P.J., and Hunt, J.E. (2014) Are landslide-turbidite recurrence intervals random and what are the implications of a common distribution for triggers, regional controls and climatic influence?, International Association of Sedimentology, Geneva, August 2014.

Clare, M.A., Talling, P.J., and Hunt, J.E. (2014) Extreme global warming and submarine landslide activity – cause and effect at the Initial Eocene Thermal Maximum and implications for the future, International Association of Sedimentology, Geneva, August 2014.

Clare, M.A., Talling, P.J., and Hunt, J. (2014) What are the implications of rapid global warming for landslide-triggered turbidity current activity?, Geophysical Research Abstracts, Vol. 16, EGU2014-11579.

Clare, M.A., Talling, P.J., Hunt, J., and Challenor, P., (2013) Multiple distal basin plains reveal a common distribution for large volume turbidity current recurrence intervals, American Geophysical Union, San Francisco, December 2013

Clare, M.A., Talling, P.J. and Hunt, J. (2013) An ‘unexpected’ switch off in turbidity current activity during the Palaeocene-Eocene Thermal Maximum, British Sedimentological Research Group Annual Meeting, Hull, December 2013.

Clare, M.A., Talling, P.J., Challenor, P. (2013) How can we assess the processes that control recurrence intervals of landslide-generated turbidites? Geophysical Research Abstracts, Volume 15, EGU2013, EGU General Assembly, 2013

Clare, M.A., Talling, P.J., Hunt, J., and Challenor, P., (2013) What is the effect of sea-level on frequency of sediment transport to distal basin plains, and what are the global implications?” International Association of Sedimentology, Manchester, September 2013.

Clare, M.A., Talling, P.J., Malgesini, G. and Hunt, J. (2013) Distal turbidite records reveal a common distribution for large submarine landslides recurrence intervals?, Future Directions for Research on Submarine Sediment Flows: Field Workshop, Santa Sofia, Italian Apennines (9-13th September 2013).

Clare, M.A. and Talling, P.J., (2012) Is there a common distribution for the recurrence intervals of landslide-generated turbidites in distal basin plains, and what are the implications of this distribution for geohazard assessment? British Sedimentological Research Group Annual Meeting, Dublin, December 2012.

- I have also provided contributions to the following work presented at conferences:

Azpiroz, M., Cartigny, M., Talling, P.J., **Clare, M.A.**, Cooper, C., Parsons, D., Sumner, E.J., Simmons, S. and Pope, E. (2015) Direct observations of turbidity currents in the Congo Canyon reveals a new flow structure, 31st IAS Meeting of Sedimentology, 22-25 June.

Azpiroz, M., Cartigny, M., Talling, P.J., **Clare, M.A.**, Cooper, C., Parsons, D., Sumner, E.J. and Simmons, S. (2014) Temporal evolution of curvature-induced secondary flows pattern of during passage of a turbidity current in a submarine canyon bend in the Congo Canyon, 2nd International Symposium on Submarine Canyons (INCISE) 2014, Edinburgh, September 2014.

Hizzett, J.L., Cartigny, M.J., Hughes Clarke, J.L., Talling, P.J., **Clare, M.A.**, Sumner, E.J. (2015) Origin and behaviour of different types of upslope migrating bedform trains on the Squamish Delta, Geophysical Research Abstracts, Vol. 17. European Geosciences Union 2015.

Allin, J.R., Hunt, J.E., Talling, P.J., **Clare, M.A.** (2015) Variability in turbidity current frequency within a central Portuguese margin canyon, Geophysical Research Abstracts, Vol. 17. European Geosciences Union 2015.

Pope, E., Talling, P., Urlaub, M., Hunt, J., **Clare, M.A.**, and Challenor, P. (2014) Are large submarine landslides in Polar Regions temporally random, or do current observations and age constraint make it impossible to tell? Geophysical Research Abstracts, Vol. 16, EGU2014-7818.

Ramsey, N., Spinewine, B., Denis, R., **Clare, M.A.**, Rushton, D. and Thomas, S., (2013) Integrated approach for slide-induced pipeline vulnerability beyond the continental shelf: From slope stability to debris flow runout and pipeline vulnerability assessment, Society for Underwater Technology, Conference on Deepwater Pipelines.

Signed:

Date:.....

Acknowledgements

This thesis is dedicated to Emma, who allowed me to go back to University part-time, and has supported me every step of the way, as she has with everything else I have done since we have been together. She has shown tremendous patience – particularly due to the lack of time off and the fact that she finds turbidites incredibly boring I could not have done this without her. Daisy, on the other hand, has been nothing but a hindrance, so don't get a cat if you want to work on a part-time PhD in peace...

Pete Talling has been a superb supervisor – he has taught me to write (properly, and with more superlatives!), encouraged me to question more, and has provided a greater level of support than I could have hoped for. I would like to thank him for providing me with a project and funding that allowed my research to grow legs and then ramble off in many directions. His “blue sky” approach to science is refreshing and his guidance and advice over coffee, beers and poorly-drawn figures has been invaluable. When I make my fortune, I will buy him his very own Californian sea-lion as a thank you.

James “Squiddy” Hunt has been a legend throughout. His support goes far beyond his assistance with fieldwork in Spain and provision of core logs for Madeira and Iberia systems. He has provided a nest for me in Southampton, countless useful (and useless) discussions about turbidites, landslides, geochemistry, the Kraken and whiskey, and has been a great friend. Claire “The Count” Hunt also deserves a huge thank you – for rambling chats, and for putting up with me in various houses. I wish you both the best.

Matthieu Cartigny is an inspiration. His ability to listen quietly and then ask the most insightful questions is remarkable and I have been fortunate to benefit from that. Aside from this, he has also been a good friend, colleague and is a genuinely great guy. I look forward to working with him at NOC, and wish him and Sanem all the best for a happy life together.

Numerous others have helped me along the way. It has been an honour to work with John Hughes Clarke whose approach to surveying is mind-blowing. His data are pure class, and he is also a thoroughly lovely man. Peter Challenor introduced me to the joys of statistics. Ivan Haigh has been an exemplary panel chair and provided useful guidance from the perspective of someone who has trodden both industry and academic paths. Tom Gernon provided useful advice on the thesis outline. The Sedimentology and Geohazards team at NOC have provided laughs, science chat and some welcomed relief from spreadsheets. There is much more good science and fun to be had with Age, Ale, Ed, Jamie, Josh, Maria, Millie and Will. My original roommates Chris, Hector and Giuseppe – our time was brief but the science shone powerfully! I am glad to stay in

touch with each of them and hope for some good collaborations in future. Mark Vardy always provides good discussion over coffee – and there is plenty more to come. Guy Rothwell and Suzie Maclochlan were very helpful in the BOSCORF when I was core logging. Thanks also go to Marine Geology Group for funding and Tim Henstock and Damon Teagle for taking a chance on me! I thank Dorrik Stow for getting me interested in turbidites in the first place.

David Waltham and Justin Dix provided a good grilling at my viva, all of which was much appreciated and I believe it has helped to tighten up the thesis. Thanks to both for taking the time to read and scrutinise in detail!

Judy and Tim provided much-needed breaks from work in the Owl Bar. Matt and Jo provided my second nest, some good chats about “the future”, and I look forward to seeing more of them in Southampton in future.

I would like to thank Fugro GeoConsulting Limited for being so open-minded in letting me study for a PhD alongside my consultancy work in geohazards. Steve Thomas has been a great mentor from whom I have learnt huge amounts about engineering geology, geohazards, geophysics, politics and history. He set me on a good path and reminded me of the importance of observation ahead of interpretation, and a good gin and tonic. Brian Mackenzie and Nigel Kee provided much needed support and guidance when I was at my busiest. Lorraine, Grant and the rest of the EGG Team in Wallingford have been hugely supportive, provided friendship and will continue to do great things. I hope we continue to work together.

Definitions and Abbreviations

LIST OF ACRONYMS

| | |
|-----------------|--|
| ^{14}C | Radiocarbon |
| ADCP | Acoustic Doppler Current Profiler |
| AMS | Accelerator Mass Spectrometry |
| BED | Benthic Event Detector |
| BIN | Benthic Instrument Node |
| BOSCORF | British Oceanographic Sediment Core Repository Facility |
| B.P. | Before Present |
| CIE | Carbon isotopic excursion |
| ED | Energy dispersive (related to XRF) |
| GLM | Generalised Linear Model |
| HP | Hemipelagite |
| Hm | Hemipelagic mud |
| IETM | Initial Eocene Thermal Maximum |
| IODP | Integrated Ocean Drilling Program |
| MBARI | Monterey Bay Aquarium Research Institute |
| MBES | Multi-beam Echo Sounder |
| MIS | Marine Isotope Stage |
| ODP | Ocean Drilling Program |
| PDF | Probability Density Function |
| PETM | Palaeocene Eocene Thermal Maximum (former term for IETM) |
| PHM | Proportional Hazards Model |
| TBT | Turbidite |
| TED | Turbidity event detector |
| THD | Total Hemipelagic Depth |
| Tm | Turbidite Mud |
| TOC | Total organic carbon |
| XRF | X-Ray Fluorescence |

LIST OF SYMBOLS AND UNITS

| | |
|--------|--|
| A | Bed roughness constant |
| B | Width of channel base |
| C_f | Dimensionless bed resistance coefficient |
| c_v | Coefficient of consolidation |
| e^x | Exponential function |
| E^b | Hazard function |
| $f(t)$ | Failure Density Function |
| g | Gravitational acceleration |
| H | Channel height |
| $h(t)$ | Hazard rate |
| k | Coefficient of permeability |
| K | Modified Hurst exponent |
| ka | Thousand years ago |
| M | Magnitude |
| m | metre |
| Ma | Million years ago |
| m_v | Compressibility of soil skeleton |
| N | Number of observations |
| $P(x)$ | Probability of event x |
| PDF | Probability Density Function |
| Q | River discharge in cm^3/s |
| Q-Q | Quantile-Quantile |
| r^2 | Coefficient of determination (square of the correlation coefficient) |
| R_T | Recurrence interval normalised to λ |
| s | Seconds (time) |
| S | Pore fluid saturation where $S=100\%$ is 0% gas, $S=98\%$ is 2% gas etc. |
| $S(t)$ | Survival Function |

| | |
|------------|--|
| T | Time |
| u | Flow velocity |
| x | event |
| α | Shape parameter for Gamma curve or parameter affecting β |
| β | Baseline hazard function |
| γ_w | Unit weight of water |
| λ | Rate parameter (mean recurrence interval for a sample) |
| ρ | Density |
| μ | Mean value for a log-normal distribution |
| ω | Tidal frequency |
| σ | Standard deviation for a log-normal distribution |
| τ_b | Bed shear stress |

Chapter 1: Thesis introduction

Summary

Submarine landslides and turbidity currents can transport large quantities of sediment at fast speeds to the deep sea. Therefore they are a potential hazard to expensive and strategically important seafloor structures, can trigger tsunamis, and are also globally important processes for deep-water sediment transport. This chapter explores the importance of landslides and turbidity currents as hazards, outlines the current state of knowledge, and highlights some recent developments in measuring their frequency using sedimentary records and novel monitoring techniques. The aim of this section is therefore to set the scene for later chapters, and explain why the questions they tackle are of importance. This is followed by an overview of the thesis structure and a discussion of previous research into submarine landslide frequency. Finally, the key questions addressed by this thesis are posed. These key questions are addressed in the conclusions in Chapter 9.

Aspects of this chapter form contributions to two manuscripts: Clare et al. (Published May 2015; Proceedings of Offshore Technology Conference), and Clare et al. (Published June 2015; Proceedings of 3rd International Symposium for Frontiers of Offshore Geotechnics).

Why do we need to understand the frequency of large submarine landslides and turbidity currents?

1.1 The largest mass flows on earth

Submarine landslides on continental margins include the largest mass flows on Earth and can be two orders of magnitude larger than those on land. (Hühnerbach and Masson, 2004; Haflidason et al., 2005; Masson et al., 2010; Korup, 2007; Urlaub et al., 2013). Remarkably, many large landslides occur on seafloor gradients of $< 2^\circ$ that would almost always be stable on land (Urlaub et al., 2013). Mixing of the landslide mass with the surrounding seawater can form even longer run-out sediment flows called turbidity currents, which can travel for many hundreds of kilometres (Talling et al., 2007a; 2012; Figure 1.1), sometimes with fast speeds of 4 to 19 m/s (Piper et al., 1999; Cooper et al., 2013; Talling, 2014). Submarine landslides and their resultant turbidity currents can involve hundreds to several thousand cubic kilometres of material (Hühnerbach and Masson, 2004; Figure 1.2); thus making them a globally important process for sediment transport (Talling, 2014).

In this thesis (Chapters 5 to 7) distal, large deposits from turbidity currents ('turbidites') are analysed. This approach captures extensive records of large volume flows that travelled long distances, at fast speeds. It is these large volume and widespread flows that are potential hazards for seafloor infrastructure and are responsible for transporting large volumes of sediment to deep-water. While there is often a genetic link, submarine landslides and turbidity currents are different types of phenomena. Turbidity currents can also be triggered by a range of processes other than submarine landslides, such as storm waves and hyperpycnal river flood discharge (Normark and Piper, 1991; Piper and Normark, 2009). Turbidity currents with suspended sediment volumes far in excess of the largest river floods, however, are most likely to be triggered by submarine landslides (Talling et al., 2007a,b, 2013; 2014). Distal turbidite records are therefore used in Chapters 5 to 6 more specifically as a proxy for understanding large submarine landslide recurrence on the basis of their large volume and similarity with sites that have been demonstrated to feature landslide deposits. Finally, in Chapter 8 a unique dataset is analysed, including repeat seafloor mapping and direct monitoring, where it is possible to differentiate between smaller-scale, highly frequent turbidity currents triggered by

landslides, and by other processes. This combined approach provides new insights into the triggering of landslides and flows.

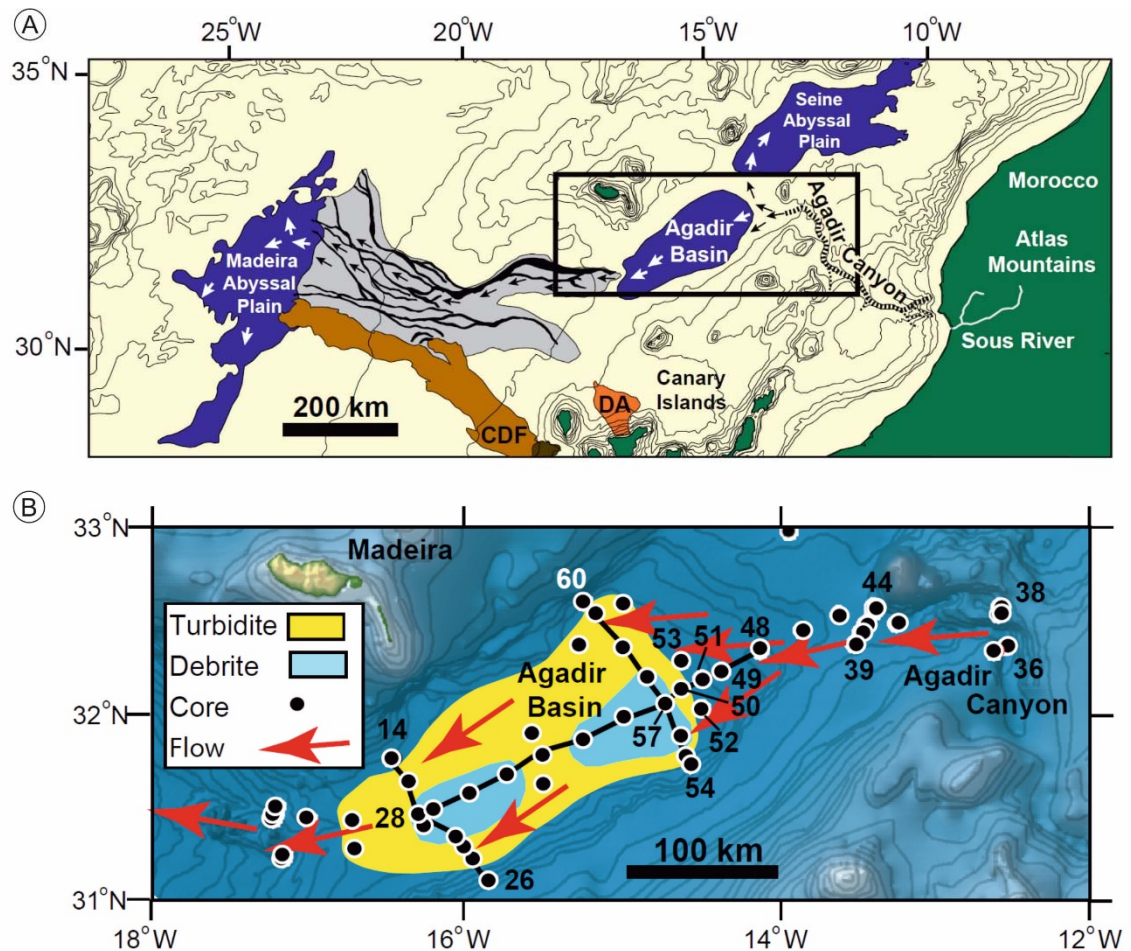


Figure 1.1: Demonstration of the potentially large volumes transported by landslide-triggered turbidity currents. This is just one example of many such deposits identified worldwide (see Figure 1.12 for more examples). Individual landslide-triggered flow volumes of $>100 \text{ km}^3$ have been correlated in the Moroccan Turbidite System, offshore NW Africa for over 1500 km between the Agadir Basin and Seine and Madeira Abyssal Plains. The Canary Debris Flow [CDF], and a volcanic debris avalanche [DA] are annotated in A. A flow of approximately 180 km width occurred about 60,000 years ago as shown in B. The location of sediment cores, and extent of turbidite sand (yellow) and cohesive debris flow (blue) deposits are annotated. Figure modified from Talling et al. (2007a).

1.2 Why landslide and turbidity current frequency is important

Understanding the frequency (or rate) at which submarine landslides and turbidity currents occur has considerable importance for understanding global sediment fluxes, tsunami hazard, risk assessment for seafloor structures, and the nature and influence of future global warming. Determining the characteristic frequency of landslides and turbidity currents, and how climate or sea-level change may (or may not) change the rate at which they may recur helps to inform future hazard assessments. Assessments may include quantification of risk for offshore oil and gas developments, landslide-triggered

tsunami predictions for coastal communities, and planning and maintenance regimes for offshore communications cables. Furthermore, the frequency of events that transport large amounts of sediment enables interpretation of longer-term depositional records that are relevant to hydrocarbon exploration, understanding carbon budgets, and palaeoceanographic reconstructions. This thesis specifically aims to investigate the effect of sea level and climate change on large submarine landslide-turbidity current frequency. When climate change is assessed in this thesis, it is primarily in relation to reconstructed global temperatures (Chapter 7), but also includes a more detailed review of the implications of relative humidity, related vegetational cover, and links with terrestrial systems (Chapter 6). This work also addresses whether landslides may themselves trigger global warming. Some studies have argued that significant volumes of methane (a potent greenhouse gas) may be released to the atmosphere during slope failure events due to dissociation of previously stable gas hydrates. Finally, this thesis explores the interaction between the two major systems for sediment transport on the surface of our planet; rivers and turbidity currents.

1.2.1 Overarching thesis aim

The overarching aim is to determine how large landslide and turbidity current frequency relates to variables, such as sea level, global temperature changes and river discharge, using statistically robust methods. In light of predicted future global and sea level rises (e.g. Haigh et al., 2014), this is a timely study. In this thesis, submarine landslide and turbidity current frequency is analysed from a range of settings worldwide, covering both modern and ancient timescales. Characterisation of landslide and turbidity current frequency over a variety of timescales and climatic conditions provides valuable new insights into their possible triggers and preconditioning mechanisms. This study is novel because the datasets analysed are unusually extensive records of landslide-turbidity current frequency and they include sufficient numbers of events ($N > 106$) for statistical analysis to be performed. This large sample number allows for the use of statistical methods that have rarely, if ever, been used before for submarine mass flow frequency. It is important to use statistics because it provides a systematic method for unbiased analysis of data. Statistics allows for the robust testing of relationships between event frequency and different hypothesised controlling factors, and determines a quantified level of significance. Datasets considered herein feature varying levels of temporal resolution, to

compare event frequency on different timescales. Thus it is possible to investigate the effect of major climatic change (>1 Myr), cycles of glacioeustatic sea level (>100 s of kyr), major hyperthermals (<10 s of kyr), and even shorter-term variations such as daily tidal range and river discharge flux (months to hours). This has not been possible in previous studies.

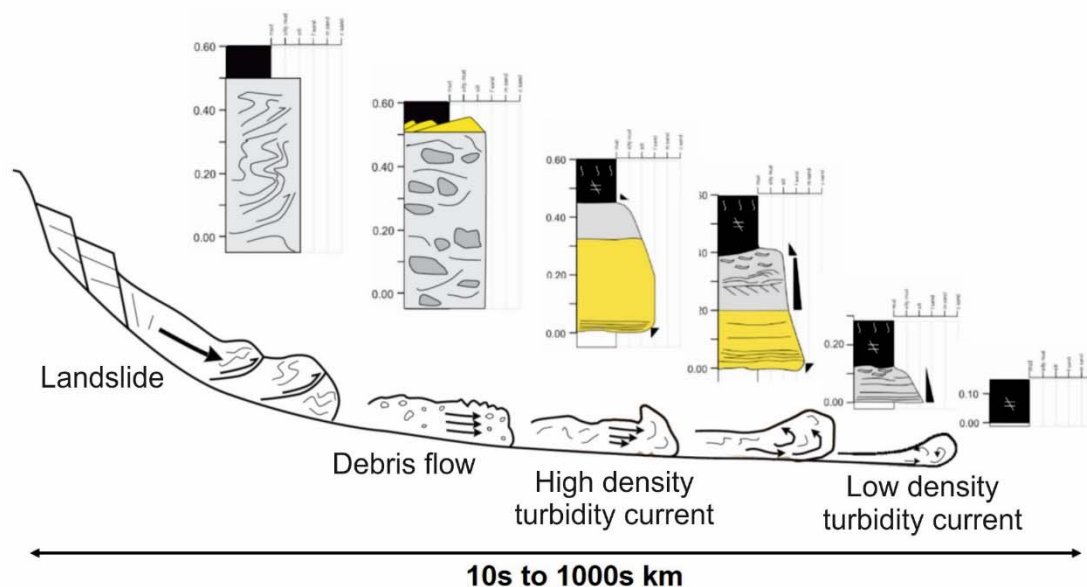


Figure 1.2: Idealised schematic showing evolution from submarine landslide (left) to turbidity current (right), illustrating potential facies evolution, associated deposits (modified from Mulder, 2011). It should be noted that turbidity currents may also be triggered by processes other than submarine landslides, such as agitation by storm waves and plunging river floodwater; however, the largest volume flows are thought to result from landslide run-out (Talling et al., 2013)

1.3 Thesis outline and key science questions posed

Chapter 2 introduces the geological settings of the study areas, followed by a discussion of the sedimentological (**Chapter 3**) and statistical (**Chapter 4**) methods employed. Chapters 5 to 9 are presented as individual scientific papers which address the key questions posed in this present chapter (Section 1.6). Specifically, **Chapter 5** addresses the frequency distribution of large submarine landslide recurrence and asks whether sea level is a dominant control on frequency of landslide activity for three different sites? The implications of dramatic short-term (**Chapter 6**) and long-term (**Chapter 7**) climate change on landslide-turbidity current frequency are then explored in relation to ancient records from the Iberia Abyssal Plain and the proto-Bay of Biscay, north-east Spain (Zumaia series). In **Chapter 8** the links between rivers and offshore delta systems, and the triggering mechanisms for delta-lip failures and turbidity currents are

investigated based on a case study from the Squamish prodelta, British Columbia. **Chapter 9** synthesises the conclusions and provides answers to the key questions posed at the end of this present chapter.

Where chapters have been submitted or accepted for publication, this is noted ahead of each chapter's abstract. At the time of submission, three lead-authored papers arising from this thesis have been accepted or are published (Chapter 4 - Submarine Mass Movements and Their Consequences, *Advances in Natural and Technological Hazards Research*; Chapter 5 - Geology; Chapter 6 – Earth and Planetary Science Letters), one has been submitted (Chapter 7 – Marine Geology) and one will be submitted in July 2015 (Chapter 8 - Geology). Parts of Chapter 1 formed contributions to two lead-authored papers which are both published (*Proceedings of International Symposium on Frontiers of Offshore Geotechnics*, and *Offshore Technology Conference*). The results and analysis of data from the Madeira Abyssal Plain (Chapter 5) contributed to a co-authored paper which was published in *Geochemistry, Geophysics and Geosystems* (Hunt, Clare et al., 2014). Some of the preliminary findings from this thesis which are now summarised in Chapter 9 were incorporated into papers published in *Geology* (Urlaub, Talling and Clare, 2014), *Oceanography* (Talling, Clare et al., 2014) and *Journal of Sedimentary Research* (Talling, Clare et al., 2015). The appendices contain copies of published papers arising from this thesis, conference abstracts, data tables, summary core logs and code for statistical analysis in *R*. These are provided on a data CD.

The main questions addressed in this thesis are listed below and expanded on in Section 1.6:

- Is there a similar frequency distribution form for large submarine landslides in different settings worldwide? Identifying if a common distribution exists can provide insights into the nature of possible triggering mechanisms.
- Does sea level act as a major, dominant control on large submarine landslide recurrence? There is some debate on this topic, but previous studies have analysed datasets with too few observations to determine a statistically meaningful answer.
- How does global warming affect large submarine landslide and turbidity current frequency and does the rate at which temperature changes have an effect? In light of future projected global warming, this is a timely question.

- Did large submarine landslides trigger past global warming? This is equally important for understanding the potential for future global warming as it is for deciphering past palaeo-climate records. There is much debate on the triggers for dramatic global warming events, such as the Initial Eocene Thermal Maximum at ~55 Ma where some authors have suggested that landslides may have triggered methane release.
- How are mass failures and flows triggered at bedload-dominated river deltas? Determining whether there is a direct connection between sediment fed by rivers and submarine transport systems is important for future hazard assessments in coastal settings, and for understanding the processes responsible for shallow to deep-water deposition on a larger scale

1.4 Research drivers: Understanding seafloor hazards and sediment transport

The following section outlines the key research drivers for this thesis, with respect to submarine landslides and turbidity currents as potential geohazards and globally important sediment transport processes.

1.4.1 Triggering of large submarine landslides

Numerous hypotheses have been proposed for how large submarine landslides are triggered and how slopes are preconditioned to fail (Table 1.1). We are yet to monitor a large submarine landslide in action, however, and these hypotheses remain poorly tested. Rapid accumulation of relatively impermeable sediment is often invoked as a preconditioning factor for failure, which may then be triggered by an earthquake. However, very large landslides also occur in areas of slow sedimentation (Urlaub et al., 2013), failure may occur several thousand years after rapid sedimentation ceases (Leynaud et al., 2009), and some recent large earthquakes do not appear to have produced widespread slope failure (Sumner et al., 2013). The headwalls of most large ($>> 0.1 \text{ km}^3$) landslides are too deep ($> 200 \text{ m}$ water depth) for triggering by cyclic wave loading, and some headwalls are too deep ($> 2,000 \text{ m}$ water depth) for triggering by gas hydrate dissociation (Hühnerbach and Masson, 2004). It has been suggested that sea level changes play a key role in preconditioning or triggering slope failure (Maslin et al., 2004; Owen et al., 2007; Lee, 2009). However, a recent analysis of large submarine landslide

frequency concluded that there was no significant association with sea level on a global scale (Urlaub et al., 2013).

Table 1.1: Factors that may contribute to the initiation of submarine landslides (modified from Masson et al., 2006)

| Historically documented | Examples | References |
|--|---------------------------------------|---|
| Earthquakes | Grand Banks | Fine et al. (2005) |
| Hurricanes of cyclic loading | Mississippi Delta | Prior and Coleman (1982a,b) |
| Loading or oversteepening of slopes | Nice, Canary Islands | Assier-Rzadkiewics et al. (2000), Dugan and Flemings (2000), Stigall and Dugan (2010), Dugan and Sheahan (2012) |
| Underconsolidation (overpressure) | Mississippi Delta | Prior and Coleman (1982a,b) |
| Rainfall (where landslides have a subaerial extension) | Norway | Longva et al. (2003) |
| Slope parallel weak layers in bedded sequence | East Coast USA, Storegga, West Africa | O’Leary (1991), Haflidason et al. (2003), Bryn et al. (2005), Masson et al. (2010), Locat et al. (2014) |
| Suggested (but less well documented) | | |
| Gas hydrate dissociation | East Coast USA, Storegga | Sultan et al. (2003) |
| Sea level change | Madeira Abyssal Plain | Weaver and Kuijpers (1983), Brothers et al. (2014) |
| Volcanic activity | Hawaii, Canaries | Moore et al. (1989), Masson et al. (2002), Hunt et al. (2013) |
| Loss of sediment structure | North-west Africa | Urlaub et al. (2012) |

Why focus on sea level as a possible control on landslide frequency?

In this thesis, one of the main foci is the possible link between sea level and submarine landslide frequency. Sea level is selected because concerted efforts have been made by the palaeoceanographic and palaeoclimate communities to reconstruct past sea levels using multi-proxy methods (e.g. Miller et al., 2005; Rohling et al., 2014). Such reconstructed curves have a compatible temporal resolution with the timescales considered for landslide recurrence in this thesis and provide useful continuous records that suit statistical analysis. The same continuity does not exist for many of the other variables considered in Table 1.1; hence a direct comparison is more problematic and

does not often suit such analyses. One important reason for investigating possible sea level controls is that many oil and gas geohazard assessments make use of global eustatic curves based on the assumption that submarine landslide frequency is inherently linked to sea level (Thomas et al., 2010). Any quantitative analysis that tests such a hypothesis is therefore useful as an input and guide to future hazard assessments.

Chapter 6 and 7 aim to investigate climate controls rather than just sea level stand for early to mid-Eocene, as concerted efforts have been made by palaeoclimate researchers on reconstructing carbon isotopic ratios and global ocean temperature curves for this time period (e.g. Kennett and Stott, 1991; Canudo and Molina, 1992; Pak and Miller, 1992; Whitmarsh et al., 1998; Pardo et al., 1997; Ladner and Wise, 2001; McGonigal and Wise, 2001; Schmitz et al., 2001; Urquhart, 2001; Schmitz et al., 2003; Tremolada and Bralower, 2004; Zachos et al., 2005; Sluijs et al., 2008). It is only for the most recent record (Squamish prodelta in Chapter 8) that it is possible to analyse the influence of shorter term variables such as loading and unloading of slopes, overpressure and earthquakes. The temporal resolution (hours to days) of landslide and flow recurrence from the Squamish prodelta site suits such an analysis.

1.4.2 Potentially fatal landslide-triggered tsunamis

Due to their potential volume and speed, submarine landslides can generate destructive tsunamis that cause fatalities and damage coastal infrastructure (Tappin et al., 2001; Bondevik et al., 2005). The 8.2 ka Storegga landslide mobilised >3000 km³ of sediment and triggered a tsunami that affected coastlines many hundreds of kilometres away from its source (Masson et al., 2006; Figure 1.5). A submarine landslide that occurred in 1999 offshore Papua New Guinea triggered a tsunami which led to 2,200 deaths (Tappin et al., 2008). Seven percent of all historical tsunamis are interpreted to have been caused by submarine landslides or combined landslide-volcanic events (Harbitz et al., 2014). Figure 1.3 highlights the south and south-east Asia region where landslide, volcanic and earthquake triggered tsunamis have been recorded.

Some studies have used the probability distribution of large earthquakes as a predictor for the future occurrence of landslide-triggered tsunamis (e.g. Ten Brink et al., 2009). This, however, assumes that each large earthquake triggers a landslide, which is not necessarily always a valid hypothesis (Sumner et al., 2013). To enable future

predictions of landslide-tsunamis, a better understanding of large submarine landslide frequency and triggers is therefore highly important.

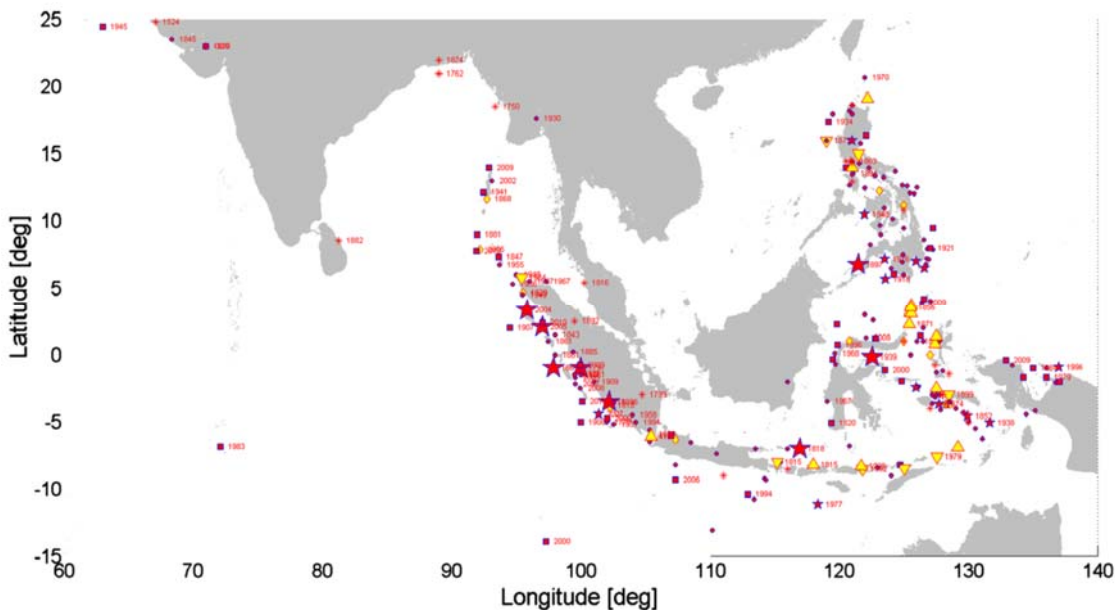


Figure 1.3: Sources of historical tsunamis in south and south-east Asia from Harbitz et al. (2014). Red marks are seismic sources, yellow upward triangles are volcano-related, yellow downward triangles are landslide-related tsunamis. Yellow rhomboids are unknown sources.

1.4.3 Hazards for strategically important subsea cable networks

The potential for submarine landslide and turbidity currents to damage seafloor structures has been shown by historical cable breaks in a variety of locations worldwide (e.g. Heezen and Ewing, 1952; Genesseeaux et al., 1980; Piper et al. 1985, 1999; Hugot, 2001; Su et al., 2012; Carter et al., 2014; Figure 1.4). Large volume (up to 100s of km³) turbidity currents may travel over many hundreds of kilometres (Talling et al., 2007a); thus, such flows have potential to damage structures over vast areas of seafloor. Indeed, it has been inferred from sequential cable breaks that turbidity currents may travel at velocities in excess of 19 m/s and can maintain velocities of up to 10 m/s on slopes as low as 0.2° (Piper et al., 1999; Figure 1.6). These velocities assume that the damage was coincident with the arrival of the head of the flow rather than the body. Even less powerful flows (~1 to 2 m/s) can cause damage (Carter et al., 2014) which is also important, as global seafloor cable networks currently carry over 95% of transoceanic data traffic, including the internet and financial services (Carter et al., 2009). Mitigating against cable breaks, by rerouting data traffic along adjacent cables, is difficult as flows can break multiple cables across a large area (Carter et al., 2014). The combination of large travel

distance, high velocity, and the impact of a moving mass of sediment also poses a credible threat to other seafloor structures (Bruschi et al., 2006; Clare et al., 2013; 2015c,d; Figure 1.8).

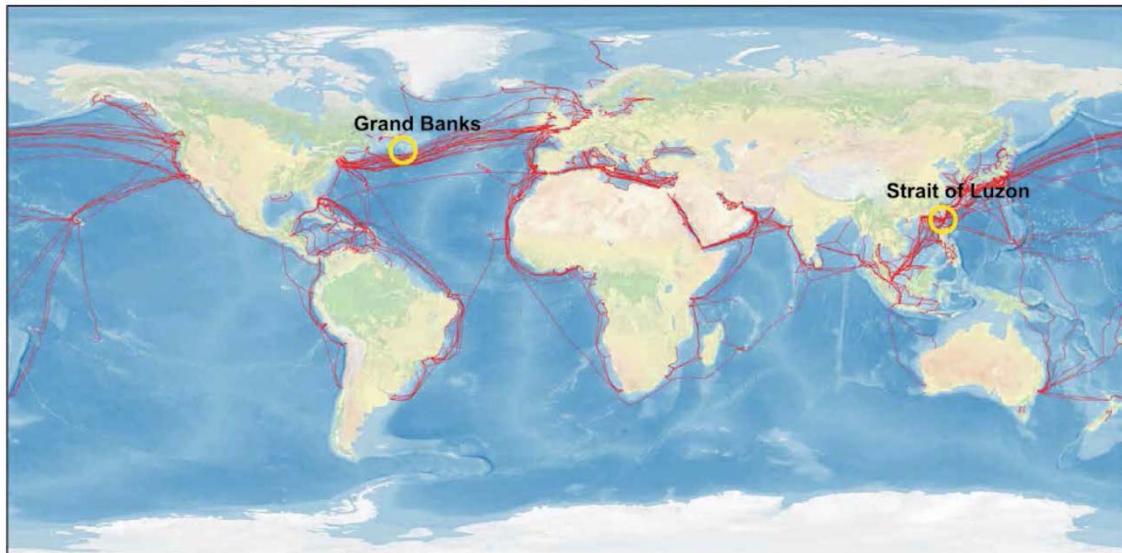


Figure 1.4: Global network of submarine fibre-optic telecommunication cables (red lines). Locations of 1929 Grand Banks, Newfoundland and 2006 Pingtung, Taiwan cable breaks outlined in yellow. From Carter et al. (2014)

To understand the impact of such flows, it is important to understand their potential to recur. While turbidity currents can be considered as geologically ‘instantaneous’ events, they may actually be sustained for several days or weeks (e.g. Mulder et al., 2003), which has implications for understanding the potential impacts to subsea structure. Recent monitoring in the deep-water Congo Canyon shows that flows can continue to travel at ~ 1 m/s for up to ten days, with as many as eleven flows observed in seven months (Cooper et al., 2013; Azpiroz et al., In Prep.). Perhaps surprisingly, flows were active in the canyon for $\sim 25\%$ of the monitored period. Sub-annual flows have also been observed in the Monterey Canyon (Xu et al., 2013,2014) and inferred for the Eel Canyon (Paull et al., 2014), therefore such a high frequency may be expected in other locations worldwide.

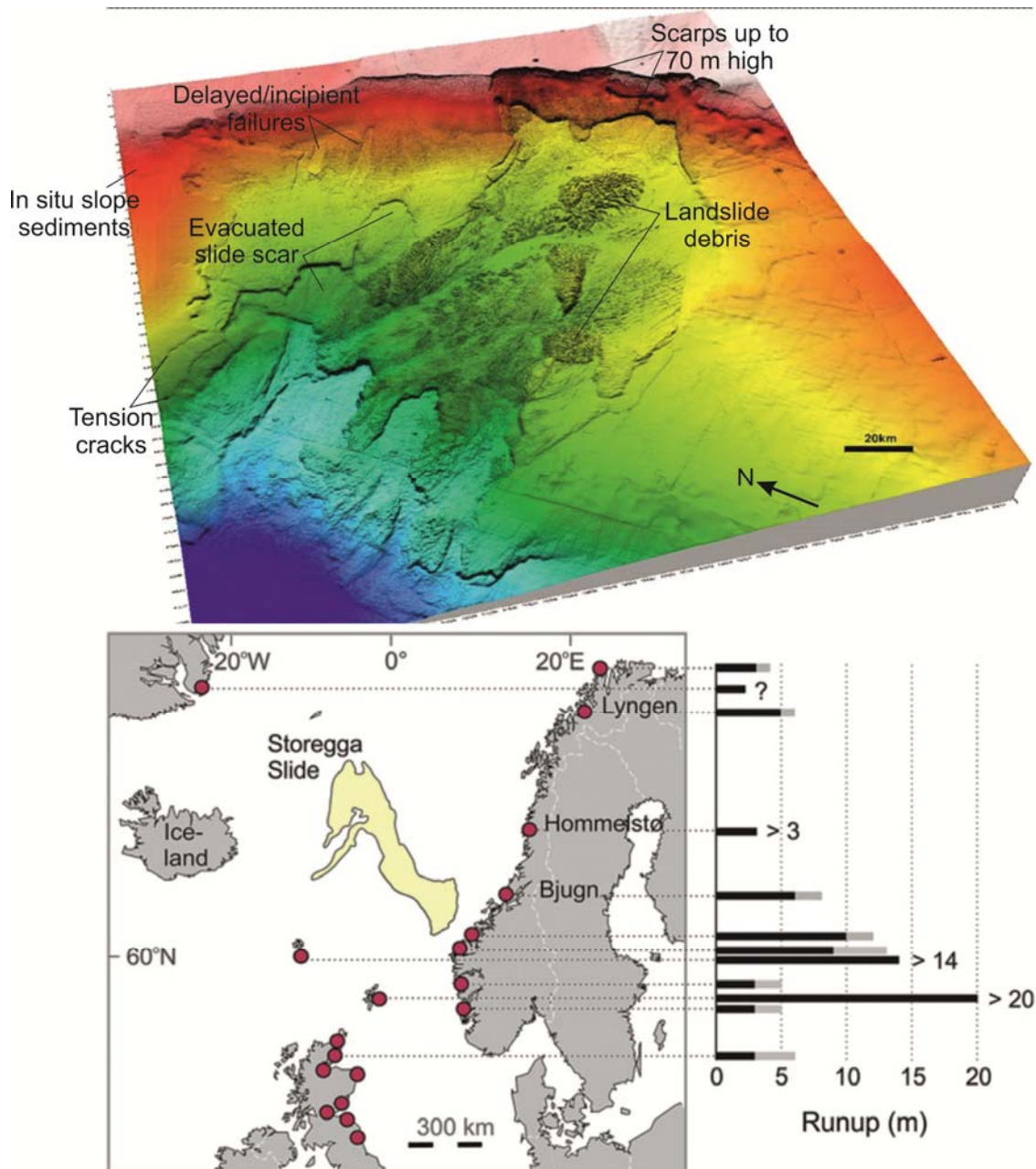


Figure 1.5: Seafloor rendering of the giant Storegga Slide (above) that occurred 8,200 years ago and comprised $>3000 \text{ km}^3$ of sediment (from Masson et al., 2006). The image below shows the location of the slide and identified tsunami deposits (red dots). Black bars illustrate minimum run-up heights and grey bars maximum run-up heights (from Talling et al., 2014).

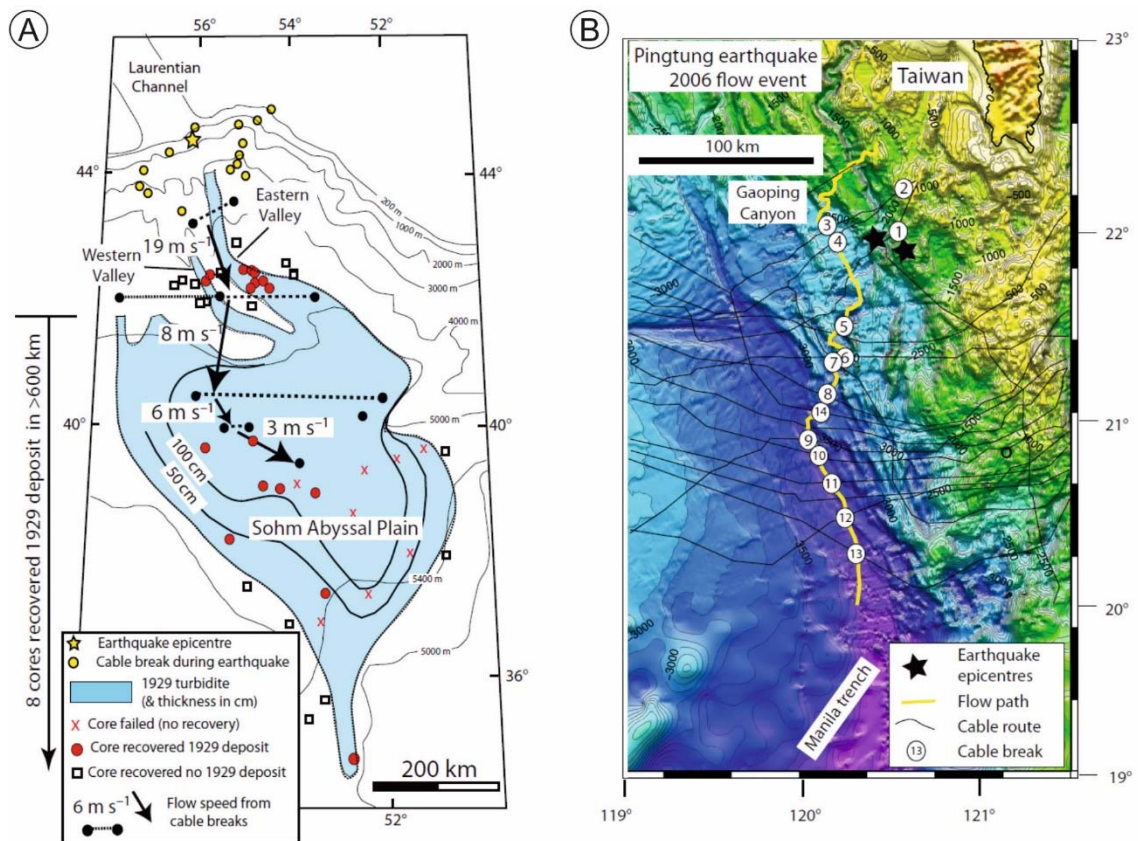


Figure 1.6: Evidence of cable breaks that demonstrate the fast speeds and long travel distance of turbidity currents. The 1929 Grand Banks earthquake-triggered turbidity current (A) reached a maximum frontal velocity of 19 m/s based on cable breaks. Sequential cable breaks are shown for the flow triggered by the 2006 Pingtung earthquake offshore Taiwan (B). (Modified from Talling et al., 2012; see also references therein).

1.4.4 Implications for expensive oil and gas infrastructure

The present day environments in which submarine landslides and turbidity currents occur are often also those which feature important oil and gas accumulations (Figure 1.7). Offshore extensions of large river deltas (e.g. Nile Delta - Thomas et al., 2010a), deep-sea canyons (e.g. Congo Canyon - Cooper et al., 2013), tectonically-deformed slopes (e.g. Offshore Borneo – Shipp and Lu, 2011), and areas of continental slope modified by submarine landslides (e.g. North-west Shelf, Australia – Hengesh et al., 2011) are a few of the settings where submarine landslides and turbidity currents have been observed or interpreted from sedimentological evidence. Large and fast landslides and flows pose a serious hazard to expensive oil and gas seafloor installations, especially in deep-water (Thomas et al., 2010b) where mitigation, re-routing or repair is costly and logistically challenging (Table 1.2). Loss of product due to rupture can have damaging environmental consequences (as demonstrated by the recent Gulf of Mexico Deepwater Horizon incident, albeit triggered by other means; Skogdalen and Vinnem, 2012) and can

lead to large financial impacts to the operator due to lost or delayed production (Kaiser et al., 2009).

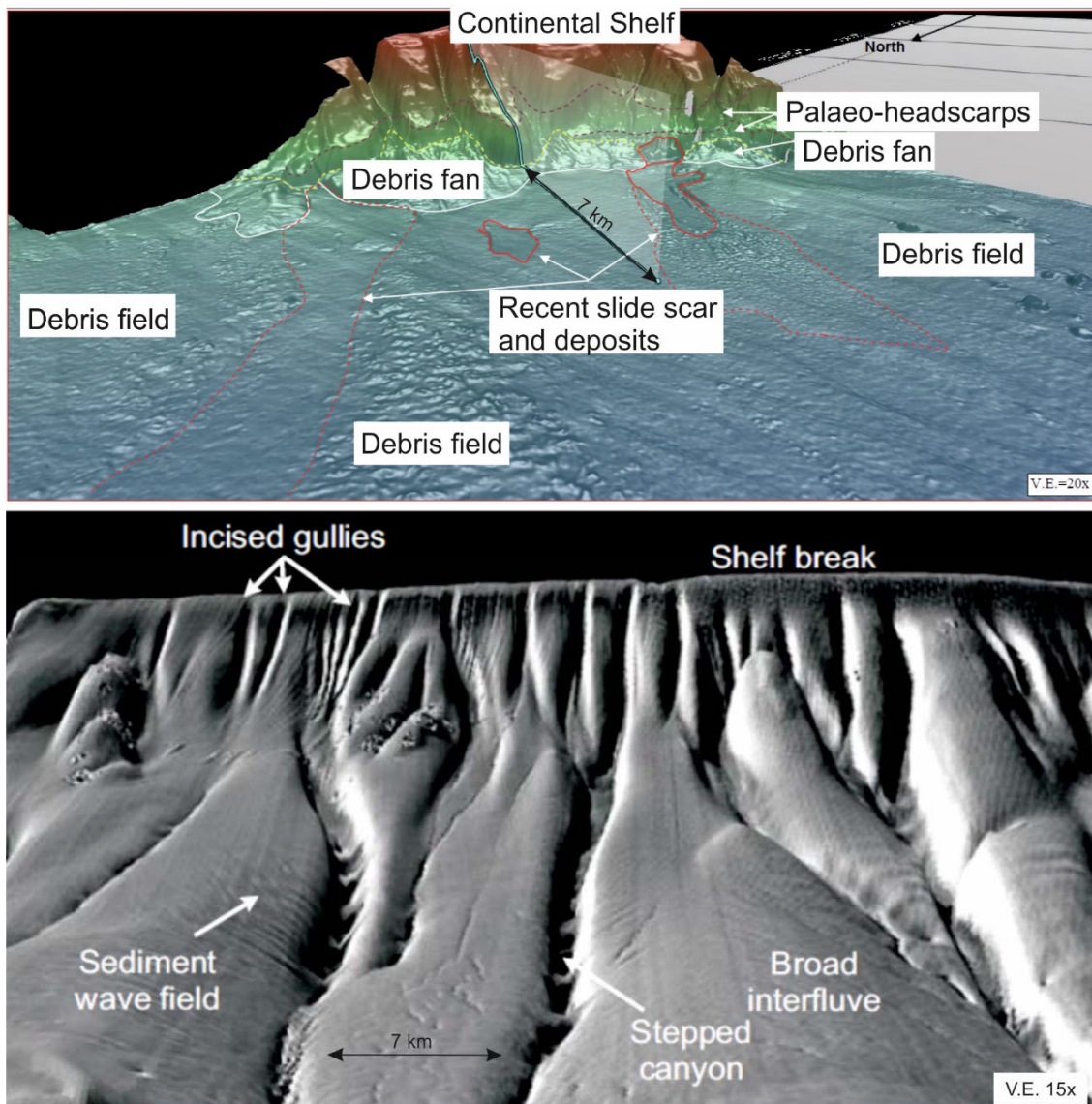


Figure 1.7: Example seafloor images from active and proposed oil and gas development areas. The North-west shelf Australia (above; Hengesh et al., 2011) shows evidence for multiple large submarine landslides with associated blocky run-out. Offshore Ghana, West Africa (below; Clare et al., 2015c) features multiple stepped canyons that have acted as a conduit for high density turbidity currents within the last 20 ka. Vertical exaggeration (V.E.) annotated.

Table 1.2: Possible mitigation measures for landslide-turbidity current hazard posed to seafloor structures (from Clare et al., 2015)

| Mitigation Strategy | Mitigation Measure | Example Case Study | Considerations |
|---|---|--|---|
| Change layout concept | Selection of different layout concept | Floating Liquefied Natural Gas (FLNG) option instead of pipeline (e.g. proposed Prelude development, NW Shelf Australia) | Unproven technology, other issues e.g. metocean hazards |
| Complete avoidance | Avoid geohazardous area entirely | Congo Canyon crossing routed beneath the canyon by directional drilling (construction costs ~\$2 billion; Chevron, 2014) | High costs and/or challenging logistics |
| Avoidance through re-routing | Select more preferable canyon/channel-crossing point, or route around area if possible | South Asia Gas Enterprise (SAGE) pipeline routed to south of Indus Fan to decrease likelihood of impact by sediment density flows (SAGE, 2010) | May not be possible to avoid Expensive to re-route (~\$3 million per km of pipeline; Smith, 2013) |
| Geohazard-resistant design | Modify pipeline design to reduce impact (e.g. Elevate pipeline above seafloor on piled foundations, or increase wall thickness) | Middle East India Deepwater Pipeline (MEIDP) may use vortex-shedding stakes to reduce turbidity current impact (Nash, 2014). Modify cable diameter (Sonoyama et al., 2013) | Expensive unconventional design which may require additional considerations |
| Shutdown and repair | Not strictly a mitigation measure - involves in-situ repair of pipelines | Deployment of diver-less deep-water repair systems (Norman, 1997; Rebello and Ayers, 2006) | Expensive to deploy such repair systems Delayed production during repair |
| Increase understanding of landslide and/or turbidity current impact on seafloor structures | Monitoring and measurement of experimental and real-world landslides and flows to determine impact forces | Flume tank experiments using novel instrumentation (Clare et al., 2015d) Deployment of novel monitoring instruments at field test-sites (Hughes Clarke et al., 2012, 2013, 2014; Cooper et al., 2013; Talling, 2014; Talling et al., 2015; Clare et al., 2015d) | Scaling effects of experimental work Limitations of existing numerical models |
| This Study: Increase understanding of large landslide and turbidity current frequency and triggers | Statistical analysis of extensive landslide and turbidity current records in relation to different triggering and preconditioning factors | Outcrop, core sample and monitoring-based data analysis | Necessary to characterise a range of settings worldwide over different timescales and climatic events |

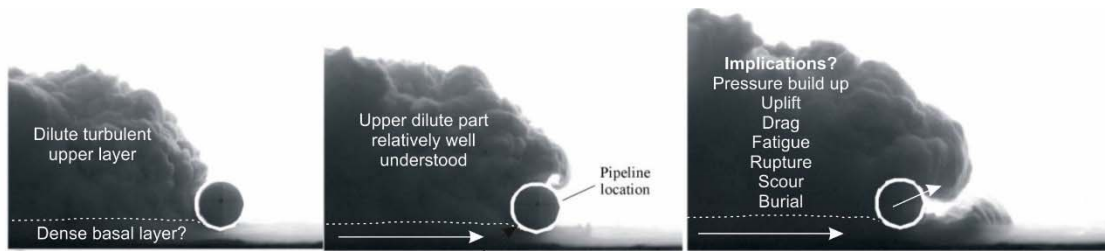


Figure 1.8: Some potential implications for pipelines, cables and umbilicals in relation to impact by a turbidity current. From Clare et al. (2015d) after De Their and Janssens (2012) and Spinewine et al. (2013)

1.4.5 Connecting the two major processes for sediment transport on earth - river systems and turbidity currents

River systems are responsible for the majority of sediment that is transported to the sea, and turbidity currents dominate the sediment transport into many parts of the deep ocean (Talling et al., 2012). It is therefore no surprise that the most extensive sediment accumulations on Earth (submarine fans) occur in association with the world's major rivers (Covault, 2011; Figure 1.9). Despite this, the precise link between terrestrial river systems and offshore turbidite systems is not well understood (Piper and Normark, 2009). As some individual turbidity currents have been documented to contain more than ten times the annual sediment flux for all of the world's rivers (Milliman and Syvitski, 1992; Talling et al., 2007a,b) there cannot always be a direct link between river discharge and transport of sediment to the deep-sea.

The generation of hyperpycnal flows has been proposed in some marine settings, due to the plunging of relatively dense river flood (Mulder and Syvitski, 1995; Mulder et al., 2003). Submarine hyperpycnal flows are considered to be less common than in freshwater settings due to the higher density of seawater; however, some rivers are thought to be capable of creating such flows during extreme flood events (Mulder et al., 2003; Dadson et al., 2005; Warrick et al., 2008). Talling (2014) recognised that there is potential for these flows to enter the ocean infrequently, but asked whether these plunging discharges are capable of generating long run-out flows that reach the deep ocean? This is a key question for understanding global sediment transport flux and the triggering of flows.

Evidence from in-situ monitoring has indicated that some flows coincide with river flood peaks (Khripounoff et al., 2009; 2012). However, it is not known whether there was a direct connection between the river discharge which plunged, or if that sediment may

have been stored on the delta lip for a brief period and was actually triggered by wave or tidal loading, or some other process.

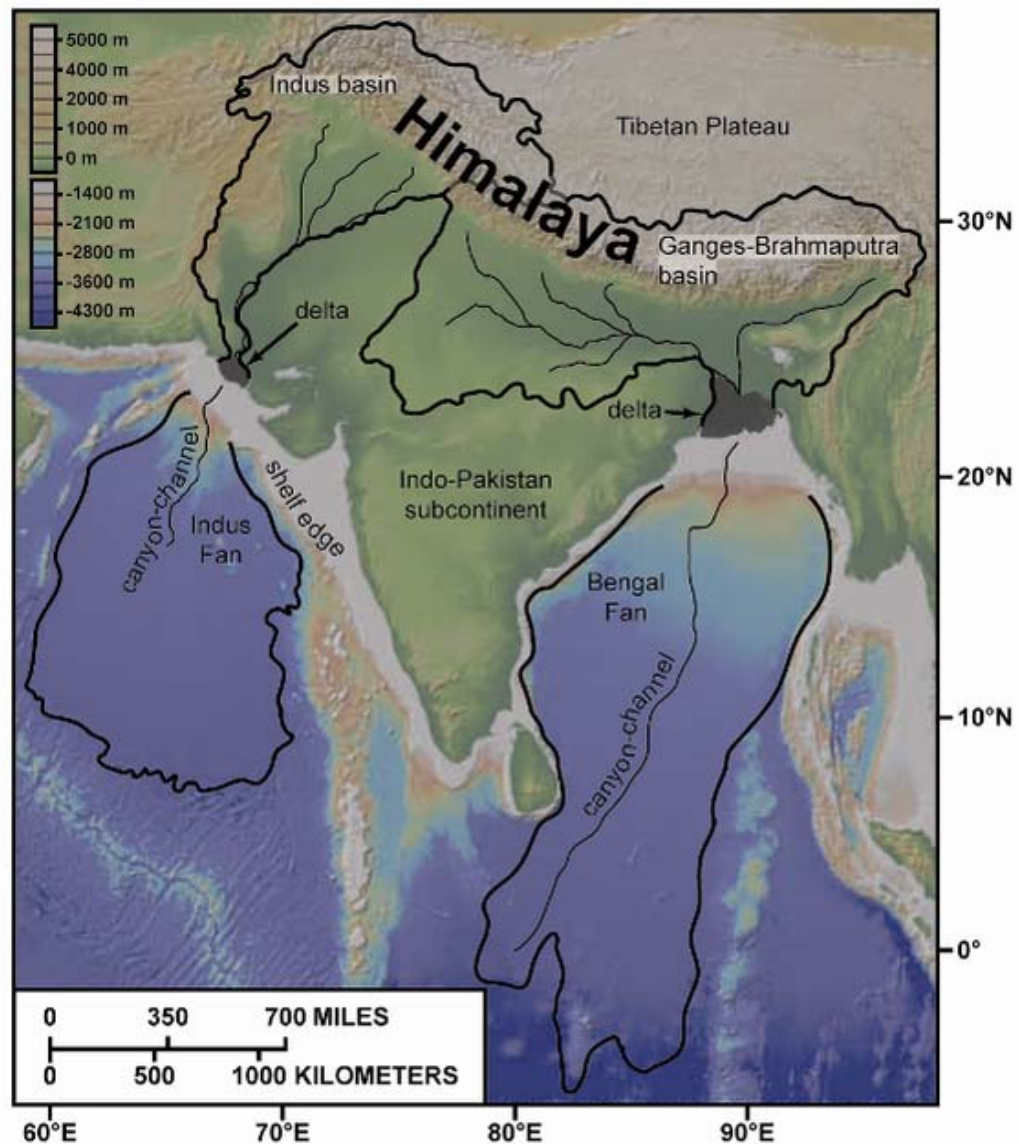


Figure 1.9: Two of the world's largest sediment accumulations, the Indus and Bengal submarine fans, occur offshore from the large watersheds that drain the Himalayas (from Covault, 2011). Turbidity currents are responsible for the submarine transport of sediment to deep-water, but the connection between onshore river and offshore systems is not well understood.

Powerful long run-out flows occurred in the Gaoping Canyon, Taiwan, including one flow that occurred two days after the 2009 Typhoon Morakot flood discharge had ceased (Carter et al., 2012; Figure 1.10). This two day lag indicates that the flow may have been triggered by failure of rapidly deposited sediment in the canyon head and not plunging river flood water. Evidence from the Congo Canyon also indicates that several flows may occur at prolonged periods after the peak in discharge; hence, they do not have a hyperpycnal origin (Heezen et al., 1964; Azpiroz et al., In Prep.). They may be attributed

to storm or wave loading, or simply due to the effects of sudden deposition of unconsolidated sediment.

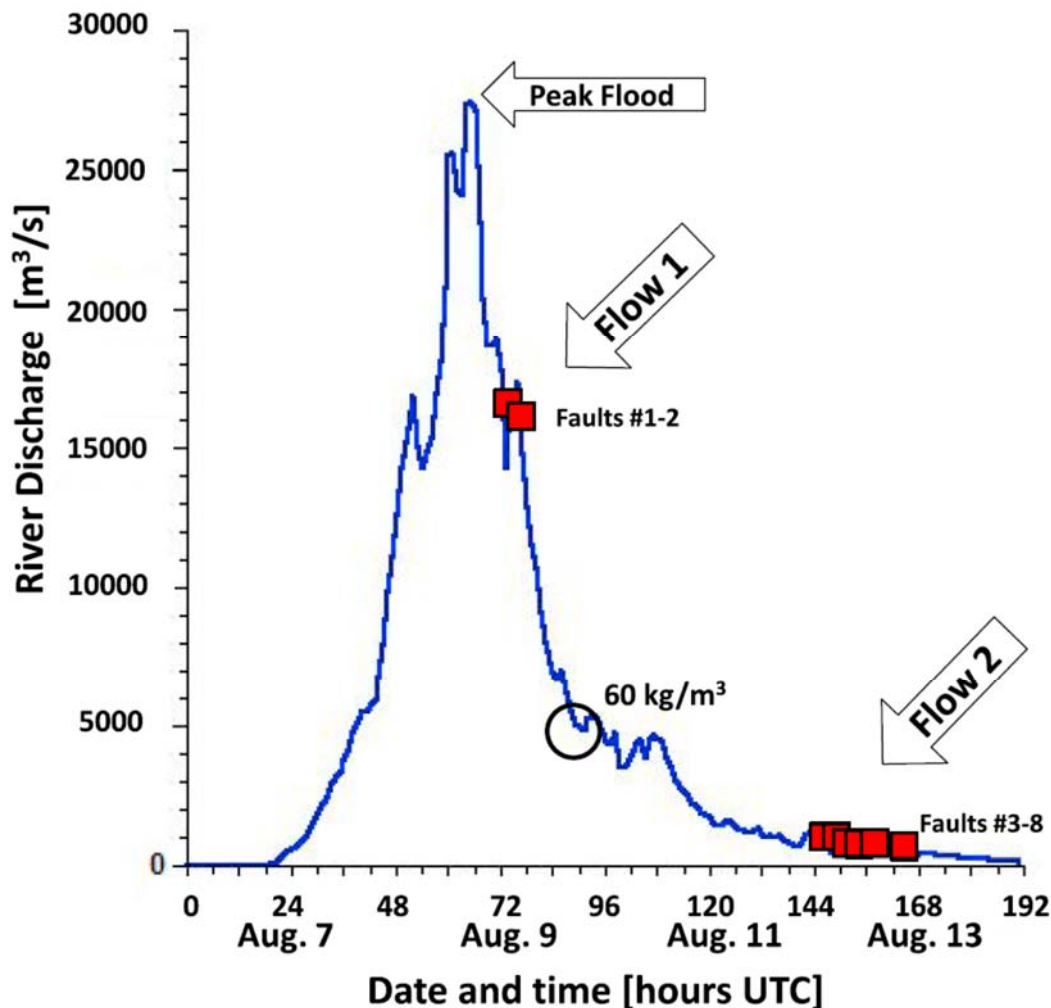


Figure 1.10: Water discharge profile for the Gaoping River during Typhoon Morakot in 2009 from Carter et al. (2014). Cable breaks are shown as red squares for: Flow 1, which occurred under near-peak flood conditions and is assumed to have been due to hyperpycnal conditions; and Flow 2 which occurred two days after the peak under near-normal fluvial discharge

Pioneering, direct flow monitoring at Bute and Knight Inlets in British Columbia, Canada, provided the accurate timing of the arrival of several turbidity currents (Bornhold et al. 1994; Figure 1.11). At both Bute and Knight Inlet, not all events closely relate to specific discharge maxima and many occurred several days after peaks in river discharge. To determine whether flows are triggered directly by plunging river floodwater, or by some other process, it is crucial to know the exact timing of flows from monitoring, the influence of other potential triggering mechanisms that may have been in operation, and also to have an understanding of the changes in morphology of the slope and delta lip. This is important, because without understanding the change in seafloor features, it is

impossible to know whether a slope failure triggered a flow coincident with an increase in river discharge, rather than triggering by plunging river flood water itself. This is only possible through high resolution repeat seafloor mapping and deployment of seafloor-mounted or moored instruments (Section 1.5.3; Table 1.5). Only one location worldwide is known to the author where this has currently been achieved and that is the Squamish prodelta, British Columbia (Hughes Clarke et al., 2012; 2013; 2014; Chapter 8).

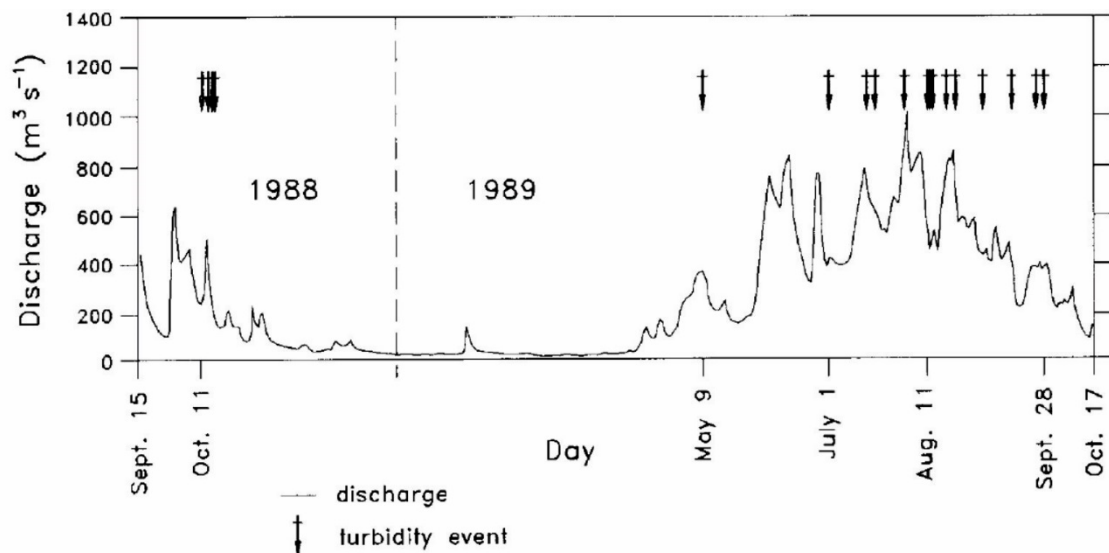


Figure 1.11: Record of Homathko River discharge at Bute Inlet, British Columbia during monitoring period from Bornhold et al. (1994). Times of turbidity current arrival as determined by the turbidity current event detector (TED) are annotated above. Note that turbidity currents appear to be coincident with periods of elevated river discharge but it is not possible to determine whether they were triggered by hyperpycnal flow, delta lip failure, or some other process / combination of processes.

1.5 How can we acquire records of landslide-turbidity current recurrence?

Given the importance of submarine landslides and turbidity currents, there is therefore a need to analyse records of their past occurrence and understand the significance of potential triggering and preconditioning factors. Obtaining continuous and long term records of submarine landslide and turbidity current activity is challenging, however. While many previous studies provide invaluable insights into system evolution, changes in sediment budget through time, and fundamental understanding of sediment transport processes, they also have shortcomings. Of most relevance to the study in this thesis, is that most previous studies typically do not include a sufficient number of events for robust statistical analysis, nor do they not allow for determination of individual inter-event recurrence intervals. A large degree of uncertainty thus remains, specifically with regard to determining the characteristic frequency distribution of recurrence and

quantifying the significance of potential triggers. The following text summarises and discusses the types of data from which event recurrence is commonly derived, which includes sedimentary records (e.g. core and outcrop studies), indirect observations (e.g. seafloor cable breaks), and direct monitoring (e.g. current meters).

1.5.1 Depositional records of submarine landslides and turbidity currents

Outcrop studies can provide records of ancient submarine events. Coring of offshore deposits can provide evidence of much more recent activity (typically gravity or piston coring) and older and longer-term records (usually requiring coring from a drillship). Deposits are diagnosed on the basis of sedimentary structures such as shown in Figure 1.13, Figure 1.14 and detailed further in Chapter 3.

Submarine landslide frequency studies based on deposits typically analyse fewer than ten events (e.g. Geist and Parsons, 2010; Figure 1.13E). Exceptions exist with up to 68 dated events (e.g. Urlaub et al., 2013; Figure 1.12); however, published global databases only extend back in time to a maximum of 180 ka. Of the previous studies that have attempted to quantify recurrence frequency of turbidity currents (e.g. Droxler and Schlager, 1985; Weaver et al., 1992; Beattie and Dade, 1996; Goldfinger et al., 2003; Romans et al., 2009; Atwater and Griggs, 2012), only a handful of studies consider large numbers of events ($N > 106$) over long (> 1 Myr) timescales (e.g. Weaver et al., 1986; Clare et al., 2014; Hunt et al., 2014). A summary of existing studies of global submarine landslide (Table 1.3) and regional to local landslide and turbidity current recurrence (Table 1.4) is now presented.

Table 1.3: Summary of global submarine landslide recurrence studies

| Number of Events [N] | Location (Data type) | Time Range | Technique / Assumptions | Recurrence between individual events possible? | Study Reference |
|----------------------|--|------------|--|--|----------------------|
| 19 landslides | Global submarine landslide record (core samples) | 0-20 ka | Radiocarbon dating individual landslide deposits | ✓ (On a global basis, but some locations only feature one dated landslide) | Lee (2009) |
| 26 landslides | Global submarine landslide record (core samples) | 0-45 ka | Radiocarbon dating individual landslide deposits | ✓ (On a global basis, but some locations only feature one dated landslide) | Owen et al. (2007) |
| 68 landslides | Global submarine landslide record (core samples) | 0-45 ka | Radiocarbon dating individual landslide deposits | ✓ (On a global basis, but some locations only feature one dated landslide) | Urlaub et al. (2013) |

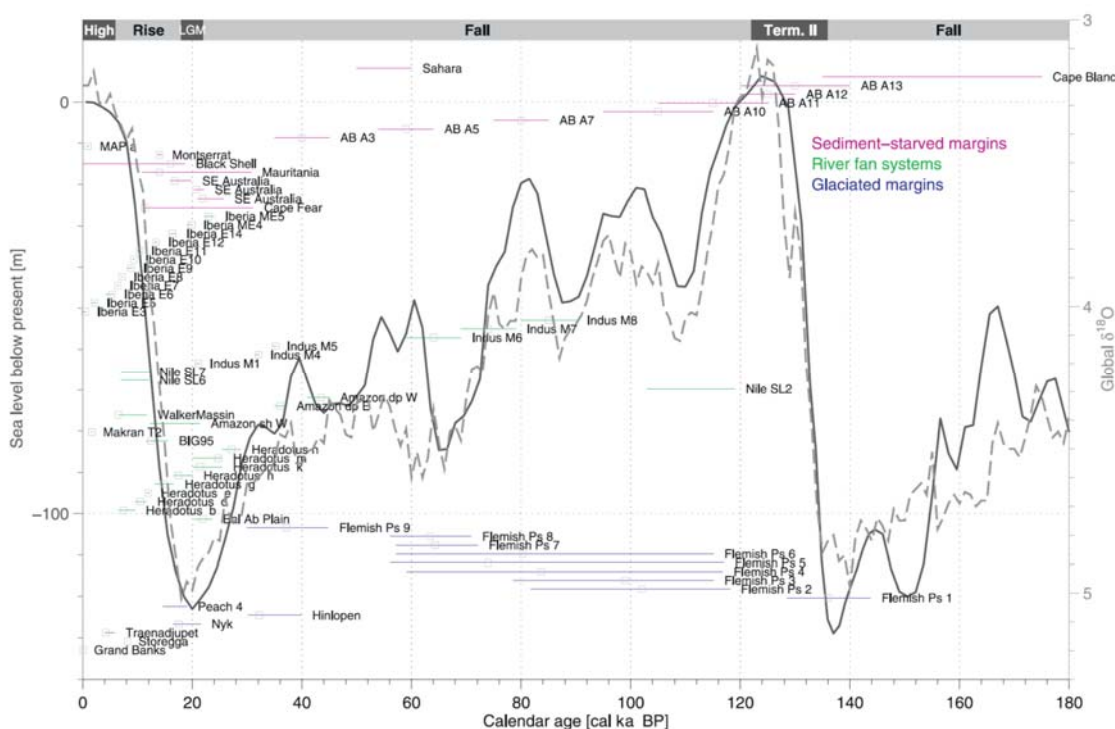


Figure 1.12: Global database of large ($>>1 \text{ km}^3$) submarine landslides from Urlaub et al. (2013). Mean sea level (dark grey) and benthic $\delta^{18}\text{O}$ (light grey) curves are shown. This database includes 68 dated submarine landslides and is the most complete global database published at the time of writing.

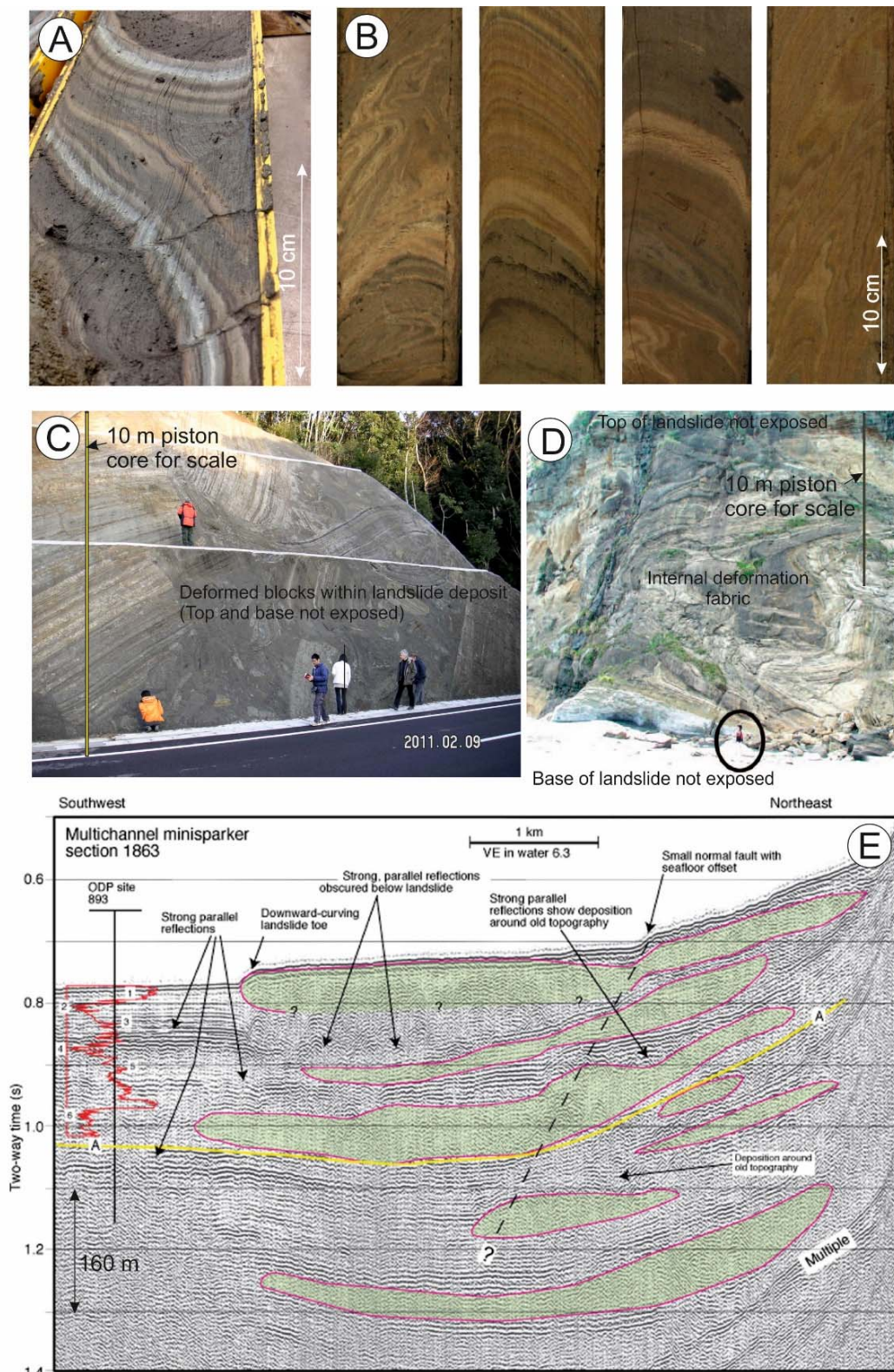


Figure 1.13: Examples of large submarine landslide deposits from core and outcrop. (A) Piston core sample from the Traenadjupet Slide, offshore Norway (Courtesy of Millie Watts, <http://slidesinthedeep.blogspot.co.uk/>). (B) Piston core samples from submarine landslides from the Western Mediterranean (Courtsey of Fugro). (C) Late Pliocene submarine landslide deposit from the Boso Peninsular Japan (<http://www.cneas.tohoku.ac.jp/labs/geo/ishiwata/SendaiSympto3.htm>), (D) Late Miocene submarine landslide deposit from the Taranaki Basin (King et al., 2011). (E) High resolution seismic reflection data from the Santa Barbara Channel, southern California (Geist and Parsons, 2010). Images C to E demonstrate the exceptional thickness of proximal landslide deposits, hence it is very difficult to sample large numbers, even by coring from a drillship.

Table 1.4: Summary of regional and local landslide and turbidity current recurrence studies

| Number of Events [N] | Location (Data type) | Time Range | Technique / Assumptions | Recurrence between individual events can be determined? | Study Reference |
|----------------------|---|-----------------|---|--|--|
| <7 landslides | Port Valdez, Alaska and Santa Barbara Channel (core and seismic data) | 0-200 ka | Sparse radiocarbon dating and age inference based on seismic profiling data | ✓ (but large assumptions made between dated horizons) | Geist and Parsons (2010) |
| 7 turbidites | SW Iberian Margin (cores) | 0-10 ka | Radiocarbon dating of individual beds | ✓ | Gracia et al. (2010) |
| 8 turbidites | Madeira Abyssal Plain (core samples) | 0-1.5 Ma | Good biostratigraphic control and hemipelagic mud can be differentiated | ✓ | Hunt et al. (2013) |
| 9 landslides | Ursa Basin, Gulf of Mexico (core samples) | 13.5-65 ka | Age model based on biostratigraphy and magnetostratigraphy | ✓ | Geist et al. (2013) |
| 9 turbidites | Madeira Abyssal Plain (core samples) | 0-190 ka | Possible to identify hemipelagic mud between turbidites. No evidence for erosion. Good biostratigraphic control. | ✓ | Weaver and Rothwell (1987) |
| 19 turbidites | Santa Monica Basin, Offshore California (ODP Site 1015; core samples) | 0-7 ka | Radiocarbon dating. Each bed not individually dated, therefore data are binned, but possible to differentiate hemipelagic mud | ✓ | Romans et al. (2009) |
| 21 turbidites | Cascadia Margin (core samples) | 0-10 ka | Radiocarbon dating | ✓ | Goldfinger et al. (2003), Atwater and Griggs, (2012) |
| 28 turbidites | Madeira Abyssal Plain (core samples) | 0 -750 ka | Possible to identify hemipelagic mud between turbidites. No evidence for erosion. Good biostratigraphic control | ✓ | Weaver et al. (1992) |
| 54 turbidites | Lake Villarica and Calafquen, Chile (core samples) | Present-1100 AD | $^{210}\text{Pb}/^{137}\text{Cs}$ dating and varve counting | ✓ | Moernaut et al. (2014) |
| 60 turbidites | Bahamas (core samples) | 0-195 ka | Radiocarbon dating. Not possible to date individual events, nor distinguish hemipelagic mud between each bed due to frequent amalgamation | ✗ (Necessary to bin data) | Droxler and Schlager (1985) |
| 73 turbidites | Poverty Bay, New Zealand | 0-18 ka | Radiocarbon dating of 28 beds and inference of ages in between | ✓ | Pouderoux et al. (2012) |
| N=106 THRESHOLD | | | | | |
| 125 turbidites | Madeira Abyssal Plain (core samples) | 0-7 Ma | Good biostratigraphic control and hemipelagic mud can be differentiated | ✓ | Hunt et al. (2014); Chapter 5, This Study |
| 151 turbidites | Balearic Abyssal Plain (core samples) | 0-150 ka | Radiocarbon and biostratigraphic dating. Hemipelagic mud can be resolved | ✓ | Clare et al. (2014) Chapter 5 This Study |

| Number of Events [N] | Location (Data type) | Time Range | Technique / Assumptions | Recurrence between individual events can be determined? | Study Reference |
|---------------------------------|--|----------------------------------|---|--|--|
| 179 turbidites | Gorrandatxe Fan-Fringe, Western Pyrenees (outcrop study) | Eocene | Binned relative to pelagic thickness. Poor age control | ✗ (Necessary to bin data) | Payros and Martinez-Braceras (2014) |
| <478 turbidites | Coral Sea Basin and Sea of Japan (DSDP Sites 210 and 287; core samples) | Late Pleistocene to Late Miocene | Poor age control. Data binned per period (e.g. late Pleistocene – Early Pleistocene) | ✗ (Necessary to bin data) | Klein (1984) |
| 532 turbidites | Izu Bonin Basin, Western Pacific Ocean (ODP Site 792 & 793; core samples) | Oligocene | No age control Recurrence calculated from mud thickness including hemipelagic and possibly turbidite mud; hence not accurate | ✗ (Inaccuracies in method) | Beattie and Dade (1996) |
| 697 turbidites | Marnoso-arenacea, Italian Apennines (outcrop study) | Mid Miocene | Biostratigraphic control at start and end of sequence. Hemipelagic mud can be differentiated | ✓ | Malgesini (2012), Chapter 5, This Study |
| 1571 turbidites | Iberia Abyssal Plain, Iberian Margin | Cretaceous-Eocene | Biostratigraphic control. Hemipelagic mud can be differentiated | ✓ | This Study, Chapter 7 |
| 2020 turbidites | Eel Fan, California (ROV observations of submarine outcrop and sediment cores) | 0-4.9 ka | Radiocarbon dating of 48 wood fragments from outcrop | ✗ (Averaged between dated points) | Paull et al. (2014) |
| 2865 turbidites | Zumaia, NE Spain (outcrop study) | 65-48 Ma | Age model based on biostratigraphy and magnetostratigraphy. Turbidites recorded per metre of hemipelagic mud and not recorded individually. Hemipelagic mud is resolvable however | ✓ (But binned in previous studies) | Winkler and Gawenda (1999), Chapter 6 This Study |
| ~6000 turbidites? (not defined) | Andøya submarine Canyon, north-Norwegian continental margin | 0-<20 ka | Age model based on biostratigraphy and radiocarbon dating. Not possible to resolve inter-event intervals | ✗ (Averaged for periods 0-15 ka and >15 ka) | Amundsen et al. (2015) |

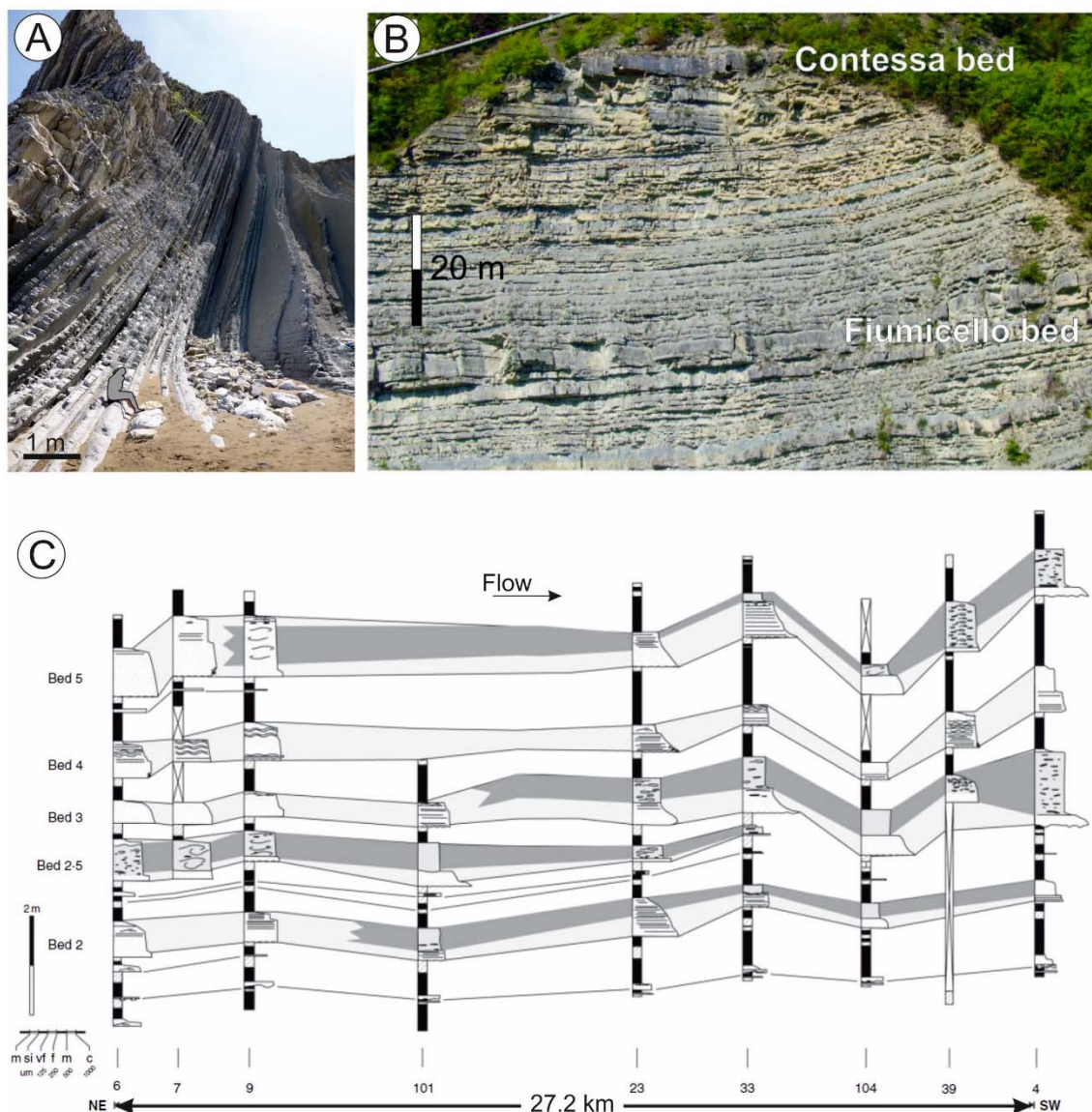


Figure 1.14: Examples of large volume distal basin plain turbidite-hemipelagite sequences from which turbidite recurrence intervals can be derived. Note they are tabular, continuous and lack erosional bases. Photos are from (A) an Eocene outcrop at Zumaia, north-east Spain, and (B) the Miocene Marnoso-arenacea Formation in the Italian Apennines where the beds can be walked out and correlated for tens of kilometres (C). B and C from Amy and Talling (2006). In both cases, hemipelagic mud can be clearly resolved from turbidite mud (see Chapter 3).

Some of the limitations of existing core and outcrop studies are now discussed, with respect to landslide and turbidity current frequency analysis, and an outline some prerequisites for suitable analysis is presented.

1.5.1.1 Limitation 1: Incomplete sedimentary records

Many deep-water settings are not suited for the study of individual landslide or turbidite deposits may not be recorded (e.g. areas of bypass on the upper slope or within canyons), may be subject to intense reworking or erosion by successive landslides or

flows (e.g. amalgamation of beds at a fan, or removal of deposits within canyons; Hubbard et al., 2014), or may themselves be remobilised (e.g. channel levee or canyon flank instability; Amundsen et al. 2015). It is generally only at the distal part of a deep-water system, the basin plain, where flows decelerate and deposit over large areas, rather than bypass or erode (Mutti 1977; Weaver and Rothwell, 1987). Therefore, distal basin plains provide good candidate locations for studying continuous sedimentary records of landslide and turbidity current frequency.

1.5.1.2 *Limitation 2: Limited number of events for analysis*

It is necessary to sample a large number of events for a robust statistical analysis of event frequency. The number of events required for statistical analysis is defined as the minimum sample size. The definition of minimum sample size can be formulated, based on three parameters: *alpha*, defined as the probability of making a Type I error (an incorrect rejection of a null hypothesis); *power* which is defined as one minus the probability of making a Type II error (not rejecting a null hypothesis); and *effect size*, the degree to which the explanatory variable is related to other predictor variables in the population (Green, 1991). The methods outlined in Harris (1975), Cohen (1988), Green (1991) and Tabachnick and Fidell (2007) set the alpha value at 0.05 (the traditional level assigned to significance, and determines the power from tables presented in Cohen (1988). Power is set at 0.8; a value proposed by Cohen (1988) as appropriate for a wide range of research areas (initially for behavioural research). As summarised in Green (1991), the setting of power is to some extent arbitrary, but should be dependent on the loss associated with making a Type II error. Power should also be a function of the loss associated with a Type I error. Cohen (1988) suggested that a 4 to 1 ratio reflects the relative seriousness of a Type I error to a Type II error. Therefore, when alpha is taken as 0.05, the probability of a Type II error should be $4 \times 0.05 = 0.20$ and power would be $1 - 0.20 = 0.80$.

Two indices of effect size can be used for regression analysis, f^2 (Cohen's effect size) and R^2 (correlation coefficient) (Green, 1991). These two variables are linked as

$$f^2 = R^2 / (1 - R^2)$$

Choices of values for effect size (R^2 or f^2) may depend on research area but Cohen (1988) states that R^2 values of 0.02, 0.13 and 0.26 and f^2 values of 0.02, 0.15 and 0.35 should serve as a general convention for describing small, medium and large effect sizes.

Various rules of thumb exist to determine the threshold limit of observations which take into account effect size, as well as the number of explanatory variables or predictors. Tabachnick and Fidell (2007) state that the number of observations required when testing for a full regression model is $N > 50 + 8(k)$ (initially from Harris, 1975) and for testing individual predictors is $N > 104 + k$ respectively; where N is the number of observations and k is the number of independent variables being tested against. This assumes that you wish to test for a medium effect size and alpha is set at 0.05. Thus, if you are interested in the influence of sea level (one predictor), you require at least $N=58$ to 105, and for two predictors the level is $N=66$ to 106. If you consider the effect of additional variables, or there is considerable uncertainty in the measurement of the observations, this minimum threshold will increase (Figure 1.15).

The method of Green (1991) computes the minimum sample size as

$$N > L/f^2$$

where

$$f^2 = R^2 / (1 - R^2)$$

$$L = 6.4 + 1.65k - 0.05k^2$$

If the effect size of the explanatory variable that we wish to investigate is small, a minimum sample size of $N=390-481$ (Cohen, 1988) or $N=400-475$ (Green, 1991) is required. Not all of the datasets presented in this thesis attain such a sample size; however, the key questions posed here (i.e. do variables such as sea level or global temperature exert a *strong* or *dominant* control) can be answered, as the datasets exceed both medium and small effect size thresholds. This present study considers one to two explanatory variables, hence, a minimum sample size of $N=24-30$ (Cohen, 1988) or $N=23-27$ (Green, 1991) is required to determine large effects and $N=53-66$ (Cohen, 1988) or $N=53-63$ (Green, 1991) for medium effects. The rule of thumb suggested by Harris (1975) for a full regression model (i.e. $N > 50 + 8(k)$) shows a reasonable similarity with the analysis considering a medium effect size, which may indicate that this is a simple rule that may

be used for testing dominant to moderate-strength variables. The rule of thumb of Tabachnick and Fidell (2007) for testing individual predictors (i.e. $N > 104 + k$) provides a much more conservative calculation of sample size for less than eight explanatory variables compared to the other methods, and assumes a medium to large effect size is in operation. Tabachnick and Fidell go on to recommend that “the data analyst choose the larger number of cases required by these decision rules”. A summary of the different sample size minima are presented graphically in Figure 1.15.

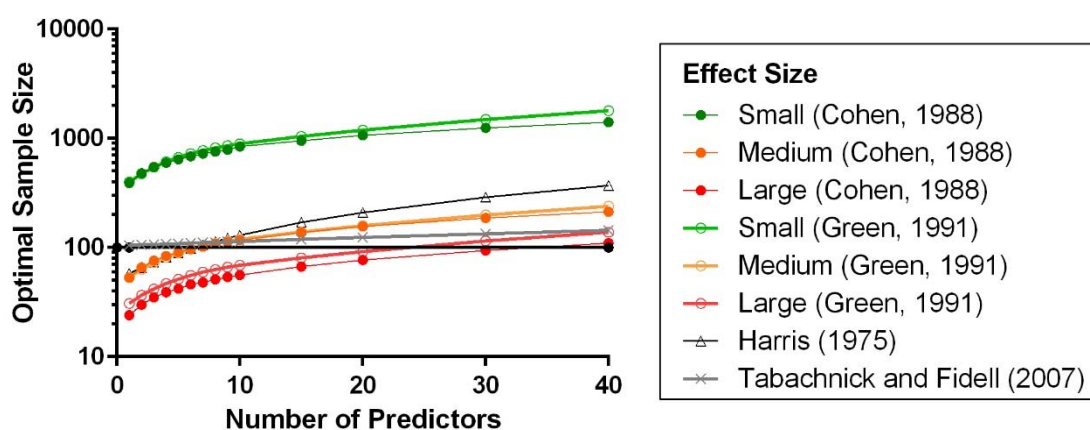


Figure 1.15: Sample size required to test the hypothesis that population multiple correlation equals zero with a power of 0.80. Plotted from data in Green (1991), after rules of thumb by Harris (1975) and Tabachnick and Fidell (2007) and analysis by Cohen (1988). $N=100$ shown by solid horizontal line.

As this study considers a maximum of two explanatory variables per analysis, at least $N=53$ to 106 observations are required for robust statistical analysis using regression-based methods that take into account a medium to large effect size and up to two explanatory variables (Figure 1.15). For conservatism, the upper threshold of $N=106$ is set as a minimum sample size, in line with recommendations made by Tabachnick and Fidell (2007).

This relatively large number ($N > 106$) of required observations is often an issue for direct sampling of large submarine landslide deposits (Geist et al., 2013), as deposits are often difficult to core or drill through and may be very thick (hundreds of metres) (Figure 1.13). In addition, it may be necessary to sample and date different lobes of the same landslide to ensure confidence in the results. For this reason, submarine landslide frequency studies that sample the initial landslide deposit generally consider less than 10 events (Geist and Parsons, 2010). Sampling of deposits from basin plains, however, has

been shown to provide continuous records of large volume turbidites which are interpreted to be the distal deposits of the largest submarine landslides from around the basin margin (Weaver et al., 1986; Rothwell et al., 1998; Talling et al., 2007a,b; Hunt et al., 2013, 2014).

1.5.1.3 Limitation 3: Issues with dating individual events

Even when large numbers of landslide-triggered turbidites are available, it may not be possible to determine recurrence between each event if there is poor or no age control, the inter-event deposits cannot be discerned or there is evidence of erosion/reworking. Recent observations by Paull et al. (2014) provide an exceptional number of events (N=2020), however, the event frequency can only be coarsely determined by averaging the number of beds observed between 48 dated horizons (Figure 1.16).

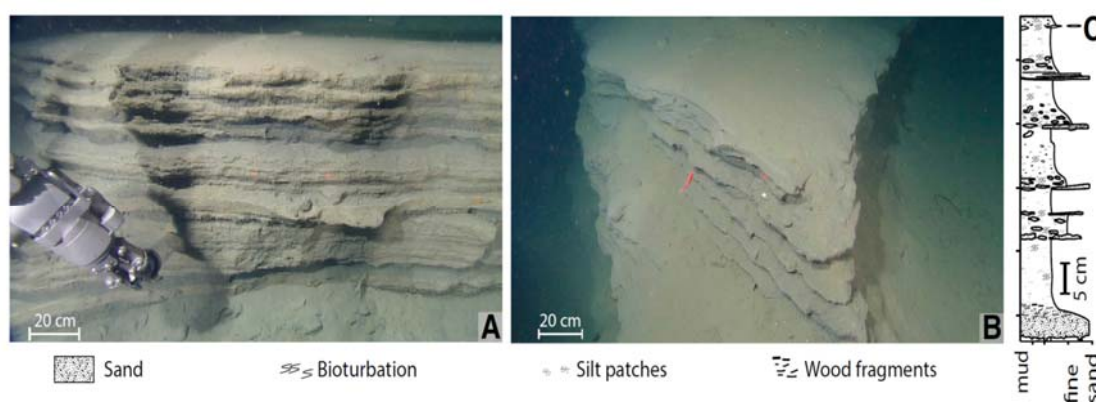


Figure 1.16: Photos of submarine outcrop of turbidites acquired using a remotely operated submarine from the Eel Canyon, offshore California (from Paull et al., 2014)

Beattie and Dade (1999) analysed turbidite recurrence from the Izu-Bonin Basin, western Pacific (N=532) based on the mud thickness between sand beds as a proxy for inter-event time. This is a valid method, but only if you can discern hemipelagic mud (i.e. background settling of sediment) from turbidite mud (i.e. the final stages of deposition following a turbidity current; see Chapter 3). In their study, Beattie and Dade (1999) cannot make this differentiation, which calls into question the validity of their results. Distal basin plain sites that meet this criterion are therefore highly valuable as they may contain continuous records of many large volume turbidites, for which individual recurrence intervals can be determined. Specific examples where this has been documented are the Miocene Marnoso-arenacea formation in the Italian Apennines (Talling et al., 2004, 2007b,c; Malgesini, 2012; Figure 1.17), the Palaeogene Zumaia

flysch, NE Spain (Chapter 6; Winkler and Gawenda, 1999), and the Madeira (Chapter 5; Weaver et al., 1987; Hunt et al., 2014), Balearic (Chapter 5; Rothwell et al., 1998; Hoogakker et al., 2004), and Iberia Abyssal Plains (Chapter 7; Figure 1.13).

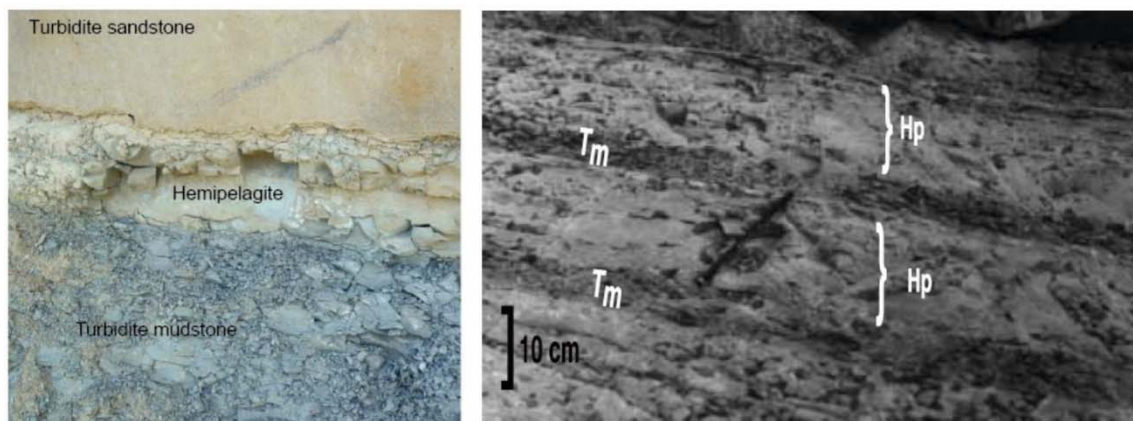


Figure 1.17: Outcrop photographs from the Miocene Marnoso-arenacea Formation, Italian Apennines where hemipelagic mud can be clearly discerned from turbidite mud on the basis of textural and colour differences. Left image from Malgesini (2012) and right image from Talling et al. (2004).

1.5.2 Indirect observations

Indirect observations typically only provide a ‘one-off’ documentation of submarine landslide or turbidity current activity. Much of this indirect data comes from submarine cable breaks (Talling et al., 2013; Carter et al., 2014; Figure 1.18), including the 1929 Grand Banks event (Heezen and Ewing, 1952; Hughes Clarke, 1988; Piper et al., 1988, 1999), Nice Airport harbour collapse in 1979 (Piper and Savoye, 1993; Mulder et al., 1997a), Gaoping Canyon, Taiwan in 2006 (Hsu et al., 2008) and 2009 (Carter et al., 2012), and offshore Algeria in 1954 (Heezen and Ewing, 1955; El Robrini et al., 1985). Of these, the two examples from the Gaoping Canyon indicate that two flows (capable of breaking cables) occurred, initiating at different places (Carter et al., 2012; Hsu et al., 2008). This limited number (i.e. $N=2$) is not, however, a sufficient number of observations for statistical analysis of frequency.

Seafloor observatories are now deployed in many parts of the ocean worldwide to measure oceanographic and seismic variations (Favali and Beranzoli, 2006). Fortuitously for studying mass movements, some of these observatories have provided evidence of submarine landslides (Figure 1.19; Figure 1.20). In 1998, an earthquake-induced landslide was interpreted from hydrophone and seismometer data offshore Papua New Guinea (Okal, 2003). The 1998 landslide is interpreted to have contributed to a deadly

tsunami (Tappin et al., 2001). A volcanic-triggered submarine landslide was detected by a hydrophone at North-west Rota-1 seamount, Mariana Arc (Chadwick et al., 2012). The landslide subsequently destroyed several instruments on the volcano flanks and its effect was clearly visible in the post-event bathymetry (Caplan-Auerback et al., 2014).

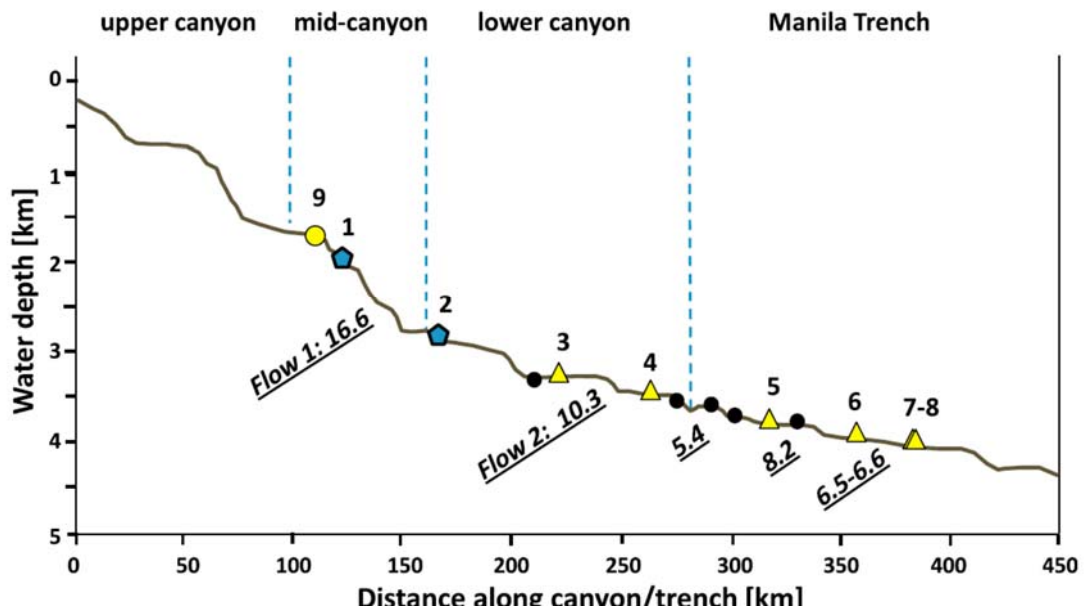


Figure 1.18: Bathymetric profile along Gaoping Canyon and into Manila Trench showing cable breaks in 2009. Flow speeds in m/s are underlined. Cable breaks are colour coded for first (blue polygons) and second (yellow triangles) turbidity currents. Black circles are cables for which no fault data was available. Yellow circle occurred after breaks 7 and 8 and may relate to a delayed failure or some other event soon after the second flow (From Carter et al., 2014)

Analysis of seismometer data on the flanks of Mount Etna, offshore Sicily, also indicates that it may be possible to discern between volcanic, earthquake and submarine landslide signals using seismometer data (Sgroi et al., 2014; Figure 1.19). Dozens of landslides were recorded on the flanks of the West Mata volcano in the Lau Basin, coincident with continuous eruptive volcanic activity (Caplan-Auerback et al., 2014; Figure 1.20). Analysis of seismic signals indicates that the submarine landslides travelled at speeds of between approximately 11 m/s and 25 m/s; however, the precise timing of submarine landslides has not been published at this time. This method seems to be a promising approach to providing longer term records of submarine landslide activity and it is hoped that valuable datasets will be available in the coming years. At this stage, however, there are insufficient records for a detailed analysis of landslide frequency.

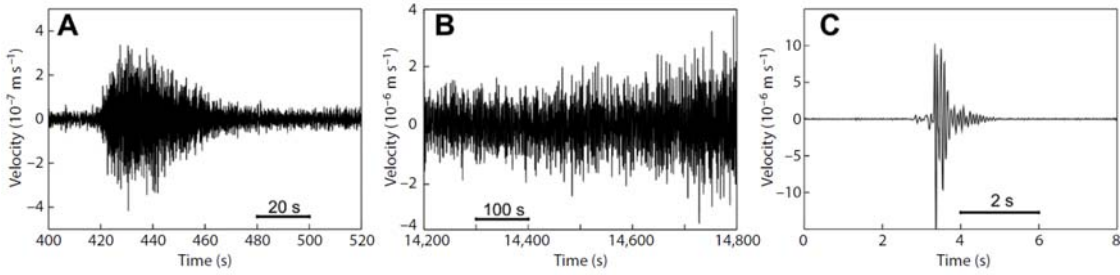


Figure 1.19: Example of waveforms (seismometer vertical component) of the three different types of signal observed in the western Ionian Sea from the NEMO-SNq Seafloor Observatory including A) submarine landslide; B) volcanic tremor recorded during onset of a lava fountain episode; C) short duration events that are interpreted to be related to hydraulic fracturing of rocks during volcanic events. From Sgroi et al. (2014)

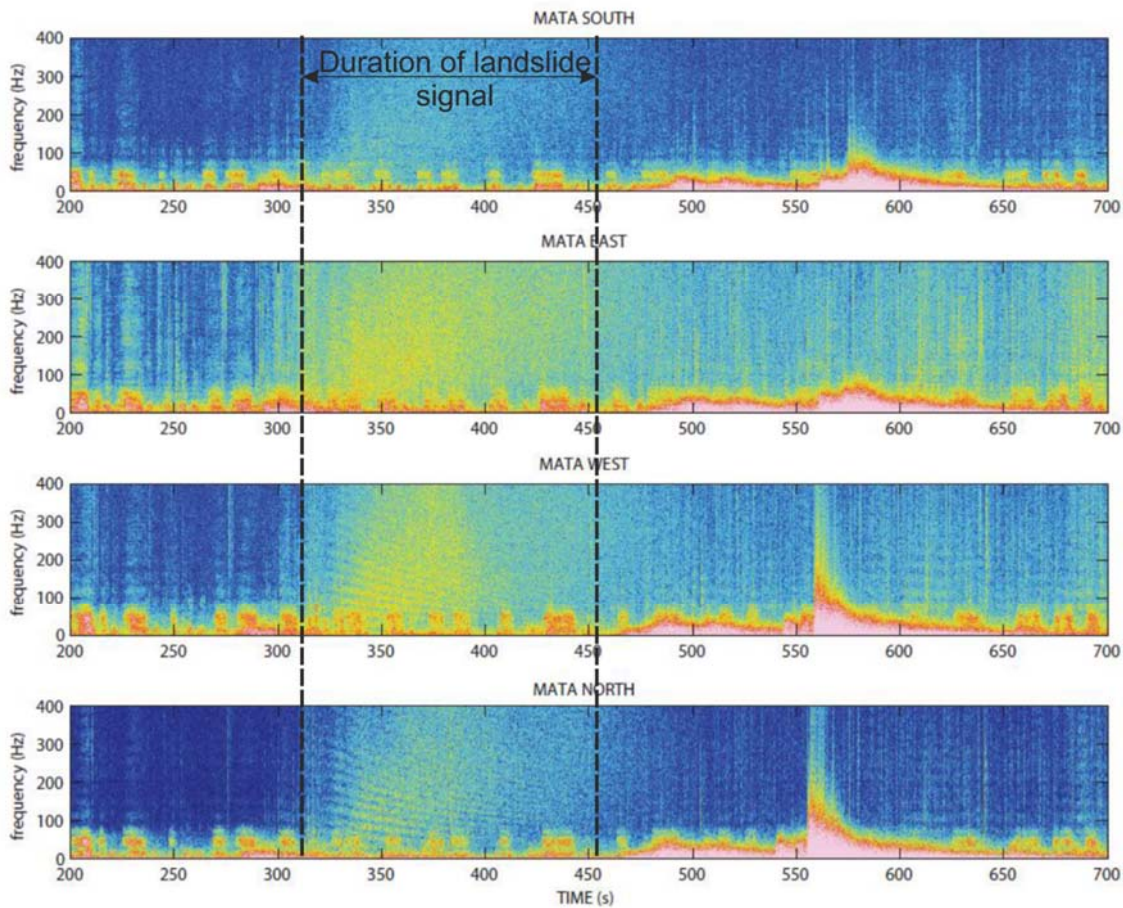


Figure 1.20: Spectrograms of four hydrophones from West Mata volcano, Lau Basin. The low frequency (<50 Hz) signals are interpreted as degassing explosions. The very low frequency signals from ~ 470 – 600 s are regional earthquakes. The signal from ~ 310 – 450 s is interpreted as a landslide, identified by its broadband spectrum and changing frequency content. From Caplan-Auerbach et al. (2014)

1.5.3 Direct Observations

Submarine sediment density flows, such as turbidity currents, are very difficult to monitor directly because of the issues in deploying instrumentation on the seafloor, their relative infrequent recurrence in many locations, and their potential to damage or destroy the monitoring instruments themselves (Khripounoff et al., 2004). Despite these issues, major steps have been made in recent years in the direct monitoring of flows, which has primarily been focused on shallow water sites (e.g. fjords and lakes). Some deployments in water depths of up to 2000 m have been successful (e.g. Cooper et al., 2013). Many of the shallow-water sites show remarkable morphological similarities to deep-water, however, and may provide useful analogues (Figure 1.21). Features that are similar include channel-levee morphology, upslope-migrating crescentic bedforms (Hughes Clarke et al., 2012), erosional nickpoints and depositional fans (Conway et al., 2012). Table 1.5 presents a summary of published studies and examples of techniques used for flow monitoring are shown in Figure 1.22.

The recent advent of in-situ monitoring is starting to provide new insights into the timing, triggering and internal structure of flows; however we are in a similar position to that of seismologists 100 years ago. Reliable global seismological records have only been kept since about 1900 AD (Lay et al., 2015); hence at the start of the 20th century there was only a very limited catalogue of seismic events – particularly of large magnitude events. In attempting to assign probability of future submarine landslide occurrence Geist et al. (2013) state “the objective of determining probability is obviously hampered by the lack of an instrumental record of submarine landslide occurrence – as is available for submarine earthquakes”. Therefore, sites that feature the monitoring of more than a handful of flows are extremely valuable. At the time of writing, the most extensive monitoring record comes from the Squamish prodelta, British Columbia, where more than 100 flows were monitored during a four month period in 2012 (Hughes Clarke et al., 2012, 2013, 2014).

Table 1.5: Summary of published monitoring data for submarine sediment density flows

| Number of Events [N] | Location | Water Depth | Monitoring Method | Monitoring Duration | Study Reference |
|---|--|---------------|---|---------------------|--|
| 1 turbidity current | Capbreton Canyon, Bay of Biscay | 500 m-1500 m | Current meter | 7 months | Mulder et al. (2012) |
| 1 turbidity current (0.1 m/s) | Tokachi-oki Earthquake, Offshore Japan | 2500 m | Downward looking ADCP | 50 months | Mikada et al. (2006) |
| 1 turbidity current (>1.5 m/s) | Congo Canyon, Deep-Water West Africa | 4000 m | Current meter | 3 months | Khripounoff et al. (2004) |
| 1 strong turbidity current (>3.5 m/s) | Congo Canyon, Deep-Water West Africa | 3420 m-4790 m | Current meter | 60 months | Vangreishheim et al. (2009) |
| 2 turbidity currents (0.6 m/s) | Mugu Canyon, California | 179 m | Upward and down-looking ADCP | 6 months | Xu (2010) |
| 2 turbidity currents (0.9 – 2.9 m/s) | Hueneme Canyon, California | 188 m | Upward and down-looking ADCP | 6 months | Xu (2010) |
| 2 turbidity currents (up to 1.6 m/s) | Gaoping Canyon, Taiwan | 650 m | Current meter | 2 months | Liu et al. (2012) |
| 2 turbidity currents, with subsequent ~6 pulses (0.5 m/s) | La Jolla Canyon, California | 260 m | Current meter | 108 hours | Shepard and Dill (1966), Dill (1964), Shepard et al. (1977), Marshall (1978) |
| 3 turbidity currents | Fraser River delta, Canada | 41 m | Upward looking ADCP | 10 months | Ayranci et al. (2012) |
| 3 turbidity currents (<0.3 m/s) | Sagami Bay, Japan | 1200 m | Current meter | 84 months | Ikehara et al. (2012) |
| 3 well defined turbidity currents at 1700 m (<0.38 m/s) | La Fonera canyon, Mediterranean | >1200 m | Current meter | 8 months | Palanques et al., (2006); Puig et al. (2012) |
| 4 turbidity currents caused by tailings discharge (0.02 to 0.6 m/s) | Rupert Inlet, Canada | >140 m | Acoustic backscatter | 2 months | Hay et al. (1982; 1987a; 1987b) |
| 4 turbidity currents (0.1 – 1.5 m/s) | Monterey Canyon, California | 820 m-1445 m | Down-looking ADCP | 12 months | Xu (2010), Xu et al. (2004; 2014) |
| 6 distinct transport events | Monterey Canyon, California | <1450 m | Homing beacons attached to 45 kg concrete monuments | 26 months | Paull et al. (2010) |
| 6 turbidity currents | Var Canyon, Mediterranean | 1200m-2000 m | Current meter | 24 months | Khripounoff et al. (2009) |
| 9 turbidity currents (<0.35 m/s) | Itirbilung Fjord, Arctic | 50 m | Current meter | 40 days | Syvitski and Farrow (1989); Hein and Syvitski (1992) |
| 11 turbidity currents (up to 3.5 m/s) | Congo Canyon, Deep-Water West Africa | 2000 m | Down-looking ADCP | 7 months | Cooper et al. (2013) |
| 12 high energy turbidity currents | Bute Inlet, British Columbia, Canada | >520 m | Current meter, vane deflectors, tilt sensors | 13 months | Prior et al. (1987); Zeng et al. (1991) |
| 35 turbidity currents | Bute Inlet, British Columbia, Canada | >520 m | Turbidity event detector | 13 months | Bornhold et al. (1994) |

| Number of Events [N] | Location | Water Depth | Monitoring Method | Monitoring Duration | Study Reference |
|--|--|-------------|---|---------------------|---|
| 39 turbidity currents (>1m/s) | Knight Inlet, British Columbia, Canada | >520 m | Turbidity event detector | 17 months | Bornhold et al. (1994) |
| N=106 THRESHOLD | | | | | |
| 106 turbidity currents. It is possible to discern large delta lip failures from smaller events (0.5 – 1.5 m/s) | Squamish River Delta, British Columbia | <200 m | Upwards looking ADCP and 93 repeat multibeam seafloor surveys | 4 months | Hughes Clarke et al. (2012; 2013); Chapter 8 This Study |

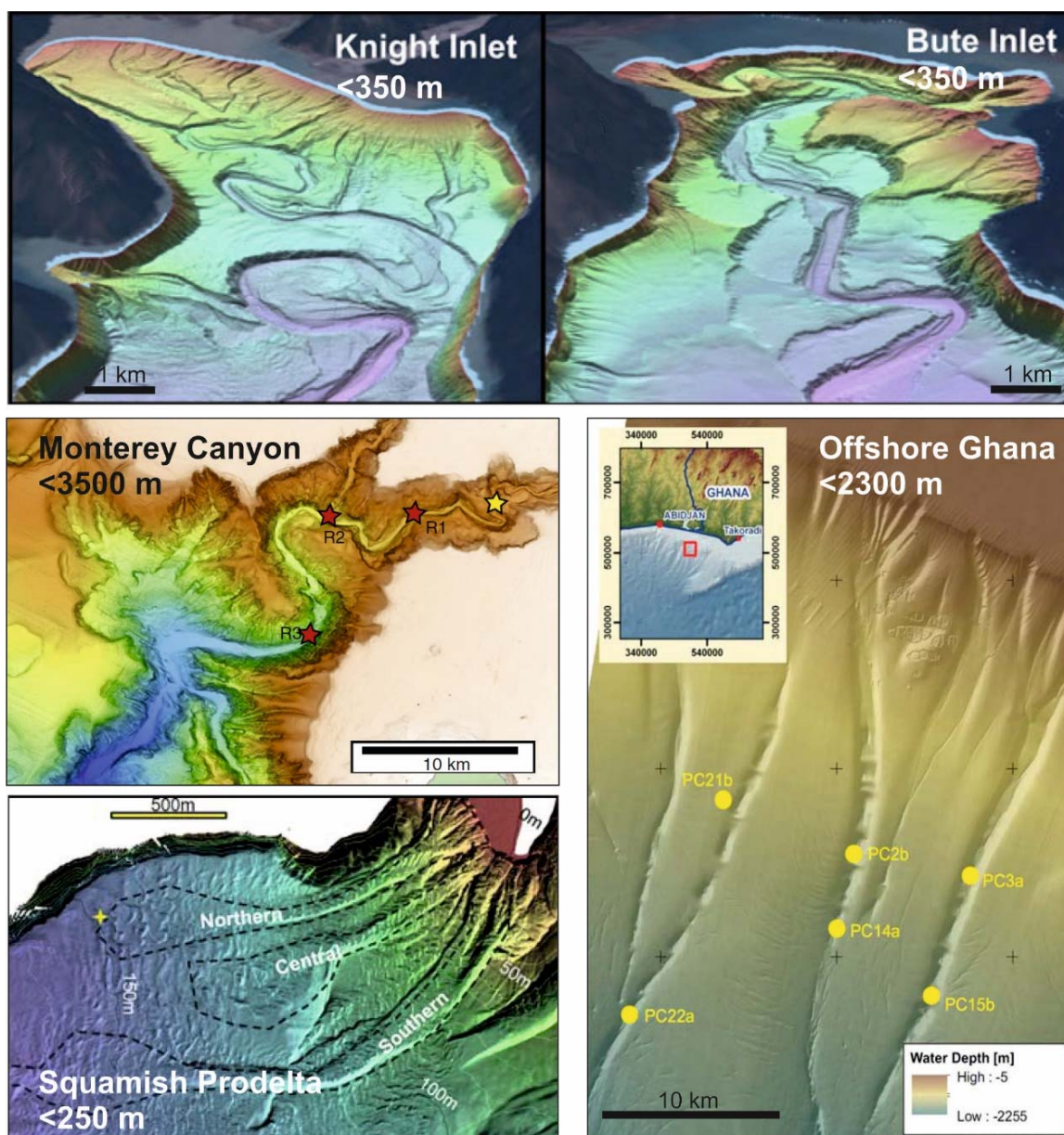


Figure 1.21: Seafloor imagery showing morphological similarities between shallow and deep water sites. Shallow water examples are from Canadian fjords at Squamish (Hughes Clarke et al., 2012), Knight and Bute Inlet (Conway et al., 2012) and deepwater examples are from offshore California (Monterey Canyon; Paull et al., 2010), and Ghana (Clare et al., 2015c).

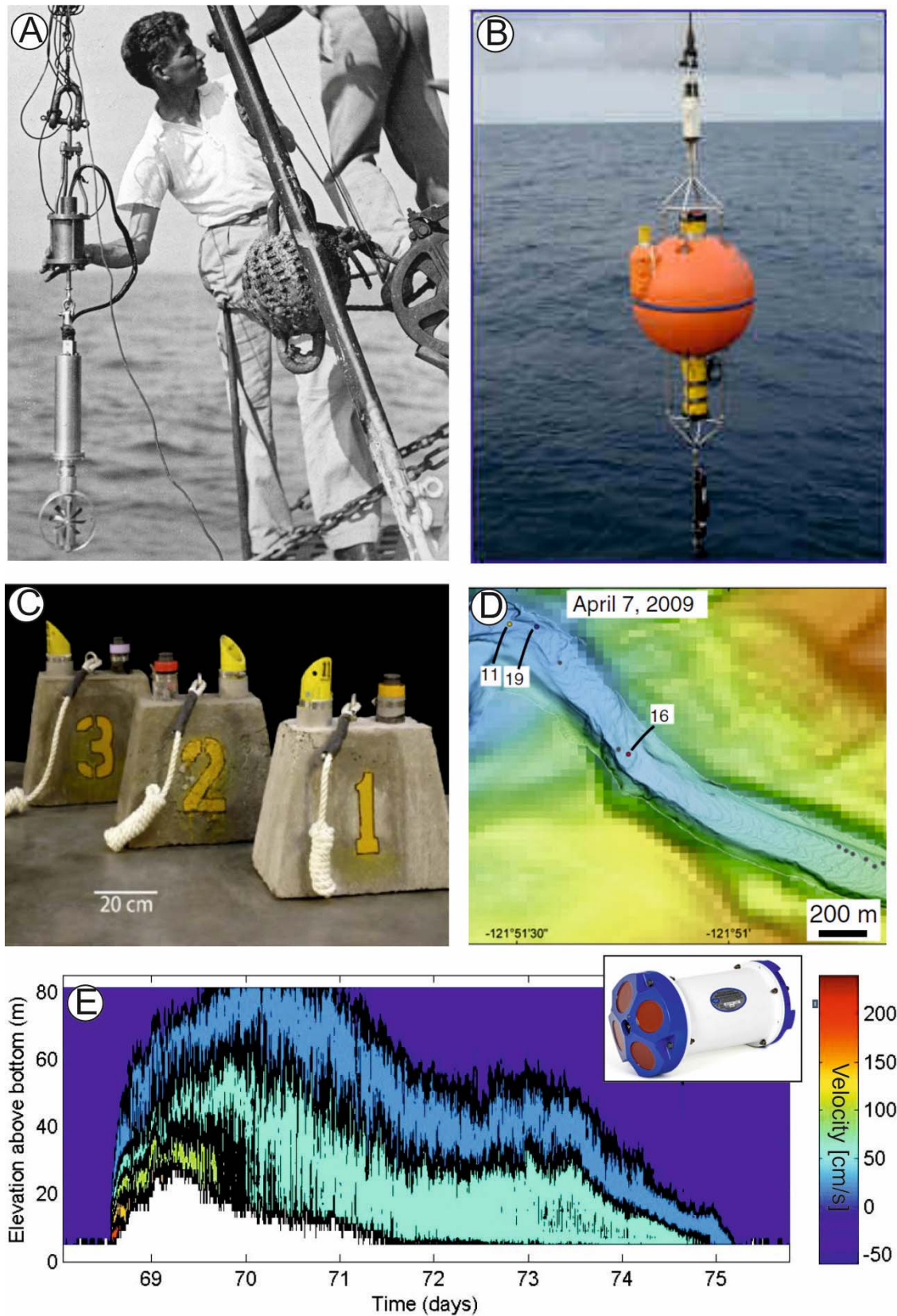


Figure 1.22: Example techniques for flow monitoring: (A) current meter (<http://www.whoi.edu>); (B) 3D current meter (<http://www.metoceanservices.com>); (C) weighted monuments deployed in the Monterey Canyon and tracked using a homing beacon to record their location (D); and remarkable time series of contoured velocity during a turbidity current is shown from a fixed ADCP mooring at 2000 m in the Congo Canyon (Cooper et al., 2013). ADCP (inset in (E), <http://www.rdinstruments.com>).

1.6 Key questions addressed by this thesis

This thesis addresses the following major questions:

Question 1: How can we measure the recurrence of potentially damaging landslides and turbidity currents?

Obtaining continuous and long term records of submarine landslide and turbidity current activity is challenging, and few studies include a large enough number of events for robust statistical analysis. A method is presented whereby the recurrence time of landslides is derived from intervals of hemipelagic mud that settles out between turbidity currents, and average accumulation rate of the hemipelagic mud (Chapter 3). The issues involved with such a method are discussed in Chapter 3, including the implications of erosion of hemipelagic deposits and the fact that not all turbidites come from landslides. This provides information on timing of many ($N > 106$) landslides and avoids the need to date prohibitively large numbers of landslides, each in a different location on the margin. This method requires data sets which satisfy a number of specific criteria as outlined in Chapter 3.

As well as geological timescales, much more recent and short-term timing of events is considered. A unique dataset is analysed in Chapter 8 which includes the monitoring 106 flow events during a period of only four months. While this dataset is from relatively shallow water depths in a Canadian fjord (Squamish Prodelta, British Columbia), it includes an unprecedented number of directly monitored events, including several delta lip failures, which provides new insights into the triggering of failures and turbidity currents. Landslides and flows are monitored by a combination of repeat seafloor multibeam surveying, which records changes in seafloor morphology caused by landslide and flow activity, and a frame-mounted ADCP which measures the velocity and backscatter intensity of flows passing a specific point.

Question 2: How can we quantitatively analyse recurrence of potentially damaging landslides and turbidity currents?

Due to the limited availability of extensive catalogues, previous statistical analysis of submarine landslide frequency has typically relied on computational techniques which are based on the probability distribution of hypothesised triggering mechanisms such as

earthquakes (Ten Brink et al., 2009) and long-term stratigraphic simulations (Hutton and Syvitski, 2004; Geist et al., 2013). However, the precise trigger is usually unknown and from a regional perspective, there may be several candidate mechanisms. Geist and Parsons (2010) used tools developed for palaeoseismological analysis, where there is also an issue of small numbers of recorded large magnitude events. They used a Bayesian approach to estimate the probability of event occurrence, and Monte Carlo analysis to determine the uncertainty. This is a sound approach for small sample sizes, however, their method necessarily assumes that landslide frequency conforms to a set distribution form (in their case, Gamma-Poisson). In this thesis, it is proposed to determine the frequency distribution form, however, so the approach taken here is first to test for different distribution forms and also to use non-parametric analyses that do not require *a priori* knowledge of the distribution form. Urlaub et al. (2013) tested goodness of fit of a global landslide database (N=68) with volumes $>1 \text{ km}^3$ to a Poisson distribution using the Chi-squared test (Swan and Sandilands, 1995). They identified that the global database is similar to a Poisson, time-independent distribution and landslide timings show no significant trends, clusters or peaks. The findings of Urlaub et al. (2013) are compelling, but they ultimately conclude that there are too few events in their database to be entirely sure.

In this thesis, the sample-size limitations of these prior studies are mitigated against, as only data sets that comprise sufficiently large numbers ($N>106$) of events for statistical analysis are considered. This means that different statistical methods that are more commonly used by medical, economic and biological disciplines can be used. A demonstration of how these statistical methods can be applied to novel analysis of submarine landslide frequency and triggering is presented in Chapter 4.

Question 3: Do large submarine landslides show time-dependent behaviour?

Determining whether large submarine landslides occur randomly in time, or whether they are controlled by variables with temporal order is important for future hazard assessment. Several studies indicate that a time-dependent behaviour is expected (e.g. Owen et al., 2007; Brothers et al., 2014); however, these studies only feature a small number of landslides. Other studies indicate that a Poisson (time-independent) distribution may be more appropriate (Urlaub et al., 2013; Geist et al., 2013), but conclude that there are too few observations to be certain. To address this, extensive records of

submarine landslides are presented from three distal basin plains in different settings in Chapter 5. Statistical analysis is used to characterise the frequency distribution of large submarine landslide recurrence and determine if there is commonality between the different basin plains.

Question 4: Is sea level a dominant control on large submarine landslide recurrence?

Despite the limited number of landslides within published catalogues, many studies have drawn strong conclusions about the influence of variables such as sea level and global temperature variations on submarine landslide recurrence rate (e.g. Owen et al., 2007; Brothers et al., 2013). It has been proposed that rapid global warming will lead to significant increases in landslide and turbidity current frequency, due to gas hydrate dissociation in response to elevated ocean temperatures (Maslin et al., 1998, 2004; Nisbet and Piper, 1998; Owen et al., 2007; Lee, 2009; Maslin, 2010). Dissociation of gas hydrate can weaken slopes and increase the probability of slope failure (Grozic, 2010). Conversely, some studies have shown that ordered processes, such as sea level change, may not exert a dominant control on landslide (Geist and Parsons, 2010; Urlaub et al., 2013) and turbidity current recurrence (Beattie and Dade, 1996; Hunt et al., 2013).

Geist and Parsons (2010) outlined the need for more age dates of both global and local landslide sequences to determine long-term variation. Thus, to make more meaningful, quantitative inferences on triggering and conditioning factors, there is a need for statistically robust ($N > 106$) datasets of landslide ages to be acquired in a variety of settings. In Chapters 5 and 7 long-term records of landslide recurrence are analysed using distal turbidite deposits to statistically test for the significance of sea level and its rate of change.

Question 5: Does millennial-scale dramatic global warming result in an increased frequency of submarine landslides and turbidity currents?

In Chapter 6 turbidity current frequency is analysed before, during and after the Initial Eocene Thermal Maximum (IETM). The IETM occurred at ~55 Ma and represents the most dramatic phase of global warming during the last 65 million years (Schmitz et al., 2001). Hence, the IETM may provide insights into the potential effects of future

global warming and into periods of elevated greenhouse gases. Sedimentary records from two deep-water basin plains (proto-Bay of Biscay and Iberia Abyssal Plain) are analysed statistically and compared with a broader global database created from other published studies to investigate if global warming at the IETM led to an increase in turbidity currents triggered by submarine landslide activity.

Question 6: Can large submarine landslides catalyse global warming? Did large submarine landslides trigger global warming at the Initial Eocene Thermal Maximum?

In addition to global warming causing variations in landslide or turbidity current frequency, it has been proposed that submarine landslides play a role in driving rapid climate change (Kennett et al., 2003; Maslin et al., 2004; Bock et al., 2012). These studies suggest that dissociation of gas hydrate within, or below, the failed slide material, may lead to significant emissions of methane – a strong greenhouse gas (Katz et al., 1999; Hornbach et al. 2007; Maslin et al., 2004, 2010). Therefore, in Chapter 6 the potential effects of submarine landslide activity on global climate change at the IETM (~55 Ma) are also explored by analysing changes in frequency in relation to palaeo-temperature and carbon isotopic records.

Question 7: How does long term (>10 Myr) global warming affect turbidity current frequency?

Deep-sea sedimentary systems are often complex, due to the various controls on the nature, amount, source and route of sediment that is supplied to the continental shelf and slope (e.g. Covault and Graham, 2010; Covault et al., 2013; Hubbard et al., 2014). Such controls may relate to climatic, oceanographic and tectonic processes as well as physiographic changes. The complexity of some deep-sea sediment transport systems, may mean that the effects of change may not be felt immediately. In Chapter 7, an investigation of turbidite frequency is performed over an exceptionally long (20 Myr) and extensive (N=1571) depositional record from the Iberia Abyssal Plain. Chapter 7 aims to characterise turbidite frequency over both long (>10 Myr) timescales and identify whether there is any significant change in relation to sea level and global temperatures.

Question 8: How are mass failures and flows triggered at offshore bedload-dominated river deltas?

There is a great amount of uncertainty in how slope failures and flows are triggered at offshore river deltas (e.g. Prior et al., 1987; Bornhold et al. 1994; Mulder et al., 2003; Piper and Normark, 2009; Talling, 2014). This is an important issue, as offshore river deltas are the point at which sediment is delivered by rivers and then transported by turbidity currents to deep-water. Determining whether there is temporal continuity in sediment transport (i.e. via plunging hyperpycnal flows during river floods) or if there is a lag (e.g. sediment accumulates on the delta lip until it fails) may be key to understanding deep-sea sediment transport in a broader sense. Most datasets do not allow for a conclusive analysis of this question. In Chapter 8 data is analysed from the Squamish prodelta, British Columbia, where the combination of monitoring and seafloor surveying provide sufficient temporal and geomorphic resolution to address this issue. The number of events identified ($N > 106$) enables statistical analysis for determining the significance of possible controlling variables on landslide and flow triggering, including sediment discharge, tidal elevation, pore pressure and bed shear stress due to river bedload transport.

Chapter 2: Geological setting of study areas

Summary

This chapter provides a summary of the geological setting for the study areas considered in this thesis. The discussion on tectonic, physiographic and sedimentary setting is intentionally brief, but provides the necessary context for more detailed discussions in later chapters. This chapter is based on a literature review and was completed entirely by me.

Geological setting of study areas

ABSTRACT *Recurrence interval records of large submarine landslides and turbidity currents are analysed from five distal basin plains over geological timescales. The sedimentary successions that are analysed come from different geological and geographic settings and include ancient outcrops (Marnoso-arenacea Formation, Italian Apennines, and Zumaia Series, north-east Spain), ancient cored sequences (Iberia Abyssal Plain, north-east Atlantic), and modern cored sequences (Madeira and Balearic Abyssal Plains). Each of these sites is a distal basin plain setting, but the nature and number of potential input sources varies, as does the morphology of the basin itself. A short-term record of landslides and flows is also analysed at the modern Squamish prodelta, British Columbia, based on the results of field-based direct monitoring. Tectonic setting, physiography and sediment input sources are discussed to provide broader context for later chapters.*

2.1. Introduction

This chapter summarises the geological setting for each study area discussed in this thesis. It starts with a discussion of the ancient records (Marnoso-arenacea, Zumaia and Iberia Abyssal Plain), then the more recent cored successions (Madeira and Balearic Abyssal Plains), and finally the modern Squamish submarine delta. The location of each of the study areas is shown in Figure 2.1 and a summary of the data is presented in Table 2.1. Rationale for the screening of sites and dataset selection is shown in Figure 2.2.

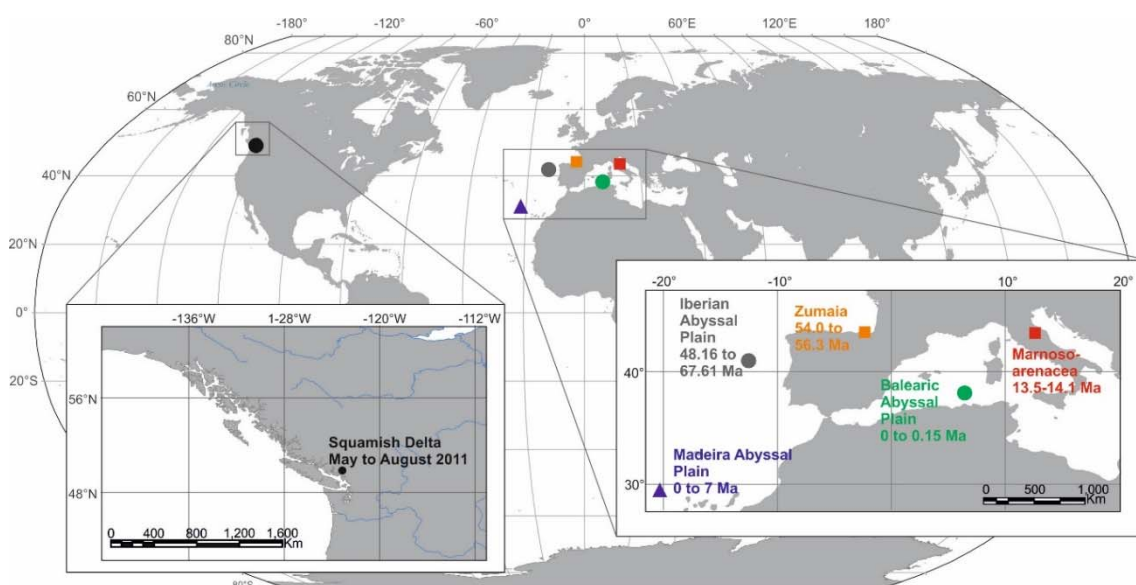


Figure 2.1: Location of the study areas analysed in this thesis. The duration of the studied interval is annotated. More details are provided in Table 2.1.

Table 2.1: Summary of sites considered in this study

| Site | Time Period Studied | Setting | Reason for Analysis | Data Type |
|---|---|---|--|--|
| Marnoso-arenacea Formation, Italian Apennines | Mid Miocene (13.5 to 14.1 Ma) | Elongate distal foreland basin, adjacent to the Apennines thrust belt (Amy and Talling, 2006) | Previously analysed data set assessing the effect of sea level on turbidity current recurrence frequency | Outcrop |
| Zumaia, North-East Spain | Palaeocene to Eocene (54.0 to 56.3 Ma) | Distal bathyal basin adjacent to the northern Iberian productive shelf and Pyrenean chain (>1000 m water depth; Winkler and Gawenda, 1999) | Assess effect of short-term global warming at the Initial Eocene Thermal Maximum on landslide frequency (and possible effects of landslide activity on global warming) | Outcrop |
| Iberia Abyssal Plain, North-Eastern Atlantic Ocean | Late Cretaceous to mid Eocene (48.1 to 67.7 Ma) | Distal deep-water (>4000 m water depth) basin plain adjacent to Iberian margin in the east (Whitmarsh et al., 1998) | Analysis of long-term climate change during the late Cretaceous to early Eocene on turbidity current frequency | ODP Core |
| Madeira Abyssal Plain, North-Eastern Atlantic Ocean | Miocene to Present (0 to 7 Ma) | Distal deep-water (>4000 m water depth) basin plain adjacent to volcanic centres of the Canaries and Madeira to the east, the north-west African margin to the south-east, and seamounts to the west (Weaver, 1994) | Assess effect of multiple cycles of sea level change on landslide frequency | ODP Cores |
| Balearic Abyssal Plain, Western Mediterranean | Late Quaternary (0 to 150 ka) | Enclosed distal, deep-water (>2800 m water depth) basin plain flanked by the north African margin to the south, the Rhone and Var fans to the north, Valencia fan and Balearic island to the west, and the Sardinian margin to the east (Rothwell et al., 1998; Hoogakker et al., 2004) | Assess effect of late Quaternary glacio-eustatic sea level variations on landslide frequency | Calypso Piston Cores |
| Squamish Prodelta, British Columbia, Canada | May to August 2011 | Submarine extent of river-fed delta within a coastal fjord (Brucker et al., 2007; Hughes Clarke et al., 2012, 2013, 2014) | Assess effect of river discharge, tidal elevation and bed shear stress on landslide-flow frequency on a very short timescale and to differentiate hyperpycnal from landslide-triggered flows | Monitoring: ADCP and repeat seafloor surveys |

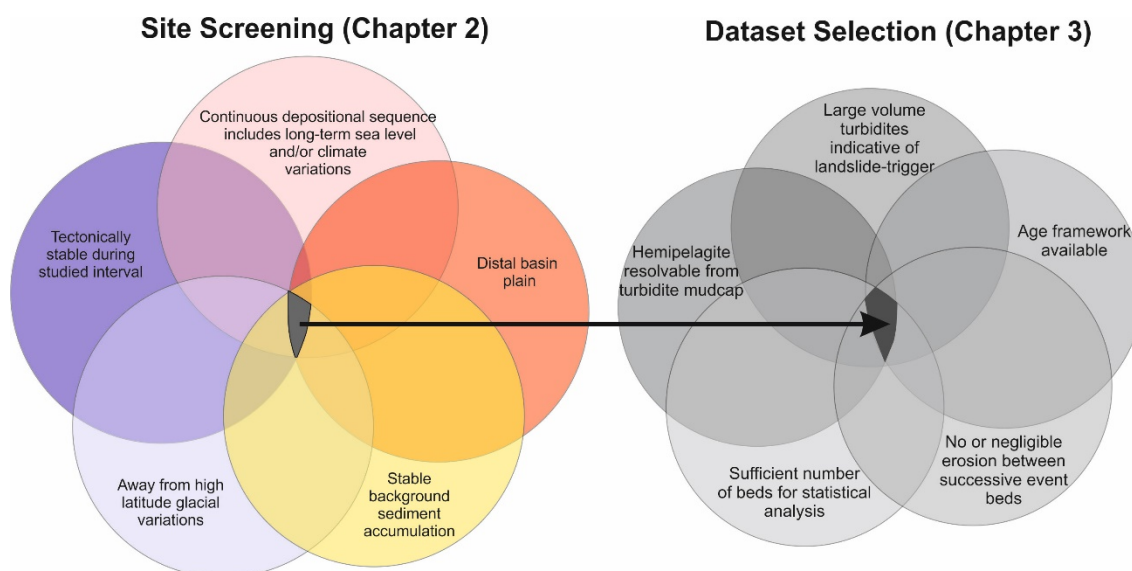


Figure 2.2: Summary of rationale for initial site screening (this chapter) and dataset selection (Chapter 3). Initial site screening is based on a review of geological and physiographic settings, while dataset selection is based on quality of the depositional sequence at the site for performing turbidite recurrence analysis.

2.2. Marnoso-arenacea Formation, Italian Apennines

The Marnoso-arenacea Formation was deposited from the late Burdegalian to Tortonian (17 to 7 Ma) and crops out over a large expanse of the northern Italian Apennines (Amy and Talling, 2006; Talling et al., 2007bc). Deposits can be correlated bed-by-bed over exceptional distances (up to 120 km) due to their continuous, tabular nature (Figure 2.3; Hesse, 1974; Ricci Luchi, 1978,1995; Ricci Lucchi and Valmori, 1980; Amy and Talling, 2006).

2.1.1 Tectonic setting

The Marnoso-arenacea Formation was deposited in an elongate foreland basin, adjacent to the Apennine thrust belt (Figure 2.4; Amy and Talling, 2006 and references therein). The deposits analysed in this study belong to the ‘inner stage’ development of the foreland basin (Amy and Talling, 2006), during which time the foredeep was relatively wide (>60 m) and unchannelised (Ricci Luchi and Valmori, 1980). Due to the structural controls on the basin morphology, the basin fill is wedge-shaped and thins to the north-east. Following the inner stage, the foredeep was disrupted by thrust faulting which led to the formation of submarine channels in response to basin narrowing (Amy and Talling, 2006).

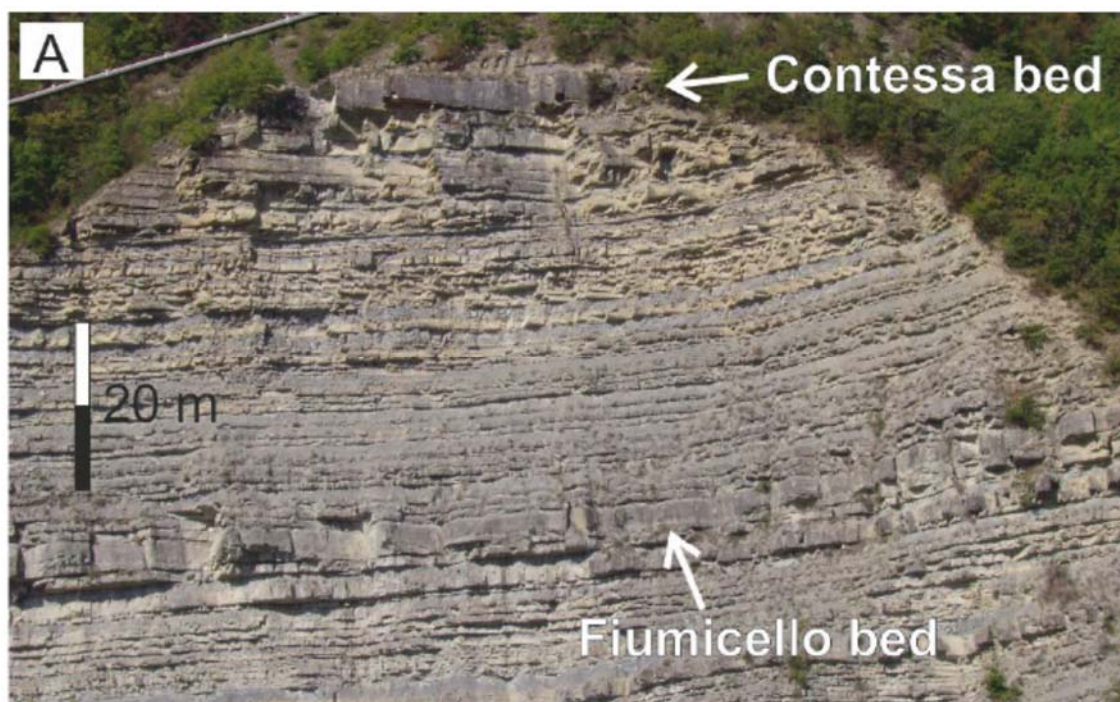


Figure 2.3: Outcrop photograph illustrating the tabular nature of beds of the Marnoso-arenacea and the basal sandstone of the Contessa and Fiumicello megaturbidites which act as a regional marker bed (from Malgesini, 2012)

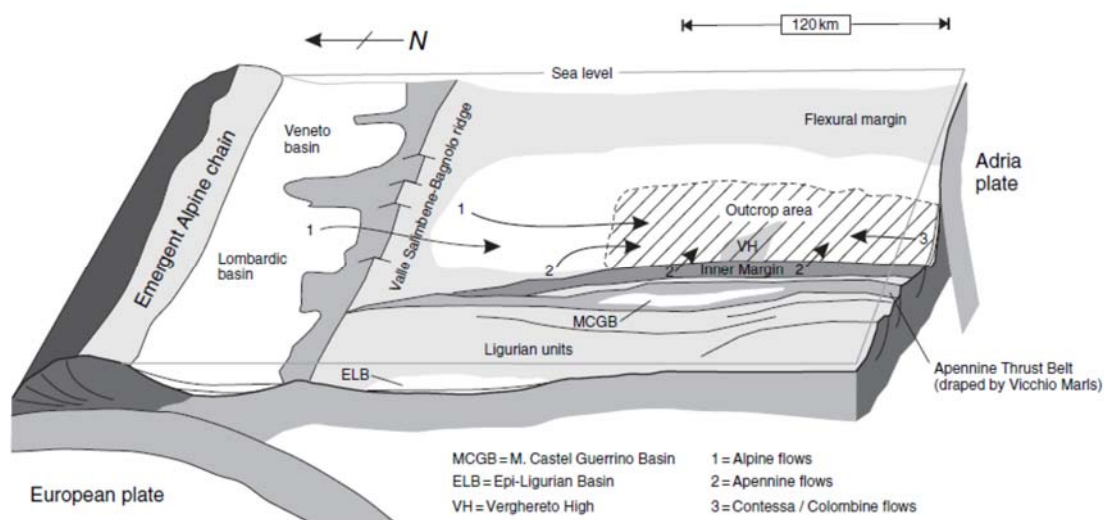


Figure 2.4: Schematic palaeogeographic reconstruction of the Marnoso-arenacea foredeep basin during the mid-Miocene (after DiBase and Mutti, 2002 and Amy and Talling, 2006)

2.1.2 Physiography and sediment input sources

The inner stage foredeep was filled mostly by submarine flows sourced from then north-east, with an Alpine or subsidiary Apennines provenance, as indicated by the lithic component of sandstone beds (Gandolfini et al., 1983). Infrequent, but substantial volume, flows also entered the foredeep from the south-east as evidenced by palaeoflow indicators and distinct composition (Figure 2.5; Amy and Talling, 2006; Malgesini,

2012). These large flows deposited carbonate-rich megaturbidites, the thickest of which is known as the Contessa Bed. The foredeep is interpreted to have been a relatively flat basin plain because palaeocurrent directions indicate flows could travel in opposite directions over long distances, deposits are not channelized, and exhibit a tabular bed geometry (Ricci Luchi and Valmori, 1980; Amy and Talling, 2006; Talling et al., 2007b,c; Malgesini, 2012). Three subtle intrabasin highs are interpreted; however, these are thought to have had a relief of less than 50 m as most flows were able to overtop the highs without significant deflection (Talling et al., 2007b).

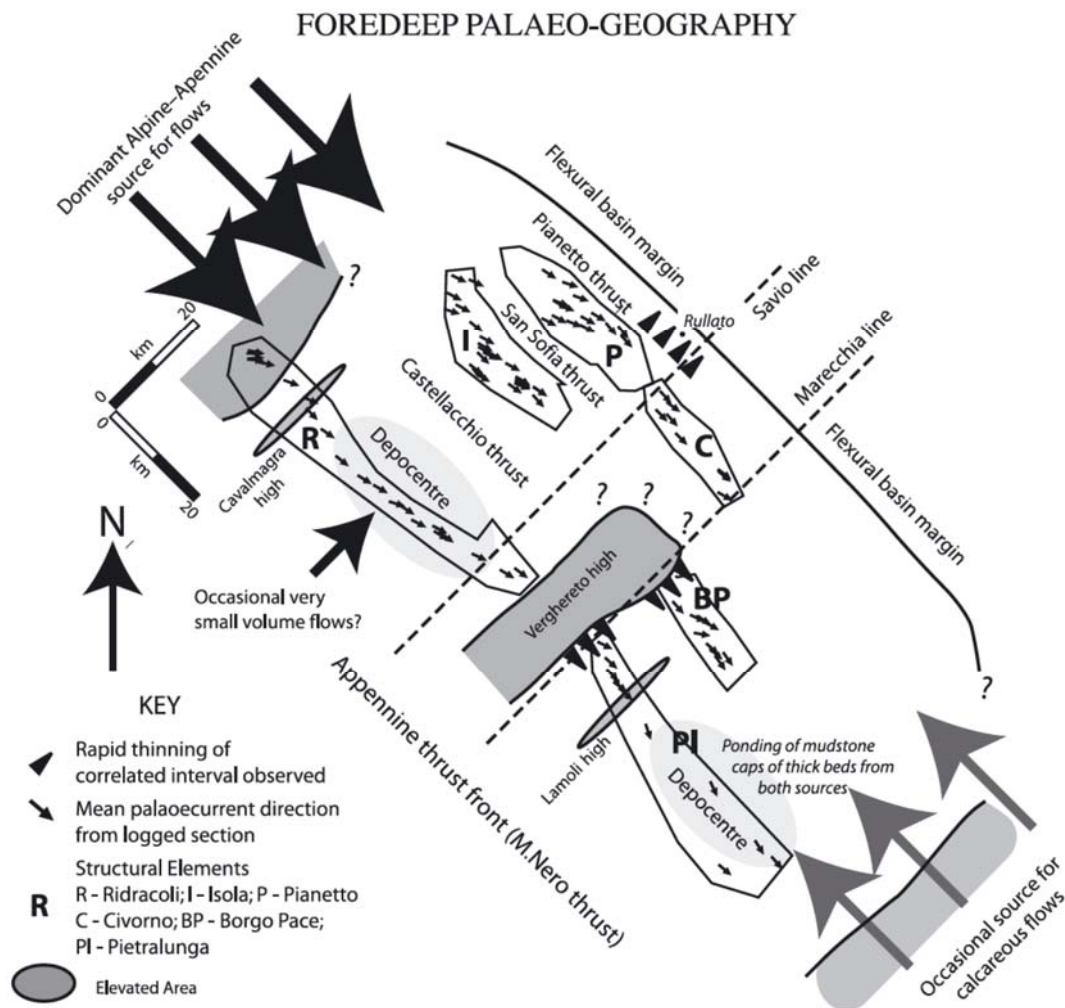


Figure 2.5: Palaeogeographic reconstruction of the Marnoso-arenacea foreland basin during the Miocene. Mean palaeocurrent direction is annotated. Structural elements are separated to illustrate post-depositional narrowing of the basin by thrust faults (from Talling et al., 2007b).

2.1.3 Interval analysed in this study

The interval that focussed on in this thesis comes from the Cabelli section below the Contessa bed and is mid-Miocene in age (13.5 to 14.1 Ma). A total of 696 turbidites

were logged in detail by Malgesini (2012) and the section was revisited by the author in April 2013. I examined the base of each turbidite to determine if the effects of erosion matched the sedimentological log of Malgesini (2012) and made regular checks on the measured hemipelagic thickness between turbidites. Turbidite recurrence intervals from the Cabelli section have previously been interpreted to be time-independent and show no correlation with sea level change (Malgesini, 2012). Testing these interpretations, and comparing them with a wider database was one of the initial motivators for this present study.

2.3. Zumaia Series, North-East Spain

This Zumaia site is a coastal exposure at Itzurun Beach in north-east Spain. The section studied forms part of a near-continuous stratigraphy that extends from the mid Cretaceous to the mid Eocene (Figure 2.6; Winkler and Gawenda, 1999).

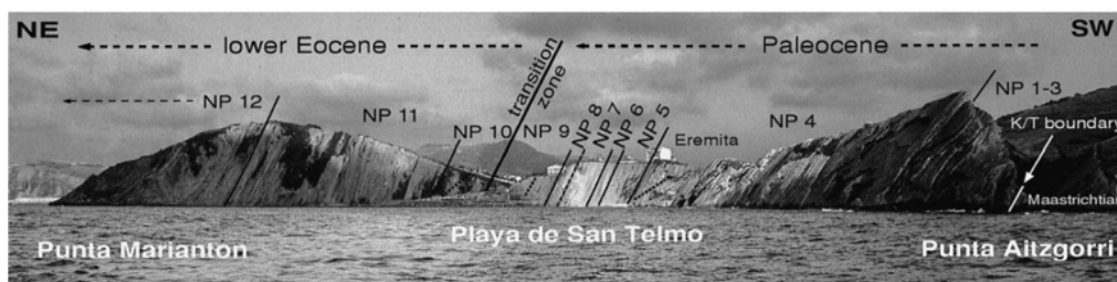


Figure 2.6: Panoramic view of the Zumaia series, north-east Spain. Positions of nannofossil zones boundaries are annotated (from Gawenda et al., 1999). The position of the Cretaceous-Tertiary boundary (K-T) is also shown.

2.1.4 Tectonic setting

During the deposition of the studied section at Zumaia, Pyrenean deformation was steady and continuous, causing minor compression landward of the Bay of Biscay (Jammes et al., 2009; 2010). The effect on deep-water sediment input was delayed, however, and only at ~53.5 Ma was a change seen from a calciclastic to siliciclastic turbidite system at Zumaia (Winkler and Gawenda, 1999). This falls after the interval of study in Chapter 6, therefore the tectonic setting at Zumaia can be considered to be one of relative tectonic quiescence (Verges et al., 1995; Rosenbaum et al., 2002).

2.1.5 Physiography and sediment input sources

The sediments were deposited in an east-south-east to west-north-west oriented elongated marine basin at a palaeolatitude of approximately 35°N (Winkler and Gawenda, 1999 and references therein; Figure 2.7). During the late Palaeocene-early Eocene, Zumaia was part of a deep-water (>1000 m) marine basin (Winkler and Gawenda, 1999) flanked by mixed carbonate-terrigenous shelf systems (Fig 1B), as verified by thinly interbedded, hemipelagic and distal calciclastic-siliciclastic turbidite deposits (Gawenda, 1999). Palaeocurrent directions indicate predominant transport of flows from the basin margins to the east and south-east (Gawenda et al., 1999; Cummings and Hodgson, 2011).

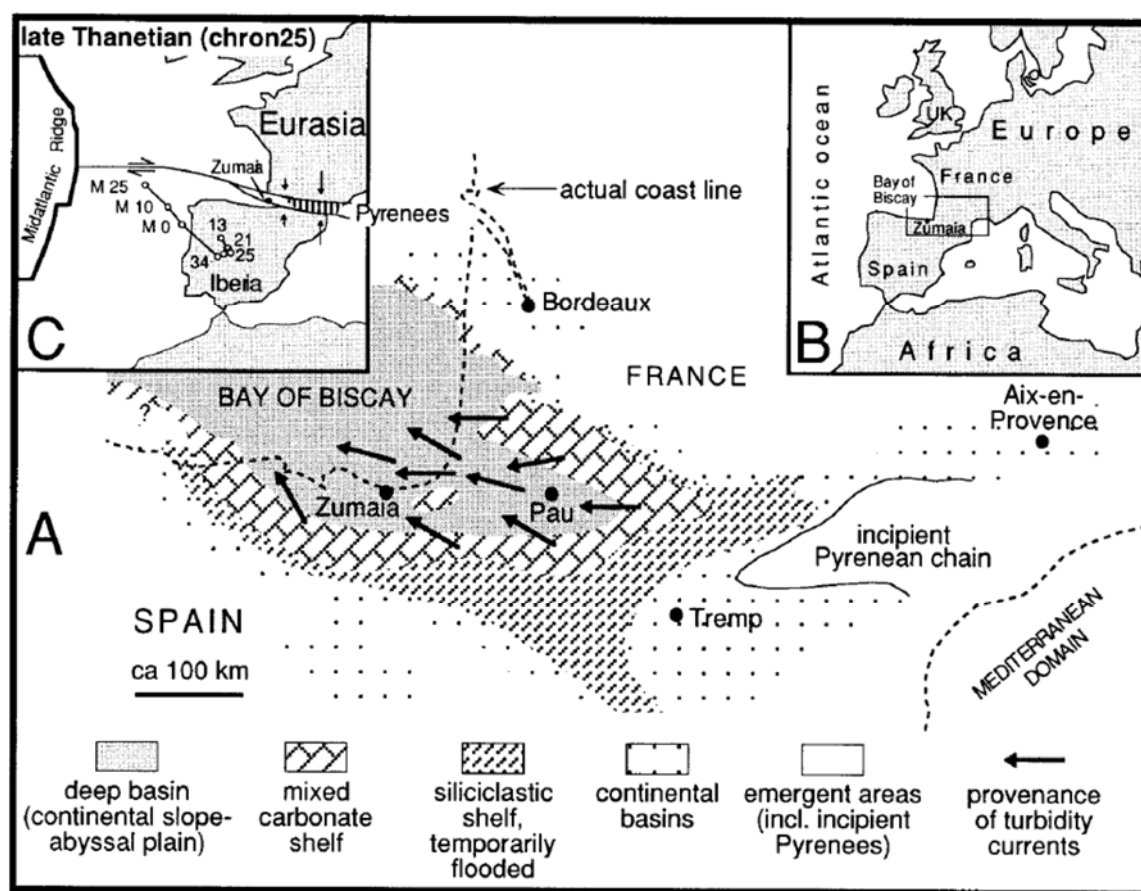


Figure 2.7: Palaeogeographic reconstruction for the Bay of Biscay during the late Palaeocene showing the deep pelagic basin flanked by mixed carbonate-siliciclastic shelves. From Gawenda et al. (1999)

2.1.6 Interval analysed in this study

A robust age and climate framework has been developed from published palaeoclimatic, palaeontologic, palaeoecologic and chronostratigraphic studies specifically for the Palaeocene and Eocene interval (Chapter 6). The stratigraphic

sequence analysed in this thesis was logged by the author with the field assistance of James Hunt in May 2013. A total of 1045 turbidites were logged; however, an interval that includes 285 of these turbidites is focused on due to uncertainties in erosion and tectonic effects (Figure 2.8). The interval selected (54.0 to 56.3 Ma) at Zumaia avoids a faulted interval where stratigraphic repetition or omission may occur and terminates prior to a transition to a submarine fan setting, in which erosional bed amalgamation is common (Cummings and Hodgson, 2011).

Zumaia is one of the most expanded and continuous sections through the Initial Eocene Thermal Maximum (IETM) worldwide (Canudo et al., 1992, 1995; Schmitz et al., 2001). Therefore the Zumaia section provides useful and high resolution insights into landslide and turbidity current frequency prior to, and following, periods of dramatic global warming and in response to enhanced greenhouse gas levels.

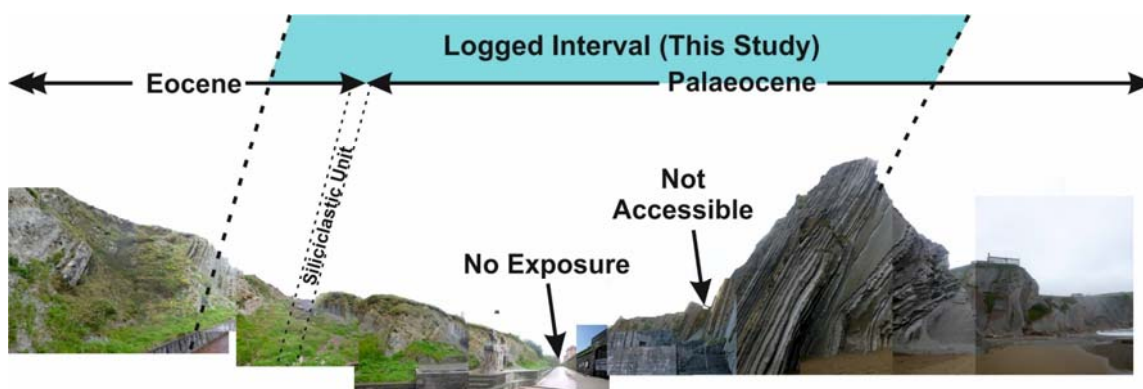


Figure 2.8: Outcrop photograph illustrating section analysed in this study from Itzurun Beach, Zumaia. Siliciclastic Unit corresponds to the IETM.

2.4. Iberia Abyssal Plain

The Iberia Abyssal Plain was located at approximately 35°N during the time of deposition in the late Cretaceous to mid Eocene (Figure 2.9). The analysis presented here focuses on the sequence of deep water deposits from Ocean Drilling Program (ODP) site 1068 which was acquired as part of leg 173.

2.1.7 Tectonic setting

Africa and Europe began to converge at ~83 Ma, with movement of Iberia virtually ceasing from 67-55 Ma (Rosenbaum, 2002; Tugend et al., 2014). This period of quiescence crosses the IETM and the start of the study intervals. Convergence resumed

in Europe, when Iberia shifted to north-westward transpression at ~55 Ma (Gawenda et al., 1999). Compression was first felt at the northern Iberian border (Grafe and Wiedmann, 1993) at ~55 Ma, progressing southward until ~46 Ma (Tugend et al., 2015). The Iberia Abyssal Plain site was distal from this tectonic centre during most of the study interval. The intensification of Iberia-Europe convergence did not occur until ~51 Ma (Roest and Srivastava, 1991; Rosenbaum et al., 2002), also postdating the study intervals.

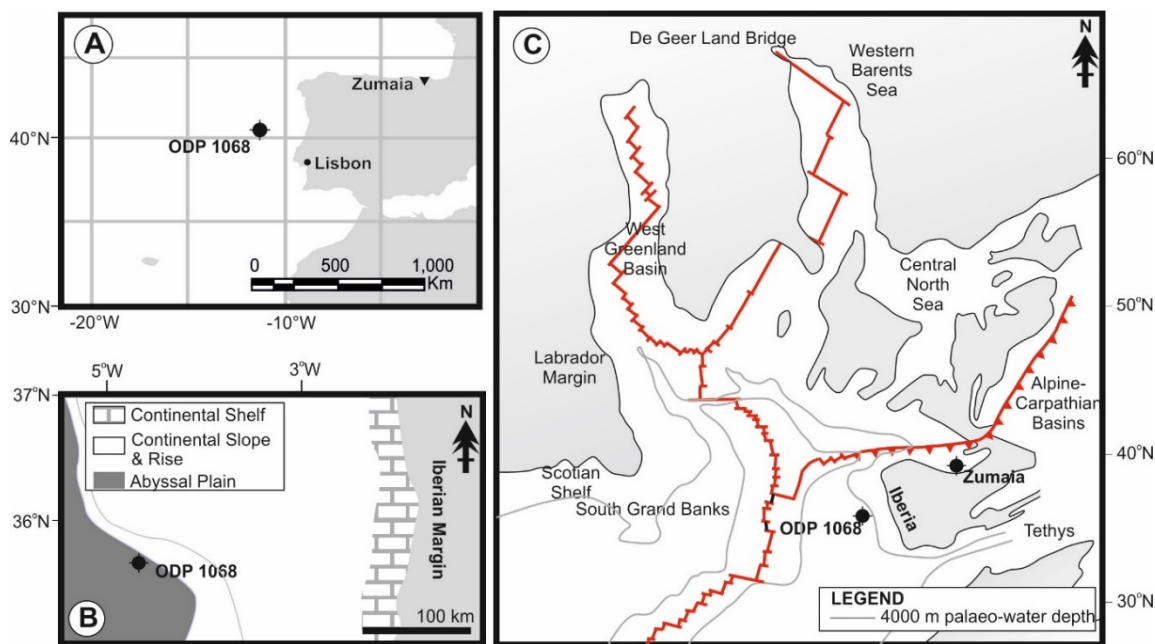


Figure 2.9: Location map (A) showing ODP Site 1068 and reference to Zumaia site in NE Spain; Palaeogeographic reconstruction (B) for Iberian Margin and ODP Site 1068 during late Palaeocene/Early Eocene (modified from Whitmarsh et al., 1995); (C) Regional palaeogeography during late Palaeocene (modified from Kaminski et al., 1998)

2.1.8 Physiography and sediment input sources

ODP site 1068 is located on the western flank of a north-south trending basement high near the southern edge of the Iberia Abyssal Plain (Whitmarsh et al., 1998). The present day Iberia Abyssal Plain is connected to the shelf by a series of canyons and is inferred to also have been so in the Palaeogene (Marsaglia et al., 1996). Early versions of the Porto, Aveiro and Nazare Canyons and elevated areas to the east and north-east of the Iberia Abyssal Plain are inferred to have been the most likely source areas for turbidity currents (Marsaglia et al., 1996). Mineralogical analysis indicates that turbidite sands were originally derived from proto-equivalents of the major river catchments that currently drain to the Iberian shelf (Marsaglia et al., 1996); hence the onshore systems were also presumably similar to the present day.

2.1.9 Interval analysed in this study

A continuous basin plain sequence featuring an exceptional number of turbidites (N=1571) was sampled at ODP Site 1068 from 48.16 to 67.61 Ma. Crucially for this study, this includes major climatic excursions (IETM at 55 Ma, EECO from 51-53 Ma), minor hyperthermals (Eocene Thermal Maximum 2 (“Elmo”) and 3 (“X”), Late Palaeocene Thermal Event, Top Chron C27n Event, Carbon Isotopic Excursions DS1 and DS2, Dan C-2 Event) as well as the Cretaceous-Tertiary boundary. The ODP site 1068 record therefore provide valuable insights into several periods of short- and longer-term global temperature changes. The stratigraphic sequence analysed in this study was logged by James Hunt, and the measurements were checked by me using core photographs from the online ODP archives (<http://iodp.tamu.edu/database/coreimages.html>). A few minor adjustments were made to the logs following the check and discussed with James Hunt prior to the analysis.

2.5. Madeira Abyssal Plain

The Madeira Abyssal Plain represents the most distal and deepest depocentre in the Moroccan Turbidite System at water depths of 5000 m to 5500 m, and is located ~500 km west of the Canary Islands (Figure 2.10; Weaver and Kuijpers, 1983; Weaver et al., 1992; Wynn et al., 2000, 2002; Hunt et al., 2014).

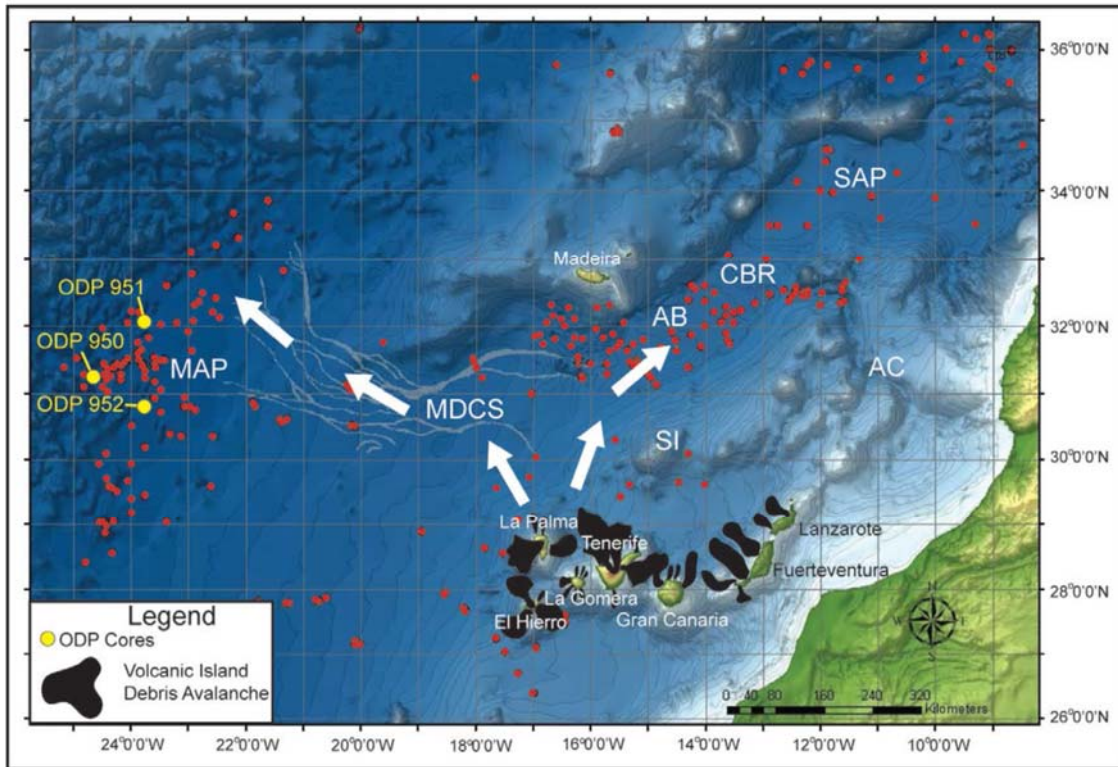


Figure 2.10: Map of the Moroccan Turbidite System, offshore Northwest Africa connecting to the Madeira Abyssal Plain (MAP). Shown are the Madeira Distributary Channel System (MDCS), Agadir Basin (AB), Seine Abyssal Plain (SAP), Selvagen Islands (SI), Agadir Canyon (AC) and Casablanca Ridge (CBR). ODP sites 950, 951 and 952 are also annotated. White arrows indicate the pathways of volcanic island-sourced turbidity currents (from Hunt et al., 2014). Other sources are indicated in Figure 2.11.

2.1.10 Tectonic setting

The Madeira Abyssal Plain is part of the larger Canary Basin, bounded to the north and west by active tectonic plate boundaries which are the Azores-Gibraltar Rise and the foothills of the Mid-Atlantic Ridge respectively (Searle, 1987; Rothwell et al., 1992). Seismic and volcanic activity is very localised along the boundaries which are a few tens of kilometres wide; hence, the Abyssal Plain is unlikely to be affected by such processes (Searle, 1987). Evidence for intraplate seismicity comes from studies of recently active volcanic islands including Madeira, Canaries and Cape Verde islands (Searle, 1987).

2.1.11 Physiography and sediment input sources

The main part of the Madeira Abyssal Plain is contained within an almost oval central basin with a thin extension that runs to the south (Rothwell et al., 1992). Numerous basement highs penetrate the plain to form abyssal hills, but generally the relief is less

than 10 m (Searle, 1987). The Madeira Distributary Channel System connects the Madeira Abyssal Plain to the Canary Islands and Agadir Basin (Wynn et al., 2003, 2010, 2012; Stevenson et al., 2014;). Flows that deposit in the Madeira Abyssal Plain may therefore have travelled a remarkable distance (up to 1500 km). Four input sources have been interpreted on the basis of core correlations and turbidite mudcap geochemistry (Figure 2.12; Weaver and Rothwell, 1987; Rothwell et al., 1992; Weaver, 1994; Hunt et al., 2014 and references therein). These include two organic sources from the north-east and south-east, volcanic-triggered flows from the Canary Islands, and calcareous flows from the seamounts to the west (Figure 2.11). The Madeira Abyssal Plain began to fill at about 22 Ma with numerous small turbidites (Weaver, 2003). The volume of turbidites then increased in volume from 16 to 11 Ma, and subsequently decreased until 7 Ma (Weaver, 2003). At 7 Ma there was a dramatic increase in the amount of turbidite input which is thought to be due to higher slope sedimentation rates and resultant mass wasting (Weaver, 2003).

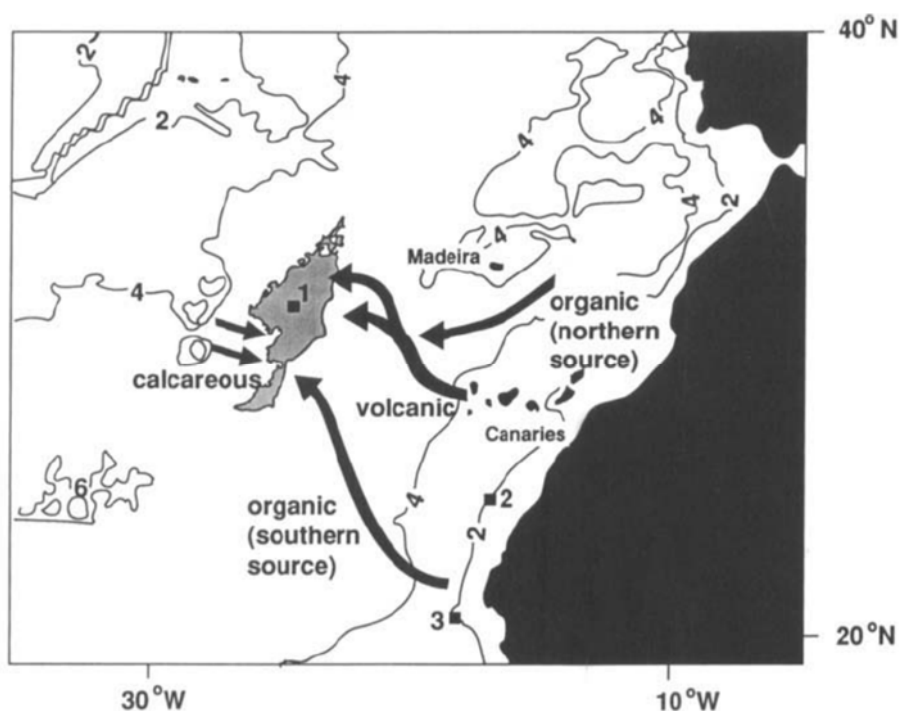


Figure 2.11: Location of the Madeira Abyssal Plain (grey) and sources of turbidites since 7 Ma. From Weaver (1994)

2.1.12 Interval analysed in this study

The post-7 Ma record from ODP sites 950, 951 and 952 is the focus in this study, where turbidites can be correlated across the basin (Weaver, 1994; Hunt et al., 2014).

This post-7 Ma time period allows for analysis of submarine landslide records to provide a better understanding of potential preconditioning and triggering factors such as sea level change (including several cycles of lowstand to highstand), climate change, and volcanic activity. The stratigraphic sequence analysed here was logged by James Hunt, but all analysis was performed by me.

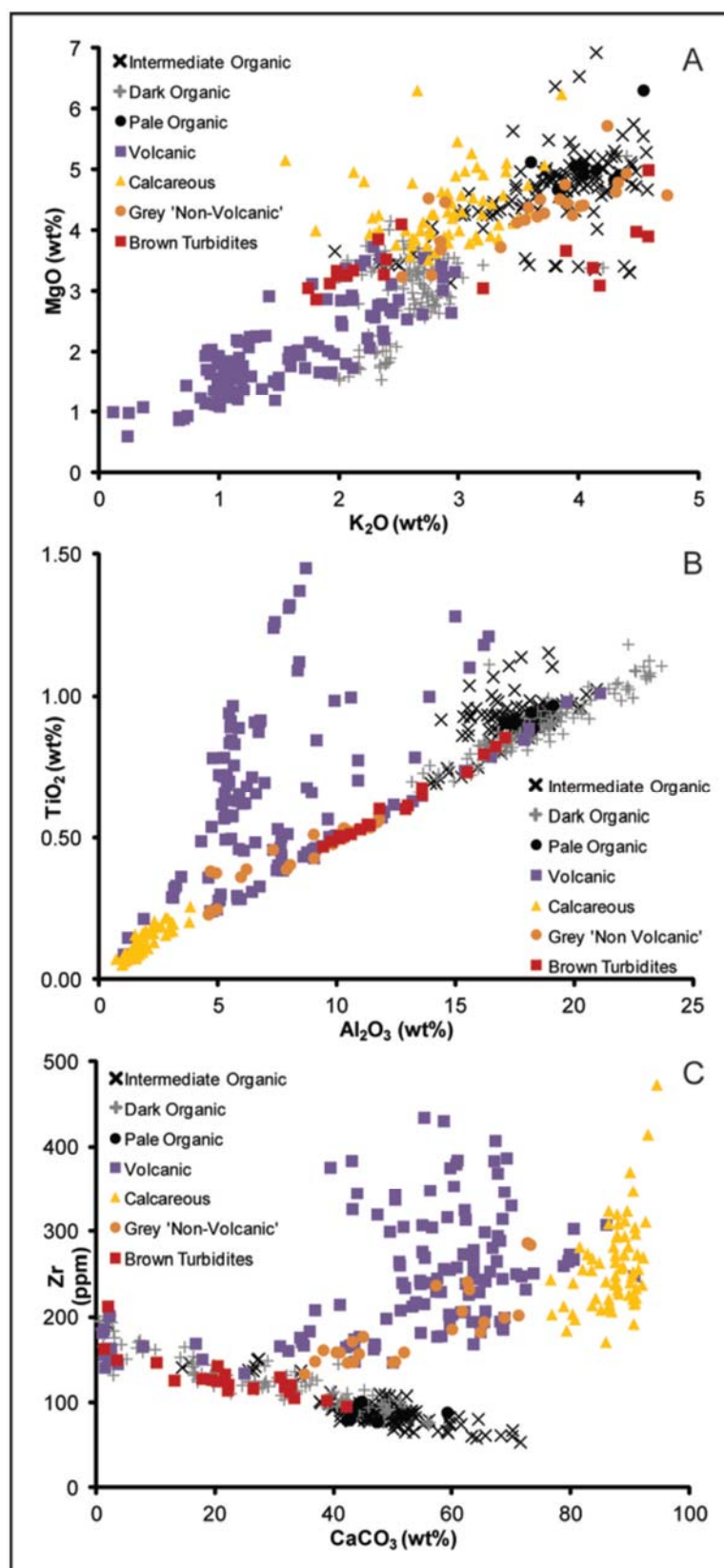


Figure 2.12: Bulk geochemical cross-plots of mudcap compositions in the Madeira Abyssal Plain that are used to infer different sources. The distinct groupings indicate organic-rich siliciclastic (subdivided into dark, intermediate and pale green), volcanoclastic, calcareous, pale grey non-volcanic and brown turbidites. From Hunt et al. (2014).

2.6. Balearic Abyssal Plain

The Balearic Abyssal Plain attains a water depth of about 2800 m and covers an area of 60,000 km², making it the largest plain in the Mediterranean Sea (Rothwell et al., 1998). An exceptional volume (500 km³) turbidite has been described from cores taken in the Balearic Abyssal Plain, as well as providing evidence for basin-wide ponding of smaller, but still large volume (>0.1 km³) turbidites (Rothwell et al., 1998; Rothwell et al., 2004).

2.1.13 Tectonic setting

The Algero-Balearic Basin is bounded in an anti-clockwise direction by the Balearic Promontory, the SE Iberian margin, the Oran Rise, the North African margin, the Tyrrhenian Trough, the Corsica-Sardinia block, the Ligurian Sea, the Gulf of Lions and the Valencia Trough (Zuniga et al., 2007). The Balearic Abyssal Plain is the central, deepest part of the Algero-Balearic Basin, in between the Balearic Promontory and the mouth of the Valencia Trough and the Sardinia-Corsica block (Zuniga et al., 2007). The seismically active North African continental margin is not only narrow but seismically active. The slope there displays a complex topography with short submarine canyons as a consequence of its collisional tectonic setting (Domzig et al., 2006).

2.1.14 Physiography and sediment input sources

The continental shelves surrounding the Balearic Abyssal Plain have widths ranging from 200 km in the Gulf of Lions to 30 km (50 km west of Corsica and Sardinia), to 20 km (54 km off North Africa; Figure 2.13; Zuniga et al., 2007). Previous studies have shown extensive turbidite deposition and large-scale bedforms along the outer rim of the Balearic Abyssal Plain and beyond that were attributed to sediment inputs mainly from the Rhone river and north-east Iberian rivers (Morris et al., 1998; Rothwell et al., 1998; Hoogakker et al., 2004) but also from the Corsican and Sardinian margins where submarine canyons are efficient in funnelling sediments to the continental rise (Got and Aloisi, 1990; Kenyon et al., 2002). Evidence of recent flow activity is provided by the run-out from the 1979 Nice harbour collapse event, which triggered a turbidity current that broke two submarine telephone cables crossing the Var Lower Valley (Mulder et al., 1998), as well as a tsunami (Genesseeux et al., 1980). One of the broken cables was

located away from the axis of the lower Var valley which means that part of the turbidity current spilled over the distal part of the Var Sedimentary Ridge and ran unconfined across the eastern part of the sediment-wave field (Migeon et al., 2001).

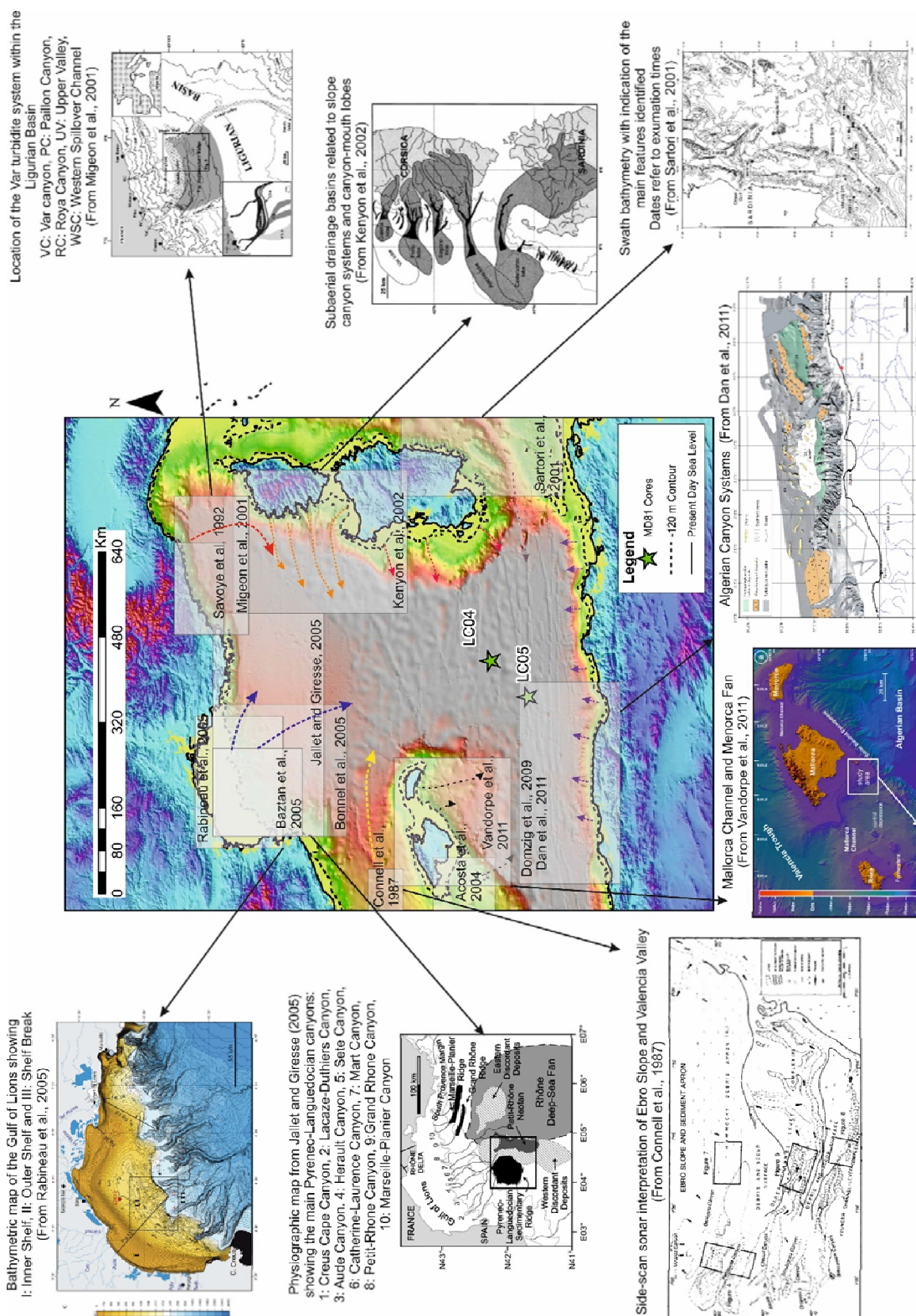


Figure 2.13: Summary of literature concerning the many potential sediment input sources to the Balearic Abyssal Plain. Core LC05 (used in this study) is annotated.

2.1.15 Interval analysed in this study

Giant piston cores taken by the RV Marion Dufresne in 1995 are analysed here, including LC04 and LC05 (Hoogakker et al., 2004). The stratigraphic sequences sampled by these cores were logged by the author both visually and using ITRAX geochemical scanning (Rothwell et al., 2004). Core LC05 provides the longest record, which spans the last 150,000 years and includes 151 turbidites. This provides a dataset for high resolution study of the effects of late Quaternary glacio-eustatic variations on landslide-triggered turbidite frequency.

2.7. Squamish Prodelta

The Squamish River delta is located at the head of the Howe Sound in British Columbia, Canada (Figure 2.14). The Howe Sound was excavated by past glacial erosion which created an approximately 150 km long trough, oriented along a fault that runs north-south through the Coast Mountain Range (Brucker et al., 2007). The delta has been prograding horizontally about 4 m per year due to large amounts of sediment delivery (approximately one million cubic metres per year; Hickin, 1989).

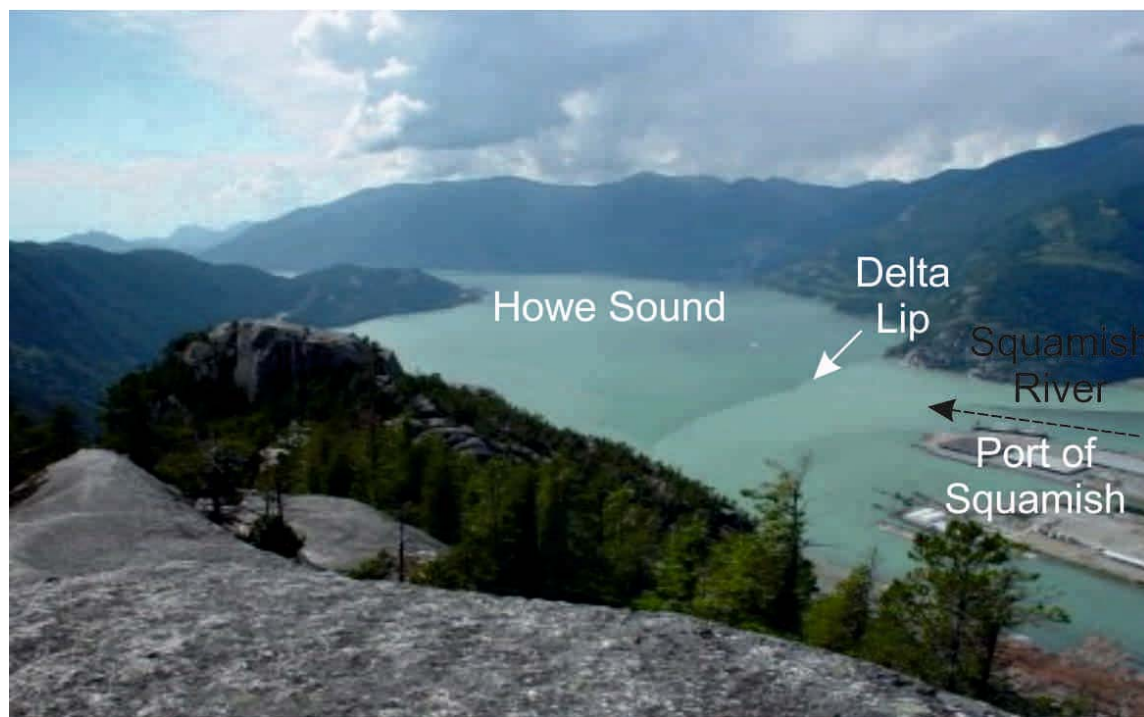


Figure 2.14: Photograph of the Howe Sound, British Columbia with the Squamish River delta lip annotated (Courtesy of John Hughes Clarke). View to the south-east.

2.1.16 Tectonic setting

The Howe Sound lies within the convergent margin of western North America and is in the most seismically active region of Canada (Bornhold et al., 1994). About 10 to 20 earthquakes are recorded annually within 100 km of the Squamish delta; however, these are usually of low magnitude (<2.5 M; Bornhold et al., 1994).

2.1.17 Physiography and sediment input sources

A terminal moraine cuts off the upper part of the Howe Sound. Inland of the terminal moraine the main source of sediment is from the Squamish River, with only minor contributions from lateral deltas of Britannia Beach and WoodFibre (Figure 2.15; Prior and Bornhold, 1987; Brucker et al., 2007). The bathymetry of the basin north of the terminal moraine increases to the south, reaching a maximum depth of 325 m (Brucker et al., 2007). The delta appears to extend across the full width of the fjord; however, the modern active delta has been modified by a training dyke that constricts almost all of the present day flow to the western side (Brucker et al., 2007). The delta lip breaks seaward to a slope of about 40° , which then rapidly shallows to a relatively constant 3° . River discharge is enhanced during the spring and summer freshet, where snowmelt contributes significantly, and may increase discharge from $100 \text{ m}^3/\text{s}$ to $>600 \text{ m}^3/\text{s}$. Multiple bathymetric surveys have identified three submarine channels that connect to the offshore delta lip (Brucker et al., 2007; Hughes Clarke et al., 2012; 2013). These channels act as conduits for turbidity currents which are most active during the freshet (Hughes Clarke et al., 2012; 2013; 2014).

2.1.18 Interval analysed in this study

The results of direct monitoring are analysed here to document the timing of more than 100 individual flow events on the offshore Squamish delta from May to August 2011 (Chapter 8). These data were acquired by Hughes Clarke et al. (2012) and comprise both observations from an ADCP mooring and 93 repeat multibeam bathymetry seafloor surveys that document the timing and character of changes in seafloor morphology. Flow velocities of between 0.5 and 1.5 m/s were recorded by the ADCP, with seafloor mapping indicating that some delta lip failures involved volumes in excess of $20,000 \text{ m}^3$. This

remarkable data set enables study of the effects of triggers for landslides and flows on very short timescales which has not been possible previously (i.e. days to minutes).

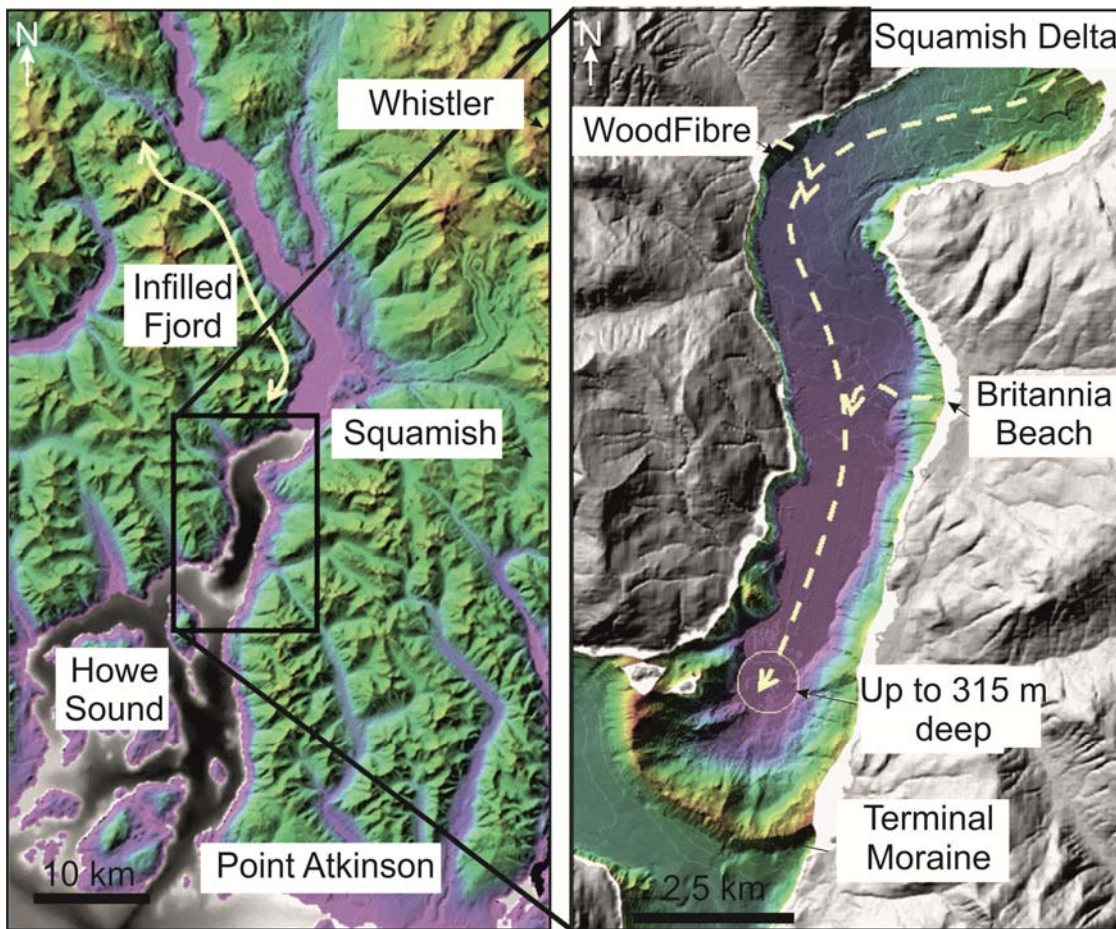


Figure 2.15: Location of the Howe Sound, with reference to the Squamish delta and other minor input sources (Modified from Brucker et al., 2007).

Chapter 3: Methods for calculating landslide and turbidite recurrence intervals

Summary

This chapter presents the methods for determining recurrence intervals for series of landslide and turbidity current events that are analysed statistically in Chapters 5, 6, 7 and 8. The age framework for each of the analysed sedimentary successions is also explained in this present chapter.

Aspects of this chapter have been incorporated into manuscripts associated with Chapters 5 to 8 and so it is not intended for subsequent stand-alone publication. All analyses and interpretations were completed by me, with editorial help provided by the co-authors during paper writing. I performed the visual and geochemical (ITRAX) logging of cores from the Balearic Abyssal Plain. James Hunt provided core logs for the Madeira and Iberia Abyssal Plains. I logged the coastal outcrop succession in Zumaia with field assistance from James Hunt in May 2013. Giuseppe Malgesini provided core logs for the Marnoso-arenacea dataset, which I checked in the field in April 2013, accompanied by Fabrizio Felletti and Andrea Squazzini (University of Milan). Alessandra Negri (University of Milan) performed biostratigraphic analyses for the Marnoso-arenacea section. John Hughes Clarke acquired and provided the 2011 Squamish dataset for analysis.

Calculating landslide and turbidite recurrence intervals from core, outcrop and monitoring

ABSTRACT *In this thesis the statistical analysis of landslide and turbidity current recurrence is considered. The datasets selected come from five distal deep-water sites, which include ancient outcrop and cored sequences, as well as more recent cored records. Distal turbidite records from these five sites cover periods of between 150 kyr and 20 Myr and each includes in excess of 100 turbidites; hence, these datasets provide valuable long term records of event frequency. These sites were selected to provide insight into the response of landslide and turbidity current triggering to sea level and climate changes. A much more recent data set from the Squamish prodelta, British Columbia, is also analysed which provides evidence of 106 turbidity currents from direct monitoring over a period of less than five months. The unique Squamish dataset provides a high enough resolution of event timing to test the significance of specific short-term triggers that cannot be determined from geological records.*

3.1 Introduction

In this chapter two approaches for measuring recurrence of landslides and sediment density flows are outlined. First, the detailed analysis of sedimentary successions is discussed, which provides extensive deep-water records across time windows of thousands to millions of years. Then a second approach is discussed, based on direct monitoring in a coastal fjord in British Columbia, Canada to characterise flow recurrence on a much shorter term (days to months). The following text explains the method for both of these approaches, including reference to the data acquisition techniques, temporal resolution of the data and potential sources of error.

3.1.1 Identifying long-term records of large landslides and flows from distal basin plains

It can be difficult to document landslide ages precisely by dating of sediment layers immediately above and below a landslide deposit, even for relatively recent deposits that are sufficiently young (< 45 ka B.P.) for AMS radiocarbon dating (Urlaub et al., 2013). Samples below the landslide may be much older than the landslide due to basal erosion. Ideally, a series of age dates are needed in the sediment drape above the landslide that provide a sediment accumulation rate, which can be used to infer the age of sediment located immediately above the top of the landslide deposit. It can be difficult to derive

this accurately, especially in areas of slow sedimentation. Dated samples are also needed from different lobes of a landslide deposit to check whether they were emplaced by a single landslide, or multiple landslides with variable ages. Therefore an alternative method is used for documenting the time periods between large landslides around a basin margin, using turbidites inferred to be generated by large slides. The recurrence time of landslides is inferred from intervals of hemipelagic fallout between turbidity currents, and the average accumulation rate of hemipelagic mud between dated horizons (Figure 3.1). Therefore, this provides information on timing of many different landslides from a small number of cores, with such large numbers ($N > 100$) of landslides needed for robust statistical analysis. It avoids the need to date prohibitively large numbers of landslides, each in a different location on the margin.

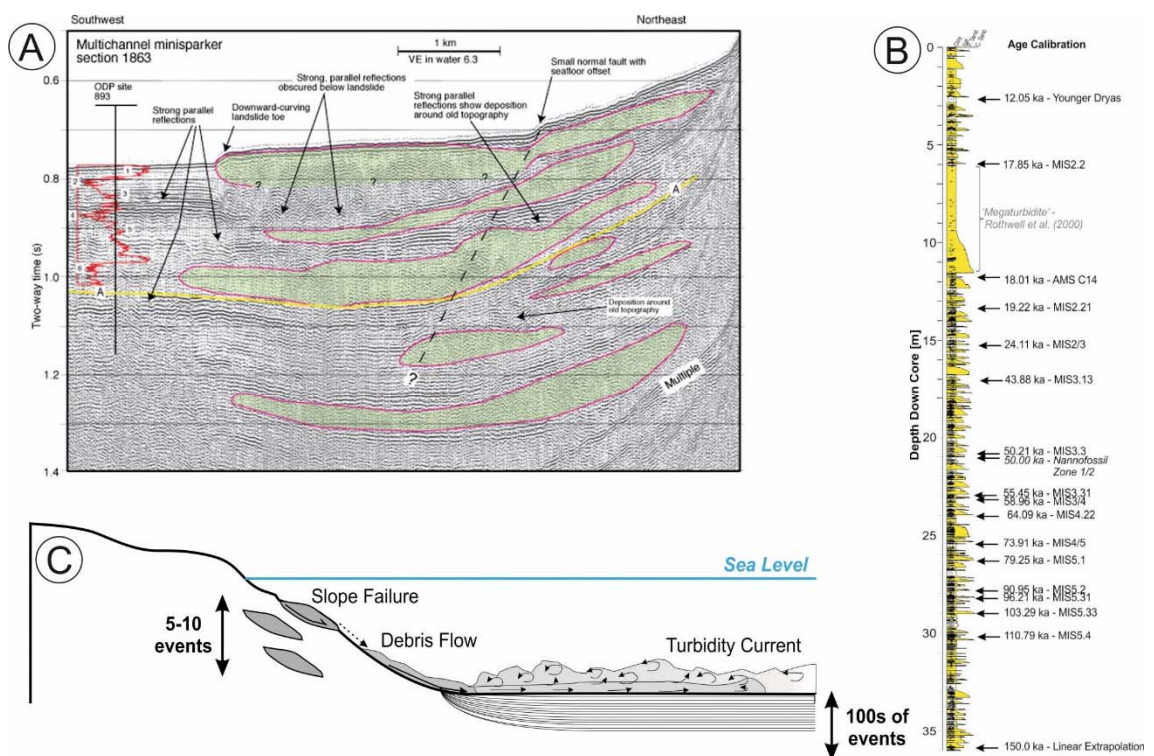


Figure 3.1: (A) Example landslide frequency study (Geist and Parsons, 2010) from the Santa Barbara Channel ($N=7$); Summary sedimentary log (B) from the Balearic Abyssal Plain ($N=151$; this study); Schematic (C) showing comparison between typical frequency of deposits in proximal and distal settings

3.1.2 Rationale for selection of distal basin plain sites

The distal basin plain datasets selected for this study satisfy the criteria listed below and illustrated in Figure 3.3. There are few (if any) other published locations worldwide that fulfil the criteria needed for this approach:

- 1) Hemipelagic mud can be distinguished clearly from turbidite mud. This allows the cumulative thickness of hemipelagic mud to be measured, and used as a proxy for time between dated horizons in the stratigraphy.
- 2) Little or no erosion occurs below turbidites; hence a continuous sedimentary record is preserved. This assumption is based on the small depth of erosion seen in the available outcrop or core. It is conceivable, however, that a uniform amount of sediment was eroded across the entire basin, thus resulting in similar, widespread thickness of hemipelagic beds. In some sites, it may be impossible to preclude this, however, geochemical and biostratigraphic evidence from the Balearic, Iberia and Madeira Abyssal Plains and Zumaia indicates that no major hiatuses exist. Continuous oxygen isotope stratigraphies, calcium carbonate curves and biozonations are observed at these sites. No correlation between thicker/coarser turbidites, and thickness of underlying hemipelagic mud was noted at any of the sites either.
- 3) Deposits include large volume ($>0.1 \text{ km}^3$) turbidites that are interpreted to have resulted from submarine landslide run-out. Calculated volumes are, however, uncertain for many of the sites considered. In the case of the Madeira Abyssal Plain it is possible to correlate deposits between boreholes and tie the lithostratigraphy into the available subsurface geophysical data (Hunt et al., 2014). Turbidites of the Marnoso-arenacea Formation have been correlated between 109 logged locations over distances of up to 120 km (Amy and Talling, 2006). There exists a lower degree of confidence for the volumes at the other sites considered in this thesis; however, the similarity in deposit type and interpreted basinal setting lends support to the interpretation that each is likely to contain similar large volume deposits.
- 4) Deposits feature sufficient ($N > 100$) turbidites which enables statistical analysis to be performed.
- 5) Minimal ($< \sim \pm 30\%$) fluctuations occur in hemipelagic mud accumulation rate between adjacent dated horizons. This is based on analysis of two recent depositional sequences that feature good age control (Figure 3.2). Locations with better age control are favoured; however, as a more accurate constraint can be placed on the variability between these fluctuations.

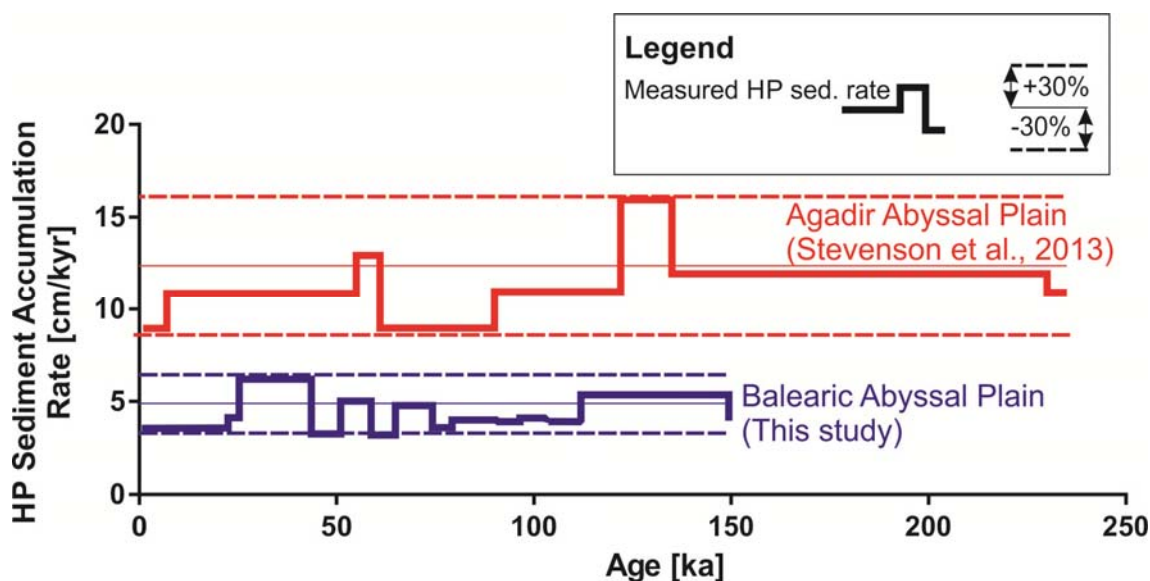


Figure 3.2: Hemipelagic accumulation rates for two sites with well constrained age frameworks. Both Agadir Basin (NW African margin) and Balearic Abyssal Plain show less than $\pm 30\%$ fluctuations in hemipelagic accumulation rate within the studied interval.

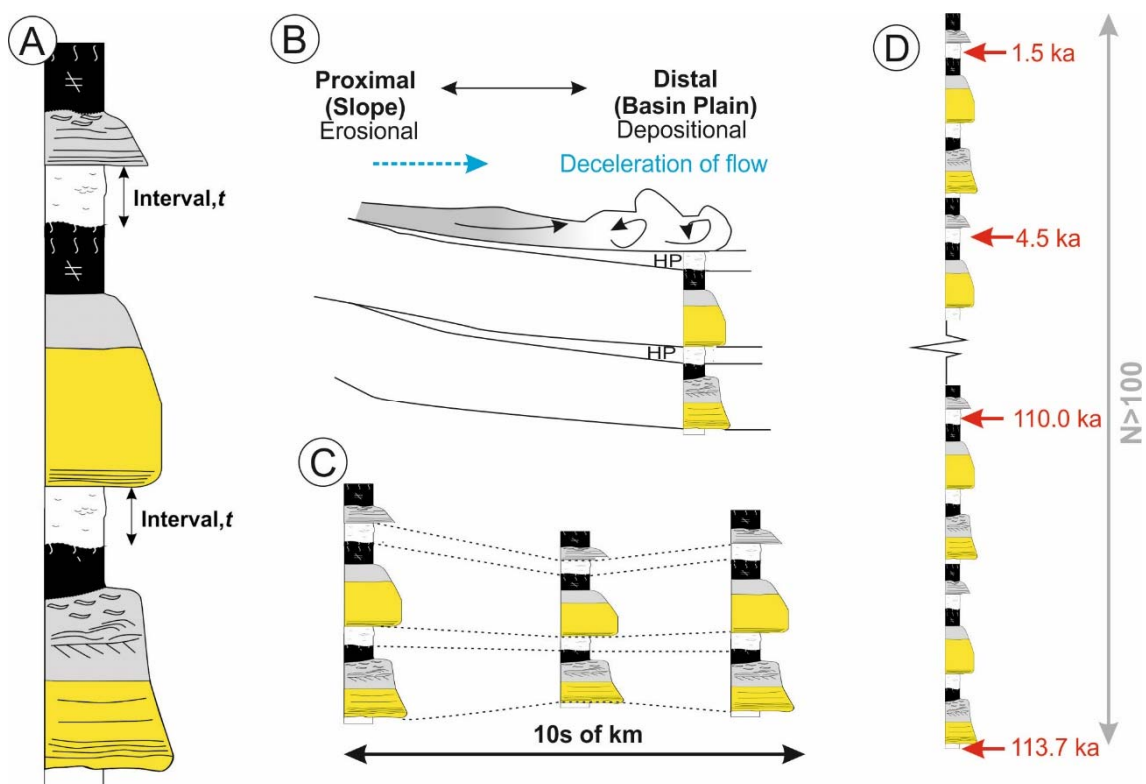


Figure 3.3: Requirements for the selection of sites. (A) Hemipelagic mud must be discernible from turbidite mud. (B) Erosion between successive flows must be negligible; hence the selection of distal basin plain settings. (C) Deposits must be large volume ($> 0.1 \text{ km}^3$) and therefore attributable to large landslides, e.g. correlated over large distances. (D) A large enough sample ($N > 106$) must exist for robust statistical analysis, and sufficient age control provides calibration of hemipelagic accumulation rates

In addition to these criteria, sedimentary records are selected that cover time periods including sea level and/or climatic variations for comparison with changes in landslide and turbidite recurrence rate. Table 3.1 summarises the sites analysed in this study, with reference to the time period, input sources to the basin, number of turbidites and criteria for identification of hemipelagic mud.

3.1.3 Visual sedimentary logging

Sedimentary logging was performed at a scale appropriate to the resolvable thickness of beds. Lithological variations were resolvable down to ~5 mm for the Balearic Abyssal Plain, Iberia Abyssal Plain and Zumaia series datasets; hence a scale of 1:5 was adopted. For the Madeira Abyssal Plain and Marnoso-arenacea datasets, the confidence in resolving bed contacts was ~10 mm to ~50 mm; therefore a scale of 1:10 was used. Where measured, grain size was estimated using a grain-size comparator (e.g. Talling et al., 2007b). Summary sedimentary logs are provided in Appendix 2. In each of the datasets, in excess of 100 discrete turbidites were observed.

Turbidites identified from the cores and outcrops studied here are generally limited to fine grained sand, with only a few instances of medium to coarse grained-basal deposits. At the Zumaia, Iberia, Balearic and Madeira Abyssal Plain sites turbidites are mostly muddy, typically missing the basal T_A Bouma division. Turbidite facies identified from the Balearic Abyssal Plain are shown in Table 3.2. Turbidites of the Marnoso-arenacea Formation are mostly muddy, but also comprise massive sand beds. The wide variety of facies observed at the Marnoso-arenacea is well discussed in many other publications (Amy and Talling, 2006; Talling et al., 2007b,c, 2012, 2013; Sumner et al., 2012). Where observed in outcrop (Marnoso-arenacea Formation, Figure 3.4; Zumaia Series, Figure 3.5), bedding surfaces are even and parallel, forming a tabular-type geometry. A broad fining-upwards trend is observed for grain size at all sites, with beds generally featuring sharp and planar basal contacts. Low to very low angle ripples are often observed in well-developed climbing patterns which indicate deceleration of a flow (Mutti, 1977; Jobe et al., 2012; Sumner et al., 2012). At both the Balearic Abyssal Plain and Marnoso-arenacea sites, infrequent, very thick basin-wide ‘megaturbidites’ exist (*sensu* Reeder et al., 2000; Figure 3.4). These megaturbidites are measured to be between 8 m and 15 m thick, with volumes of between 35 km³ (Contessa Bed at the Marnoso-arenacea; Ricci Luchi, 1975; Talling et al., 2007b,c) and 500 km³ (Balearic megaturbidite;

Rothwell et al., 1998). Palaeocurrent measurements show a different flow direction at the sandy base of the Contessa Bed, than in higher silty rippled intervals which indicates that the large volume flow may have entered the basin at one end, and was then reflected from the opposite side. This evidence of flow reflection, coupled with the other sedimentological observations of turbidites, is indicative of deposition in a low relief basin plain, where flows decelerated and erosion was inhibited (e.g. Mutti, 1977; Talling et al., 2012).

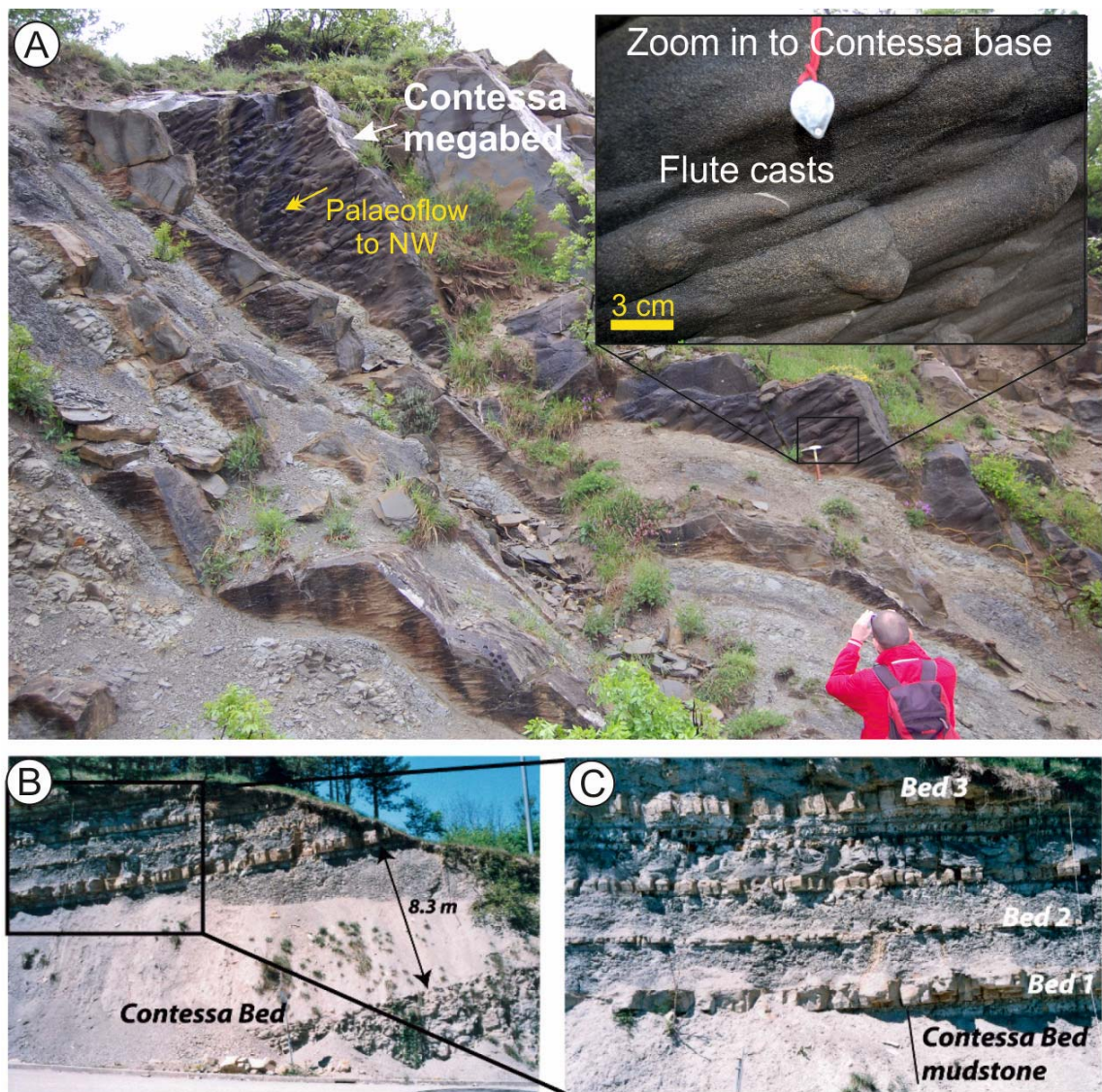


Figure 3.4: Field photographs of the Marnoso-arenacea Formation (A) Detail on Contessa megabed showing palaeocurrent indicators on base. Inset figure shows zoom in to show the flute casts. (B) Contessa megabed thickness showing considerable thickness. (C) Zoom in to beds above Contessa megabed to show more typical, thinner turbidite facies as analysed in this study. Photographs B and C from Talling et al. (2007b).

Table 3.1: Summary of datasets analysed in this study










| | Basin (Area) | Data Source (Age) | Input sources | Criteria for discerning hemipelagic mud | No. turbidites (N) | Mean Recurrence Interval, λ |
|----------------------|---|---|---|---|--------------------|---|
| Ancient Basin Plains | Marnoso-Arenacea, Italian Apennines (>4,800 km ²) | Outcrop: Mid Miocene (13.5 to 14.1 Ma) | Two sources – Dominant Alpine-Apennine source, plus occasional source for calcareous flows | Foraminifer-rich, distinct colour difference (Talling et al., 2007a,b, 2012a) | 696 | 1,400 years |
| | Zumaia Series (Unknown, but estimated to be >10,000 km ²) | Outcrop: Late Palaeocene to Early Eocene (54.0 to 56.3 Ma) | Carbonate shelf and lesser degree of terrigenous input from the east and south-east | Lighter colour, prominent less weathered limestone, foraminifer-rich (Gawenda et al., 1999) | 285 | 2,500 years |
| | Iberia Abyssal Plain (107,000 km ²) | ODP Borehole 1068: Late Cretaceous to Mid Eocene (48.16 to 67.61 Ma) | Proto-canyons linked to the Iberian Margin. Interpreted to be one main source area in the east | Foraminifer-rich (core surface appears pitted), darker colour, massive, non-laminated (Whitmarsh et al., 1996, 1998; Ladner and Wise, 2001; McGonigal and Wise, 2001) | 1571 | 12,500 years |
| Recent Basin Plains | Madeira Abyssal Plain (68,000 km ²) | ODP Boreholes 950, 951, 952: Holocene to late Miocene (0 to 7 Ma) | Two main sources – Canary Islands (predominantly volcanoclastic) and Agadir Canyon/Basin (siliciclastic and calcareous) | Foraminifer-rich, distinct colour difference (Wynn et al., 2002) | 108 | 36,500 years |
| | Balearic Abyssal Plain (60,000 km ²) | Calypso Piston Core LC05: Holocene to Late Pleistocene (0 to 0.15 Ma) | Multiple (6-7) potential sources – Rhone, Ebro, Var, Valencia Fan, Algerian Margin, Balearic Islands, Corsica/Sardinia | Foraminifer-rich (core surface appears pitted), colour difference (Hoogakker et al., 2004) | 151* / 111† | 1000 years* / 1,400 years† |
| Present Day Fjord | Squamish Prodelta, British Columbia | Repeat (daily) multibeam surveys and ADCP monitoring (April-September 2011) | Squamish River – discharge significantly elevated during Spring/Summer freshet due to glacial meltwater | Turbidity currents observed based on bathymetry differences and direct ADCP monitoring | 106 | 2 (within channels) to 3.8 days (at terminus of northern channel) |

Note: Where no intervening hemipelagic mud occurs between turbidites in the Balearic Abyssal Plain data, two recurrence intervals are presented:

*Assuming stacked turbidites represent run-out from discrete but contemporaneous slides.

†Assuming stacked turbidites represent multiple pulses of run-out from the same slide (e.g. multi-stage failure).

Table 3.2: Examples of facies identified from cores in the Balearic Abyssal Plain that are also typical of those observed at the other sites. A wider variety of facies exist at the Marnoso-arenacea, as detailed in Amy and Talling (2006), Talling et al. (2007b,c, 2012) and Magesini (2012)

| Bed Type | Type L1 | Type L2 | Type L3 | Type L4 | Type L5 | Type H1 | Type H2 | Type H3 | Type M |
|------------------------|---|---|--|---|--|--|--|--|---|
| General Description | Structureless homogeneous turbidite mud | Very thin fine grained turbidite | Upwards fining very thin fine grained turbidite couplet or triplet | Thin to medium bedded fine grained turbidite | Thin to medium fine to medium grained turbidite with convolute or rippled laminae | Thick to medium bedded sandy turbidite with ripple and cross bedded laminae | Thick to medium bedded sandy turbidite with ripple planar laminae | Thick to medium bedded sandy turbidite with thick massive poorly graded basal division | Anomalously thick deposit (megabed) fining from sand to structureless homogeneous thick upper unit |
| Thickness | 0.05 m to 0.15 m | 0.05 m to 0.20 m | 0.10 m to 0.30 m | 0.15 m to 0.30 m | 0.15 m to 0.40 m | 0.15 m to 0.50 m | 0.40 m to 0.60 m | 0.40 m to 0.60 m | 7.00 m to 10.00 m |
| Example Visual Log |  |  |  |  |  |  |  |  |  |
| | None different scale | | | | | | | | |
| Bedding and Structures | None often with speckling/mottling (bioturbation) at upper contact | Thin laminae or single lamina of sand, silt, or foraminifera fragments at base | Distinct couplet or triplet each with basal laminae | Planar laminations at base, transitioning upwards into rippled and flaser laminations | Massive basal division overlain by convoluted or rippled division, transitioning into flaser laminae | Planar spaced laminae in basal division, transitioning to climbing ripples and flaser bedding | Planar spaced laminae in basal division, transitioning to structureless and flaser laminae | Planar spaced laminae at base overlying massive sand division | Planar laminae at base, massive basal division, transitioning into cross bedded, climbing ripple and convolute laminae. Massive sand division which may include planar intra-bed contacts |
| Contacts | Sharp planar basal contact, upper contact typically gradational and bioturbated | Sharp planar basal contact, upper contact typically gradational and bioturbated | Sharp planar basal and internal contacts, upper contact typically gradational and bioturbated | Sharp irregular basal contact, upper contact typically gradational and bioturbated | Sharp irregular basal contact, upper contact typically gradational and bioturbated | Sharp irregular basal contact, upper contact typically gradational and bioturbated, sharp internal contacts due to internal cross bedding | Sharp irregular basal contact, upper contact typically gradational and bioturbated, sharp internal contact within medium sand fraction | Sharp irregular basal contact, upper contact typically gradational and bioturbated | Sharp and irregular (eroded) base, upper contact gradational and bioturbated |
| Grain Size | Clay | Silt to clay | Fine sand to clay | Fine sand to clay | Fine sand to clay | Medium sand to clay | Medium sand to clay | Coarse sand to clay | Coarse sand to clay |
| Grading | No grading apparent | Abrupt positive grading at very base | Two or three individual upwards fining intervals as part of an overall upwards fining succession | Positive, with grain size break at silt/mud contact | Inversely graded base, abrupt grain size break at medium sand to silt and silt to clay contacts | Inversely graded base, poorly graded basal unit, sharp grain size break at sand/silt and silt/mud contacts | Inversely graded base, poorly graded basal unit, sharp grain size break at silt/mud contact | No grading in mud division | Positive, although negative grading exists in coarse fraction at base, fining to upper homogenous (ungraded) mud unit, slight grain size break at transition from silt to mud fraction |
| Interpretation | Mud density flow deposit (dense) resulting from distal or waning downslope-decelerating turbidity current | Low density turbidite resulting either from distal or low energy event | Surging low density turbidite, evidencing two or three phases of flow rejuvenation | Low density turbidite with grains reworked as bedload | Grain size break (sand/silt) may mark transition from high to low density turbidite (i.e. founding of turbidity current). Convolute or rippled laminae are evidence for fully turbulent flow and slow fall out rates | High density (sandy) turbidite. Grain support via combination of damped turbulence or grain to grain interactions. Convolute or rippled laminae are evidence for dilute fully turbulent flow and slow fall out rates | High density (sandy) turbidite. Grain size break (sand/silt) may mark transition from high to low density turbidite (i.e. founding of turbidity current). Planar laminae formed from combination of deposition from traction carpet and in dilute flow | High density (sandy) turbidite. Planar laminae formed as a result of grain flow at the turbidity current head, the rest of the flow settled out due to low density turbulent suspension and/or gel strength and/or excess pore pressures | Ponded megaturbidite resulting from steady long-lived turbidity current |

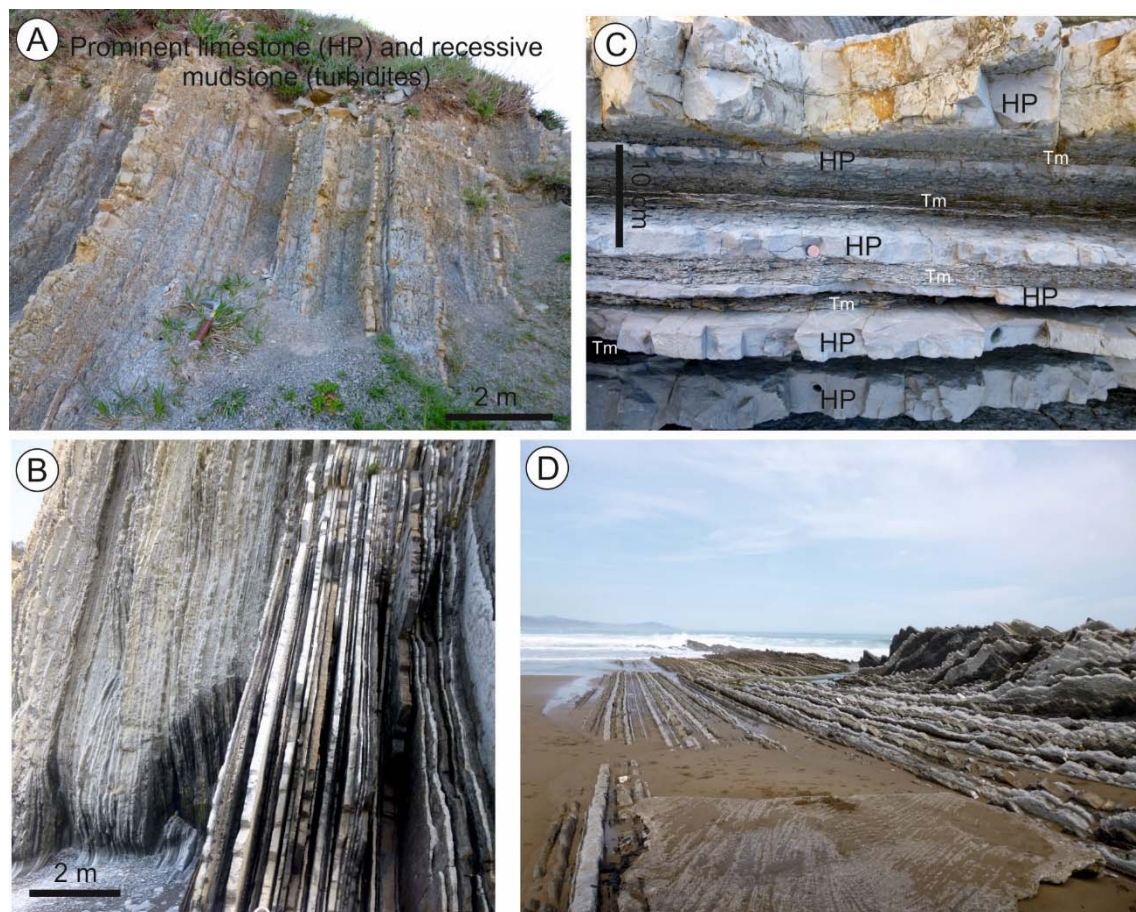


Figure 3.5: Field photographs from Zumaia, NE Spain, illustrating interbedded turbidite and hemipelagite successions. Turbidites are mostly muddy within the interval studied. (A and B) Photograph to show exposed coastal outcrop. Turbidites are generally recessive and more easily weathered than hemipelagites. (C) Zoom in to show detail of centimetre-scale beds (rotated 90 degrees). Hemipelagic mud beds (HP) are prominent relative to turbidite mud (Tm). (D) Photograph to show the tabular, laterally continuous nature of these basin plain deposits on the wave cut platform approaching low tide.

3.1.4 Geochemical logging

As part of this study, geochemical logging was performed on samples from the Balearic Abyssal Plain using the ITRAX micro-X-ray fluorescence (XRF) core scanner, based in the British Oceanographic Core Repository Facility (BOSCORF), Southampton, UK. The ITRAX makes high-resolution energy-dispersive XRF (ED-XRF) measurements along the longitudinal axis of split core samples (Rothwell et al., 2004). Core samples are moved progressively past a 3 kW Mo-tube X-Ray source and XRF Si-drift chamber detector (Rothwell et al., 2004; Croudace et al., 2006; Hunt, 2012). For this study, the instrument was operated at 60 kV and 45 mA, with an X-Ray dwell time of 800 ms and a measurement step size of 500 μm . Each ED-XRF spectrum was recorded and deconvolved to derive peak area integrals for individual elements that are nominally proportional to concentrations of major and minor elements (Rothwell et al., 2004). Data

for Al, Si, CA, K, Ti, V, Mn, Fe, Ni, Cu, Zn, As, Br, Rb, Sr and Zr were recorded and manipulated in the Itrax.PLOT software (Rothwell et al., 2004).

3.1.5 Identification of hemipelagic deposits

It is essential to be able to distinguish between mud deposited by hemipelagic fallout and that deposited from the final stages of turbidity currents, in order to measure the thickness of hemipelagic mud between each turbidite and hence calculate recurrence times. The five distal basin plain datasets were chosen because the two types of mud have distinctive features, texture and colours (Figure 3.6, Figure 3.7 and Table 3.1). In other locations, especially those below the carbonate compensation depth or ancient outcrops, it is often difficult to identify the two types of mud (Talling et al., 2012).

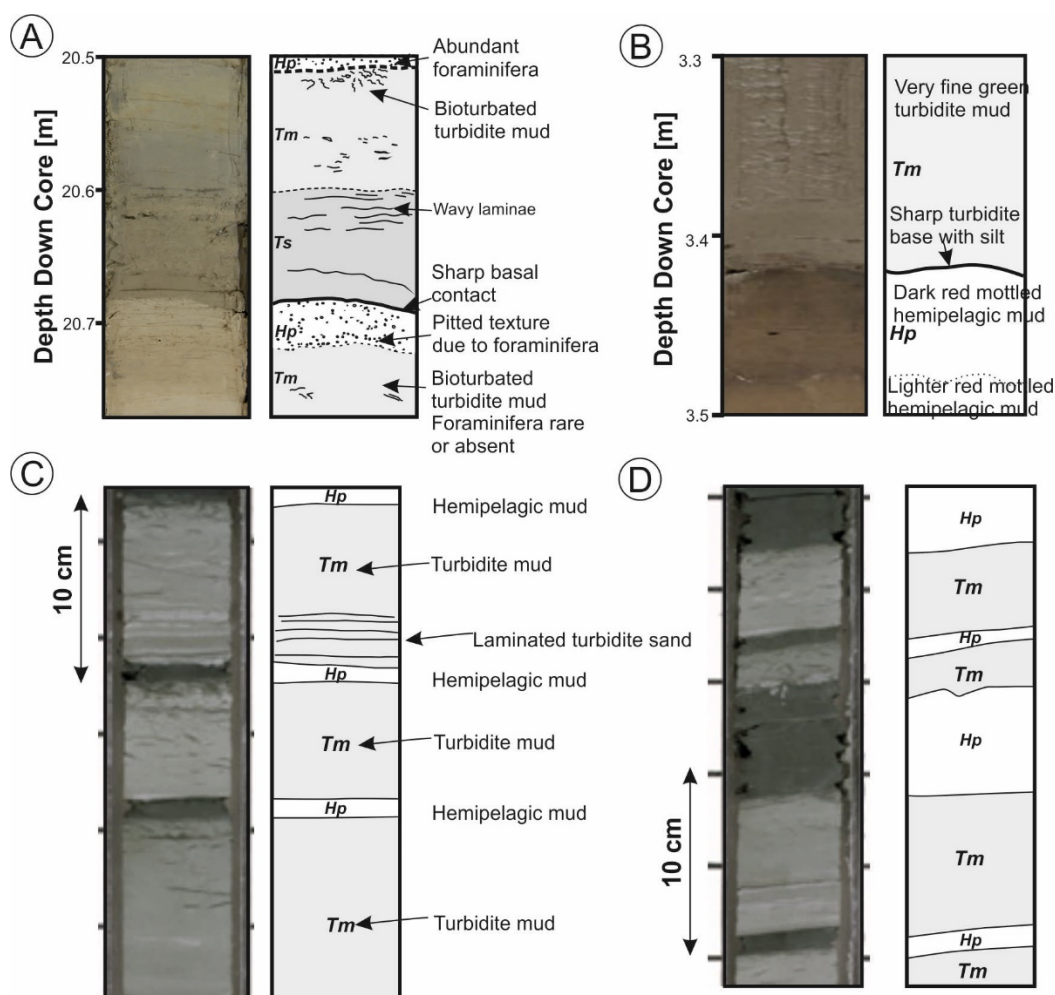


Figure 3.6: Identification of hemipelagic mud from core studies based on colour and textural differences, including Balearic Abyssal Plain (A), Madeira Abyssal Plain (B), and Iberia Abyssal Plain (C and D).

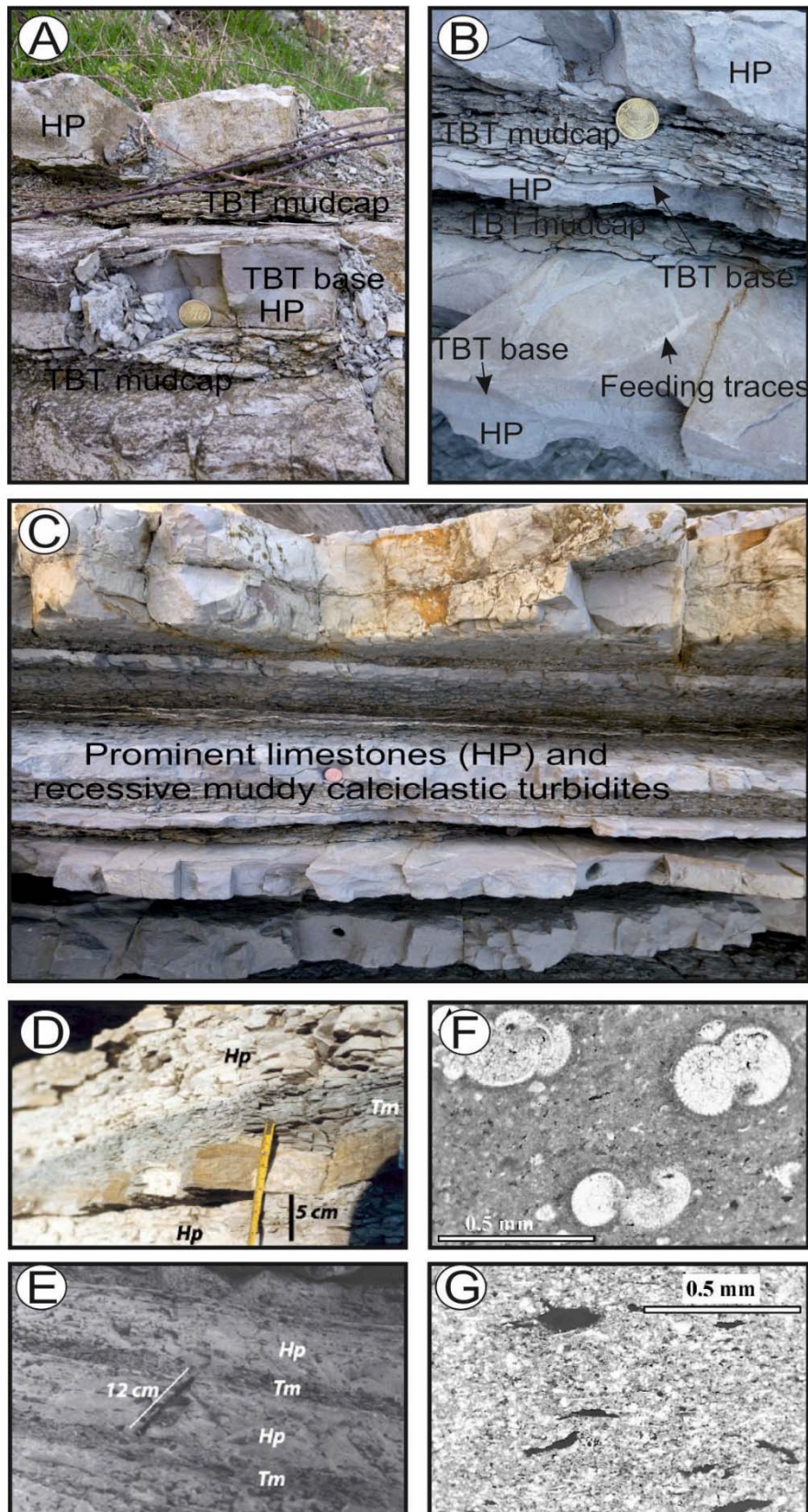


Figure 3.7: Identification of hemipelagic mud from outcrop studies. Photographs A to C from Zumaia showing prominent hemipelagic (HP) limestone beds (A to C). Photographs D and E show Marnoso-arenacea Formation where a marked colour difference can be seen between hemipelagic and turbidite mud (Tm). Thin sections also show microtextural differences where hemipelagic mud (F) features large and unbroken foraminifera tests and turbidite mud (G) contains dispersed carbonaceous matter. Images D to G from Talling et al. (2007c).

Visually diagnostic features of hemipelagic mud in these sequences are relatively common dispersed foraminifera, reduced organic carbon content, higher calcium carbonate content, different colour and the presence of bioturbation (Table 3.1; Wynn et al., 2002; Hoogakker et al., 2004; Talling et al., 2007b,c, 2012; Cummings and Hodgson, 2011). This visual differentiation has been shown to be consistent with detailed elemental (Jarvis and Higgs, 1987; Jarvis et al., 1998; Rothwell et al., 2004), and microscopic analyses (Talling et al., 2007c; Figure 3.7).

3.1.6 Erosion by turbidity currents

The method infers that significant thicknesses of hemipelagic mud were not eroded beneath turbidity currents, and a demonstration of how erosion would affect recurrence time estimates is detailed in Chapter 5. This view is supported by analyses of hemipelagic mud thickness beneath individual beds in the Marnoso-arenacea Formation, showing this thickness varies by < 5-to-10 cm over ~120 km (Talling et al., 2007b; Figure 3.8). A lack of spatial variation in coccolith assemblages and thickness of turbidite mud caps within the Madeira Abyssal Plain indicate minimal erosion - interpreted to be limited to a few centimetres (Weaver and Thomson, 1993; Weaver, 1994). The turbidite beds in the Madeira, Iberia and Balearic Abyssal Plain cores have flat bases, and lack irregular bases indicative of erosion, although the narrow core width (< 10 cm) precludes observation of larger scale erosional features (Weaver and Thomson, 1993). Hemipelagic mud intervals at Zumaia generally have thickness variations of <5 mm over distances of 50 m (extent of along-strike beach exposure; Figure 3.9) and trace fossils are not truncated (Bernaola et al., 2007; Cummings and Hodgson, 2011; Figure 3.7B).

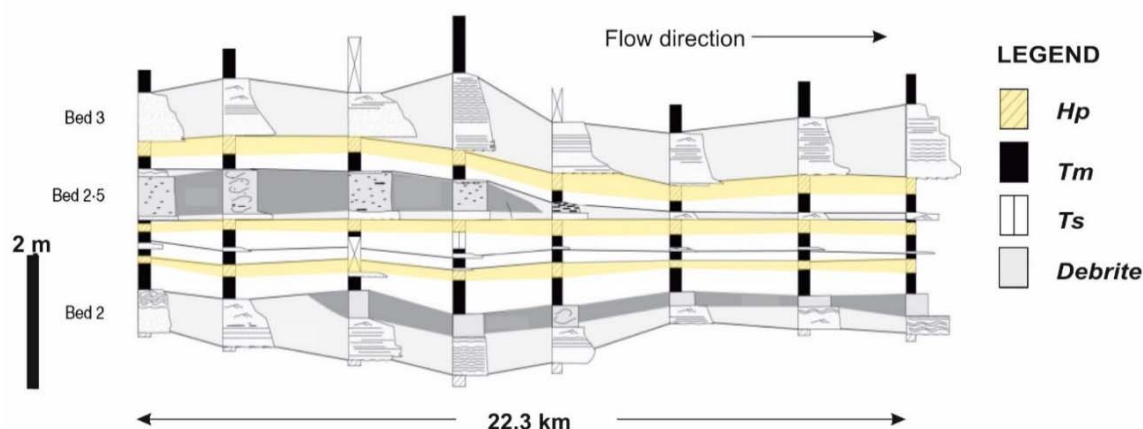


Figure 3.8: Example bed correlation in Marnoso-arenacea showing uniform hemipelagic bed thickness (Modified from Amy and Talling, 2006). Hp refers to hemipelagic mud; Tm, turbidite mud; Ts, turbidite sand.

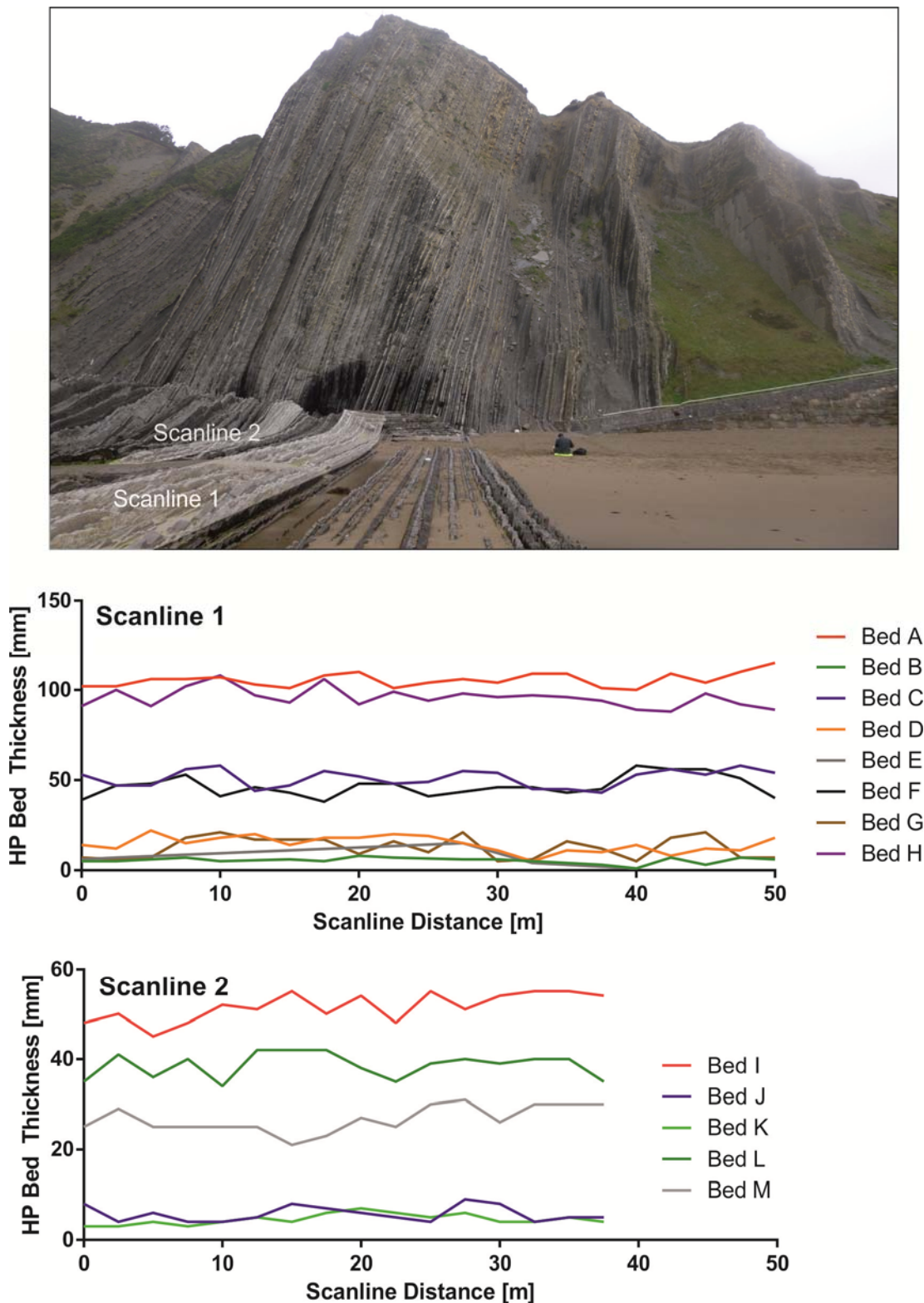


Figure 3.9: Variation in hemipelagic (HP) bed thickness determined from 2.5 m-spaced scanlines at Zumaia along two beach transects as shown in the top photograph. Geologist seated in front of outcrop for scale. The variation in hemipelagic mud thickness is generally <5 mm.

3.1.7 Age control

It was not feasible to date every hemipelagic mud interval due to the large number of beds considered at each of the study sites. The time period between turbidites was therefore derived by dividing the thickness of hemipelagic mud between turbidites by the average hemipelagic accumulation rate. The average hemipelagic accumulation rate was calculated between adjacent dated horizons by dividing their difference in age by cumulative hemipelagic mud thickness for that interval.

Marnoso-arenacea Formation

Of all the studied sites, the lowest resolution dating exists for the Marnoso-arenacea Formation. Dating of the Marnoso-arenacea Formation is provided by two biostratigraphic (nannofossil) horizons, at 13.5 and 14.1 Ma, bounding the studied interval (Figure 3.10).

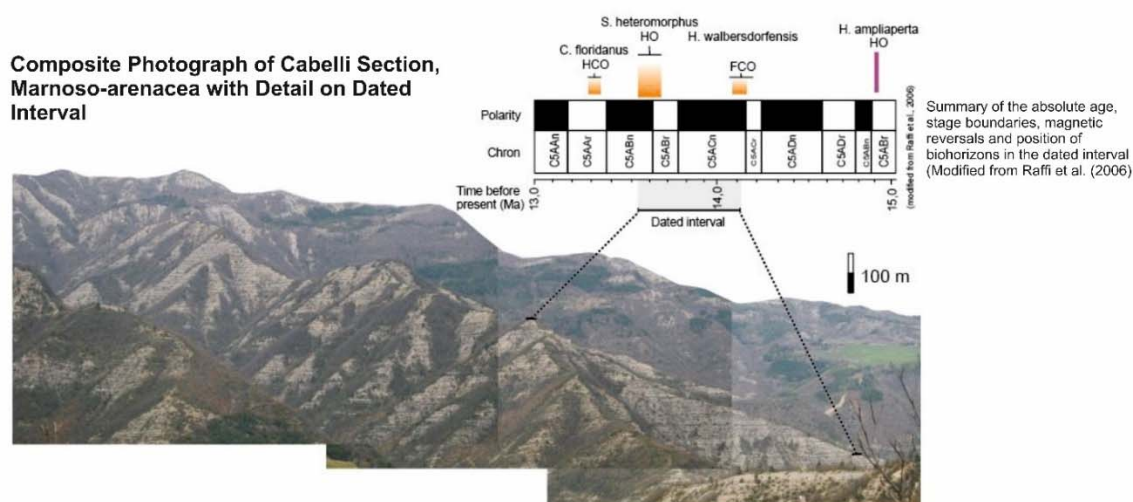


Figure 3.10: Photo of Cabelli section at the Marnoso-arenacea annotated with biostratigraphic control points (from Clare et al., 2014, after Malgesini, 2012)

Zumaia Series

Age control for the Zumaia section is based on high resolution biostratigraphy (Alegret et al., 2009; Baceta et al., 2000; Schmitz et al., 1997) as well as magnetostratigraphy (Baceta et al., 2000; Dinares-Turell et al., 2002; Storme et al., 2012). Dated horizons occur every 0.01 to 0.72 Myr within the Zumaia section and the interval containing the Initial Eocene Thermal Maximum (IETM) is particularly well dated. This includes dates for subdivisions of the IETM, including onset, core (most intense),

recovery and end phases of the Carbon Isotopic Excursion (CIE). This age control provides confidence in deriving hemipelagic accumulation rates and therefore recurrence intervals, particularly during and adjacent to the IETM. The calculated rates of hemipelagic mud accumulation show good correlation with those in previous studies (Winkler and Gawenda, 1999; Schmitz et al., 2001; Figure 3.12). The logged interval of the Zumaia series has been dated to between 56.4 and 54.8 Ma.

Iberia Abyssal Plain

Age control for Iberia ODP Site 1068 is provided by coccolith biostratigraphy (Whitmarsh et al., 1996, 1998; Figure 3.11). Dated horizons at Iberia occur every 0.7 to 1.0 Myr; hence dating is not as precise as at Zumaia; however, dates are available either side of the IETM to ensure confidence in its identification. Based on these dates and the vertical resolution, the minimum resolvable interval is 1.9 kyr at ODP Site 1068, compared to 0.5 kyr at Zumaia. The Iberia Abyssal Plain interval in this study is dated between 48.1 Ma and 67.7 Ma.

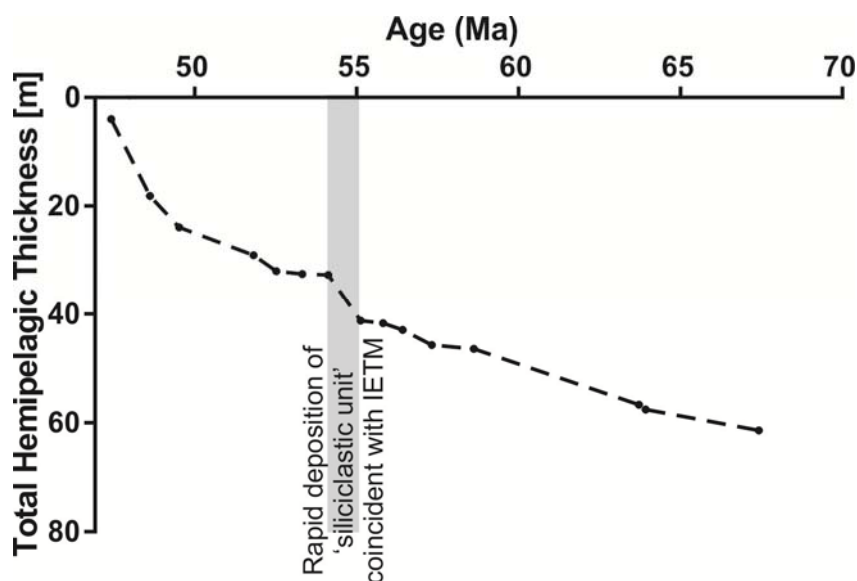


Figure 3.11: Age plot for hemipelagic sedimentation at the Iberia Abyssal Plain based on calcareous nannofossil datum points from Ladner and Wise (2001) and McGonigal and Wise (2001)

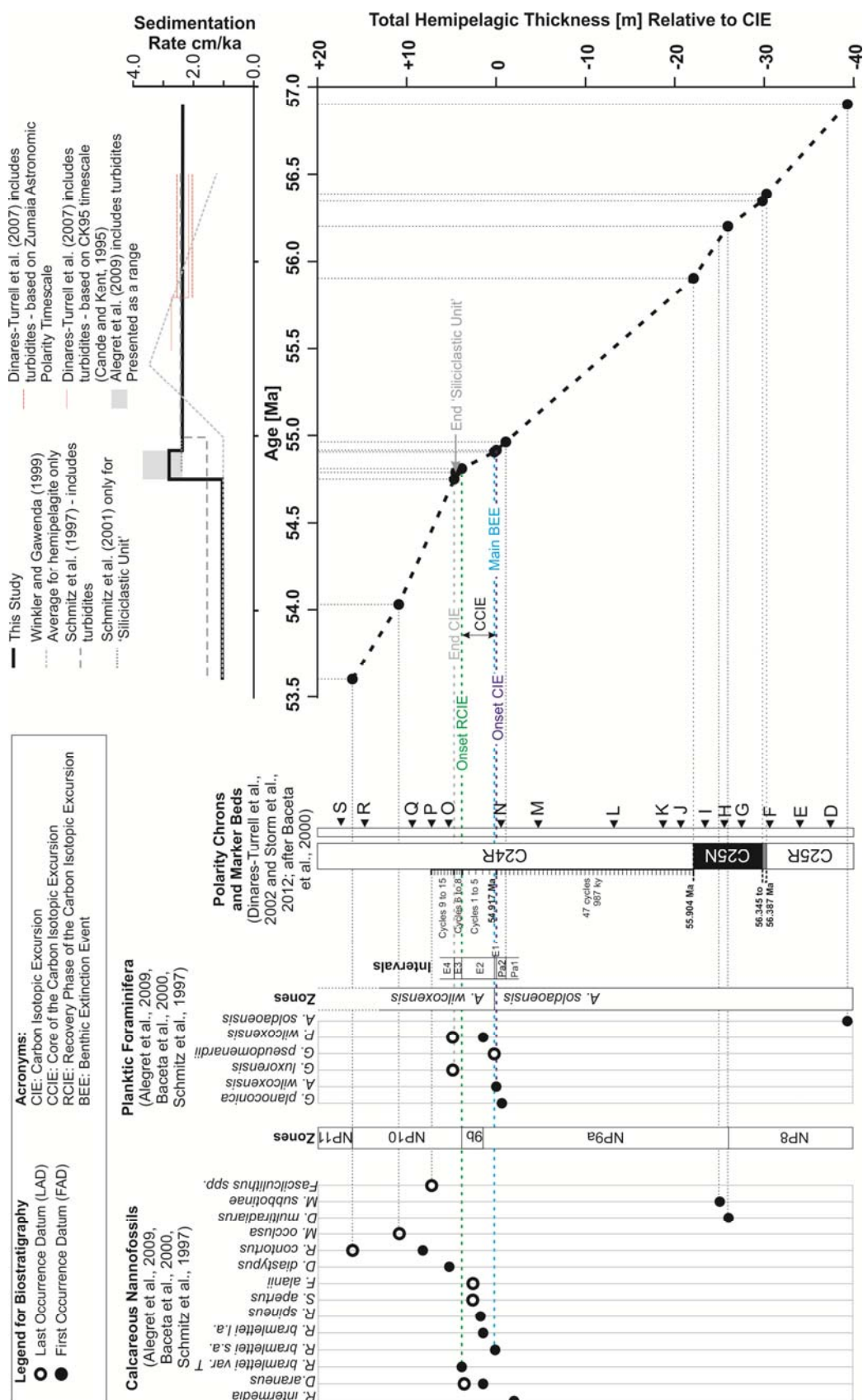


Figure 3.12: Available age control for the studied interval at Zumaia presented in relation to total hemipelagic depth after Schmitz et al. (1997), Winkler and Gawenda (1999), Baceta et al. (2000), Schmitz et al. (2001), Dinares-Turrell et al. (2002, 2007), Alegret et al. (2009) and Storme et al. (2012). The hemipelagic sedimentation rates derived for this study are compared to averaged rates for previous studies which show a good level of agreement.

Madeira Abyssal Plain

Dated horizons in the Madeira Abyssal Plain sequence are provided by detailed coccolith biostratigraphy and oxygen isotope stratigraphies (Weaver and Kuijpers, 1983; Howe and Sblendorio-Levy, 1998; Wynn et al., 2002; Hunt et al., 2014; Figure 3.13). While a record exists for the last 17 Ma, the Madeira Abyssal Plain record analysed in this study spans the last 7 Ma (Hunt et al., 2014). This is because turbidites cannot be reliably correlated across the basin plain prior to 7 Ma (Weaver, 2003).

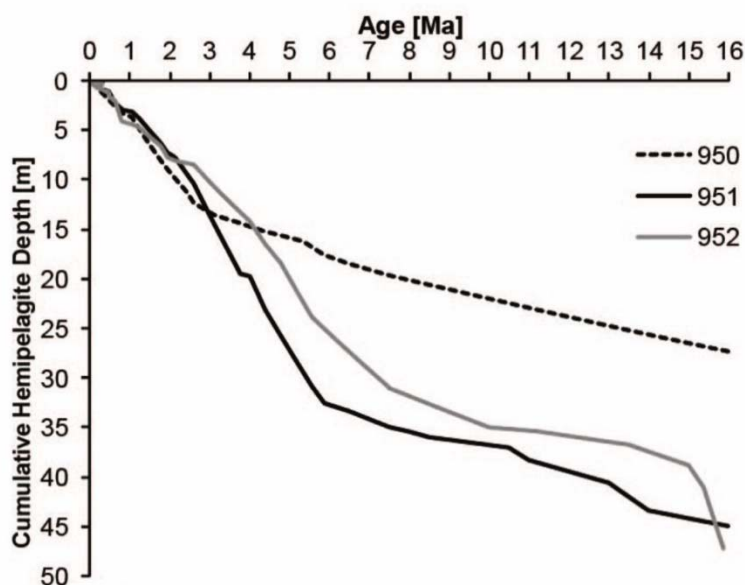


Figure 3.13: Age plot for hemipelagic sedimentation at the Madeira Abyssal Plain. The age plots are relevant for the entire basin and allow for correlation of turbidites accurately between boreholes 950, 951 and 952 (from Clare et al., 2014)

Balearic Abyssal Plain

Dating of Balearic Abyssal Plain cores is based on nannofossil biostratigraphy, radiocarbon dating (Rothwell et al., 1998), and correlation of continuous downcore elemental data (Figure 3.15) with high resolution oxygen isotope and calcium carbonate stratigraphy available for other cores in the southern part of the basin (Hoogakker et al., 2004). As shown by Hoogakker (2004) and Rothwell et al. (2004), the calcium carbonate stratigraphy of pelagic records from the Balearic Abyssal Plain closely mirrors the oxygen isotope record. High CaCO_3 contents occur when planktonic foraminifera $\delta^{18}\text{O}$ values are low (Hoogakker, 2003; Rothwell et al., 2004). Variation in pelagic calcium carbonate can therefore be used as a proxy to identify known oxygen isotope events. Based on the results of visual logging, all of the ITRAX data that includes turbidites is removed, to leave only

elemental data relating to hemipelagic mud. The ITRAX measurements of Ca from hemipelagic deposits show good correlation with the CaCO_3 and oxygen isotope records of Hoogakker et al. (2004). This reinforces the interpretation that there has been no, or only limited erosion, and provides an additional technique for proxy dating of the sedimentary record. Records of Sr also correlate well with the Ca record from ITRAX which adds additional confidence in the method (Figure 3.14).

It has been necessary to correct for stretching of the upper part of the Balearic Abyssal Plain cores due to effects of coring disturbance (Figure 3.17). The outcome of this correction agrees well with the results of Hoogakker et al. (2004; Figure 3.16), which was developed following the methodologies of Thomson et al. (2000) and Thouveny et al. (2000).

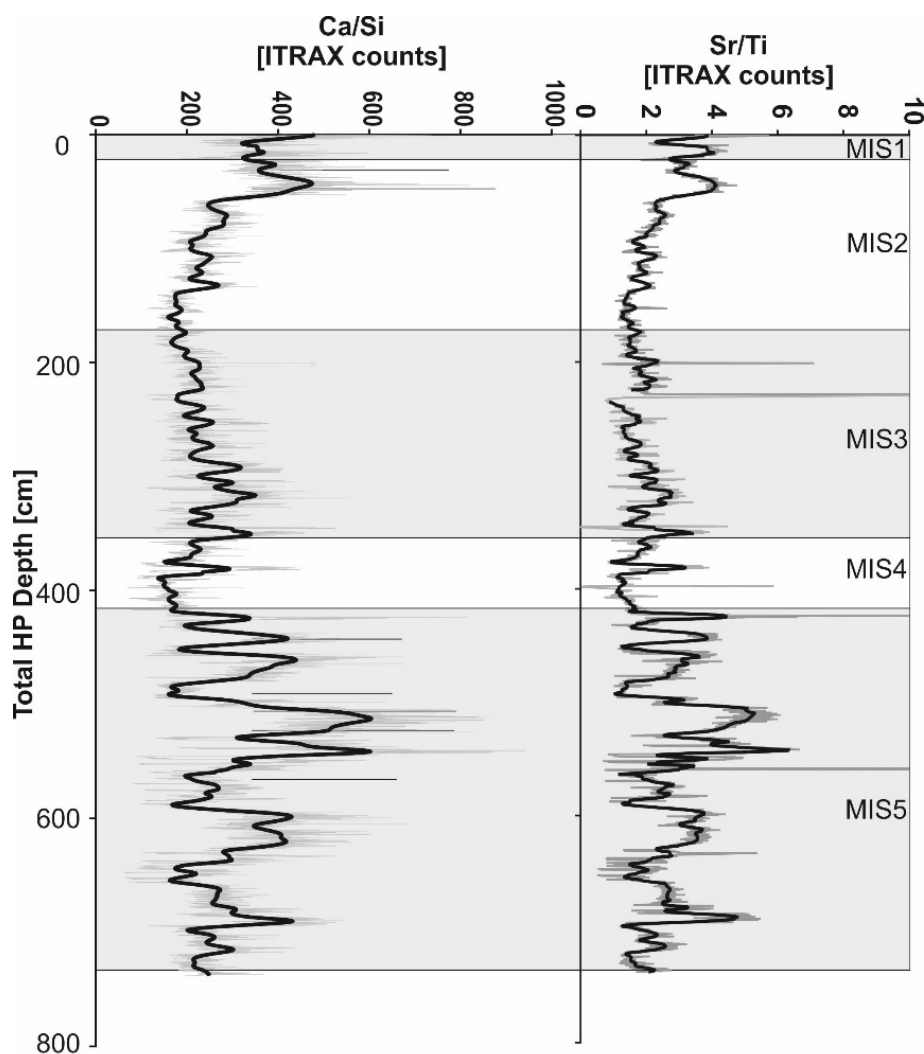


Figure 3.14: Comparison of element-normalised Sr and Ca records from hemipelagic deposits in core LC05 from the Balearic Abyssal Plain. MIS=Marine isotope stage

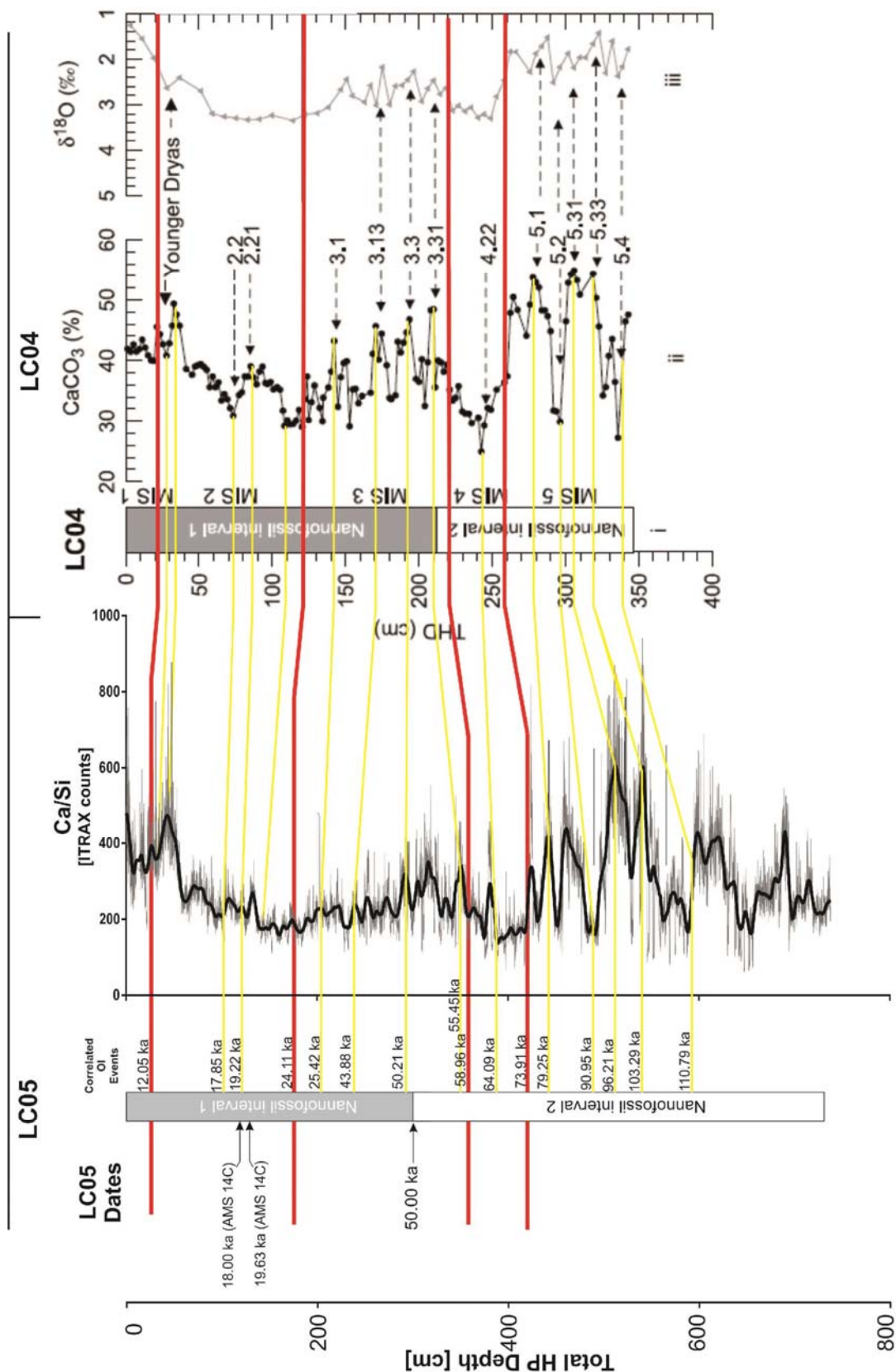


Figure 3.15: Correlation of ITRAX elemental data (Ca:Si ratio) acquired as part of this study with published calcium carbonate, oxygen isotope data (Hoogakker et al. 2004), published AMS ^{14}C and biostratigraphic dates (Rothwell et al., 1998)

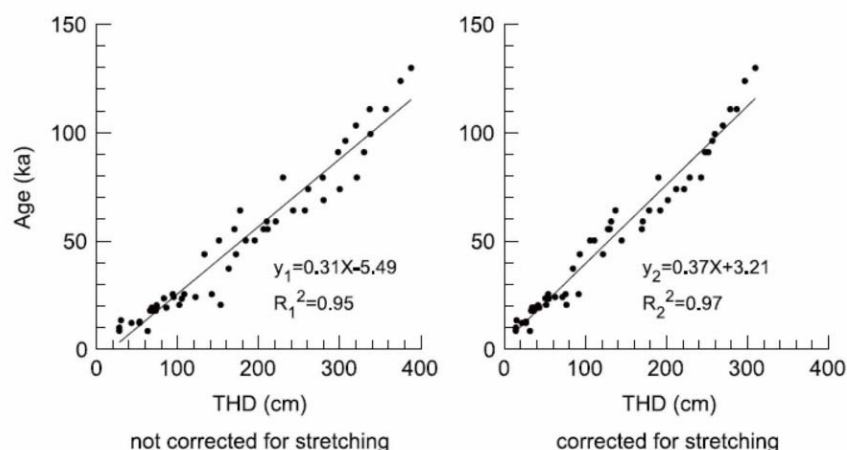


Figure 3.16: Correction for core stretching for LC06 from Hoogakker et al. (2004). THD refers to total hemipelagic depth. Note all turbidites are removed from this age-depth profile.

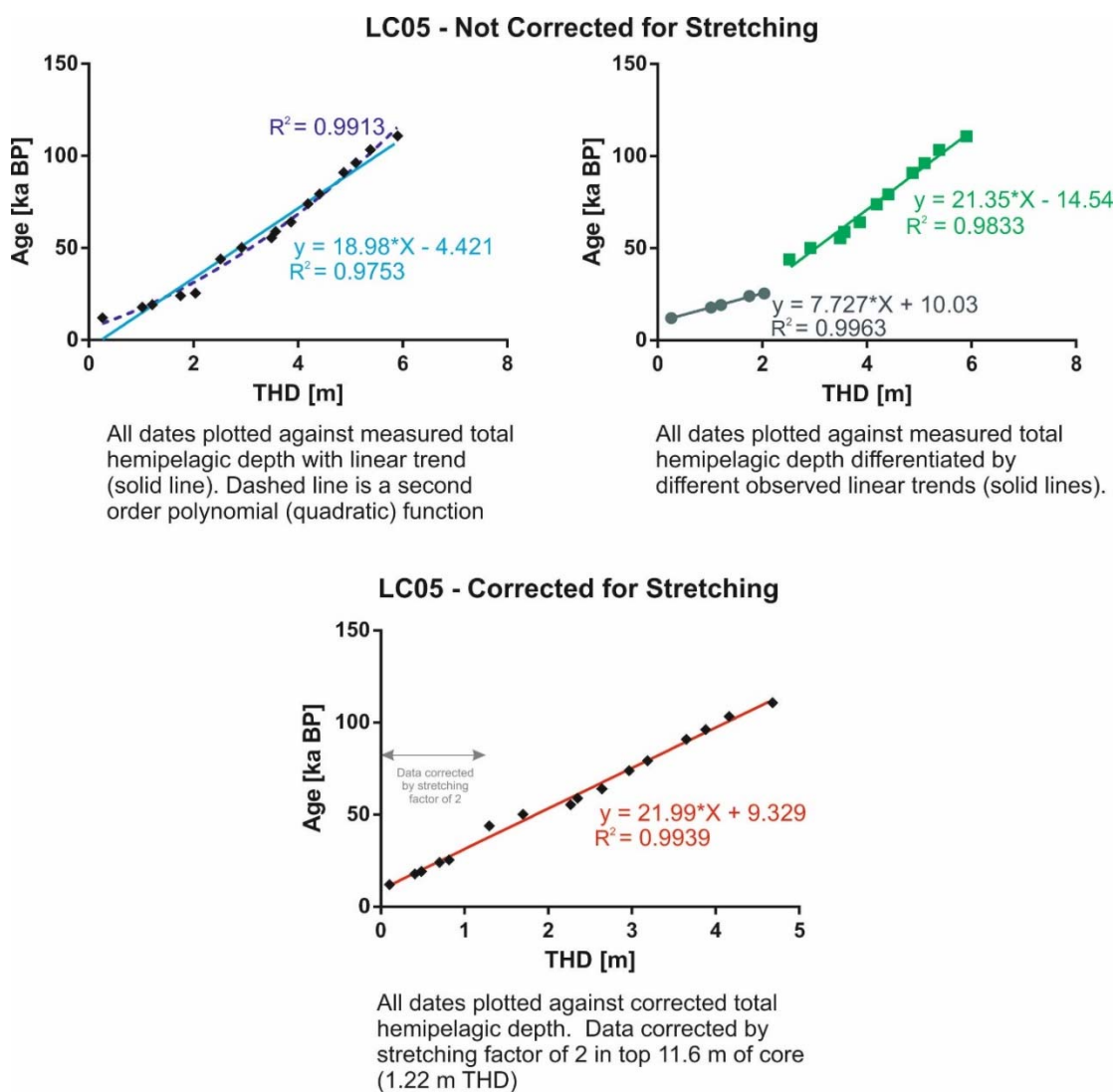


Figure 3.17: Correction for core stretching at LC05. The apparent change in gradient of hemipelagic sediment accumulation is not believed to be natural, as this is common to all the Calypso cores acquired on the MD81 Cruise and not in cores acquired by other means (Hoogakker et al., 2004). THD refers to total hemipelagic depth.

3.1.8 Short term fluctuations in hemipelagic mud accumulation rates

The method for calculating recurrence intervals also assumes no significant fluctuation in hemipelagic accumulation rates occurred within each dated sequence. Dated horizons occur approximately every 0.4 kyr to 18.5 kyr in the Balearic Abyssal Plain, every 0.18 Myr to 0.9 Myr in the Zumaia series, every 0.5 Myr to 1.3 Myr for the Iberia Abyssal Plain, and every 5 ka to 1 Myr in the Madeira Abyssal Plain. This issue is most important for the Marnoso-arenacea Formation where a constant hemipelagic accumulation rate is assumed over the entire interval. This assumption may not be unreasonable, as hemipelagic accumulation rates in the Balearic Plain and Agadir basin (Figure 3.2) only vary by $\sim \pm 30\%$ over an interval of 150 ka.

3.1.9 Minimum resolvable time intervals for study areas

The method of calculating turbidite recurrence intervals is sensitive to the minimum resolvable thickness of hemipelagic mud beds and the accumulation rate of hemipelagic sediment. In Table 3.3 the minimum resolvable recurrence interval for each of the data sets is presented, based on the limitations outlined in this chapter.

Table 3.3: Minimum resolvable time intervals for study areas

| Study Area | Minimum resolvable thickness | Minimum Sediment Accumulation Rate | Minimum resolvable interval |
|-------------------------------------|------------------------------|------------------------------------|-----------------------------|
| Balearic Abyssal Plain | 5 mm | 25 mm/ka | 0.2 ka |
| Madeira Abyssal Plain | 10 mm | 2 mm/ka | 5.0 ka |
| Marnoso-Arenacea, Italian Apennines | 50 mm | 153 mm/ka | 0.3 ka |
| Zumaia Series | 5 mm | 10 mm/ka | 0.5 ka |
| Iberia Abyssal Plain | 5 mm | 2.6 mm/ka | 1.9 ka |

Note: Sedimentation rates, and hence the time series, are assumed to be stationary in intervals between available dated horizons. The greatest uncertainty resides in the Marnoso-arenacea data as only two dated points exist

3.1.10 Reconstructed sea level curves

As part of this study, the frequency of landslides and turbidity currents are compared with reconstructed relative sea levels. These reconstructions provide global eustatic curves and have been sourced from several publications, which have themselves been compiled from a vast range of proxy data. The primary source is typically oxygen

isotope ratios over the past 100 Ma, which reflect the effects of temperature and ice volume (and hence sea level) changes in the shells of foraminifera (Miller et al., 2009). Uncertainties exist, however, as isotopic values in the surface ocean are influenced by local evaporation-precipitation effects and post-depositional diagenesis may overprint original values (Miller et al., 2005). The latter issue is typically constrained to sediments older than 100 Ma. Other sources of measurement include radiometric dating of fossil corals, submerged speleothems, shoreline markers, reefs and atolls, and the flooding history of continental margins and cratons (Miller et al., 2005).

Sea level estimates on the 10^6 scale typically have an uncertainty of ± 10 to 50 m at worst (Miller et al., 2005). The two main sources of error relate to hiatuses and palaeowater depth estimates – particularly in deep water. Errors can also arise from converting the oxygen isotope record into a sea level proxy. While benthic foraminiferal records are thought to be a close match with sea level during glacial to cool interglacials, they tend to show deviations from known sea levels during peak warm intervals (Miller et al., 2005). The amplitude of sea levels in interglacials is thus thought to be underestimated based solely on oxygen isotope data from foraminifera, with a resultant 20% uncertainty (Miller et al., 2005).

Antarctic ice records have been analysed to create a very detailed time series of carbon dioxide for the past 520 ka for which an uncertainty of ± 10 m exists (Rohling et al., 2009). Detailed studies on sea level over the last 500 ka using U/Th dating of speleothems also show a very good match with benthic oxygen isotope data. Uncertainties between 150 to 500 ka are estimated to be ± 12 m as a maximum for the global eustatic record (Grant et al., 2014). Importantly for this study, while the amplitude of sea level may show some variability due to uncertainties in the proxy method used, the timing of sea level stands and transitions is consistent between the models.

3.2 Direct monitoring of flows at Squamish

In Chapter 8 the recurrence of flows is analysed based on direct monitoring performed at the Squamish Prodelta in the Howe Sound, British Columbia. Unlike the sedimentary sequences that are discussed in Chapters 5 to 7, here one can analyse a much more resolute temporal record. The Squamish Prodelta was selected as a study site because:

- 1) *It is an exceptionally well monitored landslide and turbidity current system.* Hundreds of repeat multi-beam surveys have been conducted over eight years. The results of 93 surveys performed in 2011 are analysed. Acoustic Doppler Current Profiler (ADCP) instrumentation was also installed for 147 days which provides a temporal resolution of 30 seconds.
- 2) *It is a highly active system.* During the ten month period of study 106 flow events were recorded. This number is appropriate for quantitative statistical analysis. Other studies have monitored far fewer (see Chapter 1).
- 3) *It is a possible analogue for deep-water systems.* Many morphological features are seen at Squamish Prodelta that are typical of deep-water turbidite systems, including feeder channels, upslope-migrating crescentic bedforms and slump scars (e.g. Cartigny et al., 2011; Covault et al., 2014). While there are undoubtedly differences in terms of scale, Squamish Prodelta provides a bridge between the scale-gap of laboratory experiments and real-world deep-water sites.
- 4) *Good control is available for flow timing and possible triggers.* Hourly information is available for tidal elevation and river discharge to the delta. Combined with the 30-second precision of event arrival time from the ADCP, this provides good constraint for a quantitative comparison of the influence of tides and river discharge. The temporal uncertainties in many other data sets often preclude anything but a tentative comparison. This issue can be overcome at Squamish.

3.2.1 Repeat Seafloor Surveys

The seafloor was surveyed a total of 93 times during the studied interval using an EM710 multibeam echosounder (MBES) system operating at 70 to 100 kHz, using 1 to 2° beams. The survey area included the delta top channel and covered the prodelta slope extending to water depths of ~200 m. Surveys were performed to provide 200% coverage of the seafloor by overlapping swaths to try and minimise any uncertainty or error. The resolution is 1 m horizontally and 20 cm vertically (Hughes Clarke et al., 2013). Therefore any change in the seafloor elevation that occurs between successive surveys and that falls between these ranges can be identified. Difference maps were generated (Hughes Clarke et al., 2012) by subtracting the elevation of the seafloor from that in the previous survey and examples of surveys showing different amounts of change are shown in Figure 3.18.

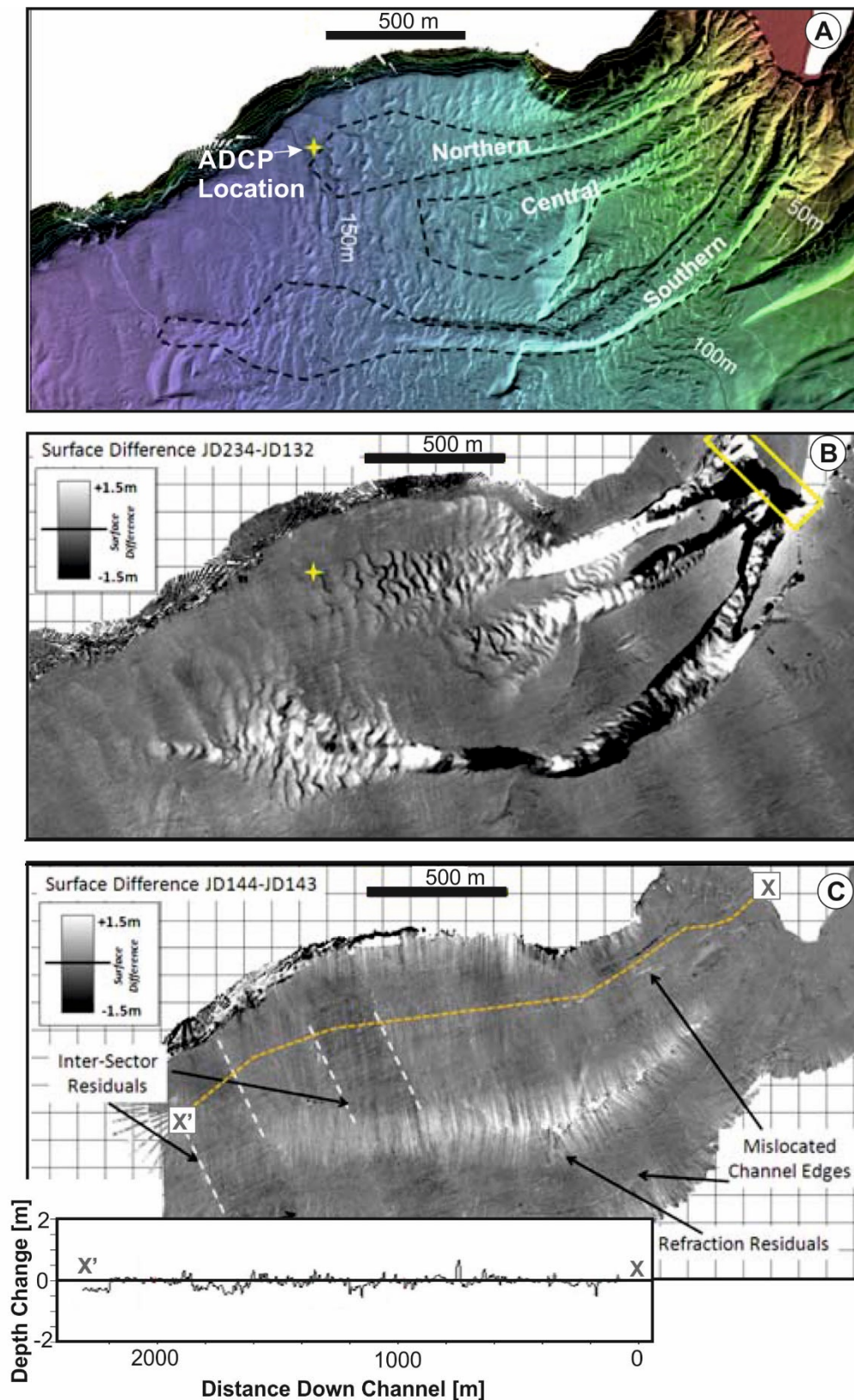


Figure 3.18: (A) Seafloor bathymetry as surveyed by multibeam echosounder at the Squamish Prodelta. The location of the ADCP is shown by a yellow star. (B) Example difference map between daily surveys showing clear change in the seafloor relief relating to a delta lip failure event. Areas of net sediment loss are shown as black, and net gain as white. Upslope migrating bedforms can be observed clearly within channels and at their downslope outspill point. (C) Example difference map where no discernible change is noted between daily surveys. The inset profile shows negligible vertical change along the profile X-X'. (Modified from Hughes Clarke et al., 2012)

Changes in the seafloor elevation have been shown to relate to delta lip failures and turbidity currents that cause the upslope migration of channel bedforms (Hughes Clarke et al., 2012; 2013; Chapter 8). The temporal resolution of the multibeam data sets is inherently tied to the timing of surveys. Surveys were performed daily on weekdays; hence, if multiple events occurred between surveys, this will result in underreporting. This is deemed sufficient for a comparison with the day to day variation in river discharge and 24-hour tidal, but for this reason, an ADCP was also deployed to provide enhanced temporal resolution of flow timing.

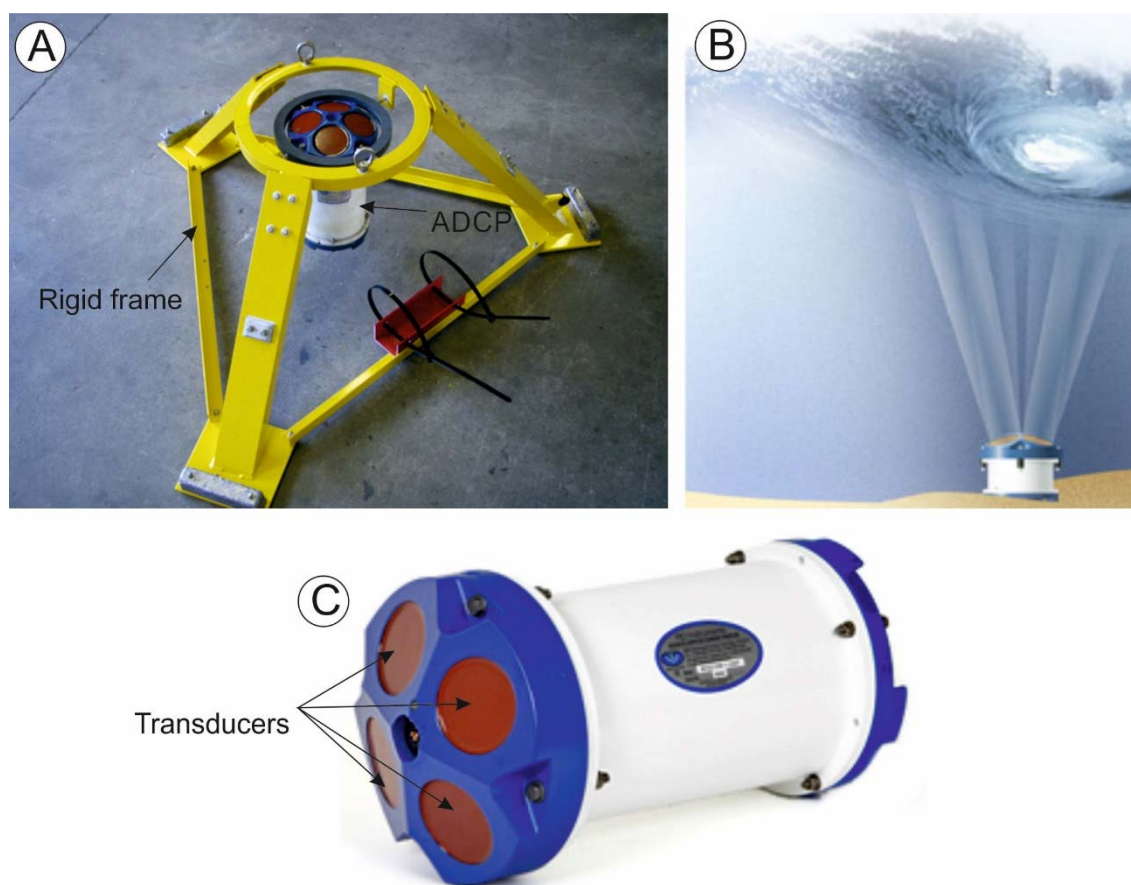


Figure 3.19: Illustrations of ADCP deployment. (A) Rigid frame and mounted upward looking ADCP (courtesy of Mooring Systems) (B) Cartoon of upward looking ADCP illustrating the spread of the four beams. In the case of the Squamish deployment, the beams recorded to approximately 47 m above the seafloor and not to sea level itself. (C) RD Instruments Workhorse Sentinel ADCP as deployed in Squamish in 2011 (B and C courtesy of RD instruments)

3.2.2 ADCP monitoring

An upwards facing 600 kHz ADCP designed by RD Instruments was deployed on a rigid frame at Squamish to provide more precise constraints on flow timing and to measure flow properties (Figure 3.19). An ADCP measures current velocities over a specified depth range by using the Doppler shift of the backscattered acoustic signal

(Griffiths et al., 1987; Wilson et al., 1997). Three beams allow for measurements of the three-dimensional velocity field, with the fourth beam allowing for an estimate of measurement error (Figure 3.19). The acoustic backscatter response also provides measurements that may relate to suspended sediment concentration (Holdaway et al., 1999).

The ADCP was located 150 m seaward from the termination of a seafloor channel (termed the North Channel), and sampled 17 ping ensembles every 30 seconds using 50 cm bins up to a maximum elevation of 47 m off the seafloor (Hughes Clarke et al., 2012). Deployment was continuous from 29th March 2011 (Julian Day 088) to 23rd August 2011 (JD235), with the exception of a 20 day period from 30th June to 20th July (JD181-201) when the ADCP was buried due to a major delta-lip failure event. Examples of the ADCP measurements of backscatter and velocity are shown in Figure 3.20.

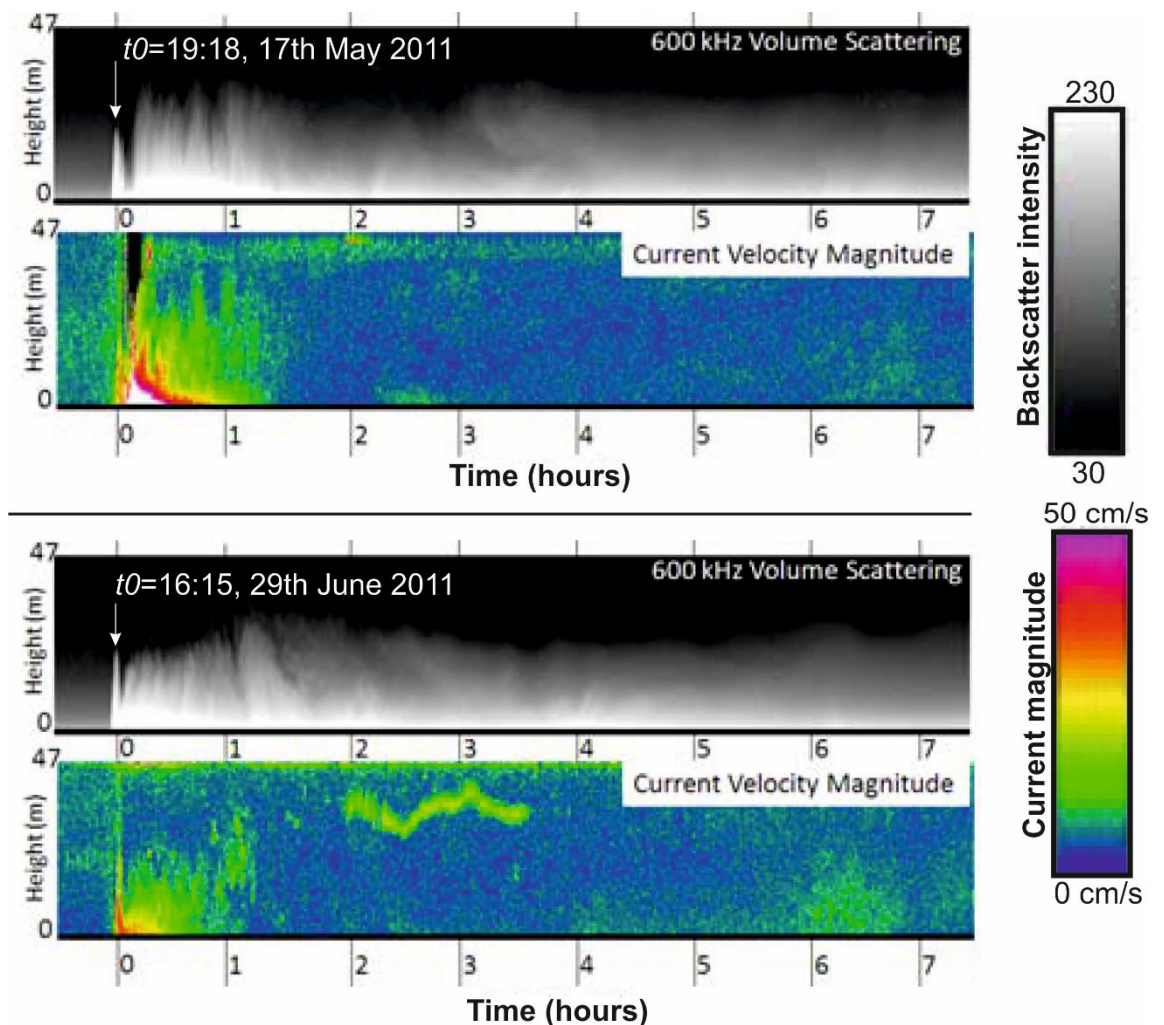


Figure 3.20: Two examples of the ADCP data from Squamish in 2011. The arrival of each turbidity current is annotated as $t=0$ and can be seen from both the measurements of velocity (lower panel) and backscatter intensity (upper panel). Modified from Hughes Clarke et al. (2012)

While the ADCP only records the largest, fastest flows that were capable of travelling to the end of the north channel, it offers an enhanced temporal resolution (>30 seconds) to that provided by the repeat seafloor surveys (>24 hours). This improved resolution in timing of flows allows for comparison of the influence of variables that change on a sub-daily basis such as tides and pulses of increased river discharge.

Chapter 4: Methodologies for statistical analysis of landslide and turbidite recurrence intervals

Summary

This chapter provides a suite of analyses that can be used to statistically test for the characteristic frequency distribution of landslide and turbidity currents and the significance of difference potential controlling or triggering mechanisms. These methods are then applied to various sites worldwide in Chapters 5, 6, 7 and 8.

An abridged version of this chapter has been accepted for publication in *Submarine Mass Movements and Their Consequences, Advances in Natural and Technological Hazards Research* (March 2014). The published manuscript benefited from the reviews of Rick Hiscott (Memorial University of Newfoundland) and Eric Geist (USGS). All analyses and interpretations were completed by me, with editorial help provided by the co-authors during paper writing. Peter Challenor provided an invaluable initial introduction to Generalised Linear Models and Proportional Hazards Models.

Tempo and triggering of large submarine landslides – Statistical analysis for hazard assessment

Clare, M.A.¹, Talling, P.J.¹ Challenor, P.², and Hunt, J.E.¹

¹National Oceanography Centre, European Way, Southampton, Hampshire, SO14 3ZH

²College of Engineering, Mathematics and Physical Sciences, University of Exeter, North Park Road, Exeter EX4 4QF

ABSTRACT *Due to their potential volume and speed, large submarine landslides can generate destructive tsunamis or damage expensive seafloor structures. Understanding their timing is therefore important for hazard assessments; however, dating large numbers of landslides close to their origin is logistically difficult. Previous landslide studies are typically limited to fewer than ten observations of ages. To address this issue, extensive, continuous and long-term turbidite records are analysed from five deep-sea basins, which are interpreted to be the distal deposits of large, disintegrative landslides. The records analysed include sufficient numbers of turbidites ($N=151$ to 1571) for robust statistical analysis of long-term controls on event timing and testing for relationships with triggering mechanisms such as earthquakes, sea level, climate change and volcanic activity. Statistical methods developed by medical, economic and biological disciplines are explored in this chapter and it is shown how they can be applied to analysis of submarine landslide frequency and triggering. Frequency analysis of field data determines the goodness-of-fit with different distribution forms for landslide recurrence, including power law, exponential and log-normal. Possible individual and combined effects of controlling factors that result in these distributions are discussed later. Rescaled range and Gaussian finite mixture models determine whether and how landslides are clustered in time. Parametric Generalised Linear Models and non-parametric Proportional Hazards Models are used to test for the significance and influence of different variables and their rate of change. The value of unusually detailed long-term landslide records is demonstrated here, and it is shown how statistical analysis can provide quantitative inputs for future hazard assessments, landslide-climate studies and understanding the tempo of deep-sea sediment flux.*

4.1 Introduction

Submarine landslides on continental margins include the largest mass flows on Earth, which can potentially generate damaging tsunamis and produce long run-out turbidity flows (Talling et al., 2014). Determining the past frequency distribution of large

slides therefore important and can inform estimates of future hazard rate (i.e. the rate of landslide recurrence during any point in time). Despite this, few studies have attempted to analyse submarine landslide frequency and probability statistically. This is largely due to uncertainties in dating individual landslides (Urlaub et al., 2013), lack of sediment for dating (Geist et al., 2013) and insufficiently large sample sizes for robust analysis (Urlaub et al., 2013; Harbitz et al., 2014). Published landslide catalogues include less than 68 dated landslides and in most cases many fewer (Urlaub et al., 2013). This is not enough to establish a confident view on past occurrence, nor to infer future potential recurrence.

Notable developments in quantifying landslide probability include techniques used in palaeoseismology (Geist and Parsons, 2010; Geist et al., 2013). These novel studies present robust approaches accounting for different frequency distributions and address uncertainties using Bayesian and Monte Carlo methods for sub-optimal sample sizes ($N < 14$). Geist and Parsons (2010) outlined the need for more age dates of global and local landslide sequences to determine longer-term variations. This is addressed here by studying landslide deposits from multiple sites (Figure 4.1), but unlike most previous studies that sample close to the landslide initiation point, a method for documenting the time periods between large landslides around a basin margin is used. Turbidites inferred to be generated by large landslides are analysed as detailed in Section 5 and Clare et al. (2014). The recurrence time of landslides is inferred from intervals of hemipelagic fallout between turbidity currents, and the average accumulation rate of hemipelagic mud between dated horizons (Chapter 3). Therefore, the method provides information on timing of many different slides from a small number of cores or outcrops, with large numbers of landslides needed for robust statistical analysis ($N > 100$). It avoids the need to date prohibitively large numbers of landslides, each in a different location on the margin.

4.2 Data

As detailed in Chapter 2, the turbidite records analysed here come from distal basin plain locations that include recent cored sediments (Madeira and Balearic abyssal plains), ancient cored records (Iberian Abyssal Plain), and ancient rock outcrops (Marnoso-arenacea, Zumaia). The sampled time windows range from 0.15 Myr to 19.45 Myr and feature up to 1571 recurrence intervals. A minimum threshold of $N=100$ observations is specified for each dataset to ensure confidence in the results. This is a

conservative approach based on conclusions from various statistical studies (Hunt et al., 2014 and references therein).

4.2.1 Data censoring

In statistics, censoring occurs when the value of an observation is only partially known. For this study, censoring results from an unknown time since the emplacement of the most recent turbidite and until the next (i.e. at some point in the future). It would be inappropriate to use the most recent hemipelagic mud thickness to calculate a recurrence interval, as the next event is at an undetermined point in the future. As a consequence, the most recent time interval is censored and removed from the analysis.

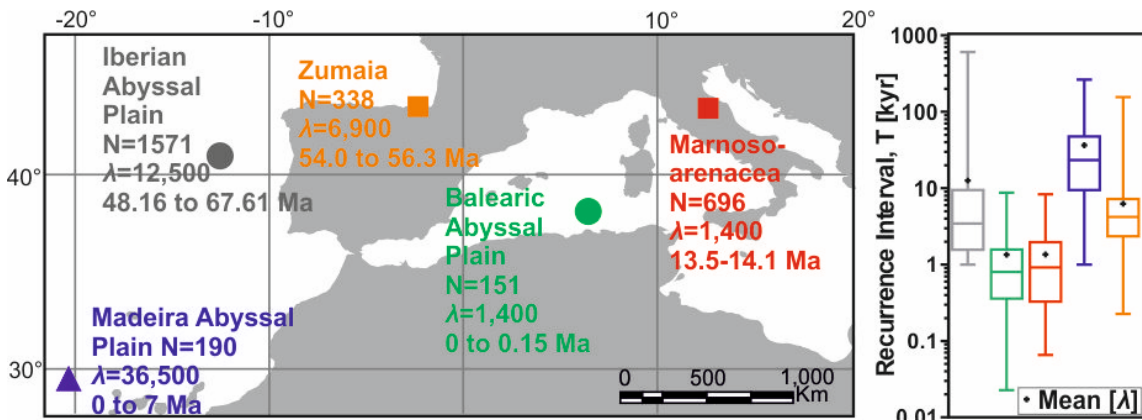


Figure 4.1. Location of sites and time windows referenced in this paper. λ refers to the mean recurrence interval of turbidites in years, N is the number of turbidites sampled at each site. Box (25-75%) and whisker (5-95%) plots on right are annotated with a black cross for λ .

4.3 Statistical analysis of landslide recurrence

First, statistical methodologies are introduced to characterise landslide recurrence that are routinely used in other disciplines, including medicine, economics, and manufacturing. These techniques are used to determine the time before fatality, major depreciation or failure, so in the same manner they can be applied to assessment of landslides. Second, it is tested as to whether landslides show time-dependence. Recent studies have indicated that large submarine landslides may occur randomly in time (or are at least indiscernible from a Poisson distribution; Geist et al., 2013; Urlaub et al., 2013; Clare et al., 2014). If landslide recurrence shows a Poisson distribution, hazard rate does not change with time. For other distributions, hazard rate varies with time (i.e. time-dependence). Finally, tests are introduced to assess whether explanatory variables, such as sea level and global temperature, exert control on recurrence intensity (i.e. hazard rate).

This provides new insights as to whether future climate change may increase, or even decrease, the likelihood of landslide recurrence.

4.3.1 What is the characteristic frequency of landslide recurrence?

The frequency distribution of recurrence intervals is identified initially by determining goodness of fit on exceedance plots (e.g. Van Daele et al., 2014). Three main forms are considered as this is appropriate for assessing variables conforming to the majority of common statistical distributions (Van Rooij et al., 2013; Figure 4.2). The forms considered include Gaussian forms relating to addition of independent variables, log-normal distributions arising from multiplication of normally or log-normally distributed independent variables, and a Power Law where interdependent processes cause an amplification of effects (Van Rooij et al., 2013).

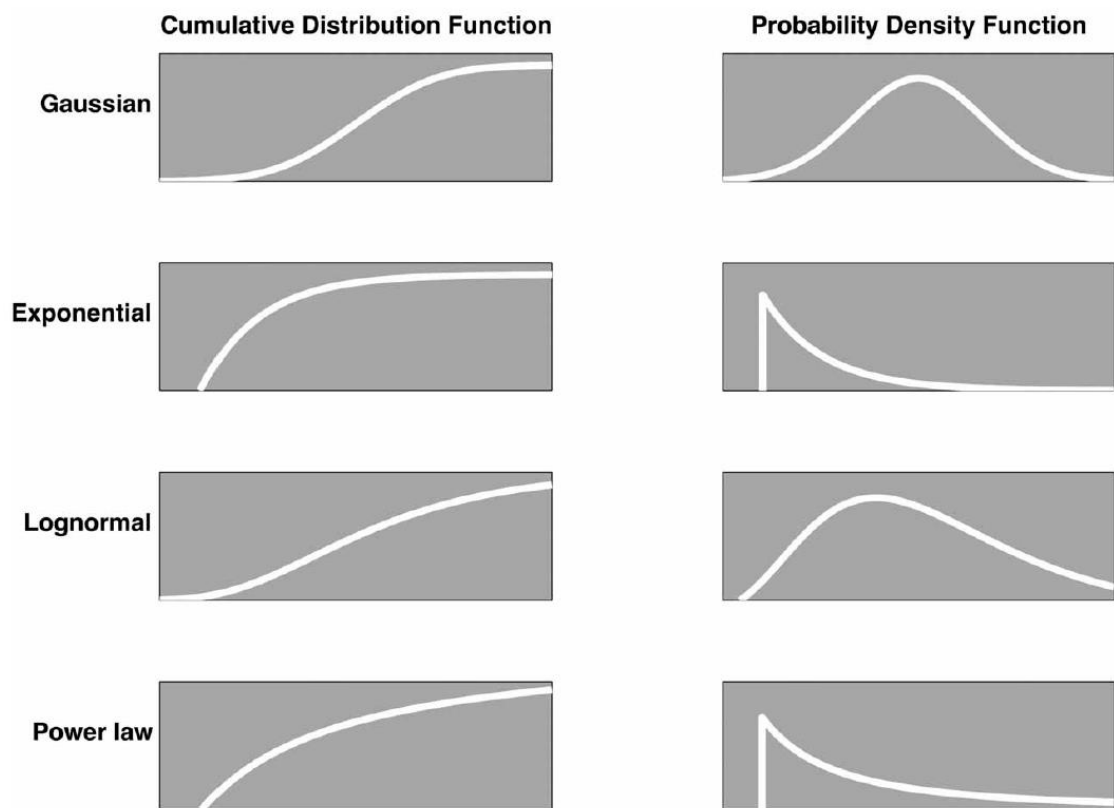


Figure 4.2: Plots showing cumulative distributions (left) and probability density (right) functions of four ideal distributions. Gaussian and exponential distributions are indicative of systems where processes occur independently, whereas lognormal and power law distributions indicate systems where processes are interdependent. By determining the frequency distribution form one may gain insights into the dynamics of the system (from Van Rooij et al., 2013)

Exceedance plots of frequency are used to visually test different distributions using different scales (Figure 4.3). A straight line trend indicates an exponential distribution on

a log-linear plot, log-normal distribution on a log-probability plot, and power law distribution on a log-log plot. Graphical methods for determination of frequency distribution have previously been applied to analysis of turbidite bed thicknesses (Talling, 2001; Sylvester, 2007), and more recently to the analysis of intervening hemipelagic mud thicknesses (Malgesini, 2012). Trendlines are applied using least squares method to provide a coefficient of determination (R^2) to test their fit. This method has limitations for Power Law distributions, however; therefore Quantile-quantile (Q-Q) plots are also used to compare the shape of theoretical frequency distributions against the observed data. In this thesis neither segmented-Power Law, nor bimodal or polymodal overlapping log-normal distributions are considered. Instead focus is placed on more broad end-member distribution scenarios that can be used to characterise major system controls (e.g. Van Rooij et al., 2013).

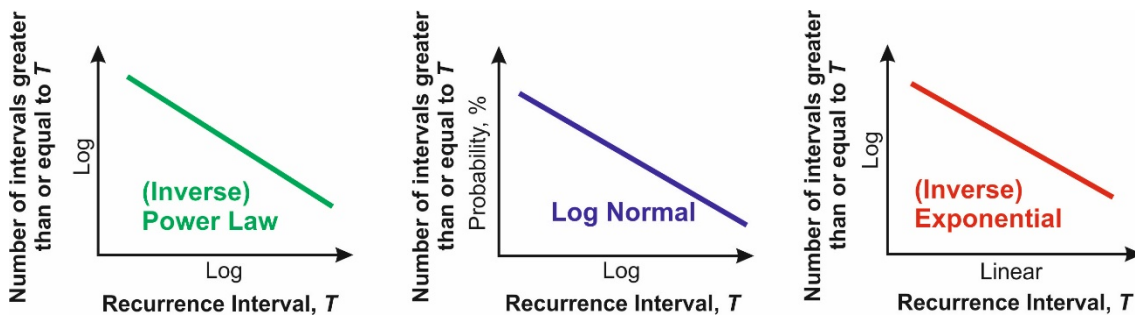


Figure 4.3: Example exceedence plots where a straight line trend would indicate (left) Power Law distribution on a log-log plot, (middle) log-normal distribution on a log-probability plot, and (right) exponential distribution on a log-linear plot.

Chi-squared (Snedecor and Cochran, 1989; Swan and Sandilands, 1995) and Kolmogorov-Smirnov tests (Massey, 1951) are employed to further assess goodness-of-fit for the different theoretical frequency distributions. The chi-squared test compares the expected number of recurrence intervals according to the specified theoretical distribution with the number of observed recurrence intervals within set bin-sizes (Urlaub et al., 2013). The Kolmogorov-Smirnov test is also used to assess the goodness-of-fit to a theoretical distribution but can be applied to continuous rather than binned data. The test statistic is the maximum discrepancy (difference in recurrence interval values) between a cumulative plot of the data and the chosen distribution (Massey, 1951).

The three theoretical trends of frequency distribution tested for indicate markedly different controls on recurrence. A Poisson (or exponential) distribution is indicative of time-independent behaviour. This may indicate a time-independent trigger, or may relate to the additive effect of different normally-distributed effects (e.g. different input sources

around the basin margin; Clare et al., 2014). A log-normal distribution indicates some degree of time-dependence. This may arise from a log-normally distributed trigger or due to multiplicative effects (e.g. probability of a trigger multiplied by the probability of failure and/or probability of the flow reaching the basin plain). Finally, a Power Law distribution is likely to represent interdependent feedback between processes (Van Rooij et al., 2013). Examples of these distributions that occur in nature are presented in Table 4.1.

Table 4.1: Examples of Power Law, log-normal and exponential distributions in the natural world

| Frequency Distribution | Generation Mechanisms | Example Occurrence |
|------------------------|--|---|
| Power Law | Time-dependent form arises from circular, interdependent feedback to generate a critical state | Topographic shape (Mandelbrot, 1967; Sayles and Thomas, 1978; Rapp, 1989) |
| | | Earthquake magnitude (Gutenberg and Richter, 1954; Sornette and Sornette, 1989; Scholz and Cowie, 1990; Sornette, 1991; Vasconcelos et al., 1991; Rothman and Grotzinger, 1996) |
| | | Critical slope stability in sand piles (Rothman et al., 1994) |
| | | Terrestrial river drainage networks (Hack, 1957) |
| | | Magnitude of subaerial landslides (Hovius et al., 2000) |
| Log-Normal | Time-dependent form arises from multiplicative interactions among independent variables | River flood discharge (Bobée et al., 1993) |
| | | Population and organism growth (Preston, 1948, 1962; Koch, 1966; Magurran, 1988) |
| | | Incubation of viral infections (Nishiura, 2007) |
| | | Survival time after diagnosis of cancer (Feinleib and McMahon, 1960) |
| Exponential | Time-independent, memoryless form arises from addition of independent variables | Rainfall (Biondini, 1976) |
| | | Growth of bacteria populations (Limpert et al., 2001) |
| | | Recurrence of large magnitude earthquakes (Corral, 2006; Mosca et al., 2012; Gomez et al., 2015) |
| | | Tsunami recurrence (Watts and Borrero, 2001) |

To a first order it may be appropriate to use the mean recurrence value for exponentially distributed data to characterise future hazard rate on a regional basis (i.e. hazard rate is constant with time). This is not the case for log-normally or Power Law distributed data which require a greater understanding of the forcing variables in order to determine how recurrence may change with time.

4.3.2 Are landslides clustered in time?

It is also important to test whether recurrence intervals fall into clusters (or periods of clustering). The tools used to test for this are rescaled range analysis and a Gaussian Finite Mixture model.

Rescaled range analysis – are recurrence intervals clustered?

The rescaled range exponent (Hurst, 1951) provides a method of determining the degree of clustering of low and high values within a sequence and has previously been applied to studies of turbidite bed thickness (Chen and Hiscott, 1999; Figure 4.4). It is used in economics to assess potential for stock market crashes and does not require any prior knowledge on the form of frequency distribution (Kristoufek, 2012). Hurst (1951) found that:

$$R/S \sim N^h \text{ (Equation 4.1)}$$

where R is the maximum range in cumulative departure from the mean, N is the number of observations, and S is the standard deviation for the N observations and h is the Hurst exponent. The basic method for deriving the Hurst exponent involves the following steps:

- i. Calculate the mean of the time series;
- ii. Create a mean-centred series by subtracting the mean from that series;
- iii. Plot the cumulative deviation of the series from the mean by a summation of the mean-centre values;
- iv. From the above plot, calculate the range, R (i.e. difference between maximum and minimum cumulative deviations);
- v. Calculate standard deviation, S of the mean-centred values;

- vi. The rescaled range refers to the division of the Range, R by the standard deviation, S .

Hurst (1951) then presented the following relationship, using K as an estimator for a modified Hurst exponent, h :

$$K = \frac{\log_{10}(R/S)}{\log_{10}(N/2)} \text{ (Equation 4.2)}$$

Values that are closer to $K=1$ show persistent or trend reinforcement (i.e. a large value is most likely followed by a large value; Mandelbrot and van Ness, 1968), and those that are closer to $K=0$ are mean-reverting or anti-persistent ((i.e. a large value is most likely followed by a small value; Barkoulas et al., 2000). Values that approximate $K=0.5$ are time-independent and are equivalent to a random walk series (Hurst, 1951). Figure 4.5 illustrates some end-member scenarios from rescaled range analysis for time-independent ($K=0.5$), mean-reverting ($K=0.1$) and persistent ($K=0.9$) examples.

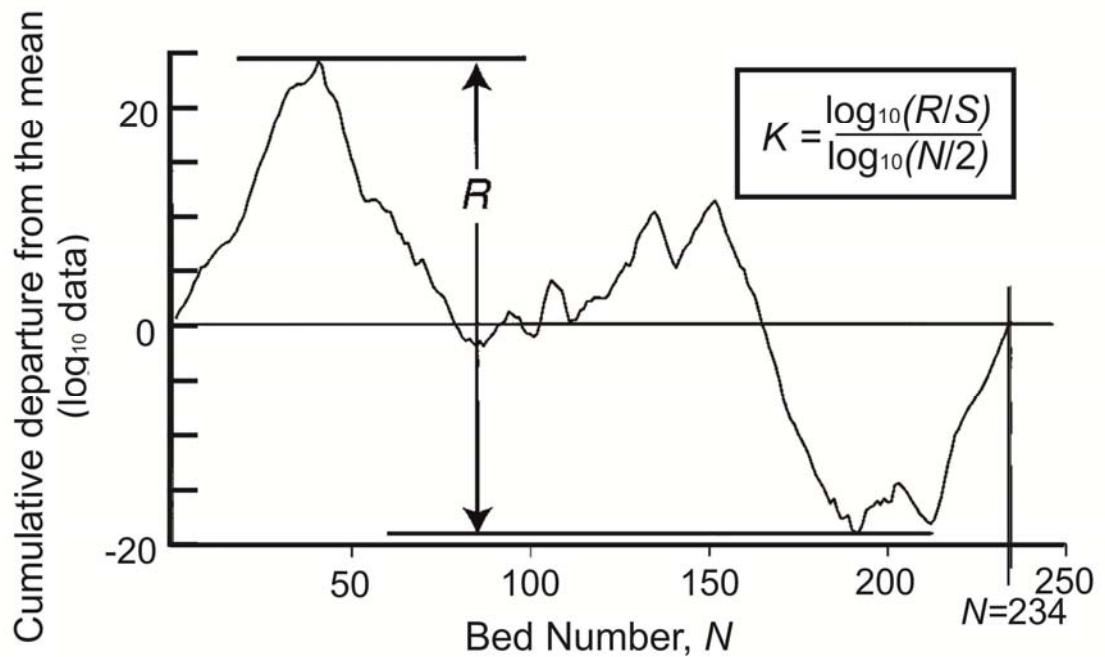


Figure 4.4: Parameters required for the rescaled range analysis from Chen and Hiscott (1999)

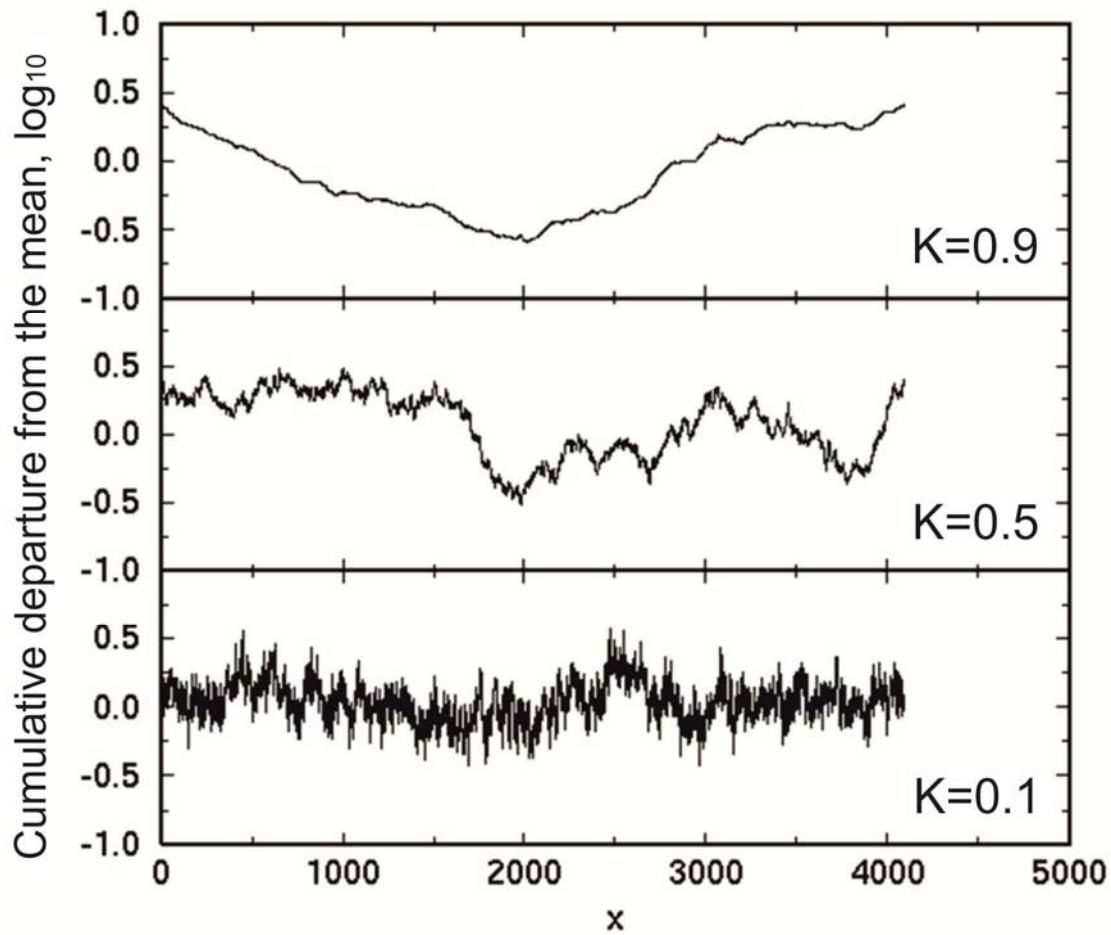


Figure 4.5: Example scenarios from rescaled range analysis for near-persistent ($K=0.9$), time-independent ($K=0.5$) and near-anti persistent ($K=0.1$) behaviour (data from http://laplace.ucv.cl/Patterns/coopphen_book97/boxes/selfAffineFractals.html)

Gaussian finite mixture model – Parameterisation of clusters

If recurrence intervals are temporally clustered (or occur within periods of clustering) a Gaussian finite mixture model (Fraley et al., 2012) is used to determine how that clustering is manifested. This model performs multiple tests to determine the best fit for different parameter scenarios to characterise the distribution of data and has recently been used to determine clustering in submarine canyon bedform metrics (Symons et al., In Review). The model uses an Expectation-Maximisation (EM) algorithm (Dempster et al., 1977) to iteratively search for the maximum likelihood estimate of parameters. Parameters considered by the model include the number of clusters, their central point (as defined by the mean), and orientation in relation to coordinate axes, volume and shape. These characteristics are estimated from the data (Figure 4.6). The EM algorithm alternates between performing an expectation (E) step, which creates a function for the expectation of the log-likelihood evaluated using the current estimate for the parameters,

and a maximisation (M) step, which computes parameters maximising the expected log-likelihood found on the E step (Dempster et al., 1977).

This approach is highly flexible and compares modelled variations between clusters, as well as considering scenarios where the parameters are the same for all clusters. The clusters are ellipsoidal, centred at the mean values, while the covariances of the data determine the other genetic features (Fraley et al., 2012).

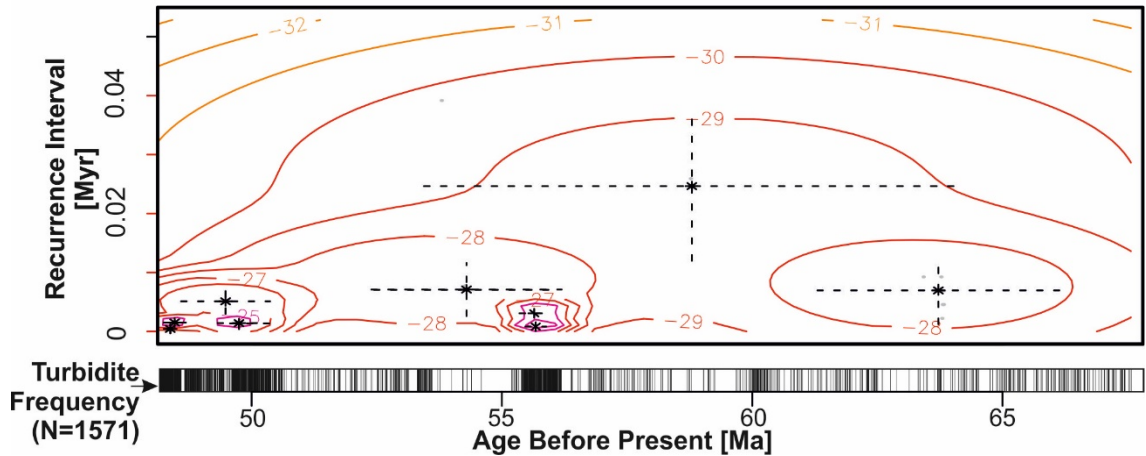


Figure 4.6: Example time series plot of the Iberian Abyssal Plain record showing individual turbidites (below as black bars) and log-likelihood density contour plots of Gaussian finite mixture model (above). Cluster centres from the finite mixture model are shown as stars. Dashed lines correspond to the 95% confidence intervals. See Chapter 7 for a full explanation of the results.

The Mclust function in *R* is used which allows for testing of all possible variations of the parameters (Fraley et al., 2012), and compares Bayesian Information Criterion (BIC; Konishi and Kitigawa, 2008) values for the best-fit parameterisations for up to nine clusters. The BIC is the maximised log-likelihood value (Dempster et al., 1977; Fraley et al., 2012). The smaller the BIC, the stronger the evidence of the model and number of clusters (Fraley et al., 2012). Thus, this method can be used to determine which model best explains the distribution of clusters and how many clusters are most likely. The output includes the best-fit parameters of the maximum BIC-model and the corresponding classification and uncertainty. Plots that summarise the analysis show the classification of data colour-coded by cluster and include ellipses that correspond to the covariances of the components (Fraley et al., 2012; Geist et al., 2013). This model therefore allows for an understanding of the nature of clustering for datasets where time dependence and/or trend-reinforcing behaviour is identified.

4.3.3 Do different time periods feature different characteristic recurrence?

If periods of clustering are identified, then it is possible to determine if the spread and the mean values of recurrence are significantly different between successive periods. To test for this two non-parametric techniques are used that compare the recurrence intervals between two unpaired groups. The Kolmogorov-Smirnov test is used again (Section 4.3.1), but instead of testing a measured sample against a hypothetical distribution, here the cumulative distributions of two periods of measured recurrence intervals are compared. The Mann-Whitney test ranks all the values from low to high, paying no attention to which group each value belongs. The smallest number is assigned a rank of 1. The largest number is assigned a rank of n , where n is the total number of values in the two groups. The ranks in each group are then averaged, and the two averages are reported. If the means of the ranks in the two groups are very different, the p value will be small. Kolmogorov-Smirnov and Mann-Whitney tests determine the chance that random sampling would result in the mean ranks and spread of the data being as far apart (or more so) as observed (Cheung and Klotz, 1997; Sheskin, 2003).

4.3.4 Is sea level a dominant control on landslide recurrence?

Generalised Linear Models

If events occur regardless of the prior and succeeding event, the distribution of the numbers of events in a period is Poissonian and the recurrence intervals have an exponential distribution. This is given by Equation 4.3:

$$P = (X < x) = 1 - e^{-\frac{x}{\lambda}} \text{ (Equation 4.3)}$$

where P is the Probability Function that a discrete random recurrence interval, X , is less than a specific value for the data series, x . The solution is related to an inverse exponential function, e^{-x} , and the rate parameter, λ . λ is the rate at which the events on average occur (MacDiarmid, et al., 1995). This is not restricted to a constant rate and it is trivial to make λ a function of time, $\lambda(t)$. One can further generalise the model and make λ a function of covariates. In principle this function can be anything, but for this analysis only linear models are considered. Linear models include polynomials and Fourier models, among others. There is a lot of latitude in the choice of model. Therefore:

$$\lambda(t) = \mu + \alpha s(t) + \dots \text{ (Equation 4.4)}$$

where μ is the mean of the distribution, α is the dispersion parameter, s is one of any possible explanatory variables, and t is time. The framework used is known as the Generalised Linear Model (GLM). These models include standard linear models with Gaussian errors as well as exponential models. Unlike a standard linear model, a Generalised Linear Model allows for response variables that have arbitrary distributions (other than just a normal distribution), and for a link function (an arbitrary function of the response variable) to vary linearly with the predicted variables (rather than assuming the response itself may vary linearly; McCullagh and Nelder, 1989). A linear model may indicate that for each 1 m increase in sea level that turbidite recurrence frequency may decrease by 100 years. However, if the initial conditions were of a recurrence of 200 years, a 100 m sea level increase would lead to an impossible turbidite recurrence of $200 - (100 \times 100) = -9800$ years! The Generalised Linear Model can instead predict a constant rate of decreased recurrence (e.g. an increase of 1 m in sea level leads to a halving of turbidite recurrence). In such an instance, an exponential-response model is most appropriate.

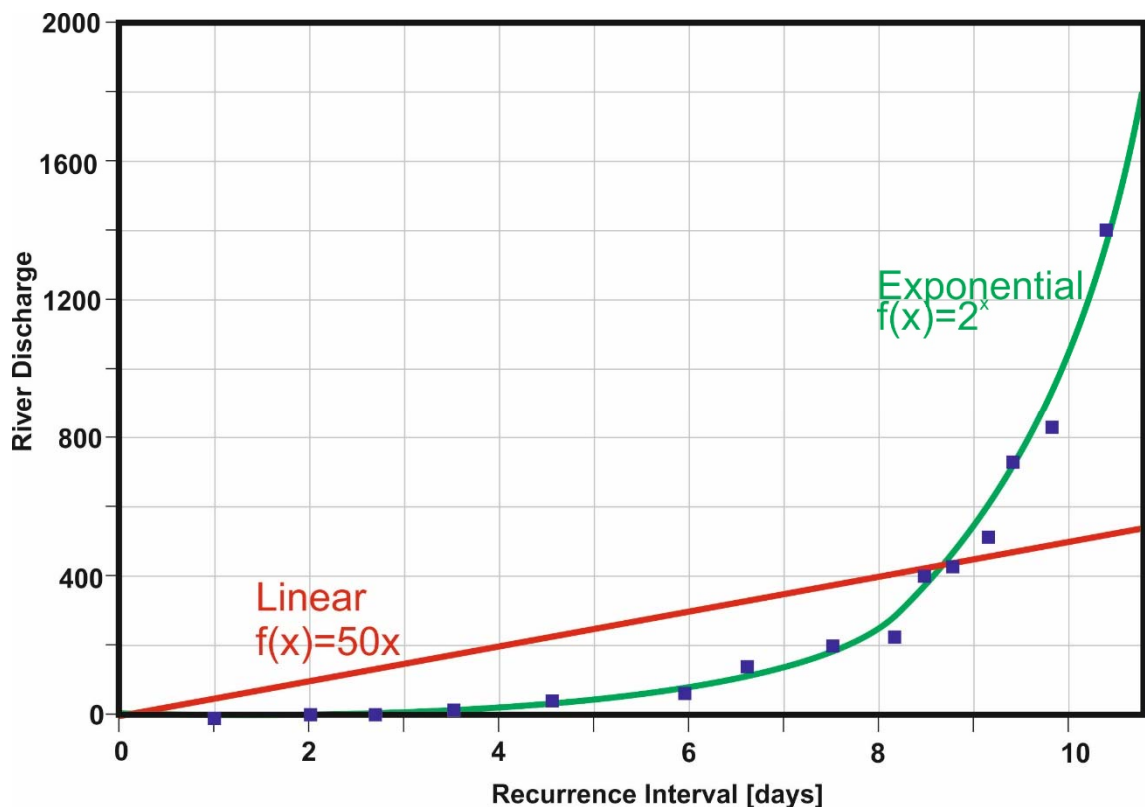


Figure 4.7: A standard linear model (red line) would not explain the relationship well between river discharge and recurrence time for the example above. Instead, an exponential distribution appears to better explain the distribution. A Generalised Linear Model could be applied with a choice of different distribution forms. As the exponential is a special case of the Gamma distribution (where the scale parameter, α , is equal to one), we opt for this in our model. Using a link function, it is also possible to compare more than one explanatory variable.

Here a more general model with Gamma is fitted (rather than just exponential errors, as the exponential is a special case of Gamma). An exponential regression is run initially to test the significance of an explanatory variable such as sea-level and/or its rate of change against event timing (Equation 4.5). The Generalised Linear Model derives an output dispersion parameter, α , for a Gamma distribution comparing event timing, t , and an explanatory variable, s .

$$\lambda(t) = \mu + \alpha s(t) \text{ (Equation 4.5)}$$

It is possible to develop this model to include the additive or multiplicative effects of explanatory variables, such as sea-level (defined here as s_1) and its rate of change (s_2). Equation 4.6 shows an additive effect model.

$$\lambda(t) = \mu + \alpha_1 s_1(t) + \alpha_2 s_2(t) \text{ (Equation 4.6)}$$

For a Poisson process (i.e. exponential) the hazard rate is constant – the system has no memory. Other processes have either decreasing or increasing hazard rates. Example values of α (determined from a GLM) are shown in Figure 4.8 in relation to hazard rate.

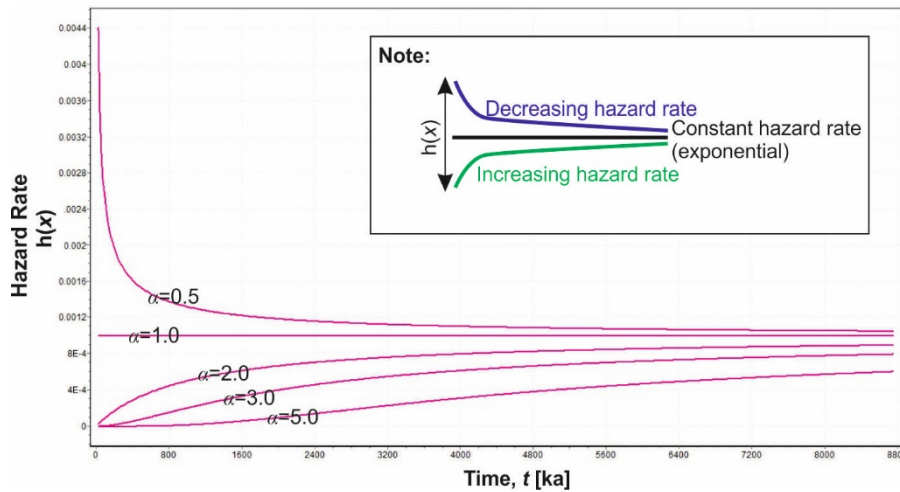


Figure 4.8: Example hazard function, $h(x)$, plot illustrating different values of α for Gamma curves showing increasing and decreasing hazard rate. Note that values close to 1.0 closely approximate an exponential distribution (i.e. near-constant hazard rate)

Cox Proportional Hazards Model

In addition to testing the timing of events in relation to sea level, recurrence rate (also termed hazard function) is considered, which is the probability that an event will occur at time t given that one occurred at time $t=0$.

$$\lambda(t) = \frac{f(t)}{S(t)} \text{ (Equation 4.7)}$$

where $f(t)$ is the failure density function and $S(t)$ is the survival function (Kleinbaum and Klein, 2005). In essence, this is the number of landslides in the database that occurred within a given time period, divided by the number of landslides in the database that did not occur within the same period. The term survival derives from biological studies of mortality, but here tells us about the repose time between landslides or turbidity currents. $S(t)$ and $f(t)$ derived by the following:

$$S(t) = P(T > t) \text{ (Equation 4.8)}$$

$$f(t) = F'(t) \text{ (Equation 4.9)}$$

where T is a random variable that denotes the time of an event, P is probability, and t is a specified time (Kleinbaum and Klein, 2005). The survival function $S(t)$ is therefore the probability that the time of an event occurring is later than some specified time. $f(t)$ is the rate of events, F' , per unit time expressed as t . If one assumes that the hazard rate, $\lambda(t)$, is proportional to a covariate vector, x (e.g. sea level and/or its rate of change) you can estimate the effect it has regardless of the form of $\lambda(t)$. This is done by applying the Cox Proportional Hazards Model (PHM; Cox, 1972) which considers the following generalisation.

$$\lambda(t, x) = \lambda_0(t, \alpha) \exp(\beta x), \text{ (Equation 4.10)}$$

The hazard is decomposed into a product of two items: $\lambda_0(t, \alpha)$ is a term that depends on time but not the covariates – α are some parameters affecting the baseline hazard function; and, $\exp(x)$ is a term that depends on the covariates but not time – β refers to baseline hazard function, x represents a covariate vector (explanatory variables). Using a model of this form tests the effects of covariates on survival and provides an estimate of β , without needing to specify the form of $\lambda_0(t, \alpha)$. Therefore you do not need to make any assumption about the distribution of the time between events for this model.

In this model, hazards are proportional to each other and do not depend on time (Smith et al., 2003). This can be understood by considering two events with covariate vectors x_1 and x_2 (which can be treated as scalars for simplicity). The ratio of their hazards at time t is:

$$\begin{aligned}\frac{\lambda(t, x_1)}{\lambda(t, x_2)} &= \frac{\lambda_0(t, \alpha) \exp(\beta x_1)}{\lambda_0(t, \alpha) \exp(\beta x_2)} \\ &= \exp\{(\beta(x_1 - x_2))\} \text{(Equation 4.11)}\end{aligned}$$

In other words, $\lambda(t, x_1)$ and $\lambda(t, x_2)$ are proportional to each other and do not depend on time. The term $\exp\{(\beta(x_1 - x_2))\}$ is called the hazard ratio, comparing x_1 to x_2 . If $\beta=0$ then the hazard ratio for that covariate is equal to $e^0=1$ (i.e. that covariate does not affect survival). The baseline hazard function is analogous to the intercept in ordinary regression (Walters, 2009).

The unique effect of a unit increase in a variable is multiplicative with respect to hazard rate. For example, in an instance where it is found to be significant, 1 m change in sea level may result in a doubling of turbidite recurrence. The $\exp(\text{coef})$ term, expressed as E^b in this thesis, indicates the hazard ratio for one unit change in the explanatory variable (e.g. how much does the recurrence rate change with 1 m change in sea level or 1 m³/s change in river discharge?). The model also outputs 95% confidence intervals that can be used to provide bounds on the predicted hazard rate. Where correlation is identified, the Proportional Hazards Model provides a powerful tool for future hazard assessments.

Cox PHM is selected as one of the statistical tools because: no parametric assumptions are required and it provides a check on other distribution-dependent tests; partial likelihood function allows for assessment of time-independent variables against other values that may be time-dependent (Smith et al., 2003); and the analysis in *R* performs three statistical tests which also allow a check on the confidence in the model outcome. These tests each compare the actual data against hypothesised values and include Likelihood, Wald and Score (logrank) tests.

An example of Cox regression analysis is shown in Table 4.2. Here, the proportional effects of sea level, its rate of change and the combination of the same two variables are analysed in relation to landslide recurrence. An approximate test of significance is determined by dividing the regression estimate b by its standard error, and comparing the results with the standard normal distribution. Values of this ratio at greater than 1.96 will be statistically significant at the 5% level (Walters, 2009). The regression coefficients in Table 4.2 include positive (higher hazard rate) and negative (lower hazard rate) values.

Therefore, sea level is associated with a lower hazard rate, whereas the rate of change of sea level is associated with a higher hazard rate. The hazard rate or ratio is estimated by the analysis as shown by E^b . For example, the estimated risk of a landslide occurring increases by $\exp(0.004)=1.004$ times if the rate of sea level increases by one unit (e.g. 4% increase in likelihood per 1 m/kyr change). However, the p-value for the rate of sea level change is 0.359; hence it is not statistically significant and the 95% confidence intervals includes values both less and greater than 1, suggesting no difference in survival. Combining the effects of sea level and its rate of change only increase the p-value. In the case shown in Table 4.2, it is only sea level as an individual variable that is found to be significant ($p=0.004$), with an increase of 1 m in sea level explaining a decrease in landslide likelihood by 0.732 times, albeit with a wide range of 95% confidence intervals (0.590-0.909).

Table 4.2: Example results for Cox Proportional Hazards Model

| Explanatory Variable(s) | Regression coefficient (b) | Standard error SE (b) | p-value | E^b Hazard ratio | 95% CI for hazard ratio |
|--|-----------------------------------|------------------------------|----------------|-----------------------------------|--------------------------------|
| Sea Level | -0.312 | 0.110 | 0.004 | 0.732 | 0.590-0.909 |
| Rate of Sea Level Change | 0.004 | 0.004 | 0.359 | 1.004 | 0.996-1.012 |
| Combined effects of sea level and rate of change | -0.033 | 0.234 | 0.887 | 0.967 | 0.61-1.530 |

4.4 Valid sample size determination

The statistical models and tests have been selected based on appropriateness with respect to the testing methodology and the available sample size for each data set. A minimum threshold of $N=106$ observations (following censoring) is specified for each dataset to ensure confidence in the results (Chapter 1). This is a conservative approach based on conclusions from various statistical studies. A minimum sample size of $N=50$ is imposed by Hurst (1951) for the rescaled range analysis and is corroborated by Chen and Hiscott (1999). Generalised Linear Models that include up to two variables and test for large to medium effect sizes require greater than $N=66-106$ (Tabachnick and Fidell, 2007). Peduzzi et al. (1995) suggest a minimum value of ten events per variable (EPV) for proportional hazards models. Vittinghoff and McCulloch (2007) go further, to suggest that this value could be relaxed even further (Figure 4.9). Given that the testing is only

for up to two variables, this would indicate a minimum sample size of $N=20$ is required. Therefore the defined threshold of $N=106$ should ensure reliable results.

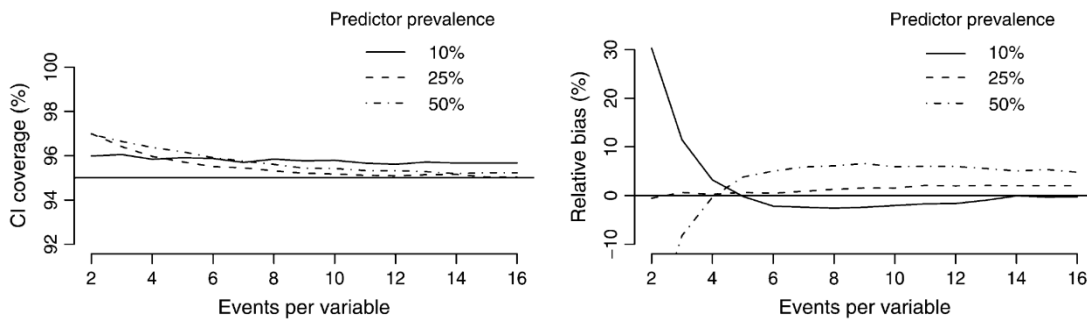


Figure 4.9: Results of a simulation study for Cox Proportional Hazards Model from Vittinghoff and McCulloch (2007) demonstrating limited variation in results for samples with six events per variable or more. CI refers to confidence interval

4.5 Conclusions

A variety of statistical analyses are outlined in this chapter that can be used to characterise recurrence of submarine slides if sufficient number of observations ($N>100$) exist. This can be achieved using extensive records of large volume distal turbidite deposits and direct monitoring of flows. The approach allows for quantification of links between recurrence and variables such as sea level or global climate, and can therefore be used to guide the inference of future hazard rate and how it may be affected by future sea level change. In Chapters 5 to 8 the above methods are applied to the field data, which were introduced in Chapters 2 and 3.

Chapter 5: Frequency distribution of large submarine landslides and implications for sea level control

Summary

This chapter provides a comparative analysis of submarine landslide recurrence based on large volume, turbidite records from distal basin plains to determine whether there is a similar frequency distribution form. The implications of the observed frequency distributions are then discussed in relation to a previously hypothesised sea level control. The main content of this chapter was published in an abridged format in *Geology* (January, 2014). The published manuscript benefited from the reviews of two anonymous reviewers and the comments of the editor, Ellen Thomas. The published paper received the 2014 Harold Reading award of the British Sedimentological Research Group.

All analyses and interpretations in this chapter were completed by me, with editorial help provided by the co-authors during paper writing. Section 5.5.4 includes results and analysis that were performed by me and included within a co-authored paper published in *Geochemistry, Geophysics, Geosystems* in 2014 (Hunt, Clare et al., 2014).

James Hunt provided recurrence intervals for the Madeira Abyssal Plain. Giuseppe Malgesini provided recurrence intervals for the Marnoso-arenacea. Alessandra Negri (University of Milan) performed biostratigraphic analyses at the Marnoso-arenacea section.

Distal turbidites reveal a common distribution form for large ($>0.1 \text{ km}^3$) submarine landslide recurrence

Clare, M.A.¹, Talling, P.J.¹, Malgesini, G.^{1,2}, Challenor, P.³, and Hunt, J.E.¹

¹National Oceanography Centre, European Way, Southampton, Hampshire, SO14 3ZH

²D'Appolonia Spa, Via San Nazaro, 16145 Genova, Italy (current address)

³College of Engineering, Mathematics and Physical Sciences, University of Exeter, North Park Road, Exeter EX4 4QF

ABSTRACT *Submarine landslides can be far larger than those on land, and are one of the most important processes for moving sediment across our planet. Landslides that are fast enough to disintegrate can generate potentially very hazardous tsunamis, and produce long run-out turbidity currents that break strategically important cable networks. It is important to understand their frequency and triggers. The distribution of recurrence intervals for large landslide-triggered turbidity currents ($>0.1 \text{ km}^3$) is documented here in three basin-plains. A common distribution form of recurrence intervals is observed, despite variable ages and disparate locations, suggesting similar underlying controls on landslide triggers and frequency. This common distribution form closely approximates a time-independent Poisson distribution, such that the probability of a large disintegrating landslide occurring along the basin margin is independent of the time since the last landslide. This distribution suggests that non-time dependent processes such as sea level are not a dominant control on frequency of these landslides. Recurrence intervals of major ($> M 7.3$) earthquakes have an approximately Poissonian distribution, suggesting they could be implicated as triggers. However, not all major earthquakes appear to generate widespread turbidites, and other as yet unknown triggers or sequential combinations of processes could produce the same distribution. This is the first study to show that large landslide-triggered turbidites have a common frequency distribution form in distal basin plains, and that this distribution is time-independent. This result has important implications for assessing hazards from landslide-tsunamis and seafloor cable breaks, and the long-term tempo of global sediment fluxes.*

5.1 Introduction

Submarine landslides on continental margins include the largest mass flows on Earth. They can involve hundreds to several thousand cubic kilometres of material (Hühnerbach and Masson, 2004), and can be far larger than those on land (Korup et al., 2007). Many large landslides initiate on sea floor gradients of $< 2^\circ$ that would almost

always be stable on land (Urlaub et al., 2013). Motion of the landslide can potentially generate damaging tsunamis that travel across the ocean for long distances. Mixing of the landslide mass with the surrounding seawater can form longer run-out sediment flows called turbidity currents, which can travel for hundreds of kilometres, sometimes with speeds of up to 19 m/s (Piper et al., 1999). Cables that carry over 95% of transoceanic global data (Carter et al., 2009), and expensive oil and gas infrastructure may be damaged by landslides and turbidity currents. The most hazardous events are large volume and fast moving landslides that disintegrate to produce turbidity currents. They are also the most important events for transporting sediment over long distances. Deposit volumes $> 0.1 \text{ km}^3$ are considered to represent large landslides – although some landslides can be up to three orders of magnitude larger (Urlaub et al., 2013). Determining whether large-volume landslides have a common frequency distribution form, and what that distribution may be, has importance for understanding regional hazards associated with tsunamis and damage to seafloor structures. The frequency distribution can also provide insights into triggers and preconditioning factors. Furthermore, the substantial volumes of sediment mobilized during landslide and turbidity current events is extremely relevant to understanding global sediment flux and the transport and ultimate burial of carbon in the deep sea.

Numerous hypotheses have been proposed for how large submarine landslides are triggered and slopes are preconditioned to fail. However, we are yet to monitor a large submarine landslide in action, and these hypotheses remain poorly tested. Rapid accumulation of impermeable sediment is often invoked as a preconditioning factor for failure, which may then be triggered by an earthquake (Stigall and Dugan, 2010). However, very large landslides also occur in areas of slow sedimentation (Urlaub et al., 2013), failure may occur thousands of years after rapid sedimentation ceases (Leynaud et al., 2009), and some recent large earthquakes did not produce widespread slope failure (Völker et al., 2011; Sumner et al., 2013). The headwalls of most large landslides are too deep ($> 200 \text{ m}$ water depth) for triggering by cyclic wave loading, and some headwalls are too deep ($> 2,000 \text{ m}$) for triggering by gas hydrate dissociation (Hühnerbach and Masson, 2004). It has been suggested that sea level changes play a key role in preconditioning or triggering slope failure (Lee, 2009). However, a recent analysis of large landslide frequency concluded that there was no significant association with sea level (Urlaub et al., 2013).

5.2 Aims

The aim is to determine the frequency distribution of recurrence intervals for turbidites triggered by large ($>0.1 \text{ km}^3$) submarine landslides in three deep-sea basins. As a similar frequency distribution of recurrence intervals is observed, the significance of this distribution is explored for understanding how large landslides are triggered. This analysis includes potential triggering of landslides by sea level changes and large magnitude earthquakes.

5.3 Methods

The recurrence time of landslides is inferred from intervals of hemipelagic mud that settles out between turbidity currents, and average accumulation rate of the hemipelagic mud (Chapter 3). This provides information on the timing of many (> 100) landslides, which aids robust statistical analysis and avoids the need to date prohibitively large numbers of landslides, each in a different location on the margin.

Turbidite sequences in three deep-water basin plains are considered in this chapter (Figure 5.1) including the Madeira Abyssal Plain (offshore NW Africa), Balearic Abyssal Plain (western Mediterranean Sea), and Marnoso-arenacea Formation (Italian Apennines). The Madeira Abyssal Plain record comes from ODP cores and spans the last $\sim 7 \text{ Ma}$, while piston coring of the Balearic Abyssal Plain provides a sequence for the last $\sim 150 \text{ ka}$. Outcrops of the Marnoso-arenacea Formation provide a record of events between 13.5 and 14.1 Ma. Visually diagnostic features of hemipelagic mud in the studied sequences are common dispersed foraminifera, reduced organic carbon content, higher calcium carbonate content, lighter color and bioturbation (Chapter 3). This visual differentiation is consistent with detailed geochemical (Rothwell et al., 2004), and microscopic analyses (Talling et al., 2007b).

5.3.1 Erosion by turbidity currents

The method used requires that significant thicknesses of hemipelagic mud were not eroded beneath turbidity currents, and the influence of how erosion would affect recurrence time estimates is shown in Section 5.4.3. This view is supported by mapping of hemipelagic mud thickness beneath individual beds in the Marnoso-arenacea Formation, showing that this thickness varies by $< 5\text{--}10 \text{ cm}$ over $\sim 120 \text{ km}$ (Chapter 3).

A lack of spatial variation in coccolith assemblages and thickness of turbidite mud caps in the Madeira Abyssal Plain indicate minimal erosion - interpreted to be less than a few centimetres (Weaver and Thomson, 1993). The turbidite beds in the Madeira and Balearic Abyssal Plain cores lack irregular bases indicative of erosion, although the narrow core width (< 10 cm) precludes observation of larger scale erosional features.

5.3.2 Short-term fluctuations in hemipelagic mud accumulation rates

The chosen method for calculating recurrence intervals assumes that no significant fluctuation in hemipelagic mud accumulation rates occurred between dated horizons. Such horizons occur every 0.4 ka to 18.5 ka in the Balearic Abyssal Plain, and every 5 ka to 1 Ma in the Madeira Abyssal Plain. This issue is most important for the Marnoso-arenacea Formation where a constant hemipelagic accumulation rate is assumed over the entire interval. This assumption may not be unreasonable, as hemipelagic accumulation rates in the Balearic Plain only vary by $\sim 30\%$ over an interval of 150 ka.

5.3.3 Were these extensive basin plain turbidity currents triggered by large landslides?

It is known that slope failures can generate turbidity currents that reach distal basin plains, from often very large landslides on the open continental slope (Piper et al., 1999) or smaller failures that lead to canyon-flushing flows (Piper and Savoye, 1993; Talling et al., 2012). However, it is possible that flows reaching basin plains can be triggered in other ways. Turbidite volume provides the best evidence of triggering by slope failure, as other triggers most likely produce small (< 0.1 km³) sediment volume flows. Even the largest flood discharges into the ocean tend to involve less than 0.1 km³ of sediment (Dadson et al., 2005), although such flood-triggered submarine flows could pick up sediment en-route to basin plains. The data sets considered here were chosen because each turbidite contains large (> 0.1 km³ to 500 km³) volumes of sediment (Appendix 3). Volume estimates are based on unusually detailed long distance (> 100 km) mapping of individual beds in the Marnoso-arenacea Formation (Talling et al., 2007b), Madeira Abyssal Plain (Weaver, 2003) and Balearic Abyssal Plain (Rothwell, et al., 1998; Rothwell et al., 2004). However, even if these turbidity currents were generated by floods and eroded very large sediment volumes during canyon flushing, understanding their recurrence times is still important for geohazards affecting seafloor infrastructure.

Not all landslides trigger long run-out turbidity currents, as some landslides may be too slow moving to disintegrate. This study only considers faster-moving and larger landslides that disintegrate to produce voluminous turbidites. It is these events that pose the greatest regional threat to seafloor infrastructure, may produce hazardous tsunamis, and are most important for continental margin evolution and global sediment transport.

5.4 Results

5.4.1 Common frequency distribution form of landslide recurrence intervals

The recurrence interval distributions form a nearly straight line on a log-linear exceedence plot for all three data sets (Figure 5.1). This linear trend indicates an exponential relationship, characteristic of a Poisson distribution, although there is a slight deviation for the longest recurrence intervals. A Poisson distribution implies a lack of memory, such that the probability of a new event occurring is independent of the time since the last. It is characterized by only one parameter (λ) - the mean recurrence interval or rate parameter. Equation 5.1 defines the Probability Function (P) that a discrete random recurrence interval (X) is less than a specific value for the data series (x). The solution is related to an exponential function (e^{-x}) and the rate parameter (λ). Values of X , x and λ are integers defined in thousands of years.

$$P(X < x) = 1 - e^{-\frac{x}{\lambda}} \text{ (Equation 5.1)}$$

A common distribution form in data sets from multiple disparate settings may indicate a common underlying control, and this has not been shown previously for large landslide-triggered turbidites preserved in distal basin plains.

5.4.2 Is this distribution time-independent (Poissonian)?

To test that the data are truly exponential and they share a common distribution, form they are normalized by sub-dividing each recurrence interval, T , by mean recurrence interval (λ) for each of the data sets to plot a normalised variable, R_T . The data sets show close agreement when plotted in this way, despite disparity in their age, location and setting. R_T values closely approximate an exponential distribution; however, some slight overpopulation is observed at the tail for $R_T > 3$, suggesting a small deviation from a strictly Poisson distribution.

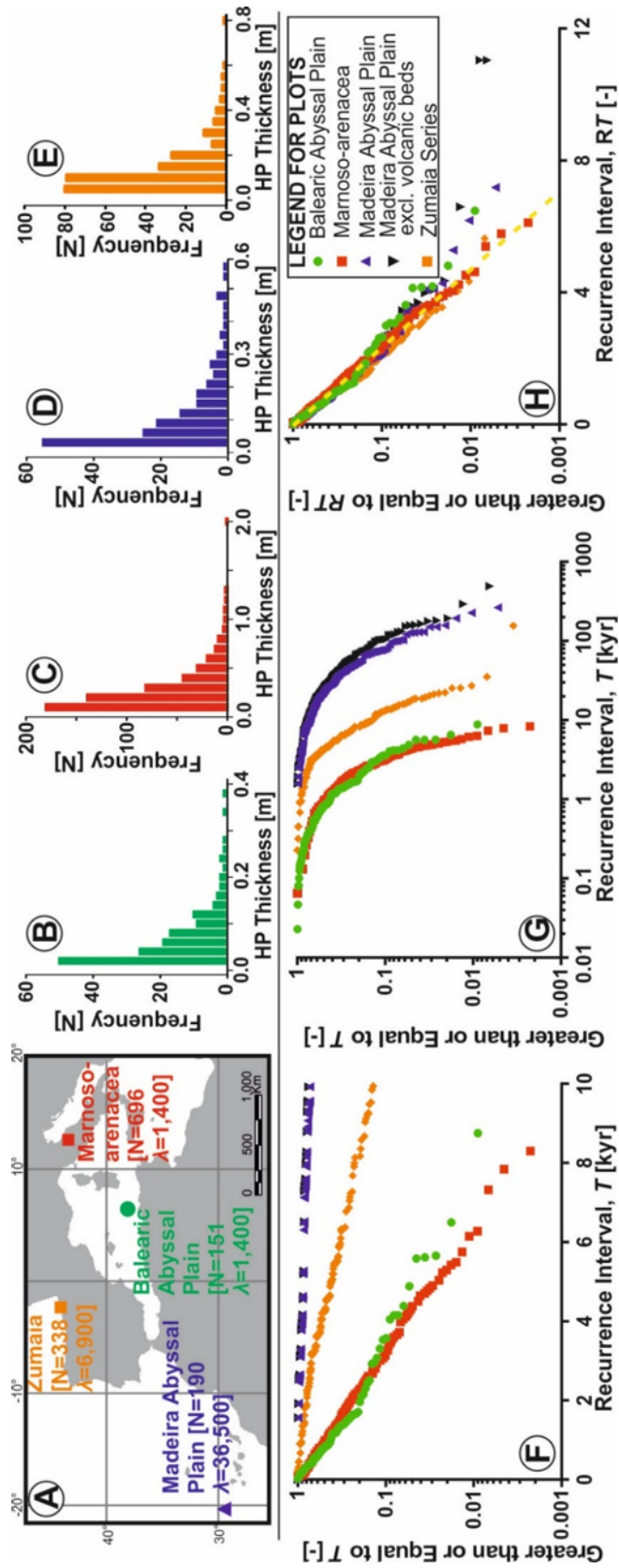


Figure 5.1: Location map (A). Frequency histograms of hemipelagic mud thickness (B to D). Recurrence intervals plotted on (E) log-linear axes, (F) log-log axes and (G) with recurrence intervals normalized by rate parameter (λ). Yellow dashed line is a true normalised exponential trend ($\log(y)=\lambda/2.3$)

To test whether this is a Poisson distribution, a Generalized Linear Model is applied to the data using a Gamma distribution (of which the exponential is a special function). This defines a dispersion parameter, α , for the curve fitted to each of the data sets. A true exponential distribution is represented by $\alpha = 1$; however, values between 1 and 2 can be treated as Poissonian. The values derived for the data sets in this study are between 1.0 (Marnoso-arenacea) and ~ 1.2 (Balearic and Madeira Abyssal Plain; Table 5.3). This indicates that they are near-exponentially distributed, albeit with some overpopulation in the tail of the data. A similar observation is made by comparing catalogues of randomly-generated synthetic data against the actual values. The synthetic data recreate the spread of the actual data, but do not show the same bias to longer inter-event times (Figure 5.3).

Table 5.1: Summary of statistical results for Generalised Linear Model and Proportional Hazards Model for the Balearic and Madeira Abyssal Plain datasets testing for significance of sea level and its first derivative

| | Dataset | Generalised Linear Model | | Cox Proportional Hazards Model | | | |
|--|------------------------|--------------------------|-----------------------------------|--------------------------------|---------------------|---------------|--------------------------|
| | | GLM [p] | Dispersion Parameter [α] | PHM [p] | Likelihood test [p] | Wald test [p] | Score (logrank) test [p] |
| Influence of Sea Level | Balearic Abyssal Plain | 0.48 | 1.179 | 0.884 | 0.884 | 0.884 | 0.884 |
| | Madeira Abyssal Plain | 0.40 | 1.240 | 0.479 | 0.503 | 0.500 | 0.500 |
| Influence of First Derivative of Sea Level | Balearic Abyssal Plain | 0.76 | 1.281 | 0.241 | 0.505 | 0.503 | 0.504 |
| | Madeira Abyssal Plain | 0.49 | 1.190 | 0.201 | 0.637 | 0.624 | 0.623 |

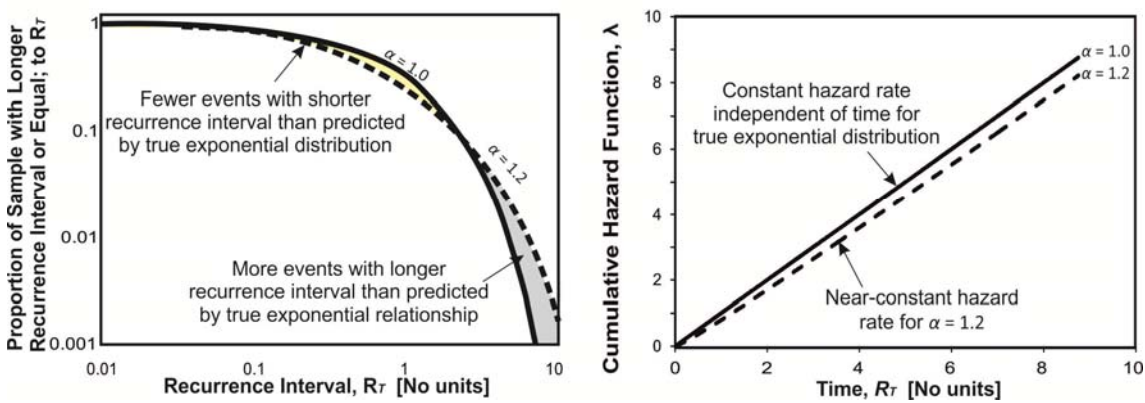


Figure 5.2: Dispersion parameters plotted for GLM results on exceedance plot (left) and cumulative hazard function plot (right)

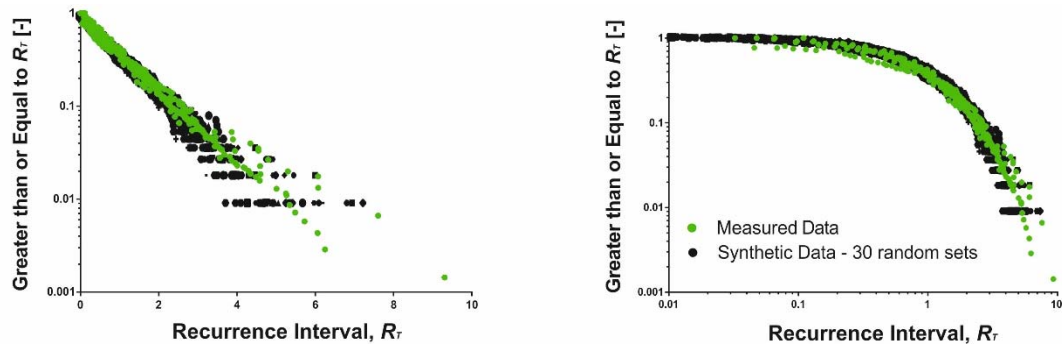


Figure 5.3: Comparison of 100 sequences of randomly generated synthetic data (black) with actual data (green) normalized to λ .

5.4.3 Effects of variable erosion beneath beds

The potential influence on the results of erosion of hemipelagic mud to variable depths by turbidity currents is now investigated. Random amounts of erosion to depths of between 0 and 10 cm are simulated for the original hemipelagic mud thickness data (Figure 5.4A). This depth range was chosen as it is the maximum difference in hemipelagic mud thickness beneath Marnoso-arenacea turbidites mapped over 120 km (Talling et al., 2007b). Additional erosion was only simulated below turbidites that are equal or thicker than the mean turbidite thickness, rather than beneath every turbidite. Erosion is likely to be greater beneath thicker beds, which represent larger and more powerful turbidity currents. Accounting for differential erosion also provides a near-exponential distribution. This supports the view that erosion of up to 10 cm between beds would not modify the main conclusion that recurrence times approximate a Poisson distribution.

5.4.4 Effects of short-term changes in hemipelagic accumulation rates

Random variations between $\pm 50\%$ of the mean recurrence interval between turbidites were applied to the data from the Madeira Abyssal Plain (Figure 5.4B). This simulates short-term temporal variations in hemipelagic accumulation rates. A near-exponential distribution of inter-event times is still observed.

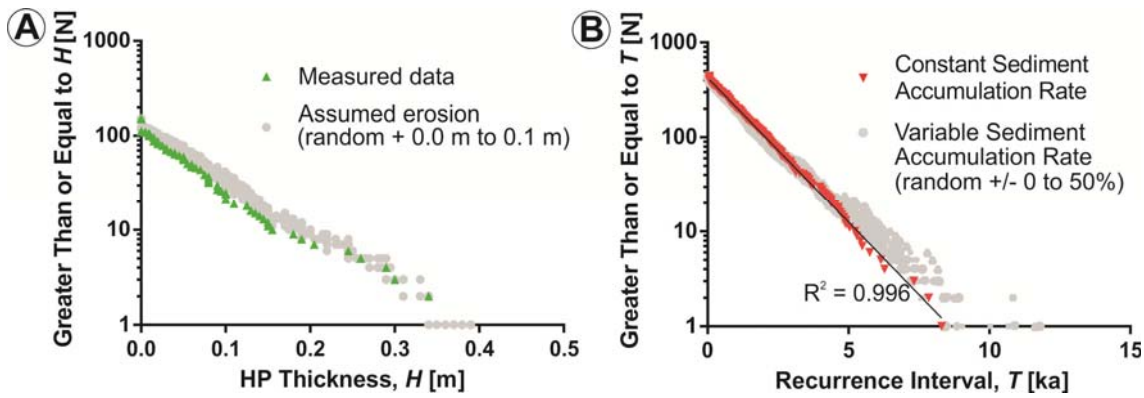


Figure 5.4: (A) Influence of erosion on hemipelagic thickness. Ten modified datasets (grey) account for random amounts of erosion (between 0.0 m and 0.1 m) below turbidites thicker than the mean bed thickness from the Balearic Abyssal Plain. (B) Influence of short term variations in hemipelagic accumulation rates – ten random datasets (grey) are plotted against the measured data for the Madeira Abyssal Plain to account for random variations between +/-50%

5.4.5 Results of tests that are independent of frequency distribution

The previous analyses are reliant upon determining the form or shape of frequency distribution. To further explore temporal relationships or other controls, the findings of two analyses that are independent of the form of frequency distribution (Cox, 1972; Kristoufek, 2012) are now presented. Outputs of the rescaled range analysis, yield K values (Hurst exponent) of 0.54 (0.47-0.68), 0.55 (0.46-0.66) and 0.59 (0.46-0.69) for the Balearic, Marnoso and Madeira datasets respectively (Figure 5.5), which indicates that there is no significant trend-reinforcement. Parenthesised ranges refer to 100 runs of data including randomly modelled variations in hemipelagic accumulation rates (Figure 5.5). In essence, the datasets can be viewed as non-clustered (such as a random walk series) with respect to the timing of preceding or succeeding events.

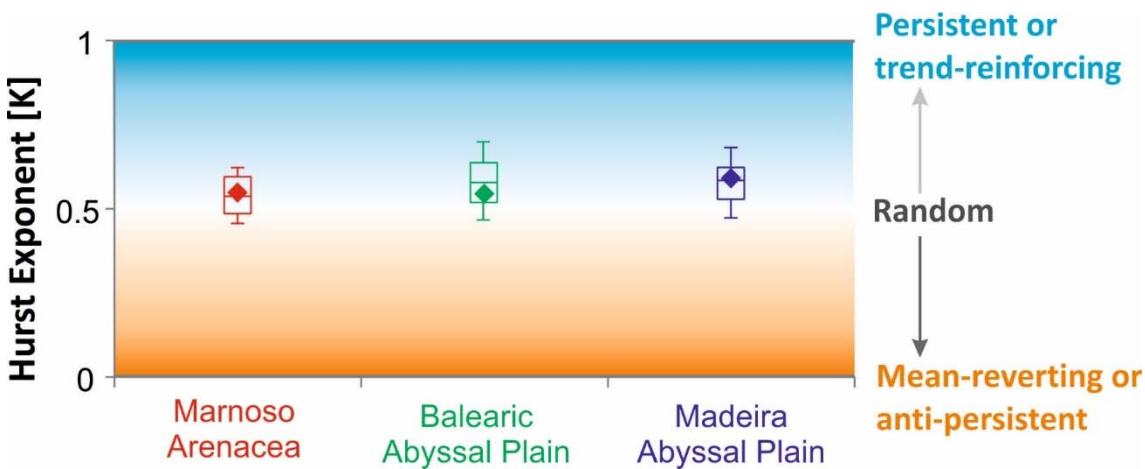


Figure 5.5: Results of rescaled range analysis: Marnoso-arenacea ($K=0.5477$), Balearic Abyssal Plain ($K=0.5438$), Madeira Abyssal Plain ($K=0.5907$). Box and whiskers represent the results for 100 runs using the same data but with +/-30% variation in hemipelagic accumulation rate to account for uncertainty. Boxes show 25%, 50% and 75% spread, while whiskers show 5% and 95% spread.

Testing the control of sea level and its first derivative (i.e. rate of change) is performed by application of the Cox Proportional Hazards Model to the Balearic and Madeira Abyssal Plain datasets. High resolution sea level curves are available for the time periods covered by these datasets, but not for the Marnoso-arenacea record (Miller et al., 2005; Rohling et al., 2009). Neither sea level, nor its first derivative, are found to have a control on recurrence rate even at the 90% significance level based on the outcomes of the Proportional Hazards, Wald, log-rank and likelihood tests (Table 5.3).

5.5 Discussion

First, the implications of the observed Poisson distribution is discussed for understanding triggers and preconditioning factors for large disintegrative landslides.

5.5.1 Geological significance of Poisson distribution

A Poisson distribution results from a process that is random and lacks memory, in the sense that the probability of an event occurring is independent of the time since the last. A Poisson distribution of landslide frequency could form in three ways. First, the distribution could result from a single basin-wide triggering process that is independent of time. Second, it could result from numerous different basin-wide triggers, or from many different triggering processes that each affects a localized area along the basin margin. Third, it could result from a sequential chain of multiple processes, each occurring one after the other. The Poisson distribution suggests that triggering of landslide is not due to a single process, or a small number of processes, whose distribution is time-dependent.

5.5.2 Landslide frequency and sea-level

It has been proposed that glacial-eustatic sea level fluctuations are a major control on the frequency of large landslides (Lee, 2009). However, all three data sets show evidence for no strong eustatic sea level control. This suggests that sea level is not a dominant triggering or preconditioning factors for large disintegrative landslides. Such a view is consistent with a recent global analysis of large landslide ages during the last 30 ka (Urlaub et al., 2013), but is contrary to that of previous workers (e.g. Lee, 2009). Processes that fluctuate in conjunction with eustatic sea level and climate cycles are also unlikely to be temporally random, and this study suggests that they too are not dominant

single controls on landslide timing. Such process may include dissociation of gas hydrates due to ocean warming, or increased sedimentation rates on continental slopes during sea-level lowstands.

5.5.3 Comparison to the frequency distribution of large magnitude earthquakes

It has been proposed that recurrence intervals of large magnitude ($M > 7.3$) earthquakes in global databases, documented by seismometers since ~1900 AD, are time-independent and follow a Poisson distribution (Corral, 2006; Figure 5.6). These analyses exclude aftershocks. Other workers have argued that this instrumental record contains too few events to be sure that the distribution is Poissonian (e.g., Daub et al., 2012). This result is only found for measurements made over large areas, as individual fault segments can have characteristic earthquake recurrence periods.

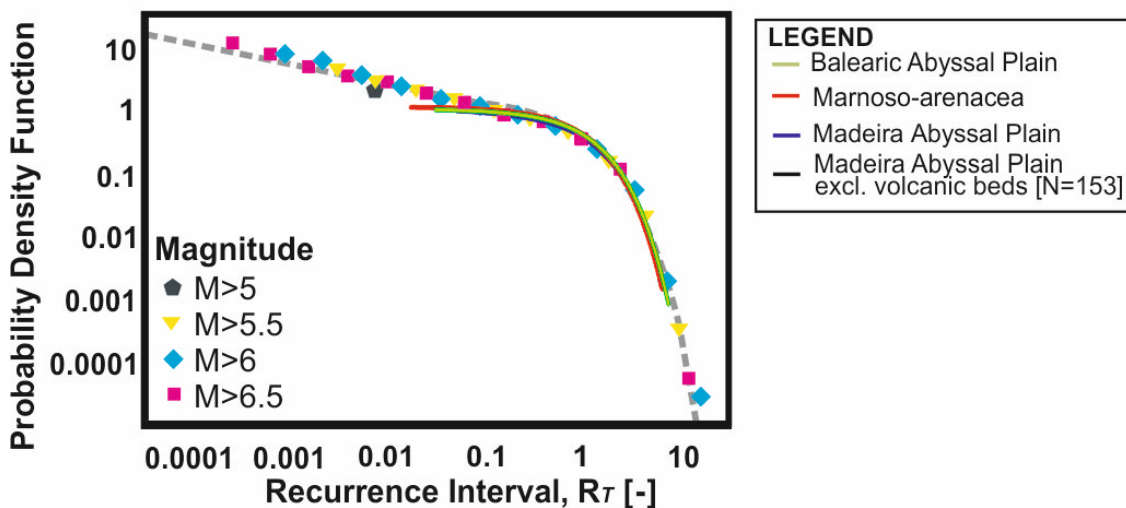


Figure 5.6: Probability density function plot shows datasets (solid lines) superimposed on global earthquake data (points and dashed line) normalised to λ (modified from Corral, 2006).

It might therefore be suggested that large landslides are triggered by major earthquakes, based on the similarity between the shape of the frequency distribution of recurrence intervals of landslides and large magnitude earthquakes (Figure 5.6). In contrast, the frequency distribution of river floods is far from an exponential Poisson distribution (Bobée et al., 1993). Although some large landslides are known to have been triggered by earthquakes (Piper et al., 1999), some large (M 8.4 and 9.1) earthquakes do not always cause widespread seafloor failure (Völker et al., 2011; Sumner et al., 2013). This suggests that only a subset of major earthquakes trigger large landslides, such that

there is not a one-to-one correlation between major earthquakes and large landslides. This view is consistent with the average recurrence intervals recorded here (1.4–36.5 ka), which tend to be significantly longer than average historical recurrence intervals of major ($> M 7.3$) earthquakes of tens to several hundred years (e.g. Meghraoui et al., 1988). It could then be argued that only very large magnitude ($M 8$ or 9) earthquakes trigger landslides, but field observations suggest that sometimes even these do not produce extensive landslides (Völker et al., 2011; Sumner et al., 2013). It is likely that sediment supply is an important control on whether an earthquake may actually trigger a landslides. If sufficient preconditioning has not occurred, a potential trigger may not result in the occurrence of a landslide. Conversely, a smaller magnitude earthquake may trigger a landslide should the slope already be predisposed or close to failure. Thus, there is unlikely to be a direct link between a large magnitude earthquake and landslide triggering. A greater understanding is thus required of sediment delivery, slope geometry and other preconditioning factors.

5.5.4 Multiple local or sequential controls along a basin margin

It is also possible that landslides are mainly triggered by one or more currently unknown factors that have a Poisson distribution, or that different factors trigger landslides locally along the margin. The latter view implies that there is not a single dominant source location for most turbidites in a basin-floor data set, and landslides are triggered in variable ways at different points around the margin. This results in a regionalized sum of landslide recurrence times that may approximate a Poisson distribution. However, a rigorous test of this model is problematic as the source of each turbidite in the data sets cannot be pinpointed with sufficient precision. It is also possible that a time-independent distribution may result from cumulative triggering by a series of factors that occur one after another, at a single location. A slope may thus be preconditioned to fail by a series of multiple factors over time.

Madeira Abyssal Plain – Discerning signals from different input sources

While it is not possible to pinpoint the exact initiation point of individual landslides, distinct source areas have been interpreted for the turbidites in the Madeira Abyssal Plain dataset (Jarvis et al., 1998; Weaver, 2003). The geochemical signature of turbidite mudcaps has been attributed to four broad types: volcanoclastic turbidites sourced from

the Canary Islands; calcareous turbidites sourced from the seamounts to the west; non-volcanic beds that most likely originate from the submarine regions around the Canary Islands; and organic-rich siliciclastic ($>0.3\%$ TOC) turbidites that are sourced from different parts of the north-west African margin (Jarvis et al., 1998; Lebreiro et al., 1998; Weaver et al., 1998; Hunt et al., 2014). Organic-rich turbidites can be further subdivided on the basis of colour and geochemical signature which is also thought to be diagnostic of source area, and are termed organic, dark organic and pale organic. Turbidites sourced specifically from the island of Tenerife have also been geochemically identified as a subset of the volcanic turbidites (Hunt et al., 2014). Thus, one can explore the frequency distribution of turbidites with different source signatures to determine whether different input sources appear to be dependent on time or not (Hunt et al., 2014; Figure 5.7).

Landslide-triggered turbidites from different source areas cannot be statistically discerned from a Poisson distribution

When plotted on exceedance plots, the recurrence intervals of the individual sources appear to show a straight line fit on log-linear axes (Figure 5.8A). The data also collapse on top of one another when normalized to the mean recurrence intervals for each sample (Figure 5.8B). Therefore, the recurrence intervals of each source area appear to conform to a Poisson distribution which is validated by the results of a Generalised Linear Model, where the dispersion parameter is close to one in all cases (Figure 5.8C). Even the subsets of organic beds appear to conform to the same trend (Figure 5.8D); however, some caution should be applied, as the number of beds is well below the optimal sample size ($N=8$ to 49).

With one exception, the results of the Generalised Linear Model and Proportional Hazards Model do not indicate any significance above a 90% level for the influence of sea level and its derivative, which may allow rejection of the hypothesis that neither sea level nor its rate of change directly controls event timing and recurrence rate (Table 5.2). The only exception is for pale organic turbidites which yield a significant result for the influence of sea level based on the Generalised Linear Model; however, the sample size [$N=8$] is so far below the optimal level that this result cannot be trusted. The results of rescaled range analysis also indicate that, when differentiated by source signature, there is generally a near-time-independent result (i.e. with values close to $K=0.5-0.6$; Table 5.3). The exceptions to this are the volcanic and Tenerife-sourced volcanic turbidites which show weak anti-persistent ($K=0.4$) and persistent ($K=0.8$) behavior respectively.

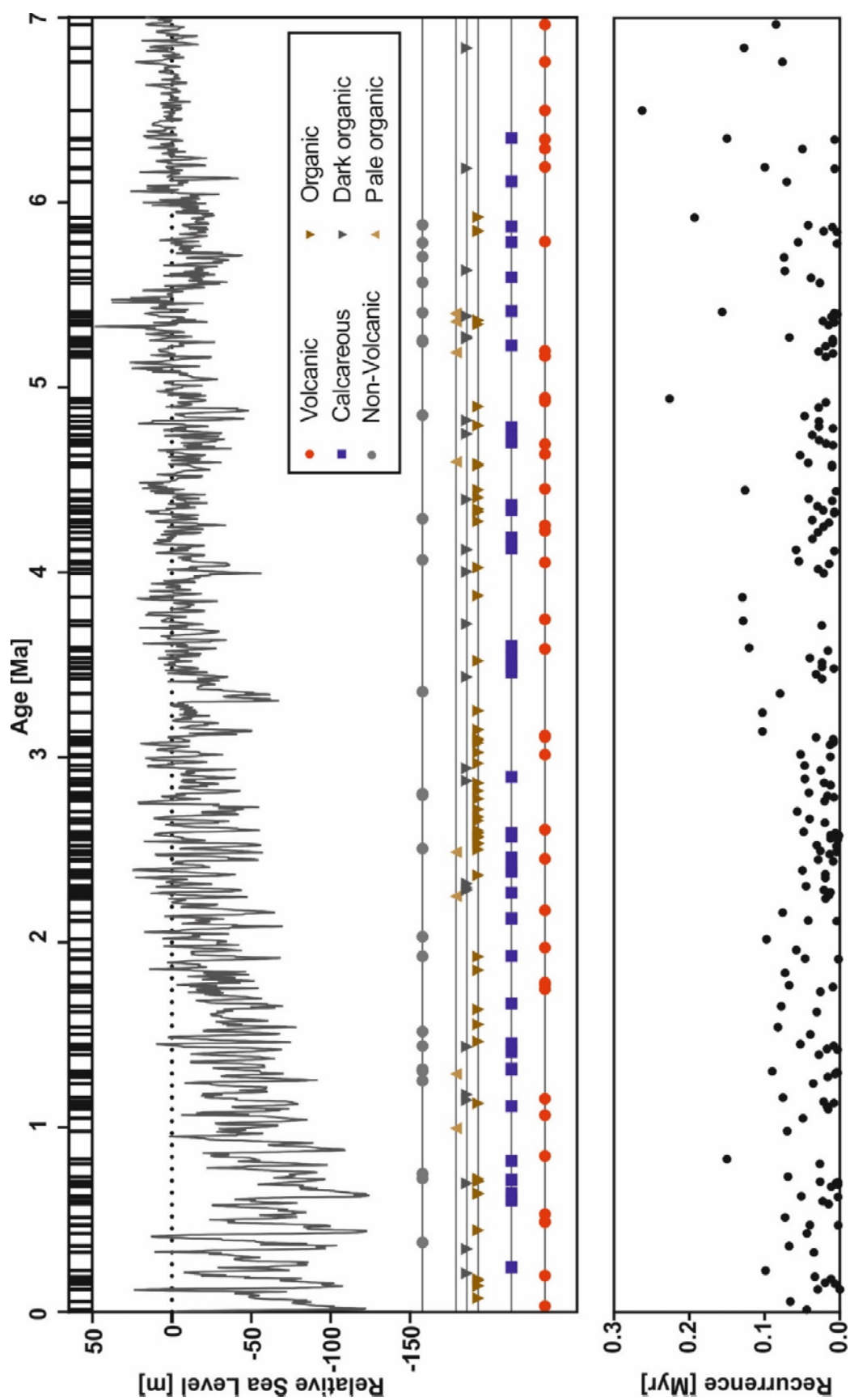


Figure 5.7: Times series plot of turbidites from the Madeira Abyssal Plain differentiated by distinct geochemical signatures. Upper panel shows global sea level curve of Miller et al. (2005), middle panel shows stave for each turbidite type and lowermost panel shows recurrence for all turbidites.

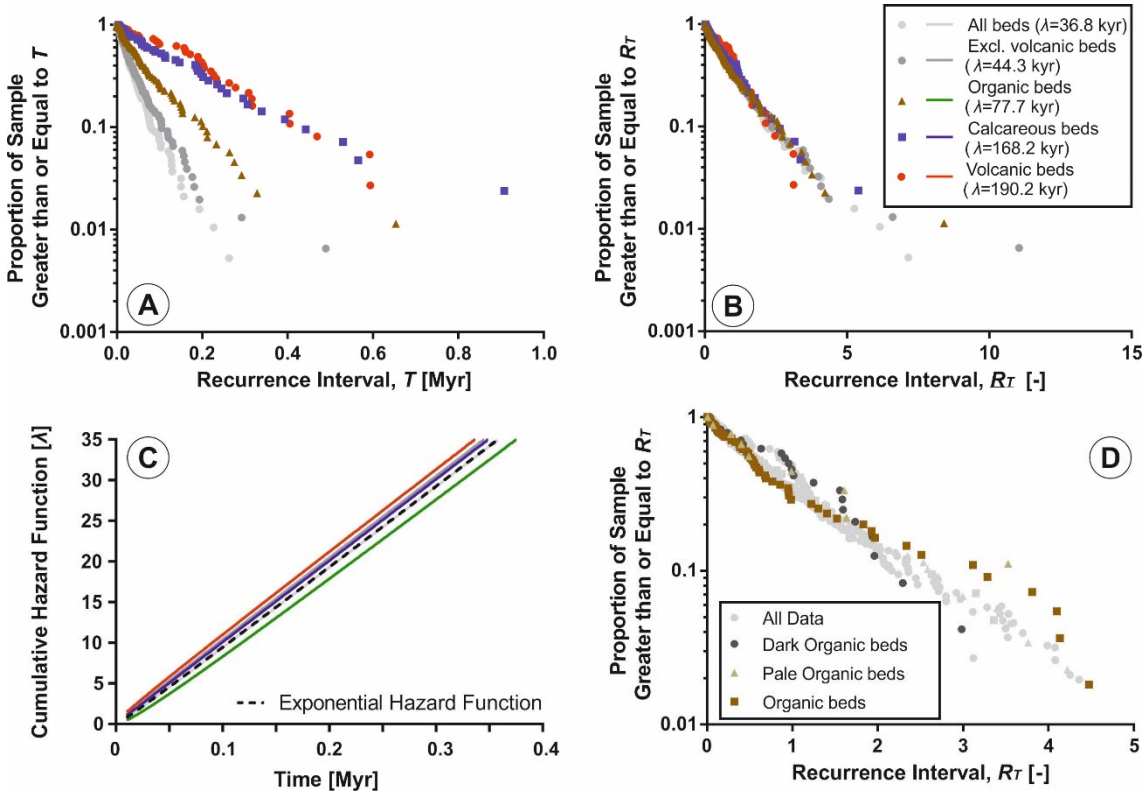


Figure 5.8: (A) Exceedence plot on log-linear scale for subsets of Madeira abyssal plain turbidites differentiated by geochemical signature, (B) As previous plot, but normalized to mean recurrence for each of the turbidite types. (C) Illustration of hazard function (using a Gamma form) using the shape parameters determined by the GLM. The hazard function only deviates slightly from a true exponential form as shown by the dashed line. (D) Subsets of the organic turbidites, which also show a near-exponential trend, however the sample size is well below the optimal level prescribed in this study.

Table 5.2: Results of rescaled range analysis for Madeira Abyssal Plain. Source areas are diagnosed on the basis of geochemical signature of turbidite mudcaps.

| Location | Hurst Exponent [K] | Number of Turbidites [N] |
|---|------------------------|------------------------------|
| Madeira Abyssal Plain | 0.591 | 186 |
| Madeira Abyssal Plain (excluding volcanic turbidites) | 0.648 | 149 |
| Madeira Abyssal Plain – Organics only | 0.620 | 82 |
| Madeira Abyssal Plain – Calcareous only | 0.593 | 42 |
| Madeira Abyssal Plain – Volcanics only | 0.401 | 37 |
| Madeira Abyssal Plain – Tenerife-sourced volcanics only | 0.794 | 26 |

Table 5.3: Summary of statistical results for Generalised Linear Model and Proportional Hazards Model for subsets of the Madeira Abyssal Plain turbidite record. Bold italicised values are significant results ($p < 0.05$).

| | Turbidite-Type | Generalised Linear Model | | Cox Proportional Hazards Model | | | |
|--|---|--------------------------|-----------------------------------|--------------------------------|---------------------|---------------|--------------------------|
| | | GLM [p] | Dispersion Parameter [α] | p-value | Likelihood test [p] | Wald test [p] | Score (logrank) test [p] |
| Influence of Sea Level | All turbidites [N=186] | 0.40 | 1.214667 | 0.479 | 0.5034 | 0.5002 | 0.5001 |
| | All turbidites except volcanics [N=148] | 0.59 | 1.668168 | 0.882 | 0.8824 | 0.8822 | 0.8822 |
| | Tenerife sourced volcanic turbidites [N=25] | 0.82 | 1.681064 | 0.29691 | 0.8136 | 0.8146 | 0.8145 |
| | All volcanic turbidites [N=36] | 0.65 | 0.698935 | 0.929 | 0.6634 | 0.6678 | 0.6676 |
| | All organic turbidites [N=81] | 0.59 | 1.671804 | 0.904 | 0.5767 | 0.581 | 0.5808 |
| | Organic turbidites [N=49] | 0.62 | 1.460223 | 0.127 | 0.7985 | 0.7999 | 0.7999 |
| | Pale organic turbidites [N=8] | 0.0033 | 1.174917 | 0.1702 | 0.01387 | 0.0299 | 0.01475 |
| | Dark organic turbidites [N=24] | 0.97 | 0.678882 | 0.733885 | 0.6441 | 0.64 | 0.6395 |
| | Non volcanic turbidites [N=23] | 0.87 | 0.884227 | 0.70266 | 0.6265 | 0.6239 | 0.6234 |
| | Calcareous turbidites [N=41] | 0.85 | 0.977137 | 0.9 | 0.8762 | 0.8766 | 0.8766 |
| Influence of First Derivative of Sea Level | All turbidites [N=186] | 0.49 | 1.190386 | 0.201 | 0.6373 | 0.6241 | 0.6237 |
| | All turbidites except volcanics [N=148] | 0.38 | 1.658606 | 0.448 | 0.5261 | 0.4474 | 0.496 |
| | Tenerife sourced volcanic turbidites [N=25] | 0.94 | 1.995476 | 0.7655 | 0.8723 | 0.8928 | 0.8917 |
| | All volcanic turbidites [N=36] | 0.92 | 0.752149 | 0.998 | 0.8792 | 0.873 | 0.8727 |
| | All organic turbidites [N=81] | 0.57 | 1.394719 | 0.33 | 0.778 | 0.8106 | 0.807 |
| | Organic turbidites [N=49] | 0.14 | 1.460223 | 0.127 | 0.3817 | 0.5291 | 0.4843 |
| | Pale organic turbidites [N=8] | 0.45 | 1.174917 | 0.1702 | 0.4022 | 0.7794 | 0.5873 |
| | Dark organic turbidites [N=24] | 0.9 | 0.807187 | 0.62418 | 0.6212 | 0.6673 | 0.6546 |
| | Non volcanic turbidites [N=23] | 0.95 | 0.980392 | 0.6879 | 0.8328 | 0.8358 | 0.8349 |
| | Calcareous turbidites [N=41] | 0.26 | 0.960476 | 0.998 | 0.3482 | 0.2125 | 0.1603 |

Therefore, one may consider that if an environmental control is operating, then it is either weak (and therefore not proven by the statistical analysis) or there may be a dynamic interrelationship between multiple controlling variables (e.g. sea level, climate, weathering, unroofing processes). These are not all currently understood, and many processes may not operate immediately in response to changes in sea level (Hunt et al., 2014). This trend, showing a weak or non-significant correlation of submarine landslide occurrence with sea level change, is being found in an increasing number of study areas (Hunt et al., 2014). Indeed, the 600 ka to recent record of continental slope-derived turbidites in Agadir Basin demonstrates a Poisson-like process as the trigger mechanism, demonstrating a reduced influence of climatically-induced sea level (Hunt et al., 2013).

5.6 Conclusions

Analysis of large volume turbidites ($>0.1 \text{ km}^3$) in three basin plains indicates that there is a common frequency distribution form of inter-event times for larger and faster-moving landslides that disintegrate. Such landslides tend to form relatively large tsunamis, pose the greatest regional hazard to seafloor infrastructure, and are most important for global sediment fluxes. This novel conclusion may indicate similar controls on landslide frequency and triggers occur in disparate areas. The common frequency distribution form approximates a Poisson distribution, such that the time to the next landslide is independent of the time since the last. This suggests that temporally non-random processes, such as glacio-eustatic sea level change, are not dominant single controls on landslide frequency, contrary to the conclusions of some previous work. It appears that processes that fluctuate in conjunction with eustatic sea-level and climate cycles (e.g., shelf edge sedimentation rates or hydrate dissociation driven by ocean warming) are also not dominant single controls on landslide timing. Major earthquakes have an approximately Poisson distribution of recurrence intervals suggesting they may play a role in landslide triggering, although not all major earthquakes appear to generate large disintegrating landslides. Alternatively, landslides may be triggered by processes that are yet unknown which are time independent, by many disparate processes acting locally along a basin margin, or by a series of processes that occur one after another at a single location. It is feasible that the records analysed may also include large volume canyon flushing events; however, regardless of this, this study has important implications for predicting frequency of landslide-tsunamis, the occurrence of cable breaks, and the

global tempo of sediment transport. It suggests that the frequency of large volume flows, such as those triggered by disintegrative landslides is unlikely to change significantly due to rapid eustatic sea level rise during forthcoming decades.

Chapter 6. Implications of millennial-scale dramatic climate change for landslide and turbidite recurrence

Summary

This chapter presents a statistical analysis of two distal basin plain sites that include turbidite records over the most pronounced period of millennial-scale global warming in the last 65 million years; the Initial Eocene Thermal Maximum (IETM). A comparison is made with the datasets analysed in Chapter 5 and implications for millennial-scale climate change on landslide frequency are discussed. The potential triggering of climate change by increased landslide activity, and related hydrate dissociation during periods of global ocean warming, is also discussed.

This chapter has been published in its current format in *Earth and Planetary Science Letters* (April, 2015). The published manuscript benefited from the reviews of Kyle Straub (Tulane University) and two anonymous reviewers. All analyses and interpretations were completed by me, with editorial help provided by the co-authors during paper writing.

James Hunt provided initial measurements of bed thicknesses for the ODP 1068 record and assisted with fieldwork in Zumaia, Spain. This research used samples and data provided by the Ocean Drilling Program (ODP). ODP is sponsored by the U.S. National Science Foundation (NSF) and participating countries under management of Joint Oceanographic Institutions (JOI), Inc. A sub-set of the full ODP 1068 record is discussed in this chapter, as the full record is discussed in Chapter 7.

Implications of reduced turbidity current and landslide activity for the Initial Eocene Thermal Maximum - evidence from two distal, deep-water sites

Clare, M.A.¹, Talling, P.J.¹ and Hunt, J.E.¹

¹National Oceanography Centre, European Way, Southampton, Hampshire, SO14 3ZH

ABSTRACT *Previous studies propose that submarine landslides and turbidity currents may become more likely due to future rapid global warming. Determining whether global warming increases likelihood assists in assessment of landslide-triggered tsunami hazards and risk to seafloor structures. Other studies propose that landslides helped to trigger past rapid climate change due to sudden release of gas hydrates. Two deep-water turbidite records show prolonged hiatuses in turbidity current activity during the Initial Eocene Thermal Maximum (IETM) at ~55 Ma. The IETM represents a possible analogue for future anthropogenically-induced climate change. It is likely that the records analysed here mainly represent large and fast moving disintegrative submarine landslides. Statistical analysis of long term (>2.3 Myr) records shows that turbidity current frequency significantly decreased after the IETM. These results indicate that rapid climate change does not necessarily cause increased turbidity current activity, and do not provide evidence for landslides as a primary trigger for the IETM.*

6.1 Introduction

A period of unusually rapid global warming occurred at ~55 Ma (McInerney and Wing, 2011), termed the Initial Eocene Thermal Maximum (IETM). This hyperthermal represents the warmest period on Earth during the Cenozoic (Schmitz et al., 2001), featuring, at its peak, a dramatic 6-8°C warming of global deep waters over a period of approximately 10 kyr (Kennett and Stott, 1991). The IETM is marked globally by a negative carbon isotopic ratio ($\delta^{13}\text{C}$) excursion, which has been linked to methane emissions due to dissociation of gas hydrate in marine sediment. Other causal mechanisms have been invoked (Dunkley-Jones et al., 2010), but emissions of methane from marine hydrates are one of the most widely held explanations for IETM (Dickens et al., 1995; Katz et al., 1999; 2001). The IETM has been used as an analogue for present-day anthropogenically-induced global warming (Agnini et al., 2007; Dunkley-Jones et al., 2010).

6.1.1 *Landslide and turbidity current recurrence frequency and climate change*

Understanding changes in the frequency of landslides and turbidity currents in response to the IETM may help predict future changes in landslide and turbidity current frequency as climate warms. It has been proposed that rapid global warming will lead to significant increases in landslide and turbidity current frequency, due to gas hydrate dissociation in response to elevated ocean temperatures (Maslin et al., 1998; Nisbet and Piper, 1998; Owen et al., 2007; Lee, 2009; Maslin et al., 2010). Dissociation of gas hydrate can weaken slopes and increase the probability of slope failure (Grozic, 2010).

In addition to climate change causing variations in landslide or turbidity current frequency, it has been proposed that submarine landslides play a role in driving rapid climate change (Kennett et al., 2003; Maslin et al., 2004; Bock et al., 2012). These studies suggest that dissociation of gas hydrate within, or below, the failed slide material, may lead to significant emissions of methane (Katz et al., 1999; Hornbach et al. 2007; Maslin et al., 2010). It was proposed that release of methane (a strong greenhouse gas) from gas hydrate within marine sediment, due to landslides or other processes, was the major control on atmospheric methane abundance (Kennett et al., 2003). The validity of this “clathrate gun hypothesis” is contentious. Methane emissions from wetlands may exceed those from gas hydrates hosted in marine sediments, as suggested by isotopic analysis of methane within ice core records (Sowers, 2006). Here it is considered whether the two study locations provide evidence that landslides may have helped to drive climate change through methane emissions. This has not previously been investigated using continuous turbidite records across well dated climatic excursions.

6.1.2 *Turbidites as a record of disintegrative landslides*

It is logistically difficult to accurately date a sufficient number of landslides ($N > 100$) around a basin margin for robust statistical analysis of recurrence intervals during the IETM. However, records of turbidity current frequency across the IETM contain distal landslide deposits. The large number ($N = 285$ to 421) of turbidites in the records analysed here enables statistical analysis of recurrence intervals. Turbidity currents can be triggered by a range of processes other than submarine landslides, however, such as storm waves and hyperpycnal river flood discharge (Normark and Piper, 1991; Piper and Normark, 2009; Talling et al., 2013). It is therefore important to assess

the level of certainty that these turbidites are landslide triggered. Turbidity currents with suspended sediment volumes far in excess of the largest river floods are likely to be triggered by submarine landslides (Talling et al., 2007a,b; 2014; Talling, 2014), although other triggers may cause flows that pick up sediment en-route. Individual turbidite beds cannot be mapped over large areas to determine volumes for either of the chosen study areas. Thus, it cannot be shown unequivocally that the turbidites are landslide triggered. It is probable that some landslides occurred, but failed to disintegrate to form long run-out turbidity currents that reached the study areas. Therefore not all landslides are likely to be recorded in the datasets.

However, both datasets are inferred to come from distal basin plain depositional sequences, featuring minimal erosion (Weaver and Thomson, 1993; Whitmarsh et al., 1998; Schmitz et al., 2001). It is thought that landslides trigger many of the turbidites seen in other basin plain sequences, where volumes can be constrained (Elmore et al., 1979; Pilkey, 1988; Talling et al., 2007a,b, 2012; Hunt et al., 2013; Clare et al., 2014; Chapter 5) or cables have been damaged by flows (Piper and Savoye, 1993; Piper et al., 1999). It is thus reasonable to infer that a predominant fraction of turbidites within the studied basin plain sequences were triggered by landslides.

6.1.3 *Geohazards and global sediment flux*

Due to their potential volume and speed, submarine landslides can generate destructive tsunamis that cause fatalities, or damage expensive seafloor structures (Tappin et al., 2001; Bondevik et al., 2005). The morphology and extent of a landslide will affect its hazard potential. Deep-seated, fast moving landslides may be more prone to tsunami-genesis and release of gas hydrate, whereas more widespread, thinner failures triggered by seismic shaking may have a reduced influence. Regardless of initial mechanics, if a disintegrative landslide triggers a turbidity current, it may pose a hazard to pipelines and seafloor cable networks (Piper et al., 1999; Bruschi et al., 2006; Carter et al., 2012) that carry over 95% of transoceanic data traffic including the internet and financial services (Carter et al., 2009). Turbidity currents that result from disintegration of submarine landslides, as well as from other triggers, may reach speeds of up to 19 m/s (Piper et al., 1999). Understanding the frequency of submarine landslides and turbidity currents, regardless of trigger, is therefore important for geohazard assessments.

An individual landslide may comprise up to thousands of cubic kilometres of sediment, two orders of magnitude greater than the largest terrestrial landslides (Hühnerbach and Masson, 2004; Haflidason et al., 2005; Korup, 2007; Masson et al., 2010). Turbidity currents have also been shown to transport hundreds of cubic kilometres of sediment for several hundreds of kilometres (Talling et al., 2012). Submarine landslides and turbidity currents are therefore major contributors to global sediment flux.

6.1.4 Previous work

Of the previous studies that have attempted to quantify turbidity current recurrence frequency (e.g. Droxler and Schlager, 1985; Weaver et al., 1992; Beattie and Dade, 1996; Goldfinger et al., 2003; Romans et al., 2009; Atwater and Griggs, 2012), only a handful consider large numbers of events ($N > 100$) over long (> 1 Myr) timescales (e.g. Weaver et al., 1986; Clare et al., 2014; Hunt et al., 2014). Submarine landslide frequency studies typically analyse fewer than ten events (e.g. Geist and Parsons, 2010). Exceptions exist with up to 68 dated events (e.g. Owen et al., 2007; Urlaub et al., 2013); however, these global databases only extend back in time to a maximum of 180 ka.

Despite this, many studies have drawn conclusions about the influence of variables such as sea level and global temperature variations on landslide recurrence rate (e.g. Owen et al., 2007; Brothers et al., 2013). Conversely, some studies have shown that non-random processes, such as sea level change, may not exert a dominant control on landslide (Geist and Parsons, 2010; Urlaub et al., 2013; 2014) and turbidite recurrence (Beattie and Dade, 1996; Hunt et al., 2013; Clare et al., 2014; Chapter 5). To make more meaningful, quantitative inferences on triggering and conditioning factors, there is a need for statistically robust ($N > 100$) datasets of landslide ages to be acquired in a variety of settings.

6.2 Aims

The first aim is to test whether rapid global ocean warming at the IETM (~ 55 Ma) coincides with an increase in turbidity current activity. This is to determine whether global warming may have promoted slope instability, or vice-versa through dissociation of gas hydrates. Deep-water turbidite records (Figure 6.1) are analysed here from the Zumaia coastal outcrop in NE Spain (2.3 Myr) and from ODP borehole records on the

Iberian Margin (5.5 Myr). Here it is assumed that these turbidity currents were mainly triggered by submarine landslides. The datasets contain sufficient bed quantities for statistical analysis (i.e. $N > 100$).

The second aim is to determine if recurrence intervals of turbidity currents were significantly different prior to, and after, the IETM interval over a window of ~ 1 Myr. This is to assess if the IETM exerted a longer-term influence on turbidity current activity. Here no assumption is made on the nature of turbidity current trigger.

The third aim is to determine whether the results obtained are consistent with previously published deep-water records across the IETM. The implications of this work are discussed for predicting future submarine landslide and turbidity current activity, and whether landslides may contribute to rapid climate change through gas hydrate dissociation and methane emissions.

6.3 Study areas

The datasets selected for this study satisfy four main criteria. Firstly, they represent a continuous sedimentary record including the IETM. Second, they feature sufficient ($N > 100$) turbidites for statistical analysis. Third, hemipelagic mud can be distinguished clearly from turbidite mud. This allows the cumulative thickness of hemipelagic mud to be measured, and used as a proxy for time between dated horizons in the stratigraphy. This method (Chapter 4; Clare et al., 2014) allows turbidite recurrence times to be estimated. Fourth, the sections have good age dating.

The first site is a coastal exposure at Itzurun Beach, Zumaia in NE Spain (Figure 6.1B). This is one of the most expanded and continuous sections through the IETM worldwide (Canudo and Molina, 1992; Canudo et al., 1995; Schmitz et al., 2001). A robust age and climate framework was developed from palaeoclimatic, palaeontologic, palaeoecologic and chronostratigraphic studies specifically for the Palaeocene and Eocene interval. During the IETM, Zumaia was part of a deep-water (> 1000 m) marine basin (Winkler and Gawenda, 1999) flanked by mixed carbonate-terrigenous shelf systems (Figure 6.1B), as verified by thinly interbedded, hemipelagic and distal calciclastic-siliciclastic turbidite deposits. The interval selected (54.0 to 56.3 Ma) at Zumaia avoids a faulted interval where stratigraphic repetition or omission may occur and terminates prior to a transition to a submarine fan setting, in which erosional bed

amalgamation is common (Cummings and Hodgson, 2011). A coarse resolution study of turbidite frequency has previously been performed at Zumaia (Winkler and Gawenda, 1999; Gawenda and Winkler, 2000); however, it did not specifically focus on the IETM, nor were individual recurrence intervals calculated.

The second record comes from Ocean Drilling Program (ODP) Site 1068 located on the western flank of a N-S trending basement high near the southern edge of the Iberian Abyssal Plain (Figure 6.1C; Whitmarsh et al., 1998). The setting during the IETM was that of a distal continental rise-abyssal plain transition dominated by hemipelagic muds with thin, interbedded turbidites (Whitmarsh et al., 1998). The studied interval of core in this chapter extends from 51.0-56.5 Ma.

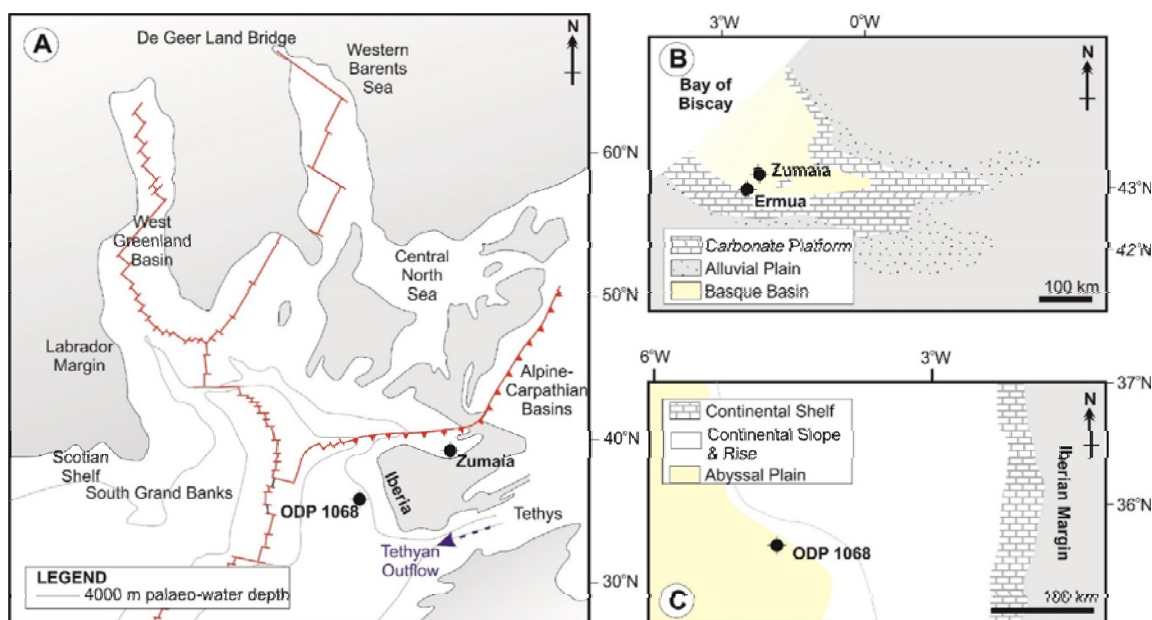


Figure 6.1: Palaeogeographic reconstructions at the end-Palaeocene to show: A) Relative location of sites (modified from Kaminski et al., 1989); B) Zumaia and surrounding region (modified from Schmitz et al., 2001); C) ODP Site 1068 (modified from Whitmarsh et al., 1998)

6.3.1 Regional tectonic setting

While the Palaeocene to early Eocene was relatively tectonically quiet at the study sites (Vergés et al., 1995; Rosenbaum et al., 2002), there is evidence of regional variation (Figure 6.2). The most pronounced intervals of deformation postdate the study intervals,

including mid to late Eocene (Masson et al., 1994) and Miocene compression (Pinheiro et al., 1996).

Africa and Europe began to converge at ~83 Ma, with movement of Iberia virtually ceasing from 67-55 Ma (Rosenbaum et al., 2002; Tugend et al., 2015). This period of quiescence crosses the IETM and the start of the study intervals.

Convergence resumed in Europe, when Iberia shifted to north-westward transpression at ~55 Ma (Gawenda et al., 1999). The resultant Pyrenean deformation was initially steady and continuous, causing minor compression landward of the Bay of Biscay (Jammes et al., 2009; 2010). The effect on deep-water sediment input was delayed, however, and only at ~53.5 Ma was a change seen from a calciclastic to siliciclastic turbidite system at Zumaia (Winkler and Gawenda, 1999). Variations in clay mineralogy at Zumaia are attributed to climatic variations and not to changing provenance or tectonic influence (Gawenda et al., 1999).

Initial stages of compression were felt at the northern Iberian border (Gräfe and Wiedmann, 1993) at ~55 Ma, progressing southward until ~46 Ma (Tugend et al., 2015). The Iberia Abyssal Plain site was distal from this tectonic centre during the study interval. The intensification of Iberia-Europe convergence did not occur until ~51 Ma (Roest and Srivastava, 1991; Rosenbaum et al., 2002), also postdating the study intervals.

6.3.2 *Palaeoceanographic setting*

Turbidites were generally sourced from a mixed carbonate shelf in the east at Zumaia (Gawenda, 1999). Turbidite sands were derived from proto-equivalents of major river catchments that currently drain to the Iberian shelf (Marsaglia et al., 1996); hence a similar setting to the present day.

Circulation was predominantly driven by deep-water formation in the Southern Ocean during the Palaeocene and Eocene (Miller et al., 1987; Katz and Miller, 1991; Pak and Miller, 1992; Bralower et al., 1997; Norris et al., 2001), except around the IETM, where it reduced significantly (Figure 6.2; Kaminski et al., 1996; Norris et al., 2001, and references therein). Tethyan outflow temporarily dominated circulation, (Kaminski et al., 1996; Norris et al., 2001), which was probably similar to modern Mediterranean outflow (Corfield and Norris, 1996). The east Tethys was a probable source of high evaporation

(Kaminski et al., 1996), which accelerated during intense warming at the IETM (Barron and Peterson, 1990). The short-term ocean circulation change intensified boundary currents in the west Atlantic, causing erosion at the Bermuda Rise between ~55.5 and 60 Ma (Norris et al., 2001). Lower Eocene hiatuses also exist in the North and South Atlantic at ~49 Ma (Tucholke, 1981; Aubry, 1995); however, these postdate the studied intervals (Figure 6.2).

Neither of the study sites, nor any other Iberian and Bay of Biscay Deep Sea Drilling Program sites, show evidence for major erosion during the studied intervals. These sites show continuous sediment accumulation, absence of unconformities or hiatuses in deposition, and all biozones/subzones are identified (Canudo and Molina, 1992; Pak and Miller, 1992; Whitmarsh et al., 1998; Pardo et al., 1997; Ladner and Wise, 2001; McGonigal and Wise, 2001; Urquhart, 2001; Tremolada and Bralower, 2004).

Late Palaeocene-early Eocene Tethyan outflow flowed northward around the Iberian margin (Kaminski et al., 1996). The northern Bay of Biscay showed the influence of Tethyan waters; however, the Zumaia site registered only an Atlantic source (Kaminski et al., 1996), indicating it was unaffected by bottom-currents.

Site 900, the shallowest continental slope site of Iberian ODP leg 149, sampled fine grained Palaeocene and Eocene contourites, but shows no evidence for erosion (Whitmarsh et al., 1998). The deeper water ODP sites locally show minor bottom-current influence but this is limited to slight winnowing of sandy turbidite tops (Whitmarsh et al., 1998); hemipelagic sediment accumulation rates are shown to be constant (Ladner and Wise, 2001; McGonigal and Wise, 2001).

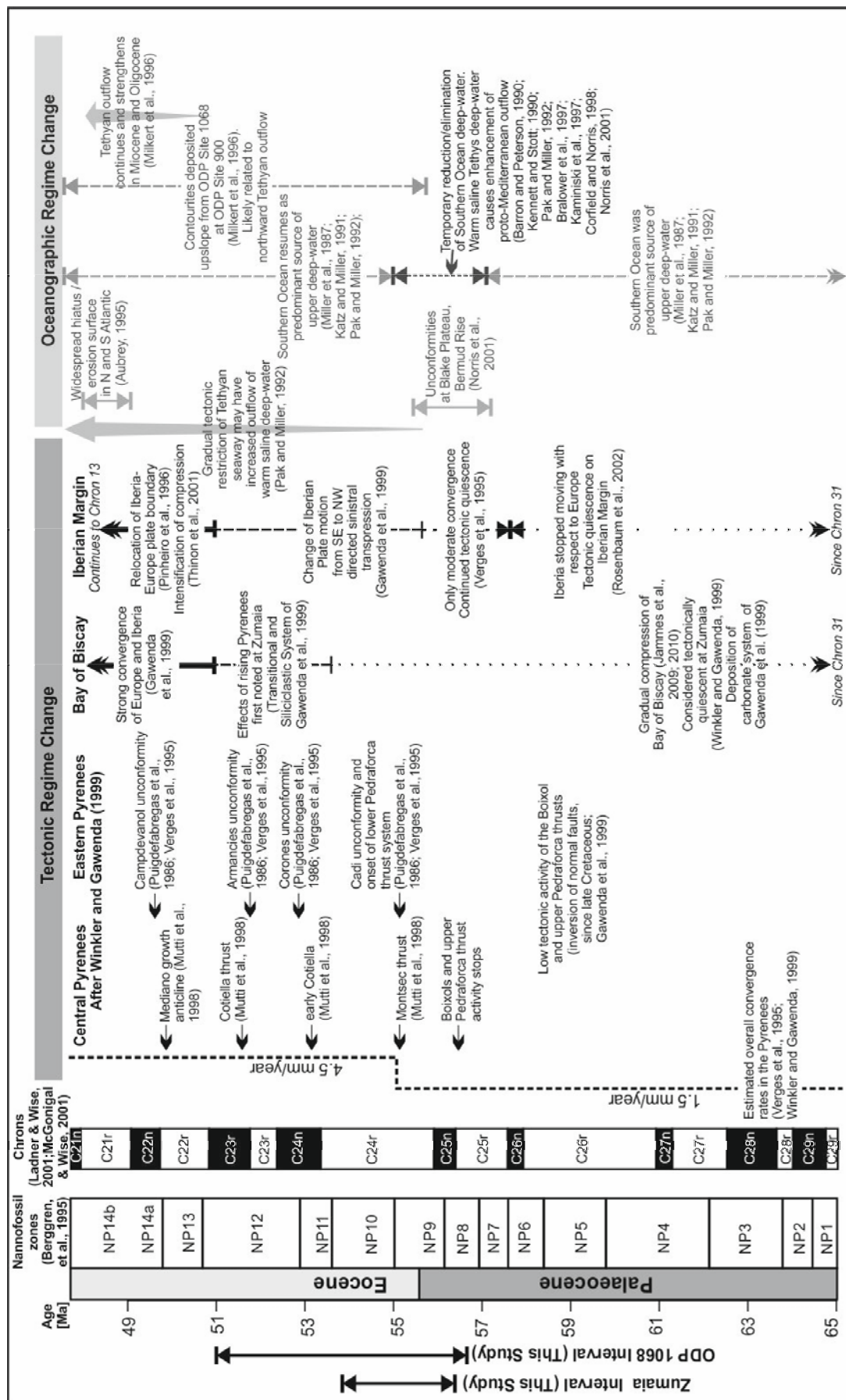


Figure 6.2: Summary of tectonic and palaeoceanographic variations with reference to the time intervals of this study. Pyrenean tectonic history adapted from Winkler and Gawenda (1999)

6.4 Methods

6.4.1 *Calculating recurrence intervals*

Hemipelagic mud was deposited progressively in the time periods between turbidity currents. The thicknesses of hemipelagic mud intervals were converted to time periods by dividing by the rate of hemipelagic mud accumulation (Chapter 4; Clare et al., 2014). Average hemipelagic mud accumulation rates were calculated using cumulative hemipelagic thickness between dated horizons. To do this, one must be able to identify hemipelagic mud intervals, and measure their thicknesses. The method assumes minimal fluctuations in hemipelagic mud accumulation rate between adjacent dated horizons. Locations with better age control are therefore favoured. It is also assumed there is little or no erosion of hemipelagic mud beneath turbidites. This assumption is based on the small depth of erosion seen in the available outcrop or core.

Hemipelagic mud intervals at Zumaia have thickness variations of <5 mm over distances of 50 m (extent of beach exposure) and trace fossils are not truncated (Bernaola et al., 2007). Turbidites logged from ODP site 1068 have flat bases and lack irregular bases indicative of erosion. The core is ~10cm in diameter. Erosional features with longer length scales would not be identified (Weaver and Thomson, 1993).

6.4.2 *Identification of hemipelagic mud*

Deposits logged visually by the authors have a vertical resolution of 5 mm. Hemipelagic mud can be clearly resolved from turbidite mud on the basis of colour and textural differences (Winkler and Gawenda, 1999; Bernaola et al., 2007; Figure 6.3 and Figure 6.4). Turbidite thicknesses at Zumaia range from <5 to 170 mm over the studied interval, with a mean thickness of 16 mm. Turbidites in ODP 1068 range from 5 to 675 mm in thickness, with a mean thickness of 40 mm. The present day location of ODP Site 1068 is near the southern edge of the Iberia Abyssal Plain in 5044 m water depth, and its physiography is not interpreted to have changed much since the late Palaeocene (Whitmarsh et al., 1998). Both sites are interpreted as distal basin plain settings in accordance with the criteria of Mutti (1977). Bedding surfaces are even and parallel, turbidites are thin, typically base-missing Bouma sequences, grain size is limited to fine sand, with low to very low angle ripples often occurring in well-developed climbing

patterns. Additionally, the considerable stratigraphic thickness of the sequences, trace fossils (Whitmarsh et al., 1998; Cummings and Hodgson, 2011) and benthic foraminiferal assemblages (Whitmarsh et al., 1998; Baceta et al., 2000) indicate a deep-water basin setting.

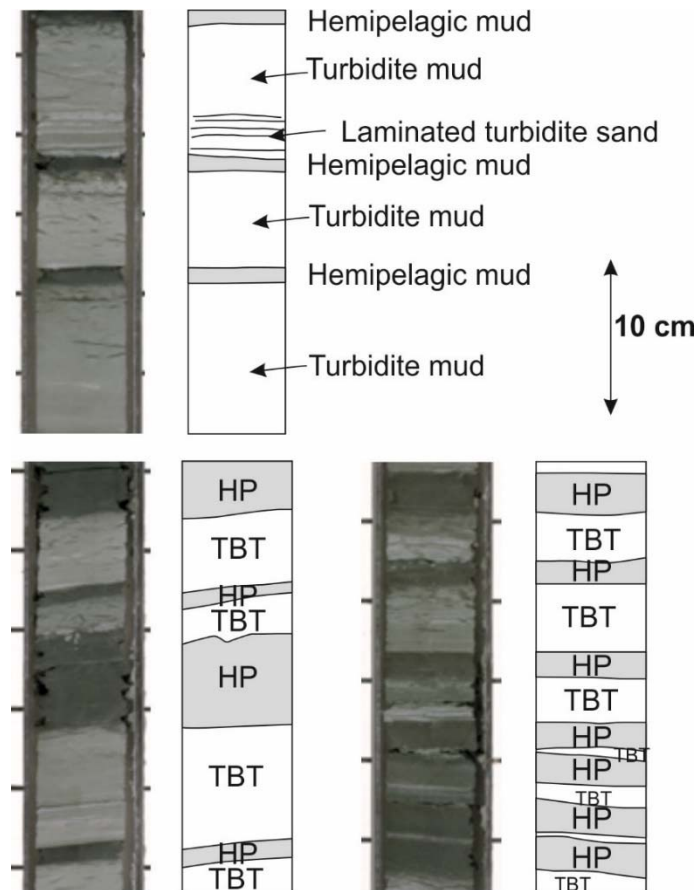


Figure 6.3: Identification of hemipelagic mud from turbidite mudcap from ODP 1068 borehole samples. HP refers to hemipelagic mud, TBT is turbidite.

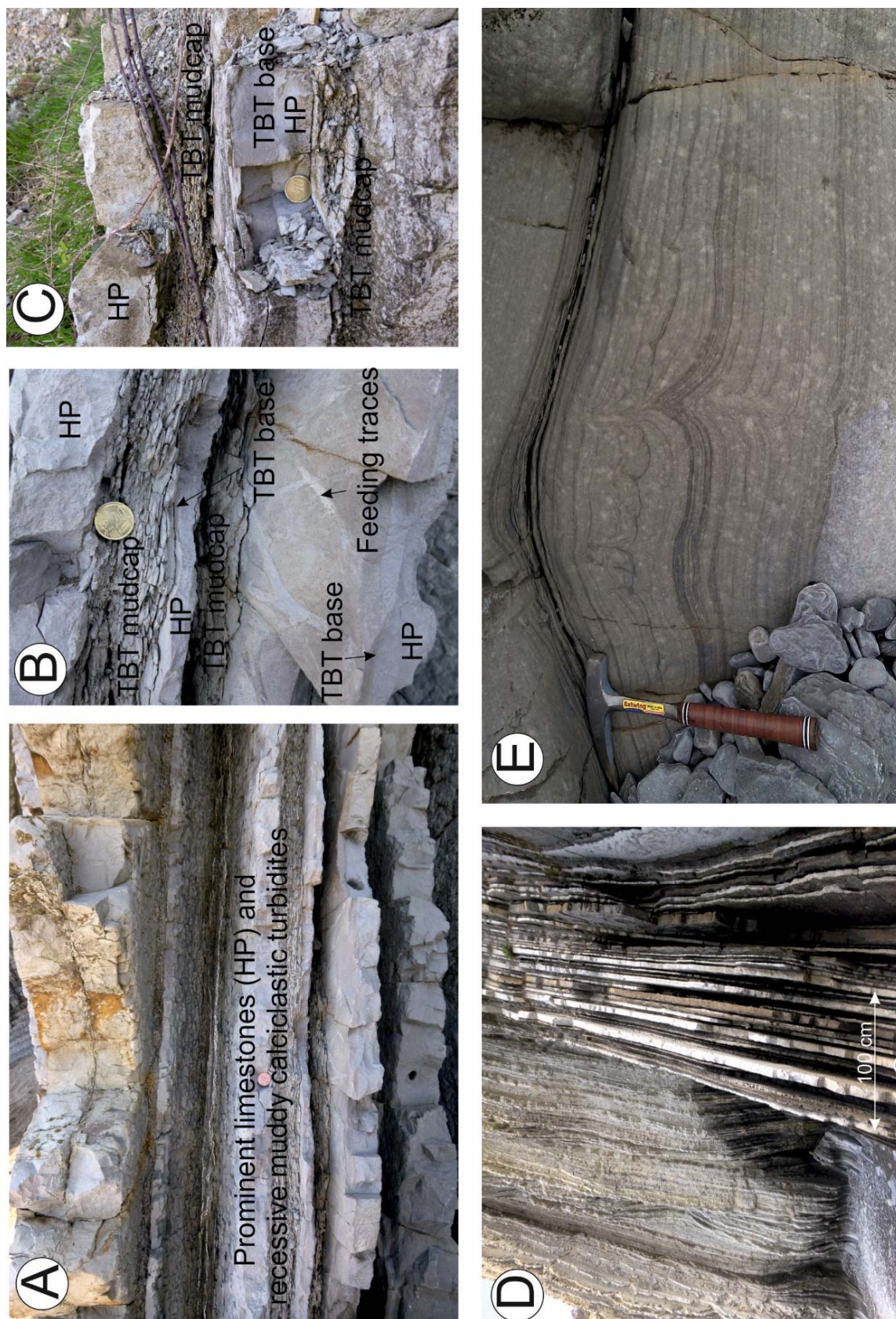


Figure 6.4: Identification of hemipelagic (HP) mud from turbidite (TBT) mudcap deposits (A-C), example photo of interbedded sequence (D), example of sand-rich mid-Eocene fan deposits that are excluded from this study (E)

6.4.3 *Age framework*

Age control for the Zumaia section is based on biostratigraphy (Schmitz et al., 1997; Baceta et al., 2000; Alegret et al., 2009) and magnetostratigraphy (Baceta et al., 2000; Dinares-Turell et al., 2002; Storme et al., 2012). Dated horizons occur every 0.01 to 0.72 Myr within the Zumaia section and the interval containing the IETM is particularly well dated. This includes dates for subdivisions of the IETM, including onset, core (most intense), recovery and end phases of the Carbon Isotopic Excursion (CIE). This age control provides confidence in deriving hemipelagic accumulation rates and therefore recurrence intervals, particularly during and adjacent to the IETM. The rates of hemipelagic mud accumulation that is calculated show good correlation with those in previous studies (Winkler and Gawenda, 1999; Schmitz et al., 2001; Figure 6.5).

Age control for Iberia ODP Site 1068 is provided by biostratigraphy (Whitmarsh et al., 1996; Ladner and Wise, 2001; McGonigal and Wise, 2001). Dated horizons occur every 0.7 to 1.0 Myr; hence dating is not as precise as at Zumaia, however, dates are available either side of the IETM to ensure confidence in its identification. Based on these dates and the vertical resolution, the minimum resolvable interval is 1.9 kyr at ODP Site 1068, compared to 0.5 kyr at Zumaia.

Table 6.1: Summary of study area locations, turbidite records and diagnostic criteria for hemipelagic mud identification

| | Itzurun Beach, Zumaia, NE Spain | ODP Site 1068, Iberian Margin |
|---|---|---|
| Coordinates (Lat, Long) | 43.3000, -2.2600 | 40.7520, -11.6190 |
| Depositional Environment | Deepwater basin plain | Continental rise-abyssal plain transition |
| Time Interval Studied | 54.0 to 56.3 Ma | 51.0 to 56.5 Ma |
| Number of Turbidites [N] | 285 | 421 |
| Diagnostic Criteria for Hemiplegic Mud Identification | Lighter colour, prominent less weathered limestone, foraminifer-rich, massive, non-laminated (Gawenda et al., 1999) | Foraminifer-rich (core surface appears pitted), darker colour, massive, non-laminated |
| Minimum Resolvable Thickness | 5 mm | 5 mm |
| Minimum Sediment Accumulation Rate | 10 mm/kyr | 2.6 mm/kyr |
| Minimum Resolvable Interval | 0.5 kyr | 1.9 kyr |

Note: Sedimentation rates, and hence the time series, are assumed to be stationary in intervals between available dated horizons

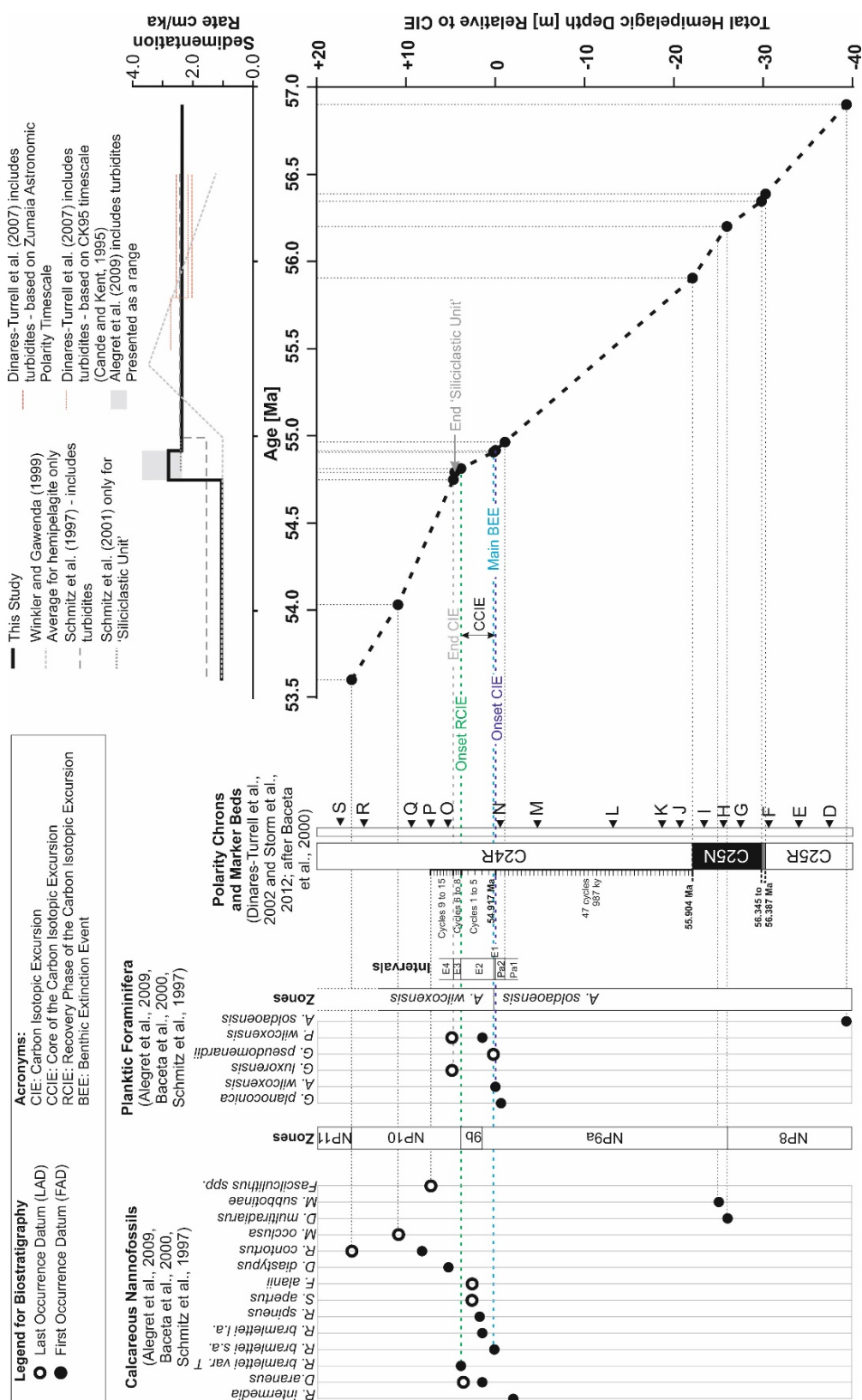


Figure 6.5: Available age control for the studied interval at Zumaia presented in relation to total hemipelagic depth after Schmitz et al. (1997), Winkler and Gawenda (1999), Baceta et al. (2000), Schmitz et al. (2001), Dinares-Turrell et al. (2002 & 2007), Alegret et al. (2009) and Storme et al. (2012). The hemipelagic sedimentation rates derived for this study are compared to averaged rates for previous studies which show a good level of agreement.

6.4.4 Carbon isotopic records

Negative $\delta^{13}\text{C}$ excursions are important because it has been proposed that they may relate to release of methane from gas hydrate in seafloor sediment, including via submarine landslides (Kennett et al., 2003; Maslin et al., 2004, 2010). Outcrop-specific $\delta^{13}\text{C}$ records based on whole-rock records are available for Zumaia (Gawenda et al., 1999; Schmitz et al., 2001). A direct comparison between turbidite frequency and the CIE can thus be made.

6.4.5 Comparison with sea level curve

Contrasting views of global sea level during the IETM exist (Sluijs et al., 2008). A sea level lowstand is inferred based on records from the North Atlantic (Neal and Hardenbol, 1998) and elsewhere (Schmitz et al., 2003), whereas Speijer and Morsi (2002) indicate a highstand in North Africa. Given these uncertainties, turbidite recurrence intervals are not specifically compared with sea level curves across the IETM.

6.5 Results

6.5.1 Turbidite switch off during IETM

Turbidite recurrence intervals are broadly similar for most of the duration of two records studied here. The frequency distribution of turbidite recurrence intervals in the Zumaia section shows a good fit ($r^2=0.99$ based on least squares fit) to an exponential (Poisson) distribution (Figure 6.6C). Some scatter is expected in the tail of exceedence plots due to limited data; however, five points lie well above the trend for a true Poisson distribution at Zumaia. Four of these relate to relatively long (25.1-35.2 kyr) recurrence intervals after the IETM, and one occurs during the IETM. The frequency distribution of turbidite recurrence intervals at the Iberian ODP Site 1068 location conform more closely to a log-normal distribution (Figure 6.6B; $r^2=0.99$).

Running values of mean and standard deviation for recurrence intervals generally show variations of <10%, over a moving window of 50 beds (Figure 6.8). However, a single anomalously long turbidite recurrence interval (Figure 6.6D) occurs in both Zumaia (54.854-54.699 Ma) and ODP 1068 (55.2-54.595 Ma) datasets. The 155 kyr turbidite recurrence interval at Zumaia is far longer than the average recurrence interval

of 7 kyr. Turbidites occur on average every 13 kyr in the ODP Site 1068 record, with an anomalous recurrence interval of 605 kyr. Interestingly, both anomalously long turbidite recurrence intervals coincide with the IETM. This perturbation in recurrence is also observed in the running median values, albeit to a slightly less pronounced degree (Figure 6.8),

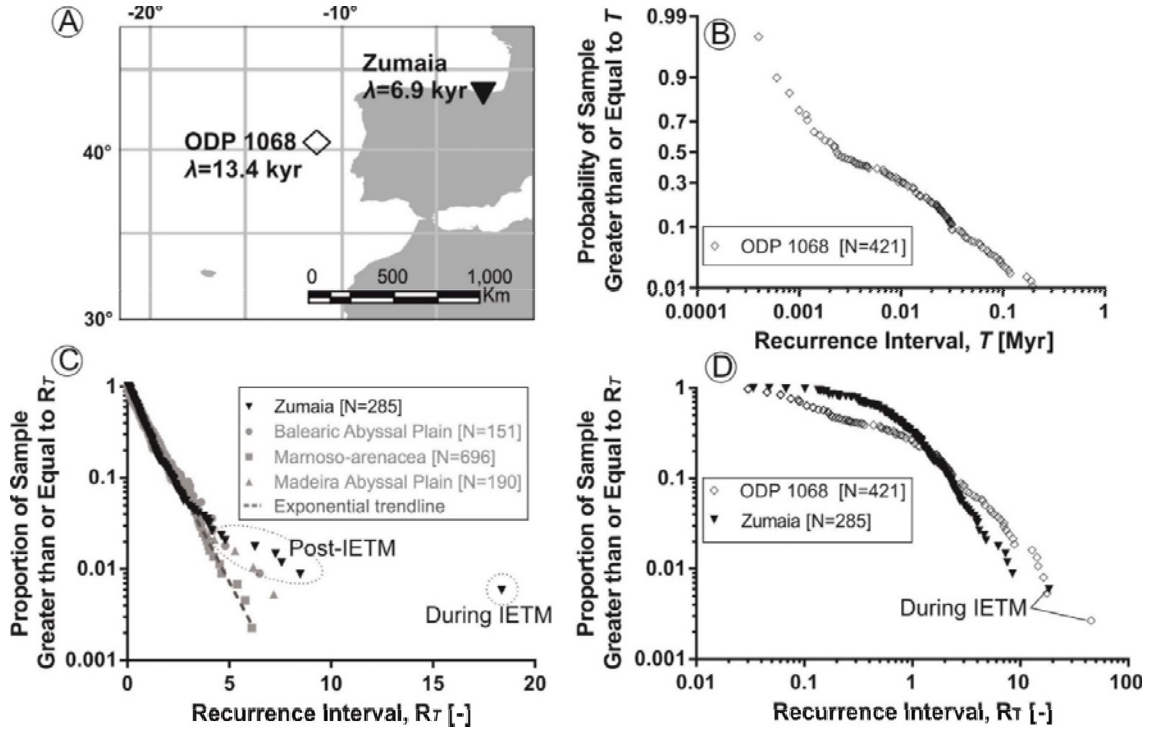


Figure 6.6: A) Location of study areas annotated with mean turbidite recurrence interval, λ . B) Log-probability exceedence plot for ODP 1068 turbidite recurrence intervals showing a close approximation to a log-normal (straight line) trend. C) Comparison of recurrence intervals on log-linear axes for Zumaia and sites in Clare et al. (2014) – data are normalised to mean recurrence interval, λ and generally show good agreement with an exponential (straight line) trend, except for data during IETM and some points following the IETM. D) Comparison of Zumaia and ODP 1068 datasets on log-log axes showing outlying hiatuses found during the IETM.

6.5.2 Modelling of uncertainty in recurrence intervals

The precision of derived recurrence intervals can be affected by several variables. Erosion by successive turbidity currents, differential compaction and dewatering, and short-term decreases in background sedimentation rate may result in thinner hemipelagic beds. In contrast, short term increases in background sedimentation will yield thicker hemipelagic beds. Uncertainty in absolute dating of intervals may also arise from biostratigraphic and magnetostratigraphic data, which can lead to over- or under-estimation of recurrence intervals. To address these uncertainties, variations in accumulation rate are modelled based on the measured data for each site to account for

random variations of $\pm 30\%$ (Clare et al., 2014). The overall trends are well recreated, thus providing support for use of the data (Figure 6.7). For ODP site 1068, there is some deviation from a straight line trend on a log-probability plot for intervals <0.001 Myr; however, these intervals are well below the resolution of the data and should not be considered valid (Figure 6.7).

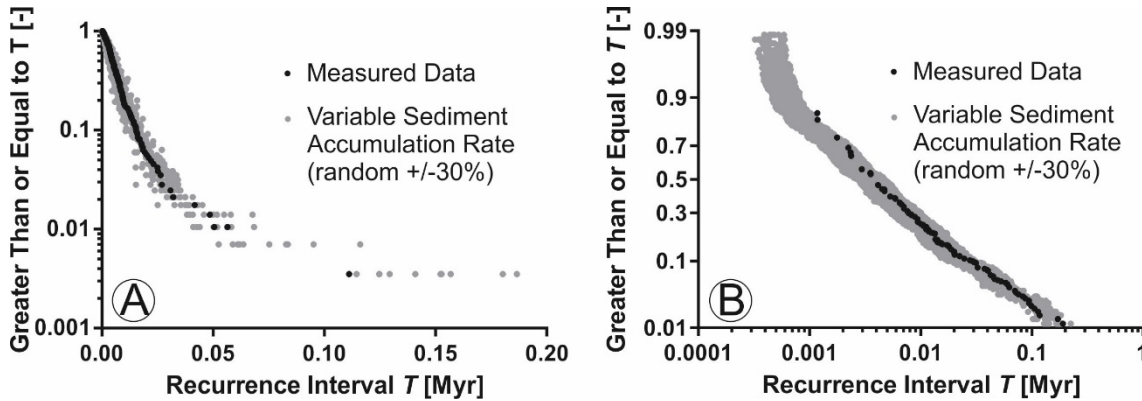


Figure 6.7: Modelling of random variations (grey) in sediment accumulation rate between $\pm 30\%$ for Zumaia (A) and ODP site 1068 (B) compared with measured data (black) analysed in this study. Note that the general trends are well recreated providing confidence in the use of these data. This modelling accounts for short-term variations in hemipelagic sedimentation rates, as well as differential compaction, localised erosion, and uncertainties in age control of $\pm 30\%$.

6.5.3 *Is the switch off genuine?*

At both sites, the IETM interval is characterised by an approximately two to four-fold increase in background (hemipelagic) sediment accumulation rates, as noted by Winkler and Gawenda (1999) and Schmitz et al. (2001). Unlike the rest of the sequence which features hemipelagic marls and limestones, the non-turbidite deposits during the IETM comprise calcite-depleted clay – referred to as the ‘siliciclastic unit’ (Orue-Etxebarria et al., 1996; Schmitz et al., 1997; Schmitz et al., 2001). The paucity of calcite is attributed to dissolution in response to global ocean warming (Zachos et al., 2005). As both sites have age control points bounding the IETM, background hemipelagic accumulation rates can be determined for the ‘siliciclastic unit’. At Zumaia, for example, hemipelagic accumulation rate increases from $\sim 1\text{cm/kyr}$ to 3cm/kyr at the start of the IETM (i.e. deposition was three times faster during the IETM). This is corrected for using the age model and ensures that recurrence intervals are not overestimated based solely on bed thickness. Were just hemipelagic mud thickness to be used, the anomalous interval during the IETM would be >450 kyr; however the corrected value (which accounts for the increase in accumulation rates) is 155 kyr. It is accepted that there is likely to be some

uncertainty in continuity of sediment accumulation rates between dated horizons; however, the anomalous interval is more than an order of magnitude greater than the mean trend. This is a significantly different result. Therefore it is suggested that the prolonged hiatuses in turbidity current activity at both sites are genuine.

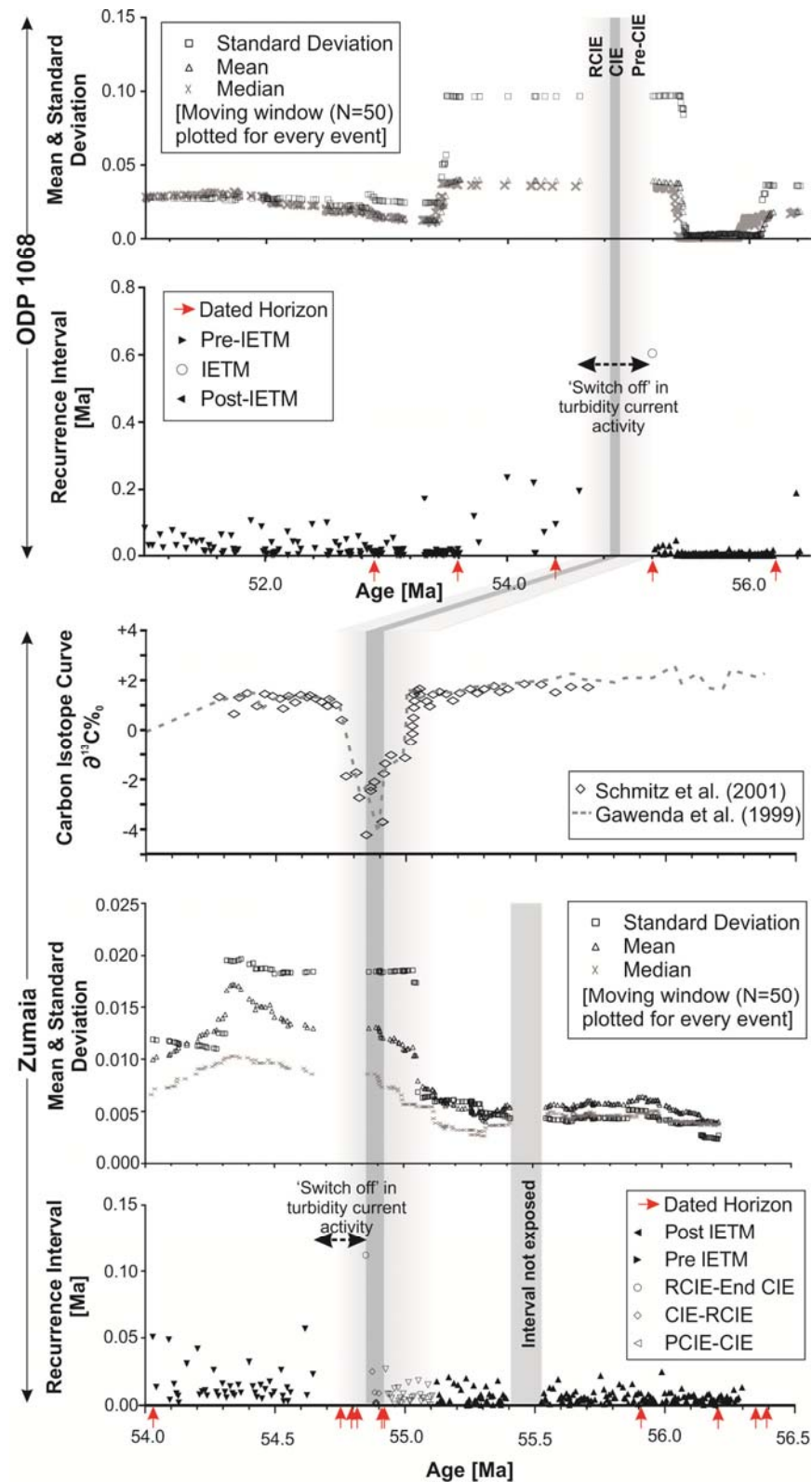


Figure 6.8: Turbidite recurrence time series for Zumaia and ODP 1068 sites. Values of running mean and standard deviation for windows of 50 beds are highly skewed by anomalous hiatuses during with the IETM. Note change in age scale between sites. CIE = Carbon Isotopic Excursion; RCIE = Recovery Phase; PCIE = Pre-CIE.

6.5.4 *Post-IETM reduction in turbidite frequency*

Now variation in recurrence intervals are considered, before, during and after the CIE at the IETM. A non-parametric approach is used as the distribution is non-Gaussian. Unpaired Mann-Whitney and Kolmogorov-Smirnov tests are performed for recurrence intervals classified into different time periods. P values <0.05 indicate that the populations are significantly distinct and that random sampling could not account for this difference. Recurrence intervals are compared from periods relating to the entire dataset, before the IETM (56.311 to 55.127 Ma), pre-CIE to CIE (55.127 to 54.917 Ma), CIE to recovery phase (54.917 to 54.854 Ma) and the interval post-IETM (54.749 to 54.482 Ma) for Zumaia. Interval dates are provided by the high resolution age and biostratigraphic framework of various authors (Section 3). Unlike ODP site1068, turbidites are identified during periods of the IETM at Zumaia; hence a higher resolution study is possible across the IETM interval. Only pre-IETM (56.390 to 55.127 Ma) and post-IETM (54.749 to 53.749 Ma) intervals are compared for the ODP 1068 site, where windows of one million years either side are selected for comparison (Figure 6.9; Table 6.2, Table 6.3). The analysis shows that:

- i) Mean and median recurrence intervals of the post-IETM window are significantly different ($p < 0.0001-0.007$) to all the other time windows. For Zumaia, the mean recurrence interval prior to the IETM is 5 kyr, but increases after the IETM to 15.3 kyr. The mean recurrence is 7 kyr before the IETM at ODP Site 1068, and increases to 28 kyr for the 1 million year period after the IETM.
- ii) At both sites, mean and median recurrence intervals before and during the $\delta^{13}\text{C}$ excursion are significantly different ($p < 0.01$) to recurrence after the IETM.

Table 6.2: Results of non-parametric unpaired Mann-Whitney and Kolmogorov-Smirnov tests for Zumaia Series considering time windows prior to the IETM (56.311 to 55.127 Ma), pre-CIE to CIE (55.127 to 54.917 Ma), CIE to recovery phase (54.917 to 54.854 Ma) and the interval post-IETM (54.749 to 54.482 Ma). Italicised p values are statistically significant.

| | Results | All Zumaia Data | Pre-IETM | PCIE-CIE | CIE-RCIE | Post-IETM | |
|-----------------|--------------|----------------------------|------------------------|-------------------------|-------------------------|-----------------------|------------------------|
| All Zumaia Data | Mann-Whitney | p value | - | <i>0.0111</i> | 0.2351 | 0.427 | < 0.0001 |
| | | U | - | 25505 | 3326 | 952.5 | 2825 |
| | | Difference of medians | - | 0.0006965 | -0.001062 | 0.002477 | -0.005359 |
| | | Difference: Hodges-Lehmann | - | 0.000854 | -0.001062 | 0.001107 | -0.005716 |
| | | 95% CI | - | ~0.000179 to 0.001438 | -0.002695 to 0.000673 | -0.001813 to 0.004098 | -0.007312 to -0.003979 |
| | K-S | p value | - | 0.0713 | 0.2503 | 0.1936 | <0.0001 |
| | | K-S D | - | 0.118 | 0.2051 | 0.3872 | 0.4948 |
| Pre-IETM | Mann-Whitney | p value | <i>0.0111</i> | - | <i>0.0142</i> | 0.7392 | <0.0001 |
| | | U | 25505 | - | 1978 | 765.5 | 1426 |
| | | Difference of medians | 0.0006965 | - | -0.001797 | 0.00178 | 0.006504 |
| | | Difference: Hodges-Lehmann | 0.000854 | - | -0.001841 | 0.000478 | 0.006504 |
| | | 95% CI | ~0.000179 to 0.001438 | - | -0.003593 to -0.0004490 | -0.003683 to 0.002768 | 0.05024 to 0.0083 |
| | K-S | p value | 0.0713 | - | <i>0.0142</i> | ~0.3237 | <0.0001 |
| | | K-S D | 0.118 | - | 0.322 | 0.3434 | 0.6128 |
| PCIE-CIE | Mann-Whitney | p value | 0.2351 | <i>0.0142</i> | - | 0.317 | <i>0.0007</i> |
| | | U | 3326 | 1978 | - | 82 | 314 |
| | | Difference of medians | -0.001062 | -0.001797 | - | -0.003577 | 0.004258 |
| | | Difference: Hodges-Lehmann | -0.001062 | -0.001841 | - | -0.002301 | 0.004707 |
| | | 95% CI | -0.002695 to 0.000673 | -0.003593 to -0.0004490 | - | -0.005823 to 0.002506 | 0.001904 to 0.007791 |
| | K-S | p value | 0.2503 | ~0.0142 | - | ~0.1208 | <i>0.0034</i> |
| | | K-S D | 0.2051 | 0.322 | - | 0.4769 | 0.4369 |
| CIE-RCIE | Mann-Whitney | p value | 0.427 | 0.7392 | 0.317 | - | <i>0.0073</i> |
| | | U | 952.5 | 765.5 | 82 | - | 73 |
| | | Difference of medians | 0.002477 | 0.00178 | -0.003577 | - | 0.007835 |
| | | Difference: Hodges-Lehmann | 0.001107 | 0.000478 | -0.002301 | - | 0.006553 |
| | | 95% CI | -0.001813 to 0.004098 | -0.003683 to 0.002768 | -0.005823 to 0.002506 | - | 0.001737 to 0.01284 |
| | K-S | p value | 0.1936 | 0.3237 | ~0.1208 | - | ~0.0147 |
| | | K-S D | 0.3872 | 0.3434 | 0.4769 | - | 0.6023 |
| Post-IETM | Mann-Whitney | p value | < 0.0001 | <0.0001 | <i>0.0007</i> | <i>0.0073</i> | - |
| | | U | 2825 | 1426 | 314 | 73 | - |
| | | Difference of medians | -0.005359 | 0.006504 | 0.004258 | 0.007835 | - |
| | | Difference: Hodges-Lehmann | -0.005716 | 0.006504 | 0.004707 | 0.006553 | - |
| | | 95% CI | -0.007312 to -0.003979 | 0.05024 to 0.0083 | 0.001904 to 0.007791 | 0.001737 to 0.01284 | - |
| | K-S | p value | <0.0001 | <0.0001 | <i>0.0034</i> | <i>0.0147</i> | - |
| | | K-S D | 0.4948 | 0.6128 | 0.4369 | 0.6023 | - |

Table 6.3: Results of non-parametric unpaired Mann-Whitney and Kolmogorov-Smirnov tests for ODP Site 1068 considering time windows before (56.390 to 55.127 Ma) and after the IETM (54.749 to 53.749 Ma). Italicised p values are statistically significant.

| | Results | All Data | Pre-IETM | Post-IETM |
|-----------|-------------------|----------------------------|------------------------|------------------|
| All Data | Mann-Whitney Test | p value | - | 0.1936 |
| | | U | - | 39289 |
| | | Difference of medians | - | 0.0 |
| | | Difference: Hodges-Lehmann | - | 0.0 |
| | | 95% CI | - | 0.0 to 0.0005906 |
| | K-S Test | p value | - | 0.7526 |
| | | K-S D | - | 0.05615 |
| Pre-IETM | Mann-Whitney Test | p value | 0.1936 | - |
| | | U | 39289 | - |
| | | Difference of medians | 0.0 | - |
| | | Difference: Hodges-Lehmann | 0.0 | - |
| | | 95% CI | 0.0 to 0.0005906 | - |
| | K-S Test | p value | 0.7526 | - |
| | | K-S D | 0.05615 | - |
| Post-IETM | Mann-Whitney Test | p value | <0.0001 | - |
| | | U | 2945 | - |
| | | Difference of medians | -0.006257 | - |
| | | Difference: Hodges-Lehmann | -0.004698 | - |
| | | 95% CI | -0.007252 to -0.002919 | - |
| | K-S Test | p value | <0.0001 | - |
| | | K-S D | 0.4242 | - |

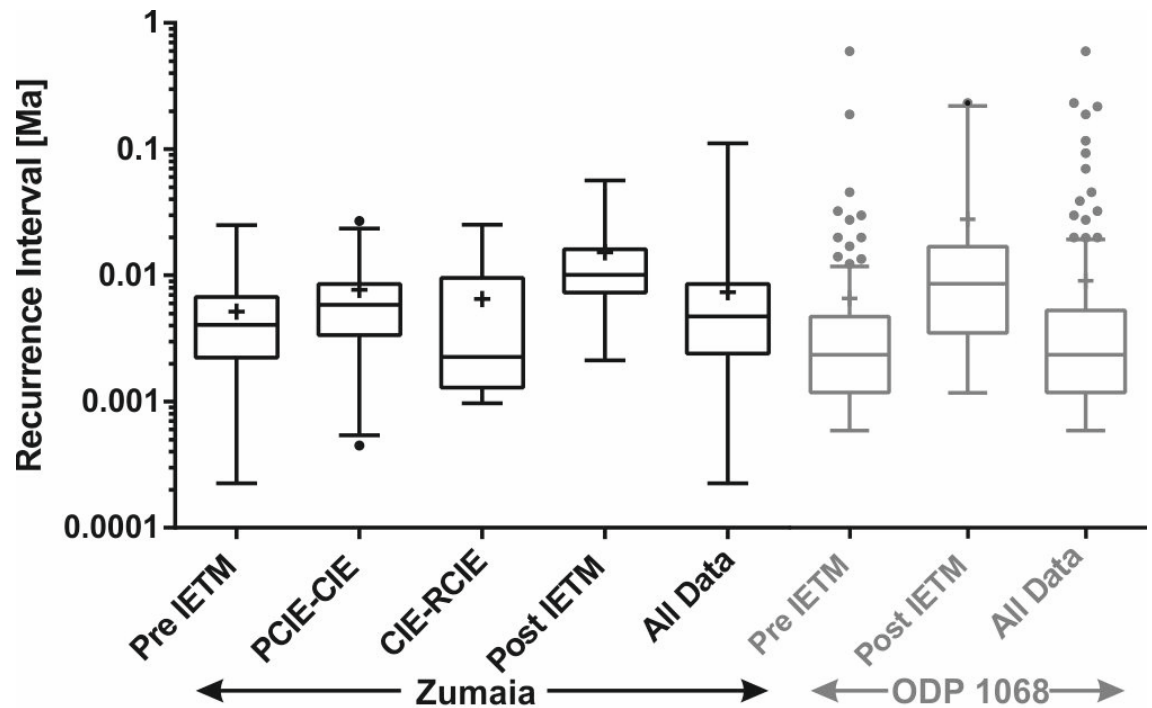


Figure 6.9: Box and whisker plots of turbidite recurrence expressed for different time windows relative to the IETM. Boxes show 25% and 75% intervals, crosses indicate arithmetic mean values, whiskers show 5% and 95% intervals, and points represent values that fall outside 5% and 95% intervals. Post-IETM recurrence intervals are significantly longer than those Pre-IETM for both datasets.

6.6 Discussion

In the following section, the overall frequency distribution of turbidite recurrence is first discussed at both sites and compared with results from other basin plains. Then the anomalous switch off in turbidity current activity identified during the IETM, and the reduction in activity following the IETM are addressed. The findings are compared with published records from other IETM sites worldwide and explain the relevance for geohazard assessment. Finally, wider implications for climate change are discussed in relation to submarine landslide activity.

6.6.1 Long term controls on turbidite recurrence

Turbidite recurrence intervals for the full record at Zumaia show a good agreement with an exponential (or Poisson) distribution for recurrence intervals < 25 kyr. A common frequency distribution is observed in three deep-water basin plain settings worldwide (Figure 6.6C; Chapter 5; Clare et al., 2014). A Poisson distribution indicates time-independent, memoryless behaviour (Parzen, 1962); hence, it is unlikely that non-random processes such as sea level change exerted a dominant control on turbidite

recurrence for most of the interval at Zumaia. However, recurrence intervals >25 kyr deviate significantly from the Poissonian background trend. These outliers either occur immediately after the IETM or during the IETM in the case of the longest recurrence interval. Effects of rapid climatic change during the IETM at Zumaia may therefore have reduced the likelihood of turbidity current activity – both immediately before and during the IETM.

In contrast with Zumaia, an approximately log-normal distribution is identified for turbidite recurrence intervals at the ODP Site 1068. In the same manner that the *sum* of independent variables may yield a normal distribution, the *product* of several independent processes may create a log-normal distribution (Van Rooij et al., 2013). This may result where a sequential series of processes controls turbidity current activity (Figure 6.10). A simple example of multiplicative effects is shown as Equation 6.1, where P is probability, LS denotes landslide and TC denotes turbidity current.

$$P(\text{TC at ODP 1068 site}) = P(\text{trigger generates LS}) \times P(\text{LS disintegrates to TC}) \times P(\text{TC runs out to site})$$

(Equation 6.1)

A Poisson distribution is generated by additive independent effects, such as a time-independent trigger, superimposition of multiple triggering processes, or several regional input sources. A hypothetical Poissonian additive probability for turbidite deposition at Zumaia, is shown in Equation 6.2. A, B and C represent different source areas around the same basin margin.

$$P(\text{TC at Zumaia}) = P(\text{LS-triggered TC from A}) + P(\text{LS-triggered TC from B}) + P(\text{hyperpycnal-triggered TC from C})$$

(Equation 6.2)

During the IETM, Zumaia was located ~30 km from the shelf break in a semi-enclosed basin setting (Schmitz et al., 2001) that may have featured sediment input from the north, south and west. ODP Site 1068 was located more distally (~200 km) from the shelf break, in an open setting, with a lower number of possible input sources. Therefore, the difference in frequency distribution form may be a function of basin morphology, nature and distance of input pathways, and the number of input sources. Regardless of frequency distribution form, however, both sites show an anomalous hiatus in turbidity current activity during the IETM (Figure 6.6), which is now the main focus of discussion.

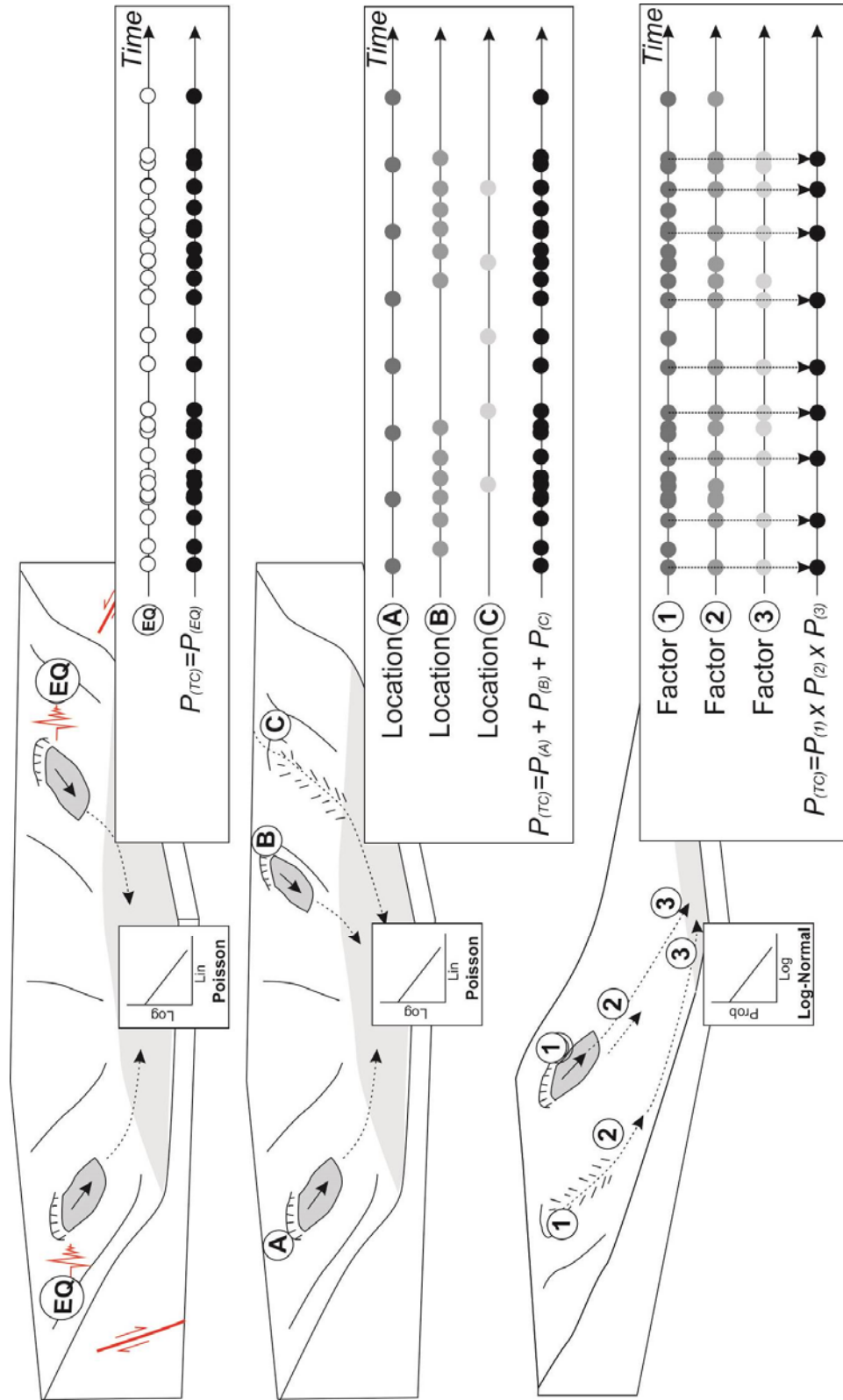


Figure 6.10: Scenarios that generate different frequency distributions. Above: Poisson distribution assuming time-independent, memoryless earthquake (EQ) trigger is responsible for each basin turbidite. Middle: Poisson distribution resulting from the sum of regional inputs to the basin which may include landslides on different margin flanks (A and B) and turbidity currents triggered by other processes (C) e.g. river floods. Below: Log-normal distribution in a more distal, open setting resulting from the product of probabilities. Basin turbidite frequency is the probabilistic product of

landslides (1), disintegrating to become turbidity currents (2), which travel the distance to the basin plain (3).

6.6.2 *IETM-related control on turbidity current recurrence intervals*

The frequency of turbidity current activity is reduced significantly at the IETM. This includes a cessation of turbidity currents during the rapid warming phase, and a decrease in recurrence intensity immediately following the IETM (Figure 6.8). The relevance to geohazard assessment and future climate changes studies is now explored.

Reduced landslide frequency during the IETM

It is hypothesised here that dramatic climatic effects during the IETM can explain the anomalous hiatuses and modifications in longer term recurrence trends. As the IETM features a major hiatus in activity, one can confidently state that no landslide-triggered turbidity currents (as well as those triggered by other processes) reached either site during that time. To account for uncertainty in whether turbidites are all landslide-triggered, one must be circumspect about stating that changes in mean recurrence intervals are solely due to changes in landslide intensity. They may also relate to turbidity currents triggered by river flood discharge, canyon-flushing events or other processes. However, it is likely that a large proportion of the turbidites at these two sites was contributed by landslides. It is therefore suggested that landslide activity decreased during the IETM at the two sites in this study, rather than increasing as predicted by previous studies (Kennett et al., 2003; Maslin et al., 2010).

Did flows route elsewhere during IETM?

The prolonged hiatuses observed at both Zumaia and ODP Site 1068 during the IETM are interpreted as a temporary “switch off” in turbidity current activity. Could it be that flows occurred, but simply did not reach these sites during this time, or else they were routed elsewhere? There is limited up-dip information that can be used to answer such questions unequivocally. A base of slope apron sequence is located 7 km to the SW of Zumaia at Ermua. Abundant turbidites and infrequent slump deposits complicate direct stratigraphic ties between Zumaia and Ermua. However, Schmitz et al. (2001) developed a high-resolution biostratigraphic and isotopic correlation across the IETM for these locations. Interpretation of stratigraphic logs (Schmitz et al., 2001) indicates a significant

(greater than ten-fold) reduction in turbidity current activity at Ermua, coincident with the peak-CIE at the IETM (Figure 6.11). Turbidites emplaced during the IETM interval at Ermua are also considerably (<30%) thinner. Mean turbidite recurrence rate at Ermua is significantly less than at Zumaia, suggesting that not all flows make it to the basin plain, which is not unexpected. However, a decrease in turbidite recurrence at the start-IETM at Ermua provides support for a prolonged break in turbidity current activity.

Was there a tectonic influence?

The westward advance of the Pyrenean chain is not interpreted to have exerted a major influence on marine sedimentation until at least approximately 51 Ma, which postdates the periods considered at the chosen study areas (Figure 6.2). There is evidence for steady, independent movement of the Iberian Plate from ~55 Ma, however. Deformation was probably felt in the Pyrenean region initially but the effect at Zumaia was delayed until ~53.5 Ma (Winkler and Gawenda, 1999; Gawenda and Winkler, 2000) which corresponds to the later progradation of a deep sea fan (Cummings and Hodgson, 2011). Thus, this deformation also postdates the studied intervals. The initial stages of compression were focused far to the north of the Iberia Abyssal Plain and did not affect it, nor the eastward hinterland until much later (Gräfe and Wiedmann, 1993; Tugend et al., 2015). Major tectonic modification of sediment routing pathways is also not likely, as the provenance of turbidites did not change before or after the IETM at either of the sites (Marsaglia et al., 1996; Gawenda et al., 1999). Sites that were affected by major tectonic activity, show an increase in turbidity current activity (e.g. Wagreich et al., 2011); instead, a decrease is observed at our sites. It is plausible that relatively small tectonic effects could have had larger implications for the overall sediment budget. While, on the regional scale, river systems may not have been modified to a major extent, tectonic activity in the Pyrenees could have routed some rivers away, thus leading to a temporary decrease in sediment supply.

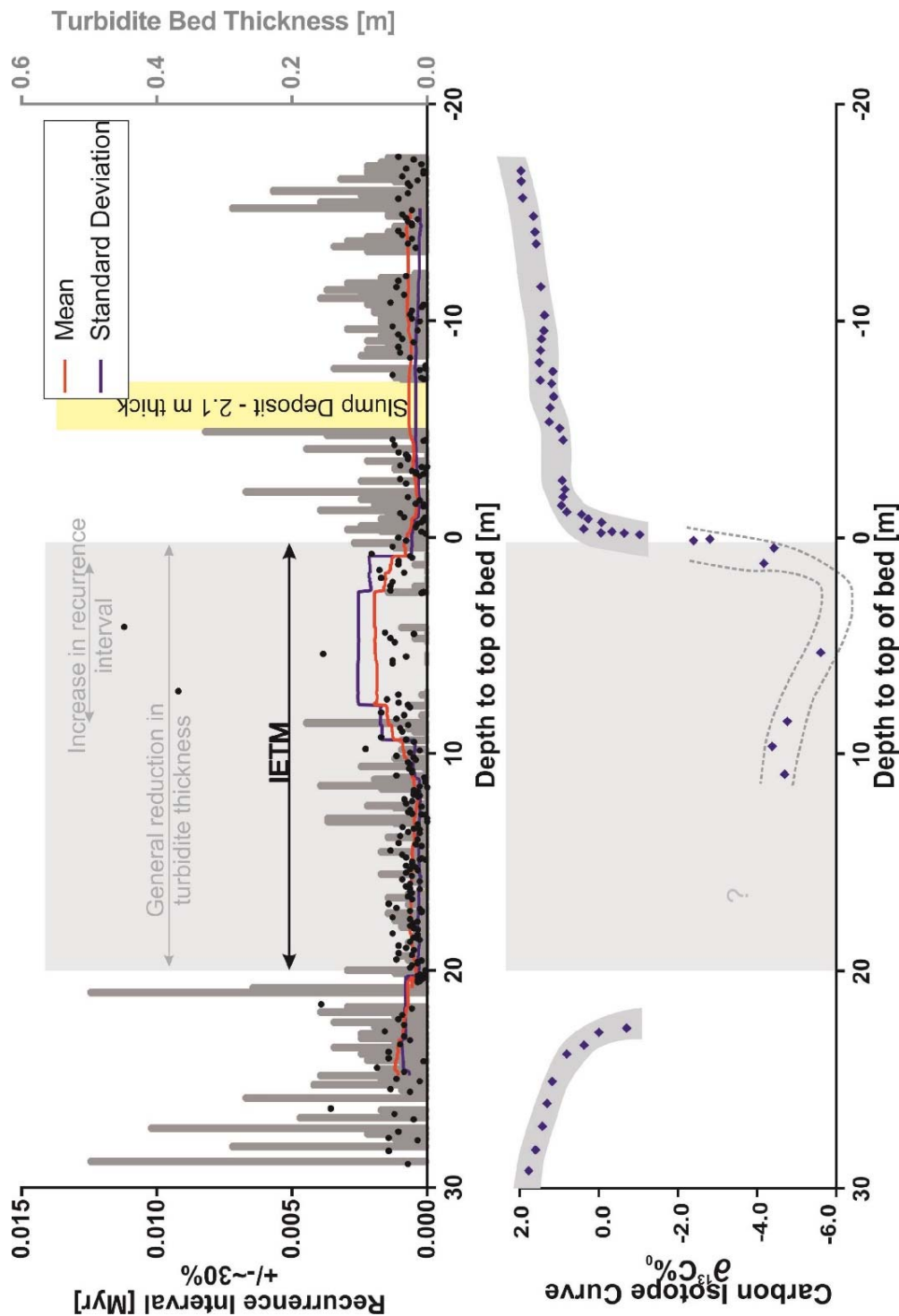


Figure 6.11: Turbidite recurrence intervals for Ermua, NE Spain based on detailed lithostratigraphic logs from Schmitz et al. (2001). N=211 turbidites. Age control is not well constrained; hence, the $\pm 30\%$ uncertainty on recurrence intervals. This is used on the basis of assumptions in Clare et al. (2014). Erosion below base of beds cannot be discounted. At the onset IETM an anomalously long period of no turbidity current activity occurs. During the IETM, turbidites are generally thinner than the periods before and after.

Did ocean circulation control turbidite frequency?

The influence of ocean warming at the IETM intensified Tethyan outflow (Norris et al., 2001 and references therein). A northward-flowing boundary current affected the Iberian margin (Whitmarsh et al., 1996). It is possible that a strengthened influence of contour currents may have temporarily starved the Iberia Abyssal Plain of turbidity flows due to interactions on the continental slope; however, other IETM sites (Section 6.3) including Zumaia (Kaminski et al., 1996) were not affected by bottom-currents and show a similar turbidite frequency response before, during and after the IETM (Kaminski et al., 1996). Therefore the localised effect of bottom-currents is not thought to have had a major effect on IETM turbidite frequency.

6.6.3 Why did turbidity current activity reduce post-IETM?

The background trend of recurrence appears to be largely insensitive to less acute, millennial oscillations in climate change. The pre-IETM interval was dominated at both sites by hemipelagic deposition interrupted by periodic turbidity currents - many of which were likely landslide-triggered. Warm and seasonally wet conditions are interpreted for the studied areas during this time (Gawenda and Winkler, 2000); but were dramatically altered to hot and arid at the onset-IETM, as indicated by terrestrial evaporite deposits (Schmitz and Pujalte, 2003). The IETM featured enhanced terrestrial erosion rates, but reduced hydrodynamic energy of freshwater outflow to the oceans in NE Spain (Schmitz et al., 2001). The elevation in deep marine background sedimentation rates (i.e. 'siliciclastic' unit) during the IETM is interpreted to be due to wind-blown transport (Schmitz et al., 2001), which also corroborates a hot, arid onshore setting. It is therefore possible that only minor fluvial/terrigenous contributions were made during the IETM to upper slope sedimentation, and did not provide conditioning for future landslides (i.e. no critical development of sediment thickness, slope steepening or excess pore pressures). This combination of factors may explain the reduction in both turbidity currents and landslides, as sediment was either locked up on land, bypassed the slope by aeolian transport, or was diverted by contour currents (Figure 6.12). The modification of sediment routing pathways on land and on the continental shelf in response to dramatic climatic changes during the IETM may also explain the significantly different turbidite recurrence intervals following the IETM.

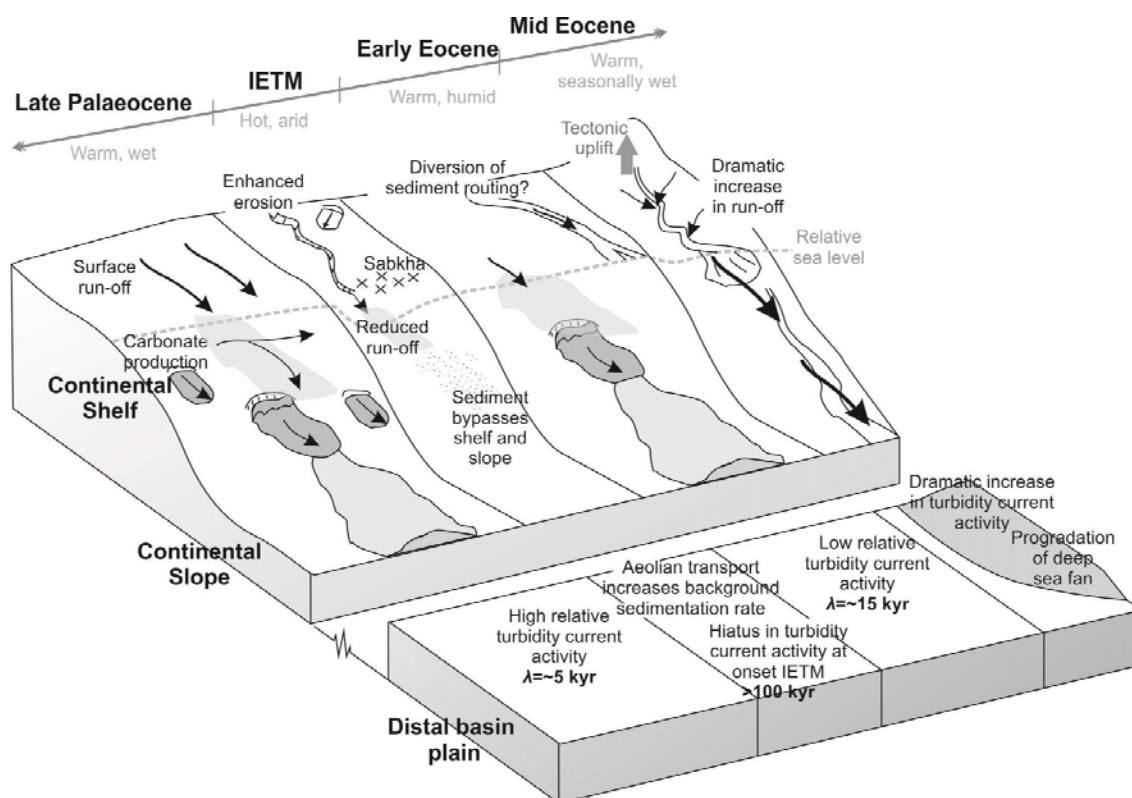


Figure 6.12: Conceptual model explaining effects of climate change on deep-water turbidity current activity at Zumaia (distal basin plain)

6.6.4 IETM turbidite frequency – global review

Most published IETM sections and boreholes were selected primarily for palaeoclimate studies, rather than turbidite frequency. As a consequence, there is a relative paucity of available data for a similar comparison. Existing studies are summarised in Figure 6.13 and Table 5.4 – many of which appear to corroborate the findings presented here, although they are mostly qualitative in nature. The literature review performed here, analysed any available deep-water data set that crossed the IETM. It should be noted, however, that as some of these previous studies were performed to understand palaeoclimates, they may have been selected to purposefully avoid turbidites. There is therefore some inherent bias, but as the records include pre- and post-IETM intervals, they provide a valuable insight into how turbidite frequency changed at several other sites worldwide. It is recommended that additional sites are selected for future analysis to further test the findings in this present study.

Eight sites from Europe, Egypt and Newfoundland show a reduction in turbidity current activity during and/or after the IETM. In particular, the Anthering section in Austria (Egger et al., 2003) shows a decrease in turbidite sedimentation rate from 20

cm/kyr (pre-IETM) to 5 cm/kyr (post-IETM) which corresponds to a drop from 45 to 2 turbidites per metre. Unlike the sites focused on in this present study, however, a dramatic increase in turbidite frequency is found immediately prior to the IETM. This may be climate-related, or could be due to an Alpine tectonic influence. Four sites from Europe, South Atlantic and Weddell Sea make no reference to turbidites, instead indicating continuous hemipelagic sequences during the IETM. A final example, in the Eastern Alps (Wagreich et al., 2011) shows a pronounced input of sand-rich turbidites during the IETM which is unlike all the other sites. This elevated sand input is interpreted to be a result of regional tectonic activity overprinting the effects of global climatic effects (Wagreich et al., 2011). This review indicates general agreement with the findings from Zumaia and ODP Site 1068; however, there is a need for more detailed study. Future efforts should focus on similar deep-water sites to Zumaia and ODP Site 1068 to provide a greater number of observations for comparison.

6.6.5 *Implications for geohazards*

The findings presented here show that periods of future global ocean warming may not necessarily result in more frequent landslide and/or turbidity current activity on non-glacially influenced margins. This is relevant for future predictions of landslide-triggered tsunamis, as well as assessment of turbidity current impact on seafloor structures and cables. It may thus be appropriate to extrapolate geologically recent records of recurrence for future assessments. If one can relate recurrence intervals from the recent past, to field measurements in the present day, this strengthens the appropriateness of using this information for future assessment and mitigation. Turbidite records from other deep sea basins should be analysed during periods of rapid climate change to enhance confidence in future assessments. The Pacific and Indian Oceans are poorly sampled, so may be good candidates for future study.

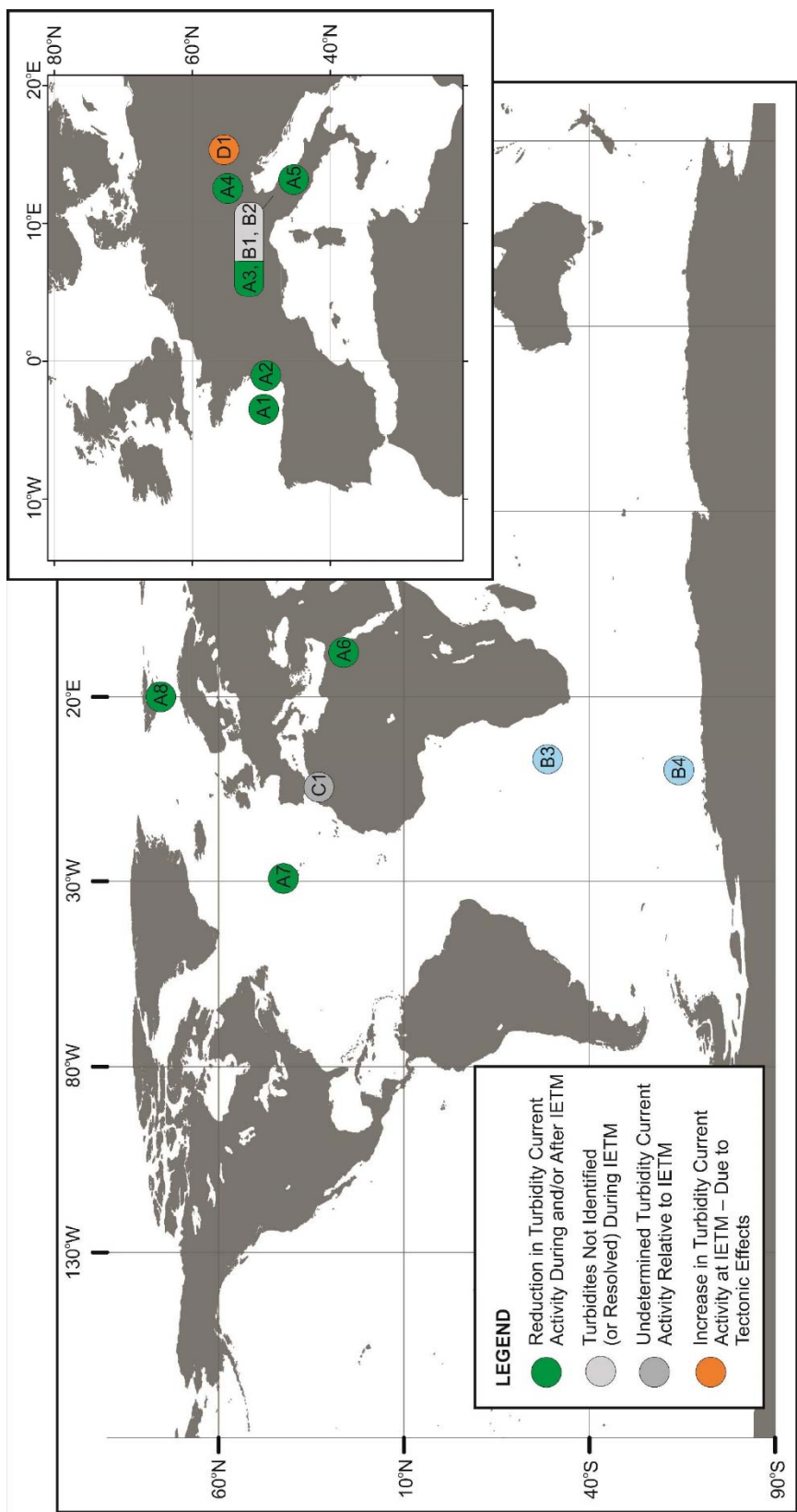


Figure 6.13: Summary of other deep-water IETM sites with reference to turbidite recurrence. See Table 6.4 for details on locations and data sources.

Table 6.4: Summary of other deep-water IETM sites with reference to turbidite recurrence. Location of sites is shown in Figure 6.13.

| Site ID | Site and Location | Palaeoenvironment (Water Depth) | Reference to Deposition Before, During and After IETM |
|--|--|---|--|
| <i>Reduction in Turbidity Current Activity During and/or After IETM</i> | | | |
| A1 | Trabakua Pass, NE Spain (Schmitz et al., 2001) | Deep basin setting (~1000 m) | One major turbidite only identified during IETM, intervals before and after IETM feature many turbidites |
| A2 | Ermua, NE Spain (Schmitz et al., 2001) | Base of slope apron | ~160 turbidites within IETM (average ~1 cm thick). Anomalous hiatus coincident with carbon isotopic excursion. Either side of the IETM turbidites are thicker >~8cm |
| A3 | South Ardo, Southern Alps, NE Italy (Dallanave et al., 2012) | Deep marine | Some turbidites identified before IETM, but predominantly hemipelagite. No turbidites immediately post-IETM. A break in sequence means that the IETM itself is not preserved, however |
| A4 | Anthering Section, Austria (Egger et al., 2003; Butt, 1981; Egger et al., 2009) | Continental rise (3000 m to 5000 m) | IETM features a threefold increase in bulk sedimentation rates. Turbidite sedimentation decreases from 20cm/kyr (pre-IETM) to 5cm/kyr (post-IETM), with a marked reduction in turbidity current activity during the IETM. Just before the IETM, a marked elevation in turbidity current activity is recorded. This record may also include tectonic effects however. |
| A5 | Umbria–Marche, Central Italy, Contessa Highway Section (Galeotti et al., 2000) | Deep marine basin | Pelagic sediments only identified during IETM |
| A6 | Galala Mountains, Egypt (Hontzsch et al., 2011; Speijer et al., 1996; Speijer and Schmitz, 1998) | Carbonate ramp and basin | Transect of boreholes show only marl and hemipelagite during IETM. Turbidites and debrites present before and after IETM interval. |
| A7 | Newfoundland Basin, ODP Leg 210 (Tucholke et al., 2004) | Below CCD in basin plain | Multiple turbidites before IETM, but once Eocene commences, a switch to grainstone deposition occurred |
| A8 | Svalbard, BH9/05 (Dypvik et al., 2011) | Open marine | Pre-IETM represented by sandy turbidites, but IETM and post-IETM appears to be shales (interpreted as hemipelagic mud) |
| <i>Turbidites Not Identified (or Resolved) During IETM</i> | | | |
| B1 | Forada Section, Belluno Basin, NE Italy (Giusberti et al., 2007; Rohl et al., 2007; Luciani et al., 2007; Agnini et al., 2007) | Deep basin (~1000 +/-500 m) | Expanded sequence of clays and marls – no reference to any turbidites IETM documented to have a five-fold increase in bulk sedimentation rate and a decrease in grain size, rate which is attributed to increased weathering and run-off, but not turbidity current activity |
| B2 | Possagno Section, Treviso, Belluno Basin, NE Italy (Agnini et al., 2006) | Deep water marine | Pink-reddish limestone to calcareous marlstone (pelagic to hemipelagic) succession is ascribed to the Scaglia Rossa. 14 m of finely bedded lower Eocene red calcareous marls identified during and post IETM. Turbidites only encountered in middle Eocene formation, not in late Palaeocene or early Eocene |
| B3 | Walvis Ridge, South Atlantic – ODP Leg 208 ODP 1262, 1263, 1266 (Zachos et al., 2002; Chun, 2010) | Deep basin ODP 1262 (1500 m), ODP 1263 (2600 m) and ODP 1266 (3600 m) | Nannofossil ooze identified before and after IETM, and calcite-depleted clay during IETM with no indication of turbidites from core photos or shipboard logs |
| B4 | Weddell Sea, ODP Site 690 (Rohl et al., 2007; Nielsen and Kelly, 2008) | Deep marine (1,100 – 3,600 m) | No reference made to turbidites before, during or after IETM |
| <i>Undetermined Turbidity Current Activity Relative to IETM</i> | | | |
| C1 | Talaa Lakrah Flysch, Moroccan Rif (Kaminski et al. (1996) | Lower bathyal or abyssal | Turbidites identified but no detail available on relative frequency in relation to IETM |
| <i>Increase in Turbidity Current Activity at IETM – Due to Tectonic Effects</i> | | | |
| D1 | Gosau Group of Gams, Eastern Alps, Austria (Wagreich et al., 2011) | Open marine | Highly expanded IETM section with increased turbidite frequency at start Eocene. The pronounced input of sand fraction is interpreted by Wagreich et al. (2011) as a result of regional tectonic activity overprinting the effects of global environmental perturbations |

6.6.6 *Implications for future short-term climate change*

It has been proposed that landslide activity, and subsequent dissociation of gas hydrates, may have triggered the IETM (e.g. Kennett et al., 2003; Maslin et al., 2004; Katz et al., 2001). The results, from local, detailed studies at two sites and a global review based on published literature, do not support this proposal. A period of enhanced turbidity current activity is not observed prior to or at the start of the IETM, which would be expected if landslides were more common. If landslides were the primary source for methane release during the IETM, evidence is not seen at the study sites here. If release of buried methane is implicated in the onset of the IETM, an explanation may come from terrestrial climate effects. The transition from more humid to arid conditions at the start IETM (Schmitz et al., 2001) led to enhanced terrestrial erosion and could also have released methane from wetlands. Methane emissions from wetlands may exceed those from gas hydrates hosted in marine sediments, as suggested by isotopic analysis of methane within ice core records (Sowers, 2006).

Recent work actually argues that the likely amount of carbon mass input at the onset CIE (4000-7000 PgC) required a major alternative source of carbon in addition to any contribution from methane hydrates (Dunkley-Jones et al., 2010). A rapid CO₂-driven warming event is instead implicated for the cause of the negative $\delta^{13}\text{C}$ excursion (Sluijs et al., 2007). This warming event may have contributed to hydrate dissociation as part of a positive feedback loop. The extent of the gas hydrate stability zone during the IETM was likely less than the present day due to higher ambient temperatures (Dunkley-Jones et al., 2010). Therefore, the influence of marine hydrate dissociation on slope stability may have been relatively limited during the IETM.

It has been suggested that the periods such as the IETM present a possible proxy for understanding future anthropogenic climate change (e.g. Bowen et al., 2004), although they are not direct analogues (Haywood et al., 2011). Despite this, such intervals do provide valuable windows into the influence of warm climate states and elevated greenhouse gases on submarine sediment transport.

6.7 **Conclusions**

Several previous predictions suggested landslide and turbidity current activity should increase during periods of rapid global warming, due to dissociation of marine hydrates. Evidence from two deep-water sites indicates that the IETM corresponds to a

reduction in turbidity current and landslide activity, and was followed by a period of reduced turbidity current and landslide activity. These results have important implications for future landslide-triggered tsunami predictions, and assessment for subsea structures that maybe vulnerable to turbidity current impacts. Finally, an increase in landslide activity is not observed prior to the IETM. It is therefore suggested that globally widespread, landslide-triggered dissociation of hydrate may not be a likely cause for the negative $\delta^{13}\text{C}$ excursion during the IETM.

Chapter 7. Implications of long-term climate change for turbidite recurrence

Summary

This chapter presents a statistical analysis of an exceptionally long (20 Myr) record of distal turbidites from the Iberia Abyssal Plain to explore long-term controls on flow recurrence, including sea level and climatic influences. In particular, this chapter explores whether a common frequency distribution for turbidite recurrence exists throughout the time series analysed. The influence of longer term climate change is investigated for comparison with the findings presented in Chapter 6 which focussed only on one short-term hyperthermal episode (IETM).

This chapter was submitted to *Marine Geology* (2014) and has been modified following comments from three reviewers prior to resubmission. David Hodgson and two anonymous reviewers are thanked for their reviews. All analyses and interpretations were completed by me, with editorial help provided by the co-authors during paper writing. James Hunt provided the initial measurements of bed thicknesses for the ODP 1068 record. This research used samples and data provided by the Ocean Drilling Program (ODP). ODP is sponsored by the U.S. National Science Foundation (NSF) and participating countries under management of Joint Oceanographic Institutions (JOI), Inc.

Long term (20 Myr) tempo of long run out turbidity currents in the Iberian Abyssal Plain: Persistent log-normal distribution and relationship to major climatic events

Clare, M.A.¹, Talling, P.J.¹ and Hunt, J.E.¹

¹National Oceanography Centre, European Way, Southampton, Hampshire, SO14 3ZH

ABSTRACT *Distal basin plains act as records of long run-out turbidity current deposits which represent unusually large-scale sediment transport events, with the largest volume events most likely triggered by submarine landslides. Understanding their future recurrence and potential triggers is important - particularly in light of projected climate and sea level change. Here a large number (N=1571) of distal turbidite recurrence intervals are analysed from the Iberian Abyssal Plain during the late Cretaceous to mid Eocene. This record covers several major climatic excursions over a period of 20 Myr and hence provides unique insights into how the frequency of turbidity currents and their initiating processes relates to major climatic events. A persistent log-normal distribution is identified for the entire record and also for sub-sets of the analysed period. The results of non-parametric and rescaled range statistics also indicate a high degree of temporal order in turbidite recurrence. The common log-normal distribution indicates that mean recurrence varies between clusters; however the parameter that governs the shape of the distribution does not vary. Therefore the controlling mechanism(s) for turbidity current generation is inferred to be broadly the same throughout the sequence. A trend of increased frequency, is observed to be coincident with long-term global warming in the mid-Eocene; however clusters of anomalously long recurrence intervals occur during the much shorter-term, intense warming at the Early Eocene Climatic Optimum and Initial Eocene Thermal Maximum. Intensification in turbidity current activity appears to show a lag of ~1.2 Myr after periods of sea level highstand. This may indicate that predicted future sea level rise and global warming may not necessarily result in significantly increased submarine landslide or turbidity current frequency on human timescales.*

7.1 Introduction

Deep sea basins provide valuable long term records of major submarine sediment transport events in the form of large volume turbidite deposits (Pilkey, 1988). Previous studies of turbidite frequency typically consider <100 events over relatively short timescales (<<1 Myr). In this chapter, distal turbidite deposits are analysed from the Iberian Abyssal Plain during the late Cretaceous to mid Eocene. The dataset presented

here is unusually large (N=1571) and covers several major climatic excursions over a period of 20 Myr. Such an extensive record provides unique insights into how the frequency of turbidity currents and their initiating processes (e.g. submarine landslides) relates to major climatic events. Determining the influence of past climate change on submarine landslide and turbidity current frequency provides valuable insights for future hazard assessments to subsea infrastructure in light of forecast man-made global warming.

7.1.1 *Climatic implications and geohazards*

Many studies have predicted that submarine landslide and turbidity current activity should increase during periods of dramatic global warming and sea level change (e.g. Lee, 2009; Brothers et al., 2014). This increase is inferred to be due to mechanisms, such as dissociation of marine gas hydrates causing weakening of slope sediments, among others (Maslin et al., 1998, 2004, 2010; Nisbet and Piper, 1998; Owen et al., 2007; Lee, 2009). Recent work has indicated that the frequency of large submarine landslides and flows in some settings may actually become less frequent in response to rapid global warming (Clare et al., 2015a; Chapter 6), or may occur independently of glacio-eustatic sea level oscillations (e.g. Romans et al., 2009; Geist et al., 2013; Clare et al., 2014; Hunt et al., 2013, 2014; Urlaub et al., 2013, 2014; Chapter 5). By analysing suitably long time series, with sufficient numbers of observations ($N > \sim 100$) for statistical analysis, it is possible to assess the implications of past major climatic variations on submarine landslide recurrence.

This present contribution is novel because it considers a much larger number of individual turbidite recurrence intervals than has been considered by previous frequency studies, and includes two major climatic events – namely the Initial Eocene Thermal Maximum (IETM; ~ 55 Ma) and the Early Eocene Climatic Optimum (EECO; 51-53 Ma). The IETM and EECO represent the most abrupt intervals of natural global warming ($\sim 10^\circ\text{C}$ increase in 10 kyr – IETM; Kennett and Stott, 1991) and the highest prolonged temperatures ($14\text{-}16^\circ\text{C}$ greater than present – EECO; Zachos et al., 2001) in the last 65 Ma. It has been suggested that these periods can help to understand the effect of future anthropogenic climate change (e.g. Bowen et al., 2004), although it should be noted that they are not perfect analogues (Haywood et al., 2011). Despite this, such intervals do

provide unique and valuable windows into the influence of warm climate states and elevated greenhouse gases on submarine sediment transport.

Some authors have argued that landslides themselves may catalyse future global warming (Kennett et al., 2003; Maslin et al., 2004; Bock et al., 2012). Dissociation of gas hydrates may result as slope sediments are unloaded or disturbed, and hence release methane to the atmosphere. This hypothesis is poorly tested and requires more observations (Talling et al., 2014). Similarly, the effects of climate-driven changes in sediment supply to the continental slope are not well understood. Urlaub et al. (2013) suggested that climate-driven variations in sediment supply to non-glaciated margins may not necessarily be a primary control on recurrence of large submarine landslides. Therefore, detailed analysis of climate effects on submarine landslide recurrence is required.

No other study is known to the author that considers the quantity of individual turbidite recurrence intervals that are analysed here. Novel work by Paull et al. (2014) provides a large number of (N=2020) turbidites sampled from deep-sea scours which provides useful insights into deep-sea sediment transport over a period of ~9 kyr; however, individual turbidite recurrence intervals cannot be determined from their method. This study thus yields unique insights into the effects of long and short-term climatic excursions, and related implications for future geohazards and deep-sea sediment transport. Specific hypotheses are tested including whether turbidity currents show time-independence, if turbidity currents show persistent frequency trends over long time periods (>10 Myr), and, if climate change affects recurrence to a significant degree.

7.1.2 *Turbidity currents as geohazards*

Turbidity currents are one of the volumetrically most important processes for transporting sediment across our planet (Talling et al., 2013). The largest volume turbidite deposits that have been identified (>0.1 to 100s of km³) are interpreted to result from the downslope disintegration of large submarine landslides (e.g. Elmore et al., 1979; Pilkey, 1988; Talling et al., 2007a,b; Wynn et al., 2010; Talling et al., 2012; Hunt et al., 2013; Clare et al., 2014). Both submarine landslide and turbidity current activity pose a threat to expensive seafloor infrastructure (Bruschi et al., 2006; Carter et al., 2012), including strategic subsea cable networks that carry 95% of all global data traffic (Carter et al.,

2012). Compounding this, submarine landslides may generate potentially fatal tsunamis (Tappin et al., 2001) due to their tremendous volume - they may be at least two orders of magnitude larger than terrestrial equivalents. Understanding the frequency of major turbidity currents thus provides insights into potential triggers and conditioning mechanisms and yields information for probabilistic assessments of their future occurrence. This is important for assessing the risk to expensive seafloor structures associated with increasing deep sea hydrocarbon exploration and production, our financial dependence on subsea communications networks, and the vulnerability of coastal communities to tsunamis (Chapter 1).

7.1.3 *Long-term records of sediment transport*

Analysis of multiple turbidite systems over the last 35 ka has shown that the timing of sediment transport by turbidity currents to the deep sea may vary greatly in response to sea level and climatic change (e.g. Covault and Graham, 2010). The quantification of the frequency of turbidity currents that reach the deep ocean is poorly understood, however, especially over longer timescales (i.e. millions of years). This is largely because long records of turbidites are often incomplete due to erosion or faulting, feature limited age control, and/or cannot be acquired due to limitations of sampling techniques (e.g. core barrel length). Sites that avoid these issues are valuable for understanding processes over geological (Myr) timescales, such as tectonism, re-routing of sediment input pathways, and major climatic shifts – as well as short-term ($\ll 10$ Myr) perturbations. The records presented here provide new insights into such effects from the Iberian Abyssal Plain.

7.1.4 *Limitations of existing studies*

Quantification of landslide hazard is problematic from submarine landslide deposits alone due to relatively few events being sampled at a given location and errors related to dating (Urlaub et al., 2013; Chapter 3). Lack of sufficient age information limits robust statistical analysis. Indeed, published submarine landslide studies currently feature no more than 68 events (Urlaub et al., 2013), and most rely on less than <10 events (e.g. Geist et al., 2013). Continuous cored, distal sequences of large volume basin plain turbidites presented in this chapter are interpreted to predominantly relate to large volume, fast-moving landslides that disintegrated downslope. This is interpreted based on the distal nature of the Iberian Abyssal Plain and similarity with deposits from other basin

plain locations (e.g. Weaver et al., 1987; Clare et al., 2014; Hunt et al., 2014; Chapter 5 and 6). It is possible that the sequence studied here includes turbidites triggered in other ways (e.g. canyon flushing; Canals et al., 2006), but these are interpreted to represent the largest events that transport sediment to abyssal depths. As such, the turbidites analysed here provide a record of the most serious hazards for strategic seafloor structures and potentially for landslide-tsunami generation, hence, underlining their importance. Understanding how dramatic past climatic perturbations such as the IETM and EECO, as well as more gradual climate shifts, have affected the tempo of turbidity current activity allows us to determine the relevance of applying past frequencies to future assessments.

7.2 Aims

The first aim is to compare the overall frequency distribution for the full record (20 Myr) of turbidite recurrence with other deep sea basin records that have been documented to show no serial dependence (i.e. the event timing is independent of the time since the last and the next). Different forms of frequency distribution provide insight into triggering mechanisms over geological timescales and this is explained later. A comparison is made of basin types with an explanation of why different frequency distributions may be anticipated due to a combination of nature, number and distance of sediment input pathways.

The second aim is to analyse sub-sets of the full turbidite record to assess whether the same frequency distribution is also observed over short timescales. This aim includes an investigation of whether the mean recurrence and frequency distribution form of distal turbidites changes through time. This provides insights into the influence of long-term climatic and tectonic effects on turbidite tempo and whether a common triggering mechanism can be implicated. The presence, and reasons for, any deviations from the background trend of recurrence are also investigated, as these may indicate temporal clustering or anomalously different recurrence intervals.

The third aim is to determine how major climatic excursions including the IETM and EECO affected turbidite frequency both on a short-term (kyr) to long-term (Myr) basis. In particular, this aim addresses whether turbidite frequency changes before, during and after these major hyperthermals and possible implications for landslide-catalysed

climate change. Implications of this work are discussed for future climate change which is a possible agent for change in submarine landslide and turbidity current frequency.

7.3 Methods

7.3.1 *Rationale for selection of study site*

The turbidite records for this study are from Ocean Drilling Program (ODP) Site 1068, located on the western flank of a N-S trending basement high at the southern edge of the Iberian Abyssal Plain (Figure 7.1; Whitmarsh et al., 1996, 1998). The first criterion for selecting ODP Site 1068 is that a continuous basin plain turbidite sequence (N=1571) was sampled from 48.16 to 67.61 Ma. Crucially for this study, this includes major climatic excursions (IETM at 55 Ma, EECO at 51 to 53 Ma), minor hyperthermals (Eocene Thermal Maximum 2 (“Elmo”) and 3 (“X”), Late Palaeocene Thermal Event, Top Chron C27n Event, Carbon Isotopic Excursions DS1 and DS2, Dan C-2 Event) as well as the Cretaceous-Tertiary boundary. The margin was subjected to right-lateral slip from 55 to 46 Ma, but the zone of deformation was distal from the study site (Roest and Sriverstava, 1991; Rosenbaum et al., 2002). The deformation was probably felt most at the study site from about 51 Ma, but the sediment input pathways are not thought to have been affected in a major way as turbidite sand mineralogy does not change significantly throughout the interval (Marsaglia et al., 1996; i.e. reflecting a consistent provenance).

The second criterion is that recurrence intervals can be derived from the sedimentary records. The method outlined Chapter 3 is used, as hemipelagic mud can clearly be discerned from turbidite mud, there is no evidence for basal erosion, and age control is available (Ladner and Wise, 2001; McGonigal and Wise, 2001). The third criterion is that the turbidite sequence is interpreted to primarily relate to major sediment transport events - predominantly submarine landslides, as well as other large-scale processes, which may include canyon flushing events. Therefore the ODP 1068 record provides long-term, dated records of major geohazard events. Turbidite sands during the studied interval were derived from proto-equivalents of major river catchments on the basis of mineralogical analysis (Marsaglia et al., 1996). The present day Iberian Abyssal Plain sedimentary sequence represents deposits from turbidity currents sourced from the Nazaré Canyon to the east (Weaver et al., 2000), associated with failures of the canyon head (Arzola et al., 2008). Early equivalents of the Nazaré Canyon were most likely fed

by similar rivers systems that currently drain to the Iberian shelf, based on mineralogical provenance analysis (Marsaglia et al., 1996). Turbidites in the studied interval are also similar in character to those of the modern Quaternary section (Milkert et al., 1996; Weaver et al., 2000; Van Weering et al., 2002). The Quaternary deposits can be correlated across the Iberian Abyssal Plain for >1000 km, and thus were deposited from long-run-out voluminous flows ranging from 1 to 20 km³ (Hunt et al., 2010). Due to their volume and long run out, these deposits are interpreted to represent flows predominantly produced by submarine landslides, rather than from flood discharge or from storm agitation (Arzola et al., 2008).

7.3.2 *Determination of recurrence intervals*

The quantity of sampled turbidites is sufficient for statistical analysis of frequency on the basis that recurrence intervals between each successive bed can be calculated. Hemipelagic mud was deposited progressively in the time periods between turbidity currents. Importantly, hemipelagic mud can clearly be discerned from turbidite mud at this site on the basis of colour and textural differences (Chapter 3). The thicknesses of hemipelagic mud intervals were converted to time periods by dividing by the rate of hemipelagic mud accumulation. Average hemipelagic mud accumulation rates were calculated using cumulative hemipelagic thickness between dated horizons. Deposits were logged visually to a vertical resolution of 5 mm. The method assumes there are minimal fluctuations in hemipelagic mud accumulation rate between adjacent dated horizons (Chapter 3). Dated horizons occur every 0.5 to 1.3 Myr and are based on biostratigraphic analysis (Whitmarsh et al., 1996, 1998; Ladner and Wise, 2001; McGonigal and Wise, 2001). Based on these dates and the vertical resolution, the minimum resolvable interval is 1.9 kyr (Chapter 3).

Finally, it is also assumed that there is little or no erosion of hemipelagic mud beneath turbidites. This assumption is based on the small depth of erosion seen in the available core and the distal basin plain setting. Turbidites have flat bases and lack irregular bases indicative of erosion. Erosional features with longer length scales than the core diameter (~10 cm) would not be identified (Weaver and Thomson, 1993).

It is recognised that variations in sediment accumulation between dated horizons, uncertainty in dating or possible erosion, may lead to some variation in results, hence the

effects of random amounts of variation are modelled between $\pm 30\%$. This reflects the variation in accumulation rates seen in a site with better constrained dates over short timescales; the Balearic Abyssal Plain (Chapter 5). The results of the modelling provides similar results to those determined from the studied interval. As this study investigates broad trends this provides confidence in the subsequent analyses.

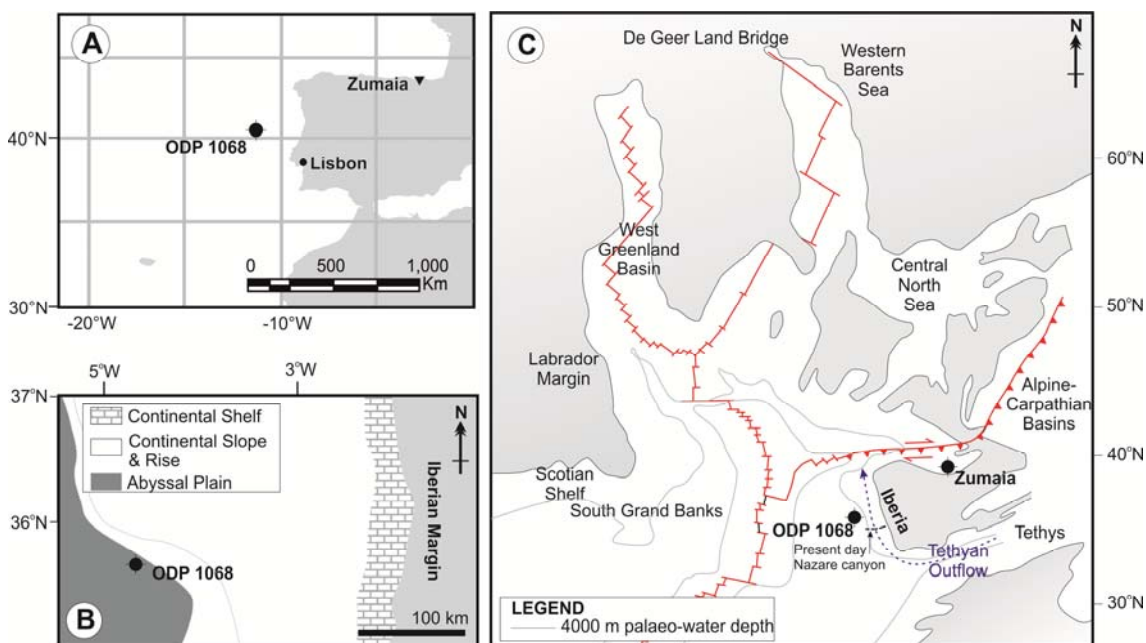


Figure 7.1: Location map (A) showing ODP Site 1068 and reference to Zumaia site in NE Spain referenced later; Palaeogeographic reconstruction (B) for Iberian Margin and ODP Site 1068 during late Palaeocene/Early Eocene (modified from Whitmarsh et al., 1995); Regional palaeogeography during late Palaeocene (C) modified from Kaminski et al., 1989. The present day Nazaré canyon is georeferenced approximately in reference to coastline. It is thought likely that a proto-equivalent of the Nazaré canyon may have funnelled sediment to the abyssal plain.

7.4 Statistical analysis

In order to analyse turbidite recurrence over different timescales a suite of statistical analyses is employed. Exceedance plots of frequency are first used to visually test different distributions on different scales. Quantile-quantile (Q-Q) plots are used to assess the goodness of fit for theoretical frequency distributions (including log-normal, power law and exponential), against the observed data. Three main distribution forms are considered in the analysis as this is appropriate for assessing variables conforming to the majority of common statistical distributions (Van Rooij et al., 2013). This includes Gaussian forms relating to addition of independent variables, log-normal distributions arising from multiplication of normally or log-normally distributed independent

variables, and a power law where interdependent processes cause an amplification of effects (Van Rooij et al., 2013). To test for shorter-term variation in recurrence intervals, non-parametric, unpaired Mann-Whitney and Kolmogorov-Smirnov (K-S) tests (Cheung and Klotz, 1997; Massey, 1951) are also used.

7.4.1 *Testing for temporal clustering*

To test whether recurrence intervals are clustered in time, rescaled range analysis (Hurst, 1951) is employed – a test that is independent of the form of frequency distribution (Kristoufek, 2012) and has been used previously in turbidite thickness studies (Chen and Hiscott, 1999). Hurst (1951) presented the following relationship (Equation 7.1), using K as an estimator for a modified Hurst exponent, h :

$$K = \frac{\log_{10}(R/S)}{\log_{10}(N/2)} \text{ (Equation 7.1)}$$

where R is the maximum range in cumulative departure form, N is the number of observations, and S is the standard deviation. Values that are closer to $K=1$ show persistent or trend reinforcement (Mandelbrot and van Ness, 1968), and those that are closer to $K=0$ are mean-reverting or anti-persistent (Barkoulas et al. 2000). Values that approximate $K=0.5$ are deemed to be time-independent and memoryless (Hurst, 1951). The *hurstexp* function in *R* is used, which calculates a theoretical K value for a truly time-independent (i.e. stationary Poisson) distribution which is compared with the K values calculated for the data.

7.4.2 *Testing for significance of sea level*

To test for the significance of sea level on turbidite recurrence, hazard rate ($\lambda(t)$) is considered. This is the probability that an event will occur at time t given that one occurred at time $t=0$. If one assumes that the hazard rate, $\lambda(t)$, is proportional to an explanatory variable, x (e.g. sea level or its rate of change), the effect it has regardless of the form of $\lambda(t)$ can be estimated. This is done by applying Cox Proportional Hazards Model (Cox, 1972) which considers the following generalisation:

$$\lambda(t, x_i) = \lambda_0(t, \alpha) \exp(coef \cdot x_i) \text{ (Equation 7.2)}$$

where h is hazard function, t is time, α represents parameters affecting the baseline hazard function, x_i is the sea level at event time i . The $\exp(coef)$ term, expressed as E^b in this

manuscript, indicates the hazard ratio for one metre change in sea level. If you use a model of this form and are interested in the effects of covariates on survival, then you do not need to specify the form of $\lambda_0(t, \alpha)$ (Cox, 1972). Therefore, it is not necessary to make any assumption about the distribution of the time between events. In this model, hazards are proportional and do not depend on time (Smith et al., 2003).

Given the uncertainties in using a global sea level curve (Miller et al., 2005), it was not deemed appropriate to attempt an absolute correlation between individual events and relative sea level. Cox Proportional Hazards Model is selected, as broad associations between hazard rate and sea level change are of greatest interest here. The model also has the benefit of not requiring any parametric assumptions.

7.5 Results

7.5.1 *Log-normal distribution of long-term (20 Myr) turbidite frequency*

Exceedance plots of recurrence intervals follow a nearly straight line trend on a log-probability scale, which suggest a good fit with a log-normal distribution (Figure 7.2A). A theoretical log-normal trend shows a good fit with the measured data ($r^2=0.984$) on Quantile-Quantile plots, while exponential ($r^2=0.688$) and power law ($r^2=0.600$) distributions show a relatively poor fit (Figure 7.2B). A subtle inflection is observed in the exceedance plots at $T=0.02$ Myr which may indicate that a segmented log-normal distribution is actually most appropriate (Figure 7.2A). A log-normal distribution indicates that a degree of time-dependence exists in the overall record of recurrence intervals.

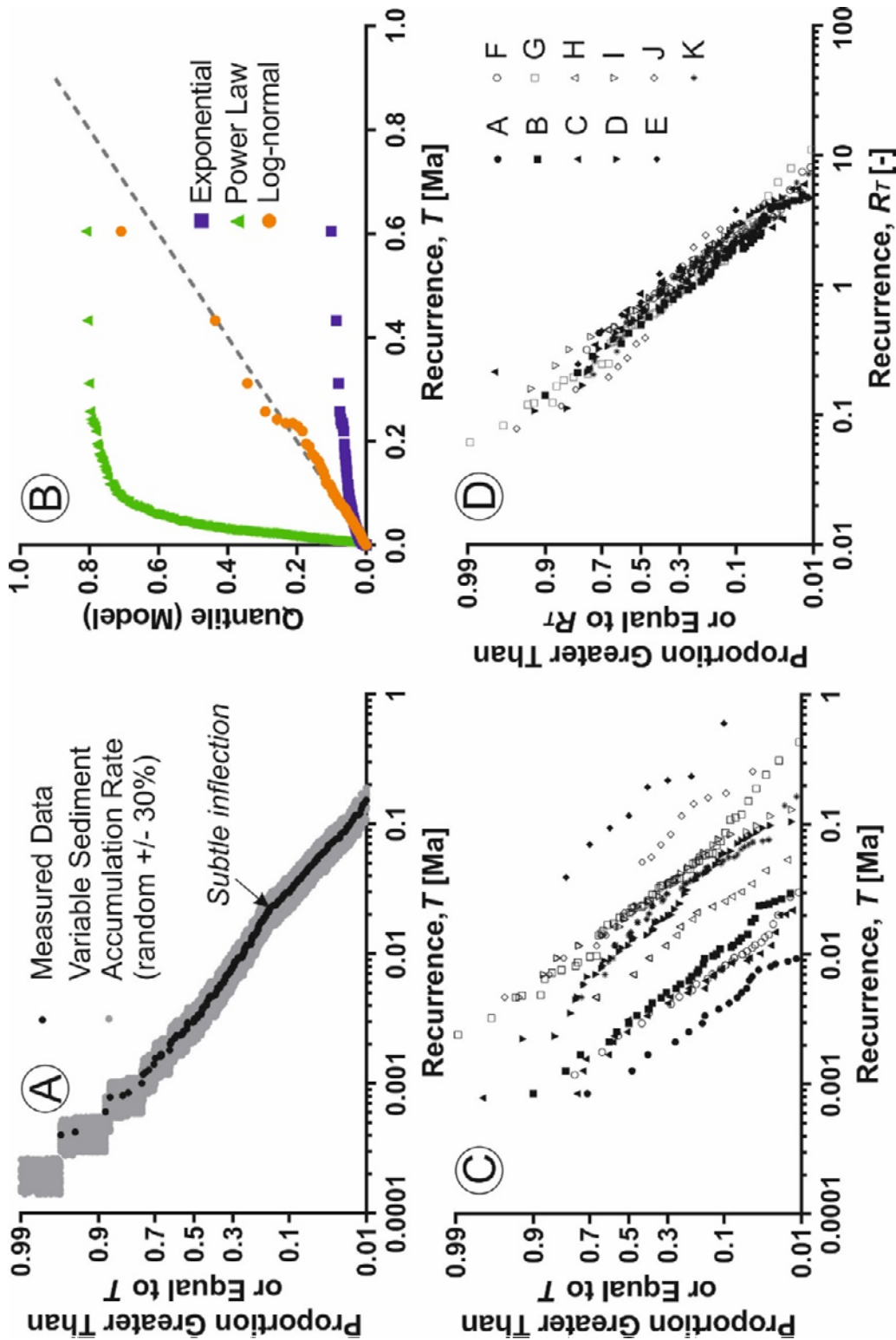


Figure 7.2: Log-probability exceedence plot for full ($N=1571$) turbidite recurrence record (A) showing a near-straight line trend indicative of a log-normal distribution. 100 runs of data that model random amounts of variation (between $\pm 30\%$) are shown in grey. This accounts for variation in hemipelagic sedimentation, differential compaction, small amounts of erosion and/or uncertainty in biostratigraphic dating. The log-normal trend is well preserved despite these variations providing confidence in the results; Quantile-quantile plot (B) testing the goodness of fit of the full turbidite recurrence record against three theoretical models; Log-probability exceedence plots for sub-sets of full record as shown in Figure 4 presented as observed values (C), and normalised to mean recurrence value (μ) for each sub-set (D).

There is a high degree of scatter when turbidite recurrence is plotted against time (Figure 7.3), which makes visual identification of trends difficult. Values of running arithmetic mean, median and standard deviation over a window of 50 beds are highly biased by a few anomalously long recurrence intervals. One such recurrence interval (605 kyr at 55 Ma) is identified during the IETM at 55 Ma (Chapter 6; Clare et al., 2015a). Therefore, the following analysis considers filtered and unfiltered versions of the data. The unfiltered data includes all observations which are analysed both as a time series of individual recurrence values (Figure 7.4A) and also as binned data to assess broad trends in different time windows of 0.25, 0.5, 1.0 and 2.0 Myr (Figure 7.4C). The filtered data exclude the longest recurrence intervals (>95%; Figure 7.4B). This filter serves to remove skew created by a few long recurrence intervals. The key observations of the analysis of filtered and unfiltered data are:

- i. Turbidite frequency generally increased from 67.61 to 48.16 Ma. However, periods of lower and greater activity are observed. Both the unfiltered (Figure 7.4A) and filtered (Figure 7.4B) recurrence records show a high degree of variation about this general trend, suggesting that neither a constant or gradually decreasing hazard rate are appropriate to explain the full variation in the data. The binned data best reveals broad trends in turbidite frequency (Figure 7.4C).
- ii. The 2 Myr bins indicate an oscillatory (~5 Myr wavelength) amplification in turbidite frequency from 67.61 to 48.16 Ma. This trend is visibly less noticeable as bin size decreases, however (Figure 7.4C);
- iii. The unfiltered data set shows a pronounced reduction in turbidity current activity at ~54 to 55 Ma (coincident with and immediately post-IETM), ~57 to 59 Ma and at ~63 Ma (Figure 7.4A);
- iv. A pronounced decrease in turbidity current activity is observed from ~51 to 52 Ma (coincident with the EECO) on the filtered data (Figure 7.4B), and to a lesser extent on the unfiltered record (Figure 7.4A);
- v. A prominent increase in turbidity current activity occurs at ~55.5 to 56.2 Ma (prior to the IETM);
- vi. A dramatic increase in turbidity current activity occurs after ~50 Ma. This is clear on the full and filtered recurrence records, and is shown as significant peaks in the binned frequency records.

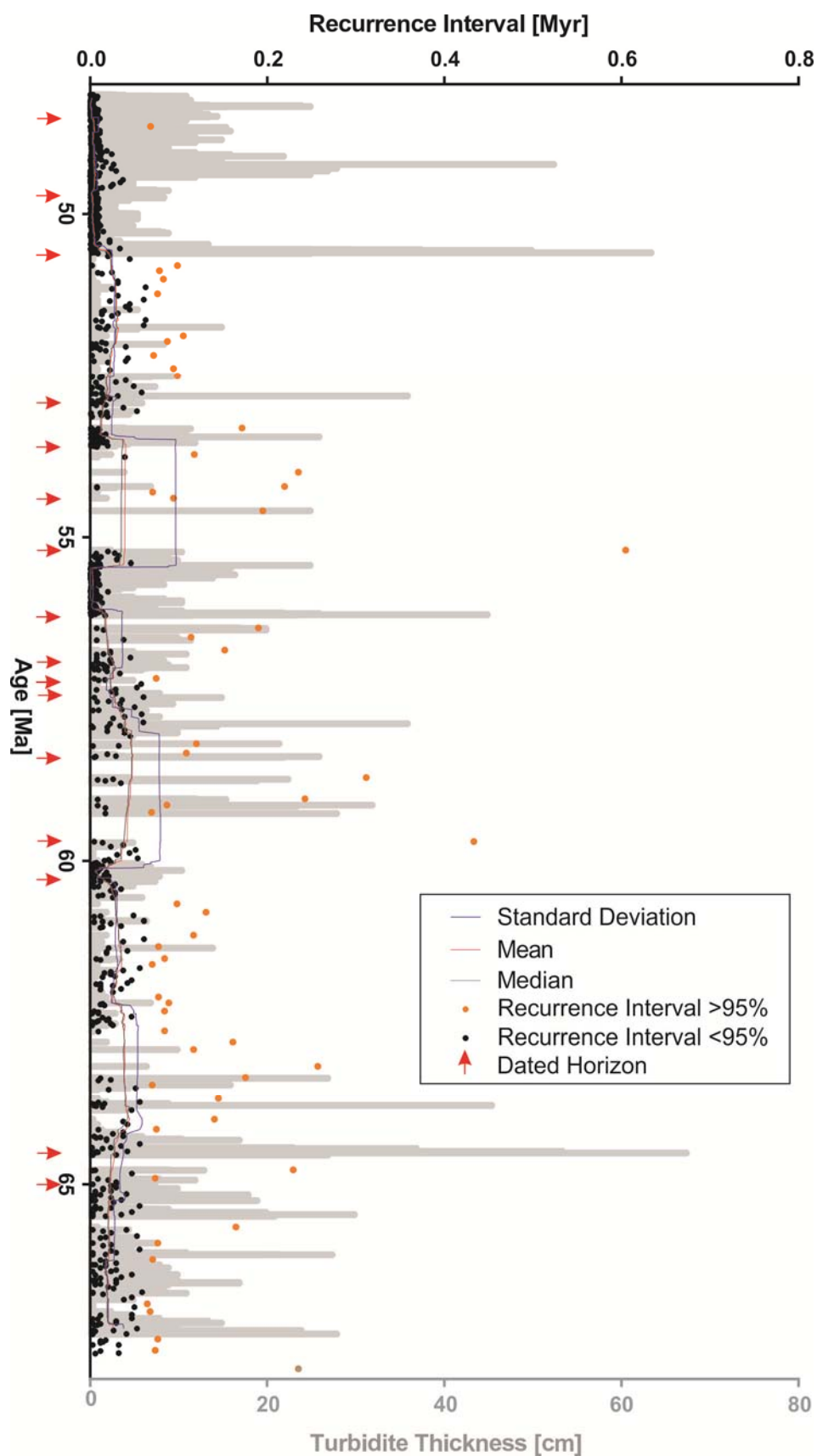


Figure 7.3: Turbidite recurrence (circles) and thickness (grey bars) time series for ODP Site 1068. The upper 5% of recurrence intervals shown as orange circles. Values of running mean and standard deviation for windows of 50 beds are occasionally highly skewed by anomalous hiatuses such as that coincident with the IETM. Note change in age scale between sites. Timing of major hyperthermals shown as yellow bars. Dated horizons shown as red arrows below.

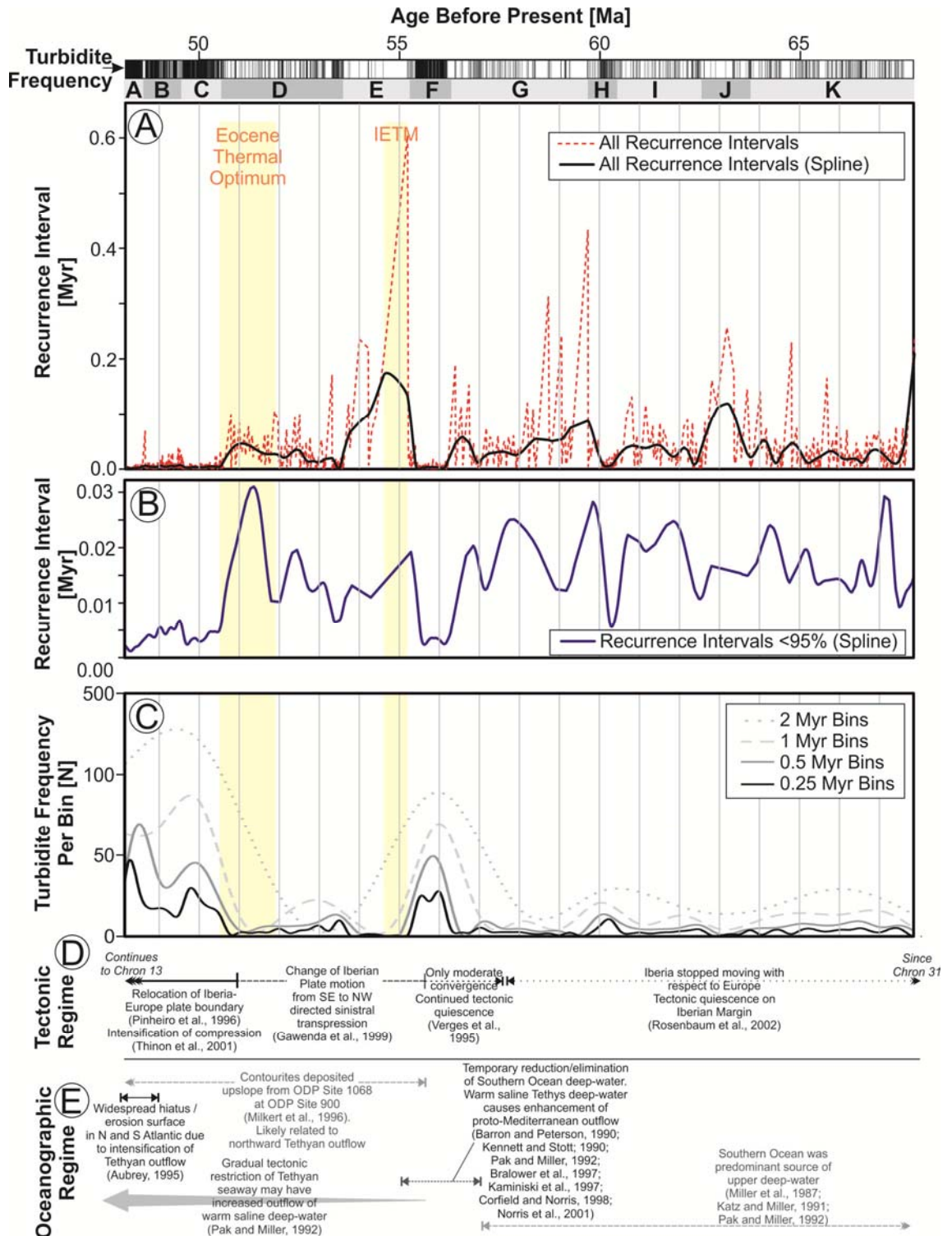


Figure 7.4: Time series including turbidite recurrence for unfiltered record (A), filtered record for excluding >95% recurrence intervals (B) and binned turbidite frequency (C). To visually track variation in recurrence a cubic spline is fitted to the recurrence and binned frequency data. (D) Major tectonic (D) and oceanographic (E) changes affecting the region based on results of published studies.

7.5.2 Common log-normal distribution of shorter-term turbidite frequency

Plotting cumulative recurrence against bed number, a general trend of more frequent turbidites is seen from 67.61 to 48.16 Ma based on a fitted curve ($y=x^2$) ($r^2=0.936$; Figure 7.5). The fitted curve smooths the data, however, and masks several periods of enhanced and reduced turbidite recurrence that do not transition gradually from one to the other.

By assigning different periods (A to K) based on the gradient of cumulative recurrence, distinctly different spreads are observed for the recurrence intervals (Figure 7.5). Mean turbidite recurrence for these periods range from 3.91 kyr to 168.34 kyr. Each of the periods shows a negative skew for the trend of recurrence intervals. Non-parametric, unpaired Mann-Whitney and Kolmogorov-Smirnov (K-S) tests demonstrate that the spread and mean of recurrence intervals are significantly different to preceding and succeeding periods with the exception of periods I and J (Table 7.2 and 7.3). The populations are significantly distinct ($p<0.05$), thus random sampling could not account for this difference. Therefore a general increase in turbidity current activity is seen from oldest to youngest parts of the sequence, but with significant short-term variations in frequency. The inflection noted at ~ 0.015 Myr on the exceedance plot for all intervals (Figure 7.2A) relates to temporal variations in recurrence rate in particular the trend for more frequent events in the younger part of the sequence – particularly noted in periods A to C (Figure 7.5).

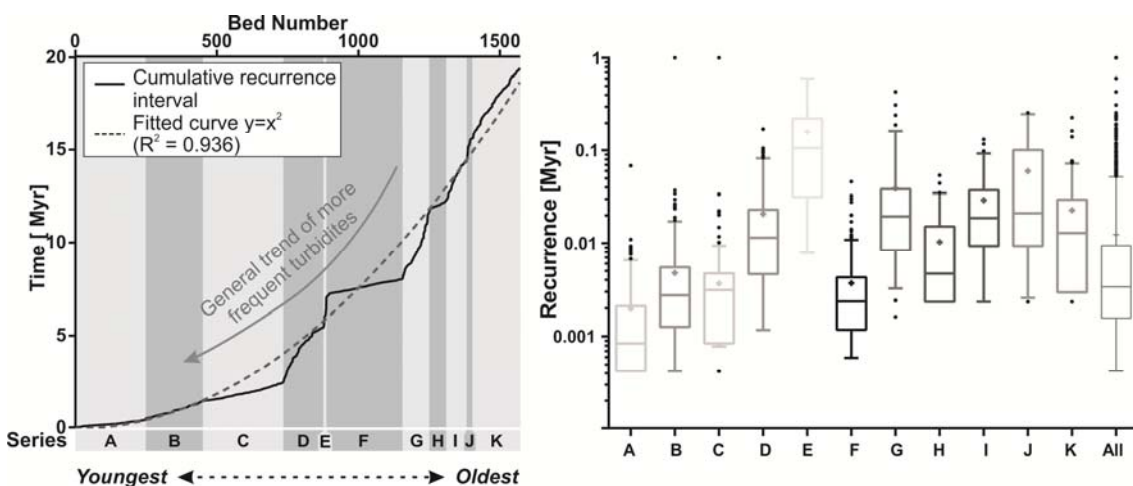


Figure 7.5: Cumulative turbidite recurrence (left) plotted against bed number 0 (young) to 1571 (old). Visually discerned changes in cumulative recurrence gradient annotated as letters below; Box and whisker plots showing recurrence intervals for lettered sub-divisions. Boxes show 25% and 75% intervals, crosses indicate arithmetic mean values, whiskers show 5% and 95% intervals, and points represent values that fall outside 5% and 95% intervals.

Exceedance plots of periods A to K individually show a good agreement with a log-normal distribution ($r^2=0.92-0.98$; Figure 7.2), albeit with different mean recurrence (μ) as shown by K-S and Mann-Whitney tests (Table 7.2 and 7.3). To test whether these periods share a common distribution form, they are normalised by subdividing each recurrence interval, T , by μ for each period to plot a dimensionless variable, R_T . The data sets show remarkably close agreement when plotted in this manner suggesting that, aside from μ , the distribution spread and form could be explained by a common variable (Figure 7.2C and D).

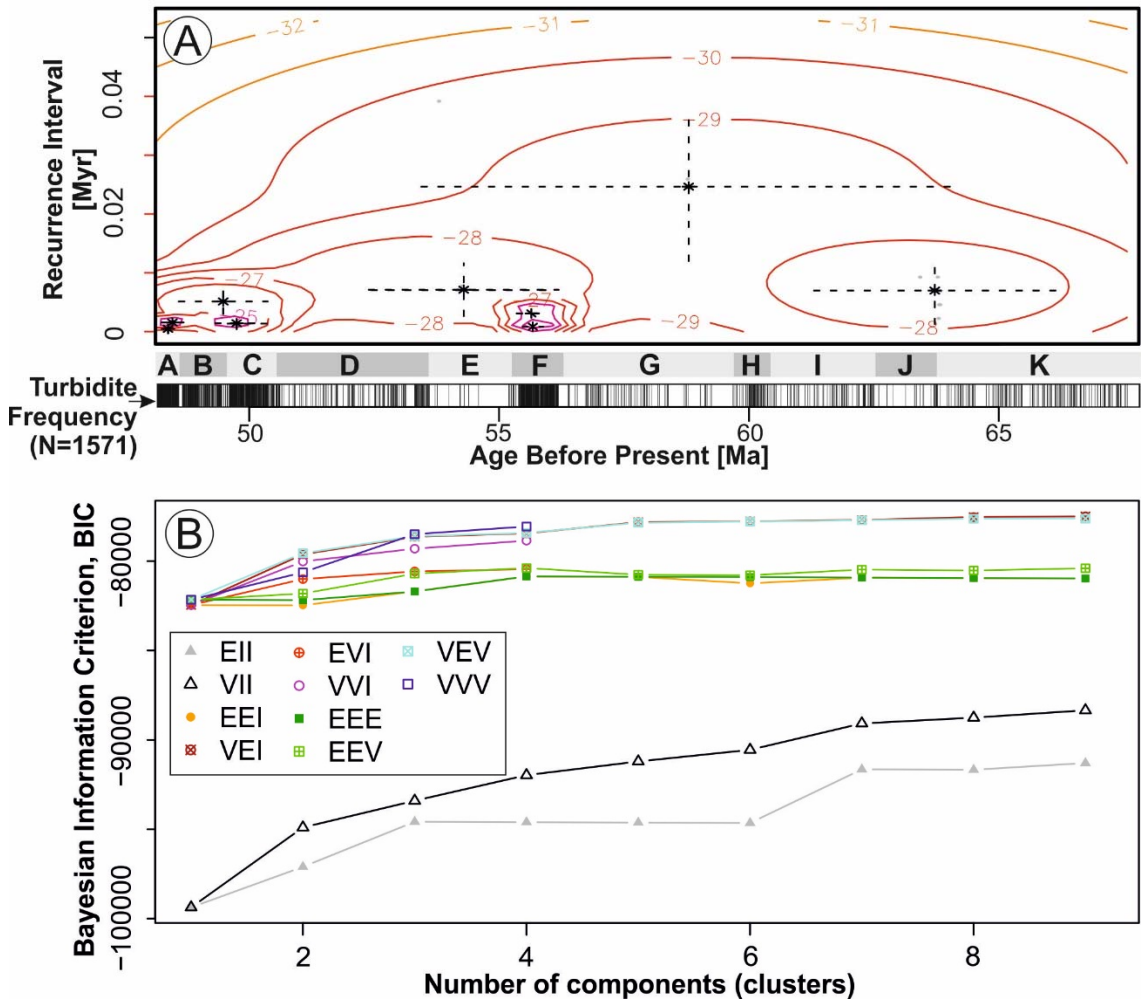


Figure 7.6: (A) Time series plot of the Iberian Abyssal Plain record showing individual turbidites (lower dashed bar), visually identified periods of characteristic recurrence (periods A to K), and log-likelihood density contour plots of Gaussian finite mixture model (upper panel). Cluster centres from the finite mixture model are shown as stars. Dashed lines correspond to 95% confidence intervals. (B) Bayesian information criterion results for the Finite Mixture Model. Highest values indicate the best parameterisation which in this case starts to plateau at fix to six clusters. The optimal fit lies above the maximum number of clusters that can be modelled (i.e. >9), but distinct cluster centres are identified by the model.

The finite mixture model detects significant clustering, with the optimal parameterisation being a diagonal equal shape (VEI) model (Fraley et al., 2012) with in excess of nine clusters (Figure 7.6A). The best model lies outside the available range of possible clusters (i.e. >9); however, the Bayesian Information Criterion starts to plateau when five to six clusters are considered so this is considered reasonable (Figure 7.6B). The finite mixture model identifies several clustered periods of relatively long (~ 0.02 Myr) to short (~ 0.002 Myr) characteristic recurrence intervals as indicated by the visual analysis. Using the rescaled range analysis, the computed value for the modified Hurst exponent is $K=0.936$. This K value indicates a very high degree of trend reinforcement (i.e. event timing is strongly related to the time of preceding and successive events). In the following section the nature of clustering is explored with respect to potential controls on turbidite recurrence.

7.5.3 *Does sea level change influence turbidite recurrence?*

It is first necessary to determine what form of recurrence interval distribution might be expected for sea level and its rate of change. Analysis of relative sea levels (Miller et al., 2005) over the time interval studied indicates a close fit to a normal ($r^2=0.96$) and 3-parameter log-normal ($r^2=0.98$) distribution (Figure 7.7A to D). Unlike a standard 2-parameter log-normal distribution, the 3-parameter variant includes a location parameter, γ , and closely approximates a normal distribution here (Sangal and Biswas, 2010). The first derivative (i.e. rate of change) of sea level also shows a good fit with a normal ($r^2=0.97$) and 3-parameter log-normal distribution ($r^2=0.97$).

A visual comparison of sea level is tentatively correlated with turbidite recurrence ($<95\%$ values) assuming a lag of approximately 1.2 Myr (Figure 7.7E). A prominent peak in sea level at 52.5 Ma is correlated with a similar increase in turbidite recurrence interval at 51.5 Ma. The general trend also appears to be replicated in both records, albeit with some minor variation. Cross correlation indicates normalised correlation coefficients of between 0.723 and 0.900, with median and mean values of 0.822 and 0.814 respectively. Values equal to 1 are perfectly correlated, and equal to zero are not correlated; hence, the results show reasonable correlation.

Sea-level estimates on the 10^6 -year scale have an uncertainty, typically, of at best ± 10 m to ± 50 m (Miller et al., 2005), however so there is a large degree of uncertainty.

The interest here is in general trends in sea level change (rather than absolute), therefore this tolerance is acceptable, but should be borne in mind nonetheless. The Cox Proportional Hazards Model provides a framework to assess the broad significance of sea level, as general trends in rate of recurrence and changes in sea level are compared (Table 7.1). When considering the sea level at 1.2 Myr prior to event recurrence, a significant relationship is observed ($p=2\times 10^{-16}$). The hazard ratio, E^b , indicates that a one metre drop in sea level corresponds to a decrease in recurrence intervals (E^b) of 1.0%. There is, however, a relatively wide spread in the 95% confidence intervals (0.8 and 1.3%).

Table 7.1: Results of Cox Proportional Hazards Modelling which tests for significance of sea level and its rate of change as a control on turbidite recurrence. Bold and italicised p-values are significant at <0.05

| Explanatory Variable | Assuming Sea Level at Time of Event | | | Sea Level 1.2 Myr Prior to Event | | |
|-------------------------------|--|--|---|---|--|---|
| | Effect of Sea Level | Effect of Smoothed Sea Level | Effect of 1 st Derivative of Sea Level | Effect of Sea Level | Effect of Smoothed Sea Level | Effect of 1 st Derivative of Sea Level |
| Regression Coefficient [b] | 0.007 | 0.007 | -7.768×10^{-5} | 0.0103 | 0.007 | -8.161×10^{-5} |
| Hazard Ratio [E^b] | 1.007 | 1.007 | 0.999 | 1.01 | 1.007 | 9.999×10^{-1} |
| <i>p</i> value | <i>1.15×10^{-11}</i> | <i>1.24×10^{-11}</i> | 0.804 | <i>2×10^{-16}</i> | <i>7.53×10^{-12}</i> | 0.795 |
| 95% Confidence Intervals [CI] | 1.005-1.009 | 1.005-1.009 | 0.993-1.001 | 1.008-1.013 | 1.005-1.009 | 0.999-1.001 |
| Likelihood ratio | 3.589×10^{-11} | 3.589×10^{-11} | 0.805 | <0.001 | 2.44×10^{-11} | 0.796 |
| Wald test | 1.148×10^{-11} | 1.241×10^{-11} | 0.805 | <0.001 | 7.53×10^{-12} | 0.795 |
| Score (logrank) test | 1.179×10^{-11} | 1.275×10^{-11} | 0.805 | <0.001 | 7.74×10^{-12} | 0.795 |

The hazard ratio should be treated cautiously, given these wide confidence intervals and the uncertainties in a reconstructed ancient global sea level curve, as well as unknown localised isostatic effects. Hence, while a statistically significant relationship is noted between sea level and turbidite recurrence, it may be weak, and there is only a small degree of improvement on a null model and other variables may also be in effect. There may well be a strong correlation between turbidite recurrence and sea level at this site, however, other factors can dilute this relationship. The changing relative distance from a sediment input source and complexity of continental shelf-slope sediment routing pathways that arise during different sea level states are possible diluting factors. The

processes involved in the delivery of sediment to areas of continental slope that may fail are unlikely to be linear in time or space.

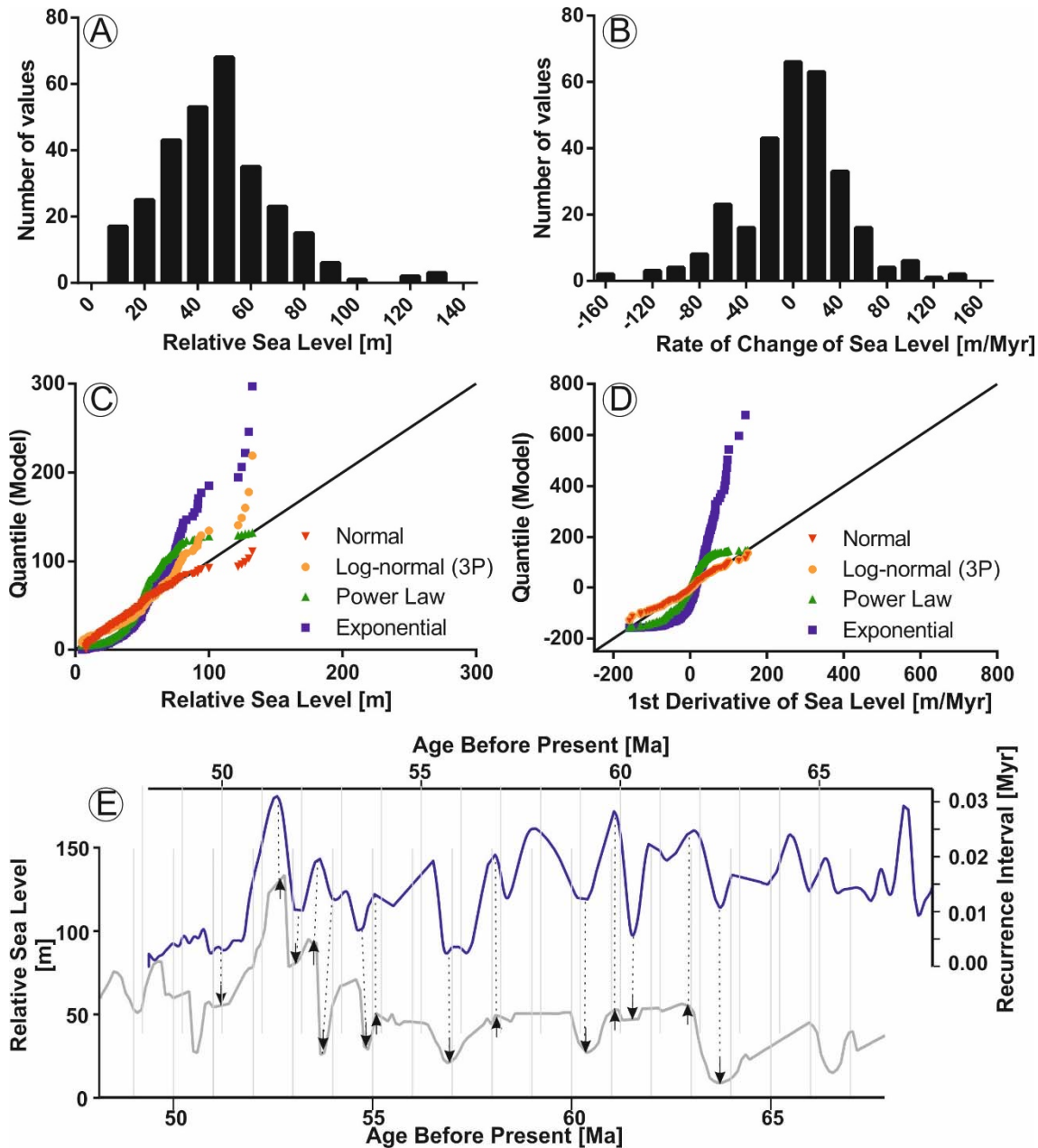


Figure 7.7: Frequency histograms of sea level (A) and rate of change (B) based on analysis of global sea level from Miller et al. (2005) during the studied interval; Quantile-quantile plots for sea level (C) and its rate of change (D) assessing fit to theoretical models; Comparison of global sea level curve and filtered (<95%) recurrence intervals with 1.2 Myr offset (E). Tentative correlation points are annotated with arrows for relative highstands (upwards pointing) and lowstands (downwards pointing).

The efficiency of triggers is inherently linked to the preconditioning of a slope to failure (e.g. through oversteepening, differential loading, development of excess pore pressures). Contribution from one or more of these factors may dilute a sea level or short-

term climatic signal, not least because they may be out of phase with eustatic variations. The timing of external triggers, such as earthquakes, is unlikely to be coincident with sea level changes (Chapter 5); however, some authors have suggested that there may be some correlation (Brothers et al., 2013). No significant result was found when considering the first derivative of sea level as an individual variable ($p=0.795$), nor when its effects are combined with sea level ($p=0.364$) (Table 7.1). This suggests that the rate of change of sea level is not of primary importance to turbidite recurrence at this location.

7.6 Discussion

7.6.1 *Implications of a log-normal distribution of turbidite recurrence for long (>10 Myr) timescales*

A log-normal distribution arises from multiplicative effects of normally or log-normally distributed different variables (Limpert et al., 2001) and, as demonstrated by the analyses here, exhibits serial dependence. A log-normal distribution is likely to be attributable to at least one temporally-ordered process, and this is supported by the results of rescaled range analysis which indicate highly ordered, trend-reinforcing behaviour. A log-normal distribution (Equation 7.3) occurs where the logarithm (\ln) of a variable (\underline{X}) is distributed according to a normal or Gaussian distribution with two parameters, the mean (μ) and the standard deviation (σ).

$$\ln[\underline{X}] \sim N(\mu, \sigma) \text{ (Equation 7.3)}$$

Distributions close to log-normal have been well documented to arise for river flood frequency (Benson, 1968; Bobée, 1975; Bobée et al., 1993, 1995), which may indicate that terrestrial sediment flux delivered by rivers may be in part responsible; however. Such a simple, unique solution to the probability equation may be unlikely, and a log-normal form may arise from all manner of independent variables (Benjamin and Cornell, 1970). It is also possible that the distal position of the Iberian Abyssal Plain has caused a log-normal distribution by a sequential aggregation of probabilities, such as the multiplied probabilities of a slope failure occurring, igniting a turbidity current and that flow making it to the basin plain (i.e. $P(x)=P(a) \times P(b) \times P(c)$). Regardless of the overall control, the key point is that the activity turbidity currents that are recorded in the Iberian Abyssal Plain shows a high degree of temporal order over geological (20 Myr) timescales.

7.6.2 *Differences in distribution form from other deep-sea basins*

The observed log-normal distribution is very different to the exponential recurrence intervals identified in Chapter 5 in three other distal basin plain settings (Clare et al., 2014). This section now explores why these differences may arise. Basin and slope physiography, sediment input, transport distance and/or triggering mechanism(s) are likely to play key roles in determining the form of frequency distribution of flows that reach the abyssal plain. The regional contribution of multiple sources, which may have their own frequency distribution form of recurrence, may lead to signal shredding (e.g. Jerolmack and Paola, 2010). Such a superposition of recurrence intervals could result in an exponential form distribution, whereas only one dominant signal may be seen at the site. Equally, the contribution of multiple triggers or enhanced complexity in sediment transport pathways may also result in a Poisson distribution of flows that travel to the basin plain. It is suggested that the exponential distributions of the Madeira and Balearic Abyssal Plains, Zumaia series and Marnoso-arenacea can be explained by an aggregation of these factors (Figure 7.8). The more complex each of the controlling factors, the closer to an exponential the distal frequency of turbidity currents becomes. The Iberian Abyssal Plain is flanked by only one, relatively broad, slope which is interpreted to have been incised by a proto-equivalent of the Nazare Canyon (Marsaglia et al., 1996; Arzola et al., 2008) which may indicate only one major regional input source. Thus, a primary signal is relatively distinct, and may explain the log-normal distribution.

7.6.3 *What does a common distribution reveal about controls on shorter-term (<1 Myr) turbidite recurrence*

Multiplying or dividing log-normal or normal random variables will result in log-normal distributions (Crow and Shimizu, 1988); hence, it is no surprise that a log-normal distributions is identified for subsets of the full turbidite recurrence record. When normalised to the mean recurrence value (μ) for each of the shorter sub-sets, the data show a very good agreement in terms of the form and spread of log-normal distribution (Figure 7.2). This indicates that only one parameter, the mean recurrence value (μ), is required to explain the variation between the different time periods. Thus, μ can be explained as a scale parameter (Limpert et al., 2001), which affects the scaling in horizontal and vertical directions on probability density function plots, but the shape of the distribution remains the same. This may indicate that, while the mean recurrence varies for different time

periods varies significantly, the mechanics behind turbidity current generation are similar throughout the full record and result in a common frequency distribution form. The mean recurrence value appears to be a key parameter to explain distal turbidite recurrence (Clare et al., 2014; Chapter 5), potentially indicating a common mechanism for landslide-triggered turbidity current generation.

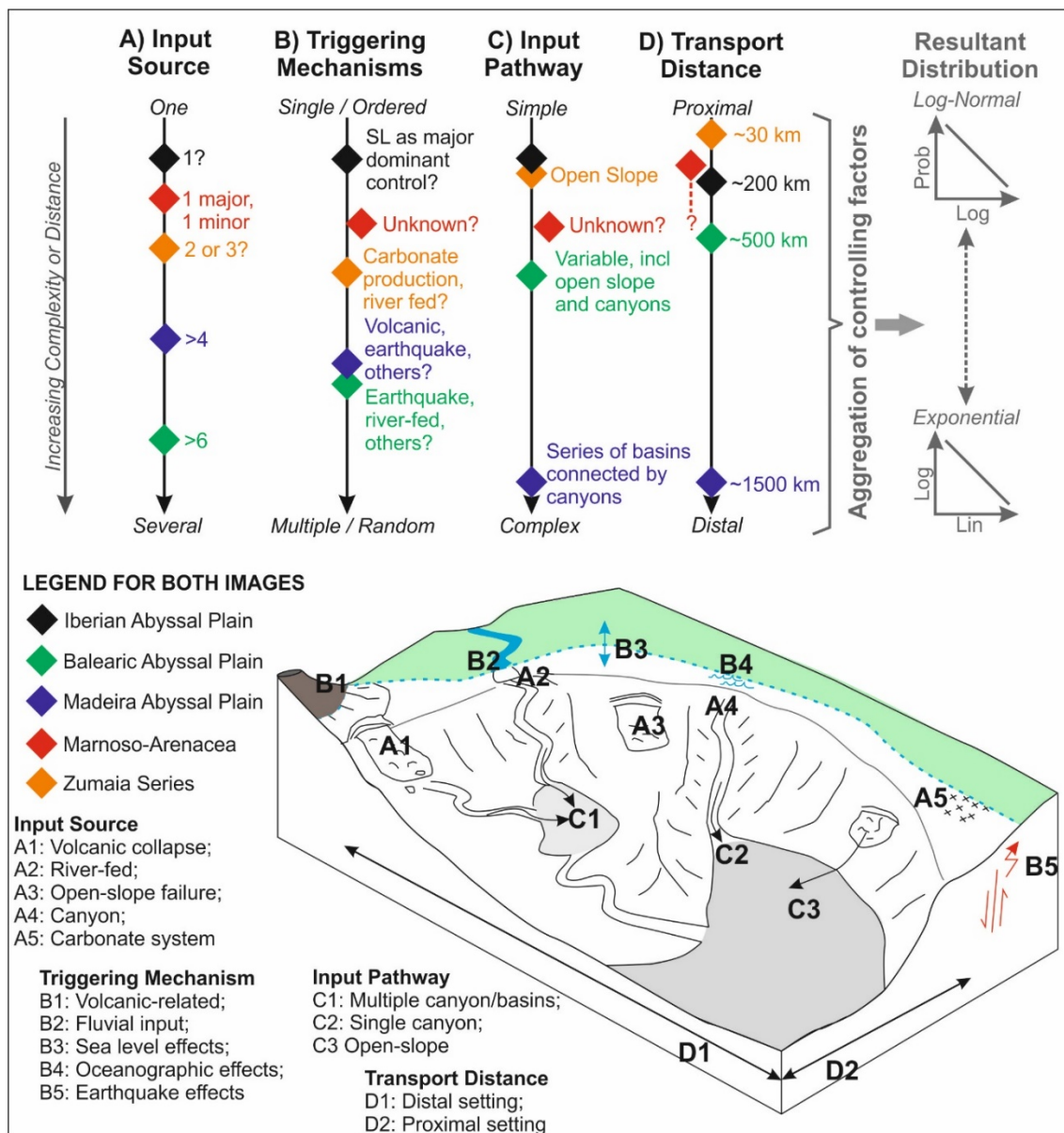


Figure 7.8: Consideration of variables that may affect the frequency distribution of turbidites in deep-sea basin plains. Scales for comparison of input source, triggering mechanism, input pathway and transport distance are relative rather than absolute.

7.6.4 *Long term intensification of turbidity current activity – Tectonic or climate control?*

An overall decrease in turbidite recurrence intervals is identified from 67.61 to 48.16 Ma, albeit with some variations due to temporal clustering (Figure 7.5). If a common frequency distribution may indicate a common triggering mechanism (or a set of mechanisms), then what might be causing this general trend? Tectonic influence might be a credible control that changes over geological (Myr) timescales. In response to variations in tectonic activity, a change in seismicity would be expected and this is a likely trigger for submarine slope instability. Alterations in the tectonic regime may also affect the nature and amount of sediment delivered to the continental shelf and slope, through processes such as rejuvenation of onshore river systems, increasing the distance or breaching barriers to sediment transport. More frequent turbidity current activity generally occurs after ~55 Ma, which is coincident with the onset of right-lateral slip on the Iberian margin which continued to 46 Ma (Roest and Sriverstava, 1991; Rosenbaum et al., 2002). A similar pattern is observed in the Zumaia basin (Bay of Biscay) where a major increase in turbidite frequency at 53.5 Ma (as well as subsequent pulses in activity) is interpreted to be related to tectonic uplift in the incipient Pyrenean chain (Winkler and Gawenda, 1999). The tectonic setting, and hence characteristic seismic activity, is not interpreted to have varied significantly over shorter timescales (<1 Myr) such as those on which eustatic variations occur.

The most pronounced warming trend in the last 65 Ma occurred from the late Palaeocene to early Eocene and peaked at the EECO as shown by a 1.5‰ decrease in $\delta^{18}\text{O}$ (Zachos et al., 2001). A general correlation is observed between the broad trend (2 Myr bins) of more frequent turbidites with gradually increasing global temperature; however, there is a large deviation about this trend (Figure 7.9). The IETM hyperthermal actually corresponds to a significant reduction in turbidity current frequency so this may not hold on short-term timescales (Chapter 6; Clare et al., 2015a). While one cannot preclude the influence of global warming over millions of years it is suggested that the general trend of increasing turbidity current frequency is probably more likely to be explained by tectonic influence or some combination of effects.

The influence of sea level change and more abrupt climatic variations (i.e. IETM, EECO) is now investigated in relation to shorter-term, clustered variations in turbidite recurrence.

7.6.5 *Is sea level a dominant control on short-term turbidite recurrence?*

Global sea level variation (Miller et al., 2005) during the studied interval shows temporal order (normal or 3-parameter log-normal distribution; Figure 7.7). This alone cannot generate the form of log-normal distribution that is seen in recurrence intervals; but, a one to one relationship is unexpected in such a distal setting. The distal turbidite frequency distribution may be due to ‘signal shredding’ related to basin effects (Jerolmack and Paola, 2010); and not all flows make it to the basin plain (Canals, et al., 2006; Talling, 2014). A visual comparison of turbidite recurrence with a global sea level curve appears to show similarity, with periods of longer recurrence intervals (excluding intervals >95%) corresponding to a ~1.2 Myr lag after sea level highstand (Figure 7.7). The results of proportional hazards modelling indicate that sea level shows a statistically significant correlation with turbidite recurrence, albeit with some scatter about the trend (Table 7.1). The rate of sea level change was not, however, observed to exert any significant effect. This may indicate that sea level is a major contributing factor to recurrence for the Iberian Abyssal Plain; however, there are large uncertainties in the model and there are likely to be other factors that cause variation in recurrence.

The apparent ~1.2 Myr lag-effect of sea level may indicate that the Iberian Abyssal Plain is either a regression-dominated system (i.e. increase in turbidite frequency during sea level fall) or a delayed lowstand-dominated (or partially buffered) system (i.e. increase in turbidite frequency after period of low sea level). Both are plausible scenarios (e.g. Allen, 2008; Romans et al., 2009; Covault and Graham, 2010; Covault et al., 2013; Talling, 2014); however, these references are focused on millennial timescales with lags over much shorter periods. Some authors argue that the poles were free of ice during the Late Cretaceous to Eocene interval (Macleod et al., 2011, 2013); however, others suggest that ephemeral, small ice sheets caused glacio-eustatic sea level fluctuations; albeit not on the same frequency as during the late Quaternary (Miller et al., 2003, 2008). As a result, the offset between sea level lowstand and increased turbidite frequency may be in response to slower rates of climate and sea level change than the present day. The

potential causative factors are now explored for a delayed lowstand-dominated or a regression-dominated system (Figure 7.10).

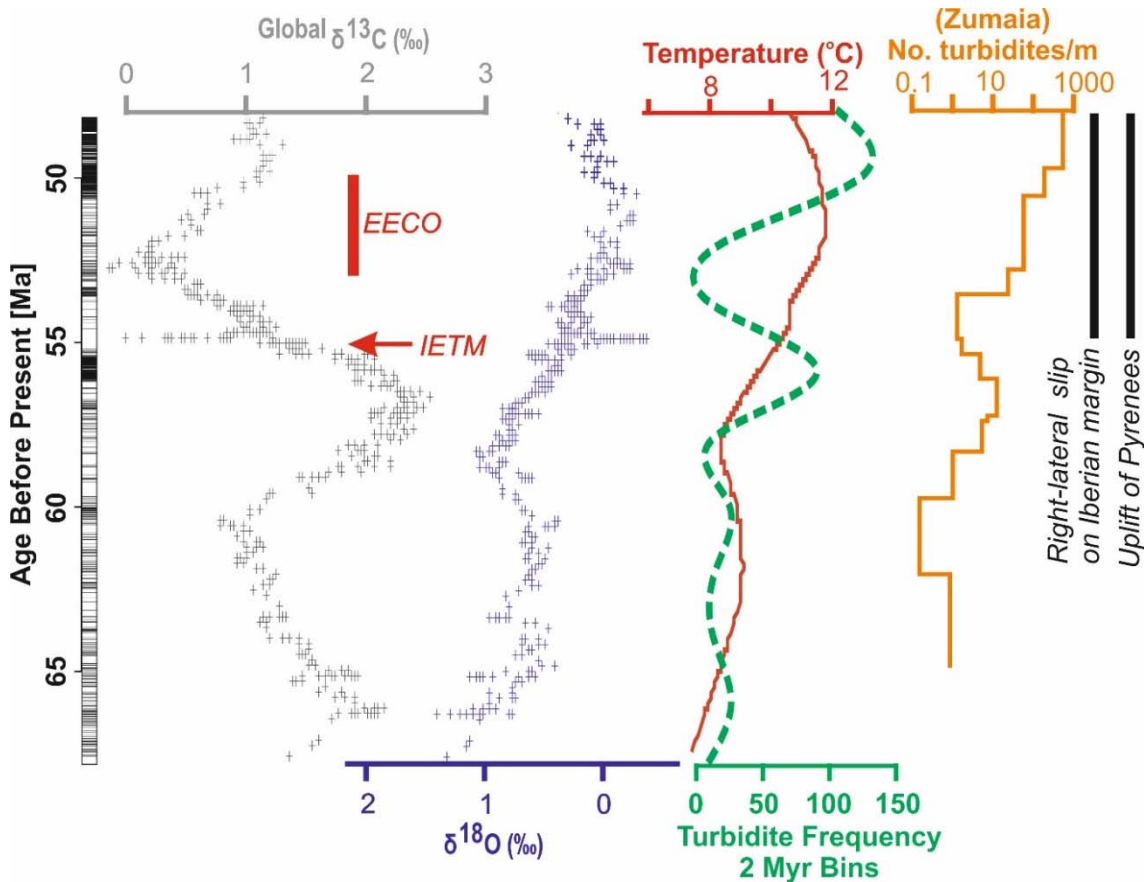


Figure 7.9: Comparison of global carbon and oxygen isotope records (from Zachos et al., 2001) with global temperature (Zachos et al., 2001), turbidite frequency from this study and from Zumaia (Winkler and Gawenda, 1999). Also annotated are key tectonic events in relation to the Iberian margin (Roest and Sriverstava, 1991) and Zumaia (Winkler and Gawenda, 1999).

Direct physiographic alteration by changing sea level state?

Lowstand-dominated systems typically arise where submarine canyons do not fully incise the continental shelf break. During a lowstand, fluvial systems may have better connectivity with the shelf than at a highstand hence supplying more sediment (Covault and Graham, 2010). If recurrence intervals relate to a lag post-highstand, this may be due to delayed onset of landslide activity (e.g. time is needed for pore pressures or slope sediment thickness to reach some critical state), delayed onset of fluvial systems transporting sediment offshore (i.e. slow rejuvenation of the lower river course), sediment being stored in a staging area on the shelf, upper slope, or even within the upper reaches of canyons which may be flushed out once sufficient sediment has accumulated. If increased turbidite frequency is related to a lag after highstand conditions, one might expect to see an effect sooner than ~ 1.2 Myr, however.

Regressive stripping of continental shelf / coastal deposits?

The lowering of sea level may lead to erosion of continental shelf deposits that accumulated during the last marine transgression and highstand. Dahlen et al. (1990) identified Plio-Pleistocene channel systems from the California borderland that were incised during abrupt regressive episodes. Ruiz-Ortiz et al. (2006) suggested that the early Cretaceous turbidite complex of the Cerrajon Formation, southern Spain, was controlled by incision of canyons during sea level regressions. The amplitude and duration of sea level falls during the studied intervals could have led to large amounts of remobilised sediment that could have contributed significantly to deposition on the continental slope and the frequency of turbidity currents.

Climatic effects controlling delivery of sediment from onshore to offshore?

The Iberia turbidite system may actually have been in-phase with long-term climatic fluxes, coincident with periods of sea level regression. That is to say, the sea level state may correlate approximately with turbidite frequency, but it may more likely be the climatic factors that are attributable rather than more simple alterations in the coastline and continental shelf physiography. The offshore Nile Delta is a good example of a turbidite system that shows higher activity during states of sea level change; not because of the relative sea level but due to complex climatic effects that affect terrestrial sediment transport and delivery offshore (rainfall, vegetation cover, surface run-off, erosion etc.; Garziglia et al., 2008; Ducassou et al., 2009). Sustained periods of climatic development may have a pronounced influence on the quantity of sediment delivered to the Iberian continental slope.

Increased contour-current activity on the Iberian margin during sea level highstands?

Periods of pronounced warming (typically coincident with highstands) during the Palaeocene-Eocene have also been hypothesised to cause high evaporation rates in the east Tethys, resulting in intensification of the Tethyan outflow (Corfield and Norris, 1996; Kaminski et al., 1996; Norris et al., 2001). The Tethyan outflow moved north along the Iberian margin and was responsible for Palaeocene-Eocene fine grained contourite deposits sampled on the middle to upper part of the Iberian continental slope (Whitmarsh et al., 1998). If sea level highstands also correspond to an intensification of contour current activity, this may have resulted in an increased thickness of sediments deposited

on the Iberian continental slope. Contourite sequences may have a mounded character creating locally steep slopes, can host more porous layers in which excess pore pressure can develop due to overloading, and may have a large degree of heterogeneity with low shear resistance (Camerlenghi et al., 2010). This combination of factors may progressively predispose contourite sediments to failure, more so than solely hemipelagic accumulations (Masson et al., 2006; Vanneste et al., 2006; Laberg and Camerlenghi, 2008; Minisini and Trincardi, 2009). Dramatic intensification of the eastern boundary current that flowed along the Iberian margin has been indicated at ~49 Ma (Tucholke et al., 1981; Aubry, 1995), which is broadly coincident with the increase in turbidity current frequency towards the end of the studied interval. The time lag of a turbidite frequency increase behind sea level highstand may be explained by the time required to “ripen” slopes to failure. The final triggering mechanism may be consistent (e.g. earthquake trigger) through time (hence a common log-normal distribution), but its efficiency may be greatest once slopes are fully ripened.

It is considered likely that a combination of some or all of the above factors may be responsible. Figure 7.10 illustrates why regressive (or a lag after highstand) conditions may result in an increase in turbidity current frequency at the Iberian margin. A similar scenario, albeit on a much shorter timeframe and on a much smaller scale, is discussed in Chapter 8 for the present day Squamish prodelta where the combination of falling tides (rather than sea level), increased river discharge, and erosion on the delta top are hypothesised to result in an increased frequency of turbidity currents.

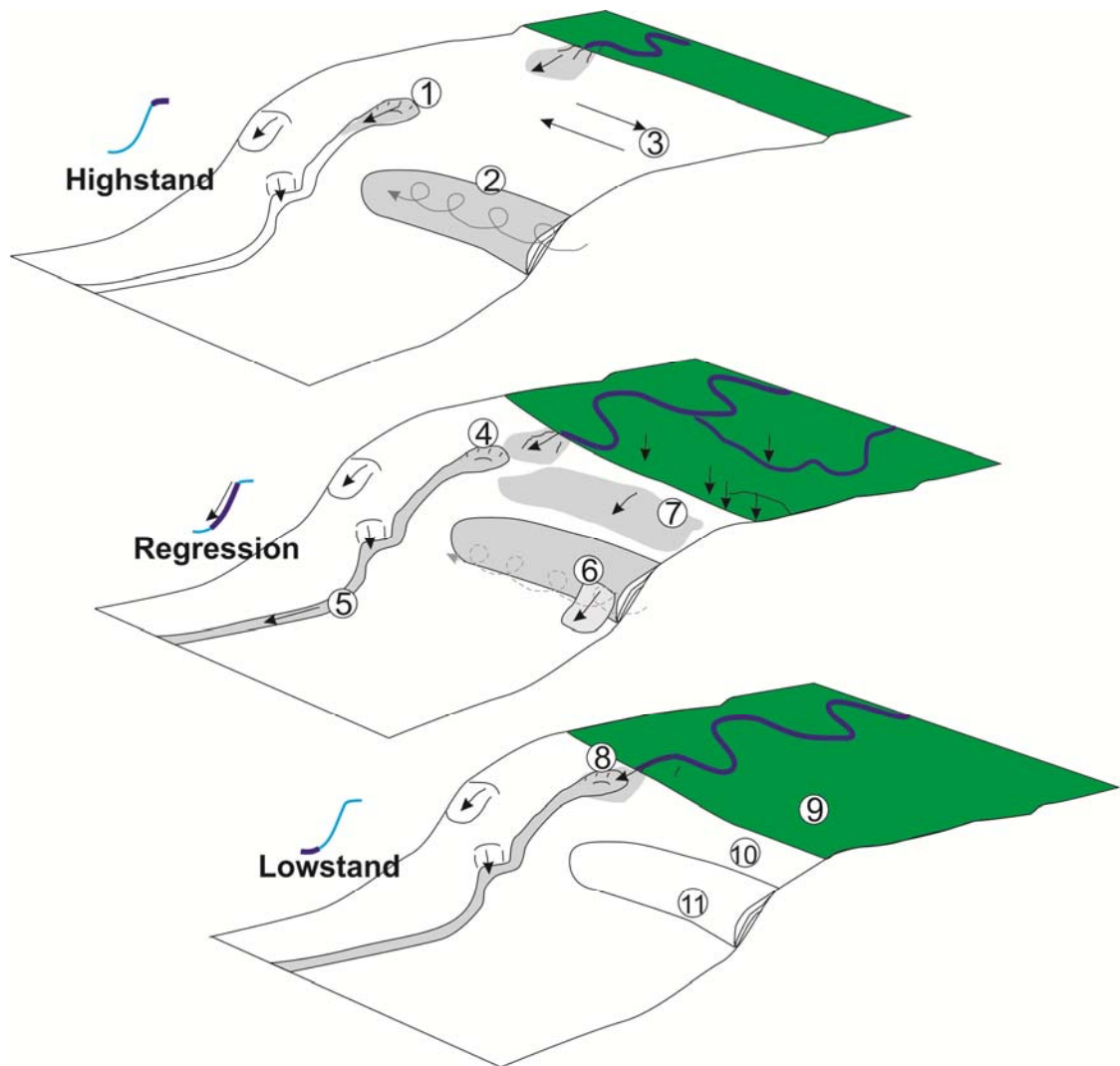


Figure 7.10: Cartoon schematics to illustrate the Iberian margin at different sea level states. Highstand conditions may include (1) disconnection of canyon heads to river input so sediment may only accumulate in the upper reaches of the canyon or the shelf, (2) intensification of contour-current activity causing deposition of contourite mounds or drifts and (3) dispersal of sediment accumulating on the continental shelf by along-shelf currents. Periods of sea level fall (regression) may include (4) improved connection between river and canyon head, (5) possible flushing of sediment accumulated in the canyon during highstand, (6) destabilisation of contourite deposits due to oversteepening, overloading and/or development of excess pore pressures, and (7) dispersal of large amounts of sediment due to incision of wave cut terraces. Contour-current activity thought to reduce as global temperatures cool. Sea level lowstands may result in (8) direct connection of rivers and the submarine canyon; however, there may only be a relatively small sediment supply as sediment was eroded from coastal regions (9) and the narrow shelf (10) during sea level regression. Contour-current activity is significantly reduced in a lowstand and pore pressures are likely to have dissipated. All scenarios may feature open slope and canyon flank failures due to external triggers such as earthquakes, but preconditioning effects may be less pronounced.

7.6.6 *Implications for short-term global warming*

What effects might climate change have on shorter term recurrence? Both the IETM and EECO correspond to periods of low relative turbidity current activity. In the case of the IETM, turbidite frequency is higher in the preceding ~1 Myr which may relate to intensified submarine landslide activity. Could this represent a period of hydrate dissociation that ultimately led to the IETM hyperthermal? This is thought to be unlikely because of the relatively long timescale over which the enhanced activity occurs (i.e. the effects should have been felt sooner). In addition to this, methane released from deep-water marine sediments would only be capable of contributing a relatively small component to the atmosphere. Methane emissions from wetlands may exceed those from gas hydrates hosted in marine sediments, as suggested by isotopic analysis of methane within ice core records (Sowers, 2006). Recent work actually argues that the likely amount of carbon mass input at the onset CIE (4000-7000 PgC) required a major alternative source of carbon in addition to any contribution from methane hydrates (Dunkley-Jones et al., 2010).

The period preceding the EECO does not show a similar intensification of activity to that pre-IETM, so it could be argued that there is no clear evidence for landslide-catalysed global warming at this site. Turbidity current activity appears to slow down during periods of much higher global temperatures in the Iberian Abyssal Plain. This may be related to climatic controls on terrestrial sediment routing. Previous work (Schmitz et al., 2001) showed that the IETM in the Bay of Biscay corresponded to a reduction in sediment delivery from rivers due to modified routing pathways and storage onshore in a sabkha-type setting. A similar scenario could be inferred for the Iberian hinterland. Interestingly, none of the other minor hyperthermals (Elmo, 'X', Late Palaeocene Thermal Event, Top Chron C27n Event, Carbon Isotopic Excursions DS1 and DS2, Dan C-2 Event) show a positive or negative correlation with recurrence, which may suggest that the influence of less dramatic climate change is not seen in the distal basin plain record.

7.6.7 *Implications for future geohazards*

While long term change in global temperature could be tentatively correlated with an overall increase in turbidite frequency, the influence of dramatic short-term climate

change does not appear to have caused any intensification in activity. In fact, these periods (IETM, EECO) correspond to a reduction in turbidity current (and therefore also submarine landslide) activity. Other short-term, minor hyperthermals do not register any significant change at all. This may indicate that climatic effects could have been significant at the Iberian Abyssal Plain for long-term changes in recurrence (i.e. over millions of years), but that increased likelihood of geohazardous events may not necessarily result from short-term man-made global warming. It may not be possible to fully strip apart the effects of gradual global warming and tectonic activity; however, changes in the tectonic regime would not change on human timescales. Therefore a possible tectonic control is of more relevance to understanding controls on sediment transport to the deep sea, rather than societally-relevant geohazards studies. If sea level does indeed exert a dominant control on turbidite recurrence at the Iberian Abyssal Plain, the implications of predicted future sea level rise may lead to a decrease in recurrence, but the effects (reduced frequency) may be delayed by up to ~1.2 Myr.

7.7 Conclusions

An unusually large (N=1571) data set of turbidite recurrence intervals was analysed in this chapter, which covers several major climatic excursions over a period of 20 Myr in the Iberian Abyssal Plain. Therefore, this data set provides unique insights into the influence of climate change on turbidite recurrence. Recurrence intervals conform closely to a log-normal distribution over both the full 20 Myr period, and also for sub-sets of the analysed period. This is in contrast to a previous study of distal basin plain turbidites which indicated an exponential distribution (Clare et al., 2014; Chapter 4). It is suggested that the difference arises from compounding factors including sediment input source, pathway, transport distance and initial triggering mechanisms. The greater the complexity of these combined factors, the less ordered the tempo of flows that make it to a deep-sea basin.

The results of non-parametric and rescaled range statistics, indicate a high degree of temporal order for turbidite recurrence in the Iberian Abyssal Plain. The common log-normal distribution indicates that the mean recurrence interval (rate parameter) varies between clusters. However, the parameter that governs the shape of the distribution does not vary. Therefore the main controlling mechanism for turbidity current generation is inferred to be the same throughout the sequence (causing a log-normal distribution).

A trend of increased turbidite frequency is observed to be coincident with long-term global warming; however clusters of anomalously long recurrence intervals actually occur during the much shorter term warming at the Early Eocene Climatic Optimum (EECO) and Initial Eocene Thermal Maximum (IETM). This is in contrast to many studies that suggest an increase in activity would be more likely (i.e. triggering by hydrate dissociation during hyperthermals can be ruled out at this site). Proportional hazards modelling indicates that sea level exerts a statistically significant control on turbidite recurrence at the Iberian Abyssal Plain, but that intensification in activity occurred approximately ~ 1.2 Myr after periods of sea level highstand. This suggests that, while sea level may exert a control, predicted future rises and global warming may not necessarily result in increased submarine landslide or turbidity current frequency on human timescales.

Table 7.2: Results of non-parametric unpaired Mann-Whitney tests comparing turbidite recurrence between periods defined in Figure 7.5. Bold italicised p-values indicate periods that feature significantly different recurrence ($p < 0.05$)

| Period | versus B | versus C | versus D | versus E | versus F | versus G | versus H | versus I | versus J | versus K |
|----------------------------|----------------------|--------------------------------------|---------------------|--------------------|--------------------------------------|--------------------|----------------------|--------------------|---------------------|---------------------|
| A | | | | | | | | | | |
| P value | < 0.0001 | < 0.0001 | < 0.0001 | < 0.0001 | < 0.0001 | < 0.0001 | < 0.0001 | < 0.0001 | < 0.0001 | < 0.0001 |
| U | 13507 | 21478 | 2774 | 15 | 20545 | 586 | 1311 | 410 | 107 | 2158 |
| Difference of medians | 0.001901 | 0.002291 | 0.01063 | 0.105 | 0.001518 | 0.01861 | 0.003833 | 0.01787 | 0.02021 | 0.01206 |
| Difference: Hodges-Lehmann | 0.001268 | 0.001146 | 0.01006 | 0.0937 | 0.000927 | 0.01861 | 0.004256 | 0.01702 | 0.01936 | 0.01134 |
| 95% CI | 0.0008450 to 0.00169 | 0.000723 to 0.001507 | 0.008545 to 0.01176 | 0.06805 to 0.1947 | 0.0006730 to 0.00135 | 0.01602 to 0.02198 | 0.003217 to 0.005978 | 0.01319 to 0.02170 | 0.01085 to 0.05318 | 0.009231 to 0.01428 |
| B | | | | | | | | | | |
| P value | - | 0.0915 | < 0.0001 | < 0.0001 | 0.041 | < 0.0001 | < 0.0001 | < 0.0001 | < 0.0001 | < 0.0001 |
| U | - | 26113 | 6025 | 64 | 24279 | 1897 | 3483 | 1402 | 405 | 6193 |
| Difference of medians | - | 0.0003905 | 0.008732 | 0.1031 | -0.0003825 | 0.01671 | 0.001933 | 0.01597 | 0.01831 | 0.01015 |
| Difference: Hodges-Lehmann | - | -0.000182 | 0.007706 | 0.0937 | -0.000429 | 0.01645 | 0.002566 | 0.01384 | 0.01641 | 0.009637 |
| 95% CI | - | -0.0007260 to 5.800x10 ⁻⁵ | 0.00588 to 0.009649 | 0.06130 to 0.1943 | -0.000931 to -6.000x10 ⁻⁶ | 0.01311 to 0.02003 | 0.001494 to 0.003866 | 0.01108 to 0.01897 | 0.008935 to 0.05104 | 0.005867 to 0.01258 |
| C | | | | | | | | | | |
| P value | - | - | < 0.0001 | < 0.0001 | 0.1562 | < 0.0001 | < 0.0001 | < 0.0001 | < 0.0001 | < 0.0001 |
| U | - | - | 7269 | 48 | 35675 | 1770 | 4591 | 1501 | 435 | 7598 |
| Difference: Actual | - | - | 0.008341 | 0.1027 | -0.000773 | 0.01632 | 0.001542 | 0.01558 | 0.01792 | 0.009764 |
| Difference: Hodges-Lehmann | - | - | 0.008218 | 0.09391 | -0.000193 | 0.01704 | 0.003098 | 0.01491 | 0.01713 | 0.0102 |
| 95% CI | - | - | 0.006505 to 0.01017 | 0.0651 to 0.1943 | -0.0003870 to 8.200x10 ⁻⁵ | 0.01420 to 0.02047 | 0.001555 to 0.003894 | 0.01165 to 0.01949 | 0.008935 to 0.05068 | 0.007256 to 0.01314 |
| D | | | | | | | | | | |
| P value | - | - | - | 0.0003 | < 0.0001 | 0.0003 | 0.0069 | 0.0014 | 0.0117 | 0.1763 |
| U | - | - | - | 222 | 7057 | 4769 | 3295 | 3684 | 982 | 10866 |

| | | | | | | | | | | |
|----------------------------|---|---|---|-------------------|-----------------------|---------------------|-------------------------|-----------------------|----------------------|------------------------|
| Difference of medians | - | - | - | 0.09441 | -0.009114 | 0.007982 | -0.006799 | 0.007236 | 0.009576 | 0.001423 |
| Difference: Hodges-Lehmann | - | - | - | 0.08953 | -0.008376 | 0.006425 | -0.004289 | 0.006433 | 0.009327 | 0.000699 |
| 95% CI | - | - | - | 0.03687 to 0.1857 | -0.01050 to -0.006604 | 0.002860 to 0.01162 | -0.007057 to -0.0009750 | 0.002329 to 0.01043 | 0.00231 to 0.03972 | -0.001165 to 0.00364 |
| E | | | | | | | | | | |
| P value | - | - | - | - | < 0.0001 | 0.0027 | < 0.0001 | 0.0029 | < 0.0001 | < 0.0001 |
| U | - | - | - | - | 53 | 195 | 50 | 147 | 417 | 6685 |
| Difference of medians | - | - | - | - | -0.1035 | -0.08642 | -0.1012 | -0.08717 | 0.01869 | 0.01054 |
| Difference: Hodges-Lehmann | - | - | - | - | -0.09353 | -0.07873 | -0.09178 | -0.08242 | 0.01751 | 0.01057 |
| 95% CI | - | - | - | - | -0.1945 to -0.06468 | -0.1758 to -0.02235 | -0.1928 to -0.04032 | -0.1787 to -0.02752 | 0.009286 to 0.05087 | 0.007585 to 0.01344 |
| F | | | | | | | | | | |
| P value | - | - | - | - | - | < 0.0001 | < 0.0001 | < 0.0001 | < 0.0001 | < 0.0001 |
| U | - | - | - | - | - | 1735 | 4186 | 1480 | 417 | 6685 |
| Difference of medians | - | - | - | - | - | 0.0171 | 0.002315 | 0.01635 | 0.01869 | 0.01054 |
| Difference: Hodges-Lehmann | - | - | - | - | - | 0.01695 | 0.00345 | 0.01517 | 0.01751 | 0.01057 |
| 95% CI | - | - | - | - | - | 0.01438 to 0.02055 | 0.001748 to 0.004087 | 0.01167 to 0.01985 | 0.009286 to 0.05087 | 0.007585 to 0.01344 |
| G | | | | | | | | | | |
| P value | - | - | - | - | - | - | < 0.0001 | 0.8447 | 0.458 | 0.0043 |
| U | - | - | - | - | - | - | 1227 | 3242 | 874.5 | 6147 |
| Difference of medians | - | - | - | - | - | - | -0.01478 | -0.000746 | 0.001594 | -0.006559 |
| Difference: Hodges-Lehmann | - | - | - | - | - | - | -0.0124 | -0.000282 | 0.00372 | -0.004668 |
| 95% CI | - | - | - | - | - | - | -0.01712 to -0.006328 | -0.005637 to 0.004492 | -0.005524 to 0.02583 | -0.009507 to -0.001737 |
| H | | | | | | | | | | |
| P value | - | - | - | - | - | - | - | < 0.0001 | < 0.0001 | < 0.0001 |
| U | - | - | - | - | - | - | - | 996.5 | 276 | 3202 |

| | | | | | | | | | | |
|----------------------------|---|---|---|---|---|---|---|---------------------|----------------------|------------------------|
| Difference of medians | - | - | - | - | - | - | - | 0.01404 | 0.01638 | 0.008222 |
| Difference: Hodges-Lehmann | - | - | - | - | - | - | - | 0.009357 | 0.01404 | 0.004679 |
| 95% CI | - | - | - | - | - | - | - | 0.007018 to 0.01637 | 0.004679 to 0.04912 | 0.001204 to 0.009426 |
| I | | | | | | | | | | |
| P value | - | - | - | - | - | - | - | - | 0.4043 | 0.0337 |
| U | - | - | - | - | - | - | - | - | 655.5 | 4930 |
| Difference of medians | - | - | - | - | - | - | - | - | 0.00234 | -0.005813 |
| Difference: Hodges-Lehmann | - | - | - | - | - | - | - | - | 0.004678 | -0.005676 |
| 95% CI | - | - | - | - | - | - | - | - | -0.004678 to 0.03275 | -0.008755 to -0.001066 |
| J | - | - | - | - | - | - | - | - | - | |
| P value | - | - | - | - | - | - | - | - | - | 0.0266 |
| U | - | - | - | - | - | - | - | - | - | 1243 |
| Difference of medians | - | - | - | - | - | - | - | - | - | -0.008153 |
| Difference: Hodges-Lehmann | - | - | - | - | - | - | - | - | - | -0.008755 |
| 95% CI | - | - | - | - | - | - | - | - | - | -0.03555 to -0.001737 |

Table 7.3: Results of non-parametric unpaired Kolmogorov-Smirnov tests comparing turbidite recurrence between periods defined in Figure 7.5. Bold italicised p-values indicate periods that feature significantly different recurrence ($p < 0.05$)

| Period | versus B | versus C | versus D | versus E | versus F | versus G | versus H | versus I | versus J | versus K |
|----------|--------------------|--------------------|--------------------|--------------------|--------------------|--------------------|--------------------|--------------------|--------------------|--------------------|
| A | | | | | | | | | | |
| P value | < 0.0001 | < 0.0001 | < 0.0001 | < 0.0001 | < 0.0001 | < 0.0001 | < 0.0001 | < 0.0001 | < 0.0001 | < 0.0001 |
| K-S D | 0.3555 | 0.3686 | 0.7137 | 0.9719 | 0.3757 | 0.8712 | 0.7912 | 0.8653 | 0.8881 | 0.8334 |
| B | | | | | | | | | | |
| P value | - | 0.015 | < 0.0001 | < 0.0001 | 0.0049 | < 0.0001 | < 0.0001 | < 0.0001 | < 0.0001 | < 0.0001 |
| K-S D | - | 0.1439 | 0.5132 | 0.8416 | 0.1612 | 0.6762 | 0.4356 | 0.7023 | 0.6808 | 0.4982 |
| C | | | | | | | | | | |
| P value | - | - | < 0.0001 | < 0.0001 | < 0.0001 | < 0.0001 | < 0.0001 | < 0.0001 | < 0.0001 | < 0.0001 |
| K-S D | - | - | 0.581 | 0.9155 | 0.2087 | 0.7407 | 0.4225 | 0.7782 | 0.7567 | 0.5807 |
| D | | | | | | | | | | |
| P value | - | - | - | 0.0012 | < 0.0001 | 0.0005 | 0.0025 | 0.0064 | 0.0519 | 0.0019 |
| K-S D | - | - | - | 0.6296 | 0.5816 | 0.2719 | 0.2801 | 0.2465 | 0.3159 | 0.2124 |
| E | | | | | | | | | | |
| P value | - | - | - | - | < 0.0001 | 0.0035 | < 0.0001 | 0.0047 | 0.1953 | 0.0008 |
| K-S D | - | - | - | - | 0.9037 | 0.5925 | 0.7672 | 0.5873 | 0.4143 | 0.6464 |
| F | | | | | | | | | | |
| P value | - | - | - | - | - | < 0.0001 | < 0.0001 | < 0.0001 | < 0.0001 | < 0.0001 |
| K-S D | - | - | - | - | - | 0.7421 | 0.4444 | 0.7532 | 0.7317 | 0.5644 |
| G | | | | | | | | | | |
| P value | - | - | - | - | - | - | < 0.0001 | 0.4838 | 0.2519 | 0.0014 |
| K-S D | - | - | - | - | - | - | 0.456 | 0.1321 | 0.2458 | 0.246 |
| H | | | | | | | | | | |
| P value | - | - | - | - | - | - | - | < 0.0001 | 0.009 | 0.0002 |
| K-S D | - | - | - | - | - | - | - | 0.4375 | 0.4161 | 0.3219 |
| I | | | | | | | | | | |
| P value | - | - | - | - | - | - | - | - | 0.2249 | 0.0043 |
| K-S D | - | - | - | - | - | - | - | - | 0.2596 | 0.2482 |
| J | | | | | | | | | | |
| P value | - | - | - | - | - | - | - | - | - | 0.0366 |
| K-S D | - | - | - | - | - | - | - | - | - | 0.3274 |

Chapter 8. Mass failure and turbidity current frequency at a modern bedload-dominated submarine river delta

Summary

Unlike the previous three chapters, this chapter considers very short-term (hours to days) recurrence of turbidity currents. An analysis of the most extensive monitoring dataset of turbidity currents yet collected is presented, comprising in excess of 100 turbidity current events, some of which were triggered by major delta lip collapses. In this analysis, for the first time, it is possible to statistically test for the significance of river discharge, tidal elevation and other related parameters in relation to flow timing and recurrence. The implications for triggers of mass failure and flows at offshore river deltas is then discussed.

This chapter will be submitted in an abridged format to *Geology* (July, 2015). All analyses and interpretations were completed by me, with editorial help provided by the co-authors during paper writing. John Hughes Clarke provided repeat multibeam echosounder survey and ADCP data. The offshore Squamish team, particularly Gord Allison, are thanked for their efforts to provide access to such high quality data.

How are mass failures and sediment flows triggered at offshore bedload-dominated river deltas?

Clare, M.A.¹, Hughes Clarke, J.E.², Talling, P.J.¹, and Cartigny, M.J.¹

¹National Oceanography Centre, European Way, Southampton, Hampshire, SO14 3ZH

²Department of Geodesy and Geomatics Engineering, University of New Brunswick, Canada

ABSTRACT

Rivers and offshore turbidity currents are probably the two most volumetrically important sediment transport processes on Earth, and form its most extensive sedimentary deposits. It is thus important to understand how these two types of sediment-and-water flow are linked. It has been proposed that processes that trigger turbidity currents at offshore river deltas may include hyperpycnal flows, tidal effects, elevated bed shear stresses, and earthquakes, but these hypotheses are poorly tested in a quantified manner. In this study, a suite of statistical tests is applied to quantify their significance, based on an unprecedented record of failures and flows. Most previous studies have observed less than ten events which has not allowed for robust statistical analysis. The submarine delta at Squamish, British Columbia provides an exceptional natural laboratory where 106 turbidity currents were monitored over 147 days during 2011. This dataset provides sufficient number of observations for statistical analysis of event timing, frequency and triggers. Elevated periods of river discharge are shown to be a significant control on when the turbidity current system ‘switches on’ (i.e. becomes active). The combined effects of river discharge and tidal elevation, interpreted to cause elevated bed shear stresses on the delta lip, are the most significant controls on flow timing. Of these two factors, river discharge is the dominant control on flow recurrence, as the seasonal discharge maximum correlates with more frequent flows. Each 1 m³/s increase in river discharge explains a 1% increase in offshore sediment flow likelihood, once a critical threshold is reached. The largest peaks in river discharge do not create hyperpycnal flows, however, and instead result in delayed delta lip failures. Delta lip failures may also occur during periods of lower sediment input, which appears to be promoted by low tide conditions. This study provides new insights into the dynamics and frequency of submarine deltas which has wide implications for hazard assessment and understanding deep-sea sediment transport.

8.1 Introduction

Rivers and offshore turbidity currents are probably the two most volumetrically important sediment transport processes on Earth, and form its most extensive sedimentary deposits. It is thus important to understand how these two types of sediment-and-water flow are linked. For instance, how do changes in discharge from the river affect the frequency and character of turbidity currents, and how exactly are turbidity currents triggered immediately offshore from river mouths?

It has been proposed that turbidity currents can be triggered in several different ways within river-fed systems (Forel, 1888; Mulder et al., 2003; Piper and Normark, 2009; Talling, 2014). First, if the river-water has enough suspended sediment to make it dense enough to plunge, it may continue to form a submerged turbidity current (Forel, 1888; Mulder and Syvitski, 1995; Parsons et al., 2001; Mulder et al., 2003). Such hyperpycnal flows will be more common in lakes than in the sea, as less sediment is necessary to cause an excess density in freshwater, but it has been suggested that hyperpycnal turbidity currents may also be common in some marine settings (Mulder et al., 1998, 2003). Required densities for generation of plunging river water have been indicated in the range of 36 to 43 kg/m³ (Mulder and Syvitski, 1995). Optical backscatter measurements of water column densities by Hughes Clarke et al. (2013) indicate sediment concentrations in the river plume do not exceed 0.4 kg/m³. Thus, the required density surfeit for hyperpycnal flow is not reached. An alternative mechanism is proposed by Hughes Clarke et al. (2013) that invokes periodic, localised mixing of the freshwater-saline interface (inferred at densities of <1 kg/m³ by Parsons et al., 2001). This convective fingering may be important for the generation of frequent, relatively small flows at the Squamish Prodelta. Second, as flow expands at the coast, rapid sediment deposition may create particularly unstable submerged slopes that are prone to fail, resulting in turbidity currents triggered by slope failure (Prior et al., 1987; Carter et al., 2012). Such rapid deposition can result from bedload transport or sediment settling from surface plumes. Third, low tides may cause sediment unloading and the expansion of gas bubbles within the sediment, thereby promoting slope failure (Christian et al., 1997a, 1998). Narrowing of mouth bar channels during low tides may also be important to focus sedimentation and offshore plumes of sediment. River discharge is typically concentrated in narrower channels at low tide, producing increased bedload transport rates, flushing of mouth bar sediments during river floods, and localised deposition (Prior et al., 1987; Hughes Clarke

et al., 2012). There is some uncertainty as to whether the sediment transported as river bedload is redeposited offshore and then fails as a two-stage process (Prior et al., 1987). Fourth, earthquakes may specifically trigger slope failure. Fifth, rapidly deposited organic carbon-rich river sediment generates gas-rich deposits that are prone to failure, especially at very low tides (Christiansen et al., 1988). Finally, it is possible that bedload swept offshore may avalanche down steeply-inclined (40°) foresets on Gilbert-type delta (Gilbert, 1885), accelerate and continue to move as a turbidity current (Postma et al., 1988) down more gentle slopes of 3° to 4° . Considerable debate surrounds the relative importance of these five different triggers for turbidity currents in river-fed systems, and there is a compelling need to test these alternative hypotheses (Figure 8.1).

Understanding what controls the frequency of turbidity currents, and offshore slope failures is important for more practical purposes. Turbidity currents may cause serious damage to communications cables that have considerable strategic importance (Carter et al., 2014), or expensive offshore infrastructure used for oil and gas recovery (Bruschi et al., 2006). Larger submarine slope failures can produce tsunamis that pose a potentially serious hazard to local coastal communities. For instance, slope failures generated tsunamis that ran up to heights of 6 to 7 m at Kitimat, British Columbia in 1974 and 1975 (Prior et al., 1982a,b). It is important to understand what controls the frequency of turbidity currents and slope failures on deltas for such geohazard analysis.

The main difficulty at present is that very few field data sets document the exact timing of turbidity currents and submerged slope failures, as these events are very difficult to monitor directly (Inman et al., 1976; Talling, 2014; Chapter 1). Such information on event timing is key for determining the relative importance of river discharge, tides, or other triggering or preconditioning factors. A significant number of events are needed for robust statistical analysis that investigates the relative importance of these factors. No previous direct monitoring study has documented the timing of more than a few tens of flows, and in most cases many fewer than ten (e.g. Prior et al., 1987 at Bute Inlet; Lambert and Giovanoli, 1988 in Lake Geneva; Carter et al., 2012, 2014 in Gaoping Canyon; Cooper et al., 2013 in Congo Canyon; Xu et al., 2014 in Monterey Canyon; Chapter 1). Statistical analysis of event frequency and triggers has therefore typically been restricted to much less precisely dated turbidity current and landslide events in the sedimentary record. The larger uncertainties in the timing of these older events has ensured that this timing cannot be compared easily to information on river discharge or individual tidal

cycles, with comparisons only being possible with longer-term processes such as sea level change (e.g. Droxler and Schlager, 1985; Weaver et al., 1992; Urlaub et al., 2012; Clare et al., 2014; Chapters 5 and 7).

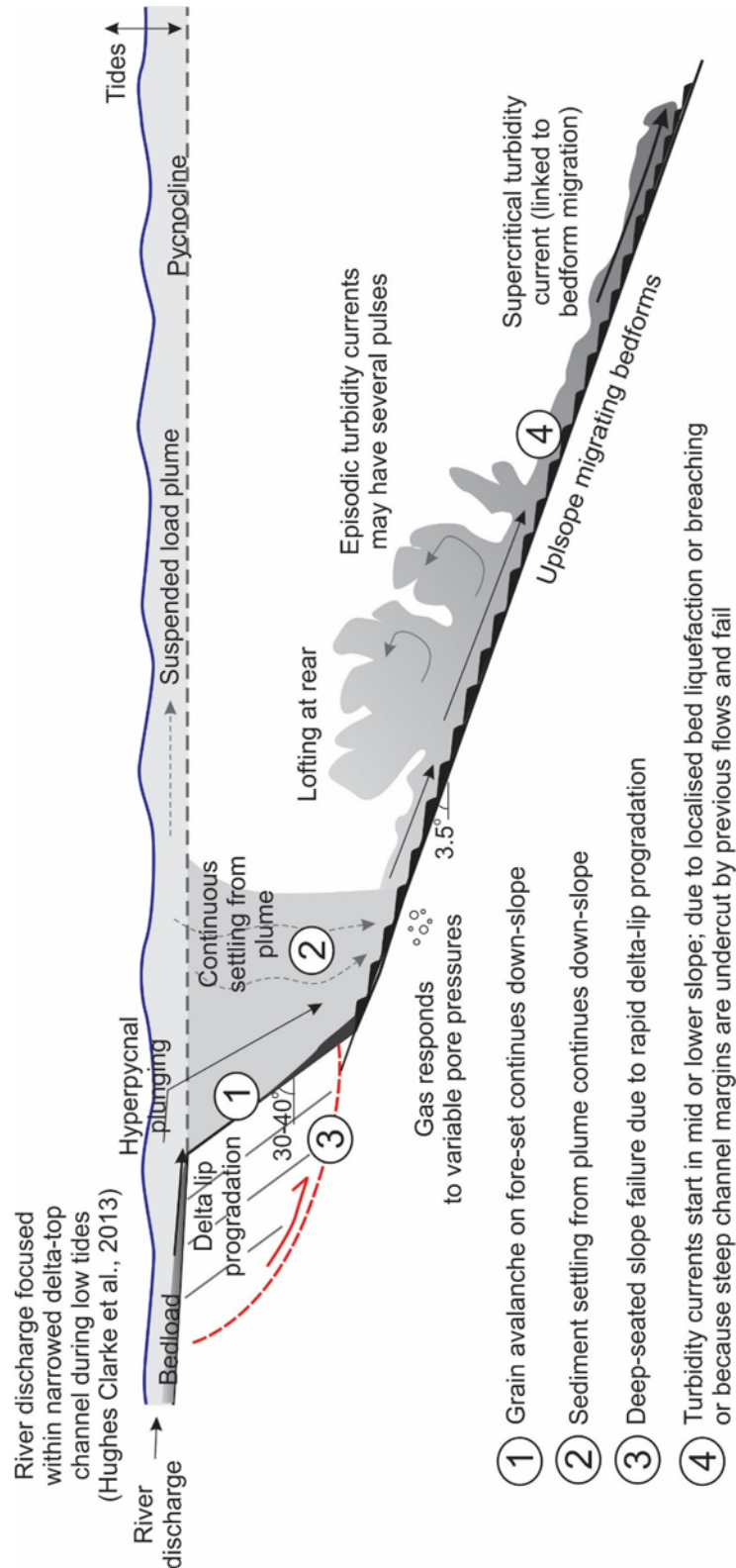


Figure 8.1: Illustration of various hypotheses for the triggering of slides and flows at offshore bedload-dominated river deltas. Slope angles based on Squamish Prodelta example.

Here the first statistical analysis is performed, of what is believed to be the only direct monitoring study to document the timing of more than 100 individual events. This unique field dataset comes from Squamish Delta in British Columbia, Canada (Hughes Clarke et al., 2012, 2013; Figure 8.2). It comprises both observations from a mooring (using an Acoustic Doppler Current Profiler or ADCP), and 93 repeat surveys of the seafloor that document the timing and character of changes in seafloor morphology. Hughes Clarke et al. (2012, 2013) have previously shown how two distinct types of event are recorded in this dataset. Large-scale, deep-seated failures of the prograding delta-lip (“delta-lip collapses”) occur relatively infrequently, and involve 20,000 to 150,000 m³ of material. Much more frequent events are associated with the up-slope migration of bedforms (“bedform events”). The events that cause bedform migration can be associated with smaller-scale failure at the delta lip, but many of these events start without a clearly discernible slope-failure scar, or at locations well beyond (>100 m) the delta-lip (Hughes Clarke, 2012, 2013).

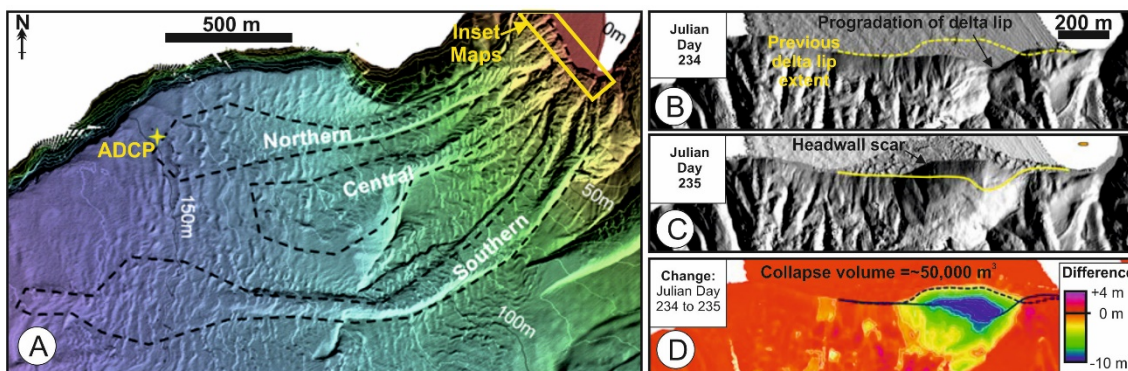


Figure 8.2: Location of northern, central and southern channels (A). ADCP location is yellow star at outflow of northern channel (modified from Hughes Clarke et al., 2012); Bathymetry before (B) and after (C) large delta lip failure. Difference map (D) clearly shows area of failure.

8.2 Aims

The first aim is to determine whether there is a statistically significant relationship between river discharge and tidal elevation, and the observed frequency of submarine flow events that (i) move bedforms or (ii) cause larger-scale delta-lip failures. If there is such a relationship, is river discharge or tidal elevation a stronger control on event frequency, and do these two factors have independent or combined effects on flow frequency? The implications of these statistical associations is then discussed for understanding the physical mechanisms that trigger these flows. The second aim is to better understand how turbidity currents and slope failures are preconditioned and

triggered in this type of delta system. The relative importance of processes is assessed, including plunging hyperpycnal river discharge, slope failure due to rapid sediment deposition, earthquakes, or expansion of gassy sediment at low tides, and avalanching bedload on steep foresets. This study is novel because it provides unique insights into the relationship between the timing and triggers of submarine flows due to the remarkable number of events observed. This chapter concludes with remarks on the implications of the results for geohazard analysis in such settings.

Table 8.1: Natural triggering mechanisms hypothesised for slope failures and flows at offshore river deltas

| Control | Trigger Mechanism | Nature of failures/flows | Reference |
|------------------------|--|--|--|
| River Discharge | Carried immediately into subaqueous channel system as turbidity currents or forms turbidity current from sediment settling out from river plume | Near-continuous flows coincident with peak of flood event | Mulder and Syvitski (1995); Mulder et al. (2003); Parsons et al. (2001); Bornhold et al. (1994); Hughes Clarke et al. (2013) |
| | Sediments reside temporarily on parts of the delta slope to be later remobilised as they become more unstable | Pulses of turbidity currents following main flood event | Bornhold et al. (1994); Hughes Clarke et al. (2012, 2013) |
| | Sediment accumulates steadily during relatively low discharge periods but is subjected to very rapid erosion due to high bed shear stresses during high river discharge. | River discharge sweeps accumulated coarse-grained bar and channel sediments (with any bedload) directly onto the steep delta front slopes | Prior and Bornhold (1989); Bornhold and Prior (1990); Bornhold et al. (1994) |
| | Bedload swept offshore may avalanche down steeply-inclined foresets on Gilbert-type delta | Sediment accelerates down inclined foresets and transitions into a turbidity current | Gilbert (1885); Postma et al. (1988) |
| Tidal Variations | Excess pore pressures in low permeability materials during low tides triggers liquefaction | Transient pore pressure changes cause liquefaction which leads to slope instability (unlikely to have any effect >1 m below seafloor) | Johns et al. (1986); Chillarige et al. (1994, 1997) |
| | Tidal drawdown on gaseous sediments | Reduction in effective stress during lowered tides where gas can be brought out of solution to trigger deep-seated failure | Christian et al. (1997); Chillarige et al. (1997); Hughes Clarke et al. (2012, 2013) |
| | Constriction of delta-top channel during low tide | Constriction of channel leads to elevated bed shear stresses causing erosion, and deposition on delta lip or triggering of sediment avalanches | Prior and Bornhold (1989); Bornhold and Prior (1990); Hughes Clarke et al. (2012, 2013) |
| Mid-prodelta processes | Localised liquefaction or breaching within submarine channels or incision of steep margins by previous flow(s) | Triggers turbidity current on mid to lower prodelta slope | Van Den Berg et al. (2002); Mastbergen and Van Den Berg (2003) |
| Earthquakes | Strong ground motion and development of transient excess pore pressures | Destabilisation of slope sediments due to shaking, liquefaction or strain softening | Prior and Bornhold (1989); Bornhold and Prior (1990); Bornhold et al. (1994) |

8.3 Methods

8.3.1 Squamish delta: An outstanding natural laboratory

The Squamish Delta receives more than one million cubic metres of sediment per year and flows into the Howe Sound (Hughes Clarke et al., 2012; Chapter 2). The delta is heavily influenced by the spring melt, as the winter discharge of $\sim 100 \text{ m}^3/\text{s}$ increases in the freshet to $>500 \text{ m}^3/\text{s}$, with peaks of up to $1,000 \text{ m}^3/\text{s}$. Spring tidal range may reach 5 m whereas neap tides have a range of $\sim 3 \text{ m}$. At low-water spring-tides, the river discharge is focused within a sub-tidal channel of 1 m depth and 200 m width where it reaches the delta lip. Seaward of the delta lip are three main channels, termed “northern”, “central” and “southern” channels (Figure 8.2). At a distance of 2 km from the delta lip, these channels open out and flows are unconfined (Figure 8.2).

Squamish Delta is an exceptionally well monitored landslide-turbidity current system as numerous multibeam surveys have been collected over eight years. Here the results of 93 surveys performed in 2011 (Hughes Clarke et al., 2012) are analysed. In addition to the multibeam surveys, an upwards-looking ADCP was installed for 147 days beyond the northern channel (yellow star in Figure 8.2). This ADCP recorded the arrival of events to within 30-seconds. During the period of study, 106 flow events were recorded, which facilitates statistical analysis. Hourly information is available for tidal elevation and river discharge to the delta. Figure 8.3 provides information on the occurrence of earthquakes during the study period.

8.3.2 Repeat multibeam echo-sounder (MBES) surveys

Surveys were conducted every month throughout the winter, but at the start of the freshet surveys were conducted on every weekday (Hughes Clarke et al., 2011, 2012). The delta-top channel and prodelta slope were surveyed to water depths of $\sim 200 \text{ m}$. Repeat surveys enabled the production of difference maps to observe daily change during the freshet (Chapter 3). Previous work has shown that vertical changes of $>0.5 \text{ m}$ (minimum resolvable interval) are related to slope failures and turbidity current processes (Hughes Clarke et al., 2012, 2013). The minimum resolution of vertical change is 0.1 % of water depth (Hughes Clarke et al., 2012). Therefore, the lowest resolution equates to 0.2 m in the deepest water (200 m), with progressive enhancement in shallower waters.

Two main types of bathymetric change are observed. The first type of events are termed “delta-lip failures” that represent large ($>20,000 \text{ m}^3$) collapses of the delta lip (Figure 8.2). Five such events were observed in the 2011 survey campaign, referred to here as events A to E. The second type of event causes the upslope migration of bedforms within channels, termed “bedform events”. This bedform migration is interpreted to be due to supercritical turbidity currents causing cyclic steps (Hughes Clarke et al., 2012, 2013; Cartigny et al., 2014). Some of these bedform events are associated with smaller-scale failures near the delta lip, but other bedform events start mid-slope without an obvious landslide scar. Channel events have been sub-classified as “major” (clearly noticeable change, significantly above resolution of MBES, $>0.5 \text{ m}$) and “minor” (discernible change, above resolution limits of MBES data, $<0.5 \text{ m}$). As the timing of an event can only be resolved to the nearest 24 hours during the freshet, the minimum recurrence interval that can be resolved is one day. All times are presented as Julian days since the start of 2011. A total of 106 discrete MBES events were identified, with 49 in the north, 29 in the central and 28 in the south channel (Figure 8.3).

8.3.3 Acoustic Doppler current profiler (ADCP) monitoring

An upwards facing 600 kHz ADCP was deployed to provide more precise constraints on flow timing and to measure flow properties on the distal lobe. The ADCP was located 150 m seaward from the termination of the North Channel, hosted on a bottom mounted tripod. It measured a velocity profile every 30 seconds, to a height of 47 m above the instrument, with 0.5 m vertical bins. Deployment was continuous from 29th March 2011 (Julian Day 088) to 23rd August 2011 (JD235), with the exception of a 20 day period from 30th June to 20th July (JD181-201) when the ADCP was buried due to a major delta-lip failure event.

MBES repeat surveys defined 49 flow events that caused morphological change in the northern channel. However, only 22 of these events were discernible at the more distal ADCP location (Figure 8.2). At the ADCP location, flow speeds were recorded the region of 0.3 to 1.5 m/s, with thicknesses from 10 m to 40 m, and lasted over one hour. Material suspended in the plume took more than 8 hours to decay away (Hughes Clarke et al., 2012).

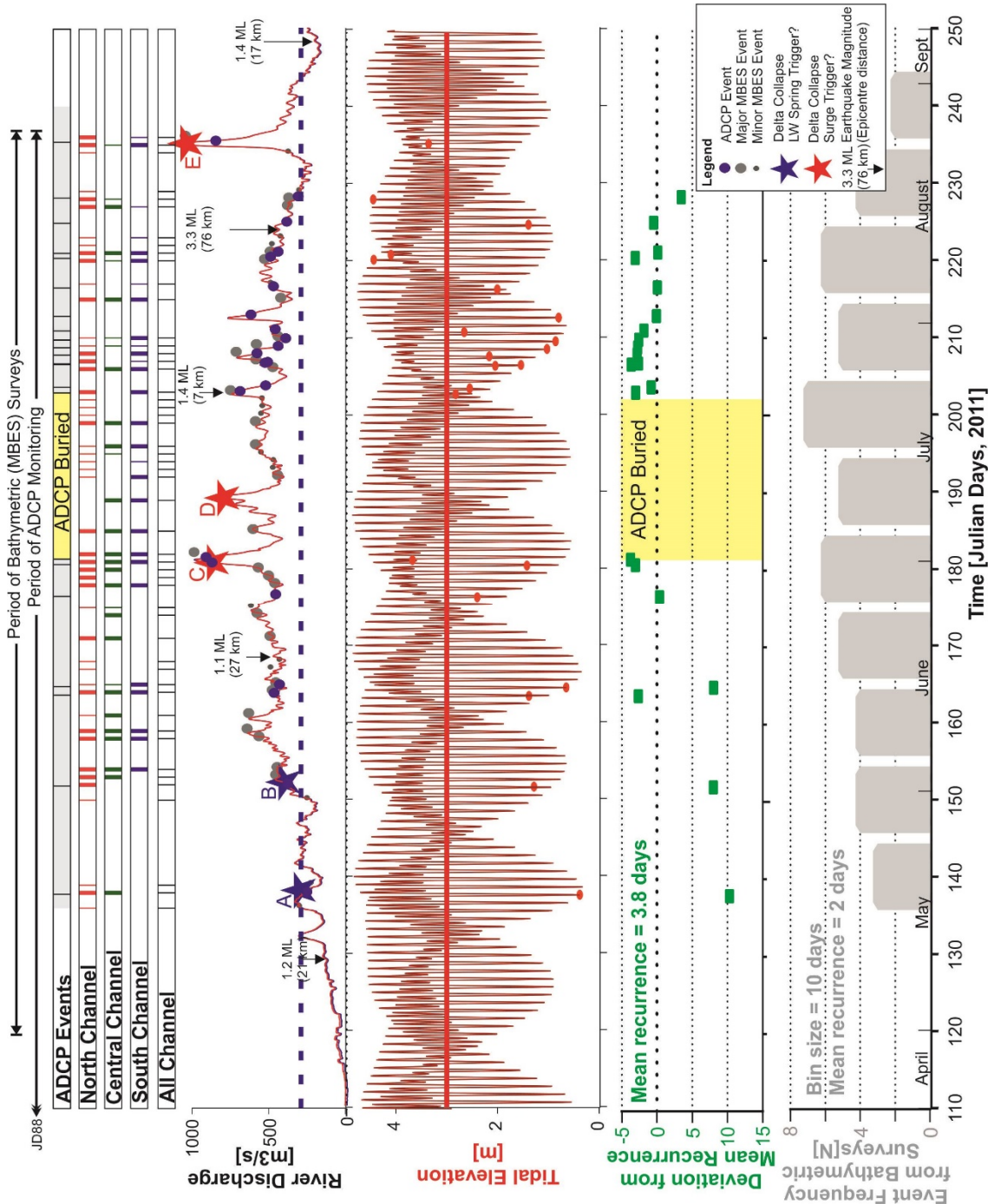


Figure 8.3: Time series of event occurrence, river discharge (annotated with earthquakes and all monitored flow events; dotted horizontal line is the mean annual river discharge), tidal elevation (with ADCP flow events; solid horizontal line is the mean annual tidal elevation), recurrence of flows at ADCP location (green), and flow frequency per 10 day bins based on MBES data (grey).

8.3.4 Tidal, river discharge and earthquake data

The variables that considered in this present analysis relate to tides, river discharge and earthquakes. Hourly tidal measurements in metres relative to mean sea level were used (Hughes Clarke et al., 2012). Hourly river discharge data, recorded in m³/s, from September 2010 to November 2011 were obtained 12 km upstream, at Brackendale,

Environmental Canada station 08GA022. Residual pore pressures were calculated theoretically at 10 m below seafloor in response to tidal variations as outlined in Section 8.3.6. In some locations worldwide, turbidity currents mainly coincide with larger wave heights (Talling et al., 2014). However, because the Squamish Delta has limited fetch, it experiences small wave heights (Stronach et al., 2006). Wave height is therefore excluded from this analysis. The timing and magnitude of earthquake events are from the Earthquakes Canada database (Earthquakes Canada, 2014).

8.3.5 Calculation of channel bed shear stress

The following text provides an explanation of the methods for calculating the channel bed shear stress variable and pore pressure in response to tidal fluctuations.

The mean velocity of river flow can be related to river discharge, and the cross sectional area of the channel.

$$U = Q/BH \text{ (Equation 8.1)}$$

where, U is the depth averaged velocity, Q is the river discharge, B is the channel width and H is the channel height. At Squamish, values of B and H depend on the cross sectional area of the sub-tidal channel which vary during low tidal elevations (Figure 8.4).

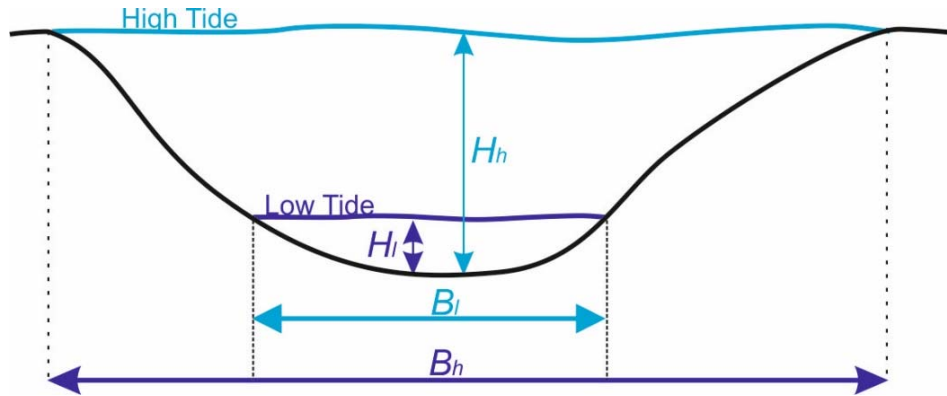


Figure 8.4: Schematic channel cross section showing how parameters H (height) and B (width of base) vary during different tidal elevations. In the case of this study, the delta top channel is assumed to be rectangular, hence any estimates of shear stress are conservative

Next the boundary shear stress at the bed, τ_b , is calculated (Parker, 2004) in order that it can be related to sediment discharge and tidal elevation.

$$\tau_b = C_f \rho U^2 \text{ (Equation 8.2)}$$

where, C_f is the dimensionless bed resistance coefficient and ρ is the flow density. Integrating this with Equation 8.1:

$$\tau_b = C_f \rho (Q/BH)^2 \text{ (Equation 8.3)}$$

C_f can be solved as follows :

$$C_f = A/\sqrt{g} \text{ (Equation 8.4)}$$

where, A is a constant that varies with the roughness of the material composing the boundary of the channel bed, and g is a gravitational constant. It is assumed here that the values of C_f is the same for high and low tidal states. Given that C_f is constant, and assuming minimal variation in ρ , τ_b can be shown to be approximately proportional to U^2 . The latter assumption of a constant flow density may not be entirely accurate, as density may increase during periods of higher river discharge due to elevated sediment concentration. Despite this, any calculation of τ_b is conservative (i.e. low estimate) and sediment concentrations within the river are likely to be very low and will not affect the calculations to a first order.

A variable, $\tau_{b[-]}$, is calculated as a proxy for bed shear stress which is approximately proportional to river discharge, Q , divided by the effect of tidal elevation on channel cross sectional area (i.e. $B \times H$).

$$\tau_{b[-]} \propto (Q/BH)^2 \text{ (Equation 8.5)}$$

8.3.6 Calculation of residual pore pressures due to tidal elevation change

In order to calculate the change in pore pressure due to tidal variations a similar approach is taken to Chillarige et al. (1997a), who analysed sediment from a broadly analogous site at the mouth of the main channel of the Fraser River, British Columbia. The total stress due to tidal loading, σ , is:

$$\sigma = \left[\frac{\gamma_w H}{2} \right] \sin(\omega t) \text{ (Equation 8.6)}$$

where, H is the tidal wave height, γ_w is the unit weight of water, ω is the tidal frequency. The tidal frequency at Squamish is 16 hours, which is the same as at the Fraser River site (Chillarige et al., 1997a). The pore-water pressure response (calculated as the stress

deviation from the mean) for the propagation of tidal cycles over a saturated porous bed can be calculated from:

$$\frac{\partial u}{\partial t} = c_v \frac{\partial^2 u}{\partial z^2} + \frac{\partial \sigma}{\partial t} \text{ (Equation 8.7)}$$

where, u is the pore-water pressure, t is time, c_v is the consolidation coefficient of water-saturated sediment, z is depth. The consolidation coefficient for water-saturated sediment, c_v , is calculated by:

$$c_v = \frac{k}{\gamma_w m_v} \text{ (Equation 8.8)}$$

where, k is the coefficient of permeability of the soil skeleton and m_v is the compressibility of the soil skeleton. In water-saturated soils, all of the stress increment applied is carried by the pore fluid as the compressibility of the soil skeleton is greater than that of the pore water (Chillarige et al., 1997a). Therefore, no change in effective stress will occur, regardless of the tidal elevation, providing the sediment remains water-saturated (i.e. it is not subaerially exposed).

This situation changes under partially saturated conditions, which may occur if gas takes up some of the pore spaces as well as water (c_{vg}). Where gas occurs within pore spaces the stress increment is shared by both the pore fluid and soil skeleton. Small amounts of gas can significantly change the pore fluid compressibility (Frelund and Rahardjo, 1993; Figure 8.5). This can be explained by the inclusion of soil structure porosity, n , and compressibility of the pore fluid, β using the same approach as in Equation 8.8. In keeping with the modelling of Chillarige et al. (1997a) an assumption is made of 2% gas saturation ($S=98\%$) of the pore fluid. Porosity is based on measurements at the Fraser River, for which an estimated lower bound of 0.49 is used (Chillarige et al., 1997a).

$$c_{vg} = \frac{k}{\gamma_w (n\beta + m_v)} \text{ (Equation 8.9)}$$

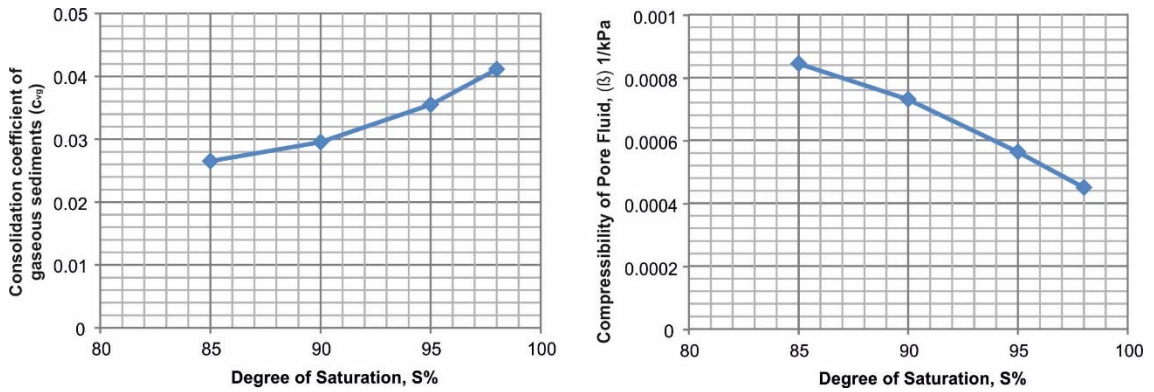


Figure 8.5: Variation in consolidation coefficient and pore fluid compressibility for different degrees of pore fluid saturation. $S=95\%$ refers to a pore fluid with 5% gas. The higher the proportion of gas in pore fluid, the higher the compressibility and the lower the consolidation coefficient become.

Based on the available tide gauge data, the maximum tidal variations are ~ 5 m with a period of ~ 16 hours, which is almost identical to that at the Fraser River. Chillarige et al. (1997a) validated their analytical results with in-situ measurements of pore-pressure using a seabed monitoring array (Christian et al., 1997b) which provides reassurance in the method. Pore pressures modified by tidal elevation changes are attenuated at depth below the seafloor. In addition, the degree of gas saturation causes a delayed dissipation of pore pressures. For 98% saturation, the effects are felt instantly at seafloor, but 0.35 hours after at 10 m depth. Based on the dimensions of delta lip failures at Squamish, 10 m is selected as the depth of consideration (Figure 8.2D) and the associated lag effect is taken into account in the analysis. Low tides result in reduced confining stresses in gaseous sediments and increased void ratios. This effect can serve to draw out gas from solution. The tidal effect on pore pressure, in particular gas held in the pore fluid, has been hypothesised as a potential agent for slope destabilization (Fredlund and Rahardjo, 1993; Chillarige et al., 1997a).

8.3.7 Statistical analysis

Non-parametric (Mann-Whitney and Kolmogorov-Smirnov) tests are used to determine if the range of tidal elevation and river discharge that corresponds with event timing is significantly different from the annual range. This allows us to determine whether the timing of events correlates with extreme values of the explanatory variables (i.e. discharge and tidal elevation). To test whether any of the variables correspond with changes in the rate at which failures and flows occur, a Generalised Linear Model (Nelder and Wedderburn, 1972) and Proportional Hazards Model (Cox, 1972) are used. Recurrence intervals (i.e. inter-event times) are calculated for events identified in each

data set and their probability density function is plotted to determine possible frequency distribution form. The Chi-Squared test is used to test for acceptance or rejection of distributions forms, including exponential (i.e. time-independent, indicating constant hazard rate, controlled by one parameter), log-normal (ordered, resulting from multiplication of normal distributions, controlled by two parameters), and log-Pearson 3 (ordered, controlled by three parameters, commonly observed in rivers for flood frequency; Bobeé et al., 1975). A Gamma form is also tested for to verify the applicability of applying a Generalised Linear Model using a Gamma distribution (Chapter 4). The Proportional Hazards Model is a non-parametric model, so does not require us to specify the frequency distribution form for recurrence intervals. This provides a useful check against the parametric Generalised Linear Model.

8.3.8 Recurrence intervals and frequency distribution form

The ADCP measured the timing of events (arrival of flow front) to the nearest 30 seconds, which can be compared to hourly measurements of tidal elevation and river discharge. Conditions in the 24 hours prior to ADCP-recorded events are also considered, as they may contribute to the preconditioning of an event. While the temporal resolution is greatest for the ADCP data, it was buried for 20 days following delta-lip failure C, hence this period cannot be analysed. Repeat MBES surveys document whether an event occurs during longer periods, typically 24 hours. MBES events are therefore compared to daily averages of river discharge, or the maximum tidal range during each day. The tidal elevation and river discharge at the timing of an event is considered, as well as the minimum tidal elevation, tidal range and river discharge maximum in the preceding 24 hours.

8.3.9 Optimal sample sizes

The larger number of events ($N=106$) observed on the MBES data are better suited for statistical analysis than the 22 ADCP-recorded events, although the timing of MBES events is known with much less precision. Small sample sizes ($N < 100$) are not optimal for statistical analysis, but Peduzzi et al. (1995) demonstrated that a minimum value of only ten events per variable is required for a Proportional Hazards Model. Vittinghoff and McCulloch (2007) proposed that this value could be relaxed even further. Given that only two variables are being tested here, this indicates a minimum sample size of 20 events is

considered adequate; hence the application of a Proportional Hazards Model can be justified. For regression models including Generalised Linear Models, where you have k predictors, the recommended minimum sample size should be $\sim 50 + 8k$ to adequately test the overall model (Green, 1991). Hence, the sample size needs to be 58 for a single explanatory variable, and 66 events are needed when there are two variables (e.g. river discharge and tidal elevation). As there are only 22 ADCP events, the statistical power of the Generalised Linear Model is not as high as would be preferred, hence the comparison with the Proportional Hazards Model to validate results.

8.4 Results

8.4.1 Recurrence distribution

The mean recurrence interval for proximal MBES events is 2 days, whereas the mean recurrence for distal ADCP events is 3.8 days. The mean recurrence may be overestimated slightly for MBES events as surveys were performed on weekdays only. It is likely that some events were therefore missed by the MBES survey. This is not an issue for the ADCP that provided continuous monitoring when it was functional. Despite this difference, Probability Density Function plots are similar for both, with a bias toward shorter recurrence intervals (<4 days for MBES events, <6 days for ADCP events). A few longer recurrence intervals are noted as outliers – this is more pronounced for ADCP events (Figure 8.6 and Figure 8.7). The data show a good fit with a Gamma distribution ($r^2 > 0.99$), which validates the selection of a Gamma-based Generalised Linear Model. However, other distributions may also characterise the data (Figure 8.6 and Figure 8.7; Table 8.2).

Table 8.2: Results of Chi Squared statistic testing for conformance of event recurrence data to different distributions. If the Chi Squared statistic exceeds the critical value we can reject the hypothesis that the data conform to the proposed distribution.

| | Normal | Log-Normal | Weibull | Exponential | Log-Pearson 3 | Gamma |
|---------------------------------|----------|-------------------------|-----------|-------------|-------------------------|-----------|
| MBES Events | | | | | | |
| Statistic | 8.636 | 19.95 | 11.676 | 8.5844 | 18.264 | 5.7306 |
| p value | 0.03454 | 1.7388×10^{-4} | 0.00858 | 0.03536 | 3.8809×10^{-4} | 0.05697 |
| Critical χ^2 Value at 0.05 | 7.8147 | 7.8147 | 7.8147 | 7.8147 | 7.8147 | 5.9915 |
| Reject distribution? | Yes | Yes | Yes | Yes | Yes | No |
| ADCP Events | | | | | | |
| Statistic | 4.6556 | 0.39403 | 0.10305 | 0.72622 | 0.29649 | 0.10555 |
| p value | 0.009751 | 0.53019 | 0.7482 | 0.39411 | 0.58609 | 0.74526 |
| Critical χ^2 Value at 0.05 | 5.9915 | 3.8415 | 3.8415 | 3.8415 | 3.8415 | 3.8415 |
| Reject distribution? | Yes | No | No | No | No | No |

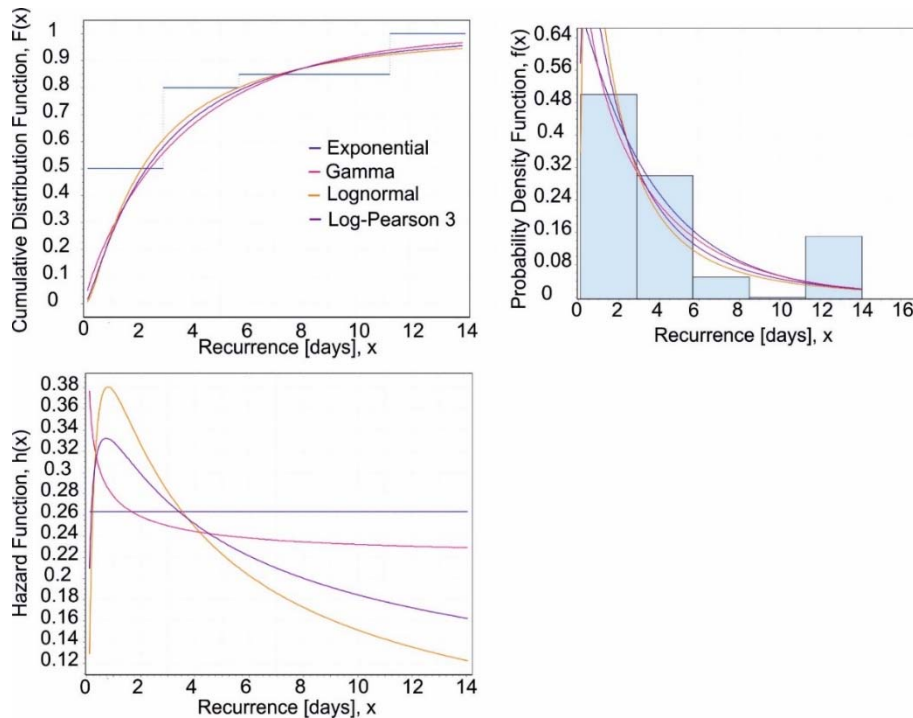


Figure 8.6:Plots of binned flow recurrence determined from the ADCP monitoring. The minimum resolvable time window is 30 seconds, hence all events that cross the ADCP are recorded. Recurrence is binned to visually assess the goodness of fit for different frequency distributions. Plots include cumulative distribution (top left) and probability density (top right). The range in potential hazard functions relating to the modelled frequency distributions is also illustrated (lower left). Only a Normal distribution is rejected by the Chi-squared statistic (Table 8.2) which is partly due to the limited number of monitored events by the ADCP.

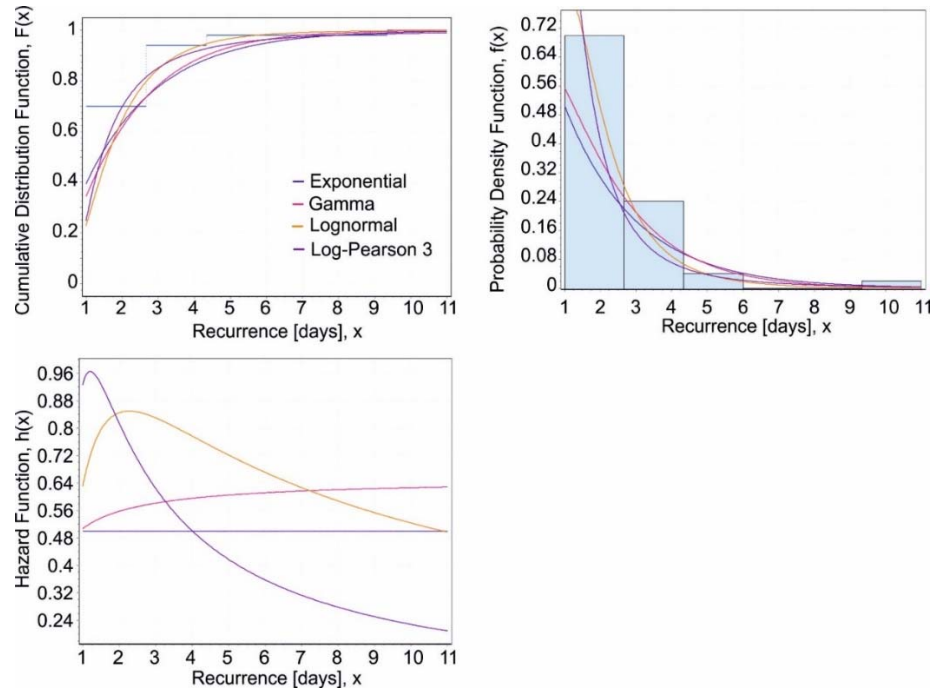


Figure 8.7: Plots of binned flow recurrence determined by MBES surveys to visually assess the goodness of fit for different frequency distributions. The minimum resolvable time window is one day; hence event recurrence below that will not be recorded. Cumulative distribution (top left), probability density (top right). The range in potential hazard functions relating to the modelled frequency distributions is also illustrated (lower left). Only a Gamma distribution is accepted by the Chi-squared statistic test (Table 8.2) so it is most appropriate to use this for hazard modelling.

8.4.2 Delta lip collapses

The first two major delta-lip collapses coincide with relatively low spring tides, but not to peaks in river discharge (Figure 8.3; Hughes Clarke et al., 2012). The subsequent delta-lip collapses (events C, D and E) occur shortly (>8 hours) after the three largest river discharge peaks ($>775 \text{ m}^3/\text{s}$) that resulted from glacier meltwater. The largest delta-lip collapse (event C) occurred ~ 8 hours after the second highest recorded river discharge. This event completely filled the lower section of the northern channel, and buried the ADCP from Julian Day 181 to 201. A statistical analysis of the five delta-lip collapses is not undertaken here, due to the small number of events. However, delta-lip failures appear to be linked to low tides and/or river floods. It appears that tidal triggers may be dominant when river discharge levels stay below a threshold level (i.e. likely to be close to the mean annual discharge level). The collapses associated with low tides occur at the start of the freshet, and it may be that tidal triggering is more pronounced in the period before sediment has built up at the delta-lip as the freshet progresses.

The spatial occurrence of the five failures appears to be important in understanding when they occurred (Figure 8.8). Failure A occurred near the most seaward extent of the

delta lip following progradation due to sediment build up. Removal of failed sediment oversteepened its western flank, coincident with where Failure B occurred 14 days later. Sediment continued to build up on the delta lip towards the peak of the freshet, until the post-failure morphology was no longer visible. The extent of the next failure, C, which corresponded to the first major peak in river discharge, covered the areas failed by both A and B which may indicate that loose, sediment rapidly deposited over the previous failure scars was more susceptible to failure. Eight days later, Failure D occurred at the seaward extent of the delta lip which adjoined the eastern flank of Failure C's headscarp. The final failure, E, occurred 46 days later, also at the most seaward extent of the delta lip, covering a similar area to Failure C; hence, also an area of loose, recently deposited sediments that may have been more prone to fail.

8.4.3 Triggering of events during river floods – is it by hyperpycnal flow or slope failure?

Previous work has suggested that plunging river floodwater may trigger flow events. ADCP data shows that delta-lip failures (C and E) occurred ~8 to 11 hours after the peak in river discharge. This cannot be determined for event D as the ADCP was temporarily buried. River discharge was measured at a station 12 km upstream from the delta lip. Based on conservative flood peak velocities of 1 to 3 m/s measured near and downstream the discharge monitoring station (Hickin, 1978), it is calculated that river discharge would reach the delta lip within 1 to 3 hours. These values are also supported by measured velocities of 1 m/s taken 1 km upstream of the delta lip during a flood peak during the summer freshet by Rood and Hicken (1989). It is also assumed that submarine flows took ~30 minutes to travel from the delta lip to the ADCP mooring at a speed of 1 m/s, which is consistent with the speeds measured by the ADCP (Hughes Clarke et al., 2012). The observed lag of 8 to 11 hours post-discharge peak is therefore not explained by the potential maximum lag of 3.5 hours for discharge to reach the ADCP (Figure 8.10). Delta-lip failure therefore post-dates the peak of flood discharge by several hours. Furthermore, headscarps seen in MBES data show clearly that the initiation mechanism for events C, D and E was slope failure, rather than plunging hyperpycnal river discharge (Figure 8.8; Hughes Clarke et al., 2013; 2014). This type of MBES data is typically not available, and it illustrates a need for caution in assuming that submarine flows that occur during river floods are triggered by plunging hyperpycnal flood-water.

It appears that increased sediment transport and rapid progradation of the delta lip preconditions the slope to failure, which occurs during the later stages of the flood. Presumably, excess pore pressures takes time to build-up in the subsurface as sediment accumulates, with peak pore pressures occurring several hours after the flood peak. The ultimate trigger may be tidally-controlled, but the set-up appears to be caused by enhanced deposition from the river.

A broadly similar relationship has been documented offshore south-east Taiwan, where a long run-out turbidity current occurred several days after the peak of an exceptional river flood (Carter et al., 2012). Work in Lake Geneva also showed that while some submarine flows (<30 cm/s) may show a near-coincidence with river flood peaks, the most powerful submarine flows (>30 cm/s to ~3 m/s) did not (Lambert and Giovanoli, 1988).

8.4.4 Did earthquakes trigger slides or flows?

Only one earthquake of >2 M_L occurred during the monitoring period (76 km to the south-east, 3.3 M_L on JD 224.25), but it did not coincide with any submarine flow or failure events. Two <2 M_L earthquakes occurred within 30 km of Squamish in the same period, one of which preceded an event observed on the ADCP by ~8 hours, and the other by ~8 days (Figure 8.3). Therefore, small <3.3 M_L earthquakes did not trigger slope failures or flows, during the 2011 monitoring period.

8.4.5 Does river discharge control the ‘switch on’ and frequency of flows?

Only the first of the ADCP-monitored flows occurred when river discharge was below the annual average discharge. The first flow at the start of the freshet did, however, occur 24 hours after a discharge peak of 342 m^3/s . More than three quarters of flows occurred when river discharge was >75% of its annual range (Figure 8.3 and Figure 8.10). Non-parametric Mann-Whitney and Kolmogorov-Smirnov tests demonstrate that the difference in river discharge at flow events is strongly significant compared to the overall annual range ($p < 0.0001$). Flow events were observed on MBES data when river discharge exceeded 253 m^3/s , but only occurred coincidentally in all three channels above 390 m^3/s . At higher rates of discharge (>600 m^3/s) when a minor MBES event occurred, it was always accompanied by a major MBES event in at least one of the other channels.

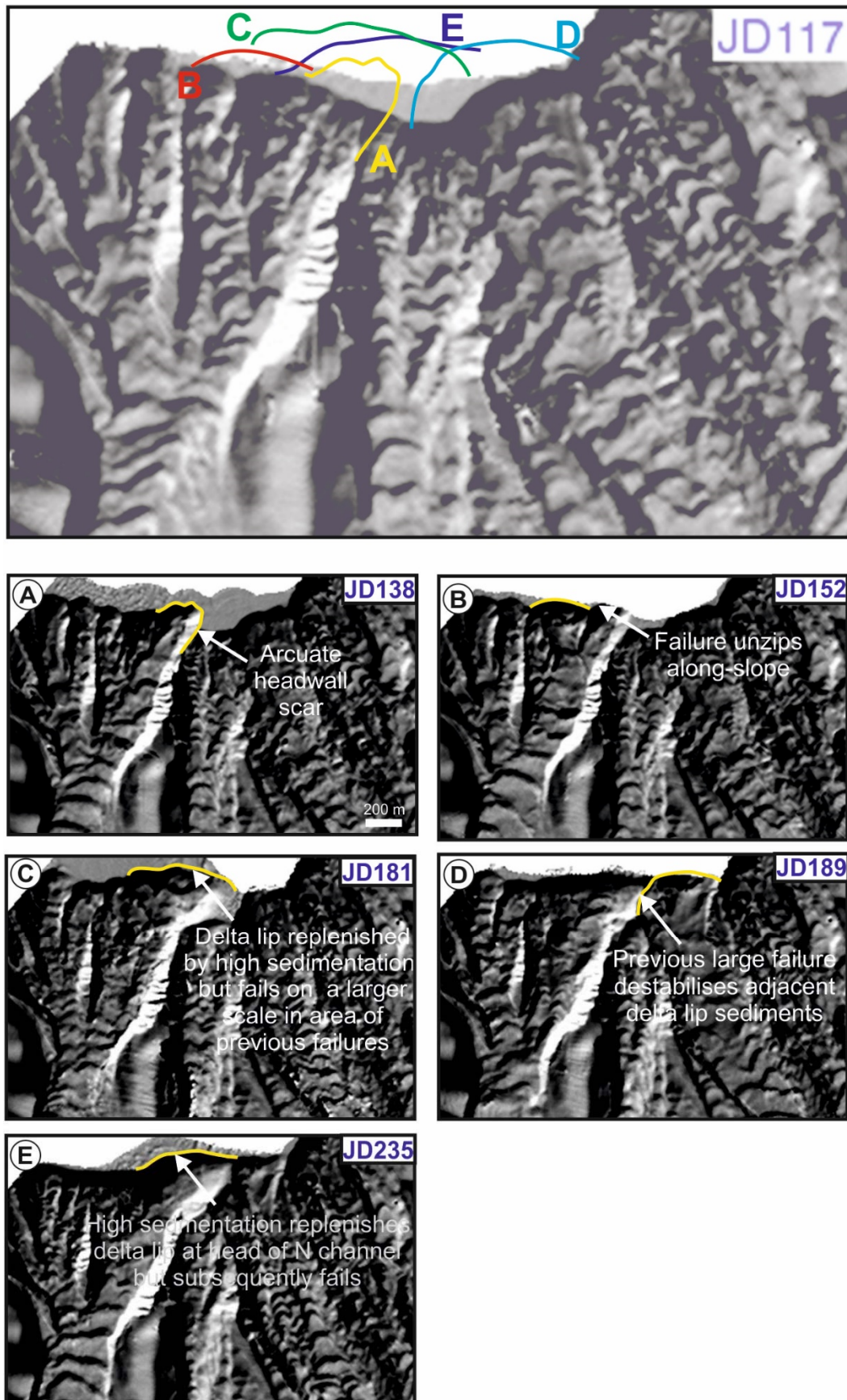


Figure 8.8: Location of headwalls of large delta lip failures seen on MBES data. Top image: Location of headwall scars of major delta failures overlain on JD117-118 difference plot. Images A to E refer to individual events and show the post-failure morphology

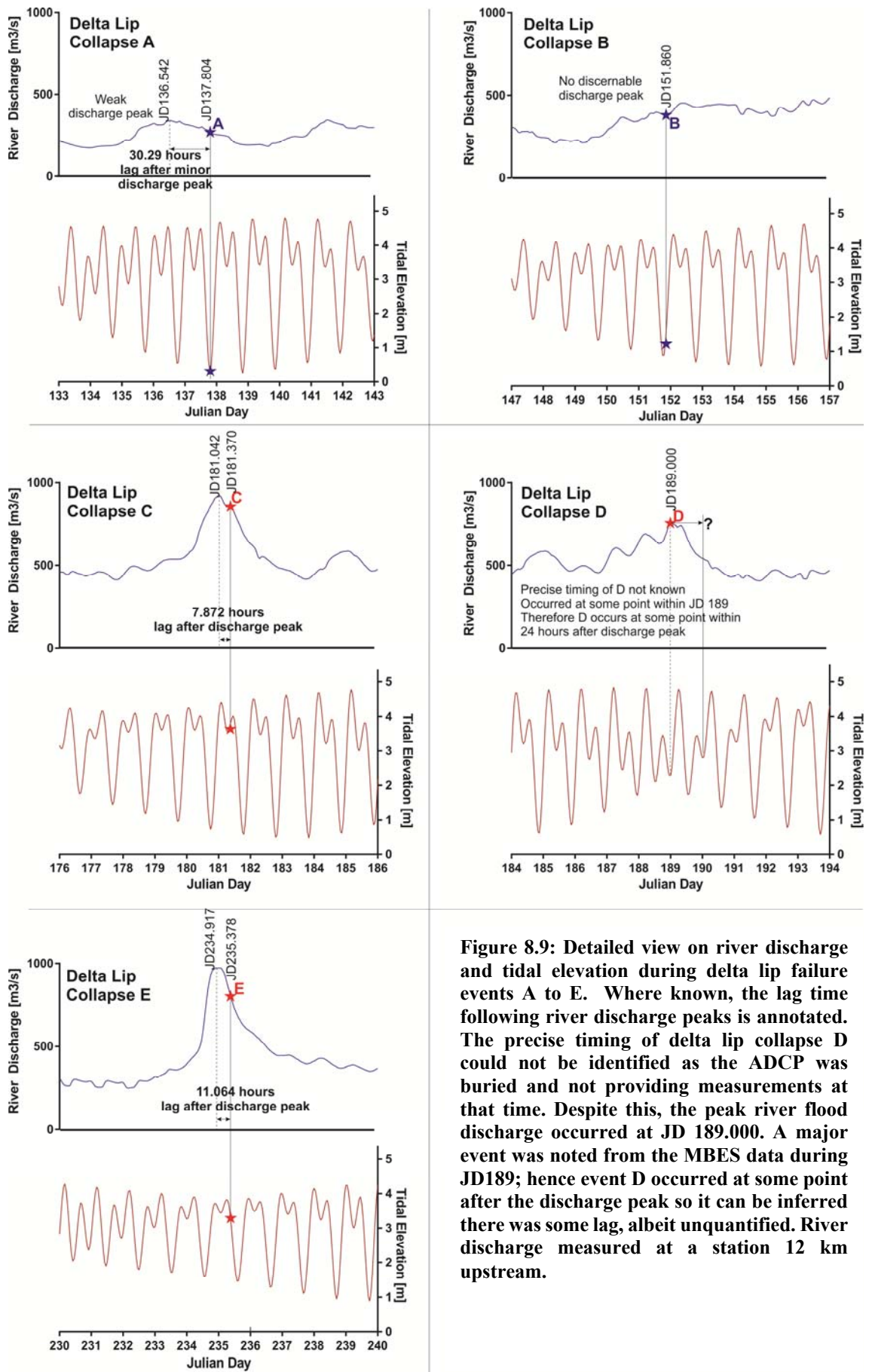


Figure 8.9: Detailed view on river discharge and tidal elevation during delta lip failure events A to E. Where known, the lag time following river discharge peaks is annotated. The precise timing of delta lip collapse D could not be identified as the ADCP was buried and not providing measurements at that time. Despite this, the peak river flood discharge occurred at JD 189.000. A major event was noted from the MBES data during JD189; hence event D occurred at some point after the discharge peak so it can be inferred there was some lag, albeit unquantified. River discharge measured at a station 12 km upstream.

The general trend of increasing river discharge towards the freshet peak in June and July is mirrored by more frequent flow activity (Figure 8.3 and Figure 8.10). The number of events per 10 day bin was more than double (1 event every 1.43 days) than at the start (1 event every 3.33 days) of the freshet (Figure 8.3). The same trend is seen when considering all MBES events, only major MBES events, and the records for each individual channel. The frequency of ADCP events also increased, particularly between JD180-225 when recurrence intervals were less than the mean flow recurrence for the freshet period (i.e. >1 flow/3.8 days). Both the Proportional Hazard ($p=0.002$ - 0.0008) and Generalised Linear Model ($p=0.002$ - 0.003) indicate that river discharge is highly significant in relation to flow recurrence rate (Figure 8.11; Table 8.5 to 8.9).

Table 8.3: Results of non-parametric statistical tests to determine significance of difference between annual range in variables against the range coincident with events detected by the ADCP. Bold italicised values are significantly different ($p<0.05$)

| Test Type | | River Discharge | Tidal Elevation | Residual Pore Pressure |
|--------------------|----------------------------|--------------------------|--------------------------|------------------------|
| Kolmogorov-Smirnov | p-value | <i>0.0005</i> | <i><0.0001</i> | <i>0.0017</i> |
| | Kolmogorov-Smirnov D | 0.4330 | 0.5492 | 0.4021 |
| Mann-Whitney | p-value | <i><0.0001</i> | <i>0.0002</i> | <i>0.0005</i> |
| | Mann-Whitney U | 25918 | 30300 | 32070 |
| | Difference: Actual | 186.7 | -1.320 | 12.12 |
| | Difference: Hodges-Lehmann | 221.1 | -1.110 | 8.929 |
| | 95% Confidence Interval | 140.1 to 301.3 | -1.630 to -0.055 | 9.09 to 19.39 |
| | | | | |

8.4.6 Do slope failures and flows coincide with low tides?

Two major delta-lip failures (A and B) correspond to relatively lower river discharge conditions compared with the rest of the freshet (<480 m³/s). These occurred during relatively low minimum tides; 2.8 m and 1.9 m below the mean annual tidal elevation for the A and B lip failures respectively (Figure 8.3). While the three other delta lip failure events correspond to extreme river discharges, they also correspond to a tidal elevation that is within the lowest 25% of the annual range (Figure 8.10). Non-parametric analysis of all of the events observed at the ADCP location demonstrates that the difference in tidal elevation at flow events is strongly significant compared to the full range (Mann-Whitney test, $p=0.0002$; Kolmogorov-Smirnov test, $p=0.0005$); however, a few events also occur during high relative tides.

Tidal loading may cause slope failure by liquefaction (Kramer, 1988). However, this process cannot explain the largest delta-lip failures, due to the depth of their failure surface (Figure 8.2). Deep deposits will not experience shear stress changes due to tidal drawdown (Chillarige et al., 1997). Changes in subsurface pore-water pressure due to tidal drawdown may, however, be more important – particularly in gas-saturated sediments. Squamish Prodelta sediments are known to be partially gas saturated (Hughes Clarke et al., 2012). Pore-water pressure response is calculated at 10 m below seafloor based on the method in Chillarige et al. (1997) which was developed for a similar site at the Fraser River Delta, British Columbia (Section 8.3.6). Similarly to the tidal analysis, pore pressures during the event are found to be significantly different to those for the annual range ($p=0.0005-0.0017$), with most events occurring at times featuring positive residual pore pressures (i.e. coincident with lowered hydrostatic pressure).

While tidal elevation may explain the final *timing* of an event, the tidal elevation is not found to be a significant variable governing the *recurrence rate* of flows ($p>>0.05$) using the Generalised Linear Model and Proportional Hazards Model (Figure 8.11; Table 8.5 to 8.9). Tidal range, does however, yield a significant result for the recurrence rate of ADCP-monitored events ($p=0.01-0.05$; Figure 8.10), indicating that periods of greater tidal variation correspond to a higher frequency of flows. This analysis of tidal state and recurrence is only robust for the ADCP-monitored events, as the time constraint on MBES-observed events (~ 24 hours) is not appropriate for comparison with shorter-term tidal fluctuations.

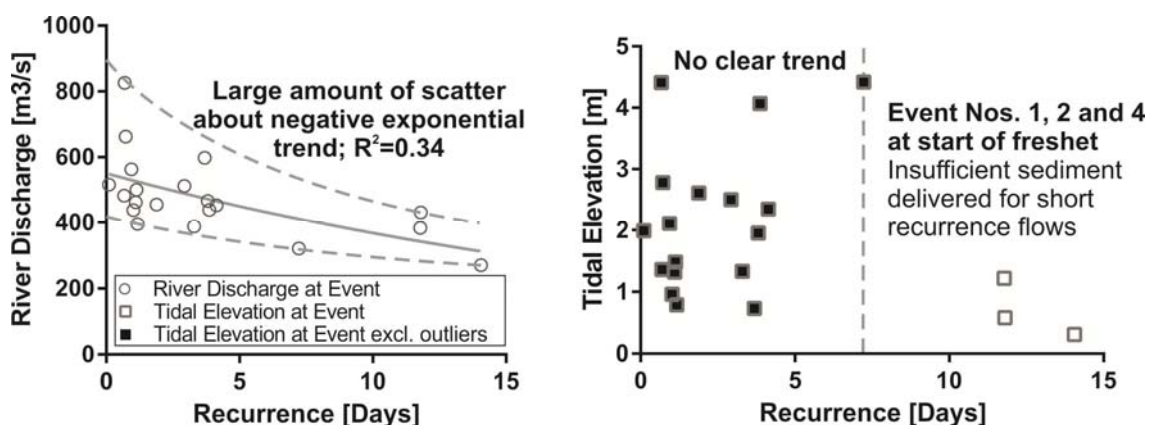


Figure 8.10: River discharge (left, $p=0.003$ based on the Generalised Linear Model) and tidal elevation (right, $p=0.210$ based on Generalised Linear Model) plotted against flow recurrence as measured from the ADCP.

8.4.7 Does flow timing relate to a combination of tide and river discharge effects?

Given that both tidal elevation and river discharge appear to be significant for event timing, statistical analysis is now performed to assess whether the significance is increased when they are combined. By analysing the results of additive and multiplicative relationships, it is possible to assess whether tides and river discharge act in unison, or if it is more appropriate to consider them as independent triggering factors.

The most significant result relates to the additive effect of tidal elevation event and river discharge based on the ADCP event data (Proportional Hazards Model, $p=0.0006$; Table 8.5; Figure 8.11). The other variants of the Generalised Linear Model and Proportional Hazards Model indicate that additive effects of tidal elevation and discharge measured at the time of a flow show a lower, but still significant correlation with the rate of recurrence (Figure 8.11; Tables 8.6 to 8.9). Multiplicative effects do not indicate any degree of significance (Figure 8.11; Tables 8.5 to 8.9).

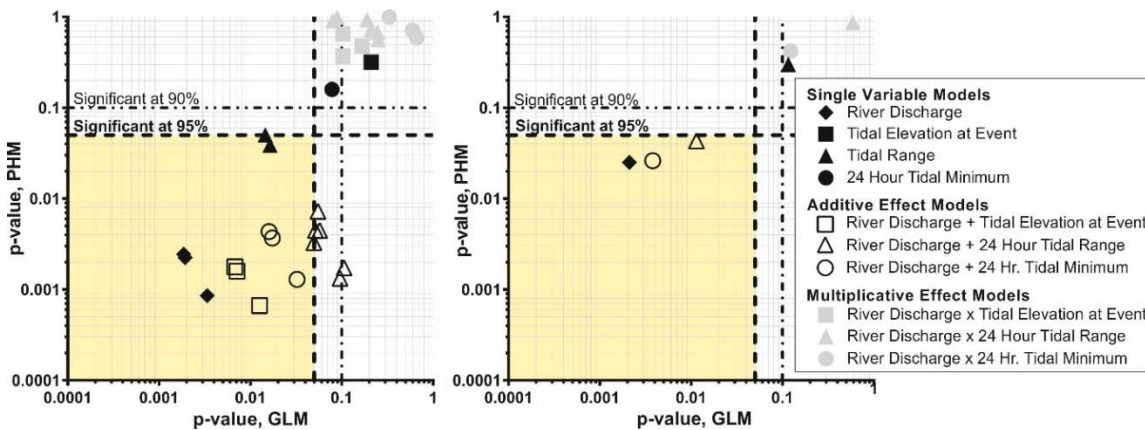


Figure 8.11: Results of Generalised Linear Model and Proportional Hazards Model analysis for events timing from ADCP (left) and MBES (right) monitoring. Results within the yellow shading (i.e. $p < 0.05$) are considered to be statistically significant. It is thus shown that none of the multiplicative effect models are significant. The most significant results are for the single influence of river discharge and the additive effects of river discharge and tidal elevation during an event.

Simply adding or multiplying variables does not explain the physics of real-world processes, however, so the next step in the analysis is to relate river discharge and tidal elevation in a simple manner to bed shear stress (Figure 8.9). Bed shear stress controls rates of bedload transport by the river to the delta lip, and hence rates of sediment deposition and lip migration. Here, a bed shear stress variable, Q/BH^2 , is derived, where Q is river discharge, and B and H are the delta-top channel width and height respectively. A rectangular channel is assumed, so that H changes in response to tidal fluctuations, but

B remains constant. Thus, the output is conservative because a U- or V-shaped channel was considered, the channel width, B, would be considerably thinner during lowered tides; providing a much higher value for the bed shear stress. More detail on the method, based on Meyer-Peter and Muller (1948) is provided in Section 8.3.5. The Generalised Linear Model and Proportional Hazards Model analyses do not indicate any degree of significance ($p > 0.89$) for this bed shear stress variable in relation to the *rate* at which flows recur (Table 8.6 to Table 8.10). However, its significance in relation to the *specific timing* of individual flows is considerably greater than just considering tidal elevation or river discharge in isolation (Mann-Whitney, $p < 0.0001$; Kolmogorov-Smirnov test, $p < 0.0001$). More than 75% of the events seen by the ADCP correspond to the upper 25% of the annual range of the bed shear stress variable (Figure 8.9 and Figure 8.13). Thus, bed shear stress may govern the instantaneous triggering of an individual flow, but not the rate at which they recur.

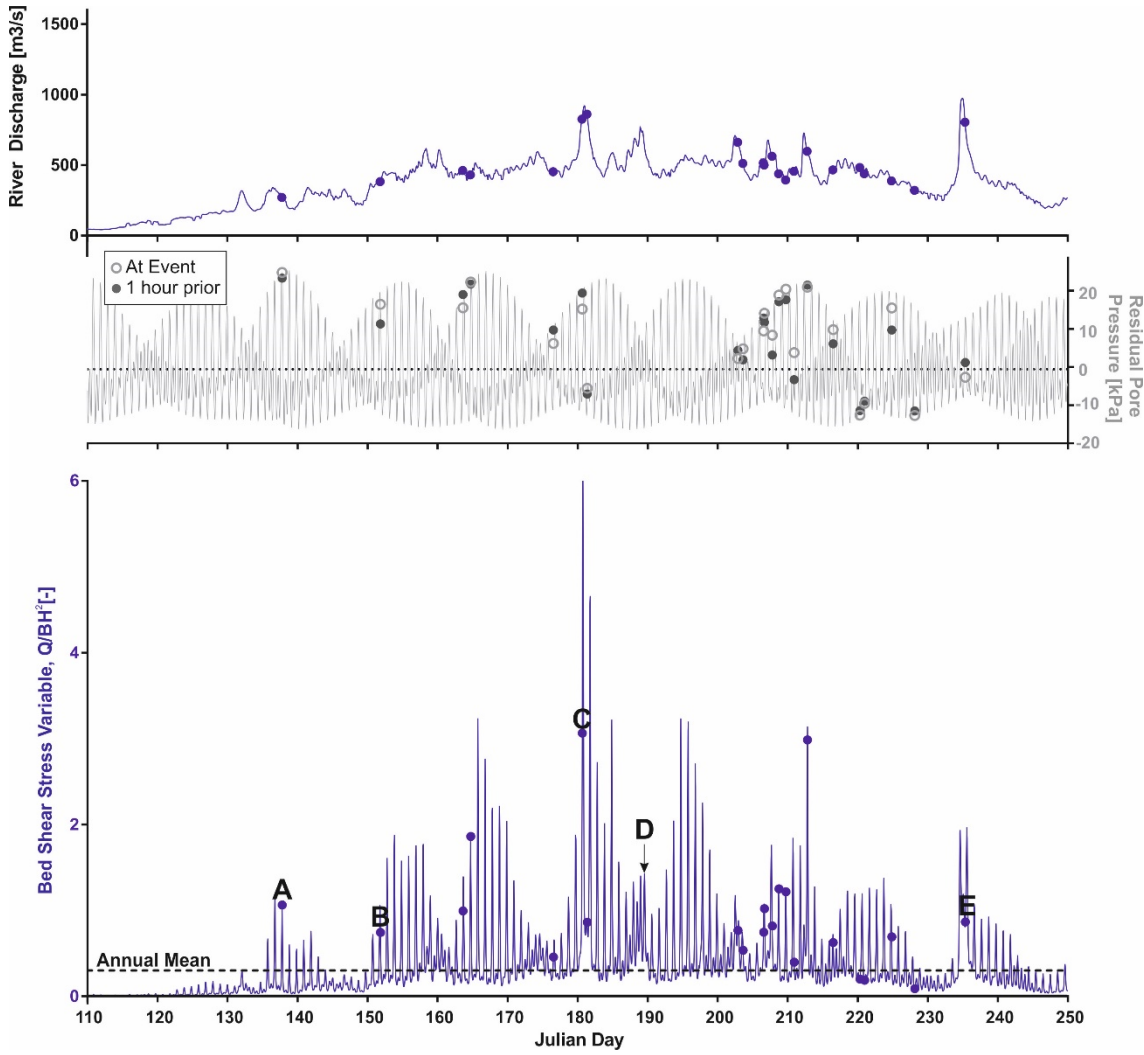


Figure 8.12: Time series of river discharge (top), residual pore pressure (middle), and bed shear stress variable as determined by Q/BH^2 (lower). Circles are events monitored by the ADCP. Letters A to E refer to delta lip failure events. As the ADCP was buried during the time of Failure D it is only indicated by an arrow on the river discharge plot.

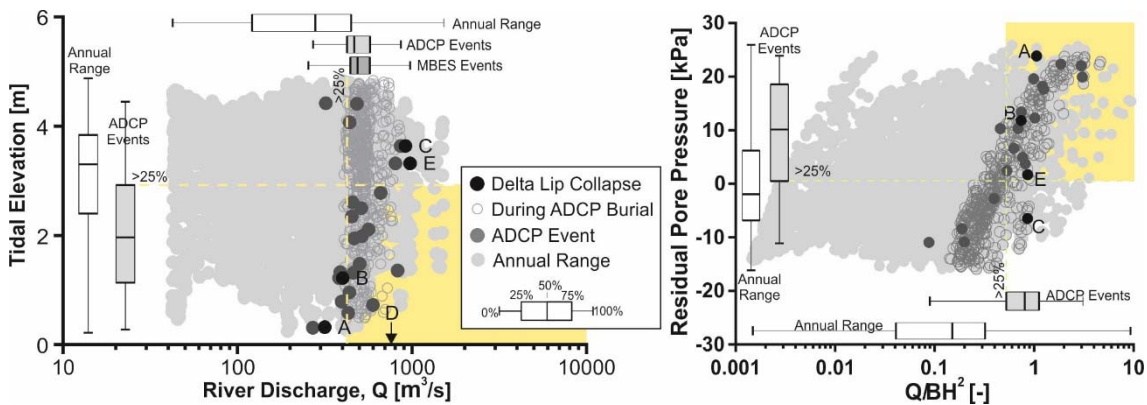


Figure 8.13: Comparison of background annual variations in variables analysed in this chapter with those at the time of observed ADCP events. Tidal elevation and river discharge shown left. Residual pore pressure at 10 m below seafloor and combined discharge and tidal elevation as a proxy for bed shear stress shown right. Box and whiskers demonstrate the range of conditions, where whiskers cover the full range of data and boxes show 25th, 50th and 75th percentiles. Dark grey solid circles are conditions at observed ADCP events. Black solid circles are conditions at delta lip collapses. Light grey solid circles are conditions during which no events were observed. Hollow circles indicate the period during which the ADCP was buried, and hence it is not known if any events occurred or not.

As the ADCP was buried during event D, only the approximate river discharge can be quantified (arrow on left plot). Yellow fill indicates range of conditions within which 75% of events occurred.

8.5 Discussion

8.5.1 Extreme river flood discharge leads to delta lip failures not hyperpycnal flows

Suspended sediment concentrations are unlikely to be high enough to generate dense, plunging hyperpycnal flow from direct river discharge at the Squamish Prodelta and other rivers in the fjords of British Columbia (Bornhold et al., 1994; Mulder and Syvitski, 1995; Hill et al., 2008). As shown here, the extreme peaks in river discharge did not trigger hyperpycnal flows, rather they correspond with large ($>20,000 \text{ m}^3$) delta lip failures a few hours after the flood peak (Figure 8.10). If the ADCP data were used in isolation, a hyperpycnal flow may have been interpreted as the initiating process from a broad correspondence in timing. This important observation is only possible due to the repeated MBES surveys which identified the occurrence of delta lip failures. The river does not appear to directly deliver substantial amounts of sediment to the offshore delta during periods of extreme discharge. Instead, sediment is stored and rapidly builds up to prograde the delta lip over a period of hours, prior to failure.

Hughes Clarke et al. (2013) noted that wholesale plunging of river water was not possible, but they did image sediment settling downwards from a surface plume using water column echo-sounders. It is inferred that convective fingering is responsible for this settling, which can occur at densities of $<1 \text{ kg/m}^3$ (Yu et al., 2000; Parsons et al., 2001). Optical backscatter measurements of density indicate that the upper part of turbidity currents are less dense than the surrounding water (Hughes Clarke et al., 2013). This density contrast may be explained by freshwater becoming entrained by sediment that settles out from the river discharge plume. As the mixture crosses the pycnocline, the sediment settles out and may start to flow downslope under its excess density. The entrained freshwater becomes an upper layer of the flow, which is less dense than the underlying sediment-rich layer and also the overlying seawater. The lower-most ($<2 \text{ m}$) part of the flow, which is presumably where the majority of sediment is transported, is not imaged by the optical backscatter measurements (Hughes Clarke et al., 2013). This mechanism of sediment settling may be important for the triggering of flows that are not associated with an obvious failure scarp (Hughes Clarke et al., 2013). Future monitoring

should focus on imaging the near-bed dense layer of flows (Clare et al., 2015d), as well as acquiring similar time series of flow recurrence.

8.5.2 Conditioning and triggering of delta lip failures

There is not an isolated variable that can explain the triggering of delta lip failures, instead a combination of factors is required (Table 8.4); however, a seismic trigger with magnitude $M_L < 3.3$ can be ruled out based on the lack of evidence in the monitoring periods. The deposition of river-fed sediment provides the source material to oversteepen, cause excess pore pressures to build, and load the top of the delta slope.

The rate of sediment discharge, as well as the amount of sediment deposited, may be important, as illustrated in Figure 8.14. Three of the largest variations in the derivative of river discharge correspond to events C, D and E. Despite this, intense bursts of river discharge are not always linked to delta lip failures (Figure 8.14, ~JD212). Thus, it may be that the effect of cumulative deposition on the delta lip is the dominant preconditioning factor.

When tidal effects are considered with river discharge – causing elevated near-bed shear stresses – the most significant relationship of the analysis is observed for flow events. There appears to be a threshold limit of cumulative bed shear stress at ~125 to 175, beyond which flows must occur (Figure 8.14), regardless of the rate of discharge or the point in the freshet. A second smaller threshold of $Q/BH^2 \approx 40$ in the shear stress variable appears to exist in the later part of the freshet (JD205-235) which may be due to the greater availability of sediment, and hence lower shear stresses are required to trigger flows.

A threshold level may also exist for the initiation of delta lip failures due to accumulation of sediment on the slope. Delta lip failures are seen to occur above river discharge levels of $>90,000 \text{ m}^3/\text{s}$ (Figure 8.14)). This may be attributed to the build-up in pore pressures under burial by accumulating river sediment and the ‘tipping over’ of some critical state (e.g. Iverson, 2000; Iverson and Vallance, 2001; Iverson, 2005). The recurrence time between delta lip failures is >9 days. Assuming at least a 2% gas saturation of the delta slope sediments, excess pore pressures would not become dissipated within a 9 day period even to a 90% level when 2 m or more of sediment are loaded (

Table 8.4). While delta lip failures A and B do not correspond to short lags after major river discharge peaks, the cumulative river discharge is approximately equivalent to that of delta lip failure D (shortly after a major river discharge peak). Sediment loading, which generates excess pore pressures that cannot dissipate through draining during consolidation, can therefore occur during large river discharge peaks, as well as progressively during the rest of the freshet. That the cumulative river discharge reaches such a high level prior to delta lip failure E, can most likely be explained by the highly frequent flows not sourced by failures (i.e. sediment during the freshet peak is quickly flushed offshore and does not reside for long on the delta lip or prodelta front).

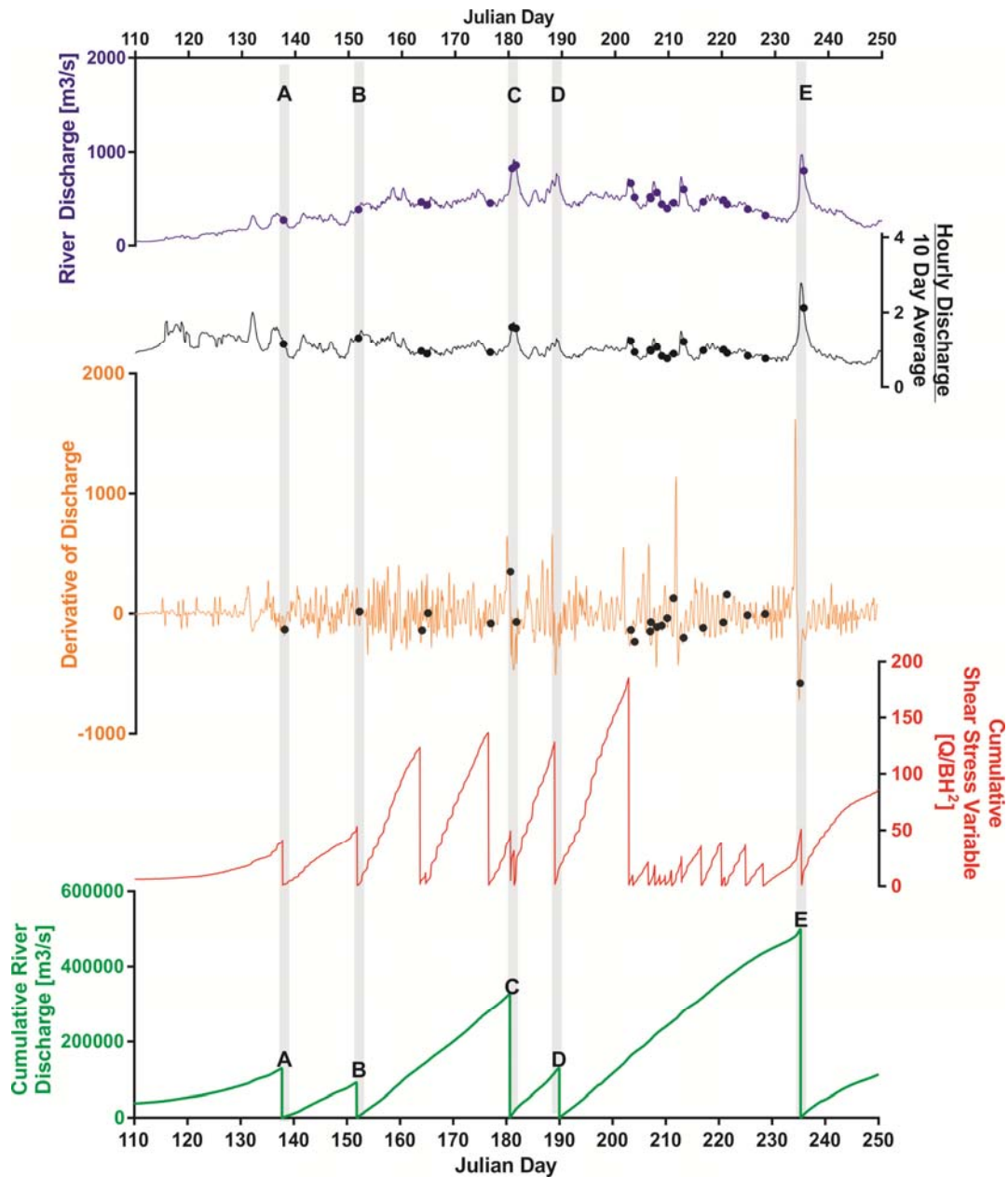


Figure 8.14: Time series variation in river discharge (blue), hourly discharge divided by ten day average (black), first derivative of river discharge (orange), cumulative shear stress build up to ADCP events (red), and cumulative hourly river discharge build up to delta lip failures (green). Delta lip failure events A to E are annotated as grey bars. ADCP events shown as solid circles.

Table 8.4: Time required for 90% dissipation of excess pore pressures following sediment loading. The time to dissipate pore pressures is highly dependent on the consolidation (or hydraulic diffusivity) coefficient (c_v ; based on values from Fraser River in Chillarige et al., 1997) as well as the rate and amount of sediment loading. Results based on methods in Terzaghi (1943) and Iverson (2005)

| Coefficient of Consolidation [c_v] (for Pore Fluid Saturation, S) | Days required for 90% dissipation of excess pore pressures due to delta lip/slope accumulation | | | | |
|--|--|-------|-------|-------|--------|
| | 1 m | 2 m | 3 m | 5 m | 10 m |
| 0.11 (S=100%) | 0.89 | 3.57 | 8.03 | 22.31 | 89.23 |
| 0.0411 (S=98%) | 2.39 | 9.55 | 21.49 | 59.70 | 238.80 |
| 0.0355 (S=95%) | 2.76 | 11.06 | 24.88 | 69.12 | 276.47 |
| 0.0295 (S=90%) | 3.33 | 13.31 | 29.94 | 83.18 | 332.71 |
| 0.0265 (S=85%) | 3.70 | 14.81 | 33.33 | 92.59 | 370.37 |

8.5.3 River discharge is the primary conditioner for flow activity

River discharge is identified as a strongly significant individual variable in relation to both flow timing and recurrence intensity. The results of the Proportional Hazards Model for the ADCP-observed flows (i.e. major channel events) determine a Hazard Ratio (E^b) of 1.006. This indicates that the rate at which flows occur increases by 0.6% (+/-0.4%; 95% confidence intervals) for every 1 m³/s increase in river discharge. This only holds for conditions where the river discharge exceeds a minimum threshold – defined here as the mean annual river discharge (~300 m³/s). If the threshold limit is exceeded, major flows are therefore 120% (40%-200%; 95% CI) more likely in the peak of the summer freshet (assuming an average discharge of ~500 m³/s) than in at the start of the spring freshet (assuming an average discharge of ~300 m³/s). Short-lived, extreme summer discharge peaks of up to 1000 m³/s result in a hazard rate that is 420% greater than the start of the spring freshet.

The Proportional Hazards Model results for the MBES data (including minor and major events) indicate a 2% increase in hazard rate per 1 m³/s increase in discharge above the threshold discharge limit, but the 95% confidence intervals range are +/- 2%; hence the results should be treated with some caution. This result may indicate that a more precise timing of event occurrence compared to that known for discharge is required, or that the combined record of events from all three channels is less responsive to fluxes in river discharge than the major flows that make it to the ADCP location. Regardless, river discharge is shown to be a significant explanatory variable on flow recurrence. Future changes in land-use or other processes that may lead to increased run-off should be

monitored, which may be aggravated by anthropogenic effects such as deforestation or diversion of sediment routing pathways.

Without increased river discharge in the freshet, the Squamish Prodelta would not be so active with respect to sediment density flows; hence, river discharge is considered to be the primary conditioning factor for triggering submarine flows. This is probably due to rapid slope deposition and small failures, or undercutting of channel bedforms, rather than hyperpycnal flows.

8.5.4 Tidal effects amplify the effects of river discharge to trigger flows

Tides may be a more instantaneous trigger than discharge. Hence, their lower significance for the timing of MBES events may be a function of temporal resolution as they appear to be important based on observations from the ADCP monitoring. Two scenarios are considered that implicate tides as an important variable for flow activity. In the first, additive effects are significant, such that the slope is preconditioned by increased sediment load and tidal influence (e.g. pore pressure change). This addition of two effects then tips the balance to trigger a failure. The second scenario is related to amplified effects, where combinations of low tides and enhanced river discharge enhance bed shear stresses thus triggering flows. Additive and amplified multiplicative effects are shown to be highly significant in relation to intensity of flow recurrence and timing of events, so both scenarios may be operational (Table 8.4).

8.6 Conclusions

The field data set from Squamish Prodelta, collected by John Hughes Clarke and others, is an unprecedented data set that provides insights into the timing and frequency of submarine delta lip collapses and sediment density flows. Many morphological features are seen at Squamish that are typical of deep-water turbidite systems, including feeder channels, upslope-migrating crescentic bedforms (e.g. Cartigny et al., 2011), and slump scars. While there are undoubtedly differences in terms of scale, Squamish provides a bridge between the scale-gap of laboratory experiments and real-world deep-water sites.

As suggested qualitatively by Hughes Clarke et al. (2012), cumulative river discharge is now quantitatively demonstrated to be a primary control for the ‘switch on’

of turbidity current activity. River discharge is a statistically significant variable in explaining the frequency at which turbidity currents occur. Each $1 \text{ m}^3/\text{s}$ increase in discharge above the threshold discharge (mean annual level) corresponds to a 1% increase in flow likelihood. Below that level the system is effectively ‘switched off’. Tidal elevation also contributed to the timing of flows, either through generation of excess pore pressures and instability, or as an amplification of the effect of river discharge causing elevated bed shear stresses on the delta lip.

The largest peaks in river discharge did not result in hyperpycnal flows, rather they caused more rapid progradation of the delta front, which ultimately led to large delta-lip failures ($>20,000 \text{ m}^3/\text{s}$). The triggers of delta-lip failures are shown to be complex, and require combinations of sediment delivery, erosion, as well as the preconditioning by former failures.

Table 8.5: Review of triggering mechanisms for failures and flows during surveyed interval at Squamish. It is most likely that a combination of factors are attributable

| Control | Trigger mechanism | Nature of failures/flows | Evidence at Squamish during 2011 surveys? |
|------------------------|--|--|---|
| River Discharge | Carried immediately into subaqueous channel system as turbidity currents or forms turbidity current from sediment settling out from river plume | Near-continuous flows coincident with peak of flood event | Not for the largest flows which are triggered by failures |
| | Sediments reside temporarily on parts of the delta slope to be later remobilised as they become more unstable due to development of excess pore pressures | Delta lip failures and pulses of turbidity currents following main flood event | Yes |
| | Sediment accumulates steadily during relatively low discharge periods but is subjected to very rapid erosion due to high bed shear stresses during high river discharge. | River discharge sweeps accumulated coarse-grained bar and channel sediments (with any bedload) directly onto the steep delta front slopes | Yes |
| | Bedload swept offshore may avalanche down steeply-inclined foresets on Gilbert-type delta | Sediment accelerates down inclined forsets and transitions into a turbidity current | Possible |
| Tidal Variations | Excess pore pressures in low permeability materials during low tides triggers liquefaction | Transient pore pressure changes cause liquefaction which leads to slope instability (unlikely to have any effect >1 m below seafloor) | No |
| | Tidal drawdown on gaseous sediments | Reduction in effective stress during lowered tides where gas can be brought out of solution to trigger deep-seated failure | Possible, but not for all failures |
| | Constriction of delta-top channel during low tide | Constriction of channel leads to elevated bed shear stresses causing erosion, and deposition on delta lip or triggering of sediment avalanches | Possible for both failures and flows |
| Mid-prodelta processes | Localised liquefaction or breaching within submarine channels or incision of steep margins by previous flow(s) | Triggers turbidity current on mid to lower prodelta slope | Possible for many major and minor MBES events that do not have obvious failure scarps |
| Earthquakes | Strong ground motion and development of transient excess pore pressures | Destabilisation of slope sediments due to shaking, liquefaction or strain softening | Not a trigger during 2011 surveyed period |

Table 8.6: Results of GLM and PHM analysis for ADCP events. Bold italicised p-values are significant at $p < 0.05$. Bold underlined p-values are close to being significant at $p = 0.05$.

| Explanatory Variables | Gamma GLM | | | | Cox PHM | | | |
|---|-----------------------|-----------------------------------|----------------------------|----------------------|------------------------|-----------------------------|--------------|--------------|
| | p-value | Dispersion Parameter (α) | Regression Coefficient (b) | Standard Error SE(b) | p-value | E ^b Hazard Ratio | Lower 95% CI | Upper 95% CI |
| River Discharge | | | | | | | | |
| 24 Hour River Discharge Maximum (or to last event) | <i>0.00193</i> | 0.6934189 | 0.006266 | 0.081 | <i>0.00224</i> | 1.006 | 1.002 | 1.01 |
| 24 Hour River Discharge Maximum (ignoring last event) | <i>0.00186</i> | 0.6844131 | 0.006196 | 0.081 | <i>0.00245</i> | 1.006 | 1.002 | 1.01 |
| River Discharge at Event | <i>0.00336</i> | 0.830337 | 0.008030 | 0.081 | <i>0.000854</i> | 1.008 | 1.003 | 1.013 |
| Tidal Elevation | | | | | | | | |
| Tidal Minimum Elevation | 0.0781 | 0.8750049 | 0.6182 | 0.081 | 0.159 | 1.855 | 0.7856 | 4.383 |
| Tidal Elevation at Event | 0.210 | 1.029678 | 0.1703 | 0.081 | 0.318 | 1.186 | 0.8487 | 1.657 |
| 24 Hour Tidal Range (or to last event) | <i>0.01455</i> | 0.8382925 | -0.4700 | 0.081 | <u>0.0503</u> | 0.6250 | 0.3904 | 1.001 |
| 24 Hour Tidal Range (ignoring last event) | <i>0.01641</i> | 0.9313773 | -0.8077 | 0.081 | <i>0.0387</i> | 0.4459 | 0.2073 | 0.9591 |
| Additive Effects | | | | | | | | |
| 24 Hour River Discharge Maximum (or to last event) + Tidal Minimum Elevation | <i>0.0174</i> | 0.7129597 | 0.006237 | 0.081 | <i>0.00369</i> | 1.006 | 1.0020 | 1.011 |
| 24 Hour River Discharge Maximum (or to last event) + Tidal Elevation at Event | <i>0.00711</i> | 0.6799712 | 0.007289 | 0.081 | <i>0.00159</i> | 1.007 | 1.0028 | 1.012 |

| Explanatory Variables | Gamma GLM | | | | Cox PHM | | | |
|--|----------------|-----------------------------------|----------------------------|----------------------|-----------------|-----------------------------|--------------|--------------|
| | p-value | Dispersion Parameter (α) | Regression Coefficient (b) | Standard Error SE(b) | p-value | E ^b Hazard Ratio | Lower 95% CI | Upper 95% CI |
| 24 Hour River Discharge Maximum (or to last event) + 24 Hour Tidal Range (or to last event) | 0.0495 | 0.6257779 | 0.006586 | 0.081 | 0.00328 | 1.0066 | 1.0022 | 1.011 |
| 24 Hour River Discharge Maximum (or to last event) + 24 Hour Tidal Range (ignoring last event) | 0.0575 | 0.6587101 | 0.006239 | 0.081 | 0.00446 | 1.0063 | 1.0019 | 1.011 |
| 24 Hour River Discharge Maximum (ignoring last event) + Tidal Minimum Elevation | 0.0160 | 0.7063904 | 0.006064 | 0.081 | 0.00434 | 1.006 | 1.0019 | 1.010 |
| 24 Hour River Discharge Maximum (ignoring last event) + Tidal Elevation at Event | 0.00677 | 0.6723156 | 0.007099 | 0.081 | 0.00178 | 1.007 | 1.0026 | 1.011 |
| 24 Hour River Discharge Maximum (ignoring last event) + 24 Hour Tidal Range (or to last event) | 0.0515 | 0.6240555 | 0.006239 | 0.081 | 0.004466 | 1.0063 | 1.0019 | 1.011 |
| Discharge Maximum (ignoring last event) + 24 Hour Tidal Range (ignoring last event) | 0.0549 | 0.6548088 | 0.005908 | 0.081 | 0.00724 | 1.0059 | 1.0016 | 1.010 |
| River Discharge at Event + Tidal Minimum Elevation | 0.0324 | 0.8401736 | 0.008211 | 0.081 | 0.00129 | 1.008 | 1.0032 | 1.013 |
| River Discharge at Event + Tidal | 0.0126 | 0.8190204 | 0.009378 | 0.081 | 0.000664 | 1.009 | 1.0040 | 1.015 |

| Explanatory Variables | Gamma GLM | | | | Cox PHM | | | |
|--|-----------|-----------------------------------|----------------------------|----------------------|----------------|-----------------------------|--------------|--------------|
| | p-value | Dispersion Parameter (α) | Regression Coefficient (b) | Standard Error SE(b) | p-value | E ^b Hazard Ratio | Lower 95% CI | Upper 95% CI |
| Elevation at Event | | | | | | | | |
| River Discharge at Event + 24 Hour Tidal Range (or to last event) | 0.0959 | 0.7354868 | 0.008282 | 0.081 | 0.00133 | 1.0083 | 1.0032 | 1.013 |
| River Discharge at Event + 24 Hour Tidal Range (ignoring last event) | 0.106 | 0.7734271 | 0.008218 | 0.081 | 0.00173 | 1.0083 | 1.0031 | 1.013 |
| Multiplicative Effects | | | | | | | | |
| 24 Hour River Discharge Maximum (or to last event) x Tidal Minimum Elevation | 0.595 | 0.7089533 | -0.001236 | 0.081 | 0.7142 | 0.9988 | 0.9922 | 1.005 |
| 24 Hour River Discharge Maximum (or to last event) x Tidal Elevation at Event | 0.167 | 0.5772344 | 0.001214 | 0.081 | 0.477 | 1.0012 | 0.9979 | 1.005 |
| 24 Hour River Discharge Maximum (or to last event) x 24 Hour Tidal Range (or to last event) | 0.1896 | 0.6019315 | 0.0002405 | 0.081 | 0.937 | 1.0002 | 1.0002 | 1.0006 |
| 24 Hour River Discharge Maximum (or to last event) x 24 Hour Tidal Range (ignoring last event) | 0.209 | 0.6638784 | 0.001184 | 0.081 | 0.720 | 1.0012 | 0.9947 | 1.008 |
| 24 Hour River Discharge Maximum (ignoring last event) x Tidal | 0.662 | 0.7166349 | -0.001752 | 0.081 | 0.5871 | 0.9982 | 0.9920 | 1.005 |

| Explanatory Variables | Gamma GLM | | | | Cox PHM | | | |
|---|-----------|-----------------------------------|----------------------------|----------------------|---------|-----------------------------|--------------|--------------|
| | p-value | Dispersion Parameter (α) | Regression Coefficient (b) | Standard Error SE(b) | p-value | E ^b Hazard Ratio | Lower 95% CI | Upper 95% CI |
| Minimum Elevation | | | | | | | | |
| 24 Hour River Discharge Maximum (ignoring last event) x Tidal Elevation at Event | 0.103 | 0.5925876 | 0.0007509 | 0.081 | 0.6470 | 1.008 | 0.9975 | 1.004 |
| 24 Hour River Discharge Maximum (ignoring last event) x 24 Hour Tidal Range (or to last event) | 0.246 | 0.6120994 | 0.001252 | 0.081 | 0.683 | 1.0013 | 0.9953 | 1.007 |
| 24 Hour River Discharge Maximum (ignoring last event) x 24 Hour Tidal Range (ignoring last event) | 0.251 | 0.6768793 | 0.0017859 | 0.081 | 0.565 | 1.0019 | 0.9957 | 1.008 |
| River Discharge at Event x Tidal Minimum Elevation | 0.331 | 0.7316621 | -6.673x10 ⁻⁶ | 0.081 | 0.9986 | 1.000 | 0.9926 | 1.007 |
| River Discharge at Event x Tidal Elevation at Event | 0.103 | 0.5925876 | 0.001874 | 0.081 | 0.3692 | 1.0019 | 0.9978 | 1.006 |
| River Discharge at Event x 24 Hour Tidal Range (or to last event) | 0.0892 | 0.5874619 | -6.421x10 ⁻⁵ | 0.081 | 0.989 | 0.9999 | 0.9909 | 1.009 |
| River Discharge at Event x 24 Hour Tidal Range (ignoring last event) | 0.0799 | 0.6490894 | -0.0005343 | 0.081 | 0.907 | 0.9995 | 0.9906 | 1.008 |

Table 8.7: Results of GLM and PHM analysis for MBES events. Bold italicised p-values are significant at $p < 0.05$. Bold underlined p-values are close to being significant at $p = 0.05$.

| Explanatory Variables | Gamma GLM | | | | Cox PHM | | | |
|--|-----------------------|-----------------------------------|----------------------------|----------------------|----------------------|-----------------------------|--------------|--------------|
| | p-value | Dispersion Parameter (α) | Regression Coefficient (b) | Standard Error SE(b) | p-value | E ^b Hazard Ratio | Lower 95% CI | Upper 95% CI |
| River Discharge | | | | | | | | |
| 24 Hour River Discharge Maximum | <i>0.00211</i> | 0.4218585 | 0.0020462 | 0.011 | <i>0.025</i> | 1.002 | 1.000 | 1.004 |
| Tidal Elevation | | | | | | | | |
| Tidal Minimum Elevation (Spline) | 0.4083 | 0.6733971 | 0.09027 | 0.11 | 0.685 | 1.094 | 0.7073 | 1.693 |
| 24 Hour Tidal Elevation Minimum | 0.5110 | 0.7075789 | 0.07576 | 0.11 | 0.749 | 1.079 | 0.6782 | 1.716 |
| 24 Hour Tidal Range | 0.11560 | 0.6107091 | -0.2133 | 0.11 | 0.301 | 1.238 | 0.5394 | 1.21 |
| Additive Effects | | | | | | | | |
| 24 Hour River Discharge Maximum + Tidal Minimum Elevation (Spline) | <i>0.00379</i> | 0.4318202 | 0.0021215 | 0.11 | <i>0.0262</i> | 1.0021 | 1.0003 | 1.004 |
| 24 Hour River Discharge Maximum + 24 Hour Tidal Elevation Minimum | <i>0.00379</i> | 0.4318202 | 0.0020749 | 0.11 | <i>0.0262</i> | 1.0021 | 1.0002 | 1.004 |
| 24 Hour River Discharge Maximum + 24 Hour Tidal Range | <i>0.0114</i> | 0.419926 | 0.0019182 | 0.11 | <i>0.0431</i> | 1.002 | 1.0001 | 1.004 |
| Multiplicative Effects | | | | | | | | |
| 24 Hour River Discharge Maximum x Tidal Minimum Elevation (Spline) | 0.12286 | 0.4255058 | -0.001157 | 0.11 | 0.4199 | 0.9988 | 0.9960 | 1.002 |

| Explanatory Variables | Gamma GLM | | | | Cox PHM | | | |
|--|-----------|-----------------------------------|----------------------------|----------------------|---------|-----------------------------|--------------|--------------|
| | p-value | Dispersion Parameter (α) | Regression Coefficient (b) | Standard Error SE(b) | p-value | E ^b Hazard Ratio | Lower 95% CI | Upper 95% CI |
| 24 Hour River Discharge Maximum x24 Hour Tidal Elevation Minimum | 0.3502 | 0.4291876 | 0.0005547 | 0.11 | 0.702 | 0.9994 | 0.9966 | 1.002 |
| 24 Hour River Discharge Maximum x 24 Hour Tidal Range | 0.588 | 0.428618 | 0.0001861 | 0.11 | 0.867 | 1.0002 | 0.9980 | 1.002 |

Table 8.8: Results of GLM and PHM analysis for Central Channel MBES events. Bold italicised p-values are significant at $p < 0.05$. Bold underlined p-values are close to being significant at $p = 0.05$.

| Explanatory Variables | Gamma GLM | | | | Cox PHM | | | |
|--|-----------------------|-----------------------------------|----------------------------|----------------------|----------------------|-----------------------------|--------------|--------------|
| | p-value | Dispersion Parameter (α) | Regression Coefficient (b) | Standard Error SE(b) | p-value | E ^b Hazard Ratio | Lower 95% CI | Upper 95% CI |
| River Discharge | | | | | | | | |
| 24 Hour River Discharge Maximum | <i>0.00708</i> | 0.5598379 | 0.0021236 | 0.111 | 0.0248 | 1.002 | 1.000 | 1.004 |
| Additive Effects | | | | | | | | |
| Tidal Minimum Elevation (Spline) | 0.28602 | 0.7104063 | 0.1449 | 0.111 | 0.5483 | 1.1559 | 0.7199 | 1.856 |
| 24 Hour Tidal Elevation Minimum | 0.54294 | 0.788507 | 0.07785 | 0.111 | 0.757 | 1.081 | 0.6606 | 1.769 |
| 24 Hour Tidal Range | 0.10978 | 0.6697619 | -0.2430 | 0.111 | 0.257 | 0.7842 | 0.5152 | 1.194 |
| Additive Effects | | | | | | | | |
| 24 Hour River Discharge Maximum + Tidal Minimum Elevation (Spline) | <i>0.0171</i> | 0.5564743 | 0.0020921 | 0.111 | <i>0.0301</i> | 1.0020942 | 1.0002 | 1.004 |
| 24 Hour River Discharge Maximum + 24 Hour Tidal Elevation Minimum | <i>0.0112</i> | 0.5719247 | -0.0077040 | 0.111 | <i>0.0261</i> | 1.0021300 | 1.0003 | 1.004 |
| 24 Hour River Discharge Maximum + 24 Hour Tidal Range | <i>0.0278</i> | 0.5385992 | 0.0019652 | 0.111 | <i>0.0439</i> | 1.0019672 | 1.000 | 1.004 |
| Multiplicative Effects | | | | | | | | |
| 24 Hour River Discharge Maximum x Tidal Minimum Elevation (Spline) | 0.5620 | 0.5823544 | -0.0004624 | 0.111 | 0.777 | 0.9995377 | 0.9964 | 1.003 |

| Explanatory Variables | Gamma GLM | | | | Cox PHM | | | |
|--|-----------|-----------------------------------|----------------------------|----------------------|---------|-----------------------------|--------------|--------------|
| | p-value | Dispersion Parameter (α) | Regression Coefficient (b) | Standard Error SE(b) | p-value | E ^b Hazard Ratio | Lower 95% CI | Upper 95% CI |
| 24 Hour River Discharge Maximum x24 Hour Tidal Elevation Minimum | 0.6873 | 0.5880479 | -0.0001222 | 0.111 | 0.938 | 0.9999 | 0.9968 | 1.003 |
| 24 Hour River Discharge Maximum x 24 Hour Tidal Range | 0.922 | 0.5534587 | 0.0001468 | 0.111 | 0.895 | 1.0001 | 0.9980 | 1.002 |

Table 8.9: Results of GLM and PHM analysis for North Channel MBES events. Bold italicised p-values are significant at $p < 0.05$. Bold underlined p-values are close to being significant at $p = 0.05$.

| Explanatory Variables | Gamma GLM | | | | Cox PHM | | | |
|--|-----------------------|-----------------------------------|----------------------------|----------------------|-----------------------|-----------------------------|--------------|--------------|
| | p-value | Dispersion Parameter (α) | Regression Coefficient (b) | Standard Error SE(b) | p-value | E ^b Hazard Ratio | Lower 95% CI | Upper 95% CI |
| River Discharge | | | | | | | | |
| 24 Hour River Discharge Maximum | <i>0.00543</i> | 0.5025395 | 0.002742 | 0.095 | <i>0.0347</i> | 1.002746 | 1.000 | 1.005 |
| Additive Effects | | | | | | | | |
| Tidal Minimum Elevation (Spline) | 0.4275 | 0.6708263 | 0.1564 | 0.095 | 0.63 | 1.1693 | 0.6191 | 2.208 |
| 24 Hour Tidal Elevation Minimum | 0.4314 | 0.6693735 | 0.1299 | | 0.705 | 1.1387 | 0.5806 | 2.233 |
| 24 Hour Tidal Range | 0.2071 | 0.6027279 | - 0.2400 | 0.095 | 0.465 | 0.7866 | 0.4129 | 1.498 |
| Additive Effects | | | | | | | | |
| 24 Hour River Discharge Maximum + Tidal Minimum Elevation (Spline) | <i>0.0151</i> | 0.5256554 | 0.002948 | 0.095 | <i>0.0376</i> | 1.002953 | 1.0002 | 1.006 |
| 24 Hour River Discharge Maximum +24 Hour Tidal Elevation Minimum | <i>0.0134</i> | 0.5202949 | 0.002783 | 0.095 | <i>0.0378</i> | 1.002786 | 1.0002 | 1.005 |
| 24 Hour River Discharge Maximum + 24 Hour Tidal Range | <i>0.0196</i> | 0.5063685 | 0.002657 | 0.095 | <i>0.0436</i> | 1.0027 | 1.0001 | 1.005 |
| Multiplicative Effects | | | | | | | | |
| 24 Hour River Discharge Maximum x Tidal Minimum Elevation (Spline) | <i>0.04771</i> | 0.432487 | -0.004632 | 0.095 | <u>0.05383</u> | 0.995379 | 0.9907 | 1.000 |

| Explanatory Variables | Gamma GLM | | | | Cox PHM | | | |
|---|-----------|-----------------------------------|----------------------------|----------------------|---------|-----------------------------|--------------|--------------|
| | p-value | Dispersion Parameter (α) | Regression Coefficient (b) | Standard Error SE(b) | p-value | E ^b Hazard Ratio | Lower 95% CI | Upper 95% CI |
| 24 Hour River Discharge Maximum x 24 Hour Tidal Elevation Minimum | 0.1580 | 0.4495916 | - 0.003529 | 0.095 | 0.1116 | 0.996477 | 0.9922 | 1.001 |
| 24 Hour River Discharge Maximum x 24 Hour Tidal Range | 0.385 | 0.4834308 | 0.003247 | 0.095 | 0.194 | 1.003252 | 0.99835 | 1.008 |

Table 8.10: Results of GLM and PHM analysis for South Channel MBES events. Bold italicised p-values are significant at $p < 0.05$. Bold underlined p-values are close to being significant at $p = 0.05$.

| Explanatory Variables | Gamma GLM | | | | Cox PHM | | | |
|--|----------------------|-----------------------------------|----------------------------|----------------------|----------------------|-----------------------------|--------------|--------------|
| | p-value | Dispersion Parameter (α) | Regression Coefficient (b) | Standard Error SE(b) | p-value | E ^b Hazard Ratio | Lower 95% CI | Upper 95% CI |
| River Discharge | | | | | | | | |
| 24 Hour River Discharge Maximum | <i>0.0995</i> | 0.6277292 | 0.003657 | 0.097 | <i>0.0226</i> | 1.003664 | 1.001 | 1.007 |
| Additive Effects | | | | | | | | |
| Tidal Minimum Elevation (Spline) | 0.319 | 0.631501 | 0.3333 | 0.097 | 0.387 | 1.3956 | 0.6558 | 2.97 |
| 24 Hour Tidal Elevation Minimum | 0.3479 | 0.6312593 | 0.2662 | 0.097 | 0.516 | 1.3050 | 0.5849 | 2.912 |
| 24 Hour Tidal Range | 0.1239 | 0.5930003 | -0.5471 | 0.097 | 0.16 | 0.5786 | 0.2698 | 1.241 |
| Additive Effects | | | | | | | | |
| 24 Hour River Discharge Maximum + Tidal Minimum Elevation (Spline) | 0.123 | 0.5723201 | 0.003571 | 0.097 | <i>0.038</i> | 1.003577 | 1.0002 | 1.007 |
| 24 Hour River Discharge Maximum + 24 Hour Tidal Elevation Minimum | 0.102 | 0.5454241 | 0.003562 | 0.097 | <i>0.0304</i> | 1.003568 | 1.0003 | 1.007 |
| 24 Hour River Discharge Maximum + 24 Hour Tidal Range | 0.108 | 0.4835237 | -0.003247 | 0.097 | <i>0.0466</i> | 1.003252 | 1.0000 | 1.006 |
| Multiplicative Effects | | | | | | | | |
| 24 Hour River Discharge Maximum x Tidal Minimum | 0.451 | 0.562399 | -0.003359 | 0.097 | 0.3050 | 0.996647 | 0.9903 | 1.003 |

| | | | | | | | | |
|----------------------------|-------|-----------|-----------|-------|-------|-----------|---------|-------|
| Elevation (Spline) | | | | | | | | |
| 24 Hour River Discharge | | | | | | | | |
| Maximum x | | | | | | | | |
| 24 Hour Tidal | 0.961 | 0.5687435 | -0.001963 | 0.097 | 0.536 | 0.998039 | 0.99185 | 1.004 |
| Elevation | | | | | | | | |
| Minimum | | | | | | | | |
| 24 Hour River Discharge | | | | | | | | |
| Maximum x | | | | | | | | |
| 24 Hour Tidal | 0.720 | 0.5033929 | 0.0011036 | 0.097 | 0.692 | 1.0011042 | 0.99564 | 1.007 |
| Range | | | | | | | | |

Chapter 9. Summary and future work

9.1 Overview

This PhD thesis concerns submarine landslide and turbidity current frequency from six sites worldwide and addresses the implications for hazards and climate change. **Chapter 1** underlined how understanding the frequency at which submarine landslides and turbidity currents occur has considerable importance for understanding global sediment fluxes, tsunami hazard, risk assessment for seafloor structures, and the nature and influence of future climate change. Sedimentary records (outcrop and core) were analysed from five different locations worldwide (**Chapter 2 and 3**). As part of this thesis, I performed fieldwork in Zumaia, NE Spain, assisted by James Hunt, and in the Marnoso-arenacea Formation, Italian Apennines, assisted by Fabrizio Feletti and Andrea Squazzini. I performed visual sedimentary and ITRAX geochemical core logging at the British Ocean Sediment Core Research Facility (BOSCORF) for cores taken from the Balearic Abyssal Plain. The primary data for the Marnoso-arenacea Formation, and Madeira/Iberia Abyssal Plains were provided by Giuseppe Malgesini and James Hunt respectively. A unique direct monitoring dataset from the Squamish Prodelta was provided by John Hughes Clarke. The analysis of each of the datasets was performed entirely by me and is the primary focus on this study.

Novel statistical methods (**Chapter 4**) are used to investigate the effect of sea level (**Chapter 5**) and climate change (**Chapters 6 and 7**) on large submarine landslide and turbidity current frequency, address whether landslides may themselves trigger global warming (**Chapter 6**), and explore the interaction between the two major systems for sediment transport on the surface of our planet; rivers and turbidity currents (**Chapter 8**).

9.2 Responses to initial questions posed in this thesis

The following text summarises the responses to the overarching questions raised in Chapter 1.

Question 1: How can we measure the recurrence of potentially damaging landslides and turbidity currents?

Figure 9.1 presents a summary of different methods, and the settings in which they have been deployed, to determine recurrence of landslides and turbidity currents. Most of these methods are deficient in providing a large enough number of events for quantitative analysis for a variety of reasons, as explained in **Chapter 1**. In **Chapter 3** we introduced two methods that, for the first time, provide large, extensive recurrence datasets suitable for statistical analysis. The first method is based on analysis of turbidite deposits (core and outcrop) from five different deep-water sites over a variety of different timescales (**Chapters 5 to 7**). This first approach relies on several assumptions that are only met at very few sites, which means the datasets such as those considered in this thesis are extremely valuable. In particular, the sites must feature hemipelagic mud that can be resolved from turbidite mud, good age control, negligible erosion between successive events and must represent large volume deposits. A full discussion on the assumptions is provided in **Chapter 5**. The second method relies on direct monitoring of flows, using seafloor surveying and fixed oceanographic instrumentation (e.g. ADCPs), for which a unique dataset was presented from the Squamish prodelta, British Columbia, in **Chapter 8**.

Determining recurrence intervals from sedimentary records is reliant on obtaining continuous, sedimentary sequences that are unaffected by the influence of erosion, for which age control exists and on being able to clearly discern hemipelagic mud from mud deposited by the final stages of a turbidity current. Sites where these criteria can be met, such as those discussed in **Chapters 5 to 7**, are therefore extremely valuable and future efforts should focus on exploring recurrence at such sites. Previous studies have not provided individual recurrence intervals for sufficient sample size that allow for statistical analysis (**Chapter 1**). Where statistical analysis has been attempted previously for submarine landslide recurrence, it was using global databases which feature geographic and temporal biases (Brothers et al., 2014; Urlaub et al., 2013,2014). The approach taken in this thesis provides new records that allow for statistical analysis, without the same systematic biases affecting such global landslide databases.

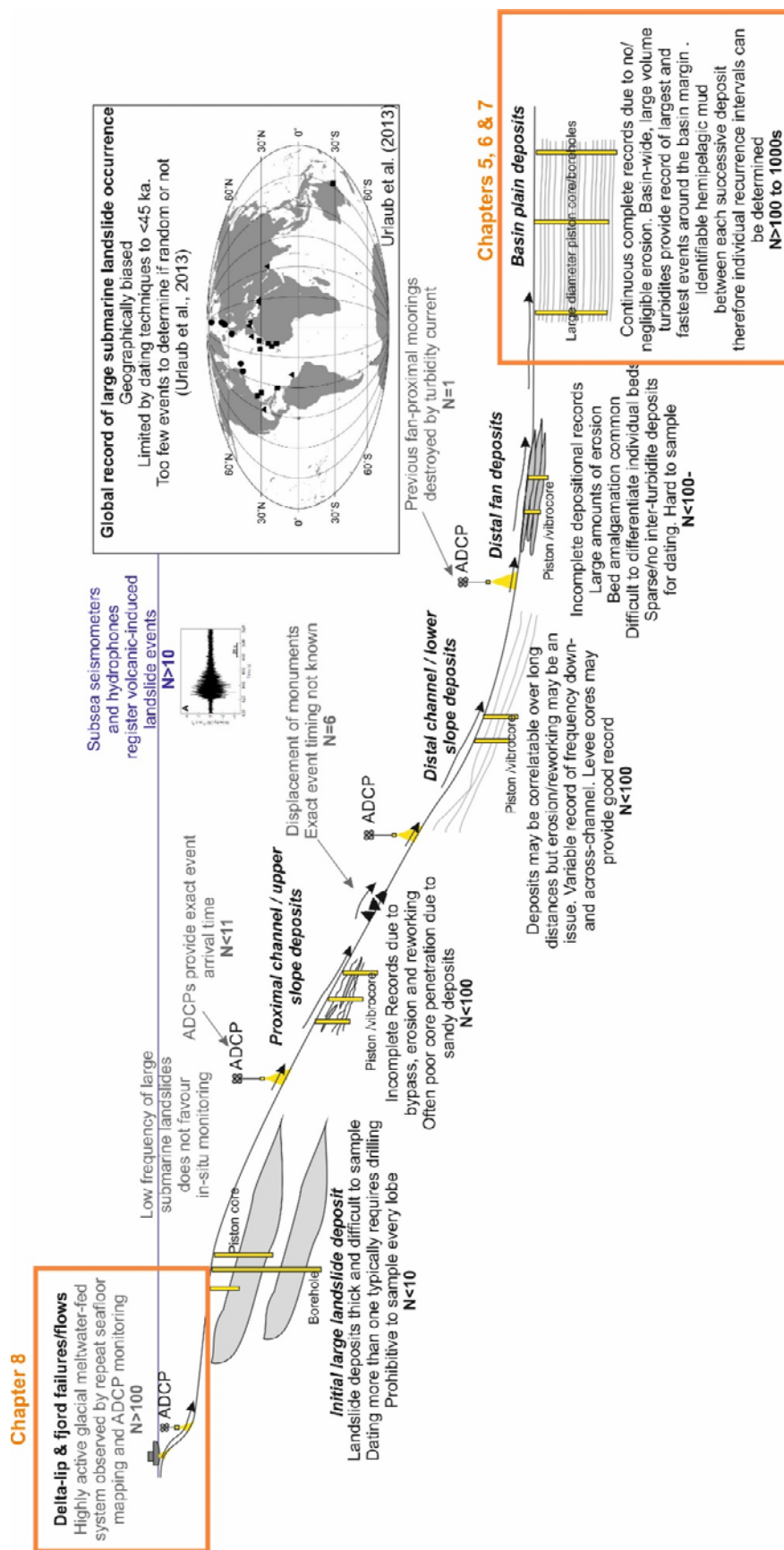


Figure 9.1: Summary of data sets used for determining landslide and turbidity current frequency. Methods used in this thesis outlined in orange. More detail on the methods is outlined in Chapter 1.

Chapter 3 summarised methods for determining recurrence intervals between landslides and turbidity currents on much shorter timescales by the use of direct monitoring. Significant developments in monitoring technology now allow us to observe flows (e.g. Hughes Clarke et al., 2012, 2013, 2014; Talling et al., 2013; Xu et al., 2014). A monitoring dataset was presented in **Chapter 8** from the Squamish Prodelta, British Columbia that captured in excess of 100 flows over a period of a few months. For the first time it is possible to statistically analyse the significance of different potential triggering mechanisms that affect flow timing and recurrence rate. It is important to perform both repeat seafloor surveying and monitoring from fixed or moored instrumentation (e.g. ADCP) in tandem, to provide a greater insight into initiation mechanisms.

Question 2: How can we quantitatively analyse recurrence of potentially damaging landslides and turbidity currents?

As most previous studies of submarine landslide and turbidite frequency have been restricted to small samples sizes, there is a paucity of literature concerning their statistical analysis. In **Chapter 4**, a novel suite of statistical analyses was outlined that can be used to characterise recurrence of submarine slides where sufficient number of observations ($N > 100$) exist. The value of unusually detailed long-term landslide records was demonstrated, and it was shown how statistical analysis provides quantitative inputs for future hazard assessments, landslide-climate studies and understanding the tempo of deep-sea sediment flux. Statistical methods have been developed by medical, economic and biological disciplines, which can be applied to analysis of submarine landslide frequency and triggering. This approach allows for quantified testing of links between recurrence and variables such as sea level or global climate, and can therefore be used to guide the inference of future hazard rate and how it may be affected by future sea level change.

Frequency analysis of field data determines the goodness-of-fit with different distribution forms for landslide recurrence, including power law, exponential and log-normal. The nature of the distribution form provides insights into potential triggering mechanisms, as discussed in **Chapters 5, 6, 7 and 8**. Rescaled range and Gaussian finite mixture models determine whether and how events are clustered in time. Parametric Generalised Linear Models and non-parametric Proportional Hazards Models were employed to test for the significance and influence of different variables and their rate of

change. All of the analyses in **Chapter 4** can be used for landslide and more widely for other hazard assessments, as well as to analyse different potential triggering or preconditioning variables than those considered in this thesis.

Question 3: Do large submarine landslides show time-dependent behaviour?

In **Chapter 5**, the analysis of large volume turbidites ($>0.1 \text{ km}^3$) in three basin plains (Marnoso-arenacea Formation, Balearic and Madeira Abyssal Plains) indicates that there is a common frequency distribution form of inter-event times for larger and faster-moving landslides that disintegrate around the basin margins. The common frequency distribution form approximates a Poisson distribution, such that the time to the next slide is independent of the time since the last. This novel conclusion may indicate similar controls on slide frequency and triggers occur in disparate areas.

In **Chapter 6**, a similar Poisson distribution form was observed for turbidite recurrence at the proto-Bay of Biscay, Zumaia, NE Spain. This lends support to the conclusion that large landslide recurrence is time-independent in distal basin plains flanked by multiple input sources. In the case of the Madeira Abyssal Plain, it was possible to discern distinct turbidite input sources based on geochemical analysis (**Chapter 5**). Each of the distinct input sources also appears to conform to a Poisson distribution. Therefore, the memoryless nature of large landslides, is not necessarily due to amalgamation of signals from different parts of the surrounding margin.

The event deposits analysed in **Chapters 5 and 6** provide a regional record of large volume flows that resulted predominantly, if not exclusively, from large submarine landslide activity. As basin plain deposits are analysed, a record is provided for the largest landslide events from all parts of the surrounding margins, and not just at a single point on the continental slope. The recognition of a characteristic Poisson distribution has important relevance for understanding global hazards including: landslide-tsunami generation that may originate at various points around basin margins; future damage to global submarine cable networks that traverse large areas of seafloor; and also understanding the tempo of deep-water sediment flux.

In **Chapter 7**, a contrasting, log-normal signature was observed for turbidite recurrence in the Iberia Abyssal Plain from ODP Site 1068. At this site, turbidite frequency shows time-dependent behaviour and appears to fall into clusters on timescales

of >1 Myr. While there is considerable variation in the mean recurrence throughout the 20 Myr sequence, a persistent log-normal distribution is identified for the entire record and also for sub-sets of the analysed period. The common log-normal distribution indicates that mean recurrence varies between clusters; however, the parameter that governs the shape of the distribution does not vary. Therefore, similarly to the findings of **Chapter 5**, the controlling mechanism(s) for landslide-turbidity current triggering is inferred to be broadly the same throughout the sequence but the preconditioning agent may vary through time.

Question 4: Is sea level a dominant control on large submarine landslide recurrence?

The Poisson distribution and lack of significance of multiple statistical analyses observed in **Chapter 5** indicates that temporally non-random processes, such as glacio-eustatic sea level change, are not dominant single controls on large submarine landslide frequency, contrary to the conclusions of some previous work (Owen et al., 2007; Lee, 2009; Brothers et al., 2013). It appears that processes that fluctuate in conjunction with eustatic sea-level and climate cycles (e.g., shelf edge sedimentation rates or hydrate dissociation driven by ocean warming) are also not dominant single controls on landslide timing. Major earthquakes have an approximately Poisson distribution of recurrence intervals, suggesting they may play a role in landslide triggering, although not all major earthquakes appear to generate large disintegrating slides. Alternatively, landslides may be triggered by processes that are yet unknown which are time-independent, by many disparate processes acting locally along a basin margin, or by a series of processes that occur one after another at a single location. It is feasible that the records analysed may also include large volume canyon flushing events; however, regardless of this, this study has important implications for predicting frequency of landslide-tsunamis, the occurrence of cable breaks, and the global tempo of sediment transport. It suggests that the frequency of large volume flows, such as those triggered by disintegrative landslides is unlikely to change significantly due to rapid eustatic sea level rise alone during forthcoming decades.

The turbidite records analysed from the Iberia Abyssal Plain in **Chapter 7** cover much longer timescales (20 Myr) and longer frequency sea level fluctuations than those in **Chapter 5**. The difference in sea level fluctuations is largely due to the more limited extent of polar ice during the Palaeocene and Eocene. Unlike the findings of **Chapter 5**, the Iberian turbidite record shows a statistically significant correlation with sea level,

albeit with a large degree of scatter. Intensification in turbidity current activity appears to show a lag of ~ 1.2 Myr after periods of sea level highstand. This pronounced lag may in fact be attributable to global temperature, and therefore climatic effects, rather than just sea level. The fact that the Iberian site is fed by a point source connected to large river system may explain the difference in signal (i.e. cleaner, less diluted climate signal in sediment discharged to the ocean), or it may relate to more simple, overall margin physiography. Despite the difference to the datasets in Chapter 5, these findings may indicate that predicted future sea level rise may not necessarily result in significantly increased submarine landslide or turbidity current frequency on human timescales.

The main conclusion that can be drawn is that the triggering mechanisms for submarine landslides and flows are shown to be non-linear and multi-faceted. Thus, a clear relationship cannot be drawn with sea level alone.

Question 5: Does millennial-scale dramatic global warming result in an increased frequency of submarine landslides and turbidity currents?

Several previous studies suggested landslide and turbidity current activity should increase during periods of rapid global warming, due to dissociation of marine sediment-hosted gas hydrates (Katz et al., 1999; Maslin et al., 2010). **Chapter 6** presented analysis of turbidite recurrence in relation to a period of unusually rapid global warming at ~ 55 Ma (McInerney and Wing, 2011), termed the Initial Eocene Thermal Maximum (IETM). The IETM hyperthermal represents the warmest period on Earth during the Cenozoic (Schmitz et al., 2001), featuring, at its peak, a dramatic 6 to 8°C warming of global deep waters over a period of approximately 10 kyr (Kennett and Stott, 1991). It has been suggested that periods such as the IETM present a possible proxy for understanding future anthropogenic climate change (e.g. Bowen et al., 2004), although they are not direct analogues (Haywood et al., 2011). Despite this, such intervals do provide valuable windows into the influence of warm climate states and elevated greenhouse gases on submarine sediment transport.

The results from two deep-water sites (Iberia Abyssal Plain and Zumaia; **Chapter 6**) indicate that the IETM corresponded to a reduction (rather than the hypothesised increase) in turbidity current and landslide activity, and was followed by a period of reduced turbidity current and landslide activity. The results may indicate that

landslide and turbidity current frequency may not necessarily increase with respect to future predicted short-term global ocean warming. This has important implications for future landslide-triggered tsunami predictions, and assessment for subsea structures that maybe vulnerable to turbidity current impacts.

Question 6: Can large submarine landslides catalyse global warming? Did large submarine landslides trigger global warming at the Initial Eocene Thermal Maximum?

It has been proposed that landslide activity, and subsequent dissociation of gas hydrates, may have triggered the IETM (e.g. Katz et al., 2001; Kennett et al., 2003; Maslin et al., 2004). The results, from local, detailed studies at two sites (Iberia Abyssal Plain and Zumaia series) and a global review based on published literature, do not support this proposal (**Chapter 6**). A period of enhanced turbidity current activity is not observed immediately prior to or at the start of the IETM, which would be expected if landslides were more common. If landslides were the primary source for methane release during the IETM, evidence is not seen at the study sites here. Therefore, it is suggested that globally widespread, landslide-triggered dissociation of hydrate may not be a likely cause for the negative $\delta^{13}\text{C}$ excursion during the IETM.

If release of buried methane is implicated in the onset of the IETM, an explanation may come from terrestrial climate effects. The transition from more humid to arid conditions at the start IETM (Schmitz et al., 2001) led to enhanced terrestrial erosion and could also have released methane from wetlands. Methane emissions from wetlands may exceed those from gas hydrates hosted in marine sediments, as suggested by isotopic analysis of methane within ice core records (Sowers, 2006).

Question 7: How does long term (>10 Myr) global warming affect turbidity current frequency?

In **Chapter 7** an unusually large (N=1571) data set of turbidite recurrence intervals was analysed, which covers several major climatic excursions over a period of 20 Myr in the Iberian Abyssal Plain. Therefore, this data set provides unique insights into the influence of pronounced global warming on turbidite recurrence. A trend of increased turbidite frequency is observed to be coincident with long-term global warming; however, clusters of anomalously long recurrence intervals actually occur during the much shorter

term warming at the Early Eocene Climatic Optimum (EECO) and Initial Eocene Thermal Maximum (IETM). This is in contrast to many studies that suggest an increase in activity would be more likely (i.e. triggering by hydrate dissociation can be ruled out during hyperthermals at this site). Proportional hazards modelling indicates that sea level exerts a statistically significant control on turbidite recurrence at the Iberian Abyssal Plain, but that intensification in activity occurred approximately ~ 1.2 Myr after periods of sea level highstand. It is hypothesised that it is long-term climatic effects, rather than sea level itself that are responsible for the shifts in turbidity current frequency.

Question 8: How are mass failures and sediment flows triggered at offshore bedload-dominated river deltas?

The unprecedented 2011 field data set acquired by Hughes Clarke et al. from the Squamish Prodelta provides insights into the timing and frequency of slope collapses and sediment density flows at an offshore river delta. In **Chapter 8**, it was demonstrated that elevated river discharge is the primary control for the ‘switch on’ of turbidity current activity and that it is a statistically significant variable in explaining the frequency at which they occur. Each $1 \text{ m}^3/\text{s}$ increase in discharge corresponds to a $\sim 0.6\%$ increase in flow likelihood above a threshold level (annual mean discharge level). Tidal elevation also contributed to the timing of flows, either through generation of excess pore pressures and instability, or as an amplification of the effect of river discharge causing elevated bed shear stresses on the delta lip.

The largest peaks in river discharge did not result in hyperpycnal flows, rather they caused more rapid progradation of the delta front, and excess pore pressures due to loading, which ultimately led to large delta-lip failures ($>20,000 \text{ m}^3/\text{s}$). The triggers of delta-lip failures are shown to be complex, and require combinations of sediment delivery, pore pressure in response to loading by sediment, erosion, as well as the preconditioning by former failures. In order to understand these, failures and flows time lapse monitoring is required, which in this case required upon both continuous moored monitoring to determine precise timing, and repeat surveys.

9.3 Future research

The following text poses some future research questions and outlines proposed directions to provide an improved understanding of submarine geohazards. The questions asked are:

- Are landslide and turbidity current geohazards time-independent, memoryless processes and can they be predicted?
 - How does this compare to recurrence of other geohazards?
- Is there a gradual continuum of geohazard frequency and magnitude?
 - If not, what are the threshold-limits for extreme events?
- How will future climate change affect geohazards and will geohazards affect climate change?

9.3.1 Are geohazards time-independent and can they be predicted?

Do different frequency distributions characterise different settings?

In this thesis it has been shown how the form of the frequency distribution for large volume turbidite recurrence may provide valuable insights into landslide triggers and preconditioning mechanisms. A Poisson distribution was identified for basin plains flanked by multiple margins (Chapter 6), and a log-normal distribution for a simpler slope setup (Chapter 7). It is important to explore whether different distribution forms characterise other, diverse settings. This can be achieved by building up a global database of regional landslide-turbidite recurrence, which should include different tectonic settings (e.g. subduction zone, volcanic, passive margins etc.), latitudes (e.g. glaciated vs non-glaciated margins), physiography, and predominant sediment inputs (volcanic, river-fed, oceanographically-controlled etc.). It will be crucial to acquire datasets specifically for statistical purposes to ensure that there are sufficient numbers of events for analysis. It should be possible to do this through specifically-targeted coring (e.g. future IODP drilling campaigns) and identification of appropriate outcrops.

Is “turbidite palaeoseismology” a valid hypothesis?

Several recent studies have suggested that the recurrence of turbidity currents matches the frequency of large magnitude earthquakes, above some specified threshold limit (typically $>M \sim 7$; Goldfinger et al., et al., 2003; 2014; Gracia et al., 2010; Goldfinger

2011; Polonia et al., 2013; Ratzov et al., 2015). In these studies, the age of turbidite emplacement is used as a proxy for earthquake timing, and aims to extend historical, monitored earthquake catalogues. This concept is appealing, as only very few large magnitude earthquakes are captured in historical record. Despite its appeal, other work has shown that not every large magnitude earthquake necessarily leads to widespread deposition of a turbidite (Völker et al., 2011; Sumner et al., 2013; Atwater et al., 2014). Palaeoseismological records are used to inform future seismic hazard predictions, hence, it is important to establish their reliability. It may be that the method is applicable in some settings, but not in others, so it is important to investigate this further.

Testing turbidite palaeoseismology using geochemical records

Ratzov et al. (2015) recently proposed that turbidites deposited on the southern margin of the Balearic Abyssal Plain were triggered by >M 7 earthquakes related to the El Asnam fault, onshore Algeria. In **Chapter 5**, it was illustrated that the frequency distribution of large landslide recurrence, including records from the distal Balearic Abyssal Plain, shows a close match with that of large magnitude earthquakes. However, this is not necessarily a unique solution and other variables are thought to be important. The mean recurrence interval for the Balearic Abyssal Plain turbidites does approximately match the mean recurrence interval for the El Asnam fault ($\lambda \sim 1.4$ kyr; Meghraoui et al., 1988). Despite this coincidence, it is hypothesised here that other seismic (and non-seismic) triggers around the margin are also important. The majority of flows that deposit in the Balearic Abyssal Plain are actually hypothesised to be sourced from the northern part of the basin (Rothwell et al., 1998; 2004); at very far-field locations from the El Asnam fault. The northern margins of the Balearic Abyssal Plain are fed by substantial river systems, in contrast to the more sediment-starved Algerian margin (**Chapter 2**). These points may support the hypothesis of Atwater et al. (2014), who suggest that turbidite frequency appears to be limited less by seismic shaking than by sediment supply (based on studies at the Cascadia subduction zone).

One method to address this is to determine the provenance of turbidites using their geochemical signature (e.g. Hunt et al., 2013, 2014). Preliminary analysis of ITRAX data (Appendix 5) appears to show an approximate correlation between the change in turbidite mudcap geochemistry and the activity of different sedimentary systems in the northern part of the Balearic Abyssal Plain (Figure 9.2 and Figure 9.3). Future analysis of these

records and proximal cores will provide greater insight into the provenance of flows, and whether basin plains can be used for turbidite palaeoseismology.

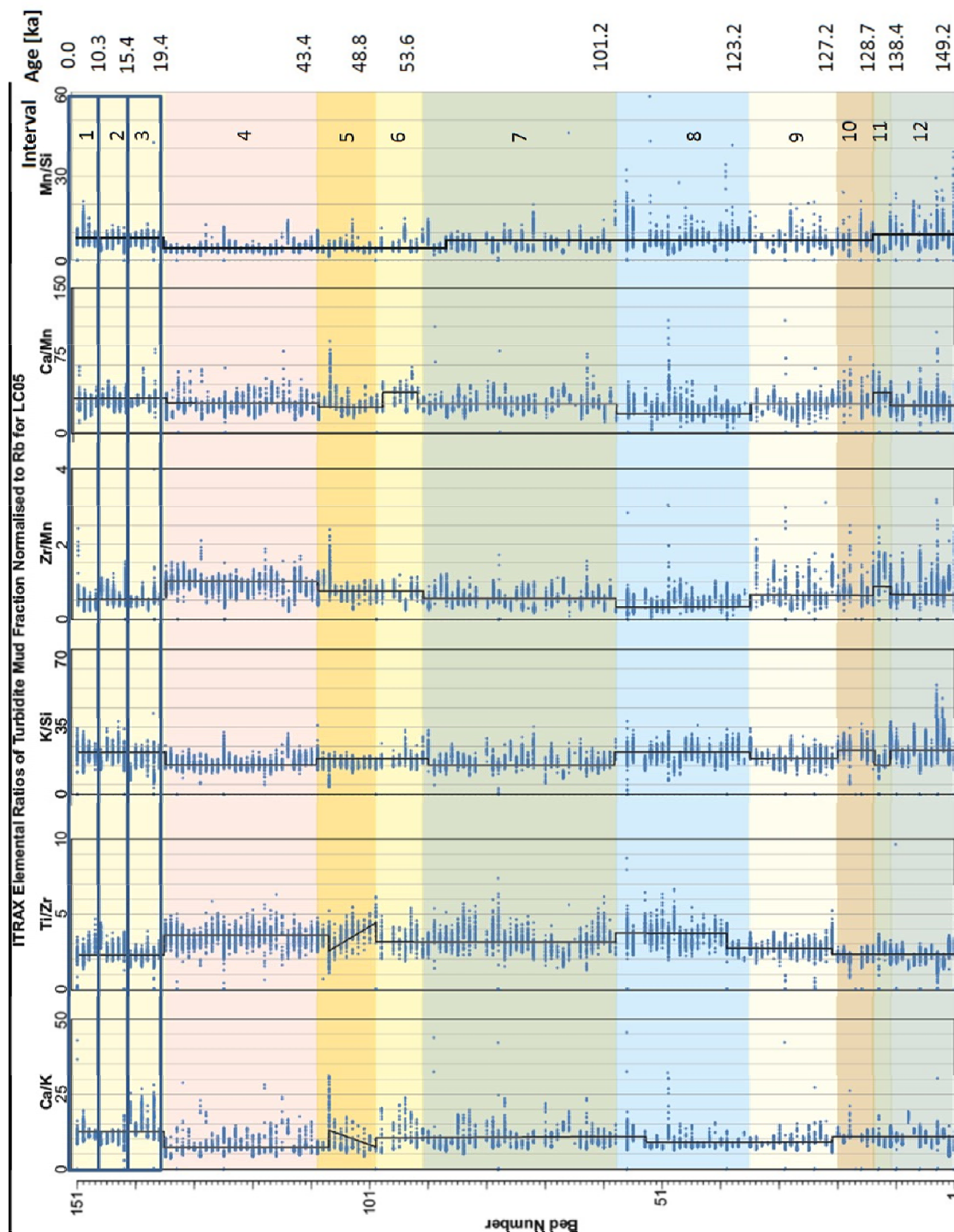


Figure 9.2: Initial compilation of mudcap geochemistry for individual turbidites in core LC05 (Balearic Abyssal Plain). Subtle changes in geochemistry may indicate shifts in the point or nature of sediment input

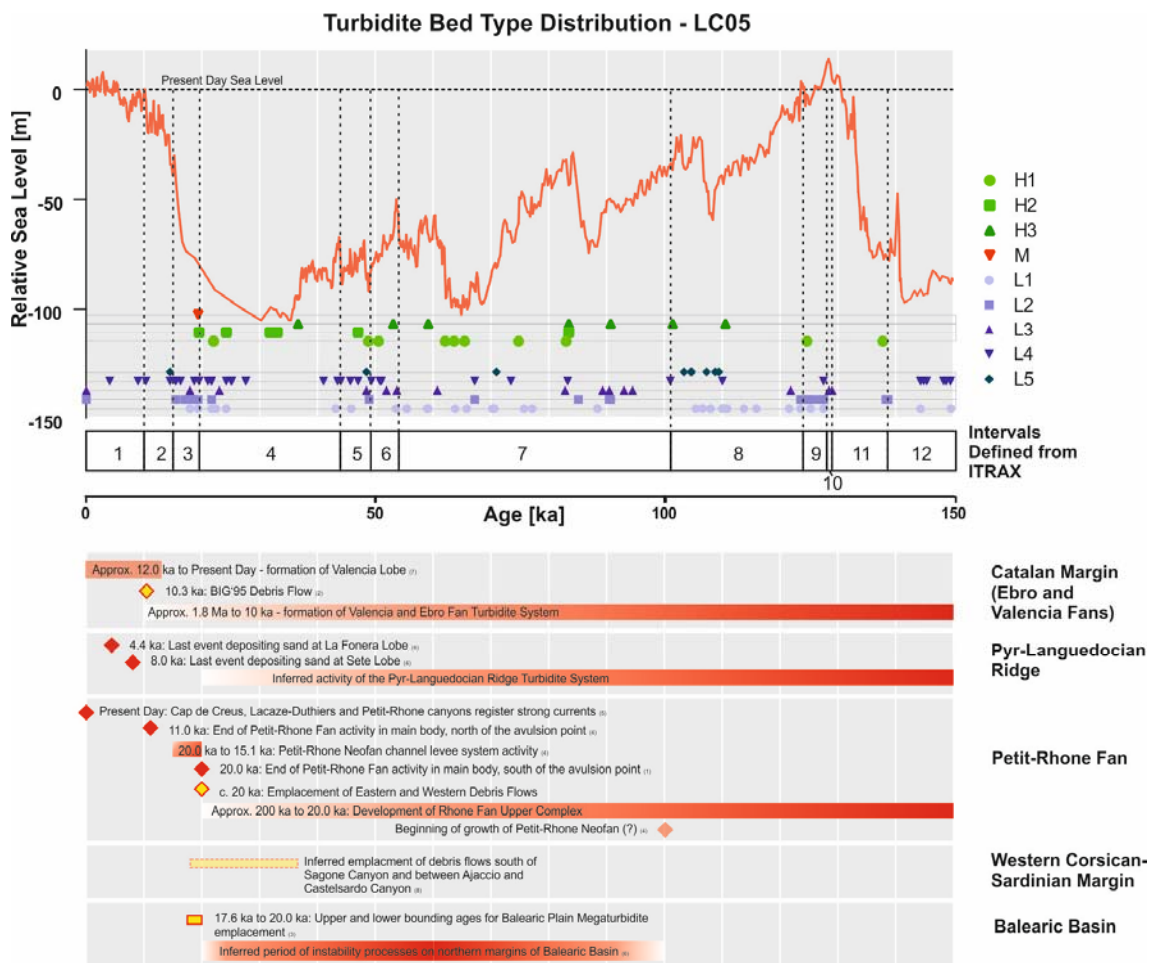


Figure 9.3: Comparison of periods defined by ITRAX analysis from Figure 9.2 with published variations in sediment input from published studies (Mear, 1984; Morris et al., 1998; Kenyon et al., 2002; Hoogakker et al., 2004; Lastras et al., 2004; Bonnel et al., 2005; Droz et al., 2006;). Future research will investigate whether there is a correlation. Turbidites are colour and symbol coded by the facies. L prefix refers to low density, H prefix to high density (sandy) turbidites and M prefix to the one megaturbidite of Rothwell et al. (1998)

Testing turbidite palaeoseismology using lake records

As highlighted above, testing the validity of turbidite palaeoseismology may be inhibited in deep-sea basins where sediment input is provided at multiple points around the margins. Many lakes have been proposed as candidate sites for turbidite palaeoseismology (Monecke et al., 2006; Strasser et al., 2006; Goldfinger, 2011; Gomez et al., 2015); however, similar issues arise, such as where delta lip failures at river fronts cannot be discerned from earthquake-triggered events. Therefore, lakes that avoid such complications are good candidate sites (e.g. they feature no direct river inflow and equal amounts of sediment input around the basin). Lake Riñihue, Calafquen, Villarica and Panguipulli in south Chile meet these criteria and provide >5.2 kyr records of landslide-triggered turbidites, which can be dated accurately using varve-counting, lead-caesium, radiocarbon and reflectivity methods (Moernaut et al., 2014; Figure 9.4). Earthquake

hazard, and related landslide activity, is of specific relevance to the south Chilean region as it has experienced several large magnitude earthquakes in historical times, including one M 9.5 event in 1960 (Moernaut, 2010). These Chilean lake sites will be used as a basis for testing the validity of turbidite palaeoseismology in a setting uncomplicated by different sediment input sources.

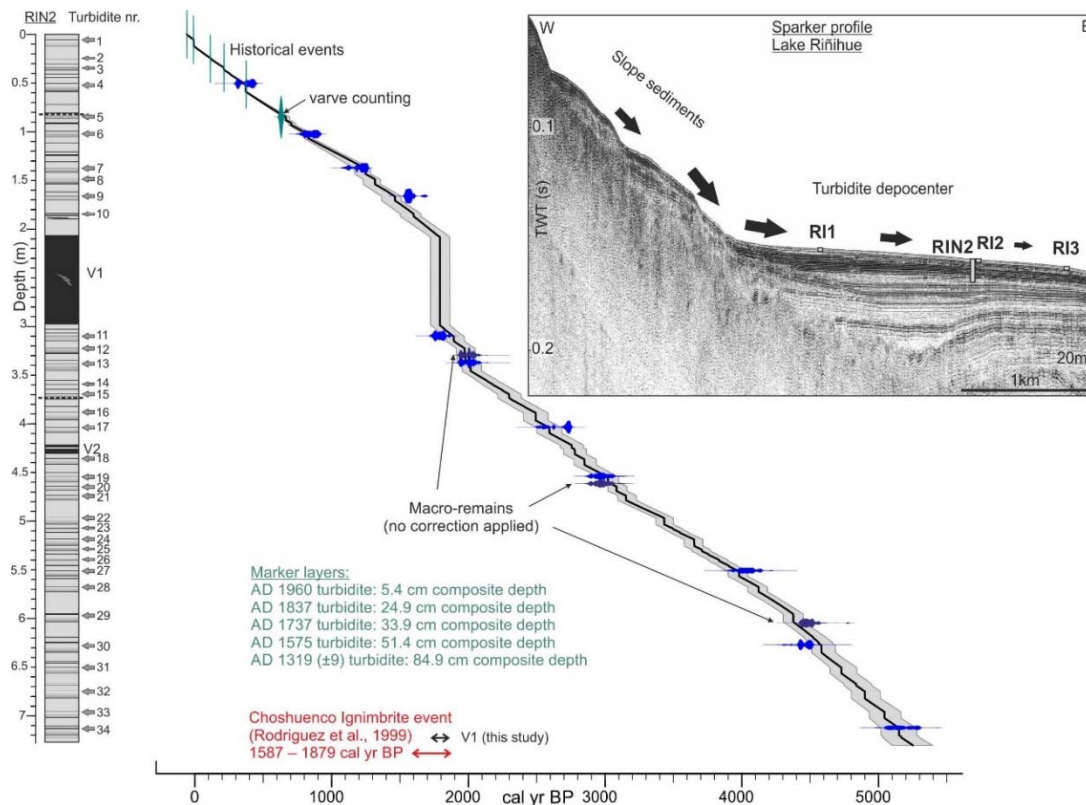


Figure 9.4: AMS radiocarbon data and their calibrated (and corrected) ages for Lake Riñihue turbidite record (from Moernaut, Clare et al., In Review)

Do different frequency distributions characterise different geohazards?

Statistical methods for the analysis of landslide frequency were introduced in **Chapter 3**. These same methods can be applied more widely to the analysis of other recurrent geohazards, such as earthquakes and oceanic island flank collapses and eruptions. Such analysis will address whether different geohazards conform to distinct frequency distribution forms, and also enable an enhanced understanding of the efficiency of seismic and/or volcanic triggering of submarine landslides. Initial work indicates that recurrence intervals of large earthquake-triggered turbidites deviate significantly from both Poisson and power law distributions, based on analysis of core data from Lake Riñihue, south Chile (Moernaut, Clare et al., In Review.). Instead, a log-normal distribution appears to be a close match, which may indicate time-dependent behaviour

for large earthquakes in south Chile, albeit for a record of only $N=33$ (Figure 9.5). It is proposed to explore this potential time-dependence through more detailed analysis of additional cores from Lake Riñihue and Lake Villarica, Calafquen and Panguipulli.

The rate of output at individual volcanoes is known to vary through time (Singer et al., 2008; Pinel et al., 2010). Growth of volcanic islands is often punctuated by large flank collapses which may be related to eruptions as well as gravitational instabilities (Hunt et al., 2013; Coussens et al., In Review.). Both volcanic eruptions and tsunamis that result from flank collapses are potentially serious hazards. Through analysis of long-term sedimentary records offshore from volcanic islands, it may be possible to further understand relative controls on volcano growth and destruction. Where long enough records can be acquired, this will also facilitate statistical analysis of cycles of dome formation and minor explosive activity, which will inform hazard assessments. Exceptional, long-term (1 Myr) records were acquired offshore Montserrat in the Lesser Antilles, as part of IODP leg 340 (core U1395B). This site provides a unique archive of events offshore from an island arc volcano. Initial statistical analysis of tephra fall and turbidity current recurrence, interpreted to relate to periods of increase volcanic activity, indicates periods of significant clustering (Coussens, Clare et al., In Prep.). Rescaled range analysis indicates trend-reinforcing behaviour ($K=0.829$). A log-normal distribution also appears to characterise recurrence, which indicates time-dependent behaviour (Figure 9.5). More detailed analysis of both offshore and onshore records will hopefully reveal more details on how eruptive and collapse events change in response to the evolution of an island arc volcano.

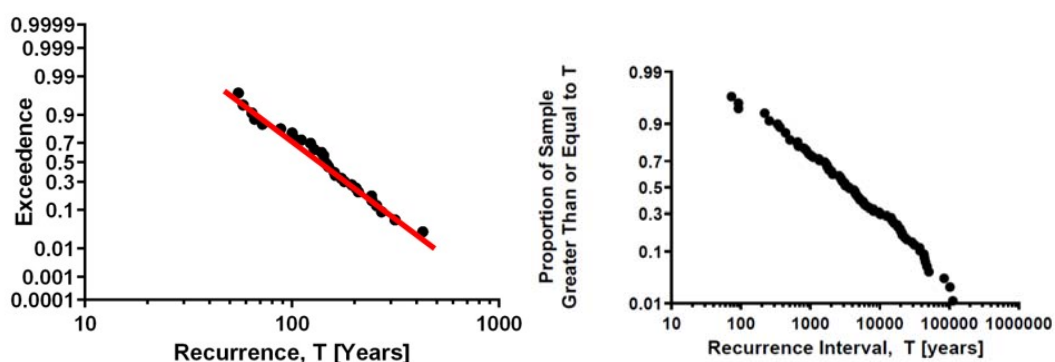


Figure 9.5: Exceedence plots of turbidite recurrence both showing close to a straight-line fit on log-probability axes which is indicative of a log-normal distribution. Left from Lake Riñihue, Chile ($N=34$; Moernaut, Clare et al., In Prep.) and right from offshore Montserrat, (IODP core U1395B; $N=88$ turbidites; Coussens, Clare et al., In Prep.)

How does event magnitude and deposit or grain size relate to recurrence periods?

This thesis is primarily concerned with characterising the *frequency* of large volume landslide and turbidity current events. It will also be important to understand the *magnitude* of these events. Future analysis should assess whether any of the controls assessed in this thesis in relation to event recurrence may instead be implicated as controls on event magnitude. Malgesini (2012) hypothesised that, while turbidite recurrence appeared to be memoryless, the thickness and amount of sand in turbidites of the Marnoso-arenacea Formation may correlate with sea level changes and show time-dependence. Initial analysis of the Balearic Abyssal Plain records presented in **Chapter 5** indicates that a similar trend may exist. Sandy, high density turbidites (*sensu* Talling et al., 2013) are much less prone during sea level highstands. Generalised linear and proportional hazards modelling indicate that turbidite bed thickness shows a significant correlation with periods of greatest sea level change (Table 9.1). The thickness of the sand and silt component of turbidites is also significantly correlated with sea level change, and is close to significant at the 90% level in relation to absolute sea level (Table 9.1). Therefore, the largest events (and perhaps the greatest availability of sediment) may correspond to periods of greatest sea level change. Further analysis should explore this possible relationship between event magnitude and sea level. A useful coupling of magnitude and frequency may then be possible for improving future hazard assessments.

Table 9.1: Preliminary results of Generalised Linear Model and Proportional Hazards Model for Balearic Abyssal Plain comparing turbidite bed thickness with sea level and its derivative. Bold italicized values indicate significance ($p < 0.005$)

| | | Turbidite bed thickness vs sea level | Turbidite bed thickness vs derivative of sea level | Turbidite bed thickness (sand and silt only) vs sea level | Turbidite bed thickness (sand and silt only) vs derivative of sea level |
|-----|----------------------|--------------------------------------|--|---|---|
| GLM | GLM alpha | 2.849 | 1.562 | 1.712 | 1.633 |
| | p-value | 0.140 | <i>0.001</i> | 0.084 | <i>0.010</i> |
| PHM | Likelihood test | 0.477 | <i>0.005</i> | 0.123 | <i>0.042</i> |
| | Wald test | 0.475 | <i>0.010</i> | 0.118 | 0.067 |
| | Score (logrank) test | 0.474 | <i>0.008</i> | 0.118 | 0.062 |

9.3.2 How will future climate change affect geohazards (and will geohazards affect climate change)?

Global inventory of climate change-submarine landslide interaction

Chapters 6 and 7 explored the implications of both relatively short and long-term climate change on large turbidite frequency. Many more examples of dramatic climate change exist in the geological record than analysed in this thesis. It is recommended that sites featuring similar records crossing other periods of climate change are investigated to further the understanding of potential links with landslide-turbidite frequency. This may include additional IETM sites like those in Figure 9.6 to develop the conclusions made in **Chapter 6**, as well as other periods of climate change (e.g. EECO, ELMO, Heinrich events etc.). Marine studies should be coupled with analysis of equivalent terrestrial and/or shallow water records where possible, to provide better constraint on sediment budgets and routing pathways. A global inventory should be compiled to provide an enhanced understanding of how climate change may affect landslide-turbidite frequency and vice versa. This could be expanded to include other geohazards and the interrelated effects of climate change, such as river floods (and hyperpycnal flow events), volcanic eruptions and flank collapses, and seismic hazards.

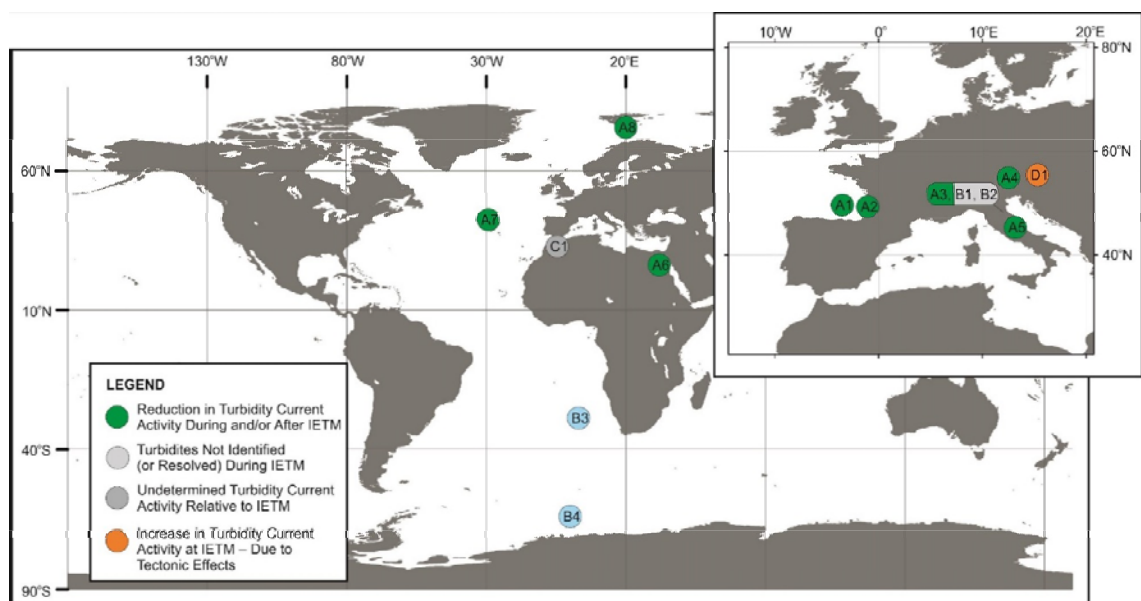


Figure 9.6: Summary of other deep-water IETM sites that could form the initial basis of a global inventory to investigate the influence of climate change on large submarine landslide-turbidite frequency. See Chapter 6 for details on locations and data sources.

Will short-term, climate change affect the stability of offshore river deltas?

Given the dramatic global warming that is forecast for the coming decades (Haigh et al., 2013), it is also important to understand whether more recent deviations in seasonal temperatures may affect the frequency of failures and flows at settings such as river deltas. In **Chapter 8** it was demonstrated that the main control on flow frequency at the Squamish Prodelta is related to periods of elevated river discharge. River discharge has historically been highest in British Columbia during the late spring and summer freshet, due to the arrival of glacial meltwater (Hughes Clarke et al., 2012). In contrast to past patterns, the winter of 2014 and spring of 2015 were the warmest on record in British Columbia, due to stagnation of the jet stream oscillations (Liu et al., 2014; NOAA, 2015). This unseasonal warmth resulted in early bursts of snow and glacier melt, as well as rainfall bursts, causing several anomalous discharge peaks of $>1000 \text{ m}^3/\text{s}$ at the Squamish prodelta from November 2014 to January 2015 (Hughes Clarke, Personal Communication). Future monitoring efforts should be made at this, and other sites, to investigate how future global warming may contribute to the dynamics of offshore river deltas.

9.3.3 Is there a gradual continuum of geohazard frequency and magnitude? If not, what are the threshold-limits for extreme events?

Chapters 5 to 7 of this thesis, investigated the frequency of large ($>0.1 \text{ km}^3$) flows capable of transporting sediment to distal basin plains. It is likely that many more, smaller slope failures and flows did not make it to the basin plain. They may deposit further upslope, providing material for future failures, or stored within canyons that is entrained or flushed out by subsequent flows. In **Chapter 8**, flows that transport much smaller volumes ($<<0.00005 \text{ km}^3$) were analysed, but it was also identified that several of the even smaller flow events either dispersed or deposited upslope of the ADCP location. It is important to understand if long run-out flows should be considered as extreme events, or if there is a progressive continuum of event frequency and magnitude. Therefore, the following questions are now asked: Is there a threshold event size that can make it to distal basin plains?; Do flows gradually decelerate, leading to a gradual transition from proximal to distal frequency distribution forms, or do they stop abruptly, resulting in two distinct frequency distributions forms? Answering these question will help to understand if the same triggers and preconditioning factors should be considered for all submarine

landslide and flow events. Determining if there is a threshold limit, and what that limit is, will require characterisation of sediment volumes and of flow frequency by considering a series of proximal to distal sites.

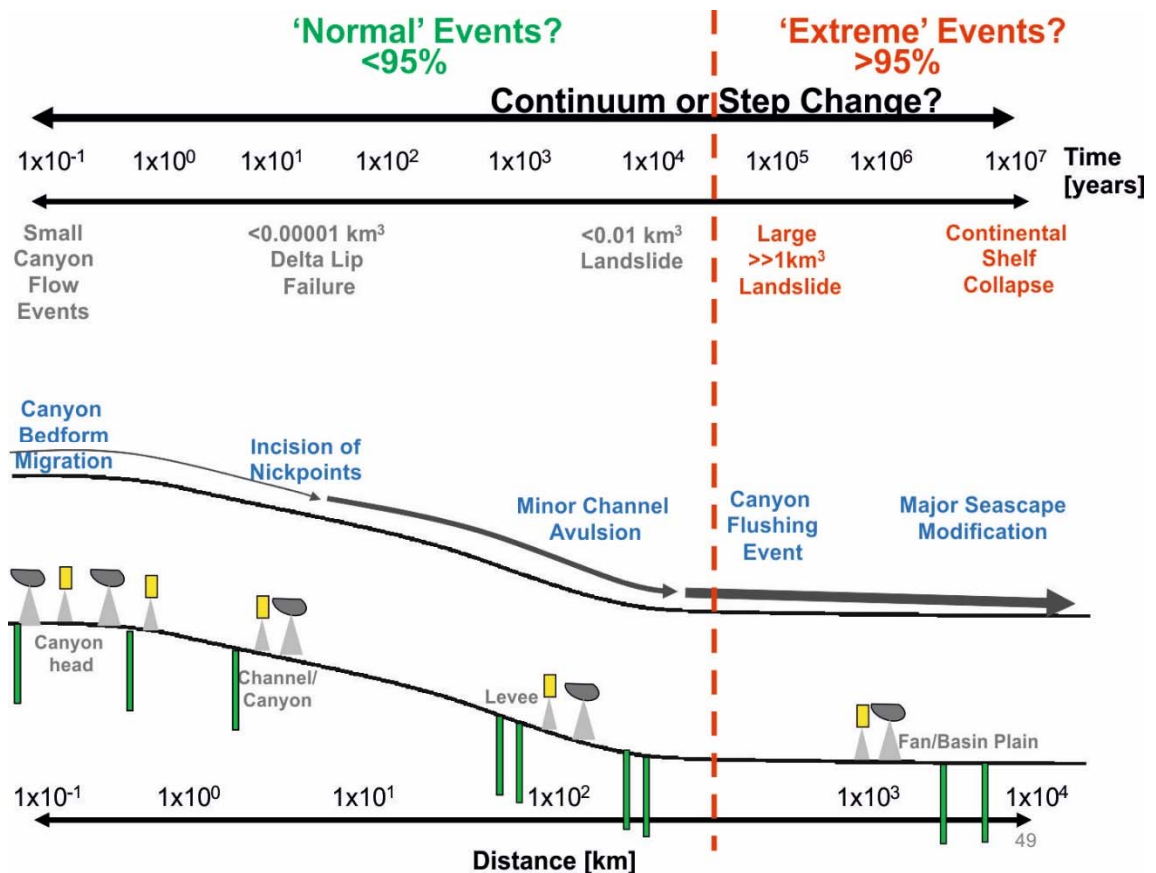


Figure 9.7: Schematic illustrating the hypothesized step-change between normal and extreme events, comparing different scales of magnitude and time. The lowermost profile is annotated with green cores, yellow fixed monitoring points, and grey repeat bathymetric and seismic surveys to illustrate the multiple techniques required to investigate whether a continuum in magnitude and frequency exists.

How does the frequency of proximal channel levee and distal basin plain deposition vary?

Future analysis of sedimentary records should include comparison of distal basin plain cores (as presented in this thesis) with more proximal cores. As outlined in **Chapter 1**, there are many limitations of using proximal sites – predominantly related to the enhanced potential for erosion. The most suitable locations for targeting cores in such settings will therefore be on channel levees where flows are predominantly depositional, as erosion is focussed in the channel axis (e.g. Hubbard et al., 2014). Statistical comparison of initial data from a channel levee site and a distal basin plain site in the modern day Iberia Abyssal Plain indicates two contrasting frequency distributions may

exist for turbidite recurrence (Allin, Clare et al., In Review). The distal basin plain record appears to conform to a Poisson distribution (Figure 9.8), whereas the proximal channel levee site shows a better fit to a log-normal, time-dependent form. The results of generalised linear and proportional hazards modelling for these initial data indicate a strong significant relationship for sea level in relation to turbidite recurrence ($p < 0.001$) for the proximal levee site. This may indicate that smaller flows are linked to a sea level control; however, the biggest events (and therefore most geohazardous), that include large landslides and canyon flushing events, may occur independently of sea level. The aggregation of probability distributions for the different factors that are required to trigger large landslides or flows that can transport to deep-water may result in a Poisson distribution for their recurrence. Additional cores will be required to validate such findings, and it is recommended that candidate sites are identified for combinations of sampling and direct flow monitoring.

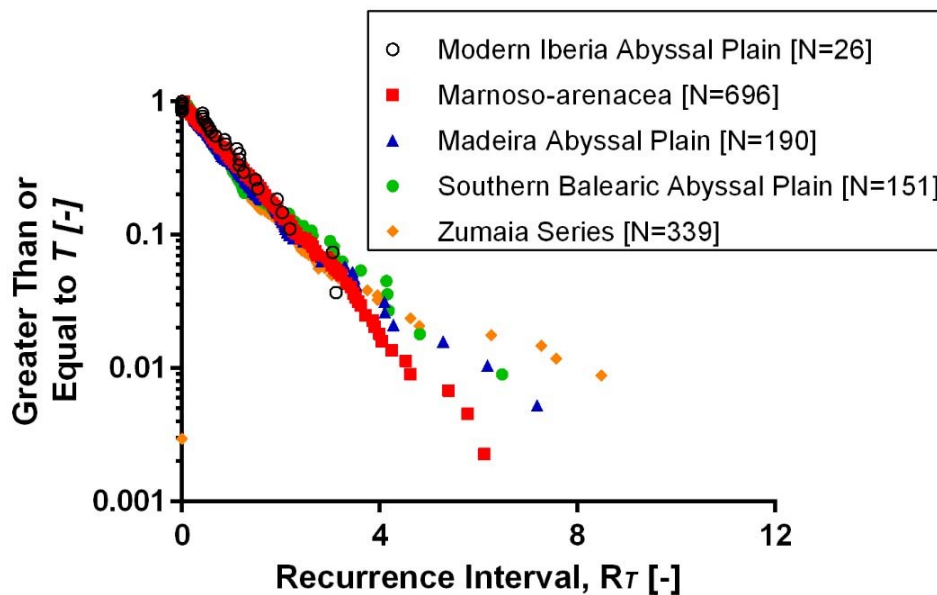


Figure 9.8: Exceedence plot comparing modern Iberia Abyssal Plain record with data sets from Chapters 5 and 6 (from Allin, Clare et al., Submitted.)

Integrated monitoring and coring efforts

It is recommended that future studies should integrate both analysis of depositional records and direct monitoring to answer the questions on both temporal and spatial scales. As shown in **Chapter 8**, sites such as the Squamish Prodelta provide a relatively easy-to-access environment in which to study highly recurrent slope failures and flows. Longer-term monitoring should be performed, should include multiple ADCP deployments down

the most active (northern) channel and further offshore, to determine whether there is a gradual reduction in frequency of flows with distance from source, or if there are locations where flows abruptly decelerate and deposit. The monitoring should be supplemented with coring from proximal to distal parts of the Howe Sound to ascertain how representative the depositional record is of flow events. It is anticipated that large events, capable of transporting sand to distal parts, may occur infrequently, but how that frequency relates to the sub-annual events is currently unclear (Talling et al., 2015).

A larger-scale three-year experiment is planned for September 2015 in the Monterey Canyon, California. The Monterey Canyon is known to feature sub-annual flows which are thought to be triggered by storm waves in the head of the canyon (Xu, 2010; Xu et al., 2014). This is a large collaborative project led by Monterey Bay Aquarium Research Institute (MBARI), United States Geological Survey (USG), National Oceanography Centre Southampton (NOC), Hull University and Ocean University of China (OUC). Instrumentation, including current meters and ADCPs will be deployed from fixed down-looking moorings and upward-looking frames at multiple points down the Monterey Canyon from ~300 m to ~2000 m water depth. Water column monitoring will be supplemented by regular repeat bathymetric surveys, which will be performed soon after flows trigger frame-mounted self-triggering event detectors (similar to a wind vane). Calibration of the depositional record will be gained by acquiring shallow cores and suspended sediment will be caught at various heights above seafloor using sediment traps. This combination of monitoring and sampling will enable the answering of questions relating to triggers, how flows evolve, and how frequency changes from proximal to distal settings.

Monitoring using existing seafloor infrastructure

The offshore geohazards sector needs to understand the potential impacts of flows on seafloor structures (Clare et al., 2015d); however, suitable information is not typically available, potentially leading to over-conservative design criteria and extra costs. Addition of flow monitoring instruments to deep-water oil and gas field developments (such as through sensors attached to manifolds, pipelines, flowlines, or risers) could provide long-term (lifetime of field) monitoring datasets. Such initiatives would involve relatively low cost, and would inform future phases of field development and geohazard assessment. Oceanographic water-column information and measurements of structural

pile settlement are already often recorded in such a manner. Future opportunities to add scientific instruments to repeater nodes in submarine telecommunication cable networks could also be explored.

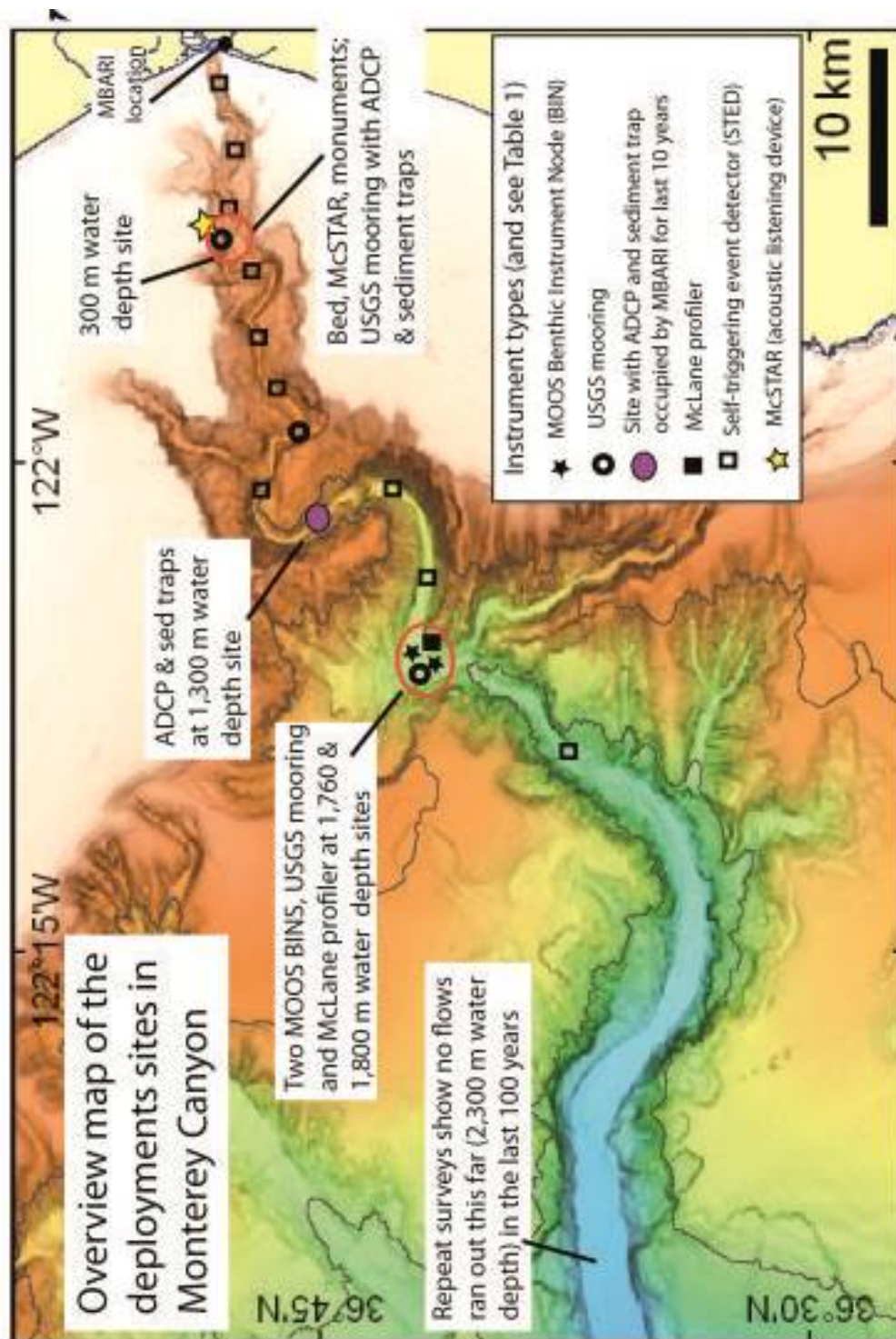


Figure 9.9 Proposed deployment of monitoring instruments for proposed 2015-2018 Monterey Canyon experiment, to include acoustic Doppler current profilers (ADCP), sediment traps (sed traps), benthic event detectors (BED). Benthic instrument nodes (BINs) will host multiple acoustic instruments on the seafloor. (Courtesy of MBARI).

9.4 Concluding remarks

This thesis presented novel methods for the determination and analysis of landslide and turbidity current frequency. Using extensive records with a large enough number of events for statistical analysis have demonstrated for the first time that:

- Large submarine landslide frequency has a common frequency distribution at three disparate deep-water sites which approximates a Poisson (memoryless, time-independent) form.
- Regional large submarine landslide recurrence does not appear to be controlled by a dominant sea level trigger.
- Submarine landslide and turbidity current frequency did not increase during the most dramatic period of global warming in the last 65 Ma (IETM); it actually decreased significantly at two deep-water sites (Iberia Abyssal Plain and Zumaia).
- Submarine landslide and turbidity current frequency may be correlated with periods of sustained (>1 Myr) global warming, but significant (up to 1.2 Myr) time lags are shown to exist. This signal may be most clear at deep-water sites with a relatively simple sediment delivery system. Other sites with more complex transport routes or variable controls may have a much more diluted signal.
- Periods of enhanced river discharge at river deltas do not necessarily cause hyperpycnal flow, and may in fact trigger delayed failures of the delta lip due to generation of excess pore pressures. This could not be deduced without repeat seafloor surveys.
- Triggers for flows at offshore river deltas are complex. Preconditioning is set up by enhanced river discharges. The ultimate triggers relate to lowered tidal elevations causing transient enhanced bed shear stresses and increased sediment transport on the delta lip.

Thus, we can conclude that:

Controls and triggering mechanisms for submarine landslides are non-linear

The fate of sediment from point of erosion onshore to deposition in the deep-sea is complex. Sediment may pass through several sediment conduits and staging areas, controlled by multiple environmental processes, before accumulating on the continental slope. The point at which that sediment fails as part of a submarine landslide event on the

continental slope is further governed by factors such as sediment accumulation rate, nature of the sediment and its relation to pre-existing topography, critical sediment thickness and slope, pore pressure regime and the effectiveness of an external trigger to cause failure. The conditioning and triggering mechanisms for large submarine landslides are therefore complex, often resulting in chaotic-looking sequences of recurrence. This may implicate a purely random, time-independent trigger, but it is more likely to indicate that the triggering mechanisms are non-linear and multi-faceted. Thus, a Poisson distribution form, which indicates time independence and a lack of memory, may characterise such apparent chaos. A constant hazard rate can be inferred through time for such systems.

River-dominated systems may partially preserve climatic signals

Some systems, such as the Iberian Abyssal Plain appear to show some time-dependence, as a persistent log-normal form was noted for the recurrence intervals. A climatic signal appears to be preserved in the recurrence of turbidites in the basin plain, albeit with a large degree of scatter which may be due to partial signal-shredding effects. The reason for the signal preservation may be due to the magnitude of the global warming during the Early Eocene Climatic Optimum. Signal preservation may be favoured in systems where rivers are the dominant, and undiluted, input to offshore canyon systems, as they may record changes in precipitation, aridity, surface runoff, and vegetation cover.

Turbidity current response to global warming is complex

The rapidity and duration of global ocean warming may be as important as its magnitude when it comes to controls on turbidity current frequency. The short-lived but intense Initial Eocene Thermal Maximum (IETM) showed a switch off in activity at the Zumaia and Iberia sites, while the prolonged Early Eocene Climatic Optimum (EECO) appeared to correspond with a steady increase in turbidite frequency. The frequency of turbidity current recurrence shows non-linear behaviour, due to the complex nature of multiple interlinked systems and external variables.

Controls on mass failures and flows at offshore river deltas are interlinked

Turbidity current frequency at the Squamish prodelta responds closely in phase with the discharge of the river, which is probably attributable to its proximity. As river discharge increases beyond a threshold limit (the annual mean), so does the frequency of

flows. This correlation is relatively undiluted, presumably because of the proximity of the river source and the quantity of sediment that is provided by the river. A secondary variable (tidal elevation) is also capable of triggering slope failures, which can result in flows occurring during lower relative river discharge periods. Thus, this serves to weakly dilute the river discharge signal. The study at Squamish shows the importance of understanding preconditioning as well as direct triggering processes. Flows appear to be preconditioned by the amount of sediment available, but are most likely during lowered tides when shear stresses are greatest on the delta top. Delta lip failures require a sufficient sediment to have accumulated which can be in a cumulative manner (over several weeks) which may be triggered by an extremely low tide, or due to sudden aggradation during a flood discharge event where no significant tidal reduction is required to trigger failure. While Squamish prodelta is a relatively small-scale system, it illustrates the potential complexity on just one slope with one sediment input source. This provides some useful context for when we try and understand the controls and variables that may affect deep-water systems and multiple margins.

References

- Agnini, C., Fornaciari, E., Rio, D., Tateo, F., Backman, J., and Giusberti, L. (2007). Responses of calcareous nannofossil assemblages, mineralogy and geochemistry to the environmental perturbations across the Paleocene/Eocene boundary in the Venetian Pre-Alps. *Marine Micropaleontology*, 63(1), 19-38.
- Agnini, C., Muttoni, G., Kent, D. V., and Rio, D. (2006). Eocene biostratigraphy and magnetic stratigraphy from Possagno, Italy: the calcareous nannofossil response to climate variability. *Earth and Planetary Science Letters*, 241(3), 815-830.
- Alegret, L., Ortiz, S., Orue-Etxebarria, X., Bernaola, G., Baceta, J. I., Monechi, S., and Pujalte, V. (2009). The Paleocene–Eocene thermal maximum: new data on microfossil turnover at the Zumaia section, Spain. *Palaaios*, 24(5), 318-328.
- Allen, P. A. (2008). Time scales of tectonic landscapes and their sediment routing systems. Geological Society, London, Special Publications, 296(1), 7-28.
- Allen, T. I., Marano, K. D., Earle, P. S., and Wald, D. J. (2009). PAGER-CAT: A composite earthquake catalog for calibrating global fatality models. *Seismological Research Letters*, 80(1), 57-62.
- Amundsen, H. B., Laberg, J. S., Vorren, T. O., Haflidason, H., Forwick, M., and Buhl-Mortensen, P. (2015). Late Weichselian–Holocene evolution of the high-latitude Andøya submarine Canyon, North-Norwegian continental margin. *Marine Geology*, 363, 1-14.
- Amy, L.A., and Talling, P.J. (2006) Anatomy of turbidites and linked debrites based on long distances (120 x 30 km) bed correlation, Marnoso Arenacea Formation, Northern Apennines, Italy, *Sedimentology*, v. 53, p. 161-212.
- Anthony, E. J. and Julian, M. (1997). The 1979 Var Delta landslide on the French Riviera: A retrospective analysis. *Journal of Coastal Research*, 27-35.
- Arzola, R. G., Wynn, R. B., Lastras, G., Masson, D. G., and Weaver, P. P. (2008). Sedimentary features and processes in the Nazaré and Setúbal submarine canyons, west Iberian margin. *Marine Geology*, 2501, 64-88

- Assier-Rzadkiewicz, S., Heinrich, P., Sabatier, P. C., Savoye, B. and Bourillet, J. F. (2000). Numerical modelling of a landslide-generated tsunami: the 1979 Nice event. *Pure and Applied Geophysics*, 157(10), 1707-1727.
- Atwater, B. F., and Griggs, G. B. (2012). Deep-sea turbidites as guides to Holocene earthquake history at the Cascadia Subduction Zone—Alternative views for a seismic-hazard workshop. *US Geological Survey Open-File Report*, 1043, 58.
- Atwater, B. F., Carson, B., Griggs, G. B., Johnson, H. P., and Salmi, M. S. (2014). Rethinking turbidite paleoseismology along the Cascadia subduction zone. *Geology*, 42(9), 827-830.
- Aubry, M.-P. (1995). From chronology to stratigraphy: interpreting the lower and middle Eocene stratigraphic record in the Atlantic Ocean. In: Berggren, W. A., Kent, D. V., Aubry, M.-P. and Hardenbol, J. (eds) *Geochronology, Time Scales and Global Stratigraphic Correlation*. SEPM Special Publications, 54, 213-274.
- Ayranci, K., Lintern, D. G., Hill, P. R., and Dashtgard, S. E. (2012). Tide-supported gravity flows on the upper delta front, Fraser River delta, Canada. *Marine Geology*, 326, 166-170.
- Azpiroz, M., Cartigny, M., Talling, P.J., Clare, M.A., Cooper, C., Parsons, D., Sumner, E.J., Simmons, S. and Pope, E. (In Prep.). The structure and dynamics of run-away turbidity currents in the deep ocean, *Nature*.
- Baceta, J.I., Pujalte, V., Dinares-Turrell, J., Payros, A., Orue-Etxebarria, X. and Bernaola, G. (2000). The Palaeocene/Eocene Boundary Interval in the Zumaia Section (Gipuzkoa, Basque Basin): Magnetostratigraphy and High –Resolution Lithostratigraphy, *Revista de la Sociedad Geológica de España*, v. 13, p. 375-391.
- Barkoulas, J., Baum, C. and Travlos, N. (2000). Long Memory in the Greek Stock Market, *Applied Financial Economics*, 10, 177–184.
- Barley, B. (1999) Deepwater problems around the world. *Leading Edge*, v. 18, p. 488-494.
- Barron, E. J. and Peterson, W. H. (1990). Mid-Cretaceous ocean circulation: Results from model sensitivity studies. *Paleoceanography*, 5(3), 319-337.

- Baztan, J., Berne, S., Olivet, J. L., Rabineau, M., Aslanian, D., Gaudin, M., and Canals, M. (2005). Axial incision: the key to understand submarine canyon evolution (in the western Gulf of Lion). *Marine and Petroleum Geology*, 22(6), 805-826.
- Beattie, P. D., and Dade, W. B. (1996). Is scaling in turbidite deposition consistent with forcing by earthquakes?. *Journal of Sedimentary Research*, 66(5).
- Benjamin, J.R. and Cornell, C.A. (1970). *Probability, Statistics, and Decision for Civil Engineers*, McGraw Hill, New York, NY
- Benson, M.A. (1968). Uniform flood frequency estimating methods for federal agencies, *Water Resources Research*, v. 4., p. 981-908.
- Berggren, W.A., Kent, D.V., Swisher, C.C., III, and Aubry, M.-P. (1995). A revised Cenozoic geochronology and chronostratigraphy. In Berggren, W.A., Kent, D.V., Aubry, M.-P., and Hardenbol, J. (Eds.), *Geochronology, Time Scales and Global Stratigraphic Correlation*. Special Publication—Society of Economic Paleontology and Mineralogy (Society of Sedimentary Geology), 54:129–212.
- Bernaola, G., Baceta, J. I., Orue-Etxebarria, X., Alegret, L., Martín-Rubio, M., Arostegui, J., and Dinarès-Turell, J. (2007). Evidence of an abrupt environmental disruption during the mid-Paleocene biotic event (Zumaia section, western Pyrenees). *Geological Society of America Bulletin*, 119(7-8), 785-795.
- Biondini, R. (1976). Cloud motion and rainfall statistics. *Journal of Applied Meteorology*, 15(3), 205-224.
- Bobée, B. (1975). The log Pearson type 3 distribution and its application in hydrology. *Water resources research*, 11(5), 681-689.
- Bobée, B., and Rasmussen, P. F. (1995). Recent advances in flood frequency analysis. *Reviews of Geophysics*, doi: 10.1029/95RG00287.
- Bobée, B., Cavadia, G., Ashkar, F., Bernier, J., and Rasmussen, P. (1993). Towards a systematic approach to comparing distributions used in flood frequency analysis, *Journal of Hydrology*, v. 142, p. 121-136.

- Bock, J., Martinerie, P., Witrant, E., and Chappellaz, J. (2012). Atmospheric impacts and ice core imprints of a methane pulse from clathrates. *Earth and Planetary Science Letters*, 349, 98-108.
- Bondevik, S., Løvholt, F., Harbitz, C., Mangerud, J., Dawson, A., and Inge Svendsen, J. (2005). The Storegga Slide tsunami—comparing field observations with numerical simulations. *Marine and Petroleum Geology*, 22(1), 195-208.
- Bonnel, C., Dennielou, B., Droz, L., Mulder, T., and Berné, S. (2005). Architecture and depositional pattern of the Rhône Neofan and recent gravity activity in the Gulf of Lions (western Mediterranean). *Marine and Petroleum Geology*, 22(6), 827-843.
- Bornhold, B. D., and Prior, D. B. (1990). Morphology and sedimentary processes on the subaqueous Noeick River delta, British Columbia, Canada. *International Association of Sedimentologists Special Publication, Coarse-Grained Deltas*, 10, 169-181.
- Bornhold, B. D., Ren, P., and Prior, D. B. (1994). High-frequency turbidity currents in British Columbia fjords. *Geo-Marine Letters*, 14(4), 238-243.
- Bowen, G. J., Beerling, D. J., Koch, P. L., Zachos, J. C., and Quattlebaum, T. (2004). A humid climate state during the Palaeocene/Eocene thermal maximum. *Nature*, 432(7016), 495-499.
- Bralower, T. J., Thomas, D., Zachos, J. et al. (1997). High resolution records of the late Palaeocene Thermal maximum and circum-Caribbean volcanism: is there a causal link? *Geology*, 25, 963-966.
- Brothers, D. S., Luttrell, K. M., and Chaytor, J. D. (2014). Sea-level–induced seismicity and submarine landslide occurrence. *Geology*, 41(9), 979-982.
- Brown, A. R. (1999), Interpretation of three-dimensional seismic data. *American Association of Petroleum Geologists and the Society of Exploration Geophysicists, AAPG Memoir 42, SEG Investigations in Geophysics, No.9.*
- Brucker, S., Hughes Clarke, J. E., Beaudoin, J., Lessels, C., Czotter, K., Loschiavo, R. and Hill, P. (2007). Monitoring flood-related change in bathymetry and sediment distribution over the Squamish Delta, Howe Sound, British Columbia. In *US Hydrogr. Conf.*

- Bruschi, R., Bughi, S., Spinazzè, M., Torselletti, E., and Vitali, L. (2006). Impact of debris flows and turbidly currents on seafloor structures. *Norsk Geologisk Tidsskrift*, 86(3), 317.
- Bryn, P., Berg, K., Forsberg, C. F., Solheim, A., and Kvalstad, T. J. (2005). Explaining the Storegga slide. *Marine and Petroleum Geology*, 22(1), 11-19.
- Butt, A. (1981). Depositional environments of the Upper Cretaceous rocks in the northern part of the Eastern Alps, Special Publication of the Cushman Foundation for Foraminiferal Research, 20 (1981), 1–81
- Camerlenghi, A., Urgeles, R., and Fantoni, L. (2010). A database on submarine landslides of the Mediterranean Sea. In *Submarine mass movements and their consequences* (pp. 503-513). Springer Netherlands.
- Canals, M., Puig, P., de Madron, X. D., Heussner, S., Palanques, A., and Fabres, J. (2006). Flushing submarine canyons. *Nature*, 444(7117), 354-357.
- Cande, S. C., and Kent, D. V. (1995). Revised calibration of the geomagnetic polarity timescale for the Late Cretaceous and Cenozoic. *Journal of Geophysical Research: Solid Earth* (1978–2012), 100(B4), 6093-6095.
- Canudo, J. I., and Molina, E. (1992). Planktic foraminiferal faunal turnover and bio-chronostratigraphy of the Paleocene-Eocene boundary at Zumaya (Northern Spain). *Revista de la Sociedad Geológica de España*, 5(1-2), 145-157.
- Canudo, J., Keller, G., Molina, E., and Ortiz, N. (1995). Planktic foraminiferal turnover and $\delta^{13}\text{C}$ isotopes across the Paleocene-Eocene transition at Caravaca and Zumaya, Spain. *Palaeogeography, Palaeoclimatology, Palaeoecology*, 114(1), 75-100.
- Caplan-Auerbach, J., Dziak, R. P., Bohnenstiehl, D. R., Chadwick, W. W., and Lau, T. K. (2014). Hydroacoustic investigation of submarine landslides at West Mata volcano, Lau Basin. *Geophysical Research Letters*, 41(16), 5927-5934.
- Carlson, J., and Grotzinger, J. P. (2001). Submarine fan environment inferred from turbidite thickness distributions. *Sedimentology*, 48(6), 1331-1351.
- Carter, L., Burnett, D., Drew, S., Marle, G., Hagadorn, L., Bartlett-McNeil, D., and Irvine, N. (2009), *Submarine Cables and the Oceans—Connecting the World*: United Nations

- Environment Programme, World Conservation Monitoring Center (UNEP-WCMC) Biodiversity Series No. 31: Cambridge, UK, United Nations Environment Programme, World Conservation Monitoring Center: http://www.unep-wcmc.org/resources/publications/UNEP_WCMC_bio_series/31.aspx (accessed February 2014).
- Carter, L., Gavey, R., Talling, P., and Liu, J. (2014). Insights into Submarine Geohazards from Breaks in Subsea Telecommunication Cables. *Oceanography*, doi: 10.5670/oceanog.2014.40.
- Carter, L., Milliman, J., Talling, P.J., Gavey, R., and Wynn, R.B. (2012), Near-synchronous and delayed initiation of long run-out submarine sediment flows from a record breaking river flood, offshore Taiwan: *Geophysical Research Letters*, v. 39, L12603, doi:10.1029/2012GL051172.
- Cartigny, M. J., Postma, G., van den Berg, J. H., and Mastbergen, D. R. (2011). A comparative study of sediment waves and cyclic steps based on geometries, internal structures and numerical modelling. *Marine Geology*, doi: 10.1016/j.margeo.2010.11.006.
- Cartigny, M. J., Ventra, D., Postma, G., and Den Berg, J. H. (2014). Morphodynamics and sedimentary structures of bedforms under supercritical-flow conditions: New insights from flume experiments. *Sedimentology*, 61(3), 712-748.
- Cauquil, E. (2009). Geohazard Risk Assessment; Risk Matrix for Nonrecurrent Geohazards: A Tool for Risk Management, Offshore Technology Conference, 4-7 May 2009, Houston, Texas.
- Chadwick, W. W., Dziak, R. P., Haxel, J. H., Embley, R. W. and Matsumoto, H. (2012). Submarine landslide triggered by volcanic eruption recorded by in situ hydrophone. *Geology*, 40(1), 51-54.
- Chen, C., and Hiscott, R. N. (1999). Statistical analysis of facies clustering in submarine-fan turbidite successions. *Journal of Sedimentary Research*, 69(2), 505-517.
- Cheung, Y. K., and Klotz, J. H. (1997). The Mann Whitney Wilcoxon distribution using linked lists. *Statistica Sinica*, 7(3), 805-813.

- Chevron (2014) <http://www.chevron.com/documents/pdf/angolafactsheet.pdf>
- Chillarige, A. V., Morgenstern, N. R., Robertson, P. K., and Christian, H. A. (1997a). Seabed instability due to flow liquefaction in the Fraser River delta. *Canadian Geotechnical Journal*, doi: 10.1139/T97-019.
- Chillarige, A. V., Robertson, P. K., Morgenstern, N. R., and Christian, H. A. (1997b). Evaluation of the in situ state of Fraser River sand. *Canadian Geotechnical Journal*, 34(4), 510-519.
- Christian, H. A., Mosher, D. C., Barrie, J. V., Hunter, J. A., and Luternauer, J. L. (1998). Seabed slope instability on the Fraser River delta. *Bulletin-Geological Survey of Canada*, 217-230.
- Christian, H. A., Mosher, D. C., Mulder, T., Barrie, J. V., and Courtney, R. C. (1997a). Geomorphology and potential slope instability on the Fraser River delta foreslope, Vancouver, British Columbia. *Canadian geotechnical journal*, 34(3), 432-446.
- Christian, H. A., Woeller, D. J., Robertson, P. K., and Courtney, R. C. (1997b). Site investigations to evaluate flow liquefaction slides at Sand Heads, Fraser River delta. *Canadian Geotechnical Journal*, 34(3), 384-397.
- Christiansen, E. A., and Sauer, E. K. (1988). Fire Lake depression: a glacially eroded feature in southwestern Saskatchewan, Canada. *Canadian Journal of Earth Sciences*, 25(12), 2130-2138.
- Chun, C. O., Delaney, M. L., and Zachos, J. C. (2010). Paleoredox changes across the Paleocene-Eocene thermal maximum, Walvis Ridge (ODP Sites 1262, 1263, and 1266): Evidence from Mn and U enrichment factors. *Paleoceanography*, 25(4).
- Clare, M.A., Talling, P.J., Challenor, P., Malgesini, G., and Hunt, J. (2014). Distal turbidites reveal a common distribution for large (> 0.1 km³) submarine landslide recurrence. *Geology*, G35160-1.
- Clare, M.A., Talling, P.J., and Hunt, J. (2015a) "Implications of reduced turbidity current and landslide activity for the Initial Eocene Thermal Maximum – evidence from two deep-water sites" *Earth and Planetary Science Letters*

- Clare, M.A., Talling, P.J., Challenor, P.G. and Hunt, J.E. (2015b) Tempo and triggering of large submarine landslides - Statistical analysis for hazard assessment, Submarine mass movements and their consequences: 7th International Symposium, Wellington, New Zealand. (Advances in Natural and Technological Hazards Research)
- Clare, M.A., Thomas, S., Mansour, M. and Cartigny, M. (2015c) "Turbidity current hazard assessment for field layout planning", Proceedings of the 3rd International Symposium on Frontiers in Offshore Geotechnics.
- Clare, M.A., Cartigny, M.J., North, L.J., Talling, P.J., Vardy, M.E., Hizzett, J.L., Sumner, E.J., Hughes Clarke, J.E., Spinewine, B. and Cooper, C. (2015d) Quantification of Near-bed Dense Layers and Implications for Seafloor Structures: New Insights into the Most Hazardous Aspects of Turbidity Currents, Proceedings of the Offshore Technology Conference, May 2015, Houston, TX, USA
- Clare, M.A., Thomas, S. and Spinewine, B. (2013) "Sediment Density Flow Impact Assessment and Mitigation Studies for Deepwater Developments: A Challenge on Multiple Scales", Proceedings of the Offshore Technology Conference, 6 - 9 May 2013, Houston, TX, USA, <http://dx.doi.org/10.4043/23993-MS>, ISBN 978-62748-339-1
- Cohen, J. (1988). Statistical power analysis for the behavioural sciences (2nd edition). New York: Academic.
- Conway, K. W., Barrie, J. V., Picard, K., and Bornhold, B. D. (2012). Submarine channel evolution: active channels in fjords, British Columbia, Canada. *Geo-Marine Letters*, 32(4), 301-312.
- Cooper, C., Wood, J., and Andrieux, O. (2013). Turbidity Current Measurements in the Congo Canyon. Proceedings of Offshore Technology Conference, 1-4 May 2013, Houston, Texas.
- Corfield, R. M. and Norris, R. D. (1996). Deep water circulation in the Palaeocene ocean. In: Knox, R. W., Corfield, R. M. and Dunay, R. E. (eds) Correlation of the Early Palaeogene in Northwest Europe. Geological Society, London, Special Publications, 101,443-456.
- Corral, A. (2006). Dependence of earthquake recurrence times and independence of magnitudes on seismicity history, *Tectonophysics*, v. 424, p. 177-193.

- Covault, J. A. (2011). Submarine fans and canyon-channel systems: a review of processes, products, and models. *Nature Education Knowledge*, 3(10), 4.
- Covault, J. A., and Graham, S. A. (2010). Submarine fans at all sea-level stands: tectono-morphologic and climatic controls on terrigenous sediment delivery to the deep sea. *Geology*, 38(10), 939-942.
- Covault, J. A., Craddock, W. H., Romans, B. W., Fildani, A., and Gosai, M. (2013). Spatial and temporal variations in landscape evolution: Historic and longer-term sediment flux through global catchments. *The Journal of Geology*, 121(1), 35-56.
- Covault, J. A., Kostic, S., Paull, C. K., Ryan, H. F., and Fildani, A. (2014). Submarine channel initiation, filling and maintenance from sea-floor geomorphology and morphodynamic modelling of cyclic steps. *Sedimentology*, 61(4), 1031-1054.
- Cox, D. R. (1972) Regression models and life-tables. *Journal of the Royal Statistical Society. Series B (Methodological)*, 187-220.
- Croudace, I. W., Rindby, A., and Rothwell, R. G. (2006). ITRAX: description and evaluation of a new multi-function X-ray core scanner. *Special Publication - Geological Society of London*, 267, 51.
- Crow, E.L. and Shimizu, K., Eds. (1988). *Lognormal Distributions, Theory and Applications*, Marcel Dekker, New York, NY.
- Cummings, J. P., and Hodgson, D. M. (2011). Assessing controls on the distribution of ichnotaxa in submarine fan environments, the Basque Basin, northern Spain. *Sedimentary Geology*, 239(3), 162-187.
- Dadson, S., Hovius, N., Pegg, S., Dade, W. B., Horng, M. J., and Chen, H. (2005). Hyperpycnal river flows from an active mountain belt. *Journal of Geophysical Research: Earth Surface* (2003–2012), 110(F4).
- Dahlen, M. Z., Osborne, R. H., and Gorsline, D. S. (1990). Late Quaternary history of the Ventura mainland shelf, California. *Marine Geology*, 94(4), 317-340.
- Dallanave, E., Agnini, C., Muttoni, G., and Rio, D. (2012). Paleocene magneto-biostratigraphy and climate-controlled rock magnetism from the Belluno Basin, Tethys Ocean, Italy. *Palaeogeography, Palaeoclimatology, Palaeoecology*, 337, 130-142.

- Dan-Unterseh, G., Savoye, B., Gaullier, V., Cattaneo, A., Déverchère, J., and Yelles, K. (2011). Algerian margin sedimentation patterns (Algiers area, southwestern mediterranean). *Mass-Transport Deposits in Deepwater Settings*, 69-84.
- Daub, E.G., Ben-Naim, E., Guyer, R.A., and Johnson, P.A., (2012). Are megaquakes clustered?, *Geophysical Research Letters*, v. 39, doi:10.1029/2012GL051465, 2012.
- De Their, T. and Janssens de Bisthoven, D. (2012), Etude de l'impact sur les structures offshore des courants de turbidite et debris-flows sous-marins: conception d'un dispositif experimental et d'un modele numerique. MSc Thesis. Universite catholique de Louvain, Belgium.
- Dempster AP, Laird NM, Rubin B (1977) Maximum likelihood from incomplete data via the EM algorithm. *J.R. Stat. Soc. Series B (Methodological)* 1-38.
- DiBase, D. and Mutti, E. (2002) The 'Proto Adriatic Basin'. In: *Revisiting Turbidites of the Marnoso-arenacea Formation and their Basin-Margin Equivalents: Problems with Classic Models*. 64th EAGE Conference and Exhibition Excursion Guidebook, (Eds E. Mutti, F. Ricci Lucchi and M. Roveri), pp. I-1–I-4, Parma University and ENI-AGIP Division, Parma, Italy.
- Dickens, G. R., O'Neil, J. R., Rea, D. K., and Owen, R. M. (1995). Dissociation of oceanic methane hydrate as a cause of the carbon isotope excursion at the end of the Paleocene. *Paleoceanography*, 10(6), 965-971.
- Dill, R. F. (1964). Sedimentation and erosion in Scripps submarine canyon head. *Papers in Marine Geology*, 23-41.
- Dimer de Oliveira, F. (2012) Can we trust earthquake cluster detection tests, *Geophysical Research Letters*, v. 39, L17305, doi:10.1029/2012GL052130, 2012.
- Dinarès-Turell, J., Baceta, J. I., Bernaola, G., Orue-Etxebarria, X., and Pujalte, V. (2007) Closing the mid-Palaeocene gap: toward a complete astronomically tuned Palaeocene Epoch and Selandian and Thanetian GSSPs at Zumaia (Basque Basin, W Pyrenees), *Earth and Planetary Science Letters*, v. 262(3), p. 450-467.
- Dinarès-Turell, J., Baceta, J. I., Pujalte, V., Orue-Etxebarria, X., and Bernaola, G. (2002), Magnetostratigraphic and cyclostratigraphic calibration of a prospective

- Palaeocene/Eocene stratotype at Zumaia (Basque Basin, northern Spain). *Terra Nova*, v. 14(5), p. 371-378.
- Domzig, A., Yelles, K., Le Roy, C., Déverchère, J., Bouillin, J. P., Bracène, R., and Pauc, H. (2006). Searching for the Africa–Eurasia Miocene boundary offshore western Algeria (MARADJA'03 cruise). *Comptes Rendus Geoscience*, 338(1), 80-91.
- Droxler, A. W., and Schlager, W. (1985). Glacial versus interglacial sedimentation rates and turbidite frequency in the Bahamas. *Geology*, 13(11), 799-802.
- Droz, L., Dos Reis, A. T., Rabineau, M., Berne, S., and Bellaiche, G. (2006). Quaternary turbidite systems on the northern margins of the Balearic Basin (Western Mediterranean): a synthesis. *Geo-Marine Letters*, 26(6), 347-359.
- Ducassou, E., Migeon, S., Mulder, T., Murat, A., Capotondi, L., Bernasconi, S. M., and Mascle, J. (2009). Evolution of the Nile deep-sea turbidite system during the Late Quaternary: influence of climate change on fan sedimentation. *Sedimentology*, 56(7), 2061-2090.
- Dugan, B., and Flemings, P. B. (2000). Overpressure and fluid flow in the New Jersey continental slope: implications for slope failure and cold seeps. *Science*, 289(5477), 288-291.
- Dugan, B., and Sheahan, T. C. (2012). Offshore sediment overpressures of passive margins: Mechanisms, measurement, and models. *Reviews of Geophysics*, 50(3).
- Dunkley-Jones, T., Ridgwell, A., Lunt, D. J., Maslin, M. A., and Schmidt, D. N. K. and Valdes, P.J. (2010) A Palaeogene perspective on climate sensitivity and methane hydrate instability. *Philosophical Transactions of the Royal Society*, 368, 2395-2415.
- Dypvik, H., Riber, L., Burca, F., Rütther, D., Jargvoll, D., Nagy, J., and Jochmann, M. (2011). The Paleocene–Eocene thermal maximum (PETM) in Svalbard—clay mineral and geochemical signals. *Palaeogeography, Palaeoclimatology, Palaeoecology*, 302(3), 156-169.
- Dypvik, H., Riber, L., Burca, F., Rütther, D., Jargvoll, D., Nagy, J., and Jochmann, M. (2011). The Paleocene–Eocene thermal maximum (PETM) in Svalbard—clay mineral

- and geochemical signals. *Palaeogeography, Palaeoclimatology, Palaeoecology*, 302(3), 156-169.
- Earthquakes Canada, GSC, Earthquake Search (On-line Bulletin), <http://earthquakescanada.nrcan.gc.ca/stndon/NEDB-BNDS/bull-eng.php>, Natural Resources Canada, accessed 18/11/14
- Egger, H., Fenner, J., Heilmann-Clausen, C., Rogl, F., Sachsenhofer, R. F., and Schmitz, B. (2003). Paleoproductivity of the northwestern Tethyan margin (Anthering section, Austria) across the Paleocene-Eocene transition. *Special Papers-Geological Society of America*, 133-146.
- Egger, H., Heilmann-Clausen, C., and Schmitz, B. (2009). From shelf to abyss: Record of the Paleocene/Eocene-boundary in the Eastern Alps (Austria). *Geologica Acta*, 7(1-2), 215-227.
- Elmore, R. D., Pilkey, O. H., Cleary, W. J., and Curran, H. A. (1979). Black shell turbidite, Hatteras abyssal plain, western Atlantic ocean. *Geological Society of America Bulletin*, 90(12), 1165-1176.
- El-Robrini, M., Genesseeux, M., and Mauffret, A. (1985). Consequences of the El-Asnam earthquakes: Turbidity currents and slumps on the Algerian margin (Western Mediterranean). *Geo-Marine Letters*, 5(3), 171-176.
- Evans, T.G. (2010) A systematic approach to offshore engineering for multiple-project developments in geohazardous areas. *Proceedings of the Second International Symposium on Frontiers in Offshore Geotechnics*, Perth, Australia, November 2010.
- Favali, P., and Beranzoli, L. (2006). Seafloor observatory science: A review. *Annals of Geophysics*, 49(2-3).
- Field, A, Miles, J, and Field, Z (2012) *Discovering statistics using R*. SAGE Publications Ltd.; London, UK
- Fine, I. V., Rabinovich, A. B., Bornhold, B. D., Thomson, R. E., and Kulikov, E. A. (2005) The Grand Banks landslide-generated tsunami of November 18, 1929: preliminary analysis and numerical modeling. *Marine Geology*, 215(1), 45-57.

- Forel, F.A. (1888). Le ravin sous-lacustre de Rhone dans le lac Lemman. *Bulletin de la Societe Vaudoise des Sciences Naturelles*, 23:85-107
- Fraley, C., Raftery, A.E., Murphy, T.B. and Scrugga, L. (2012). Technical Report No. 597, Dep. Stat. Uni. Washington <https://www.stat.washington.edu/research/reports/2012/tr597.pdf>
- Fredlund, D. G. and Rahardjo, H. (1993). *Soil mechanics for unsaturated soils*. John Wiley and Sons.
- Galeotti, S., Angori, E., Coccioni, R., Ferrari, G., Galbrun, B., Monechi, S. and Turi, B. (2000). Integrated stratigraphy across the Paleocene/Eocene boundary in the Contessa Road section, Gubbio (central Italy). *Bulletin de la Société géologique de France*, 171(3), 355-365.
- Galeotti, S., Angori, E., Coccioni, R., Ferrari, G., Galbrun, B., Monechi, S. and Turi, B. (2000). Integrated stratigraphy across the Paleocene/Eocene boundary in the Contessa Road section, Gubbio (central Italy). *Bulletin de la Société géologique de France*, 171(3), 355-365.
- Gandolfi, G., Paganelli, L. and Zuffa, G.G. (1983) Petrology and dispersal directions in the Marnoso Arenacea Formation (Miocene, northern Apennines). *Journal of Sedimentary Petrology*, 53, 493–507.
- Garcia, M. O. (1996) *Turbidites from slope failure on Hawaiian volcanoes*. Geological Society, London, Special Publications, 110(1), 281-294.
- Garcia, M. O., and Hull, D.M. (1994). Turbidites from giant Hawaiian landslides: results from Ocean Drilling Program site 842. *Geology* 22.2: 159-162.
- Gardiner, C.W. (2003) *Handbook of stochastic methods: for physics, chemistry, and the natural sciences*, Springer Verlag.
- Garziglia, S., Migeon, S., Ducassou, E., Loncke, L., and Mascle, J. (2008). Mass-transport deposits on the Rosetta province (NW Nile deep-sea turbidite system, Egyptian margin): characteristics, distribution, and potential causal processes. *Marine Geology*, 250(3), 180-198.

- Gawenda, P. (1999). Climatic and Tectonic Controls on Turbiditic and Pelagic Sedimentation in the Deep Sea: The Paleocene–Lower Eocene Zumaia Series (Northern Spain). Swiss Federal Institute of Technology, Ph.D. thesis No. 13110, Zurich, 213 pp.
- Gawenda, P. and Winkler, W. (2000). Sedimentary evolution of the early Paleogene deep-water Gulf of Biscay (proto-Atlantic): Climatic and tectonic controls, *GFF*, 122:1, 54-55
- Gawenda, P., Winkler, W., Schmitz, B. and Adatte, (1999), Climate and bioproductivity control on carbonate turbidite sedimentation (Palaeocene to Earliest Eocene, Gulf of Biscay, Zumaia, Spain), *Journal of Sedimentary Research*, v. 69, p. 1253-1261.
- Geist, E. L., Chaytor, J. D., Parsons, T., and ten Brink, U. (2013). Estimation of submarine mass failure probability from a sequence of deposits with age dates. *Geosphere*, 9(2), 287-298.
- Geist, E.L., and Parsons T. (2010). Estimating the Empirical Probability of Submarine Landslide Occurrence, in Mosher, D.C., Shipp, R.C., Moscardelli, L., Chaytor, J.D., Baxter, C.D.P., Lee, H.J. and Urgeles, R., eds., *Submarine Mass Movements and Their Consequences*, *Advances in Natural and Technological Hazards Research*, 28, p. 463-474.
- Genesseeux, M., Mauffret, A., and Pautot, G. (1980). Submarine landslides on the continental-slope near Nice and the breaking of submarine cables in the Ligurian Sea (Western Mediterranean. *Comptes Rendus Hebdomadaires Des Seances De L Academie Des Sciences Serie D*, 290(14), 959-962.
- Giachetti, T., Paris, R., Kelfoun, K., and Pérez-Torrado, F. J. (2011). Numerical modelling of the tsunami triggered by the Güimar debris avalanche, Tenerife (Canary Islands): Comparison with field-based data. *Marine Geology*, 284(1), 189-202.
- Gilbert, G.K. (1885). The topographic features of lake shores U.S. Geol. Surv., Annu. Rep., 5, pp. 75–123
- Giusberti, L., Rio, D., Agnini, C., Backman, J., Fornaciari, E., Tateo, F., and Oddone, M. (2007). Mode and tempo of the Paleocene-Eocene thermal maximum in an expanded section from the Venetian pre-Alps. *Geological Society of America Bulletin*, 119(3-4), 391-412.

- Goldfinger, C., Morey, A.E., Nelson, C.H., Gutierrez-Pastor, J., Johnson, J.E., Karabanov, E., Chaytor, J., and Ericsson, A. (2009). Rupture lengths and temporal history of significant earthquakes on the offshore and north coast segments of the Northern San Andreas Fault based on turbidite stratigraphy, *Earth Planetary Science Letters*, v. 254, p. 9-27.
- Goldfinger, C., Nelson, C. H., and Johnson, J. E. (2003). Holocene earthquake records from the Cascadia subduction zone and northern San Andreas Fault based on precise dating of offshore turbidites. *Annual Review of Earth and Planetary Sciences*, 31(1), 555-577.
- Goldfinger, C. (2011). Submarine paleoseismology based on turbidite records. *Annual Review of Marine Science*, 3, 35-66.
- Goldfinger, C., Patton, J. R., Van Daele, M., Moernaut, J., Nelson, C. H., de Batist, M., and Morey, A. E. (2014). Can turbidites be used to reconstruct a paleoearthquake record for the central Sumatran margin?: Comment. *Geology*, 42(9), e344-e344.
- Gomez, B., Corral, Á., Orpin, A. R., Page, M. J., Pouderoux, H., and Upton, P. (2015). Lake Tutira paleoseismic record confirms random, moderate to major and/or great Hawke's Bay (New Zealand) earthquakes. *Geology*, 43(2), 103-106.
- Got, H. and Aloisi, J. C. (1990). The Holocene sedimentation on the Gulf of Lions margin: a quantitative approach. *Continental Shelf Research*, 10(9), 841-855.
- Gracia, E., Vizcaino, A., Escutia, C., Asioli, A., Rodes, A., Pallas, R. and Goldfinger, C. (2010). Holocene earthquake record offshore Portugal (SW Iberia): testing turbidite paleoseismology in a slow-convergence margin. *Quaternary Science Reviews*, 29(9), 1156-1172.
- Grant, K.M., Rohling, E.J., Ramsey, C.B., Cheng, H., Edwards, R.L., Florindo, F., Heslop, D., Marra, F., Roberts, A.P., Tamislea, M.E. and Williams, F. (2014). Sea-level variability over five glacial cycles. *Nature Communications*, 5, 5076.
- Gräfe, K. U. and Wiedmann, J. (1993). Sequence stratigraphy in the Upper Cretaceous of the Basco-Cantabrian basin (northern Spain). *Geologische Rundschau*, 82(2), 327-361.

- Green, S. B. (1991). How many subjects does it take to do a regression analysis? *Multivariate behavioural research*, 26(3), 499-510.
- Griffiths, G., and Flatt, D. (1987). A self-contained acoustic Doppler current profiler—design and operation. In *Fifth International Conference on Electronics for Ocean Technology*, Heriot-Watt University, Edinburgh (pp. 41-47).
- Grozic, J. L. H. (2010). Interplay between gas hydrates and submarine slope failure. in Mosher, D.C., Shipp, R.C., Moscardelli, L., Chaytor, J.D., Baxter, C.D.P., Lee, H.J. and Urgeles, R., eds., *Submarine Mass Movements and Their Consequences, Advances in Natural and Technological Hazards Research*, 28, p. 463-474.
- Gutenberg, B., and Richter, C. (1954). *Seismicity of the earth and associated phenomena*. Princeton University Press.
- Hack, J. (1957). Submerged river system of Chesapeake Bay. *Geological Society of America Bulletin*, 68(7), 817-830.
- Haflidason, H., Lien, R., Sejrup, H. P., Forsberg, C. F., and Bryn, P. (2005). The dating and morphometry of the Storegga Slide. *Marine and Petroleum Geology*, 22(1), 123-136.
- Haigh, I. D., Wijeratne, E. M. S., MacPherson, L. R., Pattiaratchi, C. B., Mason, M. S., Crompton, R. P., and George, S. (2014). Estimating present day extreme water level exceedance probabilities around the coastline of Australia: tides, extra-tropical storm surges and mean sea level. *Climate Dynamics*, 42(1-2), 121-138.
- Hale, R.P., Nittorouer, C.A., Liu, J.T., Keil, R.G., Ogston, A.S. (2012). Effects of a Major Typhoon on Sediment Accumulation in Fangliao Submarine Canyon, SW Taiwan, *Marine Geology*, doi:10.106/j.margeo.2012.07.008.
- Haq, B. U., Hardenbol, J., and Vail, P. R. (1988) .Mesozoic and Cenozoic chronostratigraphy and cycles of sea-level change. *Sea-level changes: an integrated approach SEPM Spec. Publ*, 42, 72-108.
- Harbitz CB, Løvholt F, Bungum H (2014). Submarine landslide tsunamis: how extreme and how likely? *Nat. Hazards* 72:1341-1374 doi:10.1007/s11069-013-0681-3

- Harbitz, C. B., Løvholt, F., and Bungum, H. (2014). Submarine landslide tsunamis: how extreme and how likely?. *Natural Hazards*, 72(3), 1341-1374.
- Harris, R.J. (1975). *A primer of multivariate statistics*, New York: Academic.
- Hay, A. E. (1982). The effects of submarine channels on mine tailing disposal in Rupert Inlet, BC. In *Marine tailings disposal* (pp. 139-182). Ann Arbor Science Ann Arbor, Michigan.
- Hay, A. E. (1987a). Turbidity currents and submarine channel formation in Rupert Inlet, British Columbia: 1. Surge observations. *Journal of Geophysical Research: Oceans* (1978–2012), 92(C3), 2875-2881.
- Hay, A. E. (1987b). Turbidity currents and submarine channel formation in Rupert Inlet, British Columbia: 2. The roles of continuous and surge-type flow. *Journal of Geophysical Research: Oceans* (1978–2012), 92(C3), 2883-2900.
- Haywood, A. M., Ridgwell, A., Lunt, D. J., Hill, D. J., Pound, M. J., Dowsett, H. J. and Williams, M. (2011). Are there pre-Quaternary geological analogues for a future greenhouse warming? *Philosophical Transactions of the Royal Society A: Mathematical, Physical and Engineering Sciences*, 369(1938), 933-956.
- Heezen, B. C., and Ewing, M. (1955). Orleansville earthquake and turbidity currents. *AAPG Bulletin*, 39(12), 2505-2514.
- Heezen, B. C., and Ewing, W. M. (1952). Turbidity currents and submarine slumps, and the 1929 Grand Banks [Newfoundland] earthquake. *American Journal of Science*, 250(12), 849-873.
- Heezen, B.C., Menzies, R.J., Schneider, E.D., Ewing, W.M., and Granelli, N.C.L. (1964). Congo Submarine Canyon, *Bulletin of the American Association of Petroleum Geologists*, p. 1126-1149.
- Hein, F. J., and Syvitski, J. P. (1992). Sedimentary environments and facies in an arctic basin, Itirbilung Fiord, Baffin Island, Canada. *Sedimentary Geology*, 81(1), 17-45.
- Hengesh, J. V., Wyrwoll, K. H., and Whitney, B. B. (2011). Neotectonic deformation of northwestern Australia and implications for oil and gas development. *Frontiers in offshore geotechnics II*, 203-208.

- Hesse, R. (1974). Long-distance continuity of turbidites: possible evidence for an early Cretaceous trench-abyssal plain in the East Alps. *Geological Society of America Bulletin*, 85, 859–870.
- Hickin, E. J. (1989). Contemporary Squamish River sediment flux to Howe Sound, British Columbia. *Canadian Journal of Earth Sciences*, 26(10), 1953-1963.
- Hill, A.J., Fiske, M., Fish, P.R., Thomas, S. (2011) Deepwater Angola: Geohazard Mitigation. *Proceedings of 2nd International Symposium on Frontiers in Offshore Geotechnics*, Perth, Australia.
- Hill, P. R., Conway, K., Lintern, D. G., Meulé, S., Picard, K., and Barrie, J. V. (2008). Sedimentary processes and sediment dispersal in the southern Strait of Georgia, BC, Canada. *Marine environmental research*, 66, S39-S48.
- Holdaway, G. P., Thorne, P. D., Flatt, D., Jones, S. E., and Prandle, D. (1999). Comparison between ADCP and transmissometer measurements of suspended sediment concentration. *Continental shelf research*, 19(3), 421-441.
- Höntzsch, S., Scheibner, C., Guasti, E., Kuss, J., Marzouk, A. M., and Rasser, M. W. (2011). Increasing restriction of the Egyptian shelf during the Early Eocene?—New insights from a southern Tethyan carbonate platform. *Palaeogeography, Palaeoclimatology, Palaeoecology*, 302(3), 349-366.
- Hoogakker, B.A.A., Rothwell, R.G., Rohling, E.J., Paterne, M., Stow, D.A.V., Herrle, J.O., and Clayton, T. (2004). Variations in terrigenous dilution in western Mediterranean Sea pelagic sediments in response to climate change during the last glacial cycle, *Marine Geology*, v. 211, p. 21-43.
- Hornbach, M. J., Lavier, L. L., and Ruppel, C. D. (2007). Triggering mechanism and tsunamogenic potential of the Cape Fear Slide complex, US Atlantic margin. *Geochemistry, Geophysics, Geosystems*, 8(12).
- Hovius, N., Stark, C. P., Hao-Tsu, C., and Jiun-Chuan, L. (2000). Supply and removal of sediment in a landslide-dominated mountain belt: Central Range, Taiwan. *The Journal of Geology*, 108(1), 73-89.

- Howe, R.W. and Sblendorio-Levy, J. (1998). Calcareous nannofossil biostratigraphy and sediment accumulation of turbidite sequences on the Madeira Abyssal Plain, Sites 950–952. In Weaver, P.P.E., Schmincke, H.-U., Firth, J.V., and Duffield, W. (Eds.), *Proc. ODP, Sci. Results, 157: College Station, TX (Ocean Drilling Program)*, 501–520, doi:10.2973/odp.proc.sr.157.147.1998.
- Hsu, S., Kuo, J., Lo, C., Tsai, C., Doo, W., Ku, C., and Sibuet, J. (2008). Turbidity currents, submarine landslides and 2006 Pingtung earthquake off SW Taiwan. In *AGU Fall Meeting Abstracts (Vol. 1, p. 1229)*.
- Huang, H. Q. (2010). Reformulation of the bed load equation of Meyer-Peter and Müller in light of the linearity theory for alluvial channel flow. *Water Resources Research*, 46(9).
- Hubbard, S. M., Covault, J. A., Fildani, A., and Romans, B. W. (2014). Sediment transfer and deposition in slope channels: Deciphering the record of enigmatic deep-sea processes from outcrop. *Geological Society of America Bulletin*, 126(5-6), 857-871.
- Hughes Clarke, J. E. (1988). The geological record of the 1929 "Grand Banks" earthquake and its relevance to deep-sea clastic sedimentation. Dalhousie University.
- Hughes Clarke, J. E., Brucker, S., Muggah, J., Church, I., Cartwright, D., Kuus, P. and Eisan, B. (2012). The Squamish Prodelta, monitoring active landslides and turbidity currents. Canadian Hydrographic Conference.
- Hughes Clarke, J. E., Marques, C. V., and Pratomo, D. (2013). Imaging active mass wasting on a fjord delta, Squamish, British Columbia. In *Submarine Mass Movements and their Consequences*, V. Springer International Publishing.
- Hughes Clarke, J. E., Marques, C. R. V., and Pratomo, D. (2014). Imaging active mass-wasting and sediment flows on a fjord delta, Squamish, British Columbia. In *Submarine Mass Movements and Their Consequences* (pp. 249-260). Springer International Publishing.
- Hugot, A., Joseph, P., Savoye, B., and Zaleski, S. (2001). New modelling of submarine gravity flows: application to the Nice collapse in 1979. *Comptes Rendus de l'Academie des Sciences-Series IIA-Earth and Planetary Science*, 333(2), 133-139.

- Hühnerbach, V., and Masson, D.G., (2004), Landslides in the North Atlantic and its adjacent seas: An analysis of their morphology, setting and behaviour: *Marine Geology*, v. 213, p. 343–362, doi:10.1016/j.margeo.2004.10.013.
- Hunt, J. E. (2012). Determining the provenance, recurrence, magnitudes and failure mechanisms of submarine landslides from the Moroccan margin and Canary Islands using distal turbidite records (Doctoral dissertation, University of Southampton).
- Hunt, J. E., Wynn, R. B., Talling, P. J., and Masson, D. G. (2013). Frequency and timing of landslide-triggered turbidity currents within the Agadir Basin, offshore NW Africa: Are there associations with climate change, sea level change and slope sedimentation rates?. *Marine Geology*, 346, 274-291.
- Hunt, J.E., Talling, P.J., Clare, M.A., Jarvis, I., Wynn, R.B. (2014) Long-term (17 Ma) turbidite record of the timing and frequency of large flank collapses of the Canary Islands. *Geochemistry, Geophysics, Geosystems*, 15 (8). 3322-3345.
- Hunt, J.E., Wynn, R.B., Masson, D.G. and Talling, P.J., (2010), Comparative development of deepwater turbidite systems along the NE Atlantic margin: variability in depositional facies and potential controls, *Proceedings of the British Sedimentological Research Group Annual General Meeting*.
- Hurst, H.E. (1951). Long term storage capacity of reservoir. *American Society of Civil Engineers*, 116,770–808.
- Hutton, E. W., and Syvitski, J. P. (2004). Advances in the numerical modeling of sediment failure during the development of a continental margin. *Marine Geology*, 203(3), 367-380.
- Ikehara, K., Ashi, J., Machiyama, H., and Shirai, M. (2012). Submarine Slope Response to Earthquake Shaking Within Western Sagami Bay, Central Japan. In *Submarine Mass Movements and Their Consequences* (pp. 539-547). Springer Netherlands.
- Inman, D. L., Nordstrom, C. E., and Flick, R. E. (1976). Currents in submarine canyons: an air-sea-land interaction. *Annual Review of Fluid Mechanics*, 8(1), 275-310.
- Iverson, R. M. (2000). Landslide triggering by rain infiltration. *Water resources research*, 36(7), 1897-1910.

- Iverson, R. M. (2005). Regulation of landslide motion by dilatancy and pore pressure feedback. *Journal of Geophysical Research: Earth Surface* (2003–2012), 110(F2).
- Iverson, R. M. and Vallance, J. W. (2001). New views of granular mass flows. *Geology*, 29(2), 115-118.
- Jallet, L., and Giresse, P. (2005). Construction of the Pyreneo-Languedocian sedimentary ridge and associated sediment waves in the deep western Gulf of Lions (Western Mediterranean). *Marine and petroleum geology*, 22(6), 865-888.
- Jammes, S., Lavier, L., and Manatschal, G. (2010). Extreme crustal thinning in the Bay of Biscay and the Western Pyrenees: From observations to modeling. *Geochemistry, Geophysics, Geosystems*, 11(10).
- Jammes, S., Manatschal, G., Lavier, L., and Masini, E. (2009). Tectonosedimentary evolution related to extreme crustal thinning ahead of a propagating ocean: example of the western Pyrenees. *Tectonics*, 28(4).
- Jarvis, I., and Higgs, N. (1987). Trace-element mobility during early diagenesis in distal turbidites: Late Quaternary of the Madeira Abyssal Plain, N Atlantic, in Weaver, P.P.E., and Thomson, J., eds., *Geology and Geochemistry of Abyssal Plains*, Geological Society [London] Special Publication 31, p. 179-213.
- Jarvis, I., Moreton, J., and Gérard, M., (1998). Chemostratigraphy of Madeira Abyssal Plain Miocene–Pleistocene turbidites, Site 950. In Weaver, P.P.E., Schmincke, H.-U., Firth, J.V., and Duffield, W. (Eds.), *Proc. ODP, Sci. Results*, 157: College Station, TX (Ocean Drilling Program), 535–558. doi:10.2973/odp.proc.sr.157.129.1998
- Jerolmack, D. J., and Paola, C. (2010). Shredding of environmental signals by sediment transport. *Geophysical Research Letters*, 37(19).
- Jobe, Z. R., Lowe, D. R., and Morris, W. R. (2012). Climbing-ripple successions in turbidite systems: depositional environments, sedimentation rates and accumulation times. *Sedimentology*, 59(3), 867-898.
- John, C.M., Karner, G.D., and Mutti, M. (2004). $\delta^{18}\text{O}$ and Marion Plateau backstripping: Combining two approaches to constrain late middle Miocene eustatic amplitude, *Geology*, v. 32, p. 829-832.

- Johns, M. W., Prior, D. B., Bornhold, B. D., Coleman, J. M., and Bryant, W. R. (1986). Geotechnical aspects of a submarine slope failure, Kitimat Fjord, British Columbia. *Marine Georesources and Geotechnology*, 6(3), 243-279.
- Kaiser, M. J., Yu, Y., and Jablonowski, C. J. (2009). Modeling lost production from destroyed platforms in the 2004–2005 Gulf of Mexico hurricane seasons. *Energy*, 34(9), 1156-1171.
- Kaminski, M. A., Gradstein, F. M., and Berggren, W. A. (1989). Paleogene benthic foraminifer biostratigraphy and paleoecology at Site 647, southern Labrador Sea. In *Proceedings of the Ocean Drilling Program: Scientific Results* (Vol. 105, pp. 705-730).
- Kaminski, M. A., Kuhnt, W., and Radley, J. D. (1996). Palaeocene–Eocene deep water agglutinated foraminifera from the Numidian Flysch (Rif, Northern Morocco): Their significance for the palaeoceanography of the Gibraltar gateway. *Journal of Micropalaeontology*, 15(1), 1-19.
- Katz, M. E. and Miller, K. G. (1991). Early Palaeogene benthic foraminiferal assemblages and stable isotopes in the Southern Ocean. *Proceedings of the Ocean Drilling Program. Scientific Results*, 114 481-512.
- Katz, M. E., Cramer, B. S., Mountain, G. S., Katz, S., and Miller, K. G. (2001). Uncorking the bottle: What triggered the Paleocene/Eocene thermal maximum methane release? *Paleoceanography*, 16(6), 549-562.
- Katz, M. E., Pak, D. K., Dickens, G. R., and Miller K. G. (1999). The source and fate of massive carbon input during the latest Paleocene thermal maximum, *Science*, 286, 1531–1533.
- Kennett, J. P. and Stott, L. D. (1990). Proteus and Proto-Oceanus: ancestral Paleogene oceans as revealed from Antarctic stable isotopic results; ODP Leg 113. In *Proceedings of the Ocean Drilling Program Scientific Results* (Vol. 113, pp. 865-880).
- Kennett, J. P., and Stott, L. D. (1991), Abrupt deep-sea warming, palaeoceanographic changes and benthic extinctions at the end of the Palaeocene, *Nature*, 353, 225–229.

- Kennett, J. P., Cannariato, K. G., Hendy, I. L., and Behl, R. J. (2003). Methane hydrates in Quaternary climate change: The clathrate gun hypothesis (Vol. 54, pp. 1-216). American Geophysical Union.
- Kenyon, N. H., Klaucke, I., Millington, J., and Ivanov, M. K. (2002). Sandy submarine canyon-mouth lobes on the western margin of Corsica and Sardinia, Mediterranean Sea. *Marine Geology*, 184(1), 69-84.
- Khripounoff A., Annick, V., Philippe, C., Joel, E. (2009). High frequency of sediment gravity flow events in the Var submarine canyon (Mediterranean Sea). *Marine Geology*, v. 263(1-4), p. 1-6.
- Khripounoff. A., Crassous, P., Lo Bue, N., Dennielouc, B., Silva Jacinto, R. (2012). Different types of sediment gravity flows detected in the Var submarine canyon (northwestern Mediterranean Sea), *Progress in Oceanography*, v. 106., p. 138-153.
- King, P. R., Ilg, B. R., Arnot, M., Browne, G. H., Strachan, L. J., Crundwell, M., and Helle, K. (2011). Outcrop and seismic examples of mass-transport deposits from a late Miocene deep-water succession, Taranaki Basin, New Zealand.
- Klein, D.G. (1984). Relative rates of tectonic uplift as determined from episodic turbidite deposition in marine basins. *Geology*, 12(1), 48-50.
- Kleinbaum, D.G. and Klein M. (2005) *Survival Analysis: A Self-Learning Text*. Statistics in the health sciences. Springer Science and Business Media.
- Koch, A. L. (1966). The logarithm in biology 1. Mechanisms generating the log-normal distribution exactly. *Journal of Theoretical Biology*, 12(2), 276-290.
- Konishi, S., and Kitagawa, G. (2008). Bayesian information criteria. *Information Criteria and Statistical Modeling*, 211-237.
- Korup, O., Clague, J. J., Hermanns, R. L., Hewitt, K., Strom, A. L. and Weidinger, J. T. (2007). Giant landslides, topography, and erosion. *Earth and Planetary Science Letters*, 261(3), 578-589.
- Kramer, S.L. (1988). Triggering liquefaction flow slides in coastal soil deposits, *Engineering Geology*, 26, 17-31.

- Kramer, S.L., and Seed, H. B. (1988). Initiation of soil liquefaction under static loading conditions. *Journal of Geotechnical Engineering*, doi: org/10.1061/(ASCE)0733-9410(1988)114:4(412) .
- Kristoufek, L. (2012). How are rescaled range analyses affected by different memory and distributional properties? A Monte Carlo study. *Physica A: Statistical Mechanics and its Applications*, 391(17), 4252-4260.
- Laberg, J. S., and Camerlenghi, A. (2008). The significance of contourites for submarine slope stability. *Developments in Sedimentology*, 60, 537-556.
- Ladner, B.C., and Wise, S.W., Jr., (2001). Calcareous nannofossil biostratigraphy of Upper Cretaceous to Paleocene sediments from Leg 173, Iberia Abyssal Plain, Sites 1067–1069. In Beslier, M.-O., Whitmarsh, R.B., Wallace, P.J., and Girardeau, J. (Eds.), *Proc. ODP, Scientific Results*, 173, 1–50
- Lambert, A., and Giovanoli, F. (1988). Records of riverborne turbidity currents and indications of slope failures in the Rhone delta of Lake Geneva. *Limnology and Oceanography*, 33(3), 458-468.
- Lastras, G., Canals, M., Urgeles, R., De Batist, M., Calafat, A. M., and Casamor, J. L. (2004). Characterisation of the recent BIG'95 debris flow deposit on the Ebro margin, Western Mediterranean Sea, after a variety of seismic reflection data. *Marine Geology*, 213(1), 235-255.
- Lay, T. (2015). The surge of great earthquakes from 2004 to 2014. *Earth and Planetary Science Letters*, 409, 133-146.
- Lebreiro, S. M., McCave, I. N., and Weaver, P. P. E. (1998). Late Quaternary turbidite emplacement on the Horseshoe abyssal plain (Iberian margin). *Oceanographic Literature Review*, 3(45), 484.
- Lee, H.J. (2009). Timing of occurrence of large submarine landslides on the Atlantic Ocean margin, *Marine Geology*, v. 264, p. 53-64.
- Lee, H.J., Orzech, K., Locat, J., Boulanger, E., Konrad, J.M. (2004). Seismic strengthening, a condition factor influencing submarine landslide development, in:

- Proceedings, 57th Canadian Geotechnical Conference, October 2004, Session 7G, G36240, p. 8–14.
- Leynaud, D., Mienert, J., and Vanneste, M. (2009). Submarine mass movements on glaciated and non-glaciated European continental margins. A review of triggering mechanisms and preconditions to failure. *Marine and Petroleum Geology*, v. 26, p. 618–632.
- Limpert, E., Stahel, W. A., and Abbt, M. (2001). Log-normal Distributions across the Sciences: Keys and Clues. *BioScience*, 51(5), 341-352.
- Liu, J. T., Wang, Y. H., Yang, R. J., Hsu, R. T., Kao, S. J., Lin, H. L., and Kuo, F. H. (2012). Cyclone-induced hyperpycnal turbidity currents in a submarine canyon. *Journal of Geophysical Research: Oceans* (1978–2012), 117(C4).
- Liu, Z., Yoshimura, K., Bowen, G. J., Buening, N. H., Risi, C., Welker, J. M., & Yuan, F. (2014). Paired oxygen isotope records reveal modern North American atmospheric dynamics during the Holocene. *Nature communications*, 5.
- Locat, J., Leroueil, S., Locat, A., and Lee, H. (2014). Weak layers: Their definition and classification from a geotechnical perspective. In *Submarine Mass Movements and Their Consequences* (pp. 3-12). Springer International Publishing.
- Lombardi, A.M. and Marzocchi, W., (2007). Evidence of clustering and nonstationarity in the time distribution of large worldwide earthquakes, *Journal of Geophysical Research*, v. 112, B02303, doi:10.1029/2006JB004568, 2007.
- Longva, O., Janbu, N., Blikra, L. H. and Boe, R. (2003). The Finneidfjord slide: seafloor failure and slide dynamics. In *Submarine mass movements and their consequences* (ed. J. Locat and J. Mienert), pp. 531–538. Dordrecht, Netherlands: Kluwer Academic Publishers
- Luciani, V., Giusberti, L., Agnini, C., Backman, J., Fornaciari, E., and Rio, D. (2007). The Paleocene–Eocene Thermal Maximum as recorded by Tethyan planktonic foraminifera in the Forada section (northern Italy). *Marine Micropaleontology*, 64(3), 189-214.

- MacDiarmid, Preston; Morris, Seymour; et al., (1995), Reliability Toolkit: Commercial Practices Edition, 35–39, Reliability Analysis Center and Rome Laboratory, Rome, New York.
- MacLeod, K. G., Huber, B. T., Berrocoso, Á. J., and Wendler, I. (2013). A stable and hot Turonian without glacial $\delta^{18}\text{O}$ excursions is indicated by exquisitely preserved Tanzanian foraminifera. *Geology*, 41(10), 1083-1086.
- MacLeod, K. G., Londoño, C. I., Martin, E. E., Berrocoso, Á. J., and Basak, C. (2011). Changes in North Atlantic circulation at the end of the Cretaceous greenhouse interval. *Nature Geoscience*, 4(11), 779-782.
- Magurran, A. E., and Magurran, A. E. (1988). Ecological diversity and its measurement (Vol. 168). Princeton: Princeton university press.
- Malgesini, G. (2012). Evolution of submarine sediment density flows deduced from long distance bed correlations, Unpublished PhD Thesis, National Oceanography Centre, Southampton.
- Mandelbrot, B. B. (1967). How long is the coast of Britain. *Science*, 156(3775), 636-638.
- Mandelbrot, B. B., and Van Ness, J. W. (1968). Fractional Brownian motions, fractional noises and applications. *SIAM review*, 10(4), 422-437.
- Marsaglia, K. M., Barragan, J. C. B., Padilla, I., and Milliken, K. L. (1996). Evolution of the Iberian passive margin as reflected in sand provenance. In *Proceedings-Ocean Drilling Program Scientific Results* (pp. 269-280). National Science Foundation.
- Marshall, N. F. (1978). Large storm-induced sediment slump reopens an unknown Scripps submarine canyon tributary. *Sedimentation in Submarine Canyons, Fans, and Trenches*: Stroudsburg, Pennsylvania, Hutchinson and Ross, 73-84.
- Maslin, M., Mikkelsen, N., Vilela, C., and Haq, B. (1998). Sea-level–and gas-hydrate–controlled catastrophic sediment failures of the Amazon Fan. *Geology*, 26(12), 1107-1110.
- Maslin, M., Owen, M., Betts, R., Day, S., Jones, T. D., and Ridgwell, A. (2010). Gas hydrates: past and future geohazard?. *Philosophical Transactions of the Royal Society A: Mathematical, Physical and Engineering Sciences*, 368(1919), 2369-2393.

- Maslin, M., Owen, M., Day, S., and Long, D. (2004), Linking continental-slope failures and climate change: Testing the clathrate gun hypothesis, *Geology*, v. 32, p. 53-56.
- Massey, F. J. (1951). The Kolmogorov-Smirnov test for goodness of fit. *Journal of the American statistical Association*, 46:253, 68-78.
- Masson, D. G., Cartwright, J. A., Pinheiro, L. M., Whitmarsh, R. B., Beslier, M. O., and Roeser, H. (1994). Compressional deformation at the ocean–continent transition in the NE Atlantic. *Journal of the Geological Society*, 151(4), 607-613.
- Masson, D. G., Harbitz, C. B., Wynn, R. B., Pedersen, G., and Løvholt, F. (2006). Submarine landslides: processes, triggers and hazard prediction. *Philosophical Transactions of the Royal Society A: Mathematical, Physical and Engineering Sciences*, 364(1845), 2009-2039.
- Masson, D. G., Watts, A. B., Gee, M. J. R., Urgeles, R., Mitchell, N. C., Le Bas, T. P., and Canals, M. (2002). Slope failures on the flanks of the western Canary Islands. *Earth-Science Reviews*, 57(1), 1-35.
- Masson, D. G., Wynn, R. B., and Talling, P. J. (2010). Large landslides on passive continental margins: processes, hypotheses and outstanding questions. In *Submarine mass movements and their consequences* (pp. 153-165). Springer Netherlands.
- Mastbergen, D. R., and Van Den Berg, J. H. (2003). Breaching in fine sands and the generation of sustained turbidity currents in submarine canyons. *Sedimentology*, doi: 10.1046/j.1365-3091.2003.00554.
- McGonigal, K.L., and Wise, S.W., Jr. (2001). Eocene calcareous nannofossil biostratigraphy and sediment accumulation of turbidite sequences on the Iberia Abyssal Plain, ODP Sites 1067–1069. In Beslier, M.-O., Whitmarsh, R.B., Wallace, P.J., and Girardeau, J. (Eds.), *Proc. ODP, Scientific Results*, 173, 1–35
- McInerney, F. A., and Wing, S. L. (2011). The Paleocene-Eocene thermal maximum: a perturbation of carbon cycle, climate, and biosphere with implications for the future. *Annual Review of Earth and Planetary Sciences*, 39, 489-516.
- McMahon, B. and Feinleib, M. (1960) Breast cancer in relation to nursing and menopausal history. *J Natl Cancer Inst*, 24 (1960),

- Mear, Y. (1984). Séquences et unités sédimentaires du glaciaire rhodanien (Méditerranée occidentale) (Doctoral dissertation).
- Meghraoui, M., Jaegy, R., Lammali, K. and Alberede, F.. (1988). Late Holocene earthquake sequences on the El Asnam (Algeria) thrust fault, *Earth and Planetary Science Letters*, v. 90, p. 187-203.
- Merckelbach, L. M., and Kranenburg, C., (2004). Determining effective stress and permeability equations for soft mud from simple laboratory experiments. *Géotechnique*, 54(9), 581-591.
- Meyer-Peter, E., and Müller, R. (1948). "Formulas for bed-load transport." In *Proceedings of the 2nd Meeting of the International Association for Hydraulic Structures Research* (pp. 39-64). Delft: International Association of Hydraulic Research.
- Michel, A.J., 2011, Random variability explains apparent global clustering of large earthquakes, *Geophysical Research Letters*, v. 38, L21301, doi:10.1029/2011GL049443, 2011.
- Migeon, S., Savoye, B., Zanella, E., Mulder, T., Faugères, J. C., and Weber, O. (2001). Detailed seismic-reflection and sedimentary study of turbidite sediment waves on the Var Sedimentary Ridge (SE France): significance for sediment transport and deposition and for the mechanisms of sediment-wave construction. *Marine and Petroleum Geology*, 18(2), 179-208.
- Mikada, H., Mitsuzawa, K., Matsumoto, H., Watanabe, T., Morita, S., Otsuka, R., and Suyehiro, K. (2006). New discoveries in dynamics of an M8 earthquake-phenomena and their implications from the 2003 Tokachi-oki earthquake using a long term monitoring cabled observatory. *Tectonophysics*, 426(1), 95-105.
- Milkert, D., Weaver, P. P. E., and Liu, L. (1996). Pleistocene and Pliocene Turbidites from the Iberia Abyssal Plain. In *Proceedings of the Ocean Drilling Program: Scientific results* (Vol. 149, p. 281).
- Miller, K. G., Janecek, T. R., Katz, M. E. and Keil, D. J. (1987). Abyssal circulation and benthic foraminiferal changes near the Paleocene/Eocene boundary. *Paleoceanography*, 2(6), 741-761.

- Miller, K. G., Sugarman, P. J., Browning, J. V., Kominz, M. A., Hernández, J. C., Olsson, R. K., and Van Sickel, W. (2003). Late Cretaceous chronology of large, rapid sea-level changes: Glacioeustasy during the greenhouse world. *Geology*, 31(7), 585-588.
- Miller, K. G., Wright, J. D., Katz, M. E., Browning, J. V., Cramer, B. S., Wade, B. S., and Mizintseva, S. F. (2008). A view of Antarctic ice-sheet evolution from sea-level and deep-sea isotope changes during the Late Cretaceous–Cenozoic. *Antarctica: a keystone in a changing world*, 55-70.
- Miller, K.G., Kominz, M.A., Browning, J.V., Wright, J.D., Mountain, G.S., Katz, M.E., Sugarman, P.J., Cramer, B.S., Christie-Blick, N., Pekar, S.F. (2005). The Phanerozoic record of global sea-level change. *Science*, v.312, p. 1293-1298.
- Miller, K.G., Wright, J.D., Fairbanks, R.G. (1991). Unlocking the ice house: Oligocene–Miocene oxygen isotopes, eustasy, and margin erosion, *Journal of Geophysical Research* v. 69, p. 6829–6848.
- Miller, K.G., Wright, J.D., Fairbanks, R.G., (1991). Unlocking the ice house: Oligocene–Miocene oxygen isotopes, eustacy and marginal erosion. *Journal of Geophysical Research*. 96, 6829–6848.
- Milliman, J. D. and Syvitski, J. P. (1992). Geomorphic/tectonic control of sediment discharge to the ocean: the importance of small mountainous rivers. *The Journal of Geology*, 525-544.
- Minisini, D., and Trincardi, F. (2009). Frequent failure of the continental slope: the Gela Basin (Sicily Channel). *Journal of Geophysical Research: Earth Surface* (2003–2012), 114(F3).
- Moernaut, J., (2010). Sublacustrine landslide processes and their paleoseismological significance: Revealing the recurrence rate of giant earthquakes in south-central Chile, PhD thesis, Ghent University, Ghent, Belgium.
- Moernaut, J., Daele, M. V., Heirman, K., Fontijn, K., Strasser, M., Pino, M., and De Batist, M. (2014). Lacustrine turbidites as a tool for quantitative earthquake reconstruction: New evidence for a variable rupture mode in south central Chile. *Journal of Geophysical Research: Solid Earth*, 119(3), 1607-1633.

- Moernaut, J., Van Daele, M., Strasser, M., Clare, M.A., Heirman, K., Viel, M., Cardenas, J., Kilian, R., Ladron de Guevara, B., Pino, M., Urrutia, R., De Batist, M., Lacustrine turbidites produced by surficial slope failure: a mechanism for continuous and sensitive turbidite paleoseismic records, *Marine Geology*, In Review.
- Monecke, K., Anselmetti, F. S., Becker, A., Schnellmann, M., Sturm, M., and Giardini, D. (2006). Earthquake-induced deformation structures in lake deposits: A Late Pleistocene to Holocene paleoseismic record for Central Switzerland. *Eclogae Geologicae Helvetiae*, 99(3), 343-362.
- Montadert, L., de Charpal, O., Roberts, D., Guennoc, P., and Sibuet, J. C. (1979). Northeast Atlantic passive continental margins: rifting and subsidence processes. Deep drilling results in the Atlantic Ocean: continental margins and paleoenvironment, 154-186.
- Moore, J. G., Clague, D. A., Holcomb, R. T., Lipman, P. W., Normark, W. R., and Torresan, M. E. (1989). Prodigious submarine landslides on the Hawaiian Ridge. *Journal of Geophysical Research: Solid Earth* (1978–2012), 94(B12), 17465-17484.
- Morris, S. A., Kenyon, N. H., Limonov, A. F., and Alexander, J. (1998). Downstream changes of large-scale bedforms in turbidites around the Valencia channel mouth, northwest Mediterranean: implications for palaeoflow reconstruction. *Sedimentology*, 45(2), 365-378.
- Mosca, I., Console, R., and D'Addezio, G. (2012). Renewal models of seismic recurrence applied to paleoseismological and historical observations. *Tectonophysics*, 564, 54-67.
- Mulder, T. (2011). Gravity processes and deposits on continental slope, rise and abyssal plains. *Deep-sea sediments: Amsterdam, Elsevier, Developments in Sedimentology*, 63, 25-148.
- Mulder, T. and Syvitski, J. P. (1995). Turbidity currents generated at river mouths during exceptional discharges to the world oceans. *The Journal of Geology*, 285-299.
- Mulder, T., Savoye, B., and Syvitski, J. P. M. (1997a). Numerical modelling of a mid-sized gravity flow: the 1979 Nice turbidity current (dynamics, processes, sediment budget and seafloor impact). *Sedimentology*, 44(2), 305-326.

- Mulder, T., Savoye, B., Syvitsky, J., and Parize, O. (1997b). Hyperpycnal turbidity currents at the head of the Var Canyon? Hydrological data and geological observations. *Oceanologica Acta*, 20(4), 607-626.
- Mulder, T., Syvitski, J. P., and Skene, K. I. (1998). Modeling of erosion and deposition by turbidity currents generated at river mouths. *Journal of Sedimentary Research*, 68(1).
- Mulder, T., Syvitski, J. P., Migeon, S., Faugeres, J. C., and Savoye, B. (2003). Marine hyperpycnal flows: initiation, behavior and related deposits. A review. *Marine and Petroleum Geology*, doi:10.1016/j.marpetgeo.2003.01.003
- Mulder, T., Zaragosi, S., Garlan, T., Mavel, J., Cremer, M., Sottolichio, A., and Schmidt, S. (2012). Present deep-submarine canyons activity in the Bay of Biscay (NE Atlantic). *Marine Geology*, 295, 113-127.
- Mutti, E. (1977). Distinctive thin-bedded turbidite facies and related depositional environments in the Eocene Hecho Group (South-central Pyrenees, Spain). *Sedimentology*, 24(1), 107-131.
- Mutti, E., Seguret, M. and Sgavetti, M. (1988). Sedimentation and deformation in the Tertiary sequences of the southern Pyrenees. In: AAPG Mediterranean Basins Conference, Field Trip 7, September 1988. Special Publication University of Parma, Italy.
- Nash, I. F. J., Burnett, C., and Smith, R. (2014, May). Middle East India Deepwater Pipeline (MEIDP) crossing of the Indus Fan. In Offshore Technology Conference. Offshore Technology Conference.
- Nash, I. F. J., and Roberts, P. M. (2011, January). MEIDP-The Deep Sea Gas Route to India. In Offshore Technology Conference. Offshore Technology Conference.
- Neal, J.E., and Hardenbol, J., (1998), Introduction to the Paleogene, in de Graciansky, P.-C., et al., eds., *Mesozoic and Cenozoic sequence stratigraphy of European basins*: SEPM (Society for Sedimentary Geology) Special Publication 60, p. 87–90
- Nelder, J.A. and Wedderburn, R.W.M. (1972), Generalized Linear Models, *Journal of the Royal Statistical Society Series A*, 135, 370-384.

- Nicholls, J. (2010). Survey assesses geohazards for record subsea pipeline. *Offshore*, 71(1).
- Nielsen, T. M., and Kelly, D. C. (2008). Planktic foraminiferal assemblage variations associated with the Paleocene-Eocene thermal maximum: high latitude ODP Site 689 (Maud Rise, Weddell Sea). *Marine Micropaleontology*.
- Nisbet, E. G., and Piper, D. J. (1998). Giant submarine landslides. *Nature*, 392 (6674), 329-330.
- Nishiura, H. (2007). Early efforts in modeling the incubation period of infectious diseases with an acute course of illness. *Emerging themes in epidemiology*, 4(2), 1-12.
- NOAA (2015). <http://www.ncdc.noaa.gov/sotc/global/2014/8>
- Norman, D. (1997). The Statoil deepwater pipeline repair system. *Proceedings, Underwater Technology International '97: Remote Intervention*, Aberdeen, UK, 75-102.
- Normark, W.R. and Piper, D.J.W. (1991). Initiation processes and flow evolution of turbidity currents: implications for the depositional record. In: *From Shoreline to Abyss: Contributions in Marine Geology in Honor of Francis Parker Shepard* (Ed. by R.H. Osborne), Spec. Publ. Soc. Econ. Paleontol. Mineral., 46, 207-230.
- Norris, R. D., Klaus, A., and Kroon, D. (2001). Mid-Eocene deep water, the late Palaeocene thermal maximum and continental slope mass wasting during the Cretaceous-Palaeogene impact. *Geological Society, London, Special Publications*, 183(1), 23-48.
- O'Connell, S., Ryan, W. B. F., and Normark, W. R. (1987). Modes of development of slope canyons and their relation to channel and levee features on the Ebro sediment apron, off-shore northeastern Spain. *Marine and petroleum geology*, 4(4), 308-319.
- Okal, E. A. (2003). T waves from the 1998 Papua New Guinea earthquake and its aftershocks: Timing the tsunamigenic slump. In *Landslide Tsunamis: Recent Findings and Research Directions* (pp. 1843-1863). Birkhäuser Basel.
- O'Leary, D. W. (1991). Structure and morphology of submarine slab slides: clues to origin and behavior. *Marine Georesources and Geotechnology*, 10(1-2), 53-69.

- Orue-Etxebarria, X., Bernaola, G., Baceta, J. I., Angori, E., Caballero, F., Monechi, S and Payros, A. (2004). New constraints on the evolution of planktic foraminifers and calcareous nannofossils across the Palaeocene-Eocene boundary interval: The Zumaia section revisited. *Neues Jahrbuch für Geologie und Paläontologie-Abhandlungen*, 234(1-3), 223-260.
- Owen, M., Day, S., and Maslin, M., (2007), Late Pleistocene submarine mass movements: occurrence and causes: *Quaternary Science Reviews*, v. 26, p. 958-978.
- Pak, D. K., and Miller, K. G. (1992). Paleocene to Eocene benthic foraminiferal isotopes and assemblages: Implications for deepwater circulation. *Paleoceanography*, 7(4), 405-422.
- Palanques, A., de Madron, X. D., Puig, P., Fabres, J., Guillén, J., Calafat, A., and Bonnin, J. (2006). Suspended sediment fluxes and transport processes in the Gulf of Lions submarine canyons. The role of storms and dense water cascading. *Marine Geology*, 234(1), 43-61.
- Pardo, A., Keller, G., Molina, E., and Canudo, J. (1997). Planktic foraminiferal turnover across the Paleocene-Eocene transition at DSDP Site 401, Bay of Biscay, North Atlantic. *Marine Micropaleontology*, 29(2), 129-158.
- Parker, E.J., Traverso, C.M., and Giudice, T.D., Evans, T., and Moore, R., (2009). Geohazard Risk Assessment - Vulnerability of Subsea Structures to Geohazards - Risk Implications, *Proceedings of the Offshore Technology Conference*, 4-7 May 2009, Houston, Texas.
- Parker, G. (2004). 1D Sediment transport morphodynamics with applications to rivers and turbidity currents, http://hydrolab.illinois.edu/people/parkerg/morphodynamics_e-book.htm
- Parsons, J. D., Bush, J. W., and Syvitski, J. P. (2001). Hyperpycnal plume formation from riverine outflows with small sediment concentrations. *Sedimentology*, 48(2), 465-478.
- Parzen, E., (1962). On estimation of a probability density function and mode. *The annals of mathematical statistics*, 33(3), 1065-1076.

- Paull, C. K., McGann, M., Sumner, E. J., Barnes, P. M., Lundsten, E. M., Anderson, K., Gwiazda, R., Edwards, B., and Caress, D. W. (2014). Sub-decadal turbidite frequency during the early Holocene: Eel Fan, offshore northern California. *Geology*, G35768-1.
- Paull, C. K., Schlining, B., Ussler III, W., Lundste, E., Barry, J. P., Caress, D. W., and McGann, M. (2010). Submarine mass transport within Monterey Canyon: Benthic disturbance controls on the distribution of chemosynthetic biological communities. In *Submarine mass movements and their consequences* (pp. 229-246). Springer Netherlands.
- Payros, A., and Martínez-Braceras, N. (2014). Orbital forcing in turbidite accumulation during the Eocene greenhouse interval. *Sedimentology*, 61(5), 1411-1432.
- Peduzzi, P., Concato, J., Feinstein, A. R., and Holford, T. R. (1995). Importance of events per independent variable in proportional hazards regression analysis II. Accuracy and precision of regression estimates. *Journal of Clinical Epidemiology*, doi:10.1016/0895-4356(95)00048-8.
- Pilkey, O. H. (1988). Basin plains; giant sedimentation events. *Geological Society of America Special Papers*, 229, 93-100.
- Pinel, V., Jaupart, C., and Albino, F. (2010). On the relationship between cycles of eruptive activity and growth of a volcanic edifice. *Journal of Volcanology and Geothermal Research*, 194(4), 150-164.
- Pinheiro, L.M., Wilson, R.C.L., Pena dos Reis, R., Whitmarsh, R.B., and Ribeiro, A. (1996). The western Iberia Margin: a geophysical and geological overview. In Whitmarsh, R.B., Sawyer, D.S., Klaus, A., and Masson, D.G. (Eds.), *Proc. ODP, Sci. Results*, 149: College Station, TX (Ocean Drilling Program), 3-23.
- Piper, D. J., and Normark, W. R. (2009). Processes that initiate turbidity currents and their influence on turbidites: a marine geology perspective. *Journal of Sedimentary Research*, 79(6), 347-362.
- Piper, D. J., and Savoye, B. (1993). Processes of late Quaternary turbidity current flow and deposition on the Var deep-sea fan, north-west Mediterranean Sea. *Sedimentology*, 40(3), 557-582.

- Piper, D. J., Cochonat, P., and Morrison, M. L. (1999). The sequence of events around the epicentre of the 1929 Grand Banks earthquake: initiation of debris flows and turbidity current inferred from sidescan sonar. *Sedimentology*, 46(1), 79-97.
- Piper, D. J., Shor, A. N., and Clarke, J. E. H. (1988). The 1929 “Grand Banks” earthquake, slump, and turbidity current. *Geological Society of America Special Papers*, 229, 77-92.
- Piper, D. J., Shor, A. N., Farre, J. A., O'Connell, S., and Jacobi, R. (1985). Sediment slides and turbidity currents on the Laurentian Fan: Sidescan sonar investigations near the epicenter of the 1929 Grand Banks earthquake. *Geology*, 13(8), 538-541.
- Polonia, A., Panieri, G., Gasperini, L., Gasparotto, G., Bellucci, L. G., and Torelli, L. (2013). Turbidite paleoseismology in the Calabrian Arc subduction complex (Ionian Sea). *Geochemistry, Geophysics, Geosystems*, 14(1), 112-140.
- Postma, G., Nemec, W., and Kleinspehn, K. L. (1988). Large floating clasts in turbidites: a mechanism for their emplacement. *Sedimentary Geology*, 58(1), 47-61.
- Pouderoux, H., Lamarche, G., and Proust, J. N. (2012). Building an 18 000-year-long paleo-earthquake record from detailed deep-sea turbidite characterisation in Poverty Bay, New Zealand. *Natural Hazards in Earth Systems Science*, 12, 2077-2101.
- Preston, F. W. (1948). The commonness, and rarity, of species. *Ecology*, 29(3), 254-283.
- Preston, F. W. (1962). The canonical distribution of commonness and rarity: Part II. *Ecology*, 410-432.
- Prior, D. B., and Bornhold, B. D. (1990). The underwater development of Holocene fan deltas. *Coarse-Grained Deltas*, 75-90.
- Prior, D. B., Bornhold, B. D., Wiseman, W. J., and Lowe, D. R. (1987). Turbidity current activity in a British Columbia fjord. *Science*, 237(4820), 1330-1333.
- Prior, D. B., Bornhold, B. D., Coleman, J. M., and Bryant, W. R. (1982a). Morphology of a submarine slide, Kitimat arm, British Columbia. *Geology*, doi: 10.1130/0091-7613(1982).

- Prior, D. B., Coleman, J. M., and Bornhold, B. D. (1982b). Results of a known seafloor instability event. *Geo-Marine Letters*, 2(3-4), 117-122.
- Puidgefabregas, C., Munoz, J.A., and Marxo, M. (1986). Thrust belt development in the eastern Pyrenees and related depositional sequences in the southern foreland basin. In: Allen, P.A. and Homewood, P. (Eds) *Foreland Basins*, Special Publication International Association of Sedimentologists, 8, 229-246.
- Puig, P., Canals, M., Company, J. B., Martín, J., Amblas, D., Lastras, G., and Calafat, A. M. (2012). Ploughing the deep sea floor. *Nature*, 489(7415), 286-289.
- Rabineau, M., Berné, S., Aslanian, D., Olivet, J. L., Joseph, P., Guillocheau, F., and Granjeon, D. (2005). Sedimentary sequences in the Gulf of Lion: a record of 100,000 years climatic cycles. *Marine and Petroleum Geology*, 22(6), 775-804.
- Ramberg, J.S., Dudewicz, E.J., Tadikamalla P.R. and Mykytka, E.F. (1979). A Probability Distribution and its Uses in Fitting Data, *Technometrics*, 21, 201-214.
- Rapp, R. H. (1989). The decay of the spectrum of the gravitational potential and the topography for the Earth. *Geophysical Journal International*, 99(3), 449-455.
- Ratzov, G., Cattaneo, A., Babonneau, N., Déverchère, J., Yelles, K., Bracene, R., and Courboux, F. (2015). Holocene turbidites record earthquake supercycles at a slow-rate plate boundary. *Geology*, 43(4), 331-334.
- Rebello, A., and Ayers, R. (2006). DW RUPE: A Low-Capex Deepwater Pipeline Repair System for the Gulf of Mexico. In *Offshore Technology Conference*. Offshore Technology Conference.
- Reeder, M. S., Rothwell, R. G., and Stow, D. A. (2000). Influence of sea level and basin physiography on emplacement of the late Pleistocene Herodotus Basin Megaturbidite, SE Mediterranean Sea. *Marine and Petroleum Geology*, 17(2), 199-218.
- Ricci Lucchi, F. (1978) Turbidite dispersal in a Miocene deepsea plain: the Marnoso-arenacea of the northern Apennines. *Geol. Mijnbouw*, 57, 559–576.
- Ricci Lucchi, F. (1995) Contessa and associated megaturbidites: long distance (120–25 km) correlation of individual beds in a Miocene foredeep. In: *Atlas of Deep-Water Environments: Architectural Style in Turbidite Systems* (Eds K.T. Pickering, R.N.

- Hiscott, N.H. Kenyon, F. Ricci Lucchi and R.D.A. Smith), pp. 300–302. Chapman and Hall, London.
- Ricci Lucchi, F., and Valmori, E. (1980). Basin-wide turbidites in a Miocene, over-supplied deep-sea plain: a geometrical analysis, *Sedimentology*, v. 27, p. 241-270.
- Roest, W. R., and Srivastava, S. P. (1991). Kinematics of the plate boundaries between Eurasia, Iberia, and Africa in the North Atlantic from the Late Cretaceous to the present. *Geology*, 19(6), 613-616.
- Röhl, U., Westerhold, T., Bralower, T. J., and Zachos, J. C. (2007). On the duration of the Paleocene-Eocene thermal maximum (PETM). *Geochemistry, Geophysics, Geosystems*, 8(12).
- Rohling, E. J., Grant, K., Bolshaw, M., Roberts, A. P., Siddall, M., Hemleben, C., and Kucera, M. (2009). Antarctic temperature and global sea level closely coupled over the past five glacial cycles. *Nature Geoscience*, 2(7), 500-504.
- Romans, B. W., Normark, W. R., McGann, M. M., Covault, J. A., and Graham, S. A. (2009). Coarse-grained sediment delivery and distribution in the Holocene Santa Monica Basin, California: Implications for evaluating source-to-sink flux at millennial time scales. *Geological Society of America Bulletin*, 121(9-10), 1394-1408.
- Rood, K.M and Hickin, E.J. (1989), Suspended sediment concentration and calibre in relation to surface-flow structure in Squamish River estuary, southwestern British Columbia, *Canadian Journal of Earth Science*, 26, 2172-2176.
- Rosenbaum, G., Lister, G. S., and Duboz, C. (2002). Relative motions of Africa, Iberia and Europe during Alpine orogeny. *Tectonophysics*, 359(1), 117-129.
- Rothman, D. H., Grotzinger, J. P., and Flemings, P. (1994). Scaling in turbidite deposition. *Journal of Sedimentary Research*, 64(1).
- Rothwell, R. G., Pearce, T. J., and Weaver, P. P. E. (1992). Late Quaternary evolution of the Madeira Abyssal Plain, Canary Basin, NE Atlantic. *Basin Research*, 4(2), 103-131.
- Rothwell, R.G., Hoogakker, B., Thomson, J., Croudace, I.W., and Frenz, M. (2004). Turbidite emplacement on the southern Balearic Abyssal Plain (western Mediterranean Sea) during Marine Isotope Stages 1–3: an application of ITRAX XRF scanning of

- sediment cores to lithostratigraphic analysis, in, Rothwell, R.G., ed., 2006, *New Techniques in Sediment Core Analysis*, Geological Society, London, Special Publications, no. 267, p. 79-98.
- Rothwell, R.G., Thomson, J. and Kahler, G. (1998). Low-sea-level emplacement of a very large Late Pleistocene 'megaturbidite' in the western Mediterranean Sea, *Nature*, 392, 377-380.
- Ruiz-Ortiz, P. A., de Gea, G. A., and Castro, J. M. (2006). Timing of canyon-fed turbidite deposition in a rifted basin: The Early Cretaceous turbidite complex of the Cerrajón Formation (Subbetic, Southern Spain). *Sedimentary Geology*, 192(3), 141-166.
- SAGE, (2010). Deepwater Pipeline Energy Corridor from the Gulf region to India, Petrotech New Delhi, November 3rd 2010.
- Sangal, B. P., and Biswas, A. K. (1970). The 3-Parameter Lognormal Distribution and Its Applications in Hydrology. *Water Resources Research*, 62, 505-515.
- Sayles, R. S., and Thomas, T. R. (1978). Surface topography as a nonstationary random process.
- Schmitz, B., and Pujalte, V. (2003). Sea-level, humidity, and land-erosion records across the initial Eocene thermal maximum from a continental-marine transect in northern Spain. *Geology*, 31(8), 689-692.
- Schmitz, B., Asaro, F., Molina, E., Monechi, S., von Salis, K., and Speijer, R. P. (1997). High-resolution iridium, $\delta^{13}\text{C}$, $\delta^{18}\text{O}$, foraminifera and nannofossil profiles across the latest Paleocene benthic extinction event at Zumaya, Spain. *Palaeogeography, Palaeoclimatology, Palaeoecology*, 133(1), 49-68.
- Schmitz, B., Asaro, F., Molina, E., Monechi, S., von Salis, K., and Speijer, R. P. (1997). High-resolution iridium, $\delta^{13}\text{C}$, $\delta^{18}\text{O}$, foraminifera and nannofossil profiles across the latest Paleocene benthic extinction event at Zumaya, Spain, *Palaeogeography, Palaeoclimatology, Palaeoecology*, 133(1), 49-68.
- Schmitz, B., Pujalte, V., and Nunez-Betelu, K. (2001). Climate and sea-level perturbations during the incipient Eocene thermal maximum: Evidence from siliciclastic

- units in the Basque Basin (Ermua, Zumaia and Trabakua Pass), northern Spain. *Palaeogeography, Palaeoclimatology, Palaeoecology*, 165(3), 299-320.
- Scholz, C. H., and Cowie, P. A. (1990). Determination of total strain from faulting using slip measurements.
- Searle, R.C. (1987). Regional setting and geophysical characterization of the Great Meteor East area in the Madeira Abyssal Plain. In: P.P.E. Weaver and J. Thomson (Editors), *Geology and Geochemistry of Abyssal Plains*. Geological Society of London Special Publication, 31: 49-70.
- Sgroi, T., Monna, S., Embriaco, D., Giovanetti, G., Marinaro, G., and Favali, P. (2014). Geohazards in the Western Ionian Sea. *Oceanography*, 27(2), 154.
- Shepard, F. P., McLoughlin, P. A., Marshall, N. F., and Sullivan, G. G. (1977). Current-meter recordings of low-speed turbidity currents. *Geology*, 5(5), 297-301.
- Shepard, F.P., Dill, R.F. (1966). *Submarine Canyons and Other Sea Valleys*. Rand McNally and Company, U.S.A., 381 pp."
- Sheskin, D. J. (2003). *Handbook of parametric and nonparametric statistical procedures*. CRC Press.
- Shipp, R. C., and Lu, H. (2011). Impact of a large mass-transport deposit on a field development in the upper slope of southwestern Sabah, Malaysia, offshore northwest Borneo. In *Mass-transport Deposits in Deepwater Settings* (Vol. 96, pp. 199-220).
- Singer, B. S., Jicha, B. R., Harper, M. A., Naranjo, J. A., Lara, L. E., and Moreno-Roa, H. (2008). Eruptive history, geochronology, and magmatic evolution of the Puyehue-Cordón Caulle volcanic complex, Chile. *Geological Society of America Bulletin*, 120(5-6), 599-618.
- Skogdalen, J. E., and Vinnem, J. E. (2012). Quantitative risk analysis of oil and gas drilling, using Deepwater Horizon as case study. *Reliability Engineering and System Safety*, 100, 58-66.
- Sluijs, A., Brinkhuis, H., Crouch, E. M., John, C. M., Handley, L., Munsterman, D. and Dickens, G. R. (2008). Eustatic variations during the Paleocene-Eocene greenhouse world. *Paleoceanography*, 23(4).

- Smith, C.E. (2013). Worldwide Pipeline Construction: Crude, products plans push 2013 construction sharply higher, <http://www.ogj.com/articles/print/volume-111/issue-02/special-report--worldwide-pipeline-construction/worldwidepipeline-construction-crude-products.html>
- Smith, T., Smith, B, Ryan and Ryan, M.A.K. (2003). Survival analysis using Cox Proportional Hazards Modelling for single and multiple event time data, Statistics and Data Analysis, SAS Users Group International Proceedings 2003.
- Snedecor, G. W. and Cochran, W. G. (1989). Statistical Methods, Eighth Edition, Iowa State University Press.
- Sonoyama, T., Wang, F., Honda, M., and Kuwada, Y. (2013). Experimental Study on the Influence of Cable Diameters on the Impact Forces Caused by Submarine Landslide. In Progress of Geo-Disaster Mitigation Technology in Asia (pp. 491-501). Springer Berlin Heidelberg."
- Sornette, A., and Sornette, D. (1989). Self-organized criticality and earthquakes. *Europhysics Letters*, 9(3), 197.
- Sornette, D. (1991). Self-organized criticality in plate tectonics. In Spontaneous formation of space-time structures and criticality (pp. 57-106). Springer Netherlands.
- Sowers, T. (2006). Late Quaternary atmospheric CH₄ isotope record suggests marine clathrates are stable. *Science*, 311(5762), 838-840.
- Speijer, R. P., and Morsi, A. M. M. (2002). Ostracode turnover and sea-level changes associated with the Paleocene-Eocene thermal maximum. *Geology*, 30(1), 23-26.
- Speijer, R. P., and Schmitz, B. (1998). A benthic foraminiferal record of Paleocene sea level and trophic/redox conditions at Gebel Aweina, Egypt. *Palaeogeography, Palaeoclimatology, Palaeoecology*, 137(1), 79-101.
- Speijer, R.P., Van der Zwaan, G.J., and Schmitz, B. (1996). The impact of Paleocene/Eocene boundary events on middle neritic benthic foraminiferal assemblages from Egypt. *Marine Micropaleontology*, 28(2), 99-132.
- Spinewine, B., Renzonnet, D., Clare, M., Capart, H., De Thier, T., and Dan-Unterseh, G. (2013). Numerical Modelling of Runout and Velocity for Slide-Induced Submarine

- Density Flows: A Building Block of an Integrated Geohazards Assessment for Deepwater Developments. In 2013 Offshore Technology Conference.
- Stevenson, C. J., Talling, P. J., Sumner, E. J., Masson, D. G., Frenz, M., and Wynn, R. B. (2014). On how thin submarine flows transported large volumes of sand for hundreds of kilometres across a flat basin plain without eroding the sea floor. *Sedimentology*, 61(7), 1982-2019.
- Stigall, J., and Dugan, B. (2010). Overpressure and earthquake initiated slope failure in the Ursa region, northern Gulf of Mexico. *Journal of Geophysical Research: Solid Earth* (1978–2012), 115(B4).
- Storme, J. Y., Devleeschouwer, X., Schnyder, J., Cambier, G., Baceta, J. I., Pujalte, V., and Yans, J., (2012), The Palaeocene/Eocene boundary section at Zumaia (Basque-Cantabric Basin) revisited: new insights from high-resolution magnetic susceptibility and carbon isotope chemostratigraphy on organic matter ($\delta^{13}\text{C}_{\text{org}}$). *Terra Nova*, v. 24(4), p. 310-317.
- Strasser, M., Anselmetti, F. S., Fäh, D., Giardini, D., and Schnellmann, M. (2006). Magnitudes and source areas of large prehistoric northern Alpine earthquakes revealed by slope failures in lakes. *Geology*, 34(12), 1005-1008.
- Strasser, M., Hilbe, M., Anselmetti, F. S. (2011). Mapping basin-wide subaquatic slope failure susceptibility as a tool to assess regional seismic and tsunami hazards, *Marine Geophysical Research* 32(1–2), 331–347. doi:10.1007/s11001-010-9100-2.
- Stronach, J., Zaremba, L., Wong, M., Neil, L. and McLennan, N. (2006). Wave and current forecast system for the mouth of the Fraser River. Hay and Company Consultants, Vancouver, 15 pp.
- Su, C. C., Tseng, J. Y., Hsu, H. H., Chiang, C. S., Yu, H. S., Lin, S., and Liu, J. T. (2012). Records of submarine natural hazards off SW Taiwan. *Geological Society, London, Special Publications*, 361(1), 41-60.
- Sultan, N., Cochonat, P., Foucher, J. P., Mienert, J., Haflidason, H., and Sejrup, H. P. (2003). Effect of gas hydrates dissociation on seafloor slope stability. In *Submarine Mass Movements and Their Consequences* (pp. 103-111). Springer Netherlands.

- Sumner, E. J., Talling, P. J., Amy, L. A., Wynn, R. B., Stevenson, C. J., and Frenz, M. (2012). Facies architecture of individual basin-plain turbidites: Comparison with existing models and implications for flow processes. *Sedimentology*, 59(6), 1850-1887.
- Sumner, E. J., Talling, P. J., and Amy, L. A. (2009). Deposits of flows transitional between turbidity current and debris flow. *Geology*, 37(11), 991-994.
- Sumner, E.J., Siti, M.I., McNeill, L.C., Talling, P.J., Henstock, T.J., Wynn, R.B., Djajadihardja, Y.S., and Permana, H. (2013). Can turbidites be used to reconstruct a palaeoearthquake record for the central Sumatran margin? *Geology*, doi: 10.1130/G34298.1
- Swan, A. R., and Sandilands, M. (1995). Introduction to geological data analysis. Blackwell science ltd.
- Sylvester, Z., (2007). Turbidite bed thickness distributions: methods and pitfalls of analysis and modelling. *Sedimentology*, 54(4), 847-870.
- Syvitski, J. P. M., and Farrow, G. E. (1989). Fjord sedimentation as an analogue for small. Geological Society, London, Special Publications, 41.
- Tabachnick, B.G. and Fidell, L.S. (2007). Using Multivariate Statistics, Fifth Edition, Boston: Pearson Education, Inc.
- Talling, P.J. (2001). On the frequency distribution of turbidite thickness. *Sedimentology*, 48(6), 1297-1329.
- Talling, P.J. (2014), On the Triggers, Resulting Flow Types and Frequencies of Subaqueous Sediment Density Flows in Different Settings. *Marine Geology*, doi:10.1016/j.margeo.2014.02.006.
- Talling, P. J., Allin, J., Armitage, D. A., Arnott, R. W., Cartigny, M. J., Clare, M. A., et al. (2015). Key future directions for research on turbidity currents and their deposits. *Journal of Sedimentary Research*, 85(2), 153-169.
- Talling, P. J., Amy, L. A., Wynn, R. B., Peakall, J., and Robinson, M. (2004). Beds comprising debrite sandwiched within co-genetic turbidite: origin and widespread occurrence in distal depositional environments. *Sedimentology*, 51(1), 163-194.

- Talling, P. J., Masson, D. G., Sumner, E. J., and Malgesini, G. (2012). Subaqueous sediment density flows: Depositional processes and deposit types. *Sedimentology*, 59(7), 1937-2003.
- Talling, P. J., Paull, C. K., and Piper, D. J. (2013). How are subaqueous sediment density flows triggered, what is their internal structure and how does it evolve? Direct observations from monitoring of active flows. *Earth-Science Reviews*, 125, 244-287.
- Talling, P., Clare, M., Urlaub, M., Pope, E., Hunt, J., and Watt, S. (2014). Large Submarine Landslides on Continental Slopes: Geohazards, Methane Release, and Climate Change. *Oceanography*, 27(2), 32-45.
- Talling P. J., Wynn, R.B., Masson, D.G., Frenz, M., Cronin, B.T., Schiebel, R., Akhmetzhanov, A.M., Dallmeier-Tiessen, S., Benetti, S., Weaver, P.P.E. Georgiopoulou, A., Zühlsdorff, C. and Amy L.A. (2007a). Onset of submarine debris flow deposition far from original giant landslide, *Nature*, v. 450, 541-544.
- Talling, P.J., Amy, L.A. and Wynn, R.B., (2007b), New insights into the evolution of large volume turbidity currents; comparison of turbidite shape and previous modelling results, *Sedimentology*, v. 54, p. 737-769.
- Talling, P.J., Amy, L.A., Wynn, R.B., Blackbourn, G., and Gibson, O., (2007c). Evolution of turbidity currents deduced from extensive thin turbidites: Marnoso Arenacea formation (Miocene), Italian Apennines, *Journal of Sedimentary Research*, v. 77, p. 172-196.
- Tappin, D. R., Watts, P., and Grilli, S. T. (2008). The Papua New Guinea tsunami of 17 July 1998: anatomy of a catastrophic event. *Natural Hazards and Earth System Science*, 8(2), 243-266.
- Tappin, D. R., Watts, P., McMurtry, G. M., Lafoy, Y., and Matsumoto, T. (2001). The Sissano, Papua New Guinea tsunami of July 1998—offshore evidence on the source mechanism. *Marine Geology*, 175(1), 1-23.
- Ten Brink, U. S., Barkan, R., Andrews, B. D., and Chaytor, J. D. (2009). Size distributions and failure initiation of submarine and subaerial landslides. *Earth and Planetary Science Letters*, 287(1), 31-42.

- Terzaghi, K. (1943) Theoretical Soil Mechanics, John Wiley and Sons, New York, 510 p.
- Thinon, I., Fidalgo-González, L., Réhault, J. P. and Olivet, J. L. (2001). Pyrenean deformations in the Bay of Biscay: Comptes Rendus de l'Académie des Sciences, Série IIa, v.332, p.561–568.
- Thomas, S., Hooper, J., and Clare, M. (2010a). Constraining Geohazards to the Past: Impact Assessment of Submarine Mass Movements on Seabed Developments. In Submarine Mass Movements and Their Consequences (pp. 387-398). Springer Netherlands.
- Thomas, S., Bell, L., Ticehurst, K., and Dimmock, P. S. (2010b). An investigation of past mass movement events in the West Nile Delta. *Frontiers in Offshore Geotechnics II*, 239.
- Thomson, J., Nixon, S., Summerhayes, C.P., Rohling, E.J., Schfnfeld, J., Zahn, R., Grootes, P., Abrantes, F., Gaspar, L., Vaqueiro, S. (2000). Enhanced productivity on the Iberian margin during glacial/interglacial transitions revealed by barium and diatoms. *J. Geol. Soc.* 157, 667– 677.
- Thouveny, N., Moreno, E., Delanghe, D., Candon, L., Lancelot, Y., Shackleton, N.J. (2000). Rock magnetic detection of distal ice-rafted debris: clue for the identification of Heinrich layers on the Portuguese margin. *Earth Planetary Science Letters*. 180, 61–75.
- Torfs, H., Mitchener, H., Huysentruyt, H., and Toorman, E. (1996). Settling and consolidation of mud/sand mixtures. *Coastal Engineering*, 29(1), 27-45.
- Tremolada, F., and Bralower, T. J. (2004). Nannofossil assemblage fluctuations during the Paleocene–Eocene thermal maximum at Sites 213 (Indian Ocean) and 401 (North Atlantic Ocean): palaeoceanographic implications. *Marine Micropaleontology*, 52(1), 107-116.
- Tucholke, B. E. (1981). Geologic significance of seismic reflectors in the deep western North Atlantic basin. *Society of Economic Palaeontologists and Mineralogists (SEPM)*, 32. 23-37.

- Tucholke, B. E., and Sibuet, J. C. (2007). Leg 210 synthesis: Tectonic, magmatic, and sedimentary evolution of the Newfoundland-Iberia rift. In *Proceedings of the Ocean Drilling Program, scientific results* (Vol. 210, pp. 1-56).
- Tugend, J., Manatschal, G., and Kuszniir, N. J. (2015). Spatial and temporal evolution of hyperextended rift systems: Implication for the nature, kinematics, and timing of the Iberian-European plate boundary. *Geology*, 43(1), 15-18.
- Urlaub, M., Talling, P. J., and Masson, D. G. (2013). Timing and frequency of large submarine landslides: implications for understanding triggers and future geohazard. *Quaternary Science Reviews*, 72, 63-82.
- Urlaub, M., Talling, P., and Clare, M. (2014). Sea-level-induced seismicity and submarine landslide occurrence: Comment. *Geology*, 42(6).
- Urlaub, M., Zervos, A., Talling, P. J., Masson, D. G. and Clayton, C. I. (2012). How do ~2° slopes fail in areas of slow sedimentation? A sensitivity study on the influence of accumulation rate and permeability on submarine slope stability. In *Submarine Mass Movements and Their Consequences* (pp. 277-287). Springer Netherlands.
- Urquhart, E. (2001). Campanian to Miocene planktonic foraminifers from the Iberia abyssal plain. In *Proceedings of the Ocean Drilling Program, Scientific Results* (Vol. 173).
- Van Daele, M., Moernaut, J., Silversmit, G., Schmidt, S., Fontijn, K., Heirman, K., et al. (2014). The 600 yr eruptive history of Villarrica Volcano (Chile) revealed by annually laminated lake sediments. *Geological Society of America Bulletin*, 126(3-4), 481-498.
- Van Den Berg, J. H., Van Gelder, A., and Mastbergen, D. R. (2002). The importance of breaching as a mechanism of subaqueous slope failure in fine sand. *Sedimentology*, 49(1), 81-95.
- Van Rooij, M. M., Nash, B. A., Rajaraman, S., and Holden, J. G. (2013). A fractal approach to dynamic inference and distribution analysis. *Frontiers in Physiology*, 4.
- Van Weering, T. C., De Stigter, H. C., Boer, W., and De Haas, H. (2002). Recent sediment transport and accumulation on the NW Iberian margin. *Progress in Oceanography*, 52, 349-371.

- Vandorpe, T. P., Van Rooij, D., Stow, D. A., and Henriët, J. P. (2011). Pliocene to Recent shallow-water contourite deposits on the shelf and shelf edge off south-western Mallorca, Spain. *Geo-Marine Letters*, 31(5-6), 391-403.
- Vangriesheim, A., Khripounoff, A., and Crassous, P. (2009). Turbidity events observed in situ along the Congo submarine channel. *Deep Sea Research Part II: Topical Studies in Oceanography*, 56(23), 2208-2222.
- Vanneste, M., Mienert, J., and Bünz, S. (2006). The Hinlopen Slide: a giant, submarine slope failure on the northern Svalbard margin, Arctic Ocean. *Earth and Planetary Science Letters*, 245(1), 373-388.
- Vardy, M. E., L'Heureux, J. S., Vanneste, M., Longva, O., Steiner, A., Forsberg, C. F. and Brendryen, J. (2012). Multidisciplinary investigation of a shallow near-shore landslide, Finneidfjord, Norway. *Near Surface Geophysics*, 10(4), 267-277.
- Vasconcelos, G. L., de Sousa Vieira, M., and Nagel, S. R. (1991). Implications of a conservation law for the distribution of earthquake sizes. *Physical Review A*, 44(12), R7869.
- Vergés, J., Millán, H., Roca, E., Muñoz, J. A., Marzo, M., Cirés, J. and Cloetingh, S. (1995). Eastern Pyrenees and related foreland basins: pre-, syn-and post-collisional crustal-scale cross-sections. *Marine and Petroleum Geology*, 12(8), 903-915.
- Vittinghoff, E., and McCulloch, C. E. (2007). Relaxing the rule of ten events per variable in logistic and Cox regression. *American Journal of Epidemiology*, 165(6), 710
- Völker, D., Scholz, F., and Geersen, J. (2011). Analysis of submarine landsliding in the rupture area of the 27 February 2010 Maule earthquake, Central Chile. *Marine Geology*, 288(1), 79-89.
- Wagreich, M., Egger, H., Gebhardt, H., Mohammed, O., Spötl, C., Koukal, V., and Hobiger, G. (2011). A new expanded record of the Paleocene-Eocene transition in the Gosau Group of Gams (Eastern Alps, Austria). *Annalen des Naturhistorischen Museums in Wien. Serie A für Mineralogie und Petrographie, Geologie und Paläontologie, Anthropologie und Prähistorie*, 35-65.

- Walters, S.J. (2009) What is a Cox model? What is...? Series, Hayward Medical Communications.
- Warrick, J. A., Xu, J., Noble, M. A., and Lee, H. J. (2008). Rapid formation of hyperpycnal sediment gravity currents offshore of a semi-arid California river. *Continental Shelf Research*, 28(8), 991-1009.
- Watts, P. (2004). Probabilistic predictions of landslide tsunamis off Southern California. *Marine Geology*, 203(3), 281-301. 718.
- Watts, P., and Borrero, J. C. (2001). Probability distributions of landslide tsunamis. In *Proceedings of the International Tsunami Symposium* (pp. 697-710).
- Weaver, P.P.E. (1994). Determination of turbidity current erosional characteristics from reworked coccolith assemblages, Canary Basin, north-east Atlantic, *Sedimentology*, v. 41, p. 1025-1038.
- Weaver, P.P.E., (2003). Northwest Africa Continental Margin: history of sediment accumulation, landslide deposits, and hiatuses as revealed by drilling the Madeira Abyssal Plain, *Paleoceanography*, v. 18, p. 1-12.
- Weaver, P. P. E. and Rothwell, R. G. (1987). Sedimentation on the Madeira Abyssal Plain over the last 300 000 years. *Geological Society, London, Special Publications*, 31(1), 71-86.
- Weaver, P. P. E., Rothwell, R. G., Ebbing, J., Gunn, D., and Hunter, P. M. (1992). Correlation, frequency of emplacement and source directions of megaturbidites on the Madeira Abyssal Plain. *Marine Geology*, 109(1), 1-20
- Weaver, P. P. E., Searle, R. C., and Kuijpers, A. (1986). Turbidite deposition and the origin of the Madeira Abyssal Plain. *Geological Society, London, Special Publications*, 21(1), 131-143.
- Weaver, P. P.E., Wynn, R. B., Kenyon, N. H., and Evans, J. (2000). Continental margin sedimentation, with special reference to the north-east Atlantic margin. *Sedimentology*, 47s1, 239-256.
- Weaver, P.P.E., and Kuijpers, A., (1983). Climatic control of turbidite deposition on the Madeira Abyssal Plain, *Nature*, v. 306, p. 360-363.

- Weaver, P.P.E., and Thomson, J., (1993). Calculating erosion by deep-sea turbidity currents during initiation and flow: *Nature*, v. 364, p. 136–138, doi:10.1038/364136a0.
- Westerhold, T., Bickert, T., and Roehl, U. (2005). Middle to late Miocene oxygen isotope stratigraphy of ODP Site 1085 (SE Atlantic); new constraints on Miocene climate variability and sea-level fluctuations. *Palaeogeography, Palaeoclimatology, Palaeoecology*, v. 217, p. 205–222.
- Whitmarsh, R. B., and Sawyer, D. S. (1996). The ocean/continent transition beneath the Iberia Abyssal Plain and continental-rifting to seafloor-spreading processes. In *Proceedings-Ocean Drilling Program Scientific Results* (pp. 713-736). National Science Foundation.
- Whitmarsh, R. B., Beslier, M. O., and Wallace, P. J. (1998). Return to Iberia. In *Proceedings of the Ocean Drilling Program, initial reports* (Vol. 173).
- Wilson, T.C., Lwiza, K.M.M., Allen, G.L. (1997). Oceans 97 MTS/IEEE Conference Proceedings. Held in Halifax, Nova Scotia, Canada, 6-9 October 1997, 120-125.
- Winkler, W., and Gawenda, P., (1999), Distinguishing climatic and tectonic forcing of turbidite sedimentation, and the bearing on turbidite bed scaling: Palaeocene-Eocene of northern Spain. *Journal of the Geological Society*, 156(4), 791-800.
- Wynn, R. B., and Masson, D. G. (2003). Canary Islands landslides and tsunami generation: Can we use turbidite deposits to interpret landslide processes?. In *Submarine Mass Movements and Their Consequences* (pp. 325-332). Springer Netherlands.
- Wynn, R. B., Masson, D. G., Stow, D. A., and Weaver, P. P. (2000). The Northwest African slope apron: a modern analogue for deep-water systems with complex seafloor topography. *Marine and Petroleum Geology*, 17(2), 253-265.
- Wynn, R. B., Talling, P. J., Masson, D. G., Stevenson, C. J., Cronin, B. T., and Le Bas, T. P. (2010). Investigating the timing, processes and deposits of one of the world's largest submarine gravity flows: the 'bed 5 event' off Northwest Africa. In *Submarine Mass Movements and Their Consequences* (pp. 463-474). Springer Netherlands.

- Wynn, R. B., Weaver, P. P., Masson, D. G., and Stow, D. A. (2002). Turbidite depositional architecture across three interconnected deep-water basins on the north-west African margin. *Sedimentology*, 49(4), 669-695.
- Wynn, R.B., Talling, P.J., Masson, D.G., Le Bas, T.P., Cronin, B.T., Stevenson, C.J. (2012). The Influence of Subtle Gradient Changes on Deep-Water Gravity Flows: A Case Study From the Moroccan Turbidite System. In: Prather, B. E., Deptuck, M. E., Mohrig, D. Van Hoorn, B. Wynn, R. B., (eds.) *Application of the Principles of Seismic Geomorphology to Continental-Slope and Base-of-Slope Systems: Case Studies from Seafloor and Near-Seafloor Analogues*. Tulsa, OK, SEPM Society for Sedimentary Geology, 371-383. (SEPM Special Publication, 99).
- Xu, J. P. (2010). Normalized velocity profiles of field-measured turbidity currents. *Geology*, 38(6), 563-566.
- Xu, J.P. (2011). Measuring currents in submarine canyons: Technological and scientific progress in the past 30 years, *Geosphere*, 7, 868–876, doi:10.1130/GES00640.1.
- Xu, J. P., Barry, J. P., and Paull, C. K. (2013). Small-scale turbidity currents in a big submarine canyon. *Geology*, 41(2), 143-146.
- Xu, J. P., Noble, M. A., and Rosenfeld, L. K. (2004). In-situ measurements of velocity structure within turbidity currents. *Geophysical Research Letters*, 31(9).
- Xu, J. P., Sequeiros, O. E., and Noble, M. A. (2014). Sediment concentrations, flow conditions, and downstream evolution of two turbidity currents, Monterey Canyon, USA. *Deep Sea Research Part I: Oceanographic Research Papers*, 89, 11-34.
- Yu, W. S., Lee, H. Y., and Hsu, S. M. (2000). Experiments on deposition behavior of fine sediment in a reservoir. *Journal of Hydraulic Engineering*, 126(12), 912-920.
- Zachos, J., Baldauf, J., & Blum, P. (2002). Ocean Drilling Program Leg 208 Scientific Prospectus Early Cenozoic Extreme Climates: The Walvis Ridge Transect.
- Zachos, J. C., Röhl, U., Schellenberg, S. A., Sluijs, A., Hodell, D. A., Kelly, D. C., Thomas, E., Nicolo, M., Raffi, I., Lourens, L.J., McCarren, H. and Kroon, D. (2005). Rapid acidification of the ocean during the Paleocene-Eocene thermal maximum. *Science*, 308(5728), 1611-1615.

- Zachos, J., Pagani, M., Sloan, L., Thomas, E., and Billups, K. (2001). Trends, rhythms, and aberrations in global climate 65 Ma to present. *Science*, 292(5517), 686-693.
- Zachos, J.C., Kroon, D., Blum, P., et al., (2004). *Proceedings of the Ocean Drilling Program, Initial Reports, 208*: College Station, TX (Ocean Drilling Program). doi:10.2973/odp.proc.ir.208.2004
- Zakeri, A. (2009). Review of the state-of-the-art: drag forces on submarine pipelines and piles caused by landslide or debris flow impact, *Journal of Offshore Mechanics and Arctic Engineering*, American Society of Mechanical Engineers (ASME), v. 131(1):014001-014008, doi:10.1115/1.1115.2957922.
- Zeng, J., Lowe, D. R., Prior, D. B., Wiseman, W. J. and Bornhold, B. D. (1991). Flow properties of turbidity currents in Bute Inlet, British Columbia. *Sedimentology*, doi: 10.1111/j.1365-3091.1991.tb00367.x.
- Zúñiga, D., Garcia-Orellana, J., Calafat, A., Price, N. B., Adate, T., Sanchez-Vidal, A., and Fabres, J. (2007). Late Holocene fine-grained sediments of the Balearic Abyssal Plain, Western Mediterranean Sea. *Marine Geology*, 237(1), 25-36.